FUTURE CLIMATE SCENARIOS: REGIONAL CLIMATE MODELLING AND DATA ANALYSIS

EDITED BY: Xander Wang, Yurui Fan, Shan Zhao, Yulei Xie and Hans Von Storch

PUBLISHED IN: Frontiers in Earth Science, Frontiers in Environmental Science and Frontiers in Ecology and Evolution

frontiers Research Topics

frontiers

ISSN 1664-8714
ISBN 978-2-88974-647-7
DOI 10.3389/978-2-88974-647-7

About Frontiers

Frontiers is more than just an open-access publisher of scholarly articles: it is a pioneering approach to the world of academia, radically improving the way scholarly research is managed. The grand vision of Frontiers is a world where all people have an equal opportunity to seek, share and generate knowledge. Frontiers provides immediate and permanent online open access to all its publications, but this alone is not enough to realize our grand goals.

Frontiers Journal Series

The Frontiers Journal Series is a multi-tier and interdisciplinary set of open-access, online journals, promising a paradigm shift from the current review, selection and dissemination processes in academic publishing. All Frontiers journals are driven by researchers for researchers; therefore, they constitute a service to the scholarly community. At the same time, the Frontiers Journal Series operates on a revolutionary invention, the tiered publishing system, initially addressing specific communities of scholars, and gradually climbing up to broader public understanding, thus serving the interests of the lay society, too.

Dedication to Quality

Each Frontiers article is a landmark of the highest quality, thanks to genuinely collaborative interactions between authors and review editors, who include some of the world's best academicians. Research must be certified by peers before entering a stream of knowledge that may eventually reach the public - and shape society; therefore, Frontiers only applies the most rigorous and unbiased reviews.
Frontiers revolutionizes research publishing by freely delivering the most outstanding research, evaluated with no bias from both the academic and social point of view. By applying the most advanced information technologies, Frontiers is catapulting scholarly publishing into a new generation.

What are Frontiers Research Topics?

Frontiers Research Topics are very popular trademarks of the Frontiers Journals Series: they are collections of at least ten articles, all centered on a particular subject. With their unique mix of varied contributions from Original Research to Review Articles, Frontiers Research Topics unify the most influential researchers, the latest key findings and historical advances in a hot research area! Find out more on how to host your own Frontiers Research Topic or contribute to one as an author by contacting the Frontiers Editorial Office: frontiersin.org/about/contact

FUTURE CLIMATE SCENARIOS: REGIONAL CLIMATE MODELLING AND DATA ANALYSIS

Topic Editors:
Xander Wang, University of Prince Edward Island, Canada
Yurui Fan, Brunel University London, United Kingdom
Shan Zhao, Shandong University, China
Yulei Xie, Guangdong University of Technology, China
Hans Von Storch, Helmholtz Centre for Materials and Coastal Research (HZG), Germany

Citation: Wang, X., Fan, Y., Zhao, S., Xie, Y., Storch, H. V., eds. (2022). Future Climate Scenarios: Regional Climate Modelling and Data Analysis. Lausanne: Frontiers Media SA. doi: 10.3389/978-2-88974-647-7

Table of Contents

frontiers in Environmental Science

EDITORIAL
published: 15 February 2022
doi: 10.3389/fenvs.2022.858153

Editorial: Future Climate Scenarios: Regional Climate Modelling and Data Analysis

Xander Wang[1,2]*, *Yurui Fan*[3], *Shan Zhao*[4], *Yulie Xie*[5] and *Hans Von Storch*[6]

[1]Canadian Centre for Climate Change and Adaptation, University of Prince Edward Island, St. Peter's Bay, PE, Canada, [2]School of Climate Change and Adaptation, University of Prince Edward Island, Charlottetown, PE, Canada, [3]College of Engineering, Design and Physical Sciences, Brunel University London, Uxbridge, United Kingdom, [4]School of Environmental Science and Engineering, Shandong University, Qingdao, China, [5]Institute of Environmental and Ecological Engineering, Guangdong University of Technology, Guangzhou, China, [6]Helmholtz Centre for Materials and Coastal Research (HZG), Geesthacht, Germany

Keywords: regional climate projections, climate change monitoring, hydrological modeling, climate change impacts and adaptation, climate modeling

Editorial on the Research Topic

Future Climate Scenarios: Regional Climate Modelling and Data Analysis

While climate change has become one of the most pressing issues around the world, adapting to it from a long-term perspective is extraordinarily challenging due to the significant spatial variations of climatic changes (e.g., different magnitudes of temperature increases from low- to high-latitude regions, precipitation increases in wet regions versus decreases in dry areas) as well as the wide variety of consequences caused by these changes (e.g., unexpected long-lasting droughts versus more frequent floods) (Giorgi, 2019; Wang et al., 2013). In order to support informed decision making and resilient engineering planning under future climate change, it is extremely important to develop reliable and high-resolution climate scenarios to facilitate the exploration of all possible changes to regional climatology and to quantify the potential climate risks to human society and natural systems (Wang et al., 2014; Wang et al., 2019).

Although global climate models (GCMs) have been widely used to develop future climate scenarios, their outputs are usually too coarse to be suitable for driving impact models which require finer-resolution projections at both spatial and temporal scales (Guo et al., 2018). Besides, there are a wide variety of uncertainties in future climate projections which are caused by different choices of greenhouse gas emissions scenarios, GCMs, physical parameterization schemes, etc. These challenges are among the most urgent issues to be addressed for climate change impact assessment and adaptation studies. High-resolution regional climate models, statistical downscaling, and advanced data analytical techniques are critically important to address these challenges, yet they are not well explored due to the research gaps among climate physicists, climate modellers, climate impacts modellers, and climate data users.

Therefore, this research topic aims to capture recent advances in regional climate modelling and data analysis in support of developing high-resolution climate scenarios and assessing regional climate change impacts. This editorial intends to provide a summary about all the papers collected in this research topic. In this research topic, we have published 22 original research articles authored by 109 researchers. The topics of these articles do span a variety of areas but can be generally grouped into four research areas: regional climate projections, climate change monitoring, hydrological modeling, and climate change impacts and adaptation. Here we endeavor to summarize the 22 published articles according to these four research areas.

Edited and reviewed by:
Hayley Jane Fowler, Newcastle University, United Kingdom

***Correspondence:**
Xander Wang
xxwang@upei.ca
xiuquan.wang@gmail.com

Specialty section:
This article was submitted to Interdisciplinary Climate Studies, a section of the journal Frontiers in Environmental Science

Received: *19 January 2022*
Accepted: *25 January 2022*
Published: *15 February 2022*

Citation:
Wang X, Fan Y, Zhao S, Xie Y and Von Storch H (2022) Editorial: Future Climate Scenarios: Regional Climate Modelling and Data Analysis. Front. Environ. Sci. 10:858153. doi: 10.3389/fenvs.2022.858153

REGIONAL CLIMATE PROJECTIONS

Due to the significant spatial variations of climate change, developing high-resolution climate scenarios is the starting point for climate change impact assessment and adaptation at regional and local scales. This is because the decision makers and local stakeholders need to first understand what would be the expected climate before taking any mitigation and adaptation actions. In this research topic, we collected five research articles related to regional climate projections.

- The paper entitled "Ensemble Temperature and Precipitation Projection for Multi-Factorial Interactive Effects of GCMs and SSPs: Application to China" by Duan et al. evaluate the plausible changes in annual precipitation and mean temperature over China using five GCMs (i.e., CESM2, GFDL-ESM4, IPSL-CM6A-LR, MIROC6, and MRI-ESM2-0) under two Shared Socioeconomic Pathways (SSPs), including SSP2-4.5 and SSP5-8.5. A multi-level factorial analysis approach is then used to help explore and quantify the sources of uncertainty associated with the future climate projections for China.
- The paper entitled "Long-Term Maximum and Minimum Temperature Projections Over Metro Vancouver, Canada" by Tian et al. use a neural-network-based statistical downscaling model to help develop future temperature projections for Metro Vancouver, Canada. The model's performance is validated and demonstrated to be effective in simulating the regional temperature patterns of Metro Vancouver through comparisons between model simulations and observations.
- The paper entitled "Detection, Attribution, and Future Response of Global Soil Moisture in Summer" by Qiao et al. use the CMIP6 global climate scenarios and two global reanalysis datasets (i.e., ERA5 and GLDAS) to help detect, attribute, and project soil moisture variations at global scale. The result suggests that the anthropogenic forcings with consideration of greenhouse gases emissions, aerosols, and land cover and land use change have much large impacts on soil moisture variations than the nature forcing only.
- The paper entitled "Evaluation of the Ability of CMIP6 Global Climate Models to Simulate Precipitation in the Yellow River Basin, China" by Wang et al. apply the rank score method with consideration of eight performance indicators to evaluate the performance of the 19 selected GCMs from CMIP6 in simulating the regional climatology over the Yellow River Basin in China. The evaluation results can be used to help choose the appropriate GCMs for projecting high-resolution regional climate over the study area.
- The paper entitled "A Stepwise-Clustered Simulation Approach for Projecting Future Heat Wave Over Guangdong Province" by Ren et al. employ a stepwise-clustered simulation approach to perform climate downscaling to multiple global climate models under two representative concentration pathways (RCPs), with the purpose of projecting the future changes in heat waves for Guangdong Province, China. Four indicators have been used to evaluate the potential changes in heat waves, including intensity, total intensity, frequency, and the longest duration.

CLIMATE CHANGE MONITORING

Monitoring the long-term climate is fundamentally important for understanding what has occurred with our global and local climates. In addition, historical climate observations are widely used by climate scientists to improve our understanding of the physical and dynamical processes of the Earth's climate system and thus to develop better climate models through model validation and continuous performance improvement. In this research topic, we collected seven research articles related to climate change monitoring.

- The paper entitled "Lidar Observed Optical Properties of Tropical Cirrus Clouds Over Gadanki Region" by Kumar and Venkatramanan use the polarization-diversity ground-based Lidar measurements to help monitor and investigate the optical properties of high-altitude cirrus clouds. The authors demonstrate that the Lidar measurements can be used to study the cloud layer statistics (i.e., altitude variations of optical depth and depolarization ratio) and the seasonal variations in the optical properties of cirrus clouds.
- The paper entitled "Quantitative Estimation on Contribution of Climate Changes and Watershed Characteristic Changes to Decreasing Streamflow in a Typical Basin of Yellow River" by Lv et al. use the observational streamflow and meteorological datasets from 1958 to 2017 to quantify the relative contributions of climate change and the changes in watershed characteristics to streamflow change in the Huangshui River Basin of the Qinghai-Tibetan Plateau, China. The Budyko hypothesis test is used to perform the statistical analysis.
- The paper entitled "Long-Term Spatial and Temporal Variation of Near Surface Air Temperature in Southwest China During 1969–2018" by Zhou and Lu employ an improved ANUSPLIN model to analyze the trends, anomalies, change points, and variations of near surface air temperature for Southwest China. The observational data from 494 weather stations during the period of 1969–2018 are used to support the analysis.
- The paper entitled "Summertime Moisture Sources and Transportation Pathways for China and Associated Atmospheric Circulation Patterns" by Zhang et al. use the Lagrangian particle dispersion model (HYSPLIT) to quantitatively analyze the impacts of major atmospheric moisture sources from Midlatitude Westerly, Siberian-Arctic regions, Okhotsk Sea, Indian Ocean, South China Sea, Pacific Ocean, and China Mainland on the summertime precipitation patterns in China. The ERA-Interim reanalysis

dataset is used to derive the input data needed for the HYSPLIT model, including 6-hourly and monthly geopotential height, horizontal and vertical wind, 2-m temperature, sea surface temperature, evaporation, precipitable water, and precipitation during the period of 1979–2017.

- The paper entitled "Interdecadal Linkage Between the Winter Northern Hemisphere Climate and Arctic Sea Ice of Diverse Location and Seasonality" by He et al. investigate the possible linkage between the mid–high-latitude atmospheric circulation and Arctic sea-ice loss on interdecadal timescales for the period of 1959–2020. The datasets used in this study include the National Centers for Environmental Prediction atmospheric reanalysis data, the monthly sea-ice concentration (SIC) from the Met Office Hadley Center, and the enhanced monthly mean precipitation from the Climate Prediction Center Merged Analysis of Precipitation.
- The paper entitled "Characteristics of Precipitation During Meiyu and Huang-Huai Rainy Seasons in Anhui Province of China" by Zhou et al. use the China's Meiyu monitoring indices to explore the precipitation characteristics of the Anhui Province, China during the Meiyu and Huang-Huai Rainy seasons. The observational climate data from 15 weather stations in the Anhui Province during the period of 1975–2020 were used to conduct the analysis.
- The paper entitled "Change in Extreme Precipitation Over Indochina Under Climate Change From a Lagrangian Perspective of Water Vapor" by Cheng et al. explores how global warming has humidified the atmosphere and increased the occurrence of extreme precipitation events over the Indochina Peninsula during the period of 1951–2015. A variety of climate observational and reanalysis datasets (e.g., the APHRODITE data, the ERA5 global reanalysis, and the NOAA ERSST.v5) are used here to support the analysis.

HYDROLOGICAL MODELING

As the hydrological cycle has been intensified by global warming, the conventional stationary assumption in many existing hydrological and hydraulic projects has been demonstrated to be inappropriate. Therefore, how to develop robust hydrological models to simulate the changing precipitation-streamflow or rainfall-runoff relationships under non-stationarity has become one of the top research priorities towards climate change. In this research topic, we collected five research articles related to hydrological modeling under climate change.

- The paper entitled "A Statistical Hydrological Model for Yangtze River Watershed Based on Stepwise Cluster Analysis" by Wang et al. propose a stepwise cluster analysis hydrological model to simulate the nonlinear and dynamic rainfall-runoff relationship. The developed model has been applied to the Yangtze River Watershed to predict the runoff responses to regional climatic conditions.
- The paper titled "Risk Assessment of Dam-Breach Flood Under Extreme Storm Events" by Lin et al. propose a hydrodynamic modelling approach to perform flood inundation simulations under various dam-breach scenarios caused by extreme rainfall events. A comprehensive case study for the Mountain Island Dam within the Catawba River Watershed of North Carolina, United States has been presented to demonstrate the effectiveness of the proposed approach in assessing the dam-breach flooding risks under extreme storm events.
- The paper entitled "A Bayesian-Model-Averaging Copula Method for Bivariate Hydrologic Correlation Analysis" by Wen et al. incorporate the Bayesian model averaging method and Archimedean Copula techniques into a general modeling framework to help analyze and quantify the correlations between rainfall and runoff. A case study for the Xiangxi River Watershed in China has been introduced to demonstrate the effectiveness of the proposed methodology.
- The paper entitled "Changes in and Modelling of Hydrological Process for a Semi-Arid Catchment in the Context of Human Disturbance" by Liu et al. investigate the applicability of a flood forecasting model (i.e., GR4J) for a semi-arid region under a changing environment. The Zhulong River Catchment in North China is used as a case study to evaluate the performance of GR4J model in simulating the hydrological processes from 1967 to 2015.
- The paper entitled "Water Resources Availability Assessment Through Hydrological Simulation Under Climate Change in Huangshui Watershed of Qinghai-Tibet Plateau" by Fu et al. propose a hydroclimate modeling framework through the integration of the Statistical Downscaling method (SDSM), Generalized Regression Neural Network (GRNN) model, Soil and Water Assessment Tool (SWAT) model, and the improved Tennant method. Through its application for the Huangshui Watershed of the Qinghai-Tibet Plateau in China, the proposed modeling framework is demonstrated to be effective in enhancing the spatial resolution of the predicted meteorological and hydrological parameters under climate change.

CLIMATE CHANGE IMPACTS AND ADAPTATION

Developing sustainable and climate-resilient communities requires a comprehensive understanding of the potential impacts of climate change on various sectors (e.g., agriculture, fisheries, tourism, transportation, energy systems, urban infrastructure, human and animal health, and so on) and a feasibility evaluation for all potential climate adaptation measures. Since climate change is essentially affecting all aspects of our daily life, the research for climate change impacts and adaptation can span many disciplines by nature.

In this research topic, we collected five research articles related to climate change impacts and adaptation.

- The paper entitled "The Effect of Precipitation on Hydropower Generation Capacity: A Perspective of Climate Change" by Wei et al. use the high-resolution precipitation data obtained from statistical climate downscaling to assess the potential changes to the hydropower potential in the Dadu River Basin in China. The results can provide a scientific basis for future water sources management, especially for the planning and operation of the hydropower station in the study area.
- The paper entitled "Facing Water Stress in a Changing Climate: A Case Study of Drought Risk Analysis Under Future Climate Projections in the Xi River Basin, China" by Wang et al. present a case study about drought risk analysis in the Xi River Basin, China under future climate change scenarios. The CMIP5 climate data and the VIC model are used to generate precipitation and runoff data for the drought risk assessment.
- The paper entitled "A Low-Impact Development–Based Multi-Objective Optimization Model for Regional Water Resource Management under Impacts of Climate Change" by Bao et al. propose a mathematical optimization model to help incorporate multiple uncertainties and climate change into a multi-objective decision making framework to support regional water resources management. The model considers a variety of adaptive water allocation alternatives and construction schemes associated with low-impact development to support climate change adaptation in an urban environment.
- The paper entitled "Impact of Climate Change on Water Availability in Water Source Areas of the South-to-North Water Diversion Project in China" by Qiao et al. evaluate the water availability challenges for the mega water project in China—the South-to-North Water Diversion project, in the context of climate change. A grid-based RCCC-WBM model is used here to develop runoff scenarios driven by GCMs, in order to assess the water supply risks under a changing climate.
- The paper entitled "Projecting Hydrological Responses to Climate Change Using CMIP6 Climate Scenarios for the Upper Huai River Basin, China" by Bian et al. investigate how global warming would affect the regional hydrological characteristics of the Upper Huai River Basin, China by using the CMIP6 climate scenarios and the Xinanjiang hydrological model. The results can provide a scientific basis for the local stakeholders and decision makers to develop appropriate flood mitigation and water utilization strategies in the context of climate change.

We hope that the readers will find this research topic interesting and the published papers will stimulate further research advancement towards climate change monitoring, modeling, impact assessment, and adaptation at regional and local scales.

AUTHOR CONTRIBUTIONS

XW wrote the first draft of this editorial. All authors contributed to manuscript revision, read, and approved the submitted version.

ACKNOWLEDGMENTS

We would like to thank all the authors for their contributions and all the reviewers for their valuable comments and feedback.

REFERENCES

Giorgi, F. (2019). Thirty Years of Regional Climate Modeling: where Are We and where Are We Going Next? *J. Geophys. Res. Atmospheres* 124 (11), 5696–5723.

Guo, J., Huang, G., Wang, X., Li, Y., and Lin, Q. (2018). Dynamically-downscaled Projections of Changes in Temperature Extremes over China. *Clim. Dyn.* 50 (3), 1045–1066. doi:10.1007/s00382-017-3660-7

Wang, X., Huang, G., Lin, Q., Nie, X., Cheng, G., Fan, Y., et al. (2013). A Stepwise Cluster Analysis Approach for Downscaled Climate Projection - A Canadian Case Study. *Environ. Model. Softw.* 49, 141–151. doi:10.1016/j.envsoft.2013.08.006

Wang, X., Huang, G., and Liu, J. (2014). Projected Increases in Intensity and Frequency of Rainfall Extremes through a Regional Climate Modeling Approach. *J. Geophys. Res. Atmospheres* 119 (23), 13–271. doi:10.1002/2014jd022564

Wang, X., Kinsland, G., Poudel, D., and Fenech, A. (2019). Urban Flood Prediction under Heavy Precipitation. *J. Hydrol.* 577, 123984. doi:10.1016/j.jhydrol.2019.123984

Conflict of Interest: The authors declare that the research was conducted in the absence of any commercial or financial relationships that could be construed as a potential conflict of interest.

frontiers in Earth Science

ORIGINAL RESEARCH
published: 09 April 2020
doi: 10.3389/feart.2020.00086

Facing Water Stress in a Changing Climate: A Case Study of Drought Risk Analysis Under Future Climate Projections in the Xi River Basin, China

*Keyi Wang[1], Jun Niu[2], Tiejian Li[3,4] and Yang Zhou[1]**

[1] Water Science and Environmental Engineering Research Center, College of Chemical and Environmental Engineering, Shenzhen University, Shenzhen, China, [2] Center for Agricultural Water Research in China, China Agricultural University, Beijing, China, [3] State Key Laboratory of Hydroscience and Engineering, Tsinghua University, Beijing, China, [4] School of Water Resources and Electric Power, Qinghai University, Xining, China

China, with its fragile environment and ecosystems, is vulnerable to climate change. Continuous changes in climatic conditions have altered precipitation patterns in most regions of China. Droughts become more frequent and severe in the Xi River basin in South China. It is expected that rapid urbanization and climate change will continue to aggravate water stress in this region. There is an urgent need to develop sustainable water management strategies in face of growing water demand and changing water availability. Projection of future climate change impacts on drought conditions has thus become imperative to support improved decision-making in sustainable water management. In this study, we assessed the risk of extreme droughts under future climate projections in the Xi River basin. The variable infiltration capacity (VIC) model was applied to simulate the hydrological processes of the basin under a multitude of future climate scenarios from CMIP5. Based on the precipitation and runoff series obtained from the VIC model, a comprehensive analysis with respect to the major characteristics of meteorological and hydrological droughts had been carried out. This study is of practical and theoretical importance to both policymakers and scholars. First, this study may be a readily available reference work for policymakers when taking consideration of building drought mitigation plans into future water management practices. Second, the findings in this study may provide some valuable insights into the inherent connection between climatic and hydrological changes under a changing climate. Recognition of the connection and interrelation may contribute to the improvement of climatic and hydrological models in practices.

Keywords: drought risk analysis, regional climate change, variable infiltration capacity (VIC) model, Xi River basin, hydrological processes

OPEN ACCESS

Edited by:
Xander Wang,
University of Prince Edward Island, Canada

Reviewed by:
Zoe Li,
McMaster University, Canada
Zoe Courville,
Cold Regions Research and Engineering Laboratory, United States

****Correspondence:***
Yang Zhou
yzhou@szu.edu.cn

Specialty section:
This article was submitted to Interdisciplinary Climate Studies, a section of the journal Frontiers in Earth Science

Received: *15 January 2020*
Accepted: *13 March 2020*
Published: *09 April 2020*

Citation:
Wang K, Niu J, Li T and Zhou Y (2020) Facing Water Stress in a Changing Climate: A Case Study of Drought Risk Analysis Under Future Climate Projections in the Xi River Basin, China. Front. Earth Sci. 8:86. doi: 10.3389/feart.2020.00086

INTRODUCTION

Both climate change and global warming have been at the center of arguments for decades, but almost all scientists and scholars now have come to an agreement that the average temperature of our planet has risen by around 1°C since the last century and the rise is expected to continue in the future (IPCC, 2007). Rising global temperatures unfreeze polar ice caps resulting in sea

level rise and regional climate change. Extreme weather events become more intense and frequent, e.g., heatwaves, floods, and droughts. As regional climate patterns change, their impacts from one location to another can be erratic (Zhou and Zhang, 2014; Wanders and Wada, 2015). While regional climate change has increased precipitation in some areas, it has also led to droughts in other regions. As a result, both short-term and long-term regional impact studies under climate change are needed to improve policymakers' understanding of the changing climate and environment, and to highlight the urgency and necessity of developing regional climate mitigation and adaptation plans.

China, with its fragile environment and ecosystems, is vulnerable to the negative effects of climate change (Xu et al., 2015). In recent years, China has experienced more frequent extreme weather events, e.g., heavy rains and droughts (Wang and Li, 2005; Chen and Sun, 2015; Tan et al., 2016). In fact, continuous changes in climatic conditions have altered precipitation patterns in most regions of China, especially, in the southern portions of China. Droughts become more frequent and severe in many regions of southern China in recent decades (Huang et al., 2010; Li et al., 2012). It is expected that rapid urbanization and climate change will continue to aggravate water stress in southern China. There is an urgent need to develop sustainable water management strategies in face of growing water demand and changing water availability. Therefore, projection of future climate change impacts on drought conditions has become imperative to support improved decision-making in sustainable water management.

The Xi River is the longest river in South China, with a total drainage area of 353,000 km^2, accounting for 78% of the total area of the Pearl River basin. The Xi River basin stretches from eastern Yunnan province into southern Guangdong province, and has a humid subtropical or tropical monsoon climate. In terms of mean annual runoff, the Xi River ranks 2nd behind the Yangtze River in China, and is almost 4.5 times that of the Rhine River in Europe. The mean annual precipitation in Xi River basin is approximately 1,447 mm (Niu and Chen, 2010). The Xi River basin is resource-rich, with fertile agricultural soils, abundant mineral resources, water and energy intensive industries, and supports fifty million people in South China. It has been positioned as a new national economic growth zone thanks to the economic development initiative of Xi River Economic Belt.

Although Xi River basin has abundant freshwater resources, there are many regions that are subject to periodic water scarcity due to maldistribution of water resources (Cui et al., 2007). About 80% of the annual precipitation falls during the wet season between April and September, while only 8% of that falls during the winter season between December and February (Duan et al., 2017). As a result of maldistribution of water resources, the Xi River basin has experienced recurring droughts and water stress (Fischer et al., 2013). An intense period of droughts occurred from 1962 to 1963 and about 5% of the basin land was affected, with an area of 16,200 km^2 (Niu et al., 2015). A continuous period of droughts lasting 9 years occurred from 1984 to 1992 (Lin et al., 2017). A frequent period of droughts occurred from 2003 to 2015 and the basin had seen widespread droughts almost every year during this period (Wu et al., 2016). In addition, the Xi River basin has encountered great economic losses because of severe droughts in recent years (Xiao et al., 2012; Chen et al., 2013; Niu et al., 2015). Increasingly frequent droughts have caused significant socioeconomic impacts and necessitate urgent actions from government and stakeholders. Improving understanding of historical variations in precipitation and future trends in climate are needed so as to aid policymakers in building drought mitigation plans into local water management practices.

The Xi River basin has long been of interest to scientist and scholars because of its social, economic and cultural importance. Most studies across the Xi River basin were focused on the assessment of the hydrological changes through trend analysis, and only a few studies aimed at investigating climate change impacts on hydrological processes (He et al., 2009; Zhang and Lu, 2009). However, few studies had been carried out with a glimpse into the future. Moreover, with respect to future hydrological changes, most studies were focused on using General Circulation Models (GCMs) and hydrological models to analyze the long-term mean values of variations in hydrological conditions (Yuan et al., 2017). There were few studies focusing on the connection between climate change and hydrometeorological extremes at a regional scale, despite the fact that large river basins with so-called abundant freshwater resources and dense population may be particularly vulnerable to extreme weather incidents (Teng et al., 2012; Li et al., 2016).

To address the aforementioned issues, the objectives of this study are: (1) to project future streamflow in the Xi River basin and evaluate future drought conditions including meteorological and hydrological droughts by using two types of drought indexes, i.e., the Standardized Precipitation Index (SPI) and the Standardized Runoff Index (SRI); (2) to investigate climate change impacts on the variations in the mean and extreme values of drought characteristics by using three parameters, i.e., frequency, duration and severity; and (3) to reveal the inherent connection between climatic and hydrological changes under a changing climate.

The remainder of this paper is organized as follows. Section "Materials and Methods" describes the data and methods. Section "Results" presents the results of the relative changes of river flows and drought characteristics, as well as a relationship analysis among precipitation, temperature and runoff. Section "Discussion" gives a discussion, while the final section contains conclusions.

MATERIALS AND METHODS

Study Area

The Xi River basin is located in South China between 21–27.00°N latitude and 102.00–114.00°E longitude. The river rises in Yunnan province, flows through Guizhou, Guangxi and Guangdong provinces, and finally reaches the Pearl River Delta on the South China Sea. The total length of the river is about 2,214 km, including several main tributaries, e.g., Nanpan River, Hongshui River, Yu River, Liu River, etc. The location of the Xi River basin is shown in **Figure 1**.

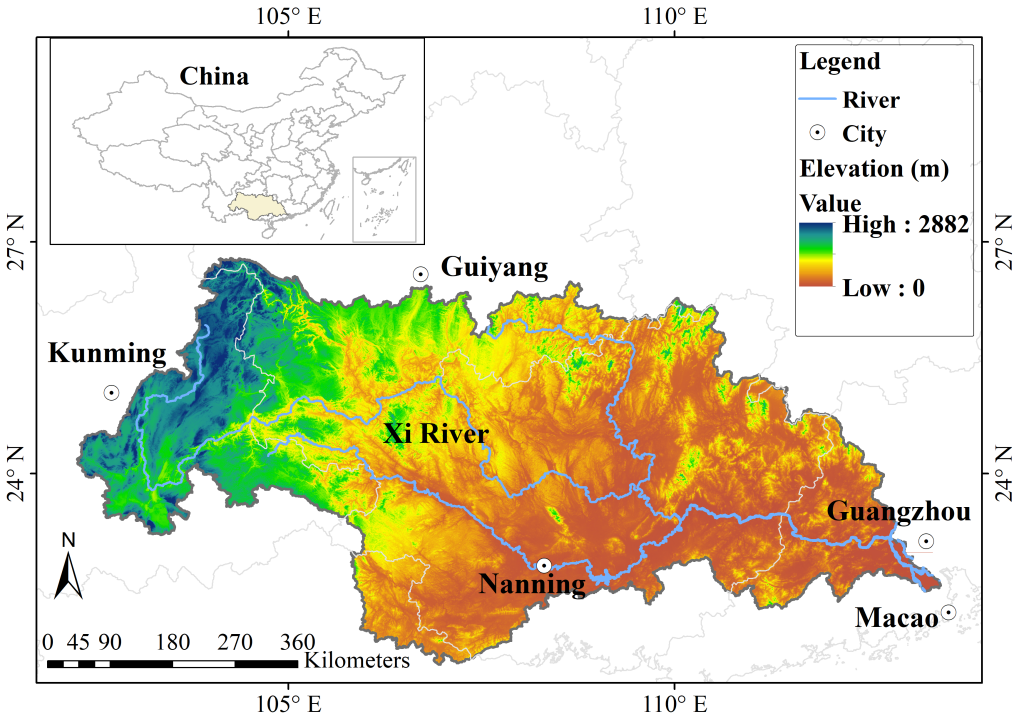

FIGURE 1 | Location of the Xi River basin.

Climate Change Scenarios

In this study, we simulated the terrestrial hydrological processes over the Xi River basin with CMIP5 multi model ensembles (MMEs). The downscaled GCMs were obtained from "Downscaled CMIP3 and CMIP5 Climate and Hydrology Projections"[1]. Then, we chose 16 GCMs based on selection criteria including data integrity of long-time series, usage frequency of numerical modeling, and variability of the downscaled data. The Bias Correction Spatial Disaggregation (BCSD) climatic data at a 0.5° × 0.5° spatial resolution and a monthly time step under the RCP4.5 scenario from 1960 to 2099 were used in this study. The summary of the selected GCMs is provided in **Table 1**.

To obtain local meteorological forcing data from the GCMs, which are the prerequisites of simulation of the Variable Infiltration Capacity (VIC) model, a stochastic weather generation method was applied to temporally disaggregate the monthly climatic data, including precipitation and temperature, into the daily meteorological forcing datasets (Wood et al., 2004). In addition, we chose RCP4.5 to study the potential impacts of future climate change. The reason is that a variety of mitigation actions have been taken in China to reduce greenhouse gas emissions; thus RCP4.5 may be an appropriate emissions scenario that can better reflect the future climate conditions in the Xi River basin (Riahi and Nakicenovic, 2007; Thomson et al., 2011; Gao et al., 2014). Therefore, the results obtained from this study may be more meaningful in terms of supporting decision-making in building future drought mitigation plans into local water management practices.

Macro-Scale Hydrological Model

The future terrestrial hydrological scenarios in the Xi River basin were derived from simulation of the VIC model. The historical meteorological forcing data required by the VIC model, such as temperature and wind speed, were obtained from the work of Feng et al. (2004). The soil and vegetation datasets required for the VIC model were obtained from the work of Nijssen et al. (2001). Previous studies demonstrated that the VIC model was capable of producing acceptable results for the purpose of runoff simulation in the Xi River basin by using the aforementioned meteorological parameters (Niu and Chen, 2010). Next, by using the BCSD climatic data as the input of the VIC model, the daily time series of the major hydrological parameters for the period 1960–2099 were obtained.

Drought Indices

The SPI and the SRI were used to analyze the meteorological and hydrological droughts, respectively. The SPI is calculated based on accumulated precipitation, which describes the degree of deviation of accumulated precipitation from climatological averages. The SPI is applicable at either monthly or multi-monthly temporal scales (e.g., 3-month) over different spatial scales so that it has been widely used to investigate the evolution of meteorological droughts (McKee, 1997). The procedure for calculating the SPI is outlined below. Firstly, an appropriate probability distribution is chosen to fit the

[1]https://gdo-dcp.ucllnl.org/downscaled_cmip_projections/

TABLE 1 | List of the Global Climate Models (GCMs) studied in this study.

	Modeling center	Country	Model
(1)	Beijing Climate Center, China Meteorological Administration	China	BCC-CSM1-1-m
(2)	College of Global Change and Earth System Science, Beijing Normal University	China	BNU-ESM
(3)	Canadian Centre for Climate Modelling and Analysis	Canada	CanESM2
(4)	National Center for Atmospheric Research	United States	CCSM4
(5)	Community Earth System Model Contributors	United States	CESM1-BGC
(6)	Centro Euro-Mediterraneo per I Cambiamenti Meteorologicali	Italy	CMCC-CM
(7)	Centre National de Recherches Météorologiques	France	CNRM-CM5
(8)	Commonwealth Scientific and Industrial Research Organization, Queensland Climate Change Centre of Excellence	Australia	CSIRO-Mk3-6-0
(9)	Laboratory of Numerical Modeling for Atmospheric Sciences and Geophysical Fluid Dynamics, Institute of Atmospheric Physics, Chinese Academy of Sciences, and Center for Earth System Science, Tsinghua University	China	FGOALS-g2
(10)	The First Institute of Oceanography, State Oceanic Administration, China	China	FIO-ESM
(11)	NOAA Geophysical Fluid Dynamics Laboratory	United States	GFDL-ESM2G
(12)	NASA Goddard Institute for Space Studies	United States	GISS-E2-R
(13)	Met Office Hadley Centre	Korean	HadGEM2-AO
(14)	Institut Pierre-Simon Laplace	France	IPSL-CM5A-LR
(15)	Japan Agency for Marine-Earth Science and Technology, Atmosphere and Ocean Research Institute (The University of Tokyo), and National Institute for Environmental Studies	Japan	MIROC-ESM
(16)	Norwegian Climate Centre	Norwegian	NorESM1-M

accumulated precipitation. Then, the cumulative probability is calculated based on the accumulated precipitation according to the selected distribution. Finally, the SPI, i.e., the standard normal deviation with mean zero and standard deviation one, can be obtained from the cumulative probability. In this study, the log-normal distribution was selected to fit the accumulated precipitation over the Xi River basin (Niu et al., 2015). Thus, the SPI can be expressed as:

$$\mathrm{SPI} = \frac{\ln(x) - \widehat{\mathrm{u}_y}}{\widehat{\sigma_y}} \quad (1)$$

where x is accumulated precipitation, $y = \ln(x)$; $\widehat{\sigma_y}$ is sample variance; $\widehat{u_y}$ is sample mean. More information about calculation of the SPI can be found in Lloyd-Hughes and Saunders (2002). The procedure for calculating the SRI is similar to that of the SPI except a key point that the SRI is calculated based on accumulated runoff. The time series of the two drought indexes were calculated by using the monthly series for the whole-basin area as well as the grid cells in the Xi River basin for every GCM. The selected threshold for drought identification is zero, and thus a drought event is defined as a consecutive and uninterrupted period, with an SPI/SRI value lower than this level (Vicente-Serrano et al., 2017). Based on this definition, three different parameters can be obtained to characterize droughts: (1) frequency—the number of drought events in a given period; (2) duration—the length of an identified drought event; (3) severity—the accumulated deficit volume of an identified drought event.

RESULTS

The projected results show that the Xi River basin would experience a temperature increase of about 1.3–1.7°C in the near future (2030–2059) and a temperature increase of about 1.9–2.4°C in the distant future (2070–2099), in comparison with the historical period (1971–2000). As shown in **Figure 2**, the largest increase would occur in the northern part of the Xi River basin, whereas the smallest increase would occur in southeastern part in the near future. Unlike the moderate temperature increase in the near-future scenario, the northern part of the Xi River basin would experience an obvious increase in temperature up to 2.4°C in the distant future. These results indicate that temperature would increase continuously across the Xi River basin in the future regardless of spatial and temporal considerations. With respect to the changes in the precipitation pattern, the results also show an upward trend in annual precipitation, increasing up to 4.5% in the near future (see **Figure 2C**) and up to 7% in the distant future over the basin (see **Figure 2D**). Overall, it is expected that both average temperature and precipitation in the Xi River basin would increase in the future.

Spatial Changes in River Flows

The relative changes in extreme river flow and average river flow between the future periods (i.e., 2030–2059 and 2070–2099) and the historical period (i.e., 1971–2000) are shown in **Figure 3**. The 95th percentile (Q95) and the 10th percentile (Q10) of the monthly flow were used to describe the extreme conditions (i.e., the low flow and the high flow) in this study. The results from MMEs shown in **Figure 3** indicate that climate change would have a significant impact on the hydrological patterns in the Xi River basin. For the near future (2030–2059), the low flow would probably decrease across the Xi River basin except several areas in the midstream region. In addition, the Xi River basin would probably see a more significant reduction in the low flow in the near future rather than in the distant future (2070–2099). For example, in the central basin, some grids show a significant decrease in the low flow by about 40–60%, while such a decrease climbs to around 20–40% in the distant future. A modest decrease in the mean flow is found across most areas of the Xi River basin. In the near future, the mean flow would probably reduce between 4 and 49%. There are only a few grids in the midstream showing an increase ranging from 2 to 13%. Similar implications could be obtained from observing the mean flow in the distant

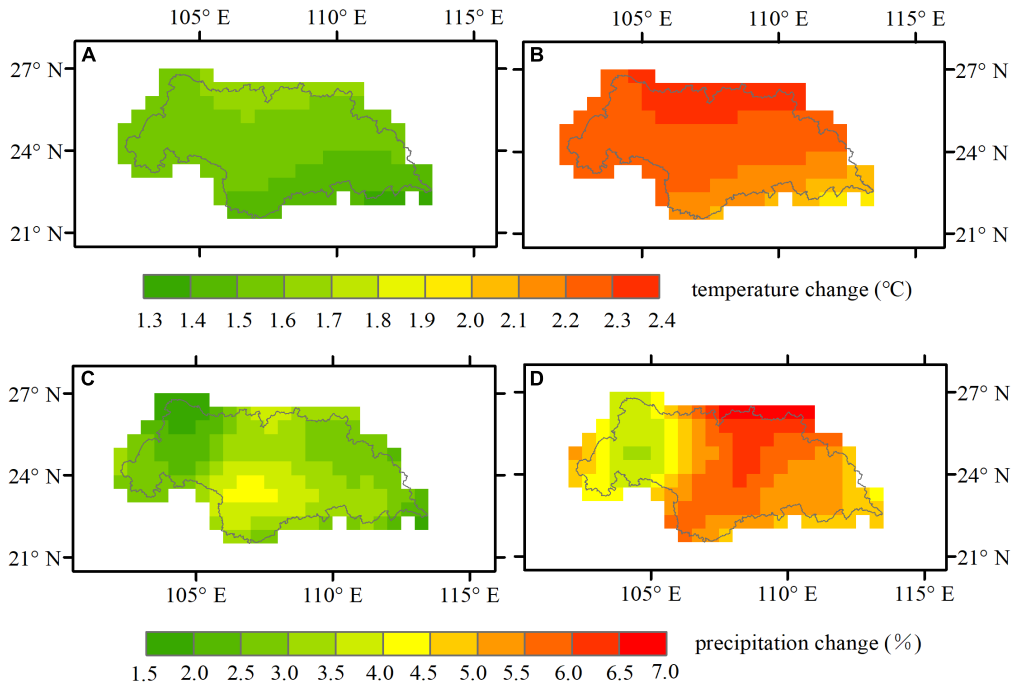

FIGURE 2 | Changes in temperature (°C) between the future periods and the historical period 1971–2000: **(A)** 2030–2059 and **(B)** 2070–2099, and changes in precipitation (%) between the future periods and the historical period 1971–2000: **(C)** 2030–2059 and **(D)** 2079–2099.

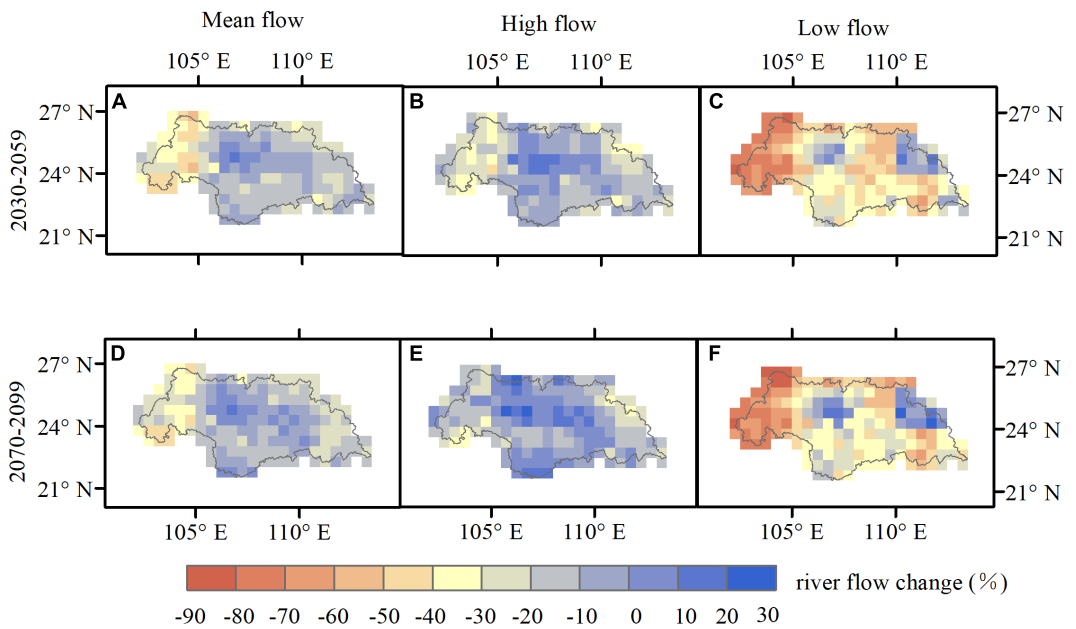

FIGURE 3 | Changes in river flows between the future period 2030–2059 and the historical period 1971–2000: **(A)** mean flow, **(B)** high flow (Q95), and **(C)** low flow (Q10), and changes in river flows between the future period 2070–2099 and the historical period 1971–2000: **(D)** mean flow, **(E)** high flow (Q95), and **(F)** low flow (Q10) over the Xi River basin.

future, but the degree of reduction with respect to the mean flow would be alleviated in some regions of the central basin. The high flow would decrease in the midstream region under RCP4.5 in the near future. The changes in the high flow in the distant future would be very similar to that case, but the magnitude of reduction could be different. In addition, more grids show

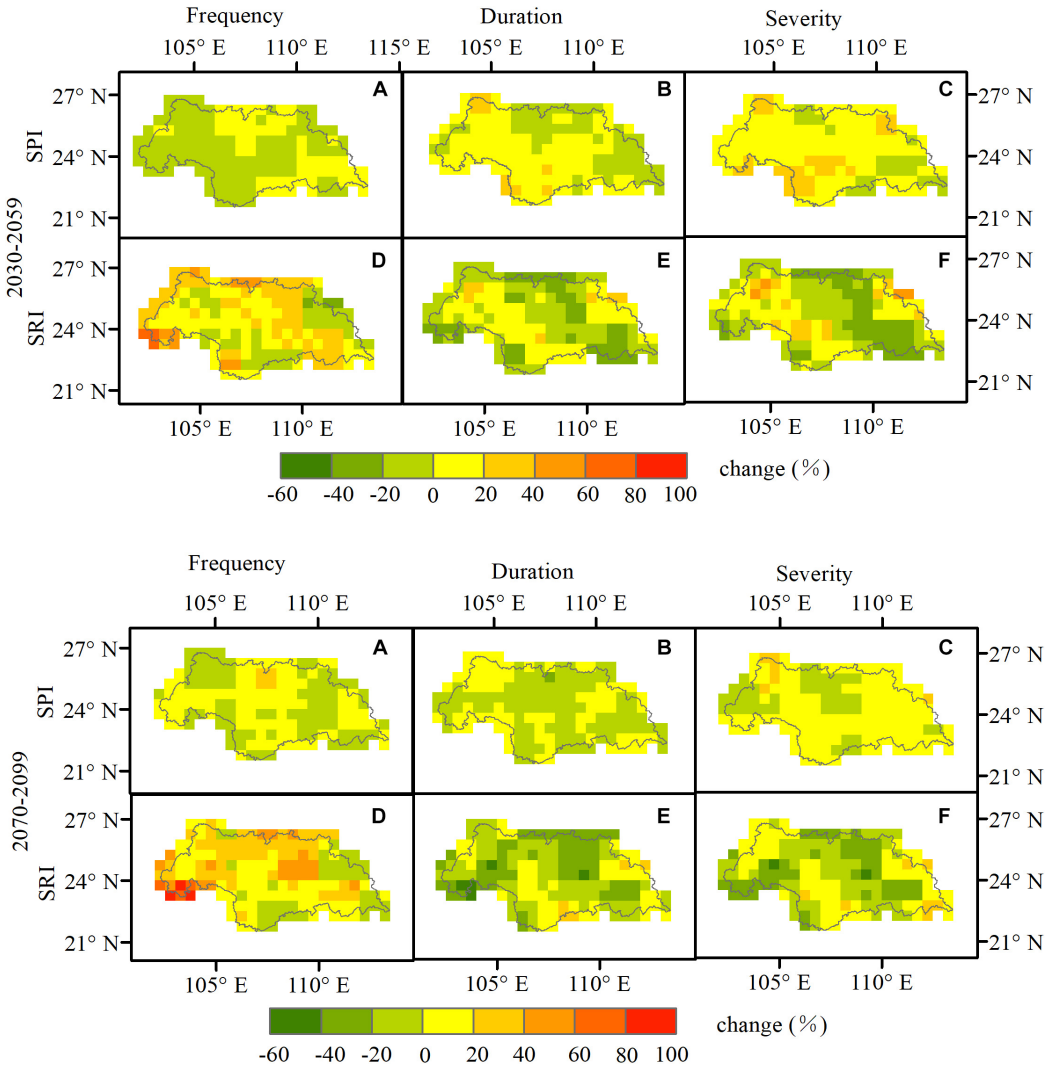

FIGURE 4 | Changes in the characteristics of meteorological droughts for the SPI between the future periods (2030–2059 and 2070–2099) and the historical period (1971–2000): **(A)** frequency, **(B)** duration, **(C)** severity, and changes in the characteristics of hydrological droughts for the SRI between the future periods (2030–2059 and 2070–2099) and the historical period (1971–2000): **(D)** frequency, **(E)** duration, and **(F)** severity.

an increase in the high flow in the midstream and downstream regions during 2070–2099.

Spatial Changes in Drought Characteristics

Mean Droughts

Figure 4 illustrates the relative changes projected by MMEs with respect to mean drought characteristics, i.e., frequency, duration and severity, between two future periods (2030–2059 and 2070–2099) and the historical period (1971–2000). Meteorological droughts described by the SPI would decrease in major areas of the Xi River basin, except the southeastern and northern parts of the Xi River basin. Meanwhile, the mean duration and severity of meteorological droughts would probably increase across most areas of the Xi River basin. However, the northern and eastern Xi River basin would experience a decrease in the mean duration. Our results indicate that global warming would result in less meteorological drought events but longer dry episodes across the Xi River basin. With respect to hydrological droughts described by the SRI, the drought frequency would increase over major parts of the Xi River basin. However, the northern and southeastern Xi River basin would experience a decrease in the mean duration and severity of hydrological droughts. Meanwhile, the increase in the mean duration and severity described by the SRI in the near future would be less than that of the SPI in the northern and southeastern Xi River basin. The reason could be attributed to the buffer processes of the land surface, leading to smaller changes in the mean duration of hydrological droughts in contrast to meteorological droughts.

The relative changes in frequency, duration and severity for the distant future, i.e., 2070–2099, is shown in the bottom panel

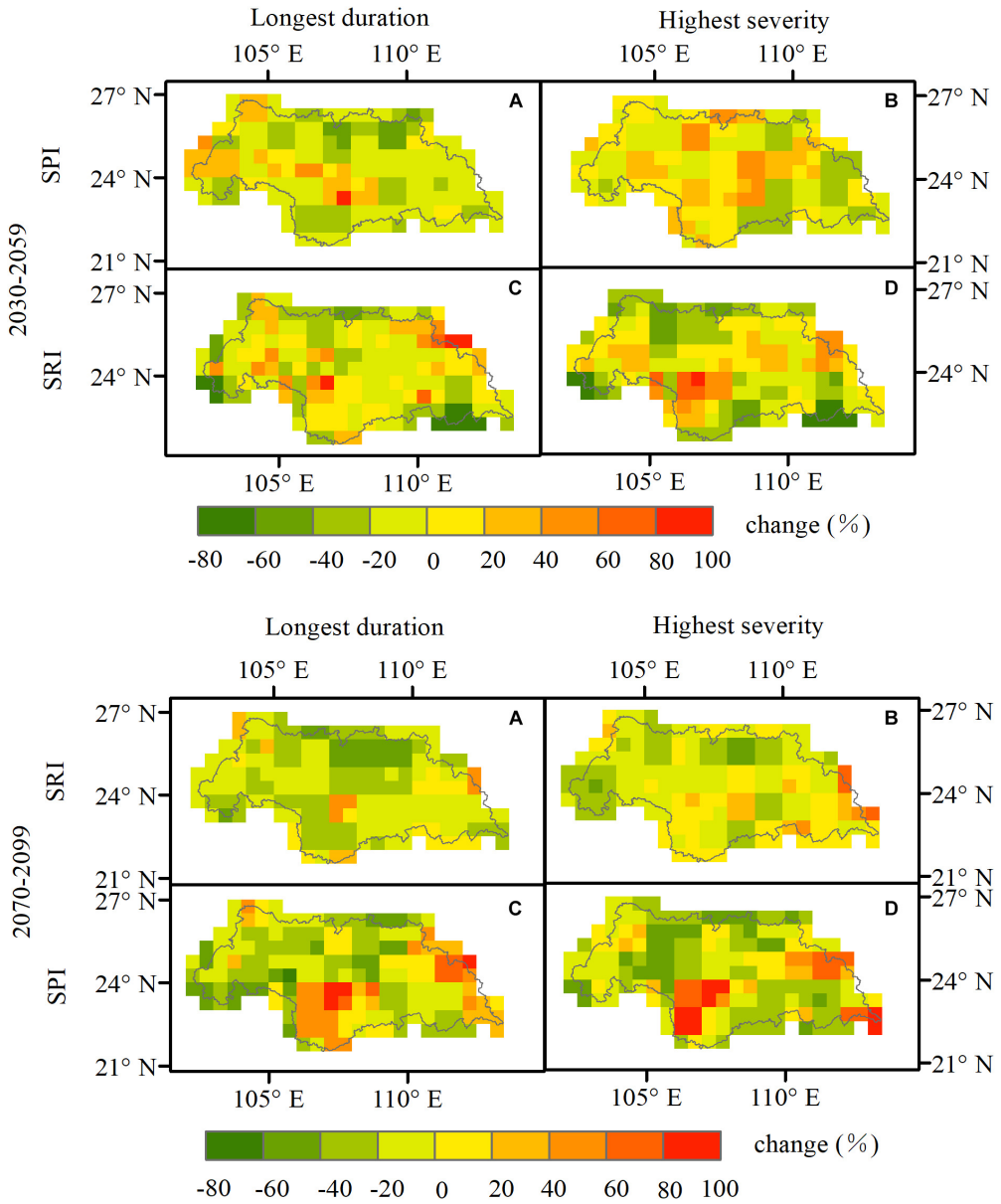

FIGURE 5 | Changes in the characteristics of extreme meteorological droughts for the SPI between the future periods (2030–2059 and 2070–2099) and the historical period (1971–2000): **(A)** longest duration and **(B)** highest severity, and changes in the characteristics of extreme hydrological droughts for the SRI between the future periods (2030–2059 and 2070–2099) and the historical period (1971–2000): **(C)** longest duration, and **(D)** highest severity.

of **Figure 4**. More grids of the Xi River basin would see a significant increase in the frequency of meteorological droughts in the distant future than in the near future. However, the mean duration of meteorological droughts would decrease significantly in most parts of the Xi River basin. The changes in the spatial pattern of hydrological droughts in the distant future would be consistent with the changes described in period 2030–2059. For example, it is expected that the drought frequency would increase in most areas of the Xi River basin, especially in the western areas, while the mean duration and severity would probably decrease in major parts of the Xi River basin.

Extreme Droughts

Figure 5 describes the relative changes in extreme drought conditions between the future and historical periods. The longest duration of meteorological droughts would decrease in most areas of the Xi River basin, while the western and central areas of the basin would experience a notable increase in the longest duration of meteorological droughts. The highest severity of meteorological droughts would probably increase over most areas of the central Xi River basin. The relative changes in extreme hydrological droughts would show more intensive variations compared with that of extreme meteorological

droughts. A decrease in the longest duration of hydrological droughts is observed affecting about 60% of the total grid cells across the Xi River basin. In the lower central part of the basin, the highest severity of hydrological droughts would be expected to increase, which is similar to the changes in meteorological droughts. The change patterns in extreme drought conditions show a multitude of changes as compared with that in mean drought conditions (**Figure 4**). For example, the mean duration of meteorological droughts would tend to increase in the lower central region of the Xi River basin, while the longest duration would tend to decrease in the same region. Moreover, with respect to both meteorological and hydrological droughts in the central Xi River basin, the increment in the longest duration and highest severity would be much greater than that in the mean duration and severity. These results describe worsening extreme drought conditions over the Xi River basin in the near future.

Similar implications could be reached for the future period 2070–2099. As shown in **Figure 5**, more areas of the Xi River basin in the distant future would experience a decrease in the longest duration and highest severity of meteorological droughts. For hydrological droughts, the maximum increment in the longest duration would be around 85% in the central basin. Except the southern part of the central basin and the eastern part of the Xi River basin, the longest duration would decrease with similar patterns as the highest severity.

Response of Runoff to Climate Change in the Future

Our study indicates that climate change could affect the timing and magnitude of average and extreme river flows as well as mean and extreme drought conditions in the Xi River basin. According to the comparison results from **Figures 2**, **3**, the changes of streamflow do not always follow the change patterns of precipitation, which indicates that both precipitation and temperature (evapotranspiration) could affect the hydrological processes. Thus, to assess the climate change impacts on streamflow, the annual percentage deviation for streamflow as a function of the annual percentage deviations for precipitation and temperature is described using the contour plot (**Figure 6**). It is observed that the percentage changes in annual streamflow are positively related to the annual precipitation changes, but negatively related to the annual temperature changes. In addition, streamflow seems to be more sensitive to the changes in precipitation than that in temperature. For example, a 30% increase in annual precipitation could result in a 60% increase in annual streamflow when temperature stays unchanged, whereas a 1.2°C decrease in temperature would lead to a relatively small increase in annual streamflow with unchanged annual precipitation (see **Figure 6**).

Figure 7 is derived from several cross sections of **Figure 6**. Streamflow changes subject to temperature changes under different precipitation scenarios across the Xi River basin are shown in **Figure 7A**. For precipitation-increase scenarios, streamflow and temperature are almost linearly related, with different changing slopes, but this relationship may turn into dissimilar non-linear patterns under the precipitation-decrease scenarios. For example, the slope of the streamflow vs. temperature line is about 3% per °C for the 20% precipitation-increase scenario, indicating that a 1°C increase in temperature would result in a decrease of 3.0% in streamflow. For the 10% precipitation-increase scenario, a 1°C increase in temperature would lead to a 2.5% decrease in streamflow. However, for the precipitation-decrease scenarios, e.g., the 20% precipitation-decrease scenario, limited changes are found in streamflow as temperature changes. **Figure 7B**

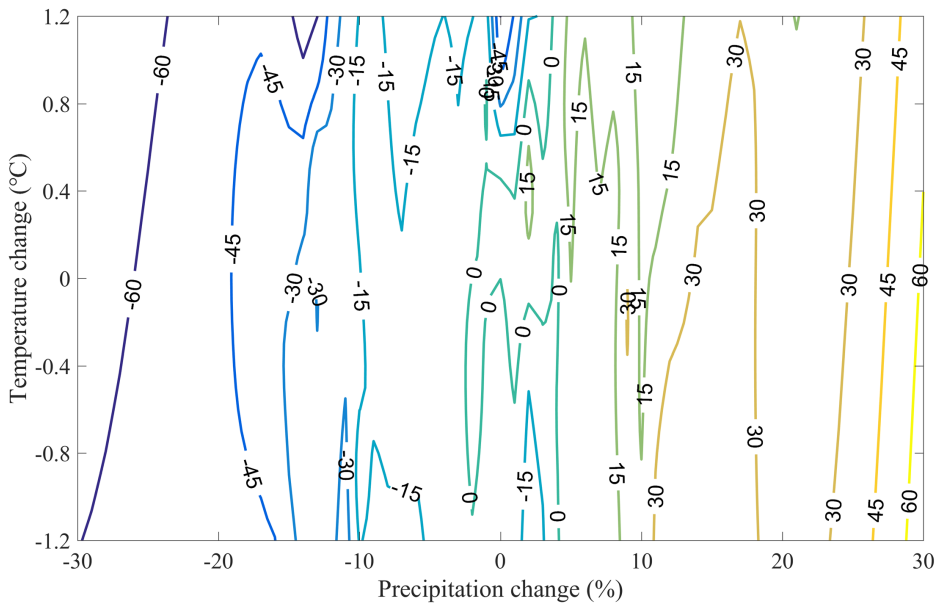

FIGURE 6 | Contour plot of annual streamflow change (%) as a function of annual precipitation and temperature changes for the Xi River basin in the future.

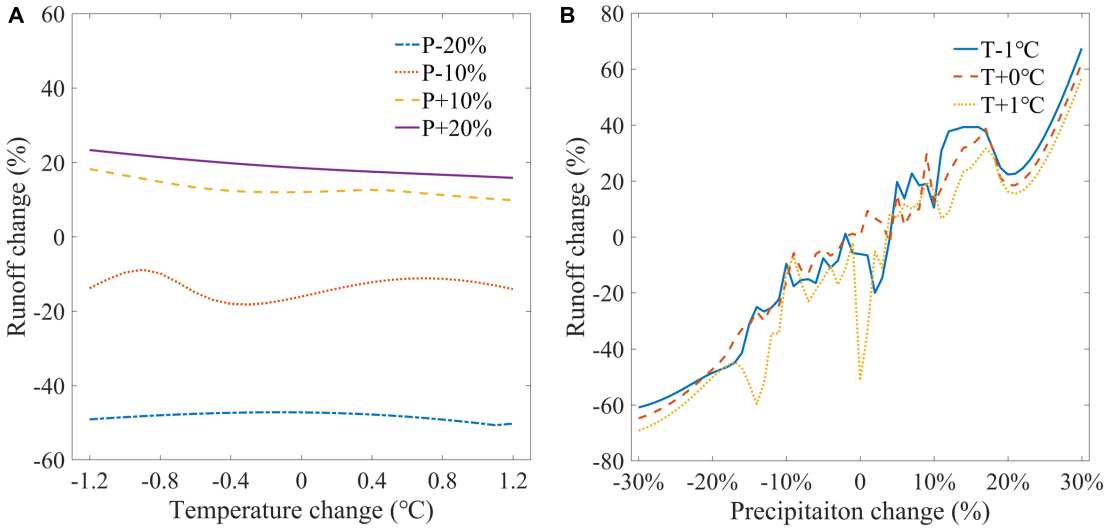

FIGURE 7 | Streamflow changes as function of precipitation changes **(A)** and temperature changes **(B)** at different scenarios for the Xi River basin.

shows streamflow changes subject to precipitation changes under different temperature scenarios for the Xi River basin. It is observed that streamflow and precipitation are almost linearly related under a fixed temperature scenario. However, some fluctuations appear, especially in the cases with precipitation changes less than 10%, which might be attributed to numerical instability (Fu et al., 2007). For the scenario with a temperature increase of 1°C, the slope of the streamflow vs. precipitation line is about 2%, indicating that a 10% increase in annual precipitation would result in an increase in annual streamflow by 20%. Moreover, the change slopes for the streamflow vs. precipitation lines under different temperature scenarios are particularly similar. In general, annual streamflow is more sensitive to the changes in precipitation than that in temperature. Moreover, the sensitivity of streamflow with respect to the changes in temperature rises along with increasing precipitation.

DISCUSSION

Uncertainties Arising From the Future Projections

In terms of drought risk analysis under climate change, projection of the variations of terrestrial hydrological processes is the first and most important procedure. However, these processes may be subject to a multitude of uncertainties owing to the selection of emission scenarios, GCMs, downscaling methods as well as impact models. The climate dataset used in this study was obtained from "Downscaled CMIP3 and CMIP5 Climate and Hydrology Projections"—a project meant to provide access to spatial and temporal climate and hydrologic projections for water resource managers and planners based on CMIP3 and CMIP5 (Bureau of Reclamation, 2014). Global and regional studies have demonstrated the superiority of multi-model integration over to a single model (Lambert and Boer, 2001; Ziehmann, 2008; Pierce et al., 2009). The references above also indicate that in terms of selection of the models, with or without a preference for the quality of simulation in study areas, there would be no systematic differences. In this study, the 16 GCMs were statistically downscaled after bias-correlation, making it possible to characterize the potential uncertainties arisen from the GCMs. Moreover, several studies have demonstrated the reliability of the selected GCMs in global and regional climate change studies (Tan et al., 2017; Srinivasa Raju et al., 2017; Sunde et al., 2017; Merabti et al., 2018).

Selection of historical reference data is another potential source of uncertainty. Maurer et al. (2002) conducted a comprehensive verification of the historical reference data used in this study. Moreover, this study is meant to investigate the hydrological response to future climate change. Hence, the analysis had been emphasized on description of the hydrological conditions in the 21st century. Since the climate projections used in this study had been corrected using the BCSD method by other researchers, we do not reassess the reliability of the reference data. In addition, the results in this study are relevant to the specific historical periods. Different researchers used different historical periods as the reference periods for climate change studies, e.g., 1915–2006 (Mantua et al., 2010), 1976–2005 (Prudhomme et al., 2014), 1961–1990 (Kay and Davies, 2008), and 1971–2000 (Dankers et al., 2014; Leng et al., 2015). The near future of 2030–2059 and the distant future period of 2070–2099 were used in our study to provide policymakers with insightful information so as to aid them in building short-term and long-term drought mitigation or adaptation plans into future water management practices.

Due to the inherent characteristics of droughts, e.g., slow onset, as well as the resulting complicated impacts, drought regimes are more ambiguous than that of other water-related incidents (Svoboda et al., 2002). Thus, there is no one universal drought index that can be used to satisfy all needs of researchers; after all, different drought indexes are only suitable for specific drought types. To precisely and visually identify drought occurrence and magnitude, many quantitative definitions of drought indexes have been proposed (Palmer, 1965; Bhalme and Mooley, 1980; McKee et al., 1993). In this study, the SPI and SRI were used to assess the risk of meteorological and hydrological droughts, respectively. It is clear that both the SPI and SRI are only based on monthly data and thus cannot fully reflect actual drought situations. Despite this limitation, both indexes have been widely applied for monitoring specific types of droughts (Hao et al., 2016; Zhang et al., 2017; Merabti et al., 2018).

Comparison Between Our Studies and Previous Studies

Our results show that there exists a substantial increase in precipitation and temperature across the Xi River basin. The high flow is likely to increase in the midstream and downstream region of the basin in the future. The relative increases are larger in the high flow than that in the mean flow, indicating an increase in the risk of floods in the central and southern parts of the basin. Wang and Chen (2014) reported the changes in temperature and precipitation over China under RCP4.5 and RCP8.5 scenarios in the future, and found annual precipitation would increase in most area of China from 2010 to 2099. Sun et al. (2015) concluded that the annual precipitation of the Pearl River basin would increase in the distant future (i.e., after 2030), which is consistent with our findings. Yan et al. (2015) reported that the high flow would increase and the low flow would decrease over the downstream region of the Pearl River basin, and both the high and low flows would decrease in the upstream region of the Pearl River basin under RCP4.5 scenario for 2070–2099. Climate change impacts on droughts were also projected in this study. Our results indicate that the meteorological drought would be more serious in the near future. Zhai et al. (2010) presented the change patterns of dryness/wetness conditions in the Pearl River basin under A1B, A2, and B1 scenarios based on the ECHAM4 model outputs, and reported a finding that future dry periods would occur in the 2020s and 2040s, which is consistent with our findings.

CONCLUSION

In this study, we assessed extreme drought risk under future climate projections in the Xi River basin. The VIC model was applied to simulate the hydrological processes of the basin under a multitude of future climate scenarios from CMIP5. Based on the precipitation and runoff series obtained from the VIC model, a comprehensive analysis with respect to the major characteristics of meteorological and hydrological droughts, i.e., frequency, duration and severity, had been carried out. The main findings of this study can be summarized as follows:

- A notable declining trend in future flows, including mean flow, high flow and low flows, has been found over the entire basin.
- Significant regional and temporal variations in flow patterns has been found. In the near future, the high flow would be likely to decrease in the midstream region while the low flow would be likely to increase, indicating that this region would face a higher risk of droughts under a changing climate. In addition, most areas of the downstream region would experience an increase in the high flow, indicating a potential risk of floods in this region.
- The changes in drought characteristics imply that meteorological droughts would be more serious and persistent, while hydrological droughts would be more frequent in the near future. In the distant future, both meteorological and hydrological droughts would become more frequent.
- In general, the changes in annual runoff are more sensitive to precipitation than temperature. However, when precipitation increases, temperature may affect runoff generation much more.

Global warming has changed climate patterns in many regions, including the Xi River basin. The changes in regional climatic conditions increase the odds of worsening droughts, and thus place additional pressure on water availability, accessibility, and supply. The Xi River basin's deteriorating drought conditions have sparked the interest of scientists and researchers and motivated major water policy modifications by providing a glimpse into the basin's climatic future. In fact, it is difficult to plan for a drought and reduce its impacts when in droughts, and while short-term response plans provide relief support during the event, local authorities can benefit from proactive, longer-term planning that includes risk mitigation strategies. Therefore, projection of future climate change impacts on drought conditions is necessary for improved policy-making in face of future water stress.

This study is of practical and theoretical importance to both policymakers and scholars, despite its limitations in the methodology and model. First, the Xi River basin has been positioned as a new national economic growth zone in South China and this region is facing recurring droughts and worsening water stress in spite of so-called abundant freshwater resources. However, few studies have been carried out for assessing the risk of extreme drought conditions under future climate projections. As a result, this study may be a readily available reference work for policymakers when taking consideration of building drought mitigation plans into future water management practices. Second, the findings in this study may provide some valuable insights into the inherent connection between climatic and hydrological changes under a changing climate. Recognition of the connection and interrelation may contribute to the improvement of climatic and hydrological models in practices.

DATA AVAILABILITY STATEMENT

The datasets generated for this study are available on request to the corresponding author.

AUTHOR CONTRIBUTIONS

KW, JN, and TL: conceptualization and methodology. KW and JN: data curation and software. KW: formal analysis, validation, and visualization. KW and YZ: writing—original draft and writing—review and editing. YZ: funding acquisition.

FUNDING

The authors are grateful to the financial support provided by an international cooperation project (No. 2016YFE0201900), National Natural Science Foundation of China (No. 51679233), a science and technology innovation project of Shenzhen (No. 0832-SFCX18SZC025), and the Shenzhen University President's Fund.

REFERENCES

Bhalme, H. N., and Mooley, D. A. (1980). Large-scale droughts/ floods and monsoon circulation. *Mon. Weather Rev.* 108, 1197–1211. doi: 10.1175/1520-0493(1980)108<1197:lsdamc>2.0.co;2

Bureau of Reclamation (2014). "Downscaled CMIP3 and CMIP5 climate and hydrology projections: release of downscaled CMIP5 climate projections," in *Comparison with Preceding Information, and Summary of User Needs US Department of the Interior*, Denver, CO.

Chen, H., and Sun, J. (2015). Changes in drought characteristics over china using the standardized precipitation evapotranspiration index. *J. Clim.* 28:150414125419009.

Chen, Z., Liu, Z., and Huang, Q. (2013). Probability of hydrologic drought duration and intensity of Xijiang River. *J. Lake Sci.* 25, 576–582. doi: 10.18307/2013.0416

Cui, W., Chen, J., Wu, Y., and Wu, Y. (2007). An overview of water resources management of the Pearl River. *Water Supply* 7, 101–113. doi: 10.2166/ws.2007.045

Dankers, R., Arnell, N. W., Clark, D. B., Falloon, P. D., Fekete, B. M., Gosling, S. N., et al. (2014). First look at changes in flood hazard in the Inter-Sectoral Impact Model Intercomparison Project ensemble. *Proc. Natl. Acad. Sci. U.S. A.* 111, 3257–3261. doi: 10.1073/pnas.1302078110

Duan, L., Zheng, J., Li, W., Liu, T., and Luo, Y. (2017). Multivariate properties of extreme precipitation events in the Pearl River basin, China: magnitude, frequency, timing, and related causes. *Hydrol. Process.* 31, 3662–3671. doi: 10.1002/hyp.11286

Feng, S., Hu, Q., and Qian, W. (2004). Quality control of daily meteorological data in China, 1951-2000: a new dataset. *Int. J. Climatol.* 24, 853–870. doi: 10.1002/joc.1047

Fischer, T., Gemmer, M., Su, B., and Scholten, T. (2013). Hydrological long-term dry and wet periods in the Xijiang River basin, South China. *Hydrol. Earth Syst. Sci.* 17, 135–148. doi: 10.5194/hess-17-135-2013

Fu, G., Charles, S. P., and Chiew, F. H. S. (2007). A two-parameter climate elasticity of streamflow index to assess climate change effects on annual streamflow. *Water Resour. Res* 43:2007

Gao, C., Zhang, Z., Chen, S., and Liu, Q. (2014). The high-resolution simulation of climate change model under RCP4.5 scenarios in the Huaihe River Basin. *Geograph. Res.* 33, 467–477.

Hao, Z., Hao, F., Singh, V. P., Xia, Y., Ouyang, W., and Shen, X. (2016). A theoretical drought classification method for the multivariate drought index based on distribution properties of standardized drought indices. *Adv. Water Resour.* 92, 240–247. doi: 10.1016/j.advwatres.2016.04.010

He, H., Lu, H., and Ou, Y. (2009). Flood characteristics of the xijiang river basin in 1959-2008. *Adv. Clim. Chang. Res.* 5, 14–18.

Huang, W., Yang, X., Li, M., Zhang, X., and Ma, J. (2010). Evolution characteristics of seasonal drought in the south of China during the past 58 years based on standardized precipitation index. *Trans. Chinese Soc. Agric. Eng.* 26, 50–59.

IPCC (2007). IPCC climate change: the physical science basis. *IPCC Clim. Chang. Phys. Sci. Basis* 9:996.

Kay, A. L., and Davies, H. N. (2008). Calculating potential evaporation from climate model data: A source of uncertainty for hydrological climate change impacts. *J. Hydrol.* 358, 221–239. doi: 10.1016/j.jhydrol.2008.06.005

Lambert, S. J., and Boer, G. J. (2001). CMIP1 evaluation and intercomparison of coupled climate models. *Clim. Dyn.* 17, 83–106. doi: 10.1007/pl00013736

Leng, G. Y., Tang, Q. H., and Rayburg, S. (2015). Climate change impacts on meteorological, agricultural and hydrological droughts in China. *Glob. Planet. Chang.* 126, 23–34. doi: 10.1016/j.gloplacha.2015.01.003

Li, W., Hou, M., Chen, H., and Chen, X. (2012). Study on drought trend in south china based on standardized precipitation evapotranspiration index. *J. Nat. Disasters* 21, 84–90. doi: 10.1016/j.scitotenv.2017.10.339

Li, Z., Huang, G., Wang, X., Han, J., and Fan, Y. (2016). Impacts of future climate change on river discharge based on hydrological inference: a case study of the Grand River Watershed in Ontario. *Canada. Sci. Total Environ.* 54, 198–210. doi: 10.1016/j.scitotenv.2016.01.002

Lin, Q., Wu, Z., Singh, V. P., Sadeghi, S. H. R., He, H., and Lu, G. (2017). Correlation between hydrological drought, climatic factors, reservoir operation, and vegetation cover in the Xijiang Basin. *South China. J. Hydrol.* 549, 512–524. doi: 10.1016/j.jhydrol.2017.04.020

Lloyd-Hughes, B., and Saunders, M. A. (2002). A drought climatology for Europe. *Int. J. Climatol.* 22, 1571–1592. doi: 10.1002/joc.846

Mantua, N., Tohver, I., and Hamlet, A. (2010). Climate change impacts on streamflow extremes and summertime stream temperature and their possible consequences for freshwater salmon habitat in Washington State. *Clim. Change* 102, 187–223. doi: 10.1007/s10584-010-9845-2

Maurer, E., Wood, A., Adam, J., Lettenmaier, D., and Nijssen, B. (2002). A long-term hydrologically-based data set of land surface fluxes and states for the conterminous United States. *J. Clim.* 15, 3237–3251. doi: 10.1175/1520-0442(2002)015<3237:althbd>2.0.co;2

McKee, D. C. E. B. (1997). Characteristics of 20th century drought in the united states at multiple time scales. *Atmos. Sci. Pap.* 634, 1–30.

McKee, T., Doesken, N., and Kleist, J. (1993). "The relationship of drought frequency and duration to timescales," in *Paper presented at 8th Conference on Applied Climatology*, Anaheim, CA.

Merabti, A., Meddi, M., Martins, D. S., and Pereira, L. S. (2018). Comparing SPI and RDI applied at local scale as influenced by climate. *Water Resour. Manag.* 32, 1071–1085. doi: 10.1007/s11269-017-1855-1857

Nijssen, B., Schnur, R., and Lettenmaier, D. P. (2001). Global retrospective estimation of soil moisture using the variable infiltration capacity land surface modl, 1980-93. *J. Clim.* 14, 1790–1808. doi: 10.1175/1520-0442(2001)014<1790:greosm>2.0.co;2

Niu, J., and Chen, J. (2010). Terrestrial hydrological features of the Pearl River basin in South China. *J. Hydro Environ. Res.* 4, 279–288. doi: 10.1016/j.jher.2010.04.016

Niu, J., Chen, J., and Sun, L. (2015). Exploration of drought evolution using numerical simulations over the Xijiang (West River) basin in South China. *J. Hydrol.* 526, 68–77. doi: 10.1016/j.jhydrol.2014.11.029

Palmer, W. (1965). *Meteorological Drought. Research Paper No.45*. Washington, DC: U.S. Department of Commerce.

Pierce, D. W., Barnett, T. P., Santer, B. D., and Gleckler, P. J. (2009). Selecting global climate models for regional climate change studies. *Proc. Natl. Acad. Sci. U.S.A.* 106, 8441–8446. doi: 10.1073/pnas.0900094106

Prudhomme, C., Giuntoli, I., Robinson, E. L., Clark, D. B., Arnell, N. W., Dankers, R., et al. (2014). Hydrological droughts in the 21st century, hotspots and uncertainties from a global multimodel ensemble experiment. *Proc. Natl. Acad. Sci. U.S.A.* 111, 3262–3267. doi: 10.1073/pnas.1222473110

Riahi, K., and Nakicenovic, N. (2007). Greenhouse gases-integrated assessment. *Technol. Forecast. Soc. Chang.* 74, 873–1108.

Srinivasa Raju, K., Sonali, P., and Nagesh Kumar, D. (2017). Ranking of CMIP5-based global climate models for India using compromise programming. *Theor. Appl. Climatol.* 128, 563–574. doi: 10.1007/s00704-015-1721-1726

Sun, Q., Miao, C., and Duan, Q. (2015). Projected changes in temperature and precipitation in ten river basins over China in 21st century. *Int. J. Climatol.* 35, 1125–1141. doi: 10.1002/joc.4043

Sunde, M. G., He, H. S., Hubbart, J. A., and Urban, M. A. (2017). Integrating downscaled CMIP5 data with a physically based hydrologic model to estimate potential climate change impacts on streamflow processes in a mixed-use watershed. *Hydrol. Process.* 31, 1790–1803. doi: 10.1002/hyp.11150

Svoboda, M., LeComte, D., Hayes, M., Heim, R., Gleason, K., Angel, J., et al. (2002). The drought monitor. *Bull. Am. Meteorol. Soc.* 83, 1181–1190. doi: 10.1175/1520-0477(2002)083<1181:tdm>2.3.co;2

Tan, H., Cai, R., Chen, J., and Huang, R. (2016). Decadal winter drought in Southwest China since the late 1990s and its atmospheric teleconnection: decadal drought in southwest china. *Int. J. Climatol* 37, 455–467. doi: 10.1002/joc.4718

Tan, M. L., Ibrahim, A. L., Yusop, Z., Chua, V. P., and Chan, N. W. (2017). Climate change impacts under CMIP5 RCP scenarios on water resources of the Kelantan River Basin. *Malaysia. Atmos. Res.* 189, 1–10. doi: 10.1016/j.atmosres.2017.01.008

Teng, J., Vaze, J., Chiew, F. H. S., Wang, B., and Perraud, J. M. (2012). Estimating the relative uncertainties sourced from GCMs and hydrological models in modeling climate change impact on runoff. *J. Hydrometeorol.* 13, 122–139. doi: 10.1175/JHM-D-11-058.1

Thomson, A. M., Calvin, K. V., Smith, S. J., Kyle, G. P., Volke, A., Patel, P., et al. (2011). RCP4.5: a pathway for stabilization of radiative forcing by 2100. *Clim. Change* 109, 77–94. doi: 10.1007/s10584-011-0151-154

Vicente-Serrano, S. M., Zabalza-Martínez, J., Borràs, G., López-Moreno, J. I., Pla, E., Pascual, D., et al. (2017). Extreme hydrological events and the influence of reservoirs in a highly regulated river basin of northeastern Spain. *J. Hydrol. Reg. Stud.* 12, 13–32. doi: 10.1016/j.ejrh.2017.01.004

Wanders, N., and Wada, Y. (2015). Human and climate impacts on the 21st century hydrological drought. *J. Hydrol.* 526, 208–220. doi: 10.1016/j.jhydrol.2014.10.047

Wang, L., and Chen, W. (2014). A CMIP5 multimodel projection of future temperature, precipitation, and climatological drought in China. *Int. J. Climatol.* 34, 2059–2078. doi: 10.1002/joc.3822

Wang, Y., and Li, Z. (2005). Observed trends in extreme precipitation events in China during 1961–2001 and the associated changes in large−scale circulation. *Geophys. Res. Lett.* 32:2005.

Wood, A. W., Leung, L. R., Sridhar, V., and Lettenmaier, D. P. (2004). Hydrologic implications of dynamical and statistical approaches to downscaling climate model outputs. *Clim. Change* 62, 189–216. doi: 10.1023/B:CLIM.0000013685.99609.9e

Wu, C., Xian, Z., and Huang, G. (2016). Meteorological drought in the Beijiang River basin, South China: current observations and future projections. *Stoch. Environ. Res. Risk Assess.* 30, 1821–1834. doi: 10.1007/s00477-015-1157-1157

Xiao, M., Qiang, Z., and Chen, X. (2012). Regionalization and changing properties of drought events along the pearl River Basin. *J. Catastrophol.* 27, 12–18.

Xu, K., Yang, D., Yang, H., Li, Z., Qin, Y., and Shen, Y. (2015). Spatio-temporal variation of drought in China during 1961-2012: a climatic perspective. *J. Hydrol.* 526, 253–264. doi: 10.1016/j.jhydrol.2014.09.047

Yan, D., Werners, S. E., Ludwig, F., and Huang, H. Q. (2015). Hydrological response to climate change: the Pearl River, China under different RCP scenarios. *J. Hydrol. Reg. Stud.* 4, 228–245. doi: 10.1016/j.ejrh.2015.06.006

Yuan, F., Zhao, C., Jiang, Y., Ren, L., Shan, H., Zhang, L., et al. (2017). Evaluation on uncertainty sources in projecting hydrological changes over the Xijiang River basin in South China. *J. Hydrol.* 554, 434–450. doi: 10.1016/j.jhydrol.2017.08.034

Zhai, J. Q., Liu, B., Hartmann, H., Su, B., Jiang, T., and Fraedrich, K. (2010). Dryness/wetness variations in ten large river basins of China during the first 50 years of the 21st century. *Quat. Int.* 226, 101–111. doi: 10.1016/j.quaint.2010.01.027

Zhang, S., and Lu, X. X. (2009). Hydrological responses to precipitation variation and diverse human activities in a mountainous tributary of the lower Xijiang. *China. Catena* 77, 130–142. doi: 10.1016/j.catena.2008.09.001

Zhang, Y., Li, W., Chen, Q., Pu, X., and Xiang, L. (2017). Multi-models for SPI drought forecasting in the north of Haihe River Basin, China. *Stoch. Environ. Res. Risk Assess.* 31, 2471–2481. doi: 10.1007/s00477-017-1437-1435

Zhou, Y., and Zhang, J. (2014). Application of GIS in downscaling regional climate model results over the province of Ontario. *Environ. Syst. Res.* 3:8. doi: 10.1186/2193-2697-3-8

Ziehmann, C. (2008). Comparison of a single−model EPS with a multi−model ensemble consisting of a few operational models. *Tellus A* 52, 280–299. doi: 10.3402/tellusa.v52i3.12266

Conflict of Interest: The authors declare that the research was conducted in the absence of any commercial or financial relationships that could be construed as a potential conflict of interest.

frontiers in Earth Science

ORIGINAL RESEARCH
published: 13 May 2020
doi: 10.3389/feart.2020.00140

Lidar Observed Optical Properties of Tropical Cirrus Clouds Over Gadanki Region

Nellore Manoj Kumar and Kannan Venkatramanan*

Department of Physics, Sri Chandrasekharendra Saraswathi Viswa Mahavidyalaya (SCSVMV Deemed University), Kanchipuram, India

The presence of cirrus cloud has its impact on the earth's radiation budget. In order to study the effect of cirrus clouds in the tropical regions, it is essential to understand, and characterize their optical properties. The optical properties of high altitude cirrus clouds are obtained using the polarization diversity ground based Mie lidar instrument at a tropical latitude station in the Indian subcontinent. Lidar measurements are taken for one year (2013) at National Atmospheric Research Laboratory (NARL), located at Gadanki (13.5°North, 79.2°East; 375 m AMSL), India and are used for the present investigation. Altitude variations of optical depth and depolarization ratio are discussed. In the altitude range of 10–17 km, the range of the optical depth and depolarization ratio of cirrus cloud was found to be 0.01–0.4 and 0.1–0.4, respectively. The interdependence of optical depth as a function of depolarization ratio is analyzed and a positive correlation is observed (0.3950). From the measured optical depth values, it is categorized that 8, 77, and 14% of the cirrus clouds are sub-visual, thin, and thick clouds. The monthly and seasonal variations of optical properties of cirrus clouds were analyzed. Summary of cirrus cloud layer statistics and the statistical variation (seasonal) of the optical properties of cirrus clouds is presented for the period of study.

Keywords: altitude, cirrus clouds, depolarization, lidar, optical depth

OPEN ACCESS

Edited by:
Xander Wang,
University of Prince Edward Island, Canada

Reviewed by:
Simone Lolli,
Institute of Methodologies for Environmental Analysis (CNR), Italy
Bijoy Vengasseril Thampi,
Science Systems and Applications, Inc., United States

****Correspondence:***
Nellore Manoj Kumar
nelloremk@gmail.com

Specialty section:
This article was submitted to Atmospheric Science, a section of the journal Frontiers in Earth Science

Received: *12 January 2020*
Accepted: *16 April 2020*
Published: *13 May 2020*

Citation:
Manoj Kumar N and Venkatramanan K (2020) Lidar Observed Optical Properties of Tropical Cirrus Clouds Over Gadanki Region. Front. Earth Sci. 8:140. doi: 10.3389/feart.2020.00140

INTRODUCTION

High altitude cirrus clouds (cold clouds) are thin and wispy, mainly composed of ice crystals (Lynch et al., 2002) of dissimilar shape and size. Cirrus clouds cover 16.7% of the earth's surface with the highest fraction of occurrence in the tropics (Sassen et al., 2008, 2009). Studies of these clouds are important to understand the climatic nature and to predict the future (Nazaryan et al., 2008). It plays a crucial role in earth's radiation budget (Liou, 1986; Mc Farquhar et al., 2000; Campbell et al., 2016; Lolli et al., 2017) as well as in the climate and weather studies. The impact of cirrus clouds (ice phase clouds) on the earth's climate system based on two radiative effects are explained by Stephens et al. (2004). A positive radiative effect known as green house effect (traps the outgoing long-wave radiation emitted by the earth and the atmosphere) and a negative radiative effect also known as albedo effect (reflects the incoming solar radiation). Both lead to warming and cooling of the earth's atmospheric system

(Lolli et al., 2017), whose significance depends on the thickness of the cloud. At the Top Of the Atmosphere (TOA) if the cirrus cloud is optically thin (0.03> cloud optical depth <0.3), then its albedo is low which causes positive radiative forcing and the greenhouse effect warms the atmosphere. If the cirrus cloud is optically thick (cloud optical depth >0.3), then its albedo is high which produces negative radiative forcing, and the albedo effect cools the atmosphere (Fu and Liou, 1993; Fahey and Schumann, 1999). The significant roles of these two competitive effects typically depend on the optical properties of cirrus clouds (Zerefos et al., 2003). Hence the radiative balance strongly depends on optical properties of cirrus clouds. Their optical properties control the radiative forcing of the earth's atmospheric system and hence the detailed measurements of cirrus clouds are important at different geographical locations. Optical properties of cirrus clouds vary during different seasons causing cooling or warming of the earth's atmospheric climate system (Ramanathan and Collins, 1991). In order to estimate the role of optical properties of cirrus clouds at the TOA, it is required to study their optical properties in terms of optical depth, depolarization ratio, and their seasonal variations.

Light Detection And Ranging (Lidar), a remote sensing tool that provides information on vertical distribution of various types of cirrus clouds like sub visual, thin and thick (or dense or opaque), and multi-layered clouds, rain and evaporation (Lolli et al., 2020), aerosols (Lolli et al., 2019), gas concentration (Foth et al., 2015), and wind speed (Lolli et al., 2013), etc. It also provides region wise information on geometrical and optical properties with high spatial and temporal resolutions. Generally, Lidar detects clouds with their back scattering signal, and provides an excellent way to obtain the optical properties of cirrus clouds. Both of these are derived by inverting lidar backscattering signals from cirrus clouds. Over tropics (Sassen and Cho, 1992; Heymsfield and McFarquehar, 1996). it is reported that the distribution of optical properties of cirrus clouds play a key role in radiative effects. Various studies are done at different seasons to analyze the variations of geometrical and optical properties of cirrus clouds using ground-based lidar over Gadanki region (Krishnakumar et al., 2014; Pandit et al., 2015; Manoj Kumar et al., 2019). Ground based lidar observations for the climatology of cirrus clouds over a fixed single location cannot be considered globally as uncertainties in the properties of the cloud vary from one region to other.

The optical properties of cirrus clouds would be highly useful in the calculation of radiative effects of climate system which greatly affects the earth's radiation budget. Also, it is essential in understanding the interaction of cloud-radiation effects. Studies related to optical properties of cirrus clouds (depolarization ratio and optical depth) and their dependence on atmospheric parameters (temperature, pressure, and relative humidity, etc.) are of great importance in cloud research. Studies on optical properties of cirrus clouds at various seasons over Gadanki region will have an immense value in playing a vital role and will help to reduce global climate model uncertainty in forecasting temperature change at the end of the century. In the present work, ground-based lidar measurements (January 2013 to December 2013) are used to investigate the optical properties of cirrus clouds at tropical latitude Gadanki, India.

INSTRUMENTATION AND DATA ANALYSIS

The present research work is carried out using Mie LIDAR situated at National Atmospheric Research Laboratory (NARL), Gadanki, a tropical rural station located at 13.5°North, 79.2°East in a height of 375 m Above Mean Sea Level (AMSL) in southern India. The lidar system is a monostatic, pulsed, biaxial, and dual polarization system. To study the properties of cirrus clouds, the lidar system usually operates for about three to 5 h during night time. This constraint in observation is due to the appearance of thick clouds at low altitudes and rain. Since 2007, the lidar transmitter uses an Nd:YAG (model : PL8050) pulsed laser operating at its wavelength (s) of 532 nm with average pulse energy of 600 mJ, pulse width of 7 ns, and Pulse Repetition Frequency (PRF) of 50 Hz (Pandit et al., 2015).

The receiver system employs two independent telescopes, one to cover middle and upper atmosphere altitudes (30 to 80 km) termed as Rayleigh receiver and another to cover Upper Troposphere and Lower Stratosphere (UTLS) altitudes (4 to 40 km) termed as Mie receiver. Data related to backscattered photon count collected from Mie receiver [consisting of 35.5 cm diameter, Schmidt–Cassegrain type, and Field of View (FOV) 1 mrad], in the altitude range of 8–20 km is used in the present study. From that data depolarization measurements can be calculated. Beam splitter is used to split the beam into cross polarized (perpendicular) and co-polarized (parallel) signal components. These parallel (designated as P-channel) and perpendicular (designated as S-channel) signal components are individually recorded through two identical and orthogonally aligned Photo Multiplier Tubes (PMT's). For Mie receiver channel, an MCS-Plus (EG and G ORTEC) multi channel photon counter is used for recording the photon counting signals as a function of time (altitude). The dwell time is 2 μs for the photon counting system, which corresponds to an altitude resolution of 300 m and the backscattered returns are summed for 250 s. The returns of backscatter signal from the cirrus clouds are received as photon counts and are analyzed by employing lidar inversion methods (Fernald, 1984; Klett, 1985). The backscattered signals in terms of photon counts are corrected with the molecular profile obtained from the co-located radiosonde measurements. In this present research work, the optical properties of cirrus clouds such as optical depth, and depolarization ratio are determined using Klett inversion algorithm. To perform this, the reference altitude should be considered as 35 km at which the backscattering contribution is mainly from the air molecules and the aerosol scattering can be neglected. Further it is used to calculate the back scattering ratio, which is defined as the ratio of total backscattering coefficient to the molecular backscattering coefficient.

The back Scatter Ratio (SR) is estimated based on the aerosol and molecular backscattering coefficients [$\beta_a(r)$ and $\beta_m(r)$] and is defined as the ratio of sum of the aerosol and molecular

backscattering coefficients divided by the molecular backscatter coefficient can be written as

$$SR_{cirrus}(r) = \frac{\beta_a(r) + \beta_m(r)}{\beta_m(r)} \quad (1)$$

where SR_{cirrus} is the cirrus clouds back SR, $\beta_a(r)$, and $\beta_m(r)$ are the backscattering coefficients of aerosols and molecules with respect to the altitude r. Throughout the analysis, a threshold value of SR > 1.5 is maintained for the determination of cirrus clouds (Sandhya et al., 2015). It can be noted that the presence of cirrus can be in the altitude region 10–18 km on many days during January-December 2013.

The lidar backscattering signals are processed separately for the co-and cross polarization channels in order to obtain the SR profile. Using the appropriate molecular density profiles (by Rayleigh theory), the molecular backscattering values (Gadanki station) at each altitude for the P and S channels were calculated. The molecular air density profile can be obtained from the co-located balloon (radiosonde) measurements. The linear depolarization ratio (LDR) is allied with the backscattering coefficients and is estimated using lidar signals from the scattering ratios of P and S channels. The LDR, denoted as $\delta(r)$, is obtained from the scattering ratios of cross polarized S-channel $S_{\perp,SR}(r)$ to the co polarized P-channel $P_{\parallel,SR}(r)$ from the lidar backscatter returns, with respect to the altitude r and is estimated as

$$\delta(r) = \left(\frac{S_{\perp,SR}(r)}{P_{\parallel,SR}(r)}\right) \quad (2)$$

The depolarization measurements provide an insight to the distribution of ice and water within the clouds. The presence of water droplets and ice crystals with different shapes in the cloud can be distinguished based on the LDR values. It is a function of the cloud altitude, temperature, and the distribution of humidity within the cloud.

The extinction coefficient $\alpha(r)$ can be calculated in terms of backscattering ratio and molecular backscattering coefficient (Klett, 1981) and is given by

$$\alpha(r) = LR\,[\beta_m(r)\,(SR_{cirrus}(r) - 1)] \quad (3)$$

where LR is the Lidar Ratio (LR) generally known as extinction-to-backscatter ratio, which is a key factor to study the nature of cloud particles. The LR values (range dependent) are then calculated from the method explained by Satyanarayana et al. (2010). The LR value of 25 sr is used for the present study.

Cloud Optical Depth (COD) denoted as τ_{cirrus}, is obtained from the integral of cloud extinction profile $\alpha(r)$ of cloud base (r_{base}) to the cloud top (r_{top}), respectively, and is expressed as

$$\tau_{cirrus} = \int_{r_{base}}^{r_{top}} \alpha(r)dr \quad (4)$$

The threshold value of COD was first proposed by Sassen and Cho (1992) and classified based on the following criteria; $\tau_{cirrus} < 0.03$ for Sub Visual Cirrus (SVC) clouds $0.03 < \tau_{cirrus} < 0.3$ for Thin Cirrus (TC) clouds and $0.3 < \tau_{cirrus} < 3$ for thick or opaque or Dense Cirrus (DC) clouds. These values are obtained from their visual appearance and the same is utilized in the present study.

RESULTS AND DISCUSSION

Lidar dataset for the year 2013 (January 2013 to December 2013) was used to study the altitude dependence, distribution, monthly, and seasonal variations of the optical properties of cirrus clouds. In order to analyze the optical properties of cirrus clouds, the annual prominent seasons at this site are categorized as winter (December–January–February), pre–monsoon (March–April–May), monsoon or South–West monsoon (June–July–August), and post–monsoon or North–East monsoon (September–October–November). The ground based lidar observations were made for 122 different nights, out of which cirrus clouds were detected during 98 nights. Even though seasonal behavior could not be attributed with this limited lidar data, a general tendency shall be observed. In the present analysis, Mie lidar dataset was used up to 40 km for measuring the vertical profiles of optical depth and depolarization ratio for the period of observation.

Optical Properties of Cirrus Clouds

Optical Depth and Depolarization Ratio

Optical depth (or thickness) is defined as the opacity of the cloud and it is a measurable quantity of extinction coefficient within the boundaries of the cloud. COD gives information about the radiative behavior and determines whether the cloud can cause positive or negative radiative effect. It significantly depends on geometrical thickness and composition of the clouds. LDR is related to the ice-crystal habits that are largely unknown for a specific type of crystal (Chen et al., 2002). Over the tropics, all cirrus clouds are formed by non-spherical ice particles and hence these particles will cause significant depolarization to the backscattered radiation. The observed LDR values range from 0.1–0.6 for non spherical ice particles of cirrus clouds and nearly zero for spherical water droplets of non cirrus clouds (Sassen, 1995; Chen et al., 2002; Manoj Kumar et al., 2019). LDR is sensitive to shape ratios (Noel et al., 2002) and crystal shape (Dai et al., 2019). The LDR values associated with the cirrus clouds indicate the presence of ice crystals with different compositions (Sassen, 1995) and help in the study of cloud formation and dynamics (Sassen and Cho, 1992).

Figures 1A,B represents the pseudo color plots (2D histograms) of variations in optical depth and depolarization ratio as a function of altitude of cirrus cloud (ranging from 9 to 19 km) for the year 2013. Colorbar from figure represent the percentage of COD and LDR cases. The lower altitude clouds below 9 km have low depolarization values suggesting that these clouds do not contain ice particles, which may be attributed due to temperature threshold (Campbell et al., 2016). It can been seen that from **Figure 1A** the majority of the cirrus clouds in the altitude ranging from 10 to 17 km shows the optical depth values ranging from 0.01–0.4, but few clouds with higher values of optical depth are also seen. Similarly at the same altitude range (**Figure 1B**) the depolarization ratio values ranging from 0.1–0.4, but quite a few higher values are also seen. It was observed that

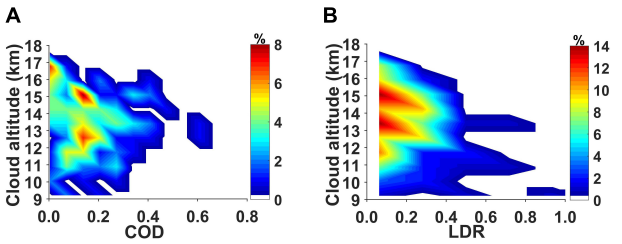

FIGURE 1 | Altitude variations of **(A)** optical depth and **(B)** depolarization ratio.

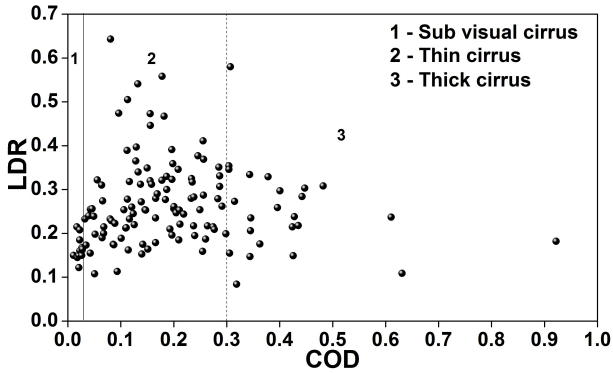

FIGURE 2 | Interdependence of measured cloud optical depth and linear depolarization ratio.

at the altitude above 12 km the LDR values are high ranging from 0.3–0.6, which shows good agreement with the values reported in literature (Sassen and Dodd, 1988; Sassen et al., 2001; Radhakrishnan et al., 2010). At higher altitudes, the ice clouds (cirrus) have larger ice crystals due to low temperature range resulting in high depolarization values (Chen et al., 2002). The lower depolarization values around 8 km indicate the presence of large water droplets which is associated with high temperature of the clouds, suggesting that the clouds at lower altitudes (<8 km) may be stratus type of clouds consisting of mixed phase due to weak ice crystal scattering.

It can be seen that the optical depth and LDR increase with cloud altitude in the range 10–14 km and above that they decrease. Above 14 km, optical depth values range from 0.1–0.3, and LDR ranges from 0.15–0.3. Almost thin cirrus clouds whose optical depth values above 0.03 and below 0.3 occur in the altitudes between 11 and 17 km. Generally, the high altitude cirrus clouds with depolarization ratios >0.3 indicate the existence of hexagonal shaped and <0.3 indicate the presence of thin plates or horizontally oriented ice crystals (Sassen, 1995). As shown in **Figure 1B**, in the altitude range between 11 and 17 km, the cirrus clouds have higher values of depolarization with the corresponding LR (25 sr) which signifies the presence of hexagonal ice crystals (Radhakrishnan et al., 2010) during the period of study. The variations in the optical depth and depolarization ratio mainly depend upon the altitudes at which cloud occurs.

Scatter plot in **Figure 2** represent the interdependence of measured optical depth of cirrus clouds categorized with depolarization ratio for the year 2013. A positive correlation (0.3950) between optical depth and the depolarization ratio is observed. The scatter plot classifies the cirrus layers into SVC clouds, TC clouds, and DC clouds. SVC clouds show lower values of depolarization which indicate that the clouds may consist of plate to column (or) aggregate type of ice crystals (Radhakrishnan et al., 2010). TC shows higher values of depolarization and DC shows moderate values of depolarization indicating the presence of randomly oriented crystals in ice clouds.

In case of thin cirrus clouds, it is observed that optical depth increases with depolarization ratio. The moderate values of depolarization ratio with higher values of optical depth show the occurrence of thick cirrus clouds. Lower values of depolarization ratio indicate the presence of super cooled water droplets in cirrus clouds (year 2013). In the present analysis, it is found that 8% of the observed cirrus clouds are sub visual ($\tau_{cirrus} < 0.03$; Campbell et al., 2016), 77% of the observed cirrus clouds are thin ($0.03 > \tau_{cirrus} < 0.3$), and 14% of the observed cirrus clouds are thick ($\tau_{cirrus} > 0.3$) over the Gadanki station (**Figure 2**). The values obtained for thin clouds are in good agreement with the values reported (Manoj Kumar et al., 2019) for the years 2014 and 2015. Hence, for the year 2013, the occurrence frequency of optical depth (figure not shown) reveals that most of the observed cirrus clouds over this region are thin clouds only. The observed values vary due to the difference in period of observation. Lidar data are collected only during night time because of the high presence of low level clouds during day time. Hence its impact may be negligible. The quality of Lidar profiles are rigorously checked based on their signal to noise ratio before using them for analysis. The data is considered mainly because of the strong backscattered signal received from the cloud. Also, the signal is corrected by the molecular contribution using ancillary computed values, i.e., the atmospheric model. Satellite observations are not analyzed because of satellite long revisit time over the site taken for study. Thus ground based observations are predominantly significant and hence they are used in the present analysis. **Table 1** gives the statistical summary of cirrus cloud layers for the period of observation. Mean optical properties of cirrus clouds and their standard deviation (in parentheses) are calculated from the mean values for the year 2013.

Monthly Variations of the Optical Properties of Cirrus

Figure 3 shows the total number of observations of lidar and cirrus clouds during the year 2013. The lidar dataset could not

TABLE 1 | Statistical details of mean optical properties of cirrus cloud.

Year (2013)	No. of cirrus layers	τ_{cirrus}	$\delta(r)$
All cirrus	6013	0.20 (0.15)	0.29 (0.21)
DC	843	0.45 (0.18)	0.29 (0.19)
TC	4665	0.16 (0.07)	0.31 (0.22)
SVC	505	0.02 (0.01)	0.16 (0.02)

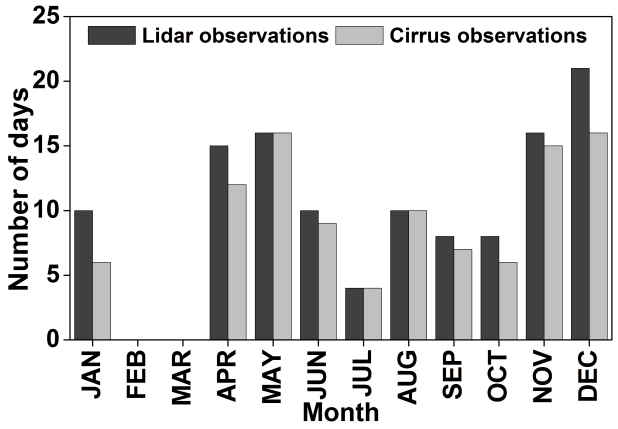

FIGURE 3 | Lidar and cirrus clouds observations during 2013.

be obtained during February and March 2013 which may be due to unforeseen circumstances. The lidar and cirrus observations are maximum in the month of December (winter season) and minimum in the month of July (monsoon season). In general, during the monsoon period, the convective activity is high at the tropical regions. The occurrence of cirrus clouds is found to be more prominent during the monsoon period.

The monthly mean variation of optical properties of cirrus clouds are depicted in **Figures 4A,B** during the period of observation. The symbolized vertical bars in both the cases represent the standard deviation from their calculated values. In this study, only single scattering effects are considered. Higher values of optical depth and depolarization ratio are observed during the post-monsoon season and lower values are observed during August (monsoon season) and January (winter season). Higher values of optical depth refer to the maximum thickness of the cloud and its variability mainly depends upon the thickness and composition of the cloud. The observed monthly mean variation in the optical depth is due to the thickness of the largely available cloud which also results in the change in microphysical properties of clouds (Motty et al., 2015).

Higher values of COD and LDR are observed due of the presence of ice crystals inside the cloud. It is observed that (**Figure 4A**) the average value of optical depth ranges between 0.15 and 0.3 which indicate the presence of optically thin clouds over this site. Similarly, from **Figure 4B** the depolarization ratio values are found to be between 0.2 and 0.45 indicating the presence of ice crystals inside the cirrus clouds. However, most of the cirrus clouds seen over Gadanki are optically thin clouds. Sassen and Campbell (2001) identified the structure of clouds as column crystals, thick plate and hexagonal (randomly oriented) thin plate based on the values of depolarization ratio. The typical mean value of optical depth and depolarization ratio of cirrus clouds occurred during different nights of corresponding months as a function of observed cloud altitude are depicted in **Figures 5A,B**. The days corresponding to the months of observations of cirrus clouds in terms of optical depth and LDR are shown in symbol square (blue) and upward pointing triangle (blue), respectively. The cloud altitude is shown as red colored circle in both the cases.

Seasonal Variation of the Optical Properties of Cirrus

The variation of optical depth as a function of depolarization ratio for the four prominent seasons of a year such as winter, pre-monsoon, monsoon, and post-monsoon are illustrated (pseudo colored plots) in **Figures 6A–D**. The colorbar denotes the number of LDR cases. It is observed that majority of cirrus clouds formed over Gadanki are optically thin having depolarization ratio ranging from 0.1 to 0.6 (Sassen and Cho, 1992). It also shows the presence of moderate thick cirrus clouds and minority SVC clouds based on their optical depth values for all seasons during 2013. **Table 2** illustrates the statistics of optical properties of cirrus clouds for the four prominent seasons along with all seasons. During each season, different numbers of cases together with all seasons are found in a year over the tropical rural site Gadanki for the year 2013.

It was observed that in all seasons, most of the thin cirrus clouds formed over Gadanki have higher values of extinction (scattering and absorption together), leading to positive radiative forcing. The depolarization ratios vary with optical depth for all

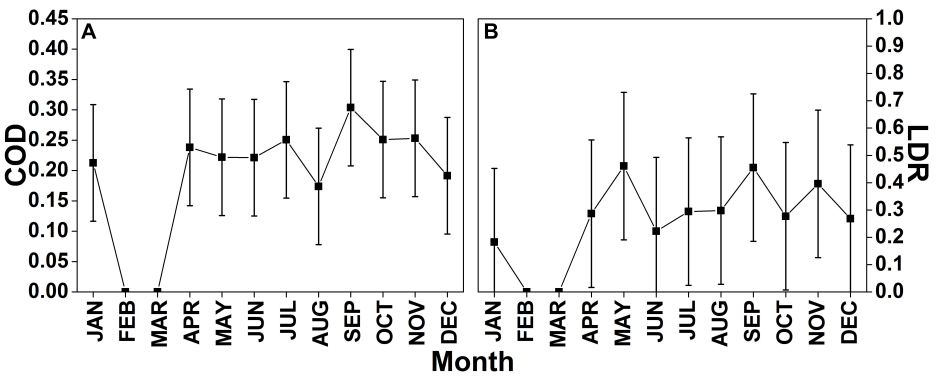

FIGURE 4 | (A) Monthly mean variation of optical depth and **(B)** depolarization ratio of cirrus clouds. Vertical bars represent standard deviation.

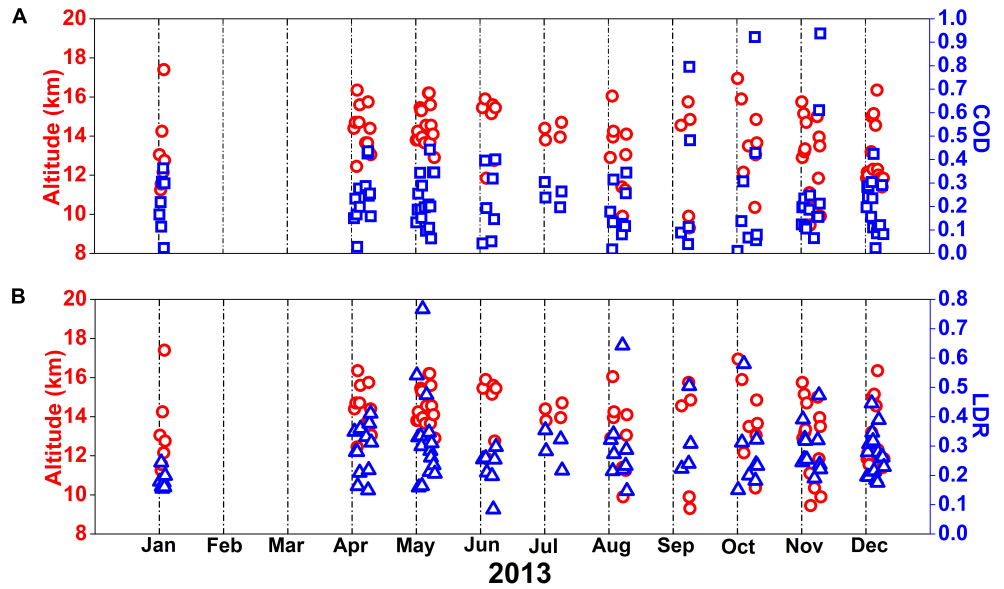

FIGURE 5 | (A) Optical depth and **(B)** linear depolarization ratio values of cirrus clouds for each case in a month with respect to cloud altitude.

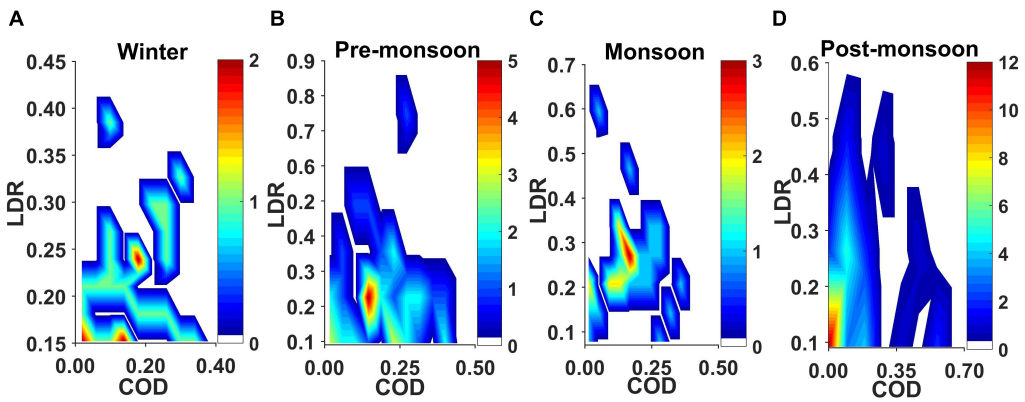

FIGURE 6 | Optical depth versus depolarization ratio of cirrus clouds for **(A)** winter, **(B)** pre-monsoon, **(C)** monsoon, and **(D)** post-monsoon seasons during the year 2013.

TABLE 2 | Statistics of optical properties of cirrus clouds over Gadanki, India for the year 2013.

Type of cirrus	Optical properties	Winter (23 cases)	Pre-monsoon (28 cases)	Monsoon (20 cases)	Post-monsoon (27 cases)	All seasons (98 cases)
Sub visual ($\tau_{cirrus} < 0.03$)	$\tau_{cirrus}\delta(r)$	0.015 (0.013) 0.172 (0.017)	0.008 (0.014) 0.078 (0.111)	0.013 (0.012) 0.119 (0.109)	0.021 (0.006) 0.161 (0.022)	0.014 (0.005) 0.132 (0.043)
Thin ($0.03 > \tau_{cirrus} < 0.3$)	$\tau_{cirrus}\delta(r)$	0.120 (0.105) 0.226 (0.042)	0.120 (0.106) 0.347 (0.101)	0.173 (0.050) 0.337 (0.059)	0.121 (0.049) 0.350 (0.112)	0.133 (0.026) 0.315 (0.059)
Thick (or) Dense ($\tau_{cirrus} > 0.3$)	$\tau_{cirrus}\delta(r)$	0.349 (0.021) 0.223 (0.081)	0.398 (0.019) 0.252 (0.028)	0.335 (0.034) 0.259 (0.082)	0.661 (0.102) 0.449 (0.190)	0.436 (0.152) 0.296 (0.103)

Parenthesis values represent the standard deviation from their respective mean value. τ_{cirrus} *is cirrus cloud optical depth and* $\delta(r)$ *is the linear depolarization ratio.*

the seasons indicating the presence of different ice crystals in the cirrus clouds. The depolarization ratio varies during winter season which shows that the cirrus clouds are composed of supercooled (like ice) particles which affect the earth's radiative budget. During the pre-monsoon season, the depolarization ratio varies due to process of heterogeneous nucleation

(DeMott et al., 2010) indicating the presence of randomly oriented of complex ice crystals inside the cirrus clouds. Low values of depolarization ratio during monsoon season indicate the presence of more water content in the clouds and its high value indicate the presence of moderate to heavy ice particles. During post monsoon season, the depolarization ratio values are almost same, indicating the presence of mixed phase of water, ice and complex ice crystals in the cirrus clouds. The optical depth is high during this season. These cirrus clouds are observed near to the tropopause layer and hence there is a chance for formation of ice crystals during the period of observation. Radiation budget of cirrus cloud depends on orientation, phase and size of cloud particles. Thus it is observed that there is a strong seasonal variation in the optical properties of cirrus clouds. In general, thin cirrus clouds occurred more frequently than the sub-visual and thick clouds. The upper portion of the cirrus clouds contain randomly oriented hexagonal ice crystals with different orientations and sizes, whereas the lower portion contains the mixed phase of ice crystals and liquid water droplets.

CONCLUSION

The optical properties of cirrus clouds were analyzed using ground-based polarization diversity lidar over the tropical site, Gadanki, India from January 2013 to December 2013. 98 days of cloud data (80.3%) were analyzed out of 122 days of lidar observation. Results show that cirrus clouds were observed in the altitude region between 8–20 km. The values of optical depth and depolarization ratio range from 0.01–0.4 and 0.1–0.4, respectively. It is observed that the optical depth and LDR increases in the altitude range of 10–14 km and then decreases. Above 12 km, the LDR values are high (0.3–0.6) which confirms the presence of ice crystals in cirrus cloud having thick plate structures. The interdependence of optical depth and LDR of cirrus clouds is analyzed and a positive correlation is observed between them. Based on the measured optical depth values, cirrus clouds are classified as sub-visual cirrus (8%), thin cirrus (77%), and thick cirrus (14%) and it is observed that most of the cirrus clouds that are formed above this site are found to be thin clouds. Monthly and seasonal variations of optical depth and LDR of cirrus clouds were presented during the period. Summary of cirrus layer statistics for the total time of observation and the statistical variation of the optical properties of cirrus clouds is presented for the period of observation.

The present research study can be relatively useful in the parameterization of cirrus clouds and can be a corresponding tool to satellite product that cannot provide vertical structure of cloud. The kind of information presented here is required as input in the calculation of radiative transfer models. Moreover, the statistics of cirrus clouds properties could also be useful in the improvement and validation of the subsequent satellite product retrievals.

DATA AVAILABILITY STATEMENT

All datasets generated for this study are included in the article/supplementary material.

AUTHOR CONTRIBUTIONS

NM: conceptualization, methodology, formal analysis, and draft preparation. KV: supervision and editing.

ACKNOWLEDGMENTS

The authors thank NARL data center, Gadanki for providing the LIDAR datasets and necessary support. The authors express their gratitude to the two reviewers for their resourceful suggestions in shaping the work as is presented now.

REFERENCES

Campbell, J., Lolli, S., Lewis, J., Gu, Y., and Welton, E. (2016). Daytime cirrus cloud top-of-the-atmosphere radiative forcing properties at a mid latitude site and their global consequences. *J. Appl. Meteorol. Clim.* 55, 1667–1679. doi: 10.1175/JAMC-D-15-0217.1

Chen, W. N., Chiang, C. W., and Nee, J. B. (2002). Lidar ratio and depolarization ratio for cirrus clouds. *Appl. Opt.* 41, 6470–6476. doi: 10.1364/AO.41.006470

Dai, G., Wu, S., Song, X., and Liu, L. (2019). Optical and Geometrical properties of cirrus clouds over the tibetan plateau measured by LiDAR and radiosonde sounding during the summertime in 2014. *Remote Sens.* 11, 1–17. doi: 10.3390/rs11030302

DeMott, J. P., Prenni, A. J., Liu, X., Kreidenweis, S. M., Petters, M. D., Twohy, C. H., et al. (2010). Predicting global atmospheric ice nuclei distributions and their impacts on climate. *PNAS* 107, 11217–11222. doi: 10.1073/pnas.0910818107

Fahey, D. W., and Schumann, U. (1999). "Aviation-Produced Aerosols and Cloudiness," in *Intergovernmental Panel on Climate Change Special Report on Aviation and the Global Atmosphere*, eds J. E. Penner, D. H. Lister, D. J. Griggs, D. J. Dokken, and M. McFarland (Cambridge: Cambridge University Press), 65–120.

Fernald, F. D. (1984). Analysis of atmospheric lidar observations: some comments. *Appl. Opt.* 23, 652–653. doi: 10.1364/AO.23.000652

Foth, A., Baars, H., Di Girolamo, P., and Pospichal, B. (2015). Water vapour profiles from Raman lidar automatically calibrated by microwave radiometer data during HOPE. *Atmos. Chem. Phys.* 15, 7753–7763. doi: 10.5194/acp-15-7753-2015

Fu, Q., and Liou, K. N. (1993). Parameterization of the radiative properties of cirrus clouds. *J. Atmos. Sci.* 50, 2008–2025. doi: 10.1175/1520-0469(1993)050<2008:potrpo>2.0.co;2

Heymsfield, J., and McFarquehar, G. M. (1996). High albedos of cirrus in the tropical pacific warm pool: microphysical interpretations from CEPEX and from Kwajalein. Marshall Islands. *J. Atmos. Sci.* 53, 2424–2451. doi: 10.1175/1520-0469(1996)053<2424:haocit>2.0.co;2

Klett, J. D. (1981). Stable analytical inversion solution for processing lidar returns. *App. Opt.* 20, 211–220. doi: 10.1364/AO.20.000211

Klett, J. D. (1985). Lidar inversion with variable backscatter/extinction ratios. *App. Opt.* 24, 1638–1643. doi: 10.1364/AO.25.000833

Krishnakumar, V., Satyanarayana, M., Radhakrishnan, S. R., Dhaman, R. K., Jayeshlal, G. S., Motty, G. N. S., et al. (2014). Lidar investigations on the optical and dynamical properties of cirrus clouds in the upper troposphere and lower stratosphere regions at a tropical station. Gadanki, India (13.5°N, 79.2°E). *J. Appl. Remote Sens.* 8, 1–22. doi: 10.1117/1.JRS.8.083659

Liou, K. N. (1986). Influence of cirrus clouds on weather and climate processes: a global perspective. *Mon. Weather Rev.* 114, 1167–1199. doi: 10.1175/1520-0493(1986)114<1167:ioccow>2.0.co;2

Lolli, S., Campbell, J. R., Lewis, J. R., Gu, Y., Marquis, J. W., Chew, B. N., et al. (2017). Daytime top-of-the-atmosphere cirrus cloud radiative forcing properties at Singapore. *J. Appl. Meteorol. Climatol.* 56, 1249–1257. doi: 10.1175/jamc-d-16-0262.1

Lolli, S., Delaval, A., Loth, C., Garnier, A., and Flamant, P. H. (2013). 0.355-micrometer direct detection wind lidar under testing during a field campaign in consideration of ESA's ADM-Aeolus mission. *Atmos. Meas. Tech.* 6, 3349–3358. doi: 10.5194/amt-6-3349-2013

Lolli, S., Khor, W. Y., Matjafri, M. Z., and Lim, H. S. (2019). Monsoon season quantitative assessment of biomass burning clear-sky aerosol radiative effect at surface by ground-based lidar observations in pulau pinang. Malaysia in 2014. *Remote Sens.* 11, 1–14. doi: 10.3390/rs11222660

Lolli, S., Vivone, G., Lewis, J. R., Sicard, M., Welton, E. J., Campbell, J. R., et al. (2020). Overview of the New Version 3 NASA micro-pulse lidar network (MPLNET) automatic precipitation detection algorithm. *Remote Sens.* 12, 1–16. doi: 10.3390/rs12010071

Lynch, D. K., Sassen, K., Starr, D., and Stephens, G. (eds.) (2002). *Cirrus*. New York, NY: Oxford University Press, 499.

Manoj Kumar, N., Venkatramanan, K., and Vellaisamy, A. L. R. (2019). A statistical method for determining optical and geometrical characteristics of cirrus clouds. *Climate* 7:72. doi: 10.3390/cli7050072

Mc Farquhar, G. M., Heymsfield, A. J., Spinhirne, J. D., and Hart, B. (2000). Thin and sub visual tropopause tropical cirrus: observations and radiative impacts. *J. Atmos. Sci.* 57, 1841–1853. doi: 10.1175/1520-0469(2000)057<1841:tasttc>2.0.co;2

Motty, S., Satyanarayana, M., Jayeshlal, G. S., Krishnakumar, V., and Mahadevan Pillai, V. P. (2015). Optical properties of cirrus clouds in the tropical tropopause region during two contrasting seasons. *Niscair* 44, 155–166.

Nazaryan, H., McCormick, M. P., and Menzel, W. P. (2008). Global characterization of cirrus clouds using CALIPSO data. *J. Geophys. Res.* 113, 1–11. doi: 10.1029/2007JD009481

Noel, V., Chepfer, H., Ledanois, G., Delaval, A., and Flamant, P. H. (2002). Classification of particle effective shape ratios in cirrus clouds based on the lidar depolarization ratio. *Appl. Opt.* 41, 4245–4257. doi: 10.1364/ao.41.004245

Pandit, A. K., Gadhavi, H. S., Venkat Ratnam, M., Raghunath, K., Rao, S. V. B., and Jayaraman, A. (2015). Long-term trend analysis and climatology of tropical cirrus clouds using 16 years of lidar data set over Southern India. *Atmos. Chem. Phys.* 15, 13833–13848. doi: 10.5194/acp-15-13833-2015

Radhakrishnan, S. R., Satyanarayana, M., Krishnakumar, V., Mahadevan Pillai, V. P., Raghunath, K., Venkata Ratnam, M., et al. (2010). Optical properties of cirrus clouds at a tropical Indian station Gadanki. Tirupati (13.5°N, 79.2°E). *J. Appl. Remote Sens.* 4, 1–17. doi: 10.1117/1.3525238

Ramanathan, V., and Collins, W. (1991). Thermodynamic regulating of ocean warming by cirrus clouds deduced from observations of the 1987 El Niño. *Nature* 351, 27–32. doi: 10.1038/351027a0

Sandhya, M., Sridharan, S., Indira Devi, M., Niranjan, K., and Jayaraman, A. (2015). A case study of formation and maintenance of a lower stratospheric cirrus cloud over the tropics. *Ann. Geophys.* 33, 599–608. doi: 10.5194/angeo-33-599-2015

Sassen, K. (1995). Lidar cloud research. *Rev. Laser Eng.* 23, 148–153. doi: 10.2184/lsj.23.148

Sassen, K., Barnett, M., Wang, Z., and Mace, G. G. (2001). Cloud and aerosol research capabilities at FARS: the facility for atmospheric remote sensing. *Bull. Amer. Meteor. Soc.* 82, 1119–1138. doi: 10.1175/1520-0477(2001)082<1119:caarca>2.3.co;2

Sassen, K., and Campbell, J. R. (2001). A midlatitude cirrus cloud climatology from the facility for atmospheric remote sensing, part I: macrophysical and synoptic properties. *J. Atmos. Sci.* 58, 481–496. doi: 10.1175/1520-0469(2001)058<0481:amcccf>2.0.co;2

Sassen, K., and Cho, B. S. (1992). Subvisual-thin cirrus lidar dataset for satellite verification and climatological research. *J. Appl. Meteor.* 31, 1275–1285. doi: 10.1175/1520-0450(1992)031<1275:stcldf>2.0.co;2

Sassen, K., and Dodd, G. C. (1988). Homogeneous nucleation rate for highly super cooled cirrus cloud droplets. *J. Atmos. Sci.* 45, 1357–1369. doi: 10.1175/1520-0469(1988)045<1357:hnrfhs>2.0.co;2

Sassen, K., Wang, Z., and Liu, D. (2008). Global distribution of cirrus clouds from Cloudsat/Cloud-Aerosol Lidar and Infrared Pathfinder Satellite Observations (CALIPSO) measurements. *J. Geophys. Res.* 113, 1–12. doi: 10.1029/2008JD009972

Sassen, K., Wang, Z., and Liu, D. (2009). Cirrus clouds and deep convection in the tropics: insights from CALIPSO and CloudSat. *J. Geophys. Res. Atmos.* 114, 1–11. doi: 10.1029/2009JD011916

Satyanarayana, M., Radhakrishnan, S. R., Mahadevan Pillai, V. P., Veerabhuthiran, S., Raghunath, K., Presennakumar, B., et al. (2010). Laser radar characterization of atmospheric aerosols in the troposphere and stratosphere using range dependent lidar ratio. *J. Appl. Remote Sens.* 4, 1–20. doi: 10.1117/1.3306573

Stephens, G. L., Wood, N. B., and Gabriel, P. M. (2004). An assessment of the parameterization of subgrid-scale cloud effects on radiative transfer. part i: vertical overlap. *J. Atmospheric Sci.* 61, 715–732. doi: 10.1175/1520-0469(2004)061<0715:aaotpo>2.0.co;2

Zerefos, C. S., Eleftheratos, K., Balis, D. S., Zanis, P., Tselioudis, G., and Meleti, C. (2003). Evidence of impact of aviation on cirrus cloud formation. *Atmos. Chem. Phys.* 3, 1633–1644. doi: 10.1039/b905334b

Conflict of Interest: The authors declare that the research was conducted in the absence of any commercial or financial relationships that could be construed as a potential conflict of interest.

frontiers in Earth Science

ORIGINAL RESEARCH
published: 08 September 2020
doi: 10.3389/feart.2020.00268

The Effect of Precipitation on Hydropower Generation Capacity: A Perspective of Climate Change

Li Wei[1], Li Jiheng[1], Guo Junhong[1]*, Bao Zhe[1], Fu Lingbo[2] and Hou Baodeng[3]*

[1] Ministry of Education Key Laboratory of Resources and Environmental Systems Optimization, North China Electric Power University, Beijing, China, [2] The Electricity Engineering School, Guangxi University, Nanning, China, [3] State Key Laboratory of Simulation and Regulation of Water Cycle in River Basin, China Institute of Water Resources and Hydropower Research, Beijing, China

Hydropower, which is the most extensively used renewable energy, is sensitive to the change of streamflow under the great impact of precipitation. According to the relationship between the hydropower station generation and local precipitation, the impact of precipitation on hydropower can be analyzed. In this paper, the global climate model and regional climate model simulations in precipitation are compared firstly, and the high-resolution precipitation data are then calculated by stepwise clustering analysis statistical downscaling method. Secondly, based on the hydropower potential (HP), the hydropower response model driven by precipitation is established. Finally, the simulated generation of a hydropower station in Dadu River basin is used as a case to validate this proposed model. The results show that precipitation will increase by around 42% from May to August in study region, while it will decrease by 40% in other months in RCP4.5. For different periods of reservoir scheduling, the precipitation will increase by about 40% in the Neutral I and Wet period, while it will decrease by around 30% in other periods, which will lead to the shortening of the peak period of hydropower generation and the peak value will be decreased. Correspondingly, the results show power generation will decrease by around 12% from June to December and increase by around 4% in the rest months. On the other hand, owing to the changes in precipitation, the future power generation will increase by 25% in Neutral I and decrease by 13.5% in other periods, but the total hydropower generation will remain. The results can provide some decision support for future water resources management in Dadu river basin, especially for the planning and operation of hydropower stations.

Keywords: hydropower, precipitation, regional climate model, stepwise clustering analysis, downscaling

OPEN ACCESS

Edited by:
Shan Zhao,
Shandong University, China

Reviewed by:
Caterina Valeo,
University of Victoria, Canada
Lidan Guo,
Hohai University, China
Huazhang Zhao,
Peking University, China

***Correspondence:**
Li Jiheng
412720716@qq.com
Guo Junhong
handangjh@163.com

Specialty section:
This article was submitted to Interdisciplinary Climate Studies, a section of the journal Frontiers in Earth Science

Received: *28 October 2019*
Accepted: *15 June 2020*
Published: *08 September 2020*

Citation:
Wei L, Jiheng L, Junhong G, Zhe B, Lingbo F and Baodeng H (2020) The Effect of Precipitation on Hydropower Generation Capacity: A Perspective of Climate Change. Front. Earth Sci. 8:268. doi: 10.3389/feart.2020.00268

INTRODUCTION

According to the IPCC AR5, with the increase of global populations and economies, the man-made emissions of greenhouse gases have remained rising and reached the industrial history peak at the beginning of the 21st century (IPCC, 2013). The global mean temperature at the end of the 21st century will probably be 1.5°C higher than that in 1899–1990 under the influence of current emission trends (Arnette, 2017).

China, which is located in East Asia, has a vast territory, abundant climate zones and complex topography (Guo et al., 2017a). Owing to the stronger regional seasonal wind led by global warming, more moisture in the atmosphere will be transported to land areas from ocean, then

resulting in more extreme precipitation events in China recently (Hui et al., 2018). For example, ten million residents were displaced and billion dollars economy cost was caused by the Yangtze River flood in 1998 (Chen and Zong, 2000). The serious urban waterlogging events in Beijing in 2012 caused thousands people death and 11.6 billion economic losses (Zhang D.L. et al., 2013).

As one of the effective energies to alleviate the greenhouse effect caused by fossil energy, renewable energy is in a fast-growing demand. Renewable energy has taken 18.2% in world total energy consumption in 2016 (REN21, 2018). In the meantime, the development of renewable energy in China is also rapidly developed. Renewable energy generation, which is up to 1676 TWh, has taken 30% in total national power generation in 2017 (CREO, 2018). Relative to other types of renewable energy, owing to the lowest cost, easier to control and manage and lower intermittent and uncertainly means, hydropower is a kind of the most widely used renewable energies (Panwar et al., 2011; Chu and Majumdar, 2012; Jiang et al., 2018). In 2017, the new generating capacity of hydropower in China is 9.12 GW, and the total installed capacity reached 341 GW. The hydropower generation has taken almost 20% of total power generation, which is far more than the generation of wind energy (5%) and solar energy (2%). Therefore, more hydropower is planned by China's government to generate electricity and replace fuel energy (IHA, 2018).

Hydropower is sensitive to climate change, especially for precipitation. Based on the change of runoff, Ali et al. (2018) evaluated and predicted the power generation of seven large hydropower stations in India. Results illustrated that the specific future climate may increase hydropower generation by about 25%. Liu et al. (2016) thought runoff and reservoir storage has a great influence on hydropower, then Generation Hydropower Potential (GHP) and Development Hydropower Potential (DHP) are tested based on 8 Global Hydro Models (GHMs), indicating that GHP will have a 3–6% increase between 2070 and 2099. Obviously, precipitation has a direct influence on basin runoff change, which will finally affect hydropower generation (Berghuijs et al., 2014; Wasko and Sharma, 2017). Based on the observed data, Chilkoti et al. (2017) found that generation of hydropower stations and the precipitation have close links, the generation of hydropower stations may rise 39% when the precipitation rise 43%. Above all, climate change has a more direct impact on precipitation, but few studies are analyzing the influence of precipitation changes under the context of global warming on hydropower generation (Guo et al., 2018). Hence, it is significant to explore the relationship between precipitation changes and hydropower generation, and the results could provide some suggestions and measures to the government policy makers in hydropower to response the climate change better.

In this study, stepwise cluster analysis (SCA) statistic method is used to downscale future climate data from PRECIS regional climate model (RCM). Then, the hydropower response model driven by precipitation (HRMDP) is established. Finally, a hydropower station in Dadu River basin is taken as a case to quantitatively analyze future climate change influence on hydropower generation.

DATA AND METHODS

As shown in the **Figure 1**, four analysis steps are divided in this paper. The first step is collecting precipitation and power generation data, which include large-scale HadGEM2-ES climate data, observation of meteorological stations and generation data of hydropower stations. Then, the statistical downscaling simulation in precipitation using SCA method is conducted. Specifically, some independent variables in large scale grids in PRECIS RCM, such as precipitation, temperature, humidity and pressure are extracted firstly, afterward, the precipitation in station scale is simulated and projected by the SCA statistic downscaling method. The third step is the establishment of a HRMDP based on the hydropower potential (HP). In the end, we use the projected precipitation under RCP4.5 and RCP8.5 climate emission scenarios to drive the HRMDP to analyze the change in hydropower in the case.

Hydropower Response Model Driven by Precipitation

In general, hydropower generation has a close relationship to precipitation. The increase in precipitation will lead to an increase in power generation, and continuous non-precipitation will cause a decrease in power generation (Chilkoti et al., 2017). **Figure 2** shows that the daily precipitation and daily power generation of station A in Dadu River basin. The high power generation can be found in a high precipitation period (such as from June to September), while low power generation in low precipitation periods (such as from January to April and December). At the same period, power generation shows an increasing trend with increasing precipitation, and vice versa. According to **Figure 2**, we can find that there is a certain relationship between precipitation and power generation, and the power generation is sensitive to the change of precipitation.

Before establishing the hydropower response model, a new conception – HP is introduced. Hydropower potential is the perfect state power generation which only considers the precipitation as the influence condition, it can be calculated by daily precipitation without considering the actual generating capacity. In this paper, HP mainly depends on the daily precipitation. In addition, continually precipitation factor and non-precipitation factor also have influence on HP, which respectively represents the increased coefficient of power generation in the period of continue precipitation and the decline coefficient of power generation in the period of non-precipitation. The detailed calculation method is as follows:

$$HP_n = \sigma_2(HP_{n-1} + \sigma_1 \times R_n) \tag{a1}$$

$$\sigma_1 = \left(\sum_{n=2}^{j} \frac{P_{n-1}-P_n}{R_{n-1}-R_n}\right)/j \tag{a2}$$

$$\sigma_2 = 1 - \left[\left(\sum_{n=2}^{j} \frac{P_{n-1}-P_n}{P_{n-1}}\right)/j\right] \tag{a3}$$

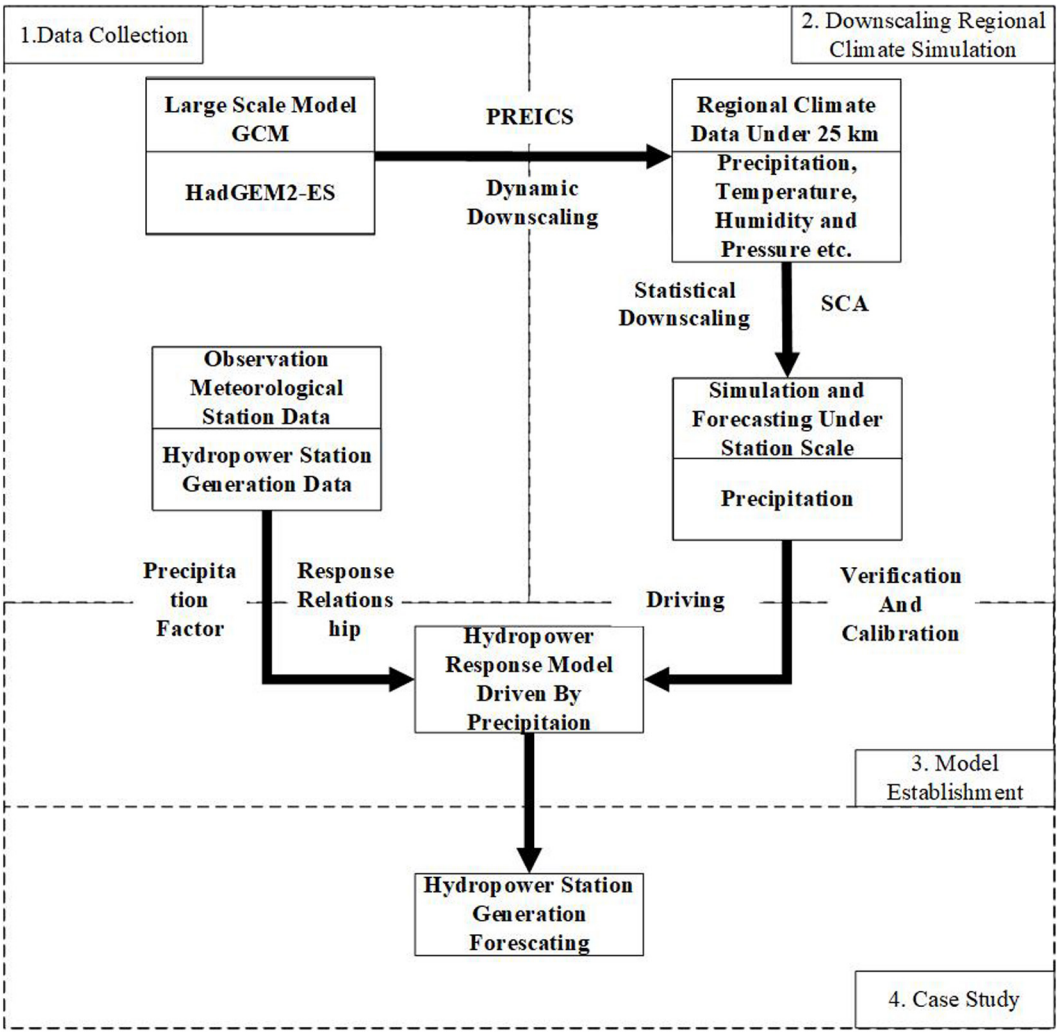

FIGURE 1 | Study flow chart.

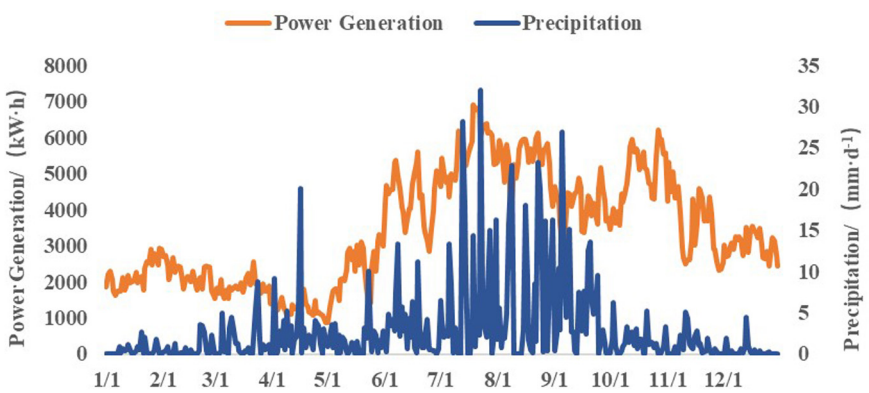

FIGURE 2 | Daily precipitation and power generation of a hydropower station in Dadu River basin.

Notations:
HP_n – HP in the day n, kWh;
R_n – Precipitation in the day n, mm;
σ_1 – The increasing coefficient of generation in the period of continue precipitation, dimensionless;
σ_2 – The decline coefficient of generation in the period of non-precipitation, dimensionless;
P_n – The power generation in the day n, kWh;
j – The number of days in some periods.

Hydropower potential represents the optimal power generation under the current precipitation status. Station power generation is not only restricted by natural factors but also influenced by human society factors (such as power policies and plans). Hence, the controllable coefficient, which represents human characteristics, is added to the formula. Formula b is used to restrict the power generation of actual production, and finally achieves the amount of constrained power generation.

$$\mathrm{HP}_a = (\mathrm{HP}_{\max} + \mathrm{HP}_{\min})/2 \quad \text{(b1)}$$

$$\mathrm{HP}_b = \mathrm{HP}_{\max} - \mathrm{HP}_{\min} \quad \text{(b2)}$$

$$P_{F,n} = [P_{\min} + (P_{\max} - P_{\min})]/ \left[\left(1 + e^{\left(-8\frac{\mathrm{HP}_n - \mathrm{HP}_a}{\mathrm{HP}_b}\right)}\right) + \delta\right] \quad \text{(b3)}$$

Notations:
$\mathrm{HP}_{\max}$ – Maximum HP during this period, kWh;
$\mathrm{HP}_{\min}$ – Minimum HP during this period, kWh;
$P_{\max}$ – Maximum power generation of generator set under the power plan of this period;
$P_{\min}$ – Minimum power generation of generator set under the power plan of this period;
$P_{F,n}$ – The constrained power generation in day n of the period;
δ – The controllable factor, which affected by actual power plan, power policy and more, and it shows as power generation fluctuates at a certain range.

Regional Climate Model

The future precipitation forecasting data are from two climate numerical simulations, which includes HadGEM2-ES and PRECIS. The former is a global climate model (GCM) and is used as the initial and boundary field data to drive the RCM PRECIS for dynamic downscaling. Developed by the UK's The Met Office Hadley Centre, PRECIS is a high-resolution (25 km) RCM and it has been widely used in regional climate simulations and extreme events forecasting (Xu et al., 2009; Kerkhoff et al., 2014; Saini et al., 2015; Guo et al., 2017b, 2018; Hui et al., 2018).

SCA Statistical Downscaling Method

Although the results from RCMs can simulate the climate change of the whole region or basin, the higher-resolution

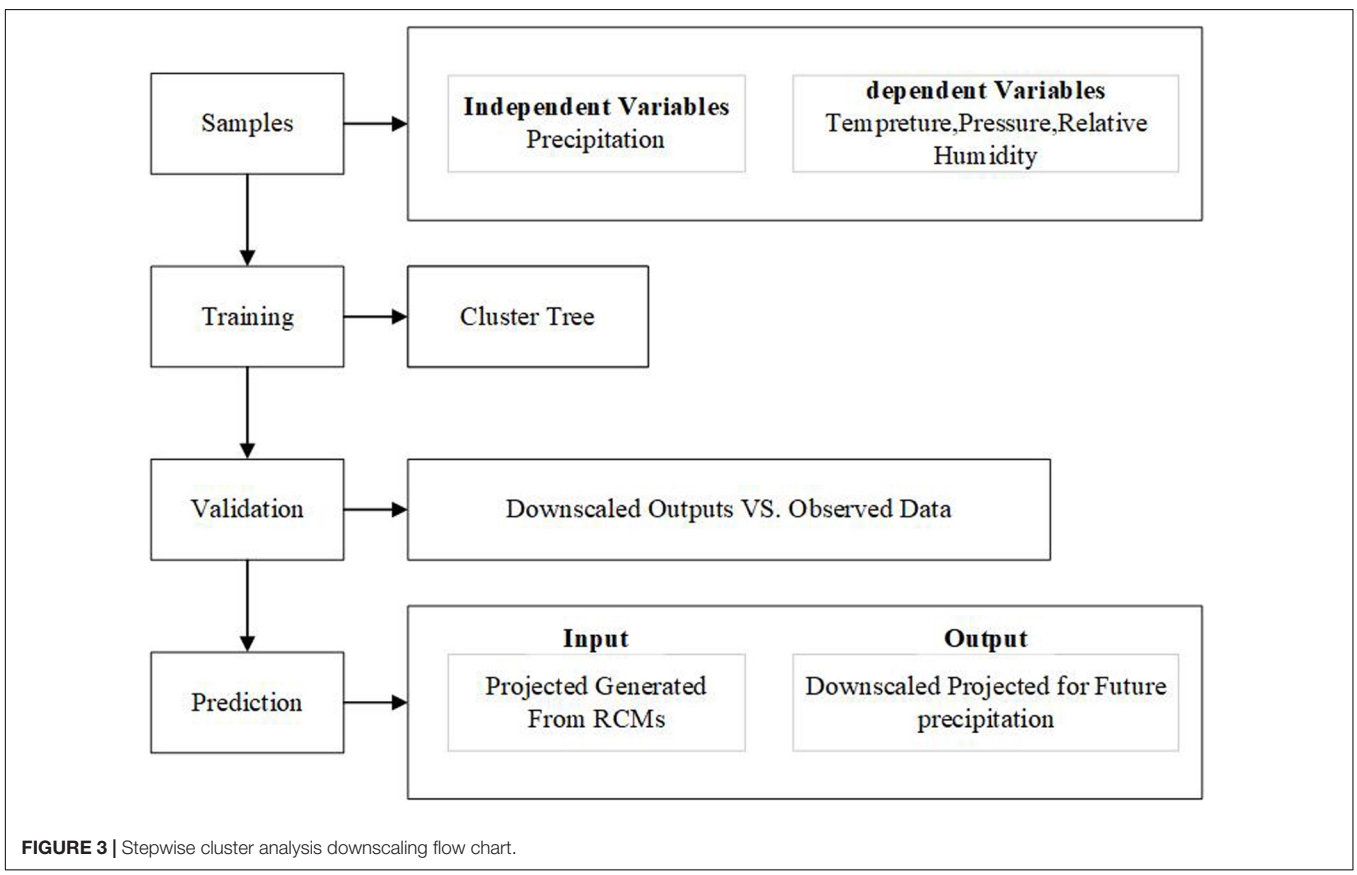

FIGURE 3 | Stepwise cluster analysis downscaling flow chart.

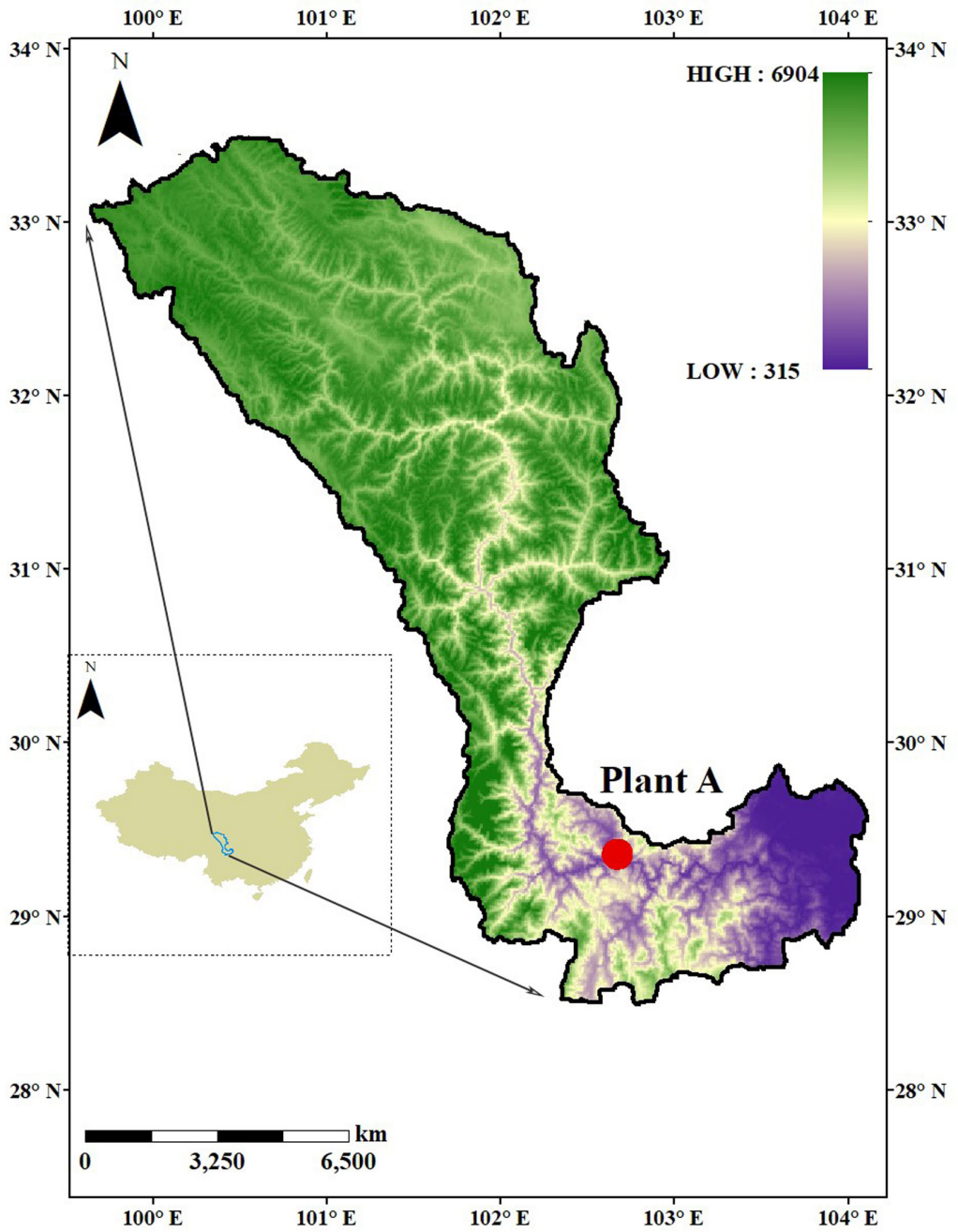

FIGURE 4 | Dadu River basin.

simulations (i.e., station scale) still cannot be met through dynamical downscaling. Therefore, based on the results of RCM, statistical downscaling can be achieved by establishing the numerical statistical relation between the large-scale circulation fields and station-scale climate variables (i.e., precipitation). There are rich methods to be applied, the statistical downscaling has been widely applied in climate change influence analysis on precipitation and hydrology (Bellouin et al., 2011; Jones et al., 2011; Wang et al., 2015). However, it is necessary to select an appropriate statistical downscaling method to reflect the discrete and random characteristics for precipitation. The SCA uses a cluster tree to illustrate the relationship between the large-scale atmosphere fields and high spatial-resolution variables, especially in effectively dealing with the stochastic and non-linear relationships. Through the integration of missing data detection, correlation analysis, model calibration, cluster tree mapping and other auxiliary function modules, SCA can rapidly develop downscaling scenarios of local weather variables

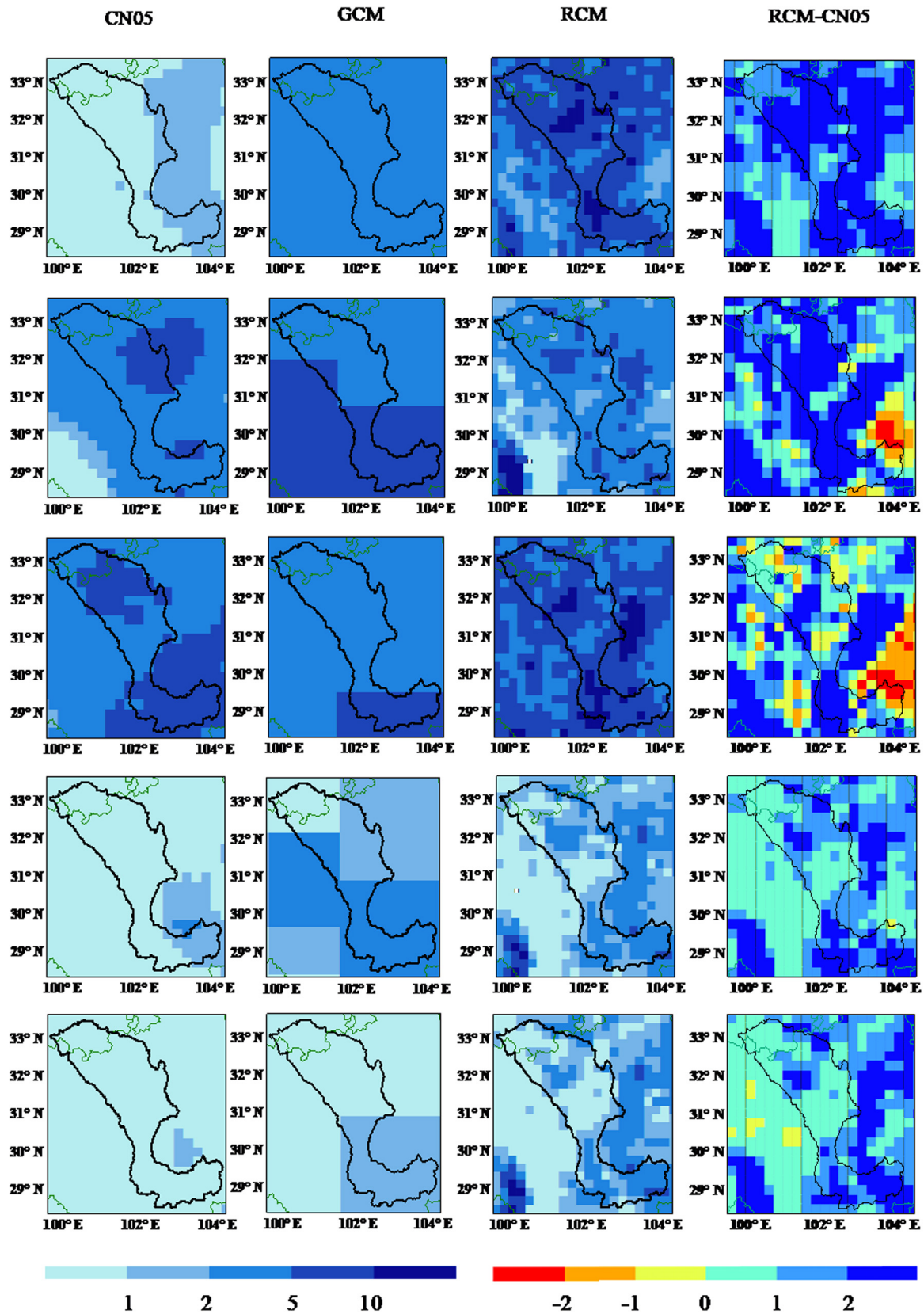

FIGURE 5 | Simulation results and deviation of difference scale models in each period.

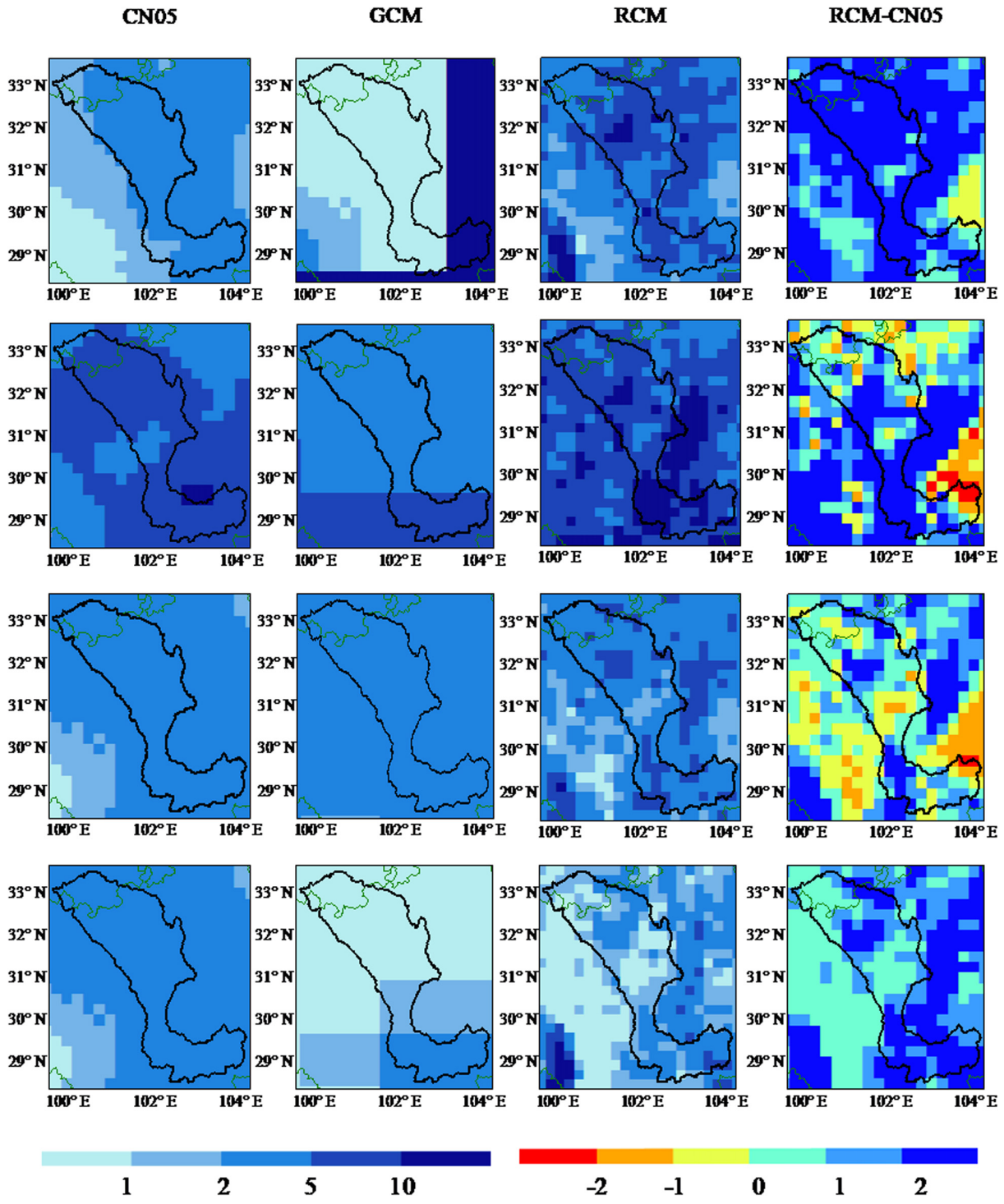

FIGURE 6 | Simulation results and deviation of difference scale models in each season.

under current and future climate forcing, and performs well in predicting precipitation during the verification (Chen et al., 2011; Yang et al., 2016).

As shown in **Figure 3**, the first step in the SCA statistical downscaling is to select large-scale forecast factors. Following previous studies, the variables, including mean sea level pressure, surface airflow strength, surface wind direction, near-surface temperature, surface specific humidity, surface relative humidity, surface divergence, surface meridional velocity and more are selected as initial variables (Duan and Mei, 2013; Li and

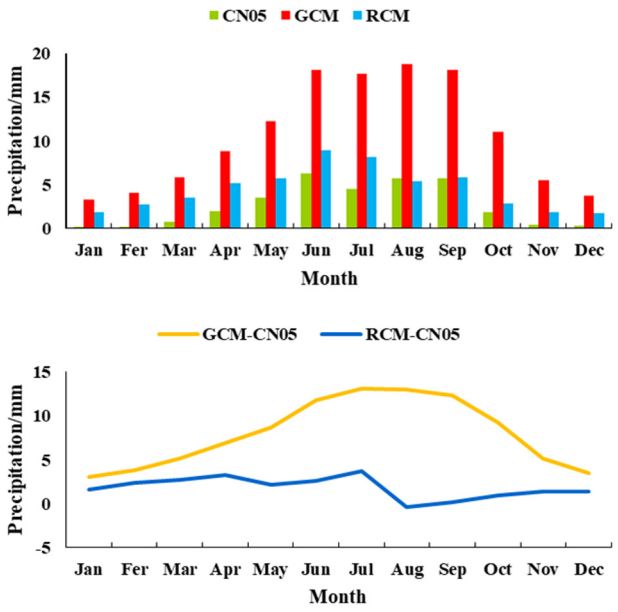

FIGURE 7 | Monthly mean precipitation and deviation of different scale models and observation data.

Yan, 2017). According to correlation analyze, Near-surface temperature, Surface relative humidity and Mean sea level pressure are selected as independent variables in statistical downscaling (Wood et al., 2004; Perkins et al., 2007; Liu et al., 2011). The meteorological station precipitation data are selected as dependent variable. Then, the independent variables of statistical downscaling are constituted as X matrix. The dependent variable is constituted as Y matrix. And using R Studio to create site scale precipitation SCA statistical downscaling training model, and build the clustering tree predictor to establish the quantitative relationship between precipitation and large-scale prediction factors.

Data

The data used for validation is divided into the following categories:

1. Climate simulation data. The future climate data from PRECIS are used to drive the power forecasting model. Its initial field and boundary field data as the driving data is from HadGEM2-ES(GCM). HadGEM2-ES is a coupled AOGCM with atmospheric resolution of N96 (1.875° × 1.25°) with 38 vertical levels and an ocean resolution of 1° (increasing to 1/3° at the equator) and 40 vertical levels. HadGEM2-ES also represents interactive land and ocean carbon cycles and dynamic vegetation with an option to prescribe either atmospheric CO_2 concentrations or to prescribe anthropogenic CO_2 emissions and simulate CO_2 concentrations as described. An interactive tropospheric chemistry scheme is also included, which simulates the evolution of atmospheric composition and interactions with atmospheric aerosols. The model time step is 30 min (atmosphere and land) and 1 h (ocean) (Jones et al., 2011). The PRECIS is able to run at two different horizontal resolutions: 0.44° × 0.44° (approximately 50 km × 50 km) and 0.22° × 0.22° (approximately 25 km × 25 km), with 19

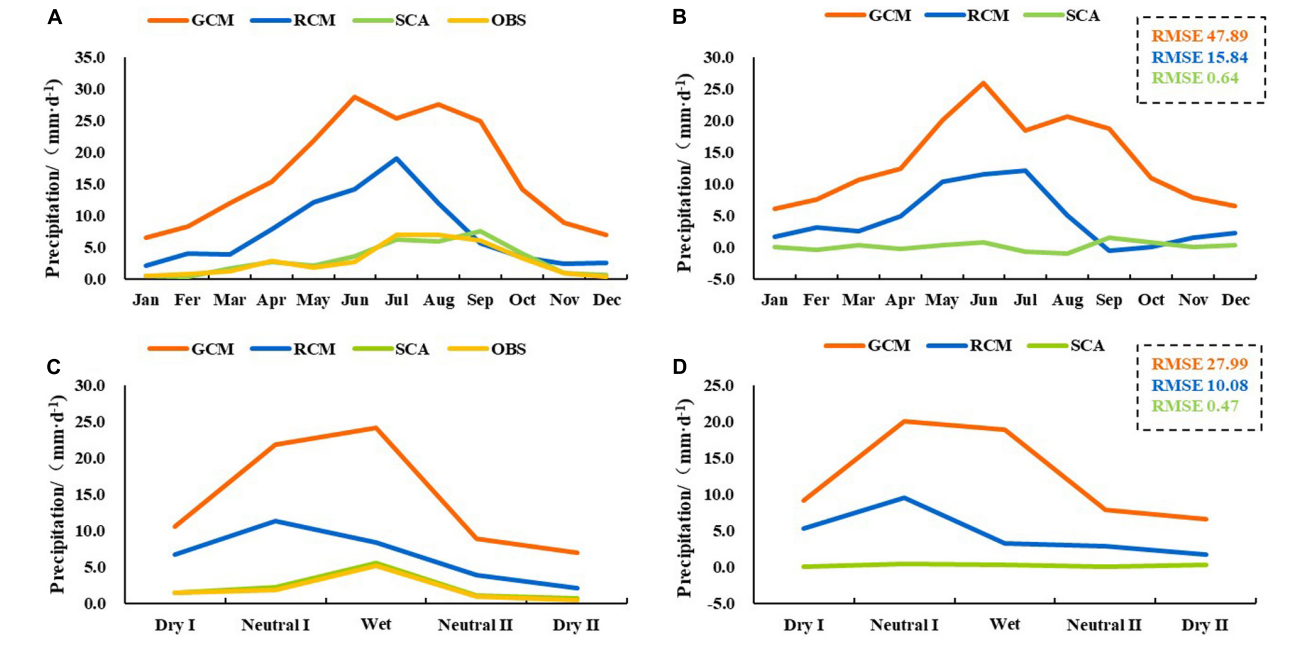

FIGURE 8 | Comparison of precipitation simulation and observed data in different scale models: **(A)** monthly precipitation; **(B)** monthly precipitation error; **(C)** precipitation in period; **(D)** precipitation error in period.

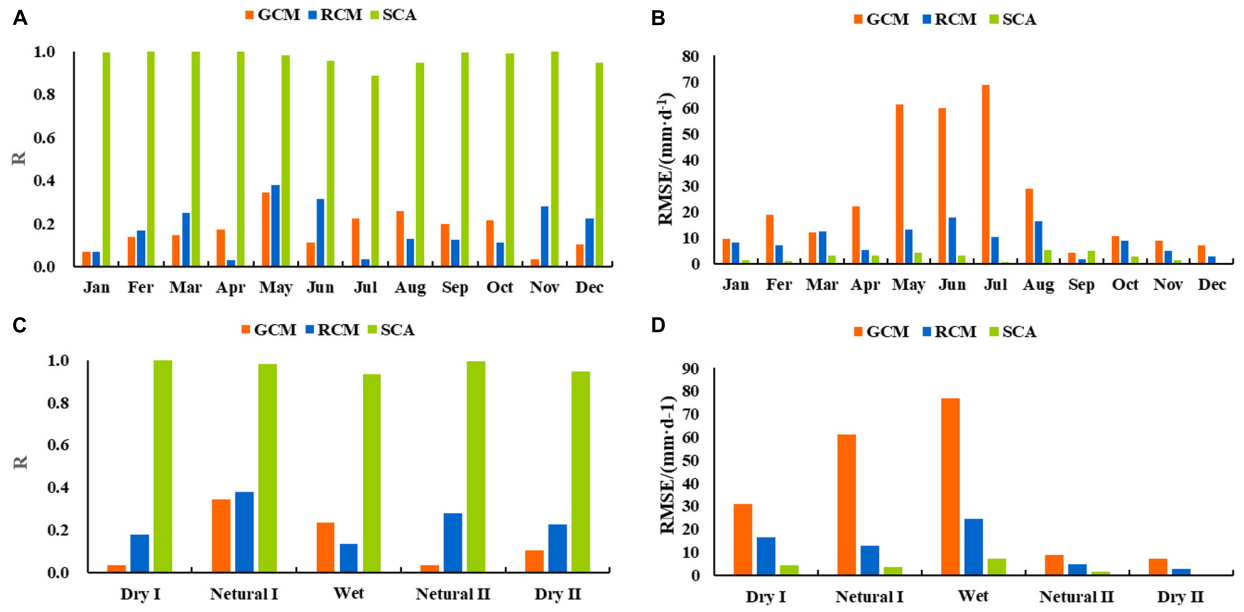

FIGURE 9 | Verification of precipitation simulation and observed data in different scale models: **(A)** monthly correlation coefficient; **(B)** monthly RMSE; **(C)** correlation coefficient in period; **(D)** RMSE in period.

atmospheric levels in the vertical using a hybrid coordinate system (Guo et al., 2017b).

2. Climate Observation data. The CN05 precipitation data set is used to validate the precipitation results of GCM and RCM. CN05 is a dataset consisting of daily mean, maximum, and minimum temperature on a 0.25 × 0.25° grid has been constructed over mainland China for the 45-years period of 1961–2005. CN05 is derived from interpolating observations from 751 stations distributed throughout the entire Chinese territory except Taiwan. The interpolation follows basically the same approach used in generating the CRU dataset, whereby a gridded climatology is calculated first, and then a gridded anomaly is added to obtain the final data (Xu et al., 2009).
3. Meteorological station data. The observation is used to validate the results of RCM and build the HRMDP. It is from the real-time monitoring stations, including daily precipitation, near-surface temperature, surface relative humidity and surface wind speed.
4. Hydropower station data. The daily power generation data is used to calibrate and verify the simulation results of the power forecasting model.

CASE STUDY

The Dadu River basin which shown in **Figure 4**, is located between 99°42'E–103°48'E and 28°15'N–33°33'N and lies in the transition area of Tibet Plateau and Sichuan Basin. Dadu River basin meets the Minjiang River in Leshan. It is the largest tributary of the Minjiang River and the secondary tributary of the Yangzi River. Dadu River Basin has an abundant hydro resource, which has 7.74 × 10^4 km^2 basin area and a total of 149 tributaries. The mainstream, which is 1062 km long and 48.8 km^3 annual net flow, and has 33730 MW water resource reserve. The annual precipitation of Dadu River Basin is about 800–1000 mm, and the precipitation from May to October takes up 80% of the whole

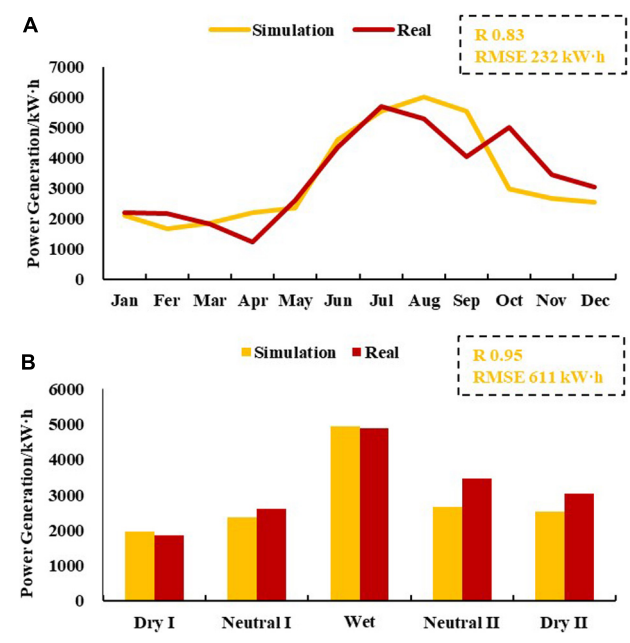

FIGURE 10 | Simulation power generation compare with actual power generation: **(A)** monthly power generation; **(B)** power generation in period.

year (Yang et al., 2017). As a key hydropower development area in China, Dadu River basin has many large power stations.

Station A is one of the largest hydropower stations in China, the power capacity of station A is nearly 3.6 million KW, and the reservoir capacity is 5.337 billion km^3. Due to the greatest power generation in Dadu River Basin and the most abundant water resources, station A is selected as the research object (Zhang and Xu, 2014).

Moreover, according to the precipitation feature of Dadu River basin and power generation plan for station A. Five main power generation periods in a year are divided, which include Dry I (from January to April), Neutral I (May), Wet (from June to October), Neutral II (November) and Dry II (December).

In this paper, we take the power station A as a case and use HRMDP model to build the relationship between meteorological factors and power generation capacity. Then based on the projection in precipitation from dynamical and statistical downscaling results, the influence of precipitation on power generation from 2025 to 2035 will be analyzed.

RESULTS

Simulation and Verification

The results of climate models and their deviations with CN05 in different periods are shown in **Figure 5**. Compared with the results of CN05, GCM underestimates the precipitation in most regions of the basin but overestimates the precipitation in the middle of basin. Due to the rough resolutions in GCM, the results of most areas only show a single value. On the other hand, PRECIS improves the spatial resolutions and shows more details in reproducing the precipitation in Dadu River basin, especially in autumn in **Figure 6**. The results in PRECIS are similar to the observation, and the deviation is between -1 mm and 1 mm in the midstream. In terms of different periods, Dry II shows a better performance (±1 mm biases) than that in Dry I (∼2 mm). From the spatial distribution, the deviation is between 0 and 1 mm in the upstream, while the value is larger (∼2 mm) in the downstream.

Figure 7 shows simulation results in annual cycle obtained from GCM and PRECIS. Compared to CN05, PRECIS can simulate the monthly precipitation in Dadu River Basin reasonably. For example, the highest precipitation occurs in June, while the precipitation in January is smaller. Meanwhile, PRECIS shows a great advantage in simulating the monthly mean precipitation relative to its driving GCM. Lots of overestimations in HadGEM2-ES (especially from May to October) are corrected by PRECIS in dynamic downscaling. Overall, the bias of RCM is kept between −0.34 and 3.67 mm, especially in August (∼−0.34 mm).

Figure 8 is the comparison results between simulation and observation in precipitation data at different spatial scales. The higher in resolutions for climate model, the simulation trend and value of precipitation are closer to the observed data. Specifically, comparing to observation, the simulation results of GCM are overestimated obviously, especially in June or Neutral I, the error is even exceeding 20 mm/day. While the results downscaled by PRECIS have numerous improvements relative to its GCM. However, PRECIS still cannot solve effectively the accuracy in simulating station-scale precipitation. For example, the error is still high in June (about 10 mm) and in Neutral I (about 8 mm). On the other hand, the results from SCA

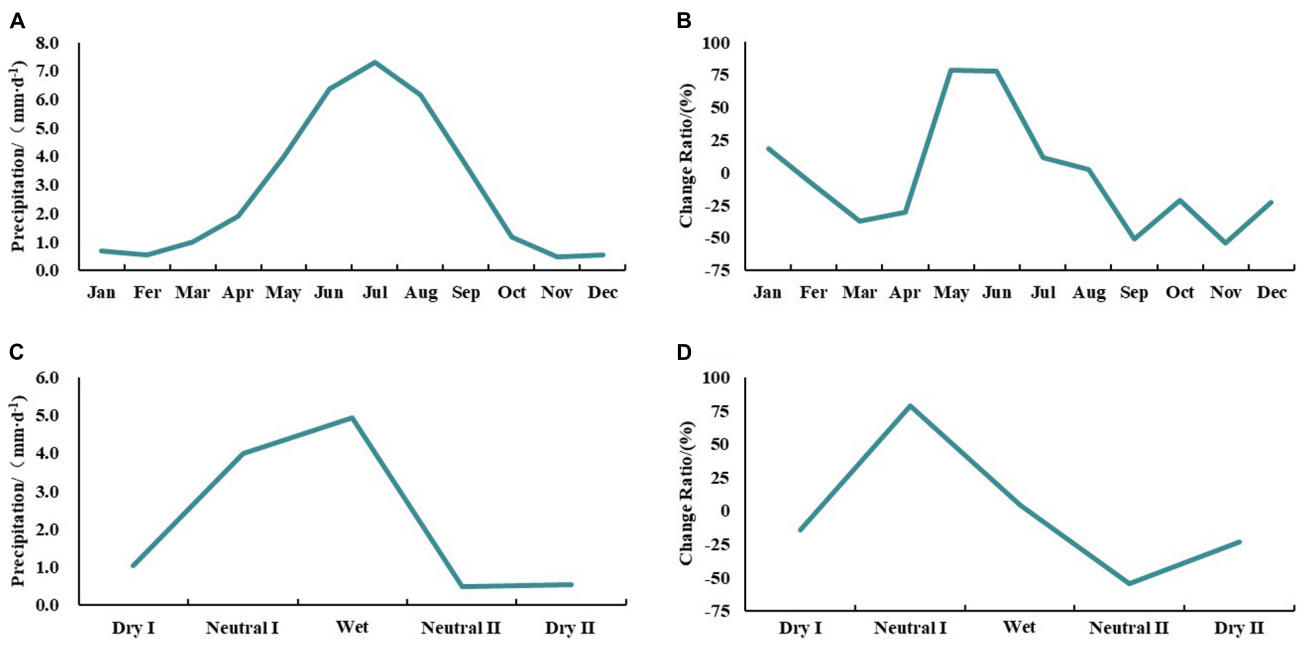

FIGURE 11 | Future precipitation forecasting: **(A)** future monthly precipitation; **(B)** monthly precipitation change; **(C)** future precipitation in period; **(D)** precipitation change in period.

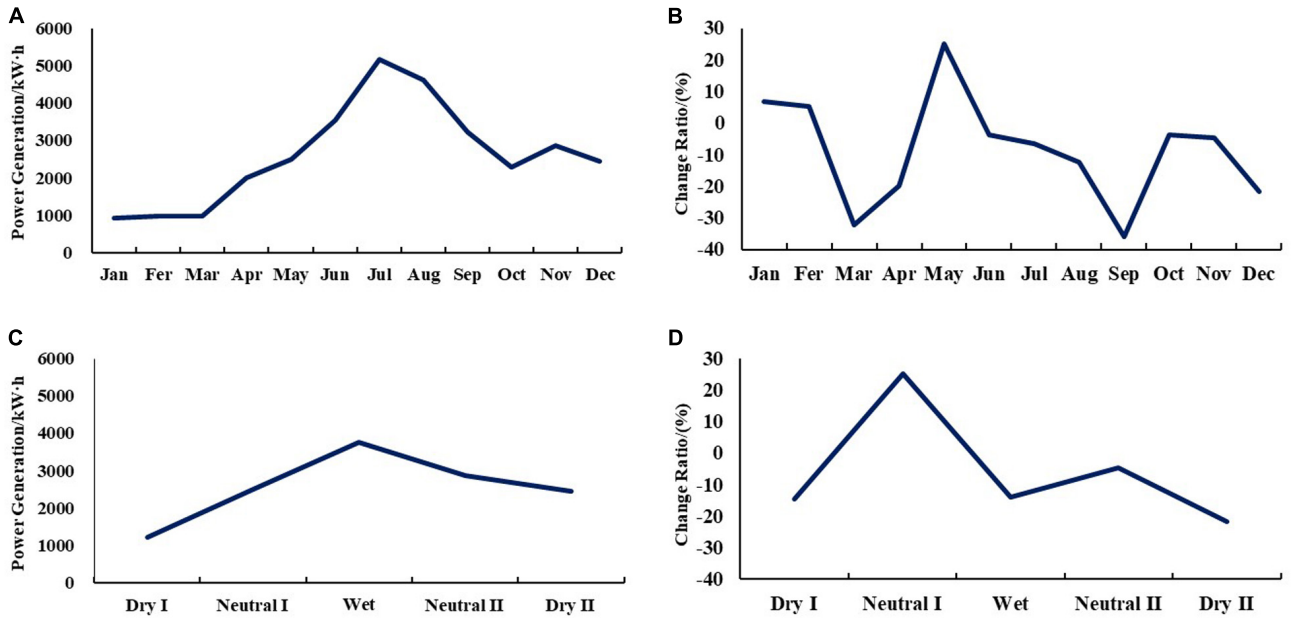

FIGURE 12 | Future power generation change: **(A)** future monthly power generation; **(B)** monthly power generation change; **(C)** future power generation in period; **(D)** power generation change in period.

statistical downscaling show the best performance than other simulations. The simulated precipitation is consistent with the observation well. The errors in GCM and PRECIS are reduced greatly, particularly in August and Dry II.

In terms of the correlations between simulations and observation, SCA downscaling also show its advantage, with a correlation coefficient (about 0.97) and low RMSE value (about 0.16), meaning that there is a great fitting degree and lower biases between the results and observation (**Figure 9**). Moreover, with the improvement of resolution, the decrease of RMSE is more pronounced. For example, the RMSE is about 68.9 mm/day in July for GCM and about 10.2mm/day for PRECIS, while the RMSE of SCA statistical downscaling is only about 0.5 mm/day. In addition, the RMSEs are different in periods and SCA shows a better performance ($\sim$ 0.16 mm/day) in Dry II periods than that in other periods.

Overall, compared with coarser-resolution climate models, the simulation results of SCA statistical downscaling can reasonably reproduce the precipitation trend and value. Thus, these results can be used as the input of a subsequent power forecasting model to simulate the power generation of hydropower stations.

Then, through the HRMDP model, we compare the simulated power generation and actual power generation in different months and periods for Station A, which is shown in **Figure 10**. Overall, the performance in correlation coefficients and RMSE values are quite satisfactory especially from May to July, which are 0.85 and 232 kWh respectively. The simulation results demonstrate a great performance in Wet period, and the correlation coefficients and RMSE values in different periods are 0.95 and 611 kWh, respectively.

Future Forecasting

The projection in precipitation is the first step to forecast the future power generation through the HRMDP model. The future precipitation and percentage change through SCA downscaling in annual cycle and different periods are shown in **Figure 11**. Compared with the historical period, the projected precipitation in annual cycle shows different change trends. Specifically, precipitation will increase by about 20–80% from May to July, while it will decrease in other months. For different periods, precipitation will increase in Neutral I and Wet, which are 79 and 4% respectively. The projected precipitation in other periods shows a decreasing trend, particularly in Neutral II (about 58%).

The changes in power generation resulting from the precipitation changes in station A in the future are shown in **Figure 12**. Compared with the historical period, there is an ascending trend in power generation in station A from January to February and May to July in the future, especially in February with the most increase by about 25%. However, in the rest months, there is a decreasing trend in power generation in station A, for example, the decrease in September will be 36%. Similarly, the power generation will increase by about 20% in future Neutral I period, while there is no obvious change in other three periods relative to the historical period.

It is noted that there is more power generation in September in tradition, but the decrease in future precipitation will lead to a decrease in power generation in this month. On the other hand, though the power generation is less in May in the historical, the value will increase because of the increased precipitation in future. In addition, the peak of the generation will change from July to August, and the value will decrease about 8%. Meanwhile,

the peak period of power generation will be shortened from June to August, because of the influence of precipitation.

CONCLUSION AND DISCUSSION

In this paper, based on the results from HadGEM2-ES and PRECIS climate models, the precipitation and power generation in power station A over Dadu River basin in China were simulated and projected using SCA statistical downscaling. The results from SCA downscaling show a great performance relative former climate models in simulating the precipitation at station scale. On the other hand, we used the observed meteorological and hydropower data in station A to establish a HRMDP. Meanwhile, we also validated the performance of HRMDP, and the results show that the HRMDP model can reflect the relationship between the precipitation and power generation, with the correlation coefficient of 0.95 and RMSE of 611 kWh.

In future, the precipitation of station A is projected an ascending trend from May to July while it will decrease in other months. For different periods, the precipitation will increase in Neutral I and Wet, but it will decrease in other periods. As the response from precipitation, the power generation will also show a similarly trend. There is an increasing trend in power generation in station A from January to February and May to July, while there is a decreasing trend in other months. For different periods, the power generation in Neutral I will increase by about 20% in future, while there is no obvious change in other three periods relative to the historical period.

Climate change has a great impact on precipitation, which affects hydropower generation. Therefore, it is of great significance to study the future precipitation change and power generation forecasting model of hydropower station to adapt climate change. As far as we know, there are many studies on future precipitation changes using climate models, but relatively few on hydropower generation forecasting model. For example, for precipitation, future climate change will lead to a general increase in precipitation over the most regions of China (Lin and Zhou, 2015; Zhao et al., 2019). Future precipitation of Dadu river basin in our study also shows an increase trend, which is consistent with other similar basins (Zhang J. et al., 2013; Zheng et al., 2017). In addition, although there are many researches on power generation forecasting methods, which focus on the runoff forecast, there are few studies on hydropower generation forecasting directly. For example,Cheng et al. (2013) used linear trend estimation method, Morlet wavelet transform and Kendall rank correlation method to forecast future runoff over the Dadu river basin, and shows that runoff will appear an increase trend. Our results show that hydropower generation has an increase trend in the future, which means the increase of precipitation will lead to increase of runoff, and further promote the increase of hydropower generation. The results can provide some decision support for future water resources management in Dadu river basin, especially for the planning and operation of hydropower stations.

DATA AVAILABILITY STATEMENT

The datasets generated for this study are available on request to the corresponding author.

AUTHOR CONTRIBUTIONS

LW, LJ, and GJ conceived and designed the research, collected the data, and performed the data analyses and manuscript preparation. LW, LJ, GJ, and BZ formulated the optimization model. LW, LJ, GJ, and FL wrote the manuscript. LW, GJ, and HB gave the comments and helped to revise the manuscript. All authors contributed to the article and approved the submitted version.

FUNDING

This research was supported by the National Key Research and Development Plan (2018YFE0196000), Natural Sciences Foundation (51190095), and the 111 Project (B14008).

REFERENCES

Ali, S. A., Aadhar, S., Shah, H. L., and Mishra, V. (2018). Projected increase in hydropower production in india under climate change. *Sci. Rep.* 8:12450.

Arnette, A. N. (2017). Renewable energy and carbon capture and sequestration for a reduced carbon energy plan: An optimization model. *Renew. Sustain. Energy Rev.* 70, 254–265. doi: 10.1016/j.rser.2016.11.218

Bellouin, N., Rae, J., Jones, A., Johnson, C., Haywood, J., and Boucher, O. (2011). Aerosol forcing in the Climate Model Intercomparison Project (CMIP5) simulations by HadGEM2-ES and the role of ammonium nitrate. *J. Geophys. Res.* 116, 2020610–2021029.

Berghuijs, W. R., Woods, R. A., and Hrachowitz, M. (2014). A precipitation shift from snow towards rain leads to a decrease in streamflow. *Nat. Climate Change* 4, 583–586. doi: 10.1038/nclimate2246

Chen, J., Brissette, F. P., and Leconte, R. (2011). Uncertainty of downscaling method in quantifying the impact of climate change on hydrology. *J. Hydrol.* 401, 190–202. doi: 10.1016/j.jhydrol.2011.02.020

Chen, X., and Zong, Y. (2000). The 1998 flood on the Yangtze, China. *Nat. Hazard* 22, 165–184.

Cheng, K., Zhou, D., Li, M., and Zhan, W. (2013). Characteristic analysis of precipitation and runoff in Daduhe River in Last 51 Years. *Water Resour. Power* 31:5-8+240.

Chilkoti, V., Bolisetti, T., and Balachandar, R. (2017). Climate change impact assessment on hydropower generation using multi-model climate ensemble. *Renew. Energy* 109, 510–517. doi: 10.1016/j.renene.2017.02.041

Chu, S., and Majumdar, A. (2012). Opportunities and challenges for a sustainable energy future. *Nature* 488, 294–303. doi: 10.1038/nature11475

CREO (2018). *China Renewable Energy Outlook 2018*. Available online at: http://boostre.cnrec.org.cn/wp-content/uploads/2018/11/China-Renewable-Energy-Outlook-2018-Folder_ENG.pdf (accessed December 23, 2018).

Duan, K., and Mei, Y. (2013). A comparison study of three statistical downscaling methods and their model-averaging ensemble for precipitation downscaling in China. *Theor. Appl. Climatol.* 116, 707–719. doi: 10.1007/s00704-013-1069-8

Guo, J., Huang, G., Wang, X., Li, Y., and Lin, Q. (2017a). Dynamically-downscaled projections of changes in temperature extremes over China. *Climate Dyn.* 50, 1045–1066. doi: 10.1007/s00382-017-3660-7

Guo, J., Huang, G., Wang, X., Li, Y., and Lin, Q. (2017b). Investigating future precipitation changes over China through a high-resolution regional climate model ensemble. *Earth's Future* 5, 285–303. doi: 10.1002/2016ef000433

Guo, J., Huang, G., Wang, X., Li, Y., and Yang, L. (2018). Future changes in precipitation extremes over China projected by a regional climate model ensemble. *Atmospher. Environ.* 188, 142–156. doi: 10.1016/j.atmosenv.2018.06.026

Hui, P., Tang, J., Wang, S., Niu, X., Zong, P., and Dong, X. (2018). Climate change projections over China using regional climate models forced by two CMIP5 global models. Part II: projections of future climate. *Int. J. Climatol.* 38, e78–e94. doi: 10.1002/joc.5409

IHA (2018). *iha_2018_hydropower_status_report_4.pdf*. London: IHA.

IPCC (2013). IPCC fifth assessment report. *Weather* 68, 310–310.

Jiang, Z., Li, R., Li, A., and Ji, C. (2018). Runoff forecast uncertainty considered load adjustment model of cascade hydropower stations and its application. *Energy* 158, 693–708. doi: 10.1016/j.energy.2018.06.083

Jones, C. D., Hughes, J. K., Bellouin, N., Hardiman, S. C., Jones, G. S., Knight, J., et al. (2011). The HadGEM2-ES implementation of CMIP5 centennial simulations. *Geosci. Model Dev.* 4, 543–570. doi: 10.5194/gmd-4-543-2011

Kerkhoff, C., Künsch, H. R., and Schär, C. (2014). Assessment of Bias assumptions for climate models. *J. Climate* 27, 6799–6818. doi: 10.1175/jcli-d-13-00716.1

Li, Y., and Yan, X. (2017). Statistical downscaling of monthly mean temperature for Kazakhstan in Central Asia. *Climate Res.* 72, 101–110. doi: 10.3354/cr01456

Lin, R., and Zhou, T. (2015). Reproducibility and future projections of the precipitation structure in east asia in four chinese gcms that participated in the CMIP5 experiments. *Chin. J. Atmosph. Sci.* 39, 338–356.

Liu, X., Tang, Q., Voisin, N., and Cui, H. (2016). Projected impacts of climate change on hydropower potential in China. *Hydrol. Earth Syst. Sci.* 20, 3343–3359. doi: 10.5194/hess-20-3343-2016

Liu, Z., Xu, Z., Charles, S. P., Fu, G., and Liu, L. (2011). Evaluation of two statistical downscaling models for daily precipitation over an arid basin in China. *International J. Climatol.* 31, 2006–2020. doi: 10.1002/joc.2211

Panwar, N. L., Kaushik, S. C., and Kothari, S. (2011). Role of renewable energy sources in environmental protection: A review. *Renew. Sustain. Energy Rev.* 15, 1513–1524. doi: 10.1016/j.rser.2010.11.037

Perkins, S. E., Pitman, A. J., Holbrook, N. J., and McAneney, J. (2007). Evaluation of the AR4 Climate Models' Simulated Daily Maximum Temperature, Minimum Temperature, and Precipitation over Australia Using Probability Density Functions. *J. Climate* 20, 4356–4376. doi: 10.1175/jcli4253.1

REN21 (2018). *Renewable 2018.pdf*. Paris: REN21.

Saini, R., Wang, G., Yu, M., and Kim, J. (2015). Comparison of RCM and GCM projections of boreal summer precipitation over Africa. *J. Geophys. Res.* 120, 3679–3699. doi: 10.1002/2014jd022599

Wang, X., Huang, G., Lin, Q., Nie, X., and Liu, J. (2015). High-resolution temperature and precipitation projections over Ontario. Canada: a coupled dynamical-statistical approach. *Q. J. R. Meteorol. Soc.* 141, 1137–1146. doi: 10.1002/qj.2421

Wasko, C., and Sharma, A. (2017). Global assessment of flood and storm extremes with increased temperatures. *Sci. Rep.* 7:7945.

Wood, A. W., Leung, L. R., Sridhar, V., and Lettenmaier, D. P. (2004). Hydrologic implications of dynamical and statistical approaches to downscaling climate model outputs. *Clim. Change* 62, 189–216. doi: 10.1023/b:clim.0000013685.99609.9e

Xu, Y., Gao, X., Shen, Y., Xu, C., Shi, Y., and Giorgi, F. (2009). A daily temperature dataset over China and its application in validating a RCM simulation. *Adv. Atmosph. Sci.* 26, 763–772. doi: 10.1007/s00376-009-9029-z

Yang, C., Wang, N., Wang, S., and Zhou, L. (2016). Performance comparison of three predictor selection methods for statistical downscaling of daily precipitation. *Theor. Appl. Climatol.* 131, 43–54. doi: 10.1007/s00704-016-1956-x

Yang, Y., Tang, G., Lei, X., Hong, Y., and Yang, N. (2017). Can satellite precipitation products estimate probable maximum precipitation: a comparative investigation with gauge data in the dadu river Basin. *Remote Sens.* 10:41. doi: 10.3390/rs10010041

Zhang, D.-L., Lin, Y., Zhao, P., Yu, X., Wang, S., Kang, H., et al. (2013). The Beijing extreme rainfall of 21 July 2012: "Right results" but for wrong reasons. *Geophys. Res. Lett.* 40, 1426–1431. doi: 10.1002/grl.50304

Zhang, J., Luo, L., Han, X., and Zhang C. (2013). Simulation and Prediction of annual Precipitation in the Yangtze River Basin by CMIP5 model. Guizhou Meteorological Society. Guizhou Meteorological Society: Guizhou Association for Science and Technology, 2013:6.

Zhang, Z., and Xu, J. (2014). Applying rough random MODM model to resource-constrained project scheduling problem: A case study of Pubugou Hydropower Project in China. *KSCE J. Civil Eng.* 18, 1279–1291. doi: 10.1007/s12205-014-0426-1

Zhao, Y., Xiao, D., and Pai, H. (2019). Projection and application for future climate in china by CMIP5 climate model. *Meteorol. Sci. Technol.* 47, 608–621. doi: 10.1002/joc.5409

Zheng, W., Cheng, X., Yang, X., and Wang, Y. (2017). Trend analysis of precipitation and temperature over the upper changjiang river basin by statistical-downscaled cmip 5 climate projections. *China Rural Water Hydropower* (09):43-47+51.

Conflict of Interest: The authors declare that the research was conducted in the absence of any commercial or financial relationships that could be construed as a potential conflict of interest.

frontiers in Earth Science

ORIGINAL RESEARCH
published: 10 November 2020
doi: 10.3389/feart.2020.527388

A Low-Impact Development–Based Multi-Objective Optimization Model for Regional Water Resource Management under Impacts of Climate Change

Zhe Bao[1], *Hansheng Yang*[1], *Wei Li*[1], *Ye Xu*[1]* *and Guohe Huang*[2]

[1] MOE Key Laboratory of Regional Energy and Environmental Systems Optimization, College of Environmental Science and Engineering, North China Electric Power University, Beijing, China, [2] Faculty of Engineering, University of Regina, Regina, Canada

Under the urgency of rational water resource allocation and effective urban flooding control, a multi-objective interval birandom chance-constrained programming (MIBCCP) model is developed for supporting regional water resource management under multiple uncertainties and climate change in this study. Two objectives were included in this model, which are the minimization of total system costs and the maximization of total pollutant treatment amounts. The major advantage of the proposed MIBCCP model is that it realized the effective combined utilization of conventional and nonconventional water sources under complexities and uncertainties through incorporating compromise programming, birandom chance-constrained programming, and interval linear programming within a general framework. This way effectively overcomes water shortage issue and reduces urban flood frequency under climate change. A water supply management system of the educational park in Tianjin was used as a study case for demonstration. A variety of adaptive water allocation alternatives and construction schemes for LID (low-impact development) projects under RCP4.5 and RCP8.5 (representative concentration pathway 4.5 and 8.5) scenarios were obtained to deal with possible changes arising from increasing rainfall and runoff in the future. It is concluded that the proposed MIBCCP model provided the effective linkage between the utilization of nonconventional water resources and urban flood prevention and offered insights into the trade-off between economic benefits and environmental protection.

Keywords: birandom variable, low-impact development, water resource management, climate change, uncertainty

OPEN ACCESS

Edited by:
Yulei Xie,
University of Science and Technology Beijing, China

Reviewed by:
Ling Ji,
Beijing Institute of Technology, China
Chuanbao Wu,
Shandong University of Science and Technology, China

***Correspondence:**
Ye Xu
xuye@ncepu.edu.cn

Specialty section:
This article was submitted to Interdisciplinary Climate Studies, a section of the journal Frontiers in Earth Science

Received: *16 January 2020*
Accepted: *01 September 2020*
Published: *10 November 2020*

Citation:
Bao Z, Yang H, Li W, Xu Y and Huang G (2020) A Low-Impact Development–Based Multi-Objective Optimization Model for Regional Water Resource Management under Impacts of Climate Change. Front. Earth Sci. 8:527388. doi: 10.3389/feart.2020.527388

INTRODUCTION

With the current rapid improvement in socioeconomic development, industrialization, and urbanization, urban water scarcity is becoming an overwhelmingly urgent issue on a global scale, and this is particularly prominent in China (Loomis et al., 2019). For example, the average annual water scarcity in China is up to $4.00 \times 108\ m^3$, nearly two-thirds of China's cities are suffering from a water shortage, and 443–525 million city people live with high water scarcity. Meanwhile, China's urban water consumption continues to increase at an annual rate of 4–8% over the most recent decade (Wang et al., 2019). The conflict between increased water demand

and limited available water resources has become particularly evident in most cities in China. Currently, urban water resource management patterns mainly focus on the reasonable exploitation and effective utilization of conventional water resources (including surface and underground water). In fact, nonconventional water resources, such as rainwater and reclaimed water, have significant advantages in regard to water resource allocation and management (Ye et al., 2018). For instance, the utilization of rainwater has the effect of reducing the water supply cost by replacing potable water used for flushing toilets and watering of gardens, and reclaimed water distributes for industrial demand with an overall positive environmental impact. The combination of conventional and nonconventional water resources from a quantity and quality viewpoint is thus expected.

In addition to water scarcity, modern urban water resource management is also confronted with the huge challenges presented by increasingly frequent urban flooding, which can cause substantial economic damage and human distress (Kundzewicz et al., 2018). Over the last decades, annual urban flooding damage in China has exceeded 10 billion USD, and the number of flood fatalities is greater than approximately 1,000 (Kundzewicz et al., 2019). Moreover, a series of research on the water resource management under climate change indicated that the climate change could aggravate water scarcity seriously and cause urban flooding frequently through affecting regional rainfall, temperature, evaporation, and hydrological cycle, leading to a huge challenge on water resource management (Shang et al., 2015; Mahmoud and Gan, 2018; Xia et al., 2019; Zhang et al., 2019). In order to deal with such challenges, the Chinese government initiated the "Sponge City" Program in 2013, which incorporates (LID) concepts to improve the urban drainage infrastructure and address urban flooding (Song et al., 2019; Xu et al., 2019). As a sustainable, innovative, and effective stormwater runoff control method, LID projects have advantages in controlling stormwater and urban runoff and storing rainwater as underground water resources compared with non-LID projects. However, the high construction cost associated with these projects may trigger excessive economic burden, which has a negative influence on the development and application of LID technologies. Moreover, many factors, including socioeconomic, meteorological, geographic, and environmental aspects, are involved in the selection and placement processes of LID projects, which bring significant difficulties to the formulation of the LID project optimization models and generation of effective solutions. Therefore, it is important to develop an effective method for optimizing LID project implementation schemes under complexities that improve water use efficiency, explore nonconventional water resources, and control urban flooding with a minimum cost.

For urban water resource management, considering system factors comprehensively, establishing LID projects rationally, combining nonconventional and conventional water resources effectively, dealing with the impact of climate change, and formulating water sources allocations optimization model are suitable methods for resolving urban water scarcity and flood control, and such approaches have been the focus of many studies in recent years (Mainuddin et al., 1997; Shangguan et al., 2002; Wang et al., 2008; Liu et al., 2011; Sample and Liu, 2014; Bekchanov et al., 2015; Palanisamy and Chui, 2015; Palla and Gnecco, 2015; Eckart et al., 2018; Xu et al., 2018; Ye et al., 2018; Helmia et al., 2019; Huang and Lee, 2019). For instance, Shangguan et al. (2002) developed a recurrence control model for regional optimal allocation of water resource for obtaining maximum efficiency. Liu et al. (2011) presented an optimization approach for the integrated management of water resources, including both nonconventional and conventional water resources. Xu et al. (2018) proposed an optimal water allocation model for industrial sectors based on water footprint accounting to optimize the allocation of nonconventional and conventional water resources in Dalian. Ye et al. (2018) presented a multi-objective optimization model to help optimize the allocation of water resources to different water users in Beijing. Sample and Liu (2014) developed a rainwater analysis and simulation model to optimize rainwater harvesting systems for water supply and runoff capture. Eckart et al. (2018) established a management model to optimize LID implementation strategies with the objective of minimizing peak flow. Huang and Lee (2019) proposed a programming model to solve water shortage of Taiwan under the impact of climate change. Helmi et al. (2019) developed a modeling tool to allocate LID projects in a cost-optimized method. However, above studies mainly sought to establish an optimization model for water resource allocation or LID projects, which considered only single objective for optimization, while in the real practice, there is more than one issue need to be taken into account simultaneously when designing and executing the water resource management strategies, for the sake of achieving a balance among them.

In fact with the increased complexity and our in-depth understanding in the urban water resource system, it is apparent that there is no absolute deterministic water allocation system. Specifically, the water demand exhibits a random nature that is subject to multiple variables, including meteorological factors, socioeconomic conditions, and deviations caused by the subjective judgments and understandings of humans. For example, the ecological water demand would be different with the change of runoff and biodiversity. Similarly, some economic and engineering factors, which are influenced by the resource availability, technical conditions, and policy regulations, fluctuate in the small ranges. For instance, the supply price of transfer water would fluctuate between 8.8 and 9.2 Yuan/m^3 due to the impact of different technical conditions. Such uncertainties lead to significant difficulties in formulating urban water resource allocation models and generating an optimal management pattern. Currently, a large amount of uncertain optimization techniques have been developed by many researchers with the aim of solving urban water resource management problems (Huang, 1988; Liu et al., 2008; Qin and Huang, 2009; Qin et al., 2011; Dai et al., 2018; Xu et al., 2018; Zhang et al., 2019). For example, Dai et al. (2018) presented a Gini coefficient–based stochastic optimization model for supporting water resource allocation on a watershed scale. Xu et al. (2018) developed a stochastic-based water allocation

optimization model on a watershed scale for supporting water supply planning and wetland restoration activities of the Xiaoqing River watershed. Zhang et al. (2019) proposed an interval multi-objective multi-stage stochastic programming model for finding a reasonable water storage scale and optimizing limited irrigation water resource. Based on the above studies, it can be concluded that many researchers have focused on dealing with the randomness inherent in urban water resource management. However, the above studies mainly utilized random variables with a known distribution type to describe the uncertainties involved in the water resource system, and they rarely observed that water demands in the real world may be subject to twofold randomness with incomplete or uncertain information. Specifically, it is first assumed that the water demands ξ are expressed as the random variables with the normal distributions, that is, $\xi \sim N(\mu, \delta^2)$, where μ and δ denote the mean value and standard deviation, respectively. Based on various survey and estimation results from n group of respondents, n groups of random variables could be obtained, that is, $(\mu_1, \delta_1{}^2)$, $(\mu_2, \delta_2{}^2)$, $(\mu_n, \delta_n{}^2)$, such that μ and δ values are more suitable to be random variables (based on the collected data above) rather than fixed values as are traditional random variables (Xu et al., 2014). Hence, the parameters μ and σ should be described as new random variables, which are the so-called birandom variables, a concept first proposed by Peng and Liu (2007). This concept has been successfully applied to the flow shop scheduling problem, vendor selection problem, and hydropower station operation planning problem (Xu and Zhou, 2009; Xu and Ding, 2011; Xu and Tao, 2012).

As mentioned above, following three aspects of urban water resource management still need to be improved. First, current optimization models often pay attention to only one aspect of water resource allocation or LID project exploration. In fact, it is necessary to develop a comprehensive optimization model that incorporates the exploration of LID projects into the urban water management scheme. Second, because water demands directly affect the accuracy and rationality of the results due to the supply–demand constraint, it is important to develop a birandom optimization method to avoid the deviation caused by the birandomness of the water demands. Third, the climate change exerts the influences on the water availability and the occurrence of urban flood, which should be incorporated into the optimization model for integrated water resource management. As such, the main goal of this study was to develop a (MIBCCP) model under climate change for supporting the urban water resource management. The proposed model aims to optimize water resource allocation and address the urban flooding under uncertainties and different climate change scenarios, while minimizing the total system costs and maximizing the treated pollutant amount. The rest of this study is organized as follows: *Materials and Methods* introduce the descriptions of the compromise programming, birandom chance-constrained programming, and interval linear programming and describe formulation and the solution procedure of the MIBCCP model. An overview of the reference education park and the MIBCCP model for this park are proposed in *Case Study*. In *Results Analysis and Discussion*, the variations in the obtained solutions and impact of climate change on water resource management are analyzed and discussed. Finally, the conclusions summarizing this study are presented in the last section.

METHODOLOGY

To establish a cost-effective and environmentally friendly water resource management pattern, multiple objectives for the programming model should be taken under consideration, so that the model is capable of tackling the economic and environmental objectives simultaneously. Moreover, the estimation and expression of uncertain factors are critical for generating a rational and reliable management strategy of the urban water system, as many of the system parameters are associated with various types of the uncertainties. Therefore, an inexact multi-objective equilibrium chance-constrained programming model with the birandom and interval variables (i.e., MIBCCP) was developed for addressing these issues.

Preliminary Definitions and Descriptions of Proposed a Multi-Objective Interval Birandom Chance-Constrained Programming Model

In this section, some definitions, conceptions, and descriptions associated with compromise programming, birandom parameters, and interval numbers are described first in order to formulate and solve the proposed MIBCCP model.

Compromise Programming

Currently, many methods are available for solving multi-objective programming problems, among which the compromise programming is the most commonly used. The solution algorithm of compromise programming is based on the concept of a distance scale d_p, a point which has the shortest distance to the ideal solution from the noninferior solution set. The total performance of all objective functions can be written as follows:

$$Min\, d_p = \min\left\{\sum_{k=1}^{K} \pi_k^p \left(\frac{Z_k^{\max}(X) - Z_k(X)}{Z_k^{\max} - Z_k^{\min}}\right)^p\right\}^{1/p} \quad (1a)$$

$$1 < p < \infty \quad (1b)$$

$$\pi_k^p > 0 \quad (1c)$$

$$\sum_{k=1}^{K} \pi_k^p = 1 \quad (1d)$$

where $Z_k^{\max}(x)$ and $Z_k^{\min}(x)$ are the maximum and minimum values of each individual objective which can be obtained through the transformation of the original multi-objective programming that is single objective. The introduction of $Z_k^{\max}(x)$ and $Z_k^{\min}(x)$ is used to normalize noncommensurable formats and units in model objectives. $Z_k(X)$ = the value of the objective k; k = the total number of objectives; π_k^p = the corresponding weight of each

objective. The distance scale d_p varies with various p, where $p = \infty$ when decision-makers focus on the specific objective; $p = 1$ is corresponded to the decision-makers, considering all the objectives. Considering the complexity of the MIBCCP model, the item p is designed as 1 for the simplicity in this research.

Introduction of Birandom Variable following the Normal Distribution

Birandom variable, a concept first proposed by Peng and Liu (2007), is a useful tool to deal with problems with twofold randomness and has been successfully applied to many fields (Xu and Zhou, 2009; Xu and Ding, 2011; Xu and Tao, 2012). In this study, the random variable following the normal distribution is considered as the example. For any ω, $\xi(\omega)$ is a birandom variable with normal distribution and is expressed as $N(\mu(\omega), \sigma^2(\omega))$, where $\mu(\omega)$ and $\sigma(\omega)$ are random variables, rather than fixed values of general random variable.

Definition 2.1. A n-dimensional birandom vector ξ is a map from the probability space (Ω, A, Pr) to a collection of n-dimensional random vectors such that $Pr\{\xi(\omega) \in B\}$ is a measurable function with respect to ω for any Borel set B of the real space R^n. Especially, ξ is called a birandom variable as $n = 1$.

Example 2.1. A birandom variable ξ is assumed to follow the normal distribution, if for each ω, $\xi(\omega)$ is a random variable with normal distribution, denoted by $N(\mu(\omega), \sigma^2(\omega))$, where $\mu(\omega)$, $\sigma(\omega)$ are the random variables defined on the probability space (Ω, A, Pr).

Lemma 2.1. Let $\xi = (\xi_1, \xi_2, \ldots, \xi_n)$ be a birandom vector and f be a Borel measurable function from R^n to R. Then $f(\xi)$ is a birandom variable.

Let ξ_1 and ξ_2 be two birandom variables defined on the probability spaces (Ω_1, A_1, Pr_1) and (Ω_2, A_2, Pr_2), respectively. Then $\xi = \xi_1 + \xi_2$ is a birandom variable on $(\Omega_1 \times \Omega_2, A_1 \times A_2, Pr_1 \times Pr_2)$ defined by $\xi(\omega_1, \omega_2) = \xi_1(\omega_1) + \xi_2(\omega_2)$, $(\omega_1, \omega_2) \in (\Omega_1 \times \Omega_2)$.

Interval Number

The interval number is composed of the lower bound and upper bound, which is depicted in **Eq. 1**, where the items a^- and a^+ are the lower and upper bounds of $a_{ij}^{\pm}$, respectively. The lower and upper bounds represent minimum value and maximum value of $a^{\pm}$, respectively. Two major advantages of the interval number are the low requirement of data information and the interval optimization model is solved without excessive computational burden (Huang et al., 1992).

$$a_{ij}^{\pm} = \left[a_{ij}^{-}, \ a_{ij}^{+}\right] \tag{2a}$$

Let $a^{\pm}$ and $b^{\pm}$ be two interval numbers defined as $a^{\pm} = [a^-, a^+]$ and $b^{\pm} = [b^-, b^+]$, respectively. Some calculation equations of two interval numbers are defined as follows:

$$a^{\pm} + b^{\pm} = [a^- + b^-, \ a^+ + b^+] \tag{2b}$$

$$a^{\pm} - b^{\pm} = [a^- - b^-, \ a^+ - b^+] \tag{2c}$$

$$a^{\pm} \times b^{\pm} = [a^- \times b^-, \ a^+ \times b^+] \tag{2d}$$

$$\frac{a^{\pm}}{b^{\pm}} = \left[\frac{a^-}{b^+}, \ \frac{a^+}{b^-}\right] \tag{2e}$$

$$ka^{\pm} = [ka^-, \ ka^+] \tag{2f}$$

$$\frac{1}{a^{\pm}} = \left[\frac{1}{a^+}, \ \frac{1}{a^-}\right] \tag{2g}$$

$$ka^{\pm} = [ka^-, \ ka^+] \tag{2h}$$

$$\frac{1}{a^{\pm}} = \left[\frac{1}{a^+}, \ \frac{1}{a^-}\right] \tag{2i}$$

Multi-Objective Interval Birandom Chance-Constrained Programming

As stated in the *Introduction* section, the uncertainties associated with the urban water resource management system not only exhibit the random characteristics but also fluctuate in the small ranges. Therefore, in this study, an integrated uncertain multi-objective optimization model including the birandom parameters and interval numbers (MIBCCP) is developed for tackling two types of uncertainties.

$$\text{Minimize } f_1^{\pm} = C_1^{\pm} X^{\pm} \tag{3a}$$

$$\text{Minimize } f_2^{\pm} = C_2^{\pm} X^{\pm} \tag{3b}$$

Subject to:

$$\tilde{\tilde{A}}(\omega) X^{\pm} \le \tilde{\tilde{B}}(\omega) \tag{3c}$$

$$D^{\pm} X^{\pm} \le E^{\pm} \tag{3d}$$

$$X^{\pm} \ge 0 \tag{3e}$$

$$C_1^{\pm}, \ C_2^{\pm}, \tilde{\tilde{A}}(\omega), \ D^{\pm} \ne 0 \tag{3f}$$

where two objective functions $f_1^{\pm}$ and $f_2^{\pm}$, decision variable $X^{\pm}$, and coefficients $C_1^{\pm}$, $C_2^{\pm}$, $A^{\pm}$, $D^{\pm}$, and $E^{\pm}$ are expressed as interval forms. The coefficients $\tilde{\tilde{A}}(\omega)$ and $\tilde{\tilde{B}}(\omega)$ are birandom variables following normal distribution, where they are described as $\tilde{\tilde{A}}(\omega) \sim N(\tilde{A}(\omega), \sigma_A^2)$ and $\tilde{\tilde{B}}(\omega) \sim N(\tilde{B}(\omega), \sigma_B^2)$, respectively. The mean values of stochastic variables also are described as normal random variables, that is, $\tilde{A}(\omega) \sim N(\mu_A, \sigma_{A'}^2)$ and $\tilde{B}(\omega) \sim N(\mu_B, \sigma_{B'}^2)$, respectively. The covariance magnitudes (i.e., σ_A^2 and σ_B^2) are assumed as fixed values, since the variations in the deviation value are limited.

The first and critical step of solving model **3** is to combine two objective functions into one objective through designing various weight coefficients (i.e., w_1 and w_2).

$$\text{Minimize } f^{\pm} = w_1 * \frac{f_1^{\max} - f_1}{f_1^{\max} - f_1^{\min}} + w_2 * \frac{f_2^{\max} - f_2}{f_2^{\max} - f_2^{\min}} \tag{4a}$$

$$w_1 + w_2 = 1 \tag{4b}$$

where w_1 is the corresponding weight of f_1; w_1 is the corresponding weight of f_2; $f_1^{\max}$, $f_2^{\max}$, $f_1^{\min}$, and $f_2^{\min}$ are the maximum and minimum values of each individual objective which can be obtained through the transformation of the original multi-objective programming, that is, single objective. In this study, depending on local conditions, we consulted 30 local managers with various backgrounds, including the environmental protection bureau, economic development

commission, and civil affairs department. According to the above managers' preferences, w_1 and w_2 were regarded as the weight coefficients of economic objective and environmental objective, and nine groups of weight coefficients (i.e., $w_1 = 0.1$ and $w_2 = 0.9$, $w_1 = 0.2$ and $w_2 = 0.8$, $w_1 = 0.3$ and $w_2 = 0.7$, $w_1 = 0.4$ and $w_2 = 0.6$, $w_1 = 0.5$ and $w_2 = 0.5$, $w_1 = 0.6$ and $w_2 = 0.4$, $w_1 = 0.7$ and $w_2 = 0.3$, $w_1 = 0.8$ and $w_2 = 0.2$, and $w_1 = 0.9$ and $w_2 = 0.1$) were designated. Among these, the first three groups were proposed by the managers from economic development commission, who tend to give priority to economic growth; the latter three groups were regulated by the managers from environmental protection bureau, who prefer the improvement in environmental quality. The rest of the groups correspond to the managers from civil affairs department, who focus on the coordinated development of economic growth and environmental protection.

Next, the constraint with birandom variables (**3c**) is converted into its interval equivalent based on the birandom equilibrium chance-constrained algorithm. The selection of the equilibrium chance measure is because it is a real number and is convenient for decision-makers to rank potential solutions (Peng and Liu, 2007). The original stochastic constraint could be reformulated as follows:

$$\begin{aligned}
&\tilde{\tilde{A}}(\omega)X^{\pm} \le \tilde{\tilde{B}}(\omega) \Leftrightarrow \mathrm{Ch}^{e}\left\{\tilde{\tilde{A}}(\omega)X^{\pm} \le \tilde{\tilde{B}}(\omega)\right\} \ge 1-\alpha_r \\
&\Leftrightarrow \Pr\left\{\omega \in \Omega \middle| \Pr\left\{\tilde{\tilde{A}}(\omega)X^{\pm} \le \tilde{\tilde{B}}(\omega)\right\} \ge 1-\alpha_r\right\} \ge 1-\alpha_r \\
&\Leftrightarrow \mu_A X^{\pm} + \Phi^{-1}(\alpha_r)\sqrt{(X^{\pm})^T \sigma_A X^{\pm} + (\sigma_B)^2} \\
&+\Phi^{-1}(\alpha_r)\sqrt{(X^{\pm})^T \sigma_{A'} X^{\pm} + \left(\sigma_{B'}\right)^2} \le \mu_B, \qquad \forall r
\end{aligned} \tag{5}$$

where α_r represent predetermined probability violation levels. The principle of designing α_r value is ensuring its ranges are wide enough. In order to generate a variety of decision alternatives and provide more choosing opportunities to decision-makers, a relatively wide range of designed parameter is necessary. Referring to the studies (Xu et al., 2009; Wang et al., 2018), in this study, the constraint violation level is designed as 0.01, 0.05, and 0.1, respectively.

Then, the interactive two-step algorithm proposed by Huang et al. (1992) is used for transforming the intermediate interval linear programming model into two submodels, which correspond to the upper and lower bounds of objective function values, respectively. The submodel corresponding to the lower bound of objective function is formulated first as (Xu and Zhou, 2009; Xu and Tao, 2012):

$$\text{Minimize } f^{-} = C^{-}X^{-} \tag{6a}$$

Subject to:

$$\begin{aligned}
&\mu_A X^{-} + \Phi^{-1}(\alpha_r)\sqrt{(X^{-})^T \sigma_A X^{-} + (\sigma_B)^2} \\
&+\Phi^{-1}(\alpha_r)\sqrt{(X^{-})^T \sigma_{A'} X^{-} + \left(\sigma_{B'}\right)^2} \le \mu_B, \qquad \forall r
\end{aligned} \tag{6b}$$

$$D^{+}X^{-} \le E^{-} \tag{6c}$$

$$X^{\pm} \ge 0 \tag{6d}$$

Based on obtained solutions from model **6**, the submodel representing the upper bound of the objective function f^{+} is formulated as follows:

$$\text{Minimize } f^{+} = C^{+}X^{+} \tag{7a}$$

Subject to:

$$\begin{aligned}
&\mu_A X^{+} + \Phi^{-1}(\alpha_r)\sqrt{(X^{+})^T \sigma_A X^{+} + (\sigma_B)^2} \\
&+\Phi^{-1}(\alpha_r)\sqrt{(X^{+})^T \sigma_{A'} X^{+} + \left(\sigma_{B'}\right)^2} \le \mu_B, \qquad \forall r
\end{aligned} \tag{7b}$$

$$D^{-}X^{+} \le E^{+} \tag{7c}$$

$$X^{+} \ge X^{-} \tag{7d}$$

Finally, the solutions of objective values and decision variables under various α_r values are obtained, that is, $f_{1,opt}^{\pm} = [f_{1,opt}^{-}, f_{1,opt}^{+}]$, $f_{2,opt}^{\pm} = [f_{2,opt}^{-}, f_{2,opt}^{+}]$ and $X_{opt}^{\pm} = [X_{opt}^{-}, X_{opt}^{+}]$, respectively. The MIBCCP model developed in this study can not only reflect two distinct objectives including the economic and environmental aspects but also describe uncertain parameters as the birandom variables and interval numbers, leading to the interval solutions under various weight combinations and violation levels for supporting the decision-making process. **Figure 1** shows the procedures for formulating and solving an MIBCCP model, which are summarized as follows:

Step 1: Investigate the water resource management system and recognize system structure and components, respectively.
Step 2: Identify all types of uncertain variables as the birandom variables and interval numbers and determine the objective function and constraints in the optimization model.
Step 3: Establish an MIBCCP model based on step 1 and step 2.
Step 4: Combine two objectives into a single objective based on the compromise programming method.
Step 5: Convert the birandom constraints into their respective interval equivalents based on equilibrium chance-constrained measure.
Step 6: Transform the interval model into two submodels through an interactive two-step algorithm, which correspond to the lower bound and upper bound models, respectively.
Step 7: Solve two submodels and generate the final solutions of objective values and decision variables under various conditions.

CASE STUDY

Overview of the Study Area

To demonstrate the advancement of the proposed optimization model for optimizing the allocation of water resource and addressing urban flooding with minimal LID project construction cost, an education park water system in Tianjin, China, was taken as an example. As shown in **Figure 2**, the reference park is a national demonstration zone of vocational education reform and innovation in China, located at latitude 38°34′–40°15′N and longitude 116°43′–118°4′E, and it covers an

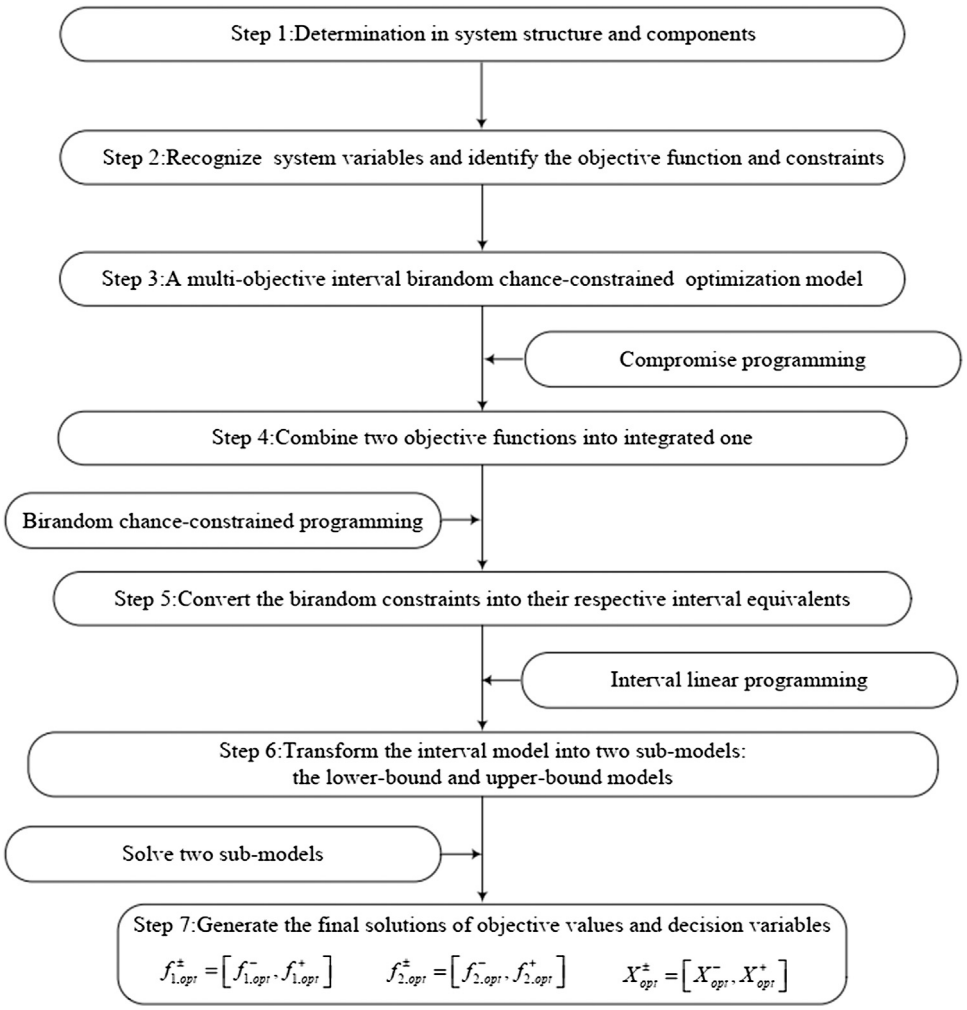

FIGURE 1 | Main procedure of formulating and solving a multi-objective interval birandom chance-constrained programming model.

area of 37 km^2 with a total population of 0.2 million. The annual rainfall is about 480 –520 mm, 75% of which is concentrated in the months of June, July, and August. As a demonstration area constructed with "three-zone linkage" (educational zone, residential zone, and industrial zone), the reference park clearly has high requirements in regard to water availability and water supply safety. However, its existing water provision is incapable of meeting the scale expansion needs of the park in the future, which is mainly reflected in the following aspects: i) water scarcity is an urgent problem in this area. The water resource per capita is 160 m^3/a, which is only about 7% of the average level in China; ii) the major water source for this park is the local reservoir, and no alternative sources are available. As such, this single water source will affect the water supply security; iii) the capability of water conservation and retention has declined due to the decrease in puddle and lake areas; moreover, increased concrete areas has also reduced the penetration of rainwater into the soil. The on-site survey result indicated that this park often undergoes flooding, which would be exacerbated under climate change; iv) intrinsic uncertainties are associated with the water resource system of this park, including the volatility in water demands and fluctuations in the prices of water resource. The current water resource management plan neglects the uncertain features and potential risk caused by climate change that can affect the accuracy and rationality of the water allocation strategy. Therefore, it is important that an effective water resource optimization model is formulated to help mitigate and/or solve the above issues.

Impact of Climate Change on the Study Area

Over the last decades, climate change has significantly aggravated water scarcity and intensified frequency of extreme weather events (such as urban flooding and droughts) in China (Niu et al., 2008; Yu et al., 2008; Guo et al., 2019). Hence, it is necessary to detect future changes in rainfall over a region by using the simulation techniques in order to identify the influence exerted by climate change and generate an optimal water resource management strategy. PRECIS is a regional climate model system developed at the Met Office Hadley Centre, United Kingdom (Rao et al., 2014). It is advantageous in simulating

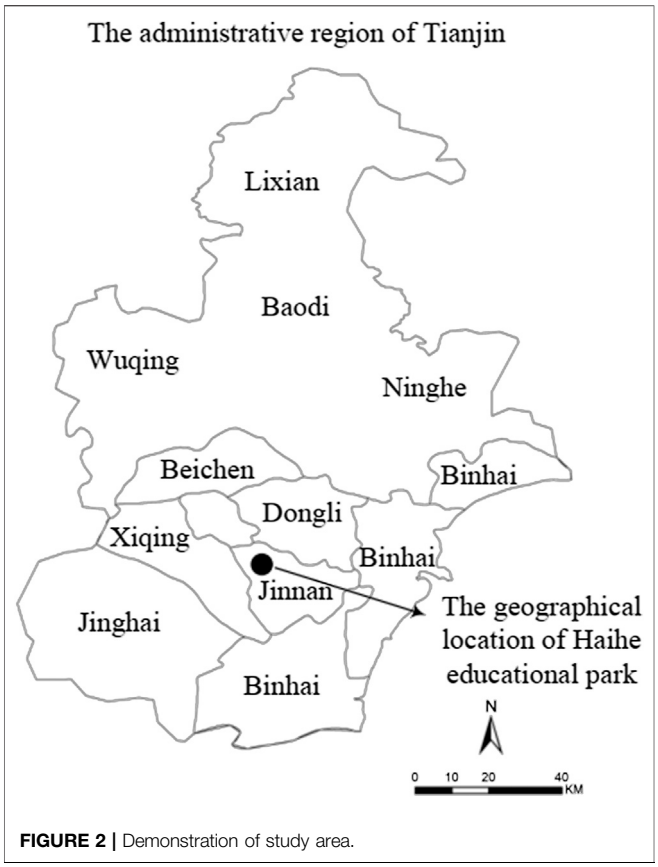

FIGURE 2 | Demonstration of study area.

TABLE 1 | Average annual rainfall under various periods and scenarios.

Item	Emission scenario	Period			
		2025 (mm)	2050 (mm)	2075 (mm)	2100 (mm)
Average annual Rainfall	RCP4.5	512.58	593.57	695.24	823.24
	RCP8.5	766.76	880.56	1,029.55	1,214.87

the change trend of climatic variables due to its easy-to-use operation, high computational precision, and wide suitability. In this study, the average annual rainfall in the reference park was predicted under four periods (2025, 2050, 2075, and 2100) and two emission scenarios (RCP4.5 and RCP8.5) by the PRECIS model, which are shown in **Table 1**. From **Table 1**, it can be seen that the average annual rainfall shows an upward trend among four periods under the impact of climate change in the future.

Description of the Water Resource System

Figure 3 presents the water network in the studied region. Based on the natural conditions, geographical position, and surface runoff of the reference park, the water resource management system for this park is conceptualized as 12 nodes, including four water sources, six water users, and LID, and non-LID projects. The major water sources are transfer water, tap water, reclaimed water, and rain water, which are used for living, industry, tertiary industry, construction, ecology, and other water users. Considering a water-saving plan, green ecological requirements, and traditional water source allocation principles of the city of Tianjin, this study made some adjustment as follows: i) "planning of recycled water utilization of Tianjin" highlights that the utilization of reclaimed water should be considered for livelihood water with the maximal value of 30 L/d per capita. Hence, the water sources for livelihood water would be transfer water, tap water, and reclaimed water. ii) According to "technical specifications for construction and community rainwater utilization engineering," rainwater can be used for green space irrigation and road watering. Therefore, the demand for ecology water could be met by reclaimed water and rainwater, which are harvested via the LID and non-LID projects in this study. iii) Other water users should include the water source loss caused by water transfer, including transfer water loss and tap water loss.

Formulation of the Multi-Objective Interval Birandom Chance-Constrained Programming Model Under Climate Change

As mentioned in the above sections, the generation and execution of a rational water resource management strategy under climate change, including the determination of the system components, design of the system operation pattern, and generation of water allocation alternatives, are directly related to the coordinated development of local socioeconomy and environmental factors.

Therefore, the MIBCCP model for tackling the water supply problem of the park was formulated, as shown in **Figure 4**. This model was used to identify and determine the optimal water allocation strategy under climate change, which could enhance the economic efficiency, reduce environmental water pollution, and avoid the negative effects caused by various uncertainties associated with the water resource management system. The formulation and solution procedures of the MIBCCP model in this study are summarized as follows:

Step 1: Investigate the water resource management system and recognize system structure and confirm the impact of climate change.
Step 2: Identify all types of uncertain variables as the birandom variables and interval numbers and determine the objective function and constraints in the MIBCCP model based on step 1.
Step 3: Establish the MIBCCP model depended on step 2.
Step 4: Solve the MIBCCP model and generate the solutions of objective values and decision variables under different conditions.
Step 5: Analyze and discuss the results obtained in step 4 and support managers to make a trade-off between the economic benefits and environmental benefits, identify the relation between the system cost and the joint constraint violation risk, and deal with the impact of climate change.

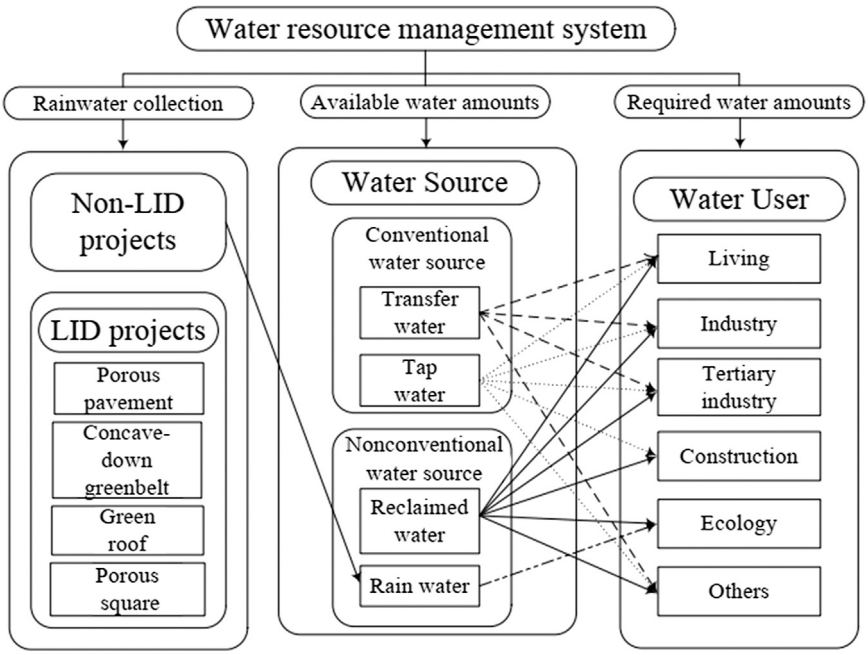

FIGURE 3 | Regional water supply system.

Objective Functions

i. Economic objective

$$\text{minimize } f_C^{\pm} = \sum_{n=1}^{N}\sum_{m=1}^{M} CA_{n,m}^{\pm} \mathrm{g} A_{n,m} + \sum_{i=1}^{I}\sum_{j=1}^{J} CX_{i,j}^{\pm} \mathrm{g} X_{i,j}^{\pm} \quad (8a)$$

where $f_C^{\pm}$ = construction costs and water resource allocation costs (RMB); $CA_{n,m}^{\pm}$ = construction price of project n in area m (RMB/m^2). n (g = 1, 2, . . ., N) = index of the project type; n = 1 represents non-LID projects; n = 2 represents LID projects; m (m = 1, 2, . . ., M) = index of the area type; m = 1 represents pavement; m = 2 represents greenbelt; m = 3 represents roofs; m = 4 represents square; $A_{n,m}$ = decision variables representing the area of project n at area m (m^2); $CX_{i,j}^{\pm}$ = water transferred cost from water source i to water user j (RMB/m^3); $X_{i,j}^{\pm}$ = decision variables representing water amounts transferred from water source i to water user j (m^3), i (i = 1, 2, . . ., I) = index of water resource type; i = 1 represents transfer water; i = 2 represents tap water; i = 3 represents reclaimed water; i = 4 represents rainwater; j (j = 1, 2, . . ., J) = index of water user type; j = 1 represents livelihood; j = 2 represents industry; j = 3 represents tertiary industry; j = 4 represents construction; j = 5 represents ecology; j = 6 represents other water user, as shown in **Figure 2**, when i = 1, j = 1, 2, 3, and 6; when i = 2, j = 1, 2, 3, 4, and 6; when i = 3, j = 1, 2, 3, 4, 5, and 6; when i = 4, j = 5. The economic target (**8a**) was designed to realize the minimization of the construction costs related to LID and non-LID projects and water resource allocation costs.

i. Environmental objective

$$\text{maximize } f_E^{\pm} = \sum_{n=1}^{N}\sum_{m=1}^{M} Lg K_m^{\pm} \mathrm{g} A_{2,m} \quad (8b)$$

where $f_E^{\pm}$ = total treatment amount of total suspended solids (TSS) (ton); L = the amount per unit area of TSS in the study area (t/m^3); $K_m^{\pm}$ = TSS treatment efficiency of LID projects at area m. The environmental objective (**8b**) endeavors to maximize the total treatment amount of TSS.

Constraints

i. Constraint for water resource availability

$$X_{1,1}^{\pm} + X_{1,2}^{\pm} + X_{1,3}^{\pm} + X_{1,6}^{\pm} \le Q \pm \quad (8c)$$

$$X_{2,1}^{\pm} + X_{2,2}^{\pm} + X_{2,3}^{\pm} + X_{2,4}^{\pm} + X_{2,6}^{\pm} \le Q \pm \quad (8d)$$

$$X_{3,1}^{\pm} + X_{3,2}^{\pm} + X_{3,3}^{\pm} + X_{3,4}^{\pm} + X_{3,5}^{\pm} + X_{3,6}^{\pm} \le Q \pm \quad (8e)$$

$$X_{4,5} \le Q_{YK} \quad (8f)$$

where $Q_W^{\pm}$ = transfer water availability (m^3); $Q_Z^{\pm}$ = tap water availability (m^3); $Q_{ZS}^{\pm}$ = reclaimed water availability (m^3); Q_{YK} = rainwater availability (m^3). The constraints (**8c**) to (**8f**) regulate the water amounts, including the transfer, tap, reclaimed, and, rainwater, so they do not exceed their maximum availability.

ii. Constraint for the water supply–demand balance

$$X_{1,1}^{\pm} + X_{1,2}^{\pm} + X_{1,3}^{\pm} \ge \tilde{Q}_S \quad (8g)$$

$$X_{1,2}^{\pm} + X_{2,2}^{\pm} + X_{3,2}^{\pm} \ge \tilde{Q}_g \quad (8h)$$

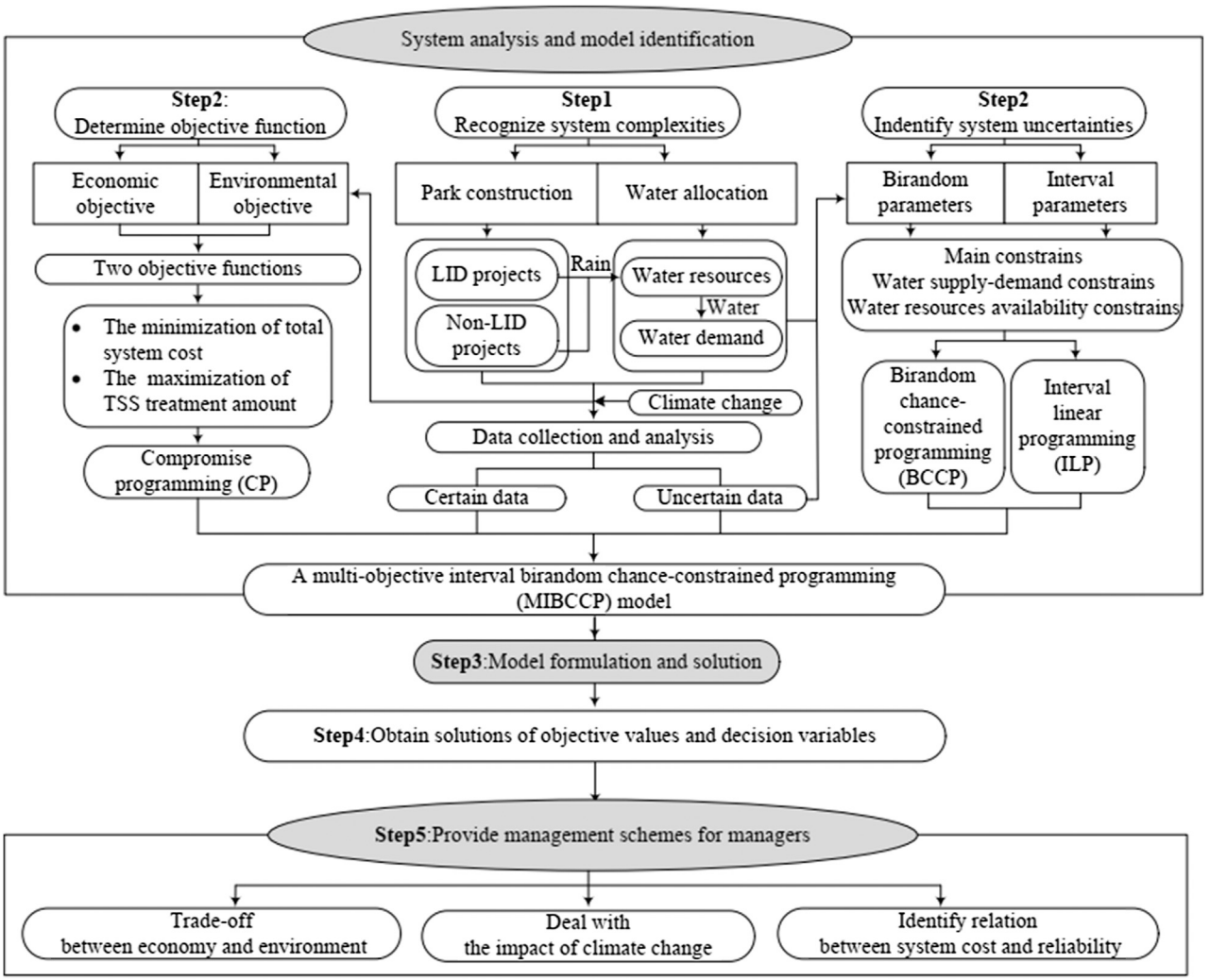

FIGURE 4 | Water supply management diagram for the educational park in Tianjin.

$$X_{1,3}^{\pm} + X_{2,3}^{\pm} + X_{3,3}^{\pm} \geq \tilde{\tilde{Q}}_{ds} \quad (8i)$$

$$X_{2,4}^{\pm} + X_{3,4}^{\pm} \geq \tilde{\tilde{Q}}_{j} \quad (8j)$$

$$X_{3,5}^{\pm} + X_{4,5} \geq \tilde{\tilde{Q}}_{e} \quad (8k)$$

$$X_{1,6}^{\pm} + X_{2,6}^{\pm} + X_{3,6}^{\pm} \geq \tilde{\tilde{Q}}_{q} \quad (8l)$$

where $\tilde{\tilde{Q}}_{S}$ = total demand of livelihood water (m^3); $\tilde{\tilde{Q}}_{g}$ = total demand of industrial water (m^3); Q_{ds} = total water demand of tertiary industry (m^3); $\tilde{\tilde{Q}}_{j}$ = total demand of construction water (m^3); $\tilde{\tilde{Q}}_{e}$ = total demand of ecological water (m^3); $\tilde{\tilde{Q}}_{q}$ = total water demand of other users (m^3). The constraints (**8g**) to (**8l**) serve to regulate the allocated water amounts from each water resource to be higher than or equal to the required water amounts.

iii. Constraint of conventional water resource utilization

$$\left(X_{1,1}^{\pm} + X_{1,2}^{\pm} + X_{1,3}^{\pm} + X_{2,1}^{\pm} + X_{2,2}^{\pm} + X_{2,3}^{\pm} + X_{2,4}^{\pm}\right) \leq R_{T}^{\pm}\, \mathrm{g}GDP \quad (8m)$$

$$X_{1,2}^{\pm} + X_{2,2}^{\pm} \leq R_{I}^{\pm}\, \mathrm{g}MAV_{I} \quad (8n)$$

$$X_{1,3}^{\pm} + X_{2,3}^{\pm} \leq R_{DS}^{\pm}\mathrm{g}MAV_{DS} \quad (8o)$$

where GDP = gross domestic product of the reference park (10^4 RMB); $R_I^{\pm}$ = maximum conventional water resource availability of the gross domestic product ($m^3/10^4$ RMB); MAV_I = added product of industry (10^4 RMB); $R_I^{\pm}$ = maximum available conventional water amounts of the added industrial product ($m^3/10^4$ RMB); MAV_{DS} = added product of tertiary industry (10^4 RMB); $R_{DS}^{\pm}$ = maximum conventional water resource availability of the added tertiary industrial product ($m^3/10^4$ RMB). The constraints (**8m**) to (**8o**) restrict the allocated water amounts of transfer water and tap water not to exceed their utilization limitations of the GDP, added industrial products, and added tertiary industrial products, respectively.

iv. Constraint of reclaimed water reuse rate

$$\frac{\left(X_{3,1}^{\pm} + X_{3,2}^{\pm} + X_{3,3}^{\pm} + X_{3,4}^{\pm} + X_{3,5}^{\pm} + X_{3,6}^{\pm}\right)}{\eta \mathrm{g}\left(Q_s + Q_g + Q_{ds} + Q_j\right)} \geq \mu^{\pm} \quad (8p)$$

where $\mu^{\pm}$ = reuse rate of reclaimed water; η = sewage discharge coefficient. The constraint (**8p**) regulates the sewage water amounts to be reclaimed following a designated ratio.

v. Constraint of the LID projects

$$A_{1,1} + A_{1,2} = A_P \quad (8q)$$

$$A_{2,1} + A_{2,2} = A_G \quad (8r)$$

$$A_{3,1} + A_{3,2} = A_R \quad (8s)$$

$$A_{4,1} + A_{4,2} = A_S \quad (8t)$$

$$\sum_{n=1}^{N} \sum_{m=1}^{M} F_{n,m} g A_{n,m} g Q_{yh} = Q_{ys} \quad (8u)$$

$$Q_{YK} = Q_{ys} \quad (8v)$$

where A_p = available area of the pavement in the lark, m^2; A_G = available area of the greenbelt in the lark, m^2; A_p = available area of the roof in the lark, m^2; A_p = available area of the square in the lark, m^2; Q_{ys} = rainfall runoff of the lark, m^3; $F_{n,m}$ = runoff coefficient of projects n at the construction area m; Q_{yh} = average rainfall of the lark during one year, m^3; Q_{yx} = storage volume of rainfall, m. The constraints (**8q**) to (**8t**) are used to control the construction area of the LID projects in the pavement, greenbelt, roof, and square areas. The constraints (**8u**) to (**8v**) regulate the rainfall runoff and the rainwater availability, respectively.

vi. Other constraints

$$X_{1,6}^{\pm} = \theta_{Ts} g \left(X_{1,1}^{\pm} + X_{1,2}^{\pm} + X_{1,3}^{\pm} \right) \quad (8w)$$

$$X_{2,6}^{\pm} = \theta_{Ta} g \left(X_{2,1}^{\pm} + X_{2,2}^{\pm} + X_{2,3}^{\pm} + X_{2,4}^{\pm} \right) \quad (8x)$$

$$A_{n,m} \geq 0 \quad (8y)$$

$$X^{\pm} \geq 0 \quad (8z)$$

where θ_{Ts} = transmission loss coefficient of transfer water; θ_{Ta} = transmission loss coefficient of tap water. The constraints (**8w**) to (**8x**) regulate the transmission losses of the transfer water and tap water, respectively. The constraints (**8y**) to (**8z**) require the decision variables to be greater or equal to zero. Based on compromise programming and stochastic equilibrium chance-constrained programming methods described in *Materials and Methods*, two objectives (including economic and environmental objectives) were first combined into a single objective; then, the birandom constraints (including water supply–demand balance constraints) were converted into their interval equivalents; next, the interval form objective function and constraints were transferred to their respective two deterministic forms. Finally, the interval solutions under various constraints violation levels (i.e., 0.01, 0.05, and 0.1) were obtained, that is,

$f_C^{\pm}{}_{opt} = [f_C^{-}{}_{opt}, f_C^{+}{}_{opt}]$, $f_E^{\pm}{}_{opt} = [f_E^{-}{}_{opt}, f_E^{+}{}_{opt}]$, $A_{n,m}^{\pm}{}_{opt} = [A_{n,m}^{-}{}_{opt}, A_{n,m}^{+}{}_{opt}]$, and $X_{i,j}^{\pm}{}_{opt} = [X_{i,j}^{-}{}_{opt}, X_{i,j}^{+}{}_{opt}]$, respectively

Data Information

The model parameters can be divided into two types in this study, which included engineering parameters and water resource system parameters.

Engineering Parameters

Engineering parameters composed of construction costs, runoff coefficients, TSS treatment efficiencies, and available areas of LID and non-LID projects, which are shown in **Table 2**. The available areas are subjected to the park-scale limitation and remain unchanged, where they are expressed as deterministic values that came from Tianjin Statistics Bureau. The construction cost and TSS treatment efficiency have significant variations caused by policy regulations and technical condition, where they exhibited the uncertain characteristics with known upper and lower bounds. Accordingly, it is essential to define them as the interval numbers.

Water Resource System Parameters

According to on-site survey results, historical data record (from 2010 to 2018), Tianjin Statistics Bureau, and Tianjin Statistics yearbook, water resource system parameters include water provision cost, available water amount, and users' requirements, and their detailed data information is displayed in **Table 3**. Among them, users' requirements are affected by population, production scale, and local meteorological condition. Therefore, they are designed as the birandom variables with normal probability distribution. The water supply cost and available water amount own the small variation range and thus are assumed to be the interval number.

RESULTS ANALYSIS AND DISCUSSION

Results Analysis

Table 4 displays the optimal solutions of the MIBCCP model under different constraint violation levels (i.e., α) and different weight combinations. Based on the description of the interval linear programming in the *Methodology* section, the solutions for the two objective function values and some decision

TABLE 2 | Parameters associated with the low-impact development and non–low-impact development projects.

Item	Type of project	
	LID projects	Non-LID projects
Runoff coefficient	0.3	0.9
Available pavement area (m^2)	9,000	9,000
Available greenbelt area (m^2)	3,200	3,200
Available roof area (m^2)	14,000	14,000
Available square area (m^2)	5,600	5,600
TSS treatment efficiencies of the pavement	[0.85, 0.92]	0
TSS treatment efficiencies of the greenbelt	[0.85, 0.92]	0
TSS treatment efficiencies of the roof	[0.85, 0.92]	0
TSS treatment efficiencies of the square	[0.50, 0.70]	0
Construction costs in the pavement (RMB/m^2)	[168.12, 222.96]	[132.64, 188.32]
Construction costs in the greenbelt (RMB/m^2)	[190.43, 294.53]	[147.95, 196.54]
Construction costs in the roof (RMB/m^2)	[225.87, 336.29]	[194.32, 298.40]
Construction costs in the square (RMB/m^2)	[443.55, 588.81]	[398.16, 544.10]

TSS, total suspended solids; LID, low-impact development; non-LID, non–low-impact development.

TABLE 3 | Parameters related to the water resource system.

Parameters	Value
Interval parameters	
Supply price of transfer water	[8.8, 9.2] RMB/m^3
Supply price of tap water	[7.2, 7.8] RMB/m^3
Supply price of reclaimed water	[4.3, 4.7] RMB/m^3
Supply price of rain water	[2.2, 2.8] RMB/m^3
Available amount of transfer water	[11,000, 14,000] 10^3 m^3
Available amount of tap water	[30,000, 35,000] 10^3 m^3
Available amount of reclaimed water	[15,000, 18,000] 10^3 m^3
Birandom parameters	
Parameters	Probability distribution
Total water demand of livelihood	$N \sim (\mu, 23.38)$ $\mu \sim (1{,}829, 16.26)$
Total water demand of industry	$N \sim (\mu, 19.09)$ $\mu \sim (1{,}168, 13.39)$
Total water demand of tertiary industry	$N \sim (\mu, 8.61)$ $\mu \sim (175, 6.41)$
Total water demand of construction	$N \sim (\mu, 7.41)$ $\mu \sim (117, 5.61)$
Total water demand of ecology	$N \sim (\mu, 19.01)$ $\mu \sim (1{,}158, 13.34)$
Total water demand of other users	$N \sim (\mu, 23.38)$ $\mu \sim (578, 10.01)$

variables could be presented as interval numbers. For instance, when $\alpha = 0.1$, $w_1 = 0.1$, and $w_2 = 0.9$, the TSS treatment amounts would range from 31.6×10^3 to 34.2×10^3 tons. The system costs would change from 35.75 to 43.77 million RMB. The transfer water amount allocated to livelihood would fluctuate from 6.07 to 8.47 million m^3. The solutions of the two objectives correspond to the upper bound of the environmental benefit and the lower bound of the system costs, which are obtained under the most optimistic conditions (e.g., high TSS treatment efficiency as well as low construction and water allocation prices) when the interval decision variables (e.g., water resource allocation amounts) are at their lower bounds; although the solutions corresponding to the lower bound of the environmental benefit and the higher bound of the system costs are associated with the most conservative conditions when the water resource allocation amounts reach their higher bound levels. In fact, the flexibility and adjustability of the interval decision variables are beneficial for the decision-maker when inserting more implicit knowledge (e.g., socioeconomic conditions) into the optimize model so that they can formulate a more satisfactory and applicable decision scheme. Moreover, some interval decision variables indicate that there is no difference between their upper bound value and lower bound value. For example, when $\alpha = 0.1$, $w_1 = 0.1$, and $w_2 = 0.9$, the solutions of 8.00 million m^3 and 1.44 million m^3 are the tap water amounts allocated to industry and tertiary industry users. This is because these decision variables are insensitive to the variations in interval parameters.

Considering that the obtained solutions are affected by the interactive influence of the above two factors (weight coefficient combination and violation level), for the sake of reflecting the impact exerted by each factor, the variation trend of the solutions was analyzed under the context of changes to one factor as the other factor remains unchanged. First, when the three violation levels were maintained as stable ($\alpha = 0.1$), the selection of the construction schemes exhibited an obvious difference under various weight combinations. The high w_1 value would help to raise the economic benefits; otherwise, as w_2 climbs, the environmental benefits would increase. For instance, the non-LID projects are favored when the system costs are more of a concern, where $w_1 = 0.9$ and $w_2 = 0.1$. Under α value of 0.1, the difference in values between the non-LID project construction area and LID project construction area for pavement, greenbelt, roof, and square areas were 9.0×10^3, 3.2×10^3, 14.0×10^3, and 5.6×103 m^2, respectively. Conversely, with the change in weight combinations from $w_1 = 0.9$ and $w_2 = 0.1$ to $w_1 = 0.1$ and $w_2 = 0.9$, the difference in values would be $3.8{\times}10^3$, $3.2{\times}10^3$, $-14.0{\times}10^3$, and 5.6×103 m^2, respectively. This variation is because LID projects can bring increased environmental benefits. Moreover, selection of the water allocation strategy is also dependent on the weight coefficients. For example, it is established that the water demand of the tertiary industry is satisfied by tap water and reclaimed water with the values of 144 and 38.01 million m^3, where $w_1 = 0.1$ and $w_2 = 0.9$. However, when the system focuses on the economic benefit ($w_1 = 0.9$ and $w_2 = 0.1$), reclaimed water with its low allocation price would be the preferred source, and thus, the water demand of the tertiary industry would be provided in total by reclaimed water. A similar situation was also reflected in the different climate change scenario and time period. For example, under the RPC 4.5 scenario, when $w_1 = 0.1$ and $w_2 = 0.9$, tap water would be used to meet the water demand of the construction industry in 2025, with the values of 123.5 million m^3. When $w_1 = 0.9$ and $w_2 = 0.1$, the water demand of the tertiary industry would be provided in total by reclaimed water due to its high economic characteristic. The function of weight coefficients was to provide different water resource management schemes for managers. If the environmental quality is relatively poor and needs to be improved, managers should focus on the environmental benefits and choose the scheme under the high w_2. Conversely, they could prefer to increase the economic benefits and select the scheme under the high w_1.

Moreover, the variable situations of the obtained solutions under the different fixed weight coefficient combinations are discussed in order to examine the influences caused by violation level design on the generated decision schemes. First, when two weight coefficients are maintained as stable ($w_1 = 0.9$ and $w_2 = 0.1$), as the increase in the probabilistic level, the total water amounts supplied to four water users were decreased. For example, at the three α levels of 0.01, 0.05, and 0.1, the water amounts transferred to meet the demands of livelihood were 18,496.3, 18,435.9, and 18,403.6 × 103 m^3, respectively; similarly, the water amounts allocated to industry and the rainwater amount collected by LID and non-LID projects increased from 9,333.0 and 11,866.8 × 103 m^3 to 9,775.8 and 11,782.9 × 103 m^3, respectively. Meanwhile, the results own the same trends under climate change. For example, under the RPC 8.5 scenario, when α increases from 0.01 to 0.1, the water demand of the construction industry provided by reclaimed water was reduced in 2,100, being from 1,288.4 × 103 to 1,235.2 × 103 m^3; the tap water allocated to industry would decrease to 3,920.8 × 103 from 4,160.6 × 103 m^3. The main reason for this result is that the decrease in α value meant the constraints with the birandom variables would be strict, such that the water demand amounts would increase. On the contrary, the increase in the violation level of α means that the satisfied extent of the constraint has become weak, leading to a decrease in the water demand.

TABLE 4 | Part of solutions of multi-objective interval birandom chance-constrained programming model under various α values and weight combinations.

Item			Water allocation amount (10^3 m^3)														
			Transfer water allocation				Tap water allocation					Reclaimed water allocation					
A	w_1	w_1	User[a]	User[b]	User[c]	User[f]	User[a]	User[b]	User[c]	User[d]	User[f]	User[a]	User[b]	User[c]	User[d]	User[e]	User[f]
0.1	0.1	0.9	[607.31, 846.56]	0	0	[48.58, 67.72]	7,751.7	8,000	1,440	1,235.2	1,474.2	4,578.8	3,782.9	380.1	0	2,349.7	3,908.5
	0.9	0.1	[607.31, 846.56]	0	0	[48.58, 67.72]	12,330.5	3,920.8	0	0	1,300.1	0	7,862.1	1,820.1	1,235.2	0	4,082.6
0.05	0.1	0.9	[608.38, 848.05]	0	0	[48.67, 67.84]	7,722.5	8,000	1,440	1,253.7	1,473.3	4,629.6	3,812.1	399.9	0	2,224.8	3,933.6
	0.9	0.1	[608.38, 848.05]	0	0	[48.67, 67.84]	12,352.1	4,004.1	0	0	1,308.5	0	7,808	1,839.9	1,253.7	0	4,098.4
0.01	0.1	0.9	[610.38, 850.83]	0	0	[48.83, 68.07]	7,667.8	8,000	1,440	1,288.4	1,471.7	4,724.7	3,866.8	437.2	0	1,990.6	3,980.7
		0.1	[610.38, 850.83]	0	0	[48.83, 68.07]	12,392.5	4,160.6	0	0	1,324.2	0	7,706.2	1,877.2	1,288.4	0	4,128.1

Item			Construction area (10^3 m^2)								Values of objectives		System costs(10^6 RMB)		Rainwater amount (10^3 m^3)
			Pavement		Greenbelt		Roof		Square		Economic objective (10^6 RMB)	Environment objective (10^4 ton)	Water allocation cost	Construction cost	
A	w_1	w_2	Non-LID	LID	Non-LID	LID	Non-LID	LID	Non-LID	LID					
0.1	0.1	0.9	6.41	2.59	3.20	0	0	14.00	5.60	0	[35.74, 43.77]	[31.6,34.2]	[7.15, 10.17]	[28.60, 33.60]	9,333.0
	0.9	0.1	9.00	0	3.20	0	14.00	0	5.60	0	[34.05, 41.97]	0	[6.62, 9.55]	[27.43, 32.42]	11,682.7
0.05	0.1	0.9	6.92	2.08	3.20	0	0	14.00	5.60	0	[35.77, 43.80]	[30.7,33.2]	[7.13, 10.15]	[28.64, 33.64]	9,487.0
	0.9	0.1	9.00	0	3.20	0	14.00	0	5.60	0	[34.14, 42.07]	0	[6.62, 9.55]	[27.53, 32.53]	11,711.8
0.01	0.1	0.9	7.89	1.11	3.20	0	0	14.00	5.60	0	[35.81, 43.86]	[28.8,31.2]	[7.13, 10.08]	[28.71, 33.74]	9,775.8
	0.9	0.1	9.00	0	3.20	0	14.00	0	5.60	0	[34.33, 42.29]	0	[6.62, 9.55]	[27.71, 32.74]	11,766.4

LID, low-impact development; non-LID, non–low-impact development projects.

The changes in the combinations of weight coefficients and violation levels exerted an influence on the decision variables, but they also influenced the objective value. The economic and environmental objectives under various weight combinations and violation levels were estimated and are shown in **Figure 5A**. From **Figure 5A**, it was apparent that regardless of the α levels, the values of two objectives both keep the same trend with the change in weight combinations, considering the obtained solutions are affected by the interactive influence of the above two factors (w and α); thus, in order to reflect the impact exerted by w, the variation trend of the solutions was analyzed under a stable constraint violation, which was selected as 0.1. Specifically, when w_1 increased from 0.1 to 0.8 and w_2 simultaneously decreased from 0.9 to 0.2 under $\alpha = 0.1$, the economic objective and environmental objective remained unchanged with the values of 35.75, 43.77 million RMB and 31.6, 34.2 $\times 10^3$ tons. When w_1 and w_2 changed to 0.9 and 0.1, the two objectives decreased especially fast to 34.05, 41.97 million RMB and 0 tons. This indicated that the values of two objectives were insensitive to the weight shift before w_1 reaches 0.8. Only when $w_1 = 0.9$ and $w_2 = 0.1$ could the solution of environmental objective would decrease, which means the decision-makers considering environmental benefits are not the key factor for determining the optimal water resource allocation strategy. Meanwhile, the solution of economic objective corresponding to the total cost of the system would decrease, which represents the decision-makers focus on the economic benefit and aim to reduce the system costs.

In order to further reflect the sensitive range of objective functions, two objectives values under different weight coefficients (changing between from $w_1 = 0.8$, $w_2 = 0.2$ and, $w_1 = 0.9$, $w_2 = 0.1$) were estimated and displayed in **Figure 5B**. As demonstrated in **Figure 5B**, it was apparent that the values of two objectives decreased fast only when w_1 shifted from 0.87 to 0.89 and w_2 ranged from 0.11 to 0.13, respectively. For example, under an α value of 0.1, TSS treatment amounts are 31.6, 34.2 $\times 10^3$ tons, 26.7, 28.9 $\times 10^3$ tons, and 0 ton under the three weight coefficient combinations (i.e., $w_1 = 0.87$ and $w_2 = 0.13$, $w_1 = 0.88$ and $w_2 = 0.12$, and $w_1 = 0.89$ and $w_2 = 0.11$). The total system costs also showed the similarly downward trend with the values of 35.75, 43.77, 35.27, 43.29, and 34.05, 41.97 million RMB. Hence, if the managers wanted other results for system costs and treatment amount of TSS, they could adjust the parameters of the optimization model by choosing different w_1 and w_2 values between the above range.

Apart from the weight coefficient combinations, the values of two objectives were also influenced by the levels of α. As shown in **Figure 5A**, various α values resulted in different solutions. The value of economic objective decreased with the increase in α value. In contrast, the value of environmental objective increased with the growth level of α. For example, when $w_1 = 0.1$ and α increased from 0.01 to 0.1, the total treatment of TSS exhibited an upward trend from 28.8, 31.2 $\times 10^3$ tons to 31.6, 34.2 $\times 10^3$ tons. Inversely, the costs of the system decreased to 35.75, 43.77 million RMB from 35.71, 43.85 million RMB. This is because the α level represents the constraint violation risk of water supply–demand balance. The low α level corresponded to a low violation risk with a high water demand, leading to a high water allocation amount, which caused an increase in the system cost. Conversely, a high α value was associated with a high violation risk, which was accompanied by a low water supply amount. The variation in the α level provides a variety of water resource management schemes to the managers, which reflected the trade-off between the system economy and risk. Generally, the water demand can be divided into two categories: rigid demand and flexible demand. For example, the industrial water demand must be satisfied in its entirety subjected to its production characteristic. Conversely, the living water demand has a high elasticity and is able to reduce the water requirement through a series of water-saving measures under the water shortage scenario. The elastic characteristics of water demand allow the managers to design the water provision schemes according to local situation. Specifically, for the area where the economic development is relatively backward and simultaneously suffers from water shortage, it is suitable to select the scheme under the high α level which is capable of increasing the economic benefits and decreasing the water provision amounts, although it also may result in the high system failure risk. Conversely, the managers could choose the strategy under the low α level so that the water supply security would be enhanced by raising water supply amounts and system costs. Tianjin, as one of the most prosperous cities in China, always faces severe water shortage and thus has the superiority on economic development and the inferiority on water resource availability at the same time. Therefore, it is suggested that a compromise alternative (i.e., $\alpha = 0.95$) be adopted as the decision basis for the generation of final water resource management scheme in this study, which is helpful in realizing the balance between system economy and failure risk.

Discussion

In order to evaluate the influence caused by climate change on the water resource management, the generated runoff of the studied region and LID project implementation scheme were estimated under the two climate change scenarios (RCP4.5 and RCP8.5) with four periods (2025, 2050, 2075, and 2100), which were displayed in **Figure 6**. As shown in **Figure 6**, under fixed α level, the runoff of the park and area of LID projects would increase from 2025 to 2100 under both two scenarios. For example, with an α value of 0.1, when the period changes from 2025 to 2100, the runoffs in the RCP4.5 and RCP8.5 scenarios would increase from 696.7 to 1,510.0 million m^3 to 1,610.26 and 2,704.3 million m^3; meanwhile, the areas of LID projects would be upward from 17.35 and 27.4 thousand m^2 to 28.8 and 31.8 thousand m^2, respectively. That is because the climate change could lead to the growths in regional rainwater and runoff, which might trigger the rainfall flood. The similar results were also reported by other studies (Zahmatkesh et al., 2014; Yoon et al., 2015; Guo et al. (2019a)). For instance, Zahmatkesh et al. (2014) found that climate change led to the increase in the urban stormwater runoff volume of the Bronx River watershed, New York City. Yoon et al. (2015) proposed a methodology for the evaluation

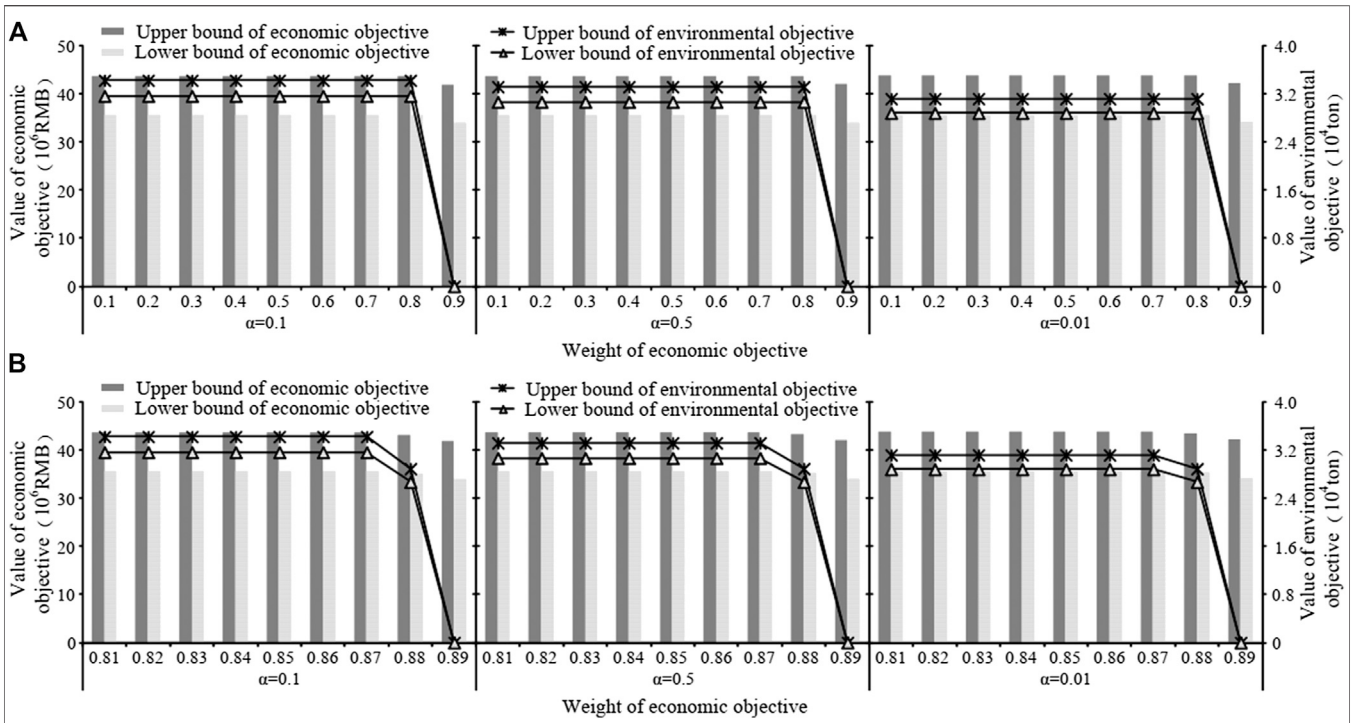

FIGURE 5 | Economic and environmental objective values under various α values and weight combinations. (A) Weight of economic objective is from 0.1 to 0.9; (B) Weight of economic objective is from 0.81 to 0.89.

of the overflow probability of urban streams under climate change in the Uicheon Basin of Korea and obtained results showed that 100-year peak flow in the future would increase by 58.1% compared with historical conditions. Moreover, to deal with the increase in the flooding risk caused by climate change, the LID project is recommended as climate mitigation measures in this research, which was capable of alleviating the adverse impact of increased stormwater based on the collection and retention facilities of the rainwater. The obtained results are consistent with the related studies, such as Guo et al. (2019b),

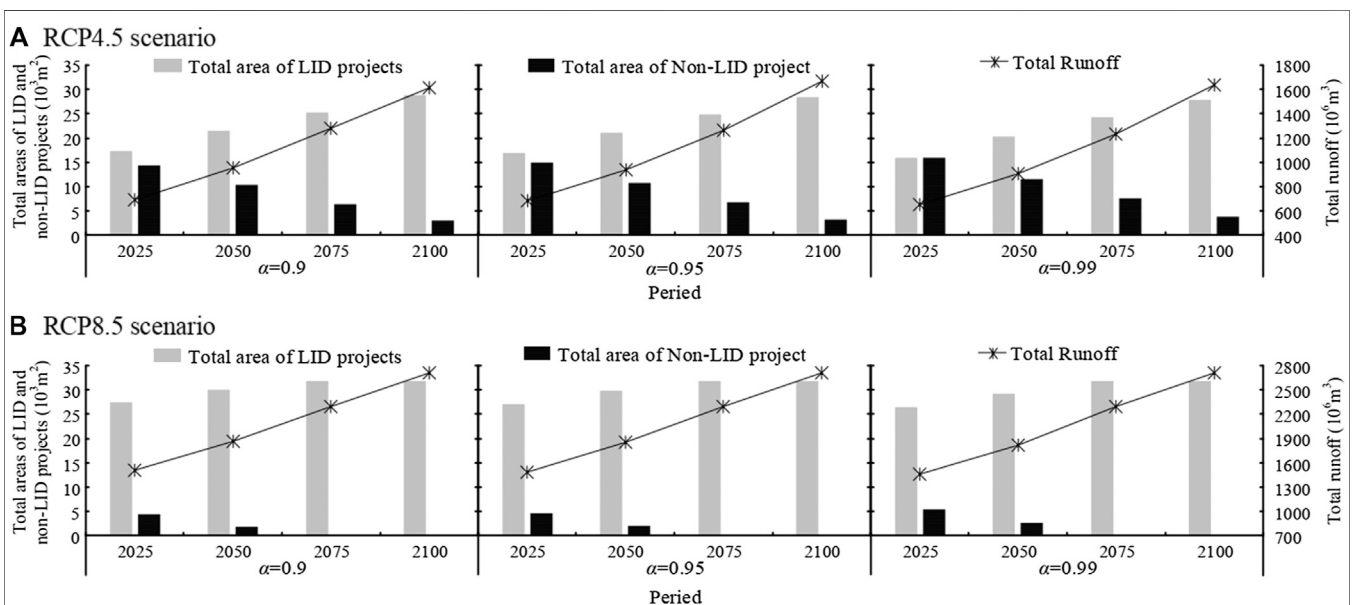

FIGURE 6 | Variations in the runoff and low-impact development projects areas under two climate change scenarios. (A) RCP 4.5 scenario; (B) RCP 8.5 scenario.

Morvarid et al. (2019), and Hou et al. (2019). Specifically, it is concluded that the LID projects are beneficial to reduce the flooding risk and cope with the stormwater management issue arising from heavy rainfall under climate change. On the other hand, the above studies formulated the urban water management model with the aid of hydrological software (i.e., SWMM), which has excellent performance in describing the hydraulic connections and relationships among various water sources and users. In this study, an MIBCCP model based on compromise programming, birandom chance-constrained programming and interval linear programming is proposed for identifying the uncertainties associated with the urban water resource management system and generating a variety of water allocation patterns reflecting the trade-off between system economy and reliability; however, it also has difficulties in obtaining more accurate solutions due to oversimplified hydrologic and hydraulic equations. Therefore, it is necessary to enhance the accuracy and applicability of the proposed model through incorporating the output of some hydrological models into the optimization process.

Moreover, the MIBCCP model still needs to be improved, especially in the following three aspects. First, the objective function in this study is assumed as a linear form; in fact, system cost could exhibit the economy-of-scale feature, and the relationship between water supply cost and distance may be nonlinear, rather than the linear one. This will lead to a nonlinear objective function. Because the focus of this research is to apply birandom variables and interval numbers for supporting water resource management issue, it is thus desired to examine the possibility of the integrated model of MIBCCP and nonlinear programming in the future. Second, the compromise programming is used to combine two objectives into an integrated one. In fact, many types of multi-objective methods are available, such as the genetic algorithm and the interactive approximation algorithm. How to select an appropriate solution method through the comparison analysis is very critical. Third, two traditional objectives are considered in the MIBCCP model. In fact, other objectives, including the ecological stability and social acceptance, also obtained more attentions and thus deserved further research.

CONCLUSION

Under the urgency of rational water resource allocation and effective urban flooding control, a (MIBCCP) model under climate change is developed in this study. The MIBCCP model incorporates compromise programming, birandom chance-constrained programming, and interval linear programming within a general framework, where each technique offers a unique contribution toward the enhancement of the model capability in tackling the complexities and uncertainties. A water supply management system of educational park in Tianjin was used to demonstrate the applicability of the proposed method. A variety of water allocation patterns are obtained through adjusting predetermined constraint violation levels and weight combinations, which indicated that MIBCCP was useful in helping local managers gain in-depth insights into the water management system under climate change, realize the utilization of nonconventional water source and application in LID projects, and analyze the trade-offs between system economy and reliability, as well as establish the cost-effective environmentally friendly water provision strategies. Meanwhile, optimal construction schemes for LID projects under two scenarios were identified by the MIBCCP model to deal with the rainfall flood control issue under climate change. The successful application in the park is expectable for providing a good demonstration to the water management problem in other regions of China. In the future, high-precision hydrological simulation models and other multi-objective programming methods should be incorporated into the proposed model for tackling more complex issues.

DATA AVAILABILITY STATEMENT

All datasets generated for this study are included in the article.

AUTHOR CONTRIBUTIONS

YX, ZB, and GH conceived and designed the research. WL, HY, and ZB collected the data. YX, ZB, GH, and HY formulated the optimization model. ZB, YX, and GH performed the data analyses and manuscript preparation. ZB, YX, WL, and HY wrote the paper. GH, WL, and YX gave the comments and helped in revising the paper.

FUNDING

This research was supported by Joint Fund of State key Lab of Hydroscience and Institute of Internet of Waters Tsinghua-Ningxia Yinchuan [sklhse-2020-Iow10] and National Key Research and Development Plan (2018YFE0196000).

REFERENCES

Bajracharya, A. R., Bajracharya, S. R., Shrestha, A. B., and BikashMaharjan, S. (2018). Climate change impact assessment on the hydrological regime of the Kaligandaki Basin, Nepal. *Sci. Total Environ.* 625, 837–848. doi:10.1016/j.scitotenv.2017.12.332

Bekchanov, M., Bhaduri, A., and Ringler, C. (2015). Potential gains from water rights trading in the Aral Sea Basin. *Agric. Water Manag.* 152, 41–56. doi:10.1016/j.agwat.2014.12.011

Dai, C., Qin, X. S., Chen, Y., and Guo, H. C. (2018). Dealing with equality and benefit for water allocation in a lake watershed: a Gini-coefficient based stochastic optimization approach. *J. Hydrol.* 561, 322–334. doi:10.1016/j.jhydrol.2018.04.012

Eckart, K., McPhee, Z., and Bolisetti, T. (2018). Multiobjective optimization of low impact development stormwater controls. *J. Hydrol.* 562, 564–576. doi:10.1016/j.jhydrol.2018.04.068

Guo, J. H., Huang, G. H., Wang, X. Q., Li, Y. P., and Yang, L. (2018). Future changes in precipitation extremes over China projected by a regional climate model ensemble. *Atmos. Environ.* 188, 142–156. doi:10.1002/2016EF000433

Guo, L. M., Shan, N., Zhang, Y. G., Sun, F. B., Liu, W. B., Shi, Z. J., et al. (2019a). Separating the effects of climate change and human activity on water use efficiency over the Beijing-Tianjin Sand Source Region of China. *Sci. Total Environ.* 690, 584–595. doi:10.1016/j.scitotenv.2019.07.067

Guo, X. C., Du, P. F., Zhao, D. Q., and Li, M. (2019b). Modelling low impact development in watersheds using the storm water management model. *Urban Water J.* 16 (2), 146–155. doi:10.1080/1573062X.2019.1637440

Helmia, N. R., Verbeirena, B., Mijicb, A., Griensvena, A., and Bauwensa, W. (2019). Developing a modeling tool to allocate low impact development practices in a cost-optimized method. *J. Hydrol.* 573, 98–108. doi:10.1016/j.jhydrol.2019.03.017

Hou, J. M., Han, H., Qi, W. C., Guo, K. H., Li, Z. B., and Reinhard, H. (2019). Experimental investigation for impacts of rain storms and terrain slopes on low impact development effect in an idealized urban catchment. *J. Hydrol.* 579, 124176. doi:10.1016/j.jhydrol.2019.124176

Huang, G. H. (1988). A hybrid inexact-stochastic water management model. *Eur. J. Oper. Res.* 107 (1), 137–158. doi:10.1016/S0377-2217(97)00144-6

Huang, G. H., Baetz, B. W., and Patry, G. G. (1992). A grey linear programming approach for municipal solid waste management planning under uncertainty. *Civil Eng. Syst.* 9, 319–335. doi:10.1080/02630259208970657

Huang, Y. C., and Lee, C. M. (2019). Designing an optimal water supply portfolio for Taiwan under the impact of climate change: case study of the Penghu area. *J. Hydrol.* 573, 235–245. doi:10.1016/j.jhydrol.2019.03.007

Kundzewicz, Z., Su, B., Wang, Y. J., Xia, J., Huang, J. L., and Jiang, T. (2018). Analysis of increasing flash flood frequency in the densely urbanized coastline of the Campi Flegrei Volcanic area. Italy. *Front. Earth Sci.* 6, 63–79. doi:10.3389/feart.2018.00063

Kundzewicz, Z., Su, B., Wang, Y. J., Xia, J., Huang, J. L., and Jiang, T. (2019). Flood risk and its reduction in China. *Adv. Water Resour.* 130, 37–45. doi:10.1016/j.advwatres.2019.05.020

Liu, S. S., Konstantopoulou, F., Gikas, P., and Papageorgiou, L. (2011). A mixed integer optimisation approach for integrated water resources management. *Comput. Chem. Eng.* 35, 858–875. doi:10.1016/j.compchemeng.2011.01.032

Liu, Y., Guo, H. C., Zhou, F., Qin, X. S., Huang, K., and Yu, Y. J. (2008). Inexact chance-constrained linear programming model for optimal water pollution management at the watershed scale. *J. Water. Res. Plan. Mang.* 134 (4), 347–356. doi:10.1061/(ASCE)0733-9496(2008)134:4(347)

Loomis, B. D., Richey, A. S., Arendt, A. A., Appana, R., Deweese, Y. J. C., Forman, B. A., et al. (2019). Water storage trends in High Mountain Asia. *Front. Earth Sci.* 7, 235–251. doi:10.3389/feart.2019.00235

Mahmoud, S. H., and Gan, T. Y. (2018). Urbanization and climate change implications in flood risk management: developing an efficient decision support system for flood susceptibility mapping. *Sci. Total Environ.* 636, 152–167. doi:10.1016/j.scitotenv.2018.04.282

Mainuddin, M., Gupta, A. D., and Onta, P. R. (1997). Optimal crop planning model for an existing groundwater irrigation project in Thailand. *Agric. Water Manag.* 33, 43–62. doi:10.1016/S0378-3774(96)01278-4

Morvarid, L., Gholamreza, R., Mohammad, R. N., and Mojtaba, S. (2019). A game theoretical low impact development optimization model for urban storm water management. *Urban Water J.* 241 (2), 118323. doi:10.1016/j.jclepro.2019.118323

Niu, S. L., Wu, M. Y., Han, Y., Xia, J. Y., Li, L. H., and Wan, S. Q. (2008). Water-mediated responses of ecosystem carbon fluxes to climatic change in a temperate steppe. *New Phytol.* 177 (1), 209–219. doi:10.1111/j.1469-8137.2007.02237.x

Palanisamy, B., and Chui, T. F. M. (2015). Rehabilitation of concrete canals in urban catchments using low impact development techniques. *J. Hydrol.* 523, 309–319. doi:10.1016/j.jhydrol.2015.01.034

Palla, A., and Gnecco, I. (2015). Hydrologic modeling of low impact development systems at the urban catchment scale. *J. Hydrol.* 528, 361–368. doi:10.1016/j.jhydrol.2015.06.050

Peng, J., and Liu, B. D. (2007). Birandom variables and birandom programming. *Comput. Ind. Eng.* 53 (3), 433–453. doi:10.1016/j.cie.2004.11.003

Qin, X. S., and Huang, G. H. (2009). An inexact chance-constrained quadratic programming model for stream water quality management. *Water Resour. Manag.* 23 (4), 661–695. doi:10.1007/s11269-008-9294-0

Qin, X. S., Xu, Y., and Hipel, K. W. (2011). Basin-wide cooperative water resources allocation. *Adv. Water Resour.* 34 (7), 873–886. doi:10.1016/j.ejor.2007.06.045

Rao, K. K., Patwardhan, S. K., Kulkarni, A., Kamala, K., Sabade, S. S., and Kumar, K. K. (2014). Projected changes in mean and extreme precipitation indices over India using PRECIS. *Global Planet. Change.* 113, 77–90. doi:10.1016/j.gloplacha.2013.12.006

Sample, D. J., and Liu, J. (2014). Optimizing rainwater harvesting systems for the dual purposes of water supply and runoff capture. *J. Clean. Prod.* 75, 174–194. doi:10.12691/ajcea-3-3-5

Shang, W., Hu, Z. G., Guo, Y., Zhang, C. C., Wang, C. J., Jiang, H., et al. (2015). The impact of climate change on landslides in southeastern of high-latitude permafrost regions of China. *Front. Earth Sci.* 3, 7. doi:10.3389/feart.2015.00007

Shangguan, Z. P., Shao, M. G., Horton, R., Lei, T. W., Qin, L., and Ma, J. Q. (2002). A model for regional optimal allocation of irrigation water resources under deficit irrigation and its applications. *Agric. Water Manag.* 52, 139–154. doi:10.1016/S0378-3774(01)00116-0

Song, J., Yang, R., Chang, Z., Li, W. F., and Wu, J. S. (2019). Adaptation as an indicator of measuring low-impact-development effectiveness in urban flooding risk mitigation. *Sci. Total Environ.* 696, 133764. doi:10.1016/j.scitotenv.2019.133764

Wang, C. Y., Wang, R. R., Hertwich, E., Liu, Y., and Tong, F. (2019). Water scarcity risks mitigated or aggravated by the inter-regional electricity transmission across China. *Appl. Energy.* 238, 413–422. doi:10.1016/j.apenergy.2019.01.120

Wang, L., Huang, G., Wang, X. Q., and Zhu, W. H. (2018). Risk-based electric power system planning for climate change mitigation through multi-stage joint-probabilistic left-hand-side chance-constrained fractional programming: a Canadian case study. *Renew. Sustain. Energy Rev.* 82, 1056–1067. doi:10.1016/j.rser.2017.09.098

Wang, L. Z., Fang, L. P., and Hipel, K. W. (2008). Basin-wide cooperative water resources allocation. *Eur. J. Oper. Res.* 190, 798–817. doi:10.1016/j.ejor.2007.06.045

Wu, J., Ma, C., Zhang, D. Z., and Xu, Y. (2018). Municipal solid waste management and greenhouse gas emission control through an inexact optimization model under interval and random uncertainties. *Eng. Optim.* 50 (11), 1963–1977. doi:10.1080/0305215X.2017.1419347

Xia, J., Duan, Q. Y., Luo, Y., Xie, Z. H., Liu, Z. Y., and Mo, X. G. (2019). Climate change and water resources: case study of eastern monsoon region of China. *Adv. Clim. Change Res.* 8, 63–67. doi:10.1016/j.accre.2017.03.007

Xu, J. P., and Ding, C. (2011). A class of chance constrained multiobjective linear programming with birandom coefficients and its application to vendors selection. *Int. J. Prod. Econ.* 131, 709–720. doi:10.1016/j.ijpe.2011.02.020

Xu, J. P., and Tao, Z. M. (2012). A class of multi-objective equilibrium chance maximization model with twofold random phenomenon and its application to hydropower station operation. *Math. Comput. Simulat.* 85, 11–33. doi:10.1016/j.matcom.2012.09.010

Xu, J. P., and Zhou, X. Y. (2009). A class of multi-objective expected value decision-making model with birandom coefficients and its application to flow shop scheduling problem. *Inf. Sci.* 179, 2997–3017. doi:10.1016/j.ins.2009.04.009

Xu, M., Li, C. H., Wang, X., Cai, Y. P., and Yue, W. C. (2018). Optimal water utilization and allocation in industrial sectors based on water footprint accounting in Dalian city, China. *J. Clean. Prod.* 176, 1283–1291. doi:10.1016/J.JCLEPRO.2017.11.203

Xu, T., Li, K., Engel, B. A., Jia, H. F., Leng, L. Y., Sun, Z. X., et al. (2019). Optimal adaptation pathway for sustainable low impact development planning under deep uncertainty of climate change: a greedy strategy. *J. Environ. Manag.* 248, 109280. doi:10.1016/j.jenvman.2019.109280

Xu, Y., Huang, G. H., Qin, X. S., and Cao, M. F. (2009). A stochastic robust chance-constrained programming model for municipal solid waste management under uncertainty. *Resour. Conserv. Recy.* 53, 352–363. doi:10.1016/j.resconrec.2009.02.002

Xu, Y., Huang, G. H., and Shao, L. G. (2014). A solid waste management model with fuzzy random parameters. *Civil Eng. Environ. Syst.* 31 (1), 64–78. doi:10.1080/10286608.2013.853744

Xu, Y., Wang, Y., Li, S., Huang, G. H., and Dai, C. (2018). Stochastic optimization model for water allocation on a watershed scale considering wetland's ecological water requirement. *Ecol. Indicat.* 92, 330–341. doi:10.3390/w9060378

Ye, Q. L., Li, Y., Zhou, L., Zhang, W. L., Xiong, W., Wang, C., et al. (2018). Optimal allocation of physical water resources integrated with virtual water trade in water scarce regions: a case study for Beijing, China. *Water Res.* 129, 264–276. doi:10.1016/j.watres.2017.11.036

Yoon, S. K., Kim, J. S., and Moon, Y. I. (2015). Urban stream overflow probability in a changing climate: case study of the Seoul Uicheon Basin, Korea. *J. Hydro-environ Res.* 13, 52–65. doi:10.1016/j.jher.2015.08.001

Yu, G. R., Song, X., Wang, Q. F., Liu, Y. F., Guan, D. X., Yan, J. H., et al. (2008). Water-use efficiency of forest ecosystems in eastern China and its relations to climatic variables. *New Phytol.* 177 (4), 927–937. doi:10.1111/j.1469-8137.2007.02316.x

Zahmatkesh, Z., Karamouz, M., Goharian, E., and Burian, S. J. (2014). Analysis of the effects of climate change on urban storm water runoff using statistically downscaled precipitation data and a change factor approach. *J. Hydrol. Eng.* 20 (7), 05014022. doi:10.1061/(ASCE)HE.1943-5584.0001064

Zhang, F., Guo, P., Engel, B. A., Guo, S. S., Zhang, C. L., and Tang, Y. K. (2019). Planning seasonal irrigation water allocation based on an interval multiobjective multi-stage stochastic programming approach. *Agric. Water Manag.* 223, 105692. doi:10.1016/j.agwat.2019.105692

Zhang, H., Wang, B., Liu, D. L., Zhang, M. X., Feng, P. Y., Cheng, L., et al. (2019). Impacts of future climate change on water resource availability of eastern Australia: a case study of the Manning River Basin. *J. Hydrol.* 573, 49–59. doi:10.1016/j.jhydrol.2019.03.067

Zhou, M., Lu, S. S., Tan, S. K., Yan, D. P., Ou, G. L., Liu, D. F., et al. (2017). A stochastic equilibrium chance-constrained programming model for municipal solid waste management of the city of Dalian, China. *Qual. Quant.* 51 (1), 199–218. doi:10.1007/s11135-015-0301-2

Conflict of Interest: The authors declare that the research was conducted in the absence of any commercial or financial relationships that could be construed as a potential conflict of interest.

frontiers in Environmental Science

ORIGINAL RESEARCH
published: 06 September 2021
doi: 10.3389/fenvs.2021.742326

Ensemble Temperature and Precipitation Projection for Multi-Factorial Interactive Effects of GCMs and SSPs: Application to China

Ruixin Duan[1,2], Guohe Huang[1], Yongping Li[1], Rubing Zheng[2], Guoqing Wang[3], Baozhen Xin[3], Chuyin Tian[1,2] and Jiayan Ren[1,2]*

[1]State Key Joint Laboratory of Environmental Simulation and Pollution Control, China-Canada Center for Energy, Environment and Ecology Research, UR-BNU, School of Environment, Beijing Normal University, Beijing, China, [2]Sino-Canada Resources and Environmental Research Academy, North China Electric Power University, Beijing, China, [3]State Key Laboratory of Hydrology–Water Resources and Hydraulic Engineering, Nanjing Hydraulic Research Institute, Nanjing, China

OPEN ACCESS

Edited by:
Shan Zhao,
Shandong University, China

Reviewed by:
Lujun Zhang,
University of Oklahoma, United States
Wei Sun,
Sun Yat-Sen University, China

***Correspondence:**
Guohe Huang
guohe.huang@outlook.com

Specialty section:
This article was submitted to Interdisciplinary Climate Studies, a section of the journal Frontiers in Environmental Science

Received: *16 July 2021*
Accepted: *23 August 2021*
Published: *06 September 2021*

Citation:
Duan R, Huang G, Li Y, Zheng R, Wang G, Xin B, Tian C and Ren J (2021) Ensemble Temperature and Precipitation Projection for Multi-Factorial Interactive Effects of GCMs and SSPs: Application to China. Front. Environ. Sci. 9:742326. doi: 10.3389/fenvs.2021.742326

Climate change has broadly impacted on the China areas. There will be severe challenges due to the variations of precipitation and temperature in the future. Therefore, a comprehensive understanding of the future climate change over China areas is desired. In this study, future annual precipitation and annual mean temperature under two SSPs over China areas were projected through multiple global climate models. Meanwhile, to explore the sources of uncertainty in projecting future climate change, the multi-factorial analysis was conducted through GCMs (five levels) and SSPs (two levels). This study can help us understand the possible changes in precipitation, temperature, and the potential extreme climate events over the China area. The results indicate that China would have more annual precipitation and higher annual mean temperature in the future. Compared with the historical period, the annual mean temperature would face a continuously increasing trend under SSPs. Regardless of SSP245 or SSP585, the growth rate of annual precipitation and annual mean temperature increase in the northern region (e.g., Northeast China, North China, and Northwest China) are higher than those in the southern parts (e.g., East China, South China, and Central China). The future temperature rise may increase the frequency of heat-related extreme climate events, which needs to be focused on in future research. Moreover, GCM was the main contributing factor to the sources of uncertainty in projecting future precipitation and SSP was the main factor for future temperature. Overall, climate change is an indisputable fact in China. The annual precipitation and annual mean temperature would increase to varying degrees in the future. Reducing the systemic bias of the climate model itself will undoubtedly be the top priority, and it would help to improve the projection and evaluation effects of relevant climate variables.

Keywords: climate change, annual precipitation, annual mean temperature, multi-factorial analysis, China

INTRODUCTION

Temperature and precipitation are the two major climatic elements that people are most concerned about under climate change (Tisseuil et al., 2012). Observations show that the average temperature of the global land area has been increasing significantly, especially in recent decades (Cheng et al., 2019). Not only that, but the precipitation has also changed to varying degrees. Changes in temperature and precipitation will cause a series of extreme climate events (Kodinariya and Makwana, 2013; Duan et al., 2020). For instance, droughts and heatwaves have increased, and floods have become more frequent (Wang et al., 2004b). There is no doubt that the intensification of climate change has affected the survival and development of humans (Feng and Hu, 2014). Besides, changes in precipitation and temperature also affect agricultural, industrial, fisheries, animal husbandry, and other aspects. Therefore, the assessment of future temperature and precipitation will help to improve the ability to deal with climate-related impacts (Wang et al., 2018). Precipitation and temperature in China have also seen significant changes in recent decades (Shivam et al., 2019). The increase in climate disasters caused by climate warming may be a more prominent problem in China. This may bring frequent climatic disasters, including excessive rainfall, extensive droughts, and sustained high temperatures, resulting in large-scale disaster losses. Therefore, the projection and analysis of future climate change have important socio-economic significance (Ghosh and Mujumdar, 2007; Zhai et al., 2020).

Previous studies have checked future changes in temperature and precipitation in China by multiple climate models (e.g., global climate models and regional climate models) (Du et al., 2018; Jacob et al., 2018). Most research focused on analyzing the temporal and spatial characteristics of key climate elements. Besides, the quantitative analysis of climate elements was also one of the current research hotspots. In particular, the changes in relative historical periods such as temperature and precipitation under different emission scenarios in the future (Cho et al., 2015; Ji et al., 2018; Batibeniz et al., 2020). There is no doubt that the climate model has become an important tool for assessing future climate change in the current period. For example Hui et al. (2018), analyzed the mean and extreme climate over China during future period through the simulations from global climate models (GCMs) under two RCPs (Representative Concentration Pathways). Ultimately, the study revealed that China area would experience much warmer climate in the future (Hui et al., 2018). Ba et al. (2018) assessed the impacts of climate change on water resources in Kaidu River Basin through multiple general circulation models under two RCPs. The results showed that both the precipitation and temperature in the study area would increase in the future relative to the historical period (Ba et al., 2018). Hou et al. (2019) compared the performance of multiple climate models for future climate change projection over different regions in China (Hou et al., 2019).

However, many studies were mainly focused on analyzing the future changes in precipitation and temperature through individual global climate models (GCMs) from CMIP5 (Manrique-Alba et al., 2020). Currently, the GCMs are the only tool available to project future climate change. They have been widely used in assessing climate change (Thomas et al., 2013). Due to the lack of a full understanding of the complex climate change process, there are inevitably many deficiencies in GCMs (Paeth and Hense, 2004; Dan et al., 2015; Spinoni et al., 2019). The grid points of GCMs are often larger than 100 km, which makes them difficult to employ for regional climate change research. Besides, due to the uncertainty of emission scenarios, climate change in the future is often uncertain (Carrão et al., 2016; Park et al., 2016; Peltier et al., 2018). Although existing studies have analyzed the uncertainties of climate models and emission scenarios for future climate projections, they have seldom considered their interactive effects (Vogel et al., 2020). Moreover, the new version of climate models has improved the ability to simulate climate elements. Therefore, it is necessary to strengthen the analysis of future climate change under the latest coupled model. (i.e., CMIP6).

Therefore, as an extension of previous studies, the objective of this research is to evaluate the possible changes in annual precipitation and annual mean temperature in China and trace the sources of uncertainty on projecting future climate change. Specifically, the objective entails 1) exploring changes in temperature and precipitation in the future from multiple perspectives through an ensemble of multiple GCMs under different Shared Socioeconomic Pathways (SSPs), 2) quantifying the main contribution (and their interactions) of climate models and emission scenarios to the sources of uncertainty on climate change projection.

METHODOLOGY AND CLIMATE DATA

Study Area

The terrain of China is high in the west and low in the east and is complex and diverse (Smirnov et al., 2016; Poschlod et al., 2018; Zhou et al., 2018). Mountains accounted for 33.3% of the total land area, plateaus accounted for 26%, basins accounted for 18.8%, plains accounted for 12%, and hills accounted for 9.9% (Sharafi et al., 2020). The terrain forms a three-level ladder from west to east. Among them, the Qinghai-Tibet Plateau is located in the west, with the highest terrain. It is composed of extremely high mountains and plateaus. Therefore, it is also called the "roof of the world". The second ladder is from the east of the Qinghai-Tibet Plateau to Daxinganling-Taihang-Wushan-Xuefeng Mountain (Tan et al., 2011; Thompson et al., 2016). The altitude is generally 1,000–2000 m, and it is mainly composed of mountains, plateaus, and basins. The broad plains and hills of eastern China are the third ladder. The annual precipitation gradually decreases from the southeast coast to the northwest inland. The annual precipitation in the southeast coastal area is more than 1,600 mm and decreases to 800 mm near the Qinling-Huaihe River. Then to the northwest to Daxinganling-Yinshan-Lanzhou-southeast of the Qinghai-Tibet Plateau, it is reduced to 400 mm. The Helan Mountain to the central part of the Qinghai-Tibet Plateau reduces to 200 mm. The annual precipitation in the Tarim Basin is less than 50 mm (Moore et al., 2013). The

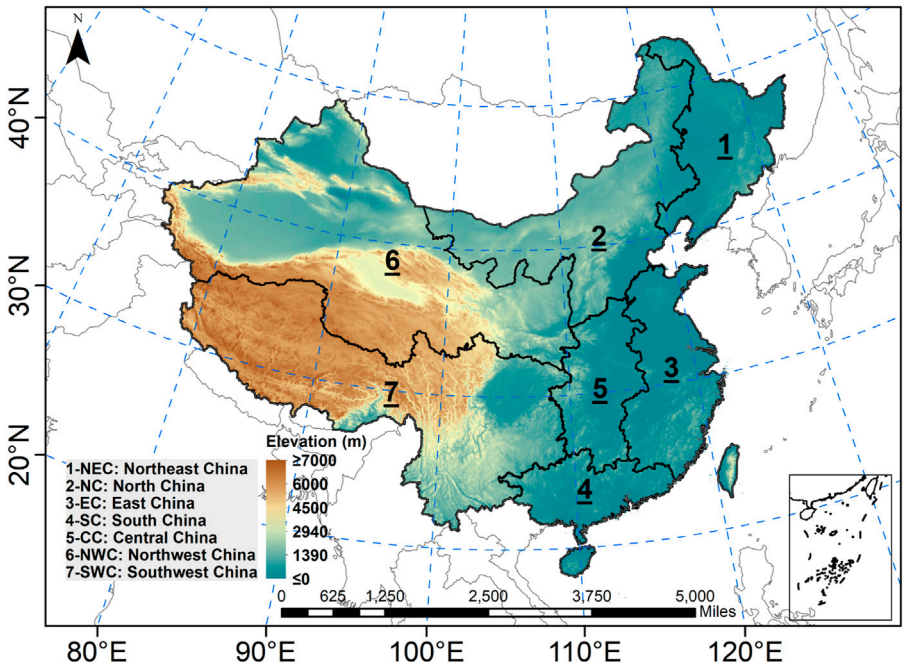

FIGURE 1 | The study area of China with seven sub-regions. The seven sub-regions are Northeast China, North China, East China, South China, Central China, Northwest China, and Southwest China.

TABLE 1 | The information of five global climate models employed in this study.

GCM model	Resolution (deg)	Experiment	Time frequency	Variant Label
CESM2	1.25 × 0.94	historical, ssp245, ssp585	Mon	r1i1p1f1
GFDL-ESM4	1.25 × 1.0	historical, ssp245, ssp585	Mon	r1i1p1f1
IPSL-CM6A-LR	2.50 × 1.27	historical, ssp245, ssp585	Mon	r1i1p1f1
MIROC6	1.41 × 1.40	historical, ssp245, ssp585	Mon	r1i1p1f1
MRI-ESM2-0	1.125 × 1.12	historical, ssp245, ssp585	Mon	r1i1p1f1

temperature difference between north and south is large in winter, while the south is warm, and the temperature gets lower as it goes north. The summer is generally high throughout the country, and the Qinghai-Tibet Plateau is the coolest place in China. Due to the combined influence of human activities and natural factors, the annual average temperature in China has risen by 0.68°C since the 1950s. Therefore, it is imminent to carry out climate change projection and assessment over China. The changes in precipitation and temperature in different regions of China are not the same. To facilitate comparative analysis, China is divided into seven subregions, including Northeast China, North China, East China, South China, Central China, Northwest China, and Southwest China, as shown in **Figure 1**. The division of subregions refers to previous studies (Smalley et al., 2019).

Dataset

Five different kinds of GCMs (i.e., CESM2, GFDL-ESM4, IPSL-CM6A-LR, MIROC6, and MRI-ESM2-0) are acquired from the WCRP Coupled Model Intercomparison Project (Phase 6) dataset archive (https://esgf-node.llnl.gov/projects/cmip6/). The details are shown in **Table 1**. Two 50-year periods are employed in this study, including the historical period (1965–2014) and the future period (2051–2100). The data in the future period is extracted under two SSPs (i.e., SSP245 and SSP585). The annual precipitation and annual mean temperature are the two variables of interest in this study. The data are all united to 0.5° × 0.5° in spatial through the bilinear interpolation method (Chen et al., 2016). The SSPs (Shared Socioeconomic Pathways) is the latest scenarios to project socioeconomic global changes up to 2100. They are broadly employed to derive greenhouse gas emissions scenarios with different climate policies. The SSP245 scenario assumes that the world follows a path where social, economic, and technological trends will not significantly deviate from historical patterns. Among them, development and income growth are not balanced. Some countries have made good progress, while others have fallen short of expectations. The environmental system has experienced degradation, but there have been some improvements, and the intensity of resource and energy use has declined overall (Ying et al., 2019). Global

population growth is modest and stabilized in the second half of this century. Income inequality persists or is slow to improve, and the challenge of reducing vulnerability to social and environmental changes remains (Roberts et al., 2019; Asif and Chen, 2020; Li et al., 2020). SSP585 assumes that the world increasingly believes that competitive markets, innovation, and a participatory society can bring rapid technological progress and human capital development as a way to sustainable development. At the same time, while promoting economic and social development, all parts of the world are developing abundant fossil fuel resources and adopting resource- and energy-intensive lifestyles. All these factors have led to the rapid growth of the global economy, while the global population has reached its peak and declined in the 21st century (Trenberth and Shea, 2005).

Multi-Factorial Analysis Method

The main content of the multi-factorial analysis method is the Analysis of variance (ANOVA) theory (Li et al., 2010). As an effective statistical method, the main contribution and the interactions of multiple factors to the sources of uncertainty can be traced. In this study, the global climate models (i.e., GCMs) and emission scenarios (i.e., SSPs) are the two sources of uncertainty on future precipitation and temperature projection. It has been broadly used to address the non-linear relationship between the independent factors and the dependent factor (Wang et al., 2004a; Wang et al., 2018; Feng and Hu, 2014). In general, a formula can be written as $y = F(x_1, x_2, x_3, ..., x_n)$ to express the complex connection. Among them, y is the dependent factor and x represents the multiple independent factors. In this study, the future precipitation or temperature is the y variable, GCMs (five levels) and SSPs (two levels) are x variables (Huang et al., 1997; Wang et al., 2021). According to the ANOVA theory, the total variance contains two aspects:

$$SS_{total} = \sum_{i=1}^{n} SS_i + SS_{int} \quad (1)$$

where SS_{total} is the total variance; SS_i represents the variance of a single factor; SS_{int} is expressed as the variance of interactions between multiple factors. The SS_{int} also can be written as:

$$SS_{int} = \sum_{i=1}^{n} \sum_{j>i}^{n} SS_{ij} + ... + SS_{1,2,...,n} = SS_{total} - \sum_{i=1}^{n} SS_i \quad (2)$$

The ratio of the variance of each part to the total variance is regarded as the contribution of the main effect and the interactive effect to the total effect, respectively. The variance fraction p can be calculated as follows:

$$p_i = \frac{SS_i}{SS_{total}} \times 100\% \quad (3)$$

$$p_{int} = \frac{SS_{int}}{SS_{total}} \times 100\% \quad (4)$$

Table 2 presents the detailed multi-factorial design for future precipitation and temperature projection. In this study, two factors (i.e., GCM with five levels and SSP with two levels) and two responses (i.e., precipitation and temperature) are employed (**Figure 2**). Therefore, there are a total of ten different level combinations in this design.

TABLE 2 | The multi-level factorial design for the sources of uncertainty of future precipitation and temperature projection.

Levels	Factors		Response	
	GCMs (x_1)	SSPs (x_2)	Precipitation	Temperature
1	CESM2	SSP245	$y_{1\text{-}1}$	$y_{2\text{-}1}$
2	CESM2	SSP585	$y_{1\text{-}2}$	$y_{2\text{-}2}$
3	GFDL-ESM4	SSP245	$y_{1\text{-}3}$	$y_{2\text{-}3}$
4	GFDL-ESM4	SSP585	$y_{1\text{-}4}$	$y_{2\text{-}4}$
5	IPSL-CM6A-LR	SSP245	$y_{1\text{-}5}$	$y_{2\text{-}5}$
6	IPSL-CM6A-LR	SSP585	$y_{1\text{-}6}$	$y_{2\text{-}6}$
7	MIROC6	SSP245	$y_{1\text{-}7}$	$y_{2\text{-}7}$
8	MIROC6	SSP585	$y_{1\text{-}8}$	$y_{2\text{-}8}$
9	MRI-ESM2-0	SSP245	$y_{1\text{-}9}$	$y_{2\text{-}9}$
10	MRI-ESM2-0	SSP585	$y_{1\text{-}10}$	$y_{2\text{-}10}$

RESULTS

Spatial-Temporal Trends in Precipitation and Temperature

Figure 3 presents the Mann-Kendall trend analysis results for annual precipitation and annual mean temperature in the historical and future periods. MK trend analysis is a non-parametric test method broadly employed to statistically evaluate whether there is a significant change trend in a time sequence of the corresponding variable. The null hypothesis, H_0, indicates that there is no monotonic trend. The alternative hypothesis, H_1, states that there is a positive or negative monotonic trend in the data series. More details can be found in previous study (Duan et al., 2021). For the annual precipitation, nearly half of the areas (47.8%) show a significant trend in the historical period. Among them, the central areas in China present a significant decreasing trend. In the Northwest China, there is a significant growth trend. The significant proportion reached 70.3%. In the Northeast China and North China, the significant proportions are relatively small, at 4.4 and 7.6%, respectively. The fraction of China areas with a significant trend will be increased to 52.7% during 2051–2100 under SSP245. Besides, the annual precipitation will be increased to varying degrees in all seven sub-regions. The central areas, South China, and Northeast China have a statistically significant (indicate by dots) increasing trend for annual precipitation. The significant proportion of precipitation increase in North China and Northeast China has increased compared with the historical period. The significant proportions in the Northeast China and North China have reached 80.3 and 24.4%, respectively. The percentage of significant trend areas will continually increase to 85.5% during 2051–2100 under SSP585. Meanwhile, there will be a significantly high increase center in Southwest China. The significant proportions in Northwest China and Northeast China exceed 90%. In North China, Central China, Southwest China, and South China, proportions exceed 80%. The trend change in annual mean temperature is in sharp contrast with

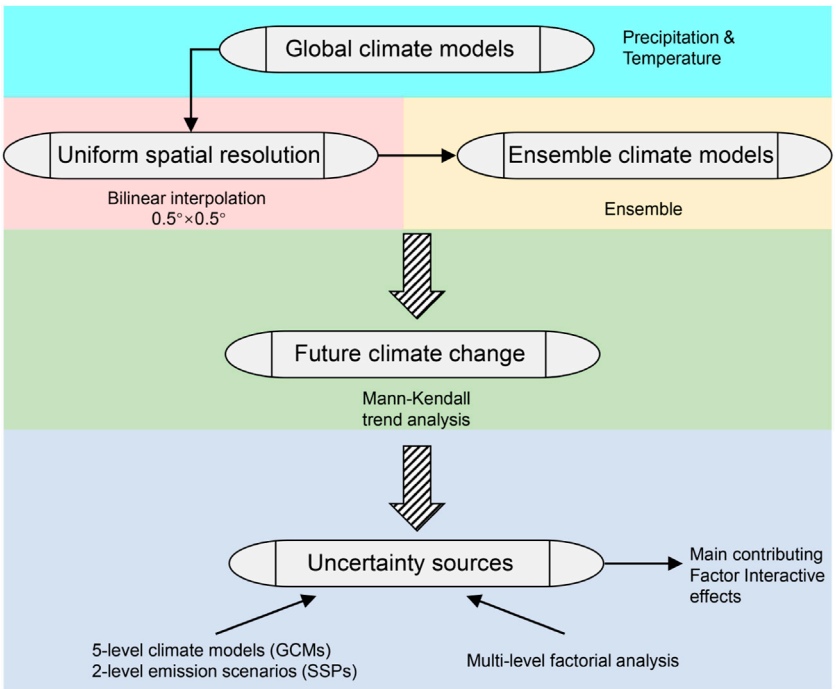

FIGURE 2 | The flowchart of this study.

annual precipitation. It has shown a significant increasing trend both in historical (99.9% significant trend areas) and future periods (100% significant trend areas) over China areas. The growth rate is the largest during 2051–2100 under SSP585, which is 0.1°C/year. In general, over China areas, the annual precipitation and annual mean temperature will increase significantly in the future, especially under SSP585. In historical and future periods, the northwestern inland temperature has increased relatively high. Compared with precipitation, the temperature has increased significantly throughout China, especially in the future. That means China will face higher temperature in the future, and there may be more temperature-related extreme climate events. It is also consistent with previous research conclusions (Chaudhuri et al., 2020; Ramil et al., 2020; Shrestha and Wang, 2020).

Projections of Future Precipitation and Temperature

Figure 4 shows the variations of future annual precipitation and annual mean temperature under SSP245 and SSP585. Compared with the historical period, the annual precipitation will increase by 11.3% over whole China areas, under SSP245. Besides, the precipitation will also increase to varying degrees in the seven sub-regions. Among them, the growth rate of the inland northwest area is higher than that of the northern and eastern coastal regions. In general, the increase in the northern part is higher than that in the southern region. The fraction of entire China areas with increasing annual precipitation will reach to 17.2% under SSP585. The growth rate of the inland northwest area is still higher than that of the eastern regions. Compared with the historical period, the whole China areas will be much wetter due to the increase annual precipitation. Among them, the proportion of precipitation increase in Northwest China, North China, and Northeast China is about 19%. The southwestern region is 18%, and the rest parts are about 10%. **Figure 4** also presents the change in annual mean temperature. Undoubtedly, temperature will increase in the future, both under SSP245 and SSP585. The increasing annual mean temperature over the whole China areas is 2.8°C under SSP245, and under SSP585, this increment will be 4.7°C. Interestingly, the spatial pattern of annual mean temperature variations is quite similar to precipitation, under both SSPs. Temperature increase in Northeast China, North China, and Northwest China is higher than that in the southern regions. The temperature increase is 3.2, 3.0, and 3.0°C, respectively, under SSP245. While under SSP585, the increase is further expanded to 5.2, 5.0, and 5.0°C, respectively. The temperature increase in the other four sub-regions was relatively small. Under SSP245, the increase is around 2°C, and under SSP585, the increase is around 4°C.

In summary, the results indicate that both annual precipitation and annual mean temperature over China will increase in the future. Regardless of SSP245 or SSP585, the growth rate of annual precipitation and annual mean temperature increase in the northern region (e.g., Northeast China, North China, and Northwest China) are higher than those in the southern parts (e.g., East China, South China, and Central China). The increase in precipitation is closely related to the rise in temperature, and it has been discussed in previous studies. Potential evapotranspiration will be increased with the

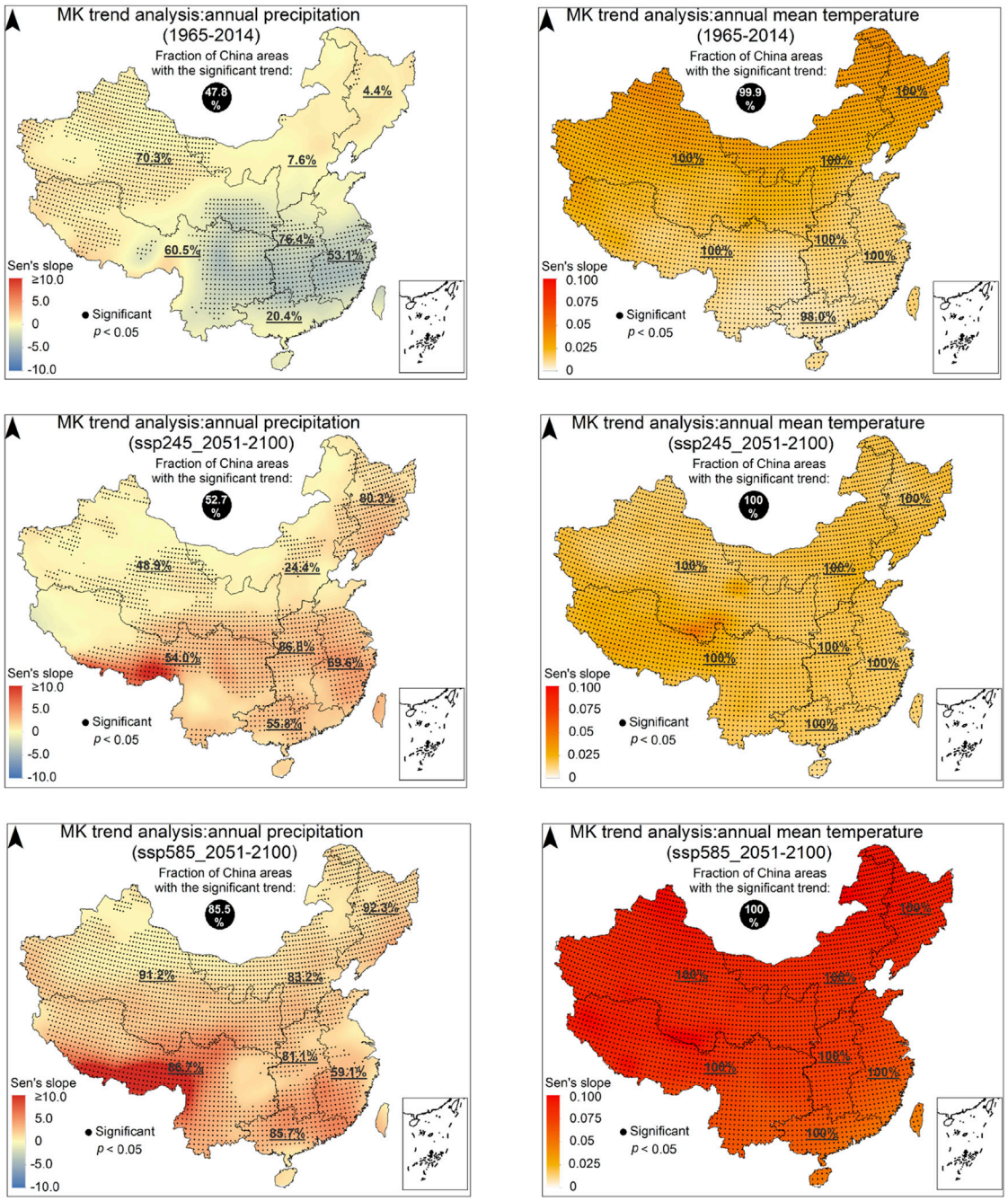

FIGURE 3 | The results of Mann-Kendall trend analysis for annual precipitation and annual mean temperature during the historical and future periods. The historical period is 1965–2014, and the future period is 2051–2100 under SSP245 and SSP585.

rise in temperature, and it may cause large amounts of moisture to converge. Eventually lead to a large increase in precipitation. Changes in precipitation and temperature will affect many aspects of China. Such as the agricultural output, human health, and infrastructure. The future temperature rise may increase the frequency of heat-related extreme climate events, which needs to be focused on in future research.

Figure 5 visually shows the historical and future changes in annual precipitation and annual mean temperature in China and the seven sub-regions. The results provide more detailed statistics

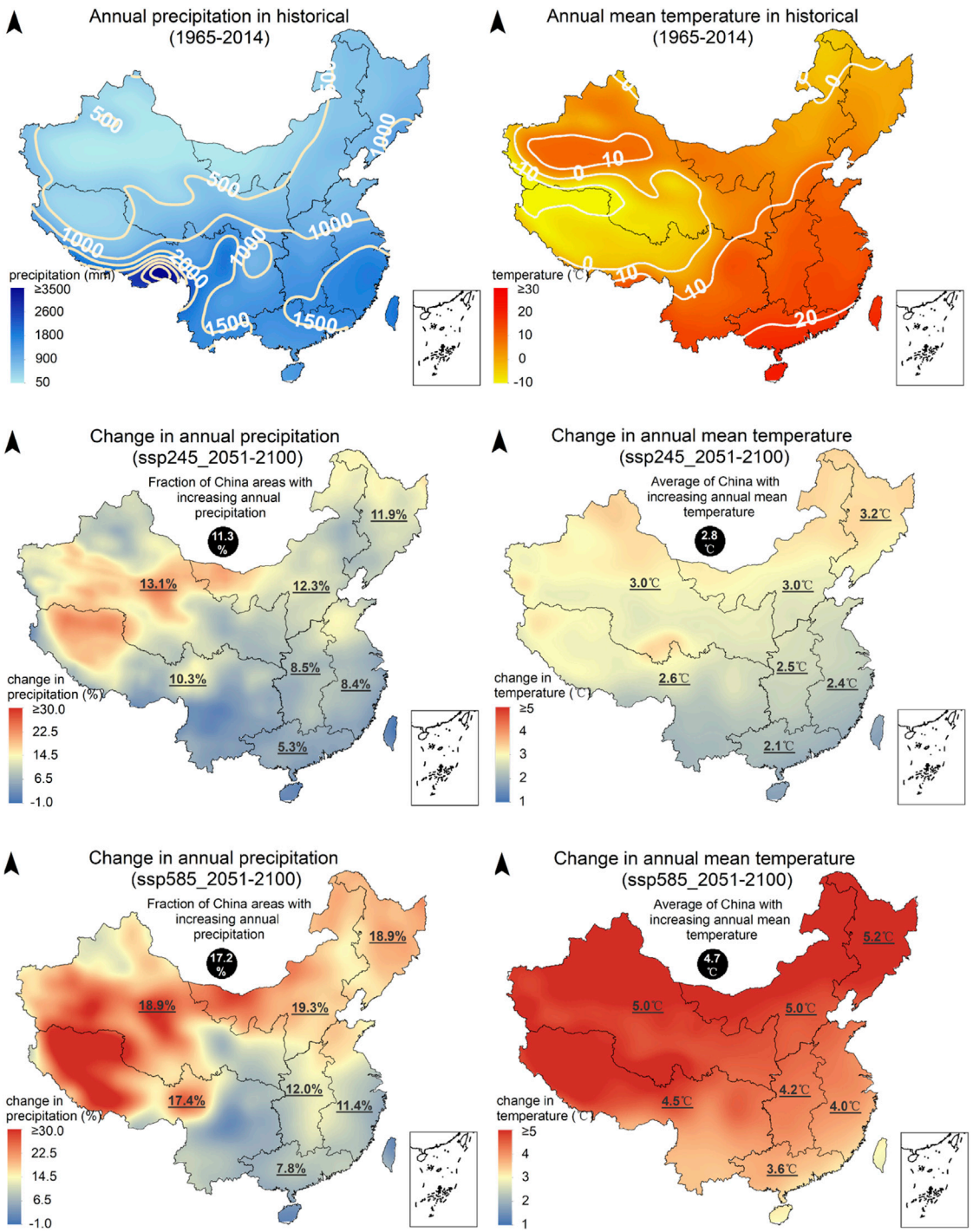

FIGURE 4 | The change in spatial distribution of annual precipitation and annual mean temperature during 2051–2100 under two SSPs relative to the historical period.

on the changes in precipitation and temperature. Precipitation in East China, South China, Central China, and Southwest China is much more. However, the growth rate in the future is significantly lower than that of other regions, as shown in **Figure 4**. The results also indicate that the previously wet areas will be wetter, while the dry areas tend to be wet. For the annual mean temperature, the East China, South China, and Central China will face higher temperature.

Figure 6 presents the changes in the probability distribution of annual precipitation and annual mean temperature. The black

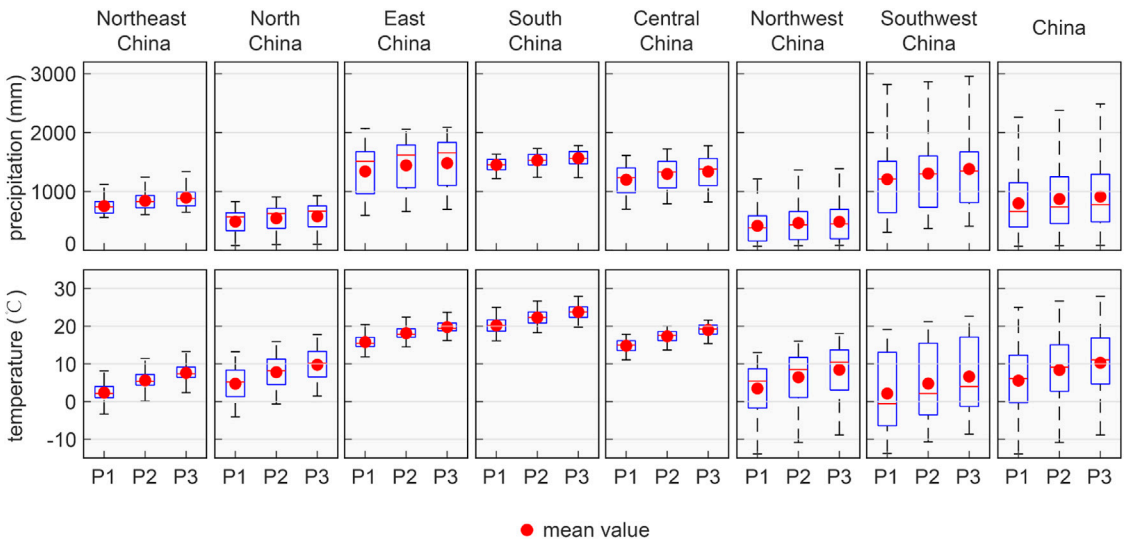

FIGURE 5 | Changes in annual precipitation and the annual mean temperature in China and its seven regions in the historical and future periods. Among them, P1 represents 1965–2014, P2 is 2051–2100 under SSP245, and P3 is 2051–2100 under SSP585.

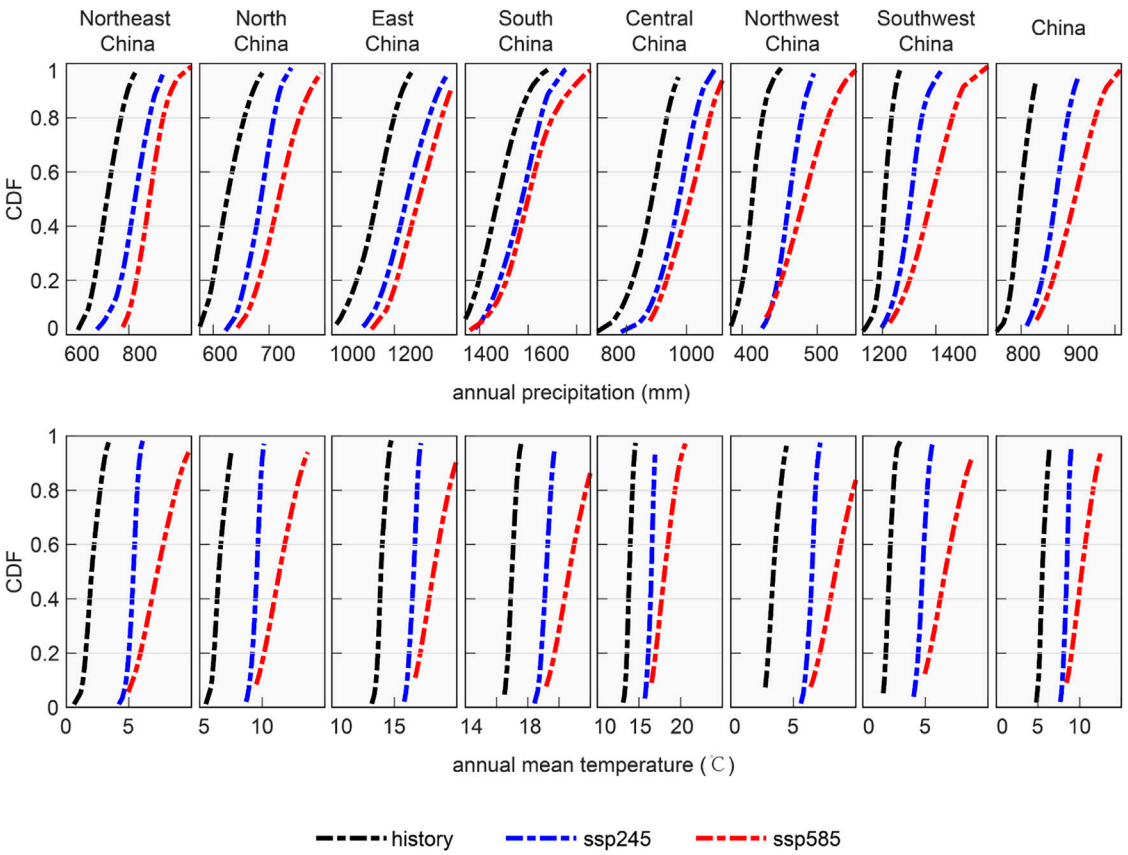

FIGURE 6 | Changes in probability distribution of annual precipitation and the annual mean temperature in China and its seven regions in the historical and future periods.

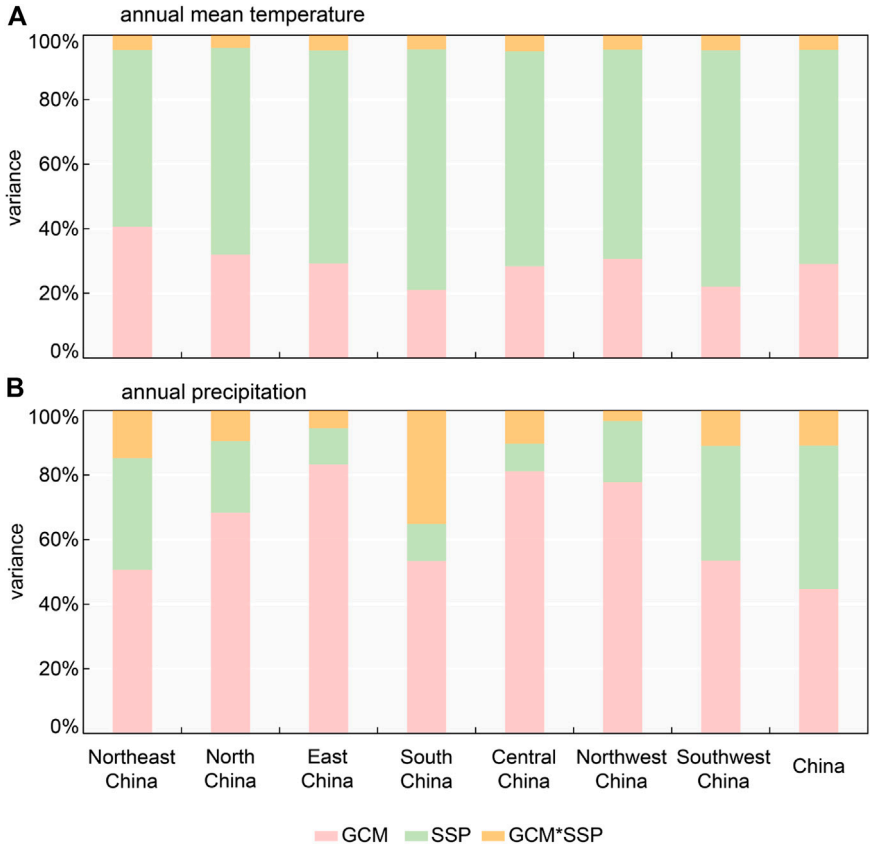

FIGURE 7 | The main contribution (and their interactions) of GCM and SSP to the sources of uncertainty on annual precipitation and annual mean temperature projections over China and seven sub-regions.

line represents the distribution of precipitation and temperature in the historical period. The blue line is the probability distribution of the two variables in 2051–2100 under SSP245, and the red line represents the probability variation of the two variables in 2051–2100 under SSP585. Compared with the historical period, the probability distribution of precipitation and temperature under SSP245 and SSP585 both shifted to the right. The results also show that under the SSP scenarios, the seven sub-regions and the entire China area will have more precipitation and higher temperature in the future. Climate change has significant impacts on China, and the regional ecological environment and human production may face severe challenges in the future due to changes in temperature and precipitation, as well as their derivative disasters (e.g., drought). Therefore, a full understanding of the possible impacts of climate change on China is desired.

Contributing Factors to Variations of Precipitation and Temperature

The uncertainties come from various factors, such as GCMs and SSPs. In this study, GCMs (with five levels) and SSPs (with two levels) are employed to quantify the main and interactive effects on precipitation and temperature projection. As presented in **Figure 7**, the total variance of precipitation and temperature projection contains three aspects: GCMs, SSPs, and their interactions. For annual precipitation, the largest contributing factor to the total variance comes from GCM, with the rate of 50.68% (Northeast China), 68.33% (North China), 83.28% (East China), 53.35% (South China), 81.20% (Central China), 77.79% (Northwest China), 53.49% (Southwest China), and 44.73% (entire China), respectively. The second contributing factor is SSP, with the rate of 34.63% (Northeast China), 22.25% (North China), 11.17% (East China), 11.52% (South China), 8.50% (Central China), 18.91% (Northwest China), 35.56% (Southwest China), and 44.36% (entire China), respectively. The contribution of the interaction is relatively small, with the rate of 14.69% (Northeast China), 9.42% (North China), 5.54% (East China), 35.13% (South China), 10.30% (Central China), 3.30% (Northwest China), 10.95% (Southwest China), and 10.91% (entire China), respectively.

For annual mean temperature, the largest contributing factor to the total variance comes from SSP, with the rate of 54.75% (Northeast China), 64.08% (North China), 65.96% (East China), 74.60% (South China), 66.66% (Central China), 64.84% (Northwest China), 73.22% (Southwest China), and 66.42% (entire China), respectively. The second contributing factor is GCM, with the rate of 40.64% (Northeast China),32.02% (North

China), 29.25% (East China), 21.04% (South China), 28.42% (Central China), 30.70% (Northwest China), 22.07% (Southwest China), and 29.09% (entire China), respectively. The contribution of the interaction is relatively small, with the rate of 4.61% (Northeast China), 3.91% (North China), 4.80% (East China), 4.35% (South China), 4.92% (Central China), 4.46% (Northwest China), 4.71% (Southwest China), and 4.49% (entire China), respectively.

The projections of future precipitation and temperature have the uncertainty of global climate models and emission scenarios. Results show that GCM is the main source of uncertainties in precipitation projection. For all sub-regions, the main contributing factor to the total variance in precipitation projection is GCM. The average contribution portions are all exceeded 50%. The interaction between GCM and SSP is relatively small. Results also present that SSP is the major contributing factor to the total variance in temperature projection. The average contribution portions are also exceeded 50%. Besides, the interaction between GCM and SSP is also quite small. Different variables have different sources of uncertainty. This may reflect the influence of different parameterization schemes of the model on the final output result.

DISCUSSION

The study on future precipitation and temperature projection, based on ensemble of global climate models, has the uncertainties of different emission scenarios and climate models. The uncertainty of future climate projection may have a profound impact on climate change projection and assessment. It is necessary to quantify different sources of uncertainty to provide reliable output achieve (Tisseuil et al., 2012; Feng and Hu, 2014). The relationship between the independent variables (i.e., climate models and emission scenarios) and the response variable is not a simple linear relationship. It is hard to explore their main and interactive effects on response variables. Nevertheless, the application of factorial analysis can roughly explore the main effects and interactions of various factors behind complex nonlinear relationships. Therefore, GCMs with five levels and SSPs with two levels are employed to trace the sources of uncertainty in projecting future precipitation and temperature, and the multi-factorial analysis method is used in this study. Results show that the major contributing factors in projecting future precipitation are all GCM over seven sub-regions and entire China. However, the major contributing factors in projecting future temperature are all SSP over seven sub-regions and entire China (Chen et al., 2016; Manrique-Alba et al., 2020). The effects explained by GCM and SSP interactions are relatively small for both future precipitation and temperature projection. To trace the different sources of uncertainty in projecting future climate change, multiple qualitative and quantitative methods have been employed in previous studies, such as the ANOVA theory.

The different kinds of uncertainties sources of multiple climate models perhaps lie in the insufficient cognizing and understanding on the natural earth change process of global climate change. Ultimately, the outputs of climate models accompany various assumptions and limitations. Due to the unpredictability of social-economic factor and human behavior in the future period, a variety of potential greenhouse gas emission scenarios have been generated (Shivam et al., 2019; Sharafi et al., 2020). For instance, the Representative Concentration Pathways (RCPs) in CMIP5 and the Shared Socioeconomic Pathways (SSPs) in CMIP6. Different emission scenarios have multiple premises and assumptions, which represent variations of development paths in the future (Du et al., 2018). Although developers try to incorporate the main physical processes of the earth's natural changes into the climate model, due to unknown emission scenarios, imperfect model structure, and complex climate systems, the simulation output of the climate model is bound to be uncertain. To reduce the system uncertainty in the modeling process as much as possible, the calculation and simulation are usually carried out through ensemble means of multiple GCMs (Moore et al., 2013; Smalley et al., 2019). A variety of ensemble methods have been developed in previous studies. In this study, five different GCMs under two SSPs are given equal weights. After the ensemble process, future annual precipitation and annual mean temperature are then projected. The simulation performance of multiple GCMs will vary with different variables and the study area. Besides, due to some GCMs share the same parameterization scheme, some modules or codes, different GCMs are not completely independent (Vogel et al., 2020; Zhai et al., 2020). Therefore, in this study, giving the same weight to all GCMs may not be the optimal solution to achieve ensemble. Wang et al. (2019) have assessed eight different weighting schemes to determine the optimal weight distribution among multiple GCMs. In addition, the effects of different weighting schemes on the final output simulation results are also compared (Wang et al., 2019). The performance of multiple GCMs ensemble has been confirmed in many studies, and the ability to project future climate change is better than a single GCM. Perhaps the multiple GCMs ensemble can reduce the systematic bias from the individual GCM, thereby improving the ability to project future variables. In the current climate change-related study, GCM is the only tool that can be used, but due to its shortcomings, the projection of some climate variables has a large deviation. In future research, reducing the systemic bias of the climate model itself will undoubtedly be the top priority (Chen et al., 2016; Wang et al., 2018).

CONCLUSION

In this study, future annual precipitation and annual mean temperature under two SSPs over China areas were projected through multiple global climate models. Meanwhile, to explore the sources of uncertainty in projecting future climate change, the multi-factorial analysis was conducted through GCMs (five levels) and SSPs (two levels). This study can help us understand the possible changes in precipitation, temperature, and the potential extreme climate events over the China area. The results indicate that China would have more annual precipitation

and higher annual mean temperature in the future. Compared with the historical period, the annual mean temperature would face a continuously increasing trend under SSPs. Regardless of SSP245 or SSP585, the growth rate of annual precipitation and annual mean temperature increase in the northern region (e.g., Northeast China, North China, and Northwest China) are higher than those in the southern parts (e.g., East China, South China, and Central China). The increase in precipitation is closely related to the rise in temperature. Potential evapotranspiration would be increased with the temperature rise, and it could cause large amounts of moisture to converge. Eventually, this leads to a large increase in precipitation. Changes in precipitation and temperature would affect many aspects of China. Such as the agricultural output, human health, and infrastructure. The future temperature rise may increase the frequency of heat-related extreme climate events, which needs to be focused on in future research. Moreover, GCM was the main contributing factor to the source of uncertainty in projecting future precipitation and SSP was the main factor for future temperature. The interactive effects are relatively unobvious on both projecting precipitation and temperature.

Overall, climate change is an indisputable fact in China. The annual precipitation and annual mean temperature will increase to varying degrees in the future. Reducing the systemic bias of the climate model itself will undoubtedly be the top priority, and it will help improve the projection and evaluation effects of relevant climate variables.

DATA AVAILABILITY STATEMENT

The original contributions presented in the study are included in the article/Supplementary Material, further inquiries can be directed to the corresponding author.

AUTHOR CONTRIBUTIONS

RD: Conceptualization, Methodology, Software, Investigation, Writing—original draft, Visualization GH: Supervision, Funding acquisition, Project administration YL: Data curation, Software GW: review and editing BX: review and editing CT: Software JR: Software.

FUNDING

This research was supported by the National Key Research and Development Plan (2016YFA0601502).

REFERENCES

Asif, Z., Chen, Z., and Chen, Z. (2020). A Life Cycle Based Air Quality Modeling and Decision Support System (LCAQMS) for Sustainable Mining Management. *J. Environ. Inform.* 35 (2), 103–117. doi:10.3808/jei.201900406

Ba, W., Du, P., Liu, T., Bao, A., Luo, M., Hassan, M., et al. (2018). Simulating Hydrological Responses to Climate Change Using Dynamic and Statistical Downscaling Methods: a Case Study in the Kaidu River Basin, Xinjiang, China. *J. Arid Land.* 10, 905–920. doi:10.1007/s40333-018-0068-0

Batibeniz, F., Ashfaq, M., Diffenbaugh, N. S., Key, K., Evans, K. J., Turuncoglu, U. U., et al. (2020). Doubling of U.S. Population Exposure to Climate Extremes by 2050. *Earth's Future* 8. doi:10.1029/2019EF001421

Carrão, H., Naumann, G., and Barbosa, P. (2016). Mapping Global Patterns of Drought Risk: An Empirical Framework Based on Sub-national Estimates of hazard, Exposure and Vulnerability. *Glob. Environ. Change.* 39, 108–124. doi:10.1016/j.gloenvcha.2016.04.012

Chaudhuri, S., Roy, M., Roy, M., and Jain, A. (2020). Appraisal of Wash (Water-sanitation-hygiene) Infrastructure Using a Composite index, Spatial Algorithms and Sociodemographic Correlates in Rural India. *J. Env Inform.* 35 (1), 1–22. doi:10.3808/jei.201800398

Chen, Y. D., Li, J., and Zhang, Q. (2016). Changes in Site-Scale Temperature Extremes over China during 2071-2100 in CMIP5 Simulations. *J. Geophys. Res. Atmos.* 121, 2732–2749. doi:10.1002/2015JD024287

Cheng, T. F., Lu, M., and Dai, L. (2019). The Zonal Oscillation and the Driving Mechanisms of the Extreme Western North Pacific Subtropical High and its Impacts on East Asian Summer Precipitation. *J. Clim.* 32, 3025–3050. doi:10.1175/JCLI-D-18-0076.1

Cho, M.-H., Boo, K.-O., Martin, G. M., Lee, J., and Lim, G.-H. (2015). The Impact of Land Cover Generated by a Dynamic Vegetation Model on Climate over East Asia in Present and Possible Future Climate. *Earth Syst. Dynam.* 6, 147–160. doi:10.5194/esd-6-147-2015

Dan, L., Cao, F., and Gao, R. (2015). The Improvement of a Regional Climate Model by Coupling a Land Surface Model with Eco-Physiological Processes: A Case Study in 1998. *Climatic Change.* 129, 457–470. doi:10.1007/s10584-013-0997-8

Du, L., Mikle, N., Zou, Z., Huang, Y., Shi, Z., Jiang, L., et al. (2018). Global Patterns of Extreme Drought-Induced Loss in Land Primary Production: Identifying Ecological Extremes from Rain-Use Efficiency. *Sci. Total Environ.* 628-629, 611–620. doi:10.1016/j.scitotenv.2018.02.114

Duan, R., Huang, G., Li, Y., Zhou, X., Ren, J., and Tian, C. (2021). Stepwise Clustering Future Meteorological Drought Projection and Multi-Level Factorial Analysis under Climate Change: A Case Study of the Pearl River Basin, China. *Environ. Res.* 196, 110368. doi:10.1016/j.envres.2020.110368

Duan, R., Huang, G., Zhou, X., Li, Y., and Tian, C. (2021). Ensemble Drought Exposure Projection for Multifactorial Interactive Effects of Climate Change and Population Dynamics: Application to the Pearl River Basin. *Earth's Future.* 9, e2021EF002215. doi:10.1029/2021EF002215

Feng, J., and Hu, D. (2014). How Much Does Heat Content of the Western Tropical Pacific Ocean Modulate the South China Sea Summer Monsoon Onset in the Last Four Decades? *J. Geophys. Res. Oceans.* 119, 4029–4044. doi:10.1002/2013JC009683

Ghosh, S., and Mujumdar, P. P. (2007). Nonparametric Methods for Modeling GCM and Scenario Uncertainty in Drought Assessment. *Water Resour. Res.* 43. doi:10.1029/2006WR005351

Hou, Y.-k., He, Y.-f., Chen, H., Xu, C.-Y., Chen, J., Kim, J.-S., et al. (2019). Comparison of Multiple Downscaling Techniques for Climate Change Projections Given the Different Climatic Zones in China. *Theor. Appl. Climatol.* 138, 27–45. doi:10.1007/s00704-019-02794-z

Huang, G. H., Baetz, B. W., Patry, G. G., and Terluk, V. (1997). Capacity Planning for an Integrated Waste Management System under Uncertainty: a North American Case Study. *Waste Manag. Res.* 15, 523–546. doi:10.1177/0734242x9701500507

Hui, P., Tang, J., Wang, S., Niu, X., Zong, P., and Dong, X. (2018). Climate Change Projections over China Using Regional Climate Models Forced by Two CMIP5 Global Models. Part II: Projections of Future Climate. *Int. J. Climatol.* 38, e78–e94. doi:10.1002/joc.5409

Jacob, D., Kotova, L., Teichmann, C., Sobolowski, S. P., Vautard, R., Donnelly, C., et al. (2018). Climate Impacts in Europe under +1.5°C Global Warming. *Earth's Future.* 6, 264–285. doi:10.1002/2017EF000710

Ji, D., Dong, W., Hong, T., Dai, T., Zheng, Z., Yang, S., et al. (2018). Assessing Parameter Importance of the Weather Research and Forecasting Model Based

on Global Sensitivity Analysis Methods. *J. Geophys. Res. Atmos.* 123, 4443–4460. doi:10.1002/2017JD027348

Kodinariya, T. M., and Makwana, P. R. (2013). Review on Determining Number of Cluster in K-Means Clustering. *Int. J. Adv. Res. Comput. Sci. Manag. Stud.* 1 (6), 90–95.

Li, L., Lei, L., Lei, L., Zheng, M. S., Borthwick, A. G. L., and Ni, J. R. (2020). Stochastic Evolutionary-Based Optimization for Rapid Diagnosis and Energy-Saving in Pilot- and Full-Scale Carrousel Oxidation Ditches. *J. Env Inform.* 35 (1), 81–93. doi:10.3808/jei.201700377

Li, Y. F., Li, Y. P., Huang, G. H., and Chen, X. (2010). Energy and Environmental Systems Planning under Uncertainty-An Inexact Fuzzy-Stochastic Programming Approach. *Appl. Energ.* 87, 3189–3211. doi:10.1016/j.apenergy.2010.02.030

Manrique-Alba, À., Beguería, S., Molina, A. J., González-Sanchis, M., Tomàs-Burguera, M., del Campo, A. D., et al. (2020). Long-term Thinning Effects on Tree Growth, Drought Response and Water Use Efficiency at Two Aleppo pine Plantations in Spain. *Sci. Total Environ.* 728, 138536. doi:10.1016/j.scitotenv.2020.138536

Moore, J. K., Lindsay, K., Doney, S. C., Long, M. C., and Misumi, K. (2013). Marine Ecosystem Dynamics and Biogeochemical Cycling in the Community Earth System Model [CESM1(BGC)]: Comparison of the 1990s with the 2090s under the RCP4.5 and RCP8.5 Scenarios. *J. Clim.* 26, 9291–9312. doi:10.1175/JCLI-D-12-00566.1

Paeth, H., and Hense, A. (2004). SST versus Climate Change Signals in West African Rainfall: 20th-century Variations and Future Projections. *Climatic Change.* 65, 179–208. doi:10.1023/B:CLIM.0000037508.88115.8a

Park, C., Min, S.-K., Lee, D., Cha, D.-H., Suh, M.-S., Kang, H.-S., et al. (2016). Evaluation of Multiple Regional Climate Models for Summer Climate Extremes over East Asia. *Clim. Dyn.* 46, 2469–2486. doi:10.1007/s00382-015-2713-z

Peltier, W. R., d'Orgeville, M., Erler, A. R., and Xie, F. (2018). Uncertainty in Future Summer Precipitation in the Laurentian Great Lakes basin: Dynamical Downscaling and the Influence of continental-scale Processes on Regional Climate Change. *J. Clim.* 31, 2651–2673. doi:10.1175/JCLI-D-17-0416.1

Poschlod, B., Hodnebrog, Ø., Wood, R. R., Alterskjær, K., Ludwig, R., Myhre, G., et al. (2018). Comparison and Evaluation of Statistical Rainfall Disaggregation and High-Resolution Dynamical Downscaling over Complex Terrain. *J. Hydrometeorol.* 19, 1973–1982. doi:10.1175/JHM-D-18-0132.1

Ramil, A., Vázquez-Nion, D., Vázquez-Nion, D., Pozo-Antonio, J. S., Sanmartín, P., and Prieto, B. (2020). Using Hyperspectral Imaging to Quantify Phototrophic Biofilms on Granite. *J. Env Inform* 35 (1), 34–44. doi:10.3808/jei.201800401

Roberts, J. L., Tozer, C. R., Ho, M., Kiem, A. S., Vance, T. R., Jong, L. M., et al. (2019). Reconciling Unevenly Sampled Paleoclimate Proxies: A Gaussian Kernel Correlation Multiproxy Reconstruction. *J. Environ. Inform* 35 (2), 1–10. doi:10.3808/jei.201900420

Sharafi, L., Zarafshani, K., Keshavarz, M., Azadi, H., and Van Passel, S. (2020). Drought Risk Assessment: Towards Drought Early Warning System and Sustainable Environment in Western Iran. *Ecol. Indicators.* 114, 106276. doi:10.1016/j.ecolind.2020.106276

Shivam, G., Goyal, M. K., Goyal, M. K., and Sarma, A. K. (2019). Index-based Study of Future Precipitation Changes over Subansiri River Catchment under Changing Climate. *J. Env Inform.* 34 (1), 1–14. doi:10.3808/jei.201700376

Shrestha, N. K., Wang, J., and Wang, J. (2020). Water Quality Management of a Cold Climate Region Watershed in Changing Climate. *J. Environ. Inform* 35 (1), 56–80. doi:10.3808/jei.201900407

Smalley, K. M., Glisan, J. M., and Gutowski, W. J. (2019). Alaska Daily Extreme Precipitation Processes in a Subset of CMIP5 Global Climate Models. *J. Geophys. Res. Atmos.* 124, 4584–4600. doi:10.1029/2018JD028643

Smirnov, O., Zhang, M., Xiao, T., Orbell, J., Lobben, A., and Gordon, J. (2016). The Relative Importance of Climate Change and Population Growth for Exposure to Future Extreme Droughts. *Climatic Change.* 138, 41–53. doi:10.1007/s10584-016-1716-z

Spinoni, J., Barbosa, P., Bucchignani, E., Cassano, J., Cavazos, T., Christensen, J. H., et al. (2020). Future Global Meteorological Drought Hot Spots: A Study Based on CORDEX Data. *J. Clim.* 33, 3635–3661. doi:10.1175/jcli-d-19-0084.1

Tan, Q., Huang, G. H., and Cai, Y. P. (2011). Radial Interval Chance-Constrained Programming for Agricultural Non-point Source Water Pollution Control under Uncertainty. *Agric. Water Manage.* 98, 1595–1606. doi:10.1016/j.agwat.2011.05.013

Thomas, D. S. K., Wilhelmi, O. V., Finnessey, T. N., and Deheza, V. (2013). A Comprehensive Framework for Tourism and Recreation Drought Vulnerability Reduction. *Environ. Res. Lett.* 8, 044004. doi:10.1088/1748-9326/8/4/044004

Thompson, G., Tewari, M., Ikeda, K., Tessendorf, S., Weeks, C., Otkin, J., et al. (2016). Explicitly-coupled Cloud Physics and Radiation Parameterizations and Subsequent Evaluation in WRF High-Resolution Convective Forecasts. *Atmos. Res.* 168, 92–104. doi:10.1016/j.atmosres.2015.09.005

Tisseuil, C., Vrac, M., Grenouillet, G., Wade, A. J., Gevrey, M., Oberdorff, T., et al. (2012). Strengthening the Link between Climate, Hydrological and Species Distribution Modeling to Assess the Impacts of Climate Change on Freshwater Biodiversity. *Sci. Total Environ.* 424, 193–201. doi:10.1016/j.scitotenv.2012.02.035

Trenberth, K. E., and Shea, D. J. (2005). Relationships between Precipitation and Surface Temperature. *Geophys. Res. Lett.* 32. doi:10.1029/2005GL022760

Vogel, M. M., Hauser, M., and Seneviratne, S. I. (2020). Projected Changes in Hot, Dry and Wet Extreme Events' Clusters in CMIP6 Multi-Model Ensemble. *Environ. Res. Lett.* 15, 094021. doi:10.1088/1748-9326/ab90a7

Wang, B., LinHoZhang, Y., and Lu, M. M. (2004a). Definition of South China Sea Monsoon Onset and Commencement of the East Asia Summer Monsoon*. *J. Clim.* 17, 699–710. doi:10.1175/2932.1

Wang, F., Huang, G. H., Fan, Y., and Li, Y. P. (2021). Development of Clustered Polynomial Chaos Expansion Model for Stochastic Hydrological Prediction. *J. Hydrol.* 595, 126022. doi:10.1016/j.jhydrol.2021.126022

Wang, H.-M., Chen, J., Xu, C.-Y., Chen, H., Guo, S., Xie, P., et al. (2019). Does the Weighting of Climate Simulations Result in a Better Quantification of Hydrological Impacts? *Hydrol. Earth Syst. Sci.* 23, 4033–4050. doi:10.5194/hess-23-4033-2019

Wang, Y., Leung, L. R., McGregor, J. L., Lee, D.-K., Wang, W.-C., Ding, Y., et al. (2004b). Regional Climate Modeling: Progress, Challenges, and Prospects. *J. Meteorol. Soc. Jpn.* 82, 1599–1628. doi:10.2151/jmsj.82.1599

Wang, Z., Zhong, R., Lai, C., Zeng, Z., Lian, Y., and Bai, X. (2018). Climate Change Enhances the Severity and Variability of Drought in the Pearl River Basin in South China in the 21st century. *Agric. For. Meteorology* 249, 149–162. doi:10.1016/j.agrformet.2017.12.077

Ying, J., Huang, P., and Lian, T. (2019). Changes in the Sensitivity of Tropical Rainfall Response to Local Sea Surface Temperature Anomalies under Global Warming. *Int. J. Climatol.* 39, 5801–5814. doi:10.1002/joc.6303

Zhai, A. F., Ding, X. W., Ding, X. W., Zhao, Y., Xiao, W. H., and Lu, B. X. (2020). Improvement of Instantaneous point Source Model for Simulating Radionuclide Diffusion in Oceans under Nuclear Power Plant Accidents. *J. Environ. Inform* 36 (2), 133–145. doi:10.3808/jei.201700380

Zhou, X., Huang, G., Wang, X., and Cheng, G. (2018). Dynamically-downscaled Temperature and Precipitation Changes over Saskatchewan Using the PRECIS Model. *Clim. Dyn.* 50, 1321–1334. doi:10.1007/s00382-017-3687-9

Conflict of Interest: The authors declare that the research was conducted in the absence of any commercial or financial relationships that could be construed as a potential conflict of interest.

Publisher's Note: All claims expressed in this article are solely those of the authors and do not necessarily represent those of their affiliated organizations, or those of the publisher, the editors and the reviewers. Any product that may be evaluated in this article, or claim that may be made by its manufacturer, is not guaranteed or endorsed by the publisher.

frontiers in Earth Science

ORIGINAL RESEARCH
published: 17 September 2021
doi: 10.3389/feart.2021.758619

Interdecadal Linkage Between the Winter Northern Hemisphere Climate and Arctic Sea Ice of Diverse Location and Seasonality

Xulong He[1], *Ruonan Zhang*[1,2,3]*, *Shuoyi Ding*[1] *and Zhiyan Zuo*[1]

[1]*Department of Atmospheric and Oceanic Sciences, Institute of Atmospheric Sciences, Fudan University, Shanghai, China,* [2]*Shanghai Qi Zhi Institute, Shanghai, China,* [3]*Innovation Center of Ocean and Atmosphere System, Zhuhai Fudan Innovation Research Institute, Zhuhai, China*

During the past few decades, Arctic sea-ice has declined rapidly in both autumn and winter, which is likely to link extreme weather and climate events across the Northern Hemisphere midlatitudes. Here, we use reanalysis data to investigate the possible linkage between mid–high-latitude atmospheric circulation and Arctic sea-ice loss in different geographical locations and seasons and associated impacts on wintertime climate on interdecadal timescales. Four critical sea-ice subregions are analyzed in this study—namely, the Pan-Arctic, Barents–Kara–Laptev Seas (BKL), East Siberia–Chukchi–Beaufort Seas (EsCB), and Bering Sea (Ber). Results suggest that interdecadal reduction of autumn sea-ice, irrespective of geographical location, is dynamically associated with the negative phase of the North Atlantic Oscillation (NAO) in the subsequent winter *via* stratospheric pathways. Specifically, autumn sea-ice loss appears to cause a weakened stratospheric polar vortex that propagates to the troposphere in the ensuing months, leading to lower surface air temperature and a deficit in precipitation over Siberia and northeastern North America. Meanwhile, an anomalous cyclone over Europe favors excessive precipitation over southern Europe. For wintertime sea-ice loss in the Pan-Arctic and BKL, a weak positive NAO phase, with a dipole pressure pattern over Greenland–northeastern North America and North Atlantic, and a shrunken Siberian high over Eurasia are observed over mid–high-latitudes. The former results in excessive precipitation over northwestern and southeastern North America, whilst the latter leads to less precipitation and mild winter over Siberia. In contrast, Ber sea-ice loss is associated with a circumglobal wave train downstream of the Bering Sea, leading to extensive warming over Eurasia. The anomalous dipole cyclone and anticyclone over the Bering Sea transport more Pacific and Arctic water vapor to North America, and the anomalous cyclone over the Barents Sea results in abundant precipitation in Siberia. Such midlatitude anomaly is dynamically linked to winter sea-ice loss, mainly through tropospheric rather than stratospheric pathways. These results have important implications for future seasonal and interdecadal forecasts in the context of ongoing sea-ice decline.

Keywords: interdecadal linkage, sea ice, midlatitudes coldness, precipitation, water vapor transport

OPEN ACCESS

Edited by:
Xander Wang,
University of Prince Edward Island, Canada

Reviewed by:
Shangfeng Chen,
Institute of Atmospheric Physics (CAS), China
Sai Wang,
Chinese Academy of Meteorological Sciences, China

***Correspondence:**
Ruonan Zhang
rn_zhang@fudan.edu.cn

Specialty section:
This article was submitted to Interdisciplinary Climate Studies, a section of the journal Frontiers in Earth Science

Received: *14 August 2021*
Accepted: *01 September 2021*
Published: *17 September 2021*

Citation:
He X, Zhang R, Ding S and Zuo Z (2021) Interdecadal Linkage Between the Winter Northern Hemisphere Climate and Arctic Sea Ice of Diverse Location and Seasonality. Front. Earth Sci. 9:758619. doi: 10.3389/feart.2021.758619

INTRODUCTION

In recent decades, the midlatitudes of the Northern Hemisphere have experienced more frequent cold winters and extreme weather events (Wu et al., 2011; Cohen et al., 2014; Li et al., 2015; Cohen et al., 2020; Wang et al., 2021). For instance, Japan suffered an extreme snowstorm in December 2005, and China suffered persistent cold and freezing rain events in January–February 2008 (WMO Regional Climate Centres 2012); and extreme cold conditions and heavy snowfall attacked North America in two consecutive winters (2013/14 and 2014/15), during which the Great Lakes were almost completely frozen for the first time in the previous 35 years and Boston experienced record-breaking snowfall reaching 2.7 m (Van Oldenborgh et al., 2015).

A range of mechanisms have been proposed for the frequent occurrence of extreme cold and snowy climates during the past 2 decades. Some studies have attributed natural variation as the primary cause of Eurasian cooling (Trenberth, 1999; Sun et al., 2016; Song et al., 2016; Screen, 2017B); whereas, in contrast, others have suggested that the increase in cold temperature events has been affected by the so-called Arctic Amplification and associated sea-ice loss (Francis and Vavrus, 2012; Mori et al., 2014, 2019; Takaya and Nakamura, 2015; Zhang et al., 2018; Zhang and Francis, 2020; Zhang et al., 2021). For instance, Wu et al. (2017) investigated a cold event that occurred in East Asia during January–February 2012 and its possible association with Arctic sea-ice loss. They found that weakening of the Aleutian low and rapid strengthening of the Siberian high, concurrent with a polar blocking high aloft, were crucial precursors for cold-air outbreaks from the Arctic. In addition to extreme temperature events, Arctic sea-ice loss further affects wintertime precipitation in northern midlatitudes. Large-scale atmospheric circulation and moisture transport are decisive for this precipitation *via* storm-scale moisture convergence (Ma et al., 2012; Sun and Wang, 2012). Using an atmospheric model, Li and Wang (2012) indicated that a negative phase of the North Atlantic Oscillation (NAO) in response to Kara–Laptev sea-ice loss in autumn acts as an atmospheric ridge over Eurasia that is favorable for moisture transport to East Asia. Liu et al. (2016) reported that the reduction of autumn sea-ice across the Arctic Ocean is accompanied by dry conditions over central China and wet conditions over South China and North China in early winter, *via* two wave-train structures.

There are two main pathways responsible for these Arctic–midlatitude linkages. First is the stratospheric pathway through which Arctic sea-ice loss causes a weakened stratospheric polar vortex in the ensuing months and has lagging effects on midlatitude climate in both winter and the subsequent spring (Mori et al., 2014; Chen and Wu, 2018; Mori et al., 2019). Second is the tropospheric pathway, in which the melting sea-ice decreases polar-to-tropics temperature gradients, which results in meandering tropospheric flow and more extreme weathers events in the midlatitudes (Nakamura et al., 2014; Sun et al., 2015; Nakamura et al., 2016). Another critical issue is the geographical location of sea-ice loss, which has distinct impacts on the midlatitude climate in both modeling and observational studies (Screen, 2017A). Specifically, rapid sea-ice loss in the Barents–Kara–Laptev (BKL) seas has tremendous impacts on the Eurasian climate (Honda et al., 2009), while in the East Siberian–Chukchi–Beaufort (EsCB) seas it has substantial implications for the climate over North America (Kug et al., 2015).

However, most previous studies have tended to focus on sea-ice change in the winter season or year-round and on interannual timescales, with limited attention having been paid to autumn and interdecadal timescales. Although recent studies argued there is diverse Eurasian temperature and precipitation responses to BKL sea-ice loss in autumn (Li and Wang, 2012; Ding et al., 2020; Zhang and Screen, 2021), their focus was on the interannual rather than interdecadal timescale. Chen and Wu (2018) and Ding and Wu (2021) explored how autumn EsCB sea-ice loss can influence spring Eurasian temperature. However, the impact on wintertime temperature and precipitation has not been thoroughly examined, particularly on interdecadal timescales.

This study aims to address two questions: 1) How does Arctic sea-ice loss in different seasons and at different locations contribute to the wintertime atmospheric circulation anomalies and associated impact on temperature and precipitation? 2) What is the Arctic-midlatitude linkage on interdecadal timescales? More specifically, this paper investigates the interdecadal linkage between Northern Hemisphere temperature and precipitation and sea-ice change in diverse regions and seasons. The underlying physical mechanisms of these linkages are thoroughly investigated *via* tropospheric and stratospheric pathways. Before we investigate the interdecadal linkage, the total variation (i.e., the sum of interannual and interdecadal variations) of sea-ice and its association with wintertime climate is primarily analyzed as a comparison.

Data and Methods

The datasets employed in this research are: 1) the National Centers for Environmental Prediction atmospheric reanalysis with a resolution of 2.58° × 2.58° (Kalnay et al., 1996), including sea level pressure (SLP), surface air temperature (SAT), horizontal wind, specific humidity, and geopotential height; 2) the monthly sea-ice concentration (SIC) from the Met Office Hadley Center with a 1° × 1° longitude/latitude resolution (Rayner et al., 2003); and 3) the enhanced monthly mean precipitation from the Climate Prediction Center Merged Analysis of Precipitation with a resolution of 2.5° × 2.5° (Xie and Arkin, 1997). For interdecadal study, the 1959–2020 period is analyzed in the present study. Regression and correlation analysis are employed in this study, and the two-tailed Student's *t*-test is applied to examine the statistical significance of the regression and correlation coefficients.

Based on topographical features (e.g., islands, straits) and conventional nomenclature, sea-ice in the Atlantic and Pacific sectors is analyzed in the present study. Specifically, we set the area-averaged SIC north of 60°N as belonging to the Pan-Arctic. Likewise, we define BKL as the (70°–80°N, 30°–135°E)-averaged SIC to represent Atlantic sea-ice index. In the Pacific sector, autumn sea-ice is mainly located in the EsCB region during September–October, and large variance of winter

(December–February) sea-ice exists in the Bering Sea (Ber) region. The reason why we choose September–October EsCB for autumn analysis is that the melting of sea-ice in EsCB is limited to occurring in September and October, which has great influence on stratospheric processes, whilst subtle sea-ice loss occurs in other months (Chen and Wu, 2018; Ding et al., 2021). Therefore, we define EsCB as the (70.5°–82.5°N, 135°E–60.5°W)-averaged SO SIC and Ber as the (55°–68°N, 165°E–125°W)-averaged DJF SIC to represent Pacific sea-ice indices. Linear trends are removed from the SIC indices prior to carrying out the analysis. In general, this paper emphasizes on autumn sea-ice in Pan-Arctic, BKL and EsCB regions and winter sea-ice in Pan-Arctic, BKL and Ber regions.

To investigate the interdecadal variation of sea-ice, we use power spectrum method to figure out the periodism of Arctic sea-ice indices in diverse regions. Three main periods are identified for autumn and winter sea-ice, which are 2-year, 10-year, and 20-year (figure not shown). Therefore, since our focus is the interdecadal timescale, a 9-year low-pass Butterworth filter is applied to all variables to derive the interdecadal component. The algorithm of the Butterworth low-pass filter (Selesnick and Burrus, 1998) can be expressed by the following formula of the amplitude squared to the frequency:

$$|H(\omega)|^2 = \frac{1}{1+\left(\frac{\omega}{\omega_e}\right)^{2n}} = \frac{1}{1+e^2\left(\frac{\omega}{\omega_p}\right)^{2n}}$$

where n is the filter order (as n increases, the smoother the curve will be), ω_e is the cut-off frequency, and ω_p is the pass-band edge frequency. For example, if we extract decadal components from the original sequence, our sampling frequency is 1 year, and the decadal cycle is 9 years. That is, the frequency is 1/9, and then the end frequency is $\omega_e = 2 \times 1/9 \approx 0.222$.

Besides, the low-pass filtered variables will have strong persistence or high autocorrelation. Therefore, the effective number of degree of freedom of the significance test (i.e., the t-test) needs to be replaced with n/T when calculating the regression and correlation coefficients. The formulae are as follows (Davis, 1976):

$$T = \sum_{j=-\infty}^{\infty} R_{xx}(j) R_{yy}(j),$$

$$R_{xx}(j) = \frac{1}{n-j} \sum_{t=1}^{n-j} x_t^* x_{t+j}^*,$$

$$R_{yy}(j) = \frac{1}{n-j} \sum_{t=1}^{n-j} y_t^* y_{t+j}^*,$$

where R_{xx} and R_{yy} are the autocorrelation coefficients of x and y, respectively; n is the sample number; j is the lag time, usually set as $n/2$; and an asterisk (*) represents normalization.

RESULTS

Interdecadal Variations in Arctic Sea Ice

Arctic sea-ice change has profound impacts on the wintertime climate of the Northern Hemisphere (Cohen et al., 2014; Cohen et al., 2020). Moreover, there is emerging evidence that the geographical location of sea-ice loss is critically important in determining the large-scale atmospheric circulation anomalies and associated impacts on the midlatitudes (Screen, 2017A). Besides, there are diverse winter circulation responses to sea-ice loss in different seasons (Zhang and Screen, 2021). **Figure 1** displays the variations in Arctic SIC in the different regions and seasons. In general, the SIC indices show substantial variations on interannual and interdecadal timescales. The interannual component of SIC indices explained roughly 52.1–78.9% of the total variance, while the interdecadal component explained 21.1–47.9% (**Table 1**). This result indicates that the interdecadal changes in SIC indices are of great importance, in addition to the interannual variability, in the total variations. We find Arctic SIC variations in autumn and winter show particularly high coherence. For instance, for the Pan-Arctic, BKL and Ber, the correlation coefficients between the autumn and winter SIC indices are 0.51, 0.42, and 0.37 respectively, with the statistical significance exceeding the 95% confidence level (**Table 2**). These high correlation coefficients indicate that a large part of the autumn sea-ice change tends to persist until winter. However, for EsCB, the autumn–winter correlation is only 0.26, consistent with the finding of Ding et al. (2021) that the melting of sea-ice in EsCB in September–October doesn't persistent into the following winter.

Such seasonal footprint characteristics in the Pan-Arctic, BKL, and Ber are also seen in the spatial pattern of correlation coefficients (**Figure 2**). When there is more (less) Pan-Arctic SIC in autumn, positive (negative) anomalies of sea-ice are located over the northern BKL and the EScB; however, in the following winter, the highly correlated region shrinks to Eurasian coastal regions, particularly over the Laptev Sea (**Figures 2A,D**). It is interesting to note that the regions of significant Pan-Arctic SIC anomalies cover the BKL and EsCB regions. That is why the correlation coefficients between the Pan-Arctic and BKL and EsCB in autumn reach 0.74 and 0.70, respectively. For BKL and EsCB, positive SIC correlations are limited to the defined region (**Figures 2B,C**), but only the southern part lasts to winter (**Figures 2E,F**).

In comparison, the wintertime sea-ice in association with winter SIC indices differs from those with autumn SIC indices. When the winter Pan-Arctic index is above average, positive SIC anomalies are located over the Atlantic sector (northern Barents–Kara–Greenland seas) and Pacific sector (Chukchi–Bering seas), which also covers the BKL and Ber regions (**Figures 2G–I**). Nevertheless, the correlation coefficients between the winter Pan-Arctic and BKL and Ber SIC indices are 0.83 and 0.30, respectively, indicating that the winter BKL makes major contributions to the variations in Pan-Arctic SIC.

Sea-ice indices in different regions and seasons show apparent interdecadal variations, which explain approximately half of the total variations. The Pan-Arctic index shows similar interdecadal changes to those of BKL in both autumn and winter, with negative phases during 1980–1990 and during 2005–2020, and a positive phase during 1990–2000. The two indices are also

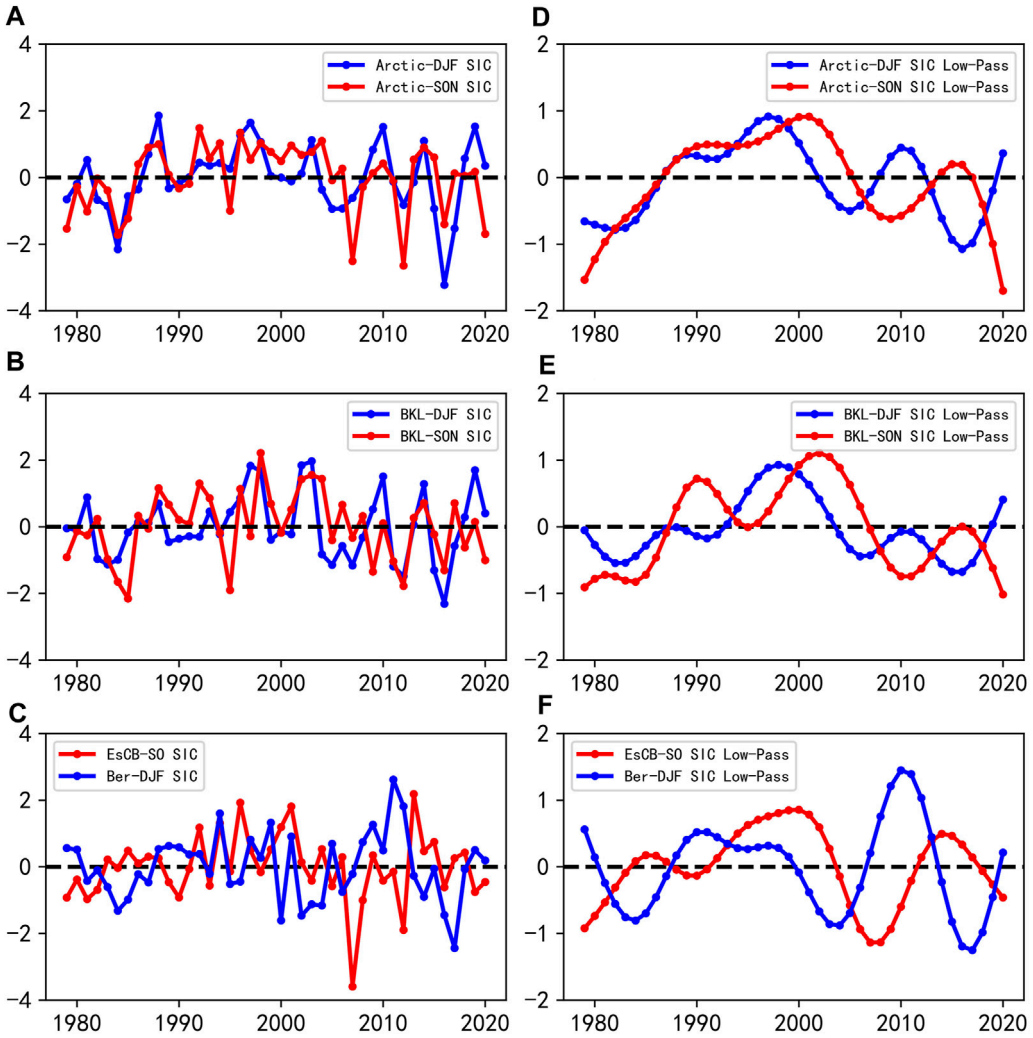

FIGURE 1 | Arctic sea-ice concentration (SIC) indices in different regions and seasons: **(A)** Pan-Arctic, **(B)** BKL in autumn (September–November) and winter (December–February), **(C)** EsCB in autumn (September–October) and Ber in winter. **(D–F)** As in **(A–C)** but for the corresponding 9-year low-pass filtered components. The blue (red) line denotes the winter (autumn) SIC index.

TABLE 1 | Explained variance of interannual and interdecadal components of raw SIC indices.

	Interannual (%)	Interdecadal (%)
Pan-arctic SON SIC	61.3	38.7
BKL SON SIC	61.8	38.2
EsCB SO SIC	68.0	32.0
Pan-Arctic DJF SIC	67.7	32.3
BKL DJF SIC	78.9	21.1
Ber DJF SIC	52.1	47.9

TABLE 2 | Correlation coefficients between Arctic SIC in diverse regions and seasons.

Pan-arctic SON SIC	Pan-arctic DJF SIC	0.51*
BKL SON SIC	BKL DJF SIC	042*
Ber SON SIC	Ber DJF SIC	0.37*
EsCB SO SIC	EsCB DJF SIC	0.26
Pan-Arctic SON SIC	BKL SON SIC	0.74*
Pan-Arctic SON SIC	EsCB SO SIC	0.70*
Pan-Arctic DJF SIC	BKL DJF SIC	0.83*
Pan-Arctic DJF SIC	Ber DJF SIC	0.30

Asterisk indicates correlation statistically significant at the 95% confidence level.

consistent in their amplitudes. Also of note is that the autumn EsCB and winter Ber are increasingly linked to the Pan-Arctic and BKL on interdecadal timescales since 2000, indicating that the interdecadal variation of Pan-Arctic sea-ice is mainly affected by sea-ice in the Atlantic sector and secondarily by sea-ice in the Pacific sector, while the contribution of Pacific sea-ice has increased since 2000. Considering the similarity in the SIC variation between the Pan-Arctic and BKL, their related atmospheric circulation and midlatitude climate anomalies should also resemble each other closely.

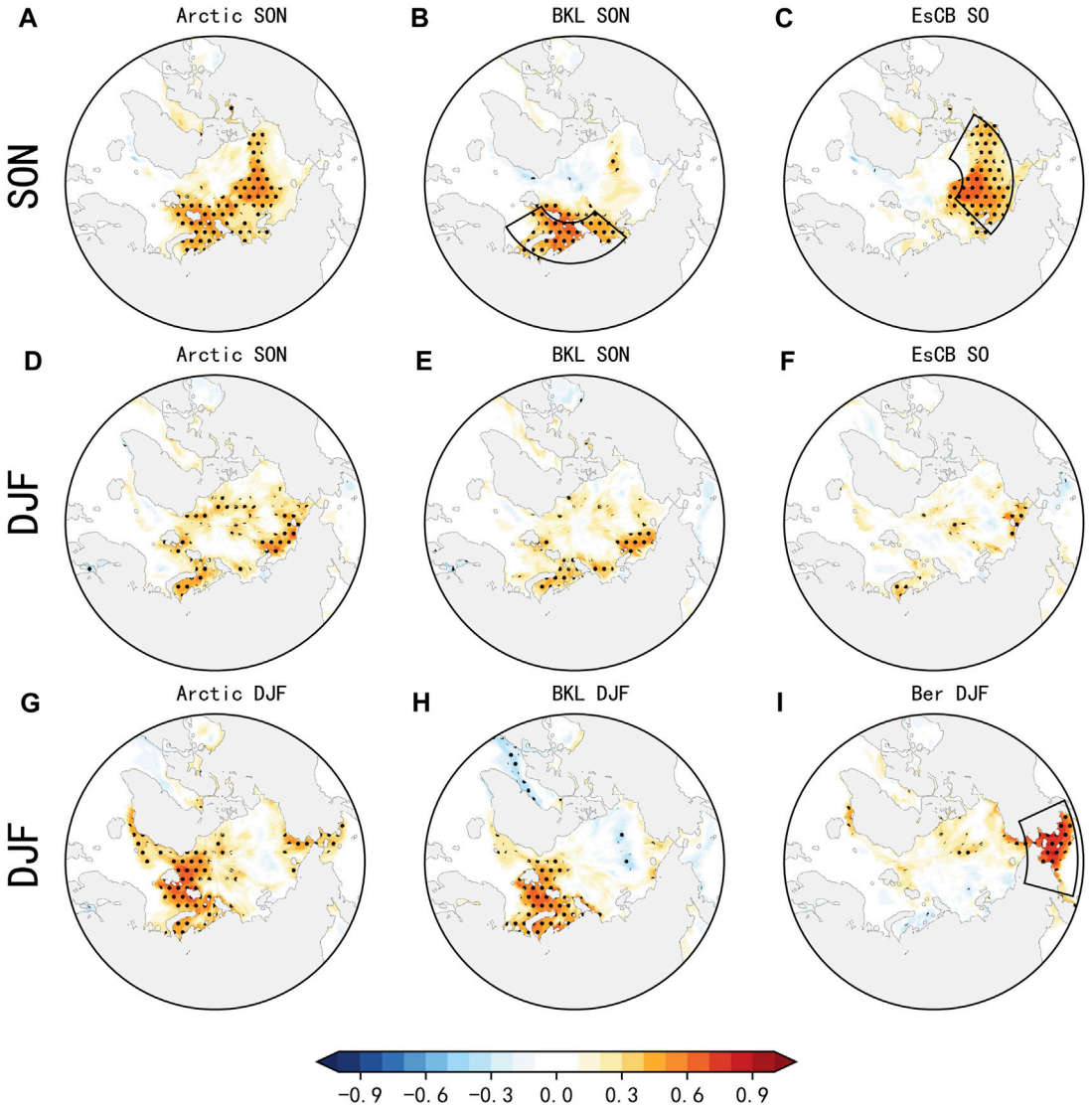

FIGURE 2 | Linear regression of **(A–C)** autumn and **(D–F)** winter Arctic SIC with respect to regional SIC indices in the Pan-Arctic, BKL and EsCB in autumn. **(G–I)** As in **(A–C)** but for winter SIC anomalies regressed upon winter indices. Rectangles denote the region to define BKL, EsCB, and Ber indices. Stippling indicates regression anomalies that are statistically significant at the 95% confidence level.

Autumn Sea-Ice–Related Temperature and Circulation

Previous studies have indicated that sea-ice loss coupled with cooling or a lack of warming in the midlatitudes causes the Arctic and midlatitude temperatures to diverge. The warm Arctic and cold continents/Eurasia (WACC/E) pattern constitutes the most robust observational evidence over the Northern Hemisphere midlatitudes in recent decades (Cohen et al., 2014; Cohen et al., 2020). However, the aforementioned studies focused mostly on year-round sea-ice change, with limited attention paid to autumn sea-ice change. **Figure 3** shows the wintertime SAT anomalies regressed upon the sea-ice indices in different regions. Consistent with previous studies, the autumn Pan-Arctic and BKL sea-ice loss have pronounced impacts on winter Eurasian coldness. There are also negative SAT anomalies over North America and positive ones over the Arctic Ocean, but the response is generally weaker and with patchy statistical significance (**Figures 3A,B**). The Northern Hemisphere midlatitude SAT anomalies are usually associated with large-scale atmospheric circulation changes. Eurasian cold anomalies are dynamically consistent with the negative phase of the NAO, enhanced and northward shifted Siberian high, and the Ural ridge of high pressure, featuring an equivalent barotropic structure (**Figures 4A,B**). These circulation changes imply meandering westerly winds, increased blocking frequency, and hence severe cold weather, which is consistent with the findings of previous studies, albeit

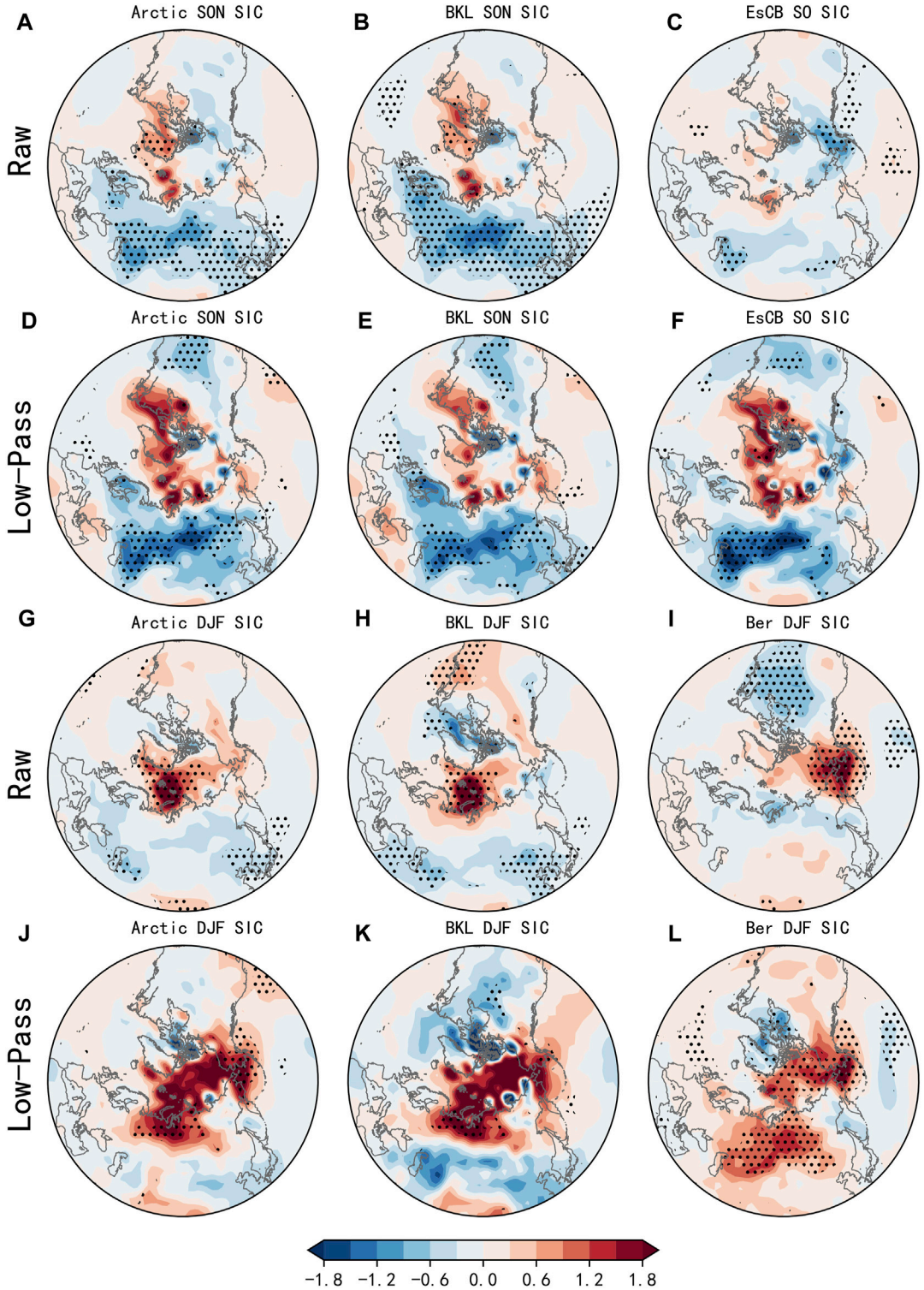

FIGURE 3 | Linear regression of winter surface air temperature (SAT; unit: K) anomalies against the Pan-Arctic, BKL and EsCB SIC indices **(A–C)** and associated interdecadal component **(D–F)** in autumn. **(G–L)** As in **(A–F)** but for SIC indices in winter. Stippling indicates SAT anomalies that are statistically significant at the 95% confidence level.

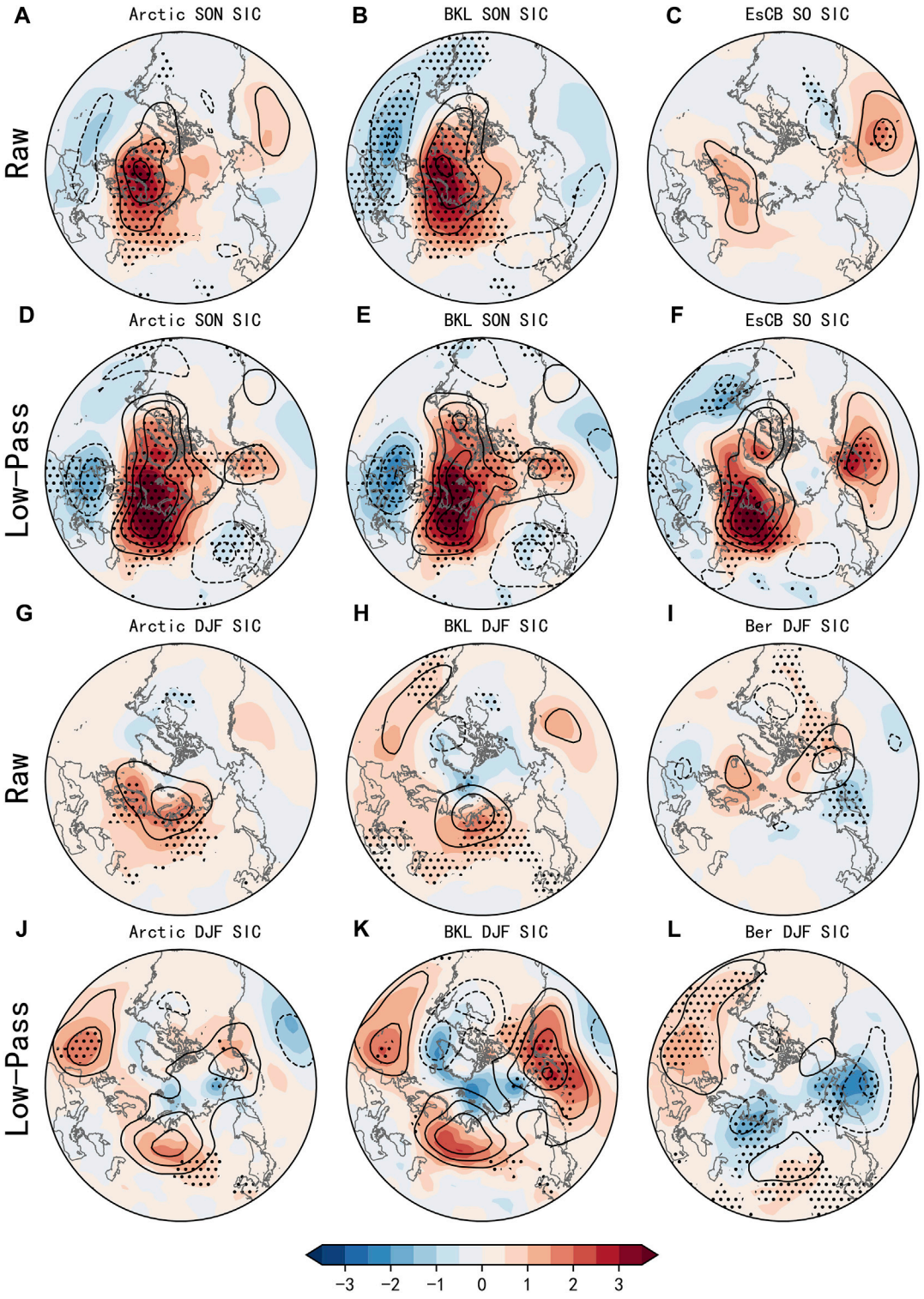

FIGURE 4 | As in **Figure 3** but for SLP (shading; unit: hPa) and 500-hPa geopotential height fields (contours; interval: 10 m).

that focused mainly on the effects of year-round or winter sea-ice loss (Mori et al., 2014; Ayarzagüena and Screen, 2016; Pedersen et al., 2016) rather than autumn sea-ice loss.

The mechanisms underpinning the influence of autumn sea-ice on the wintertime midlatitude climate are complex. Autumn sea-ice loss can modify large-scale Rossby waves by increasing the

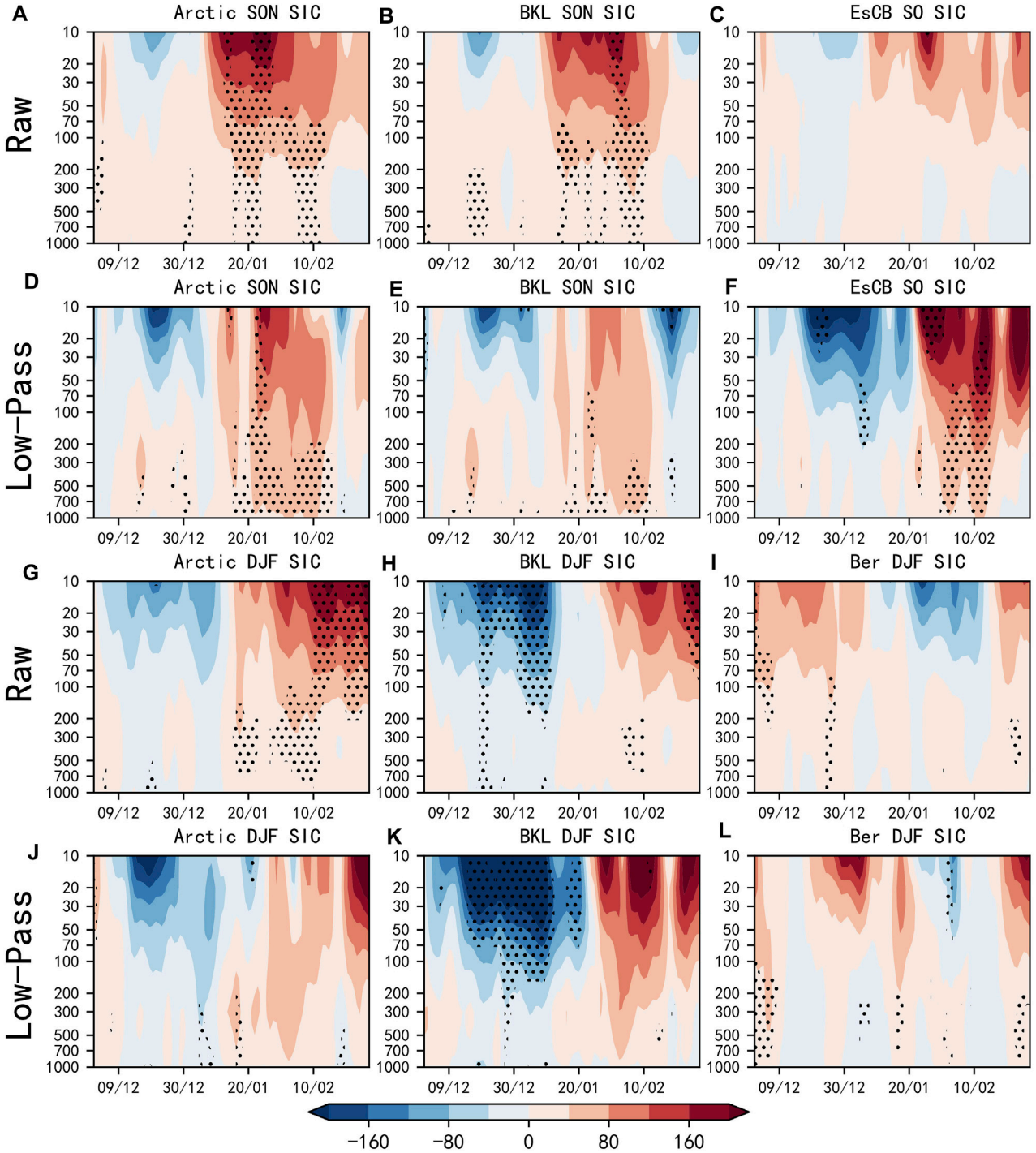

FIGURE 5 | As in **Figure 3** but for the winter daily evolution of polar cap height (PCH; 70°–90°N; unit: m).

vertical propagation of wave energy into the stratosphere, favoring a warmer and weakened stratospheric polar vortex. One common measure of such troposphere–stratosphere interaction is the evolution of polar cap height (PCH; e.g., Peings and Magnusdottir, 2014), which is calculated as the geopotential height averaged north of 70°N. **Figure 5** shows the winter PCH anomalies regressed upon the sea-ice indices in different regions and seasons. Autumn Pan-Arctic and BKL sea-ice loss favor significant positive PCH anomalies throughout the troposphere in winter, which increase in late December and January above 100 hPa, indicating a weakening of the polar vortex, consistent with Sun et al. (2015). Then, positive PCH

anomalies propagate downwards and reach the surface in mid-January and early February, leading to a negative phase of the NAO and hence significant cooling over large parts of Eurasia and North America (**Figures 5A,B**). This timing of the coldness is consistent with the findings of Peings and Magnusdottir (2014), who prescribed year-round sea-ice loss in an atmospheric model, indicating that the stratospheric pathway can be primarily attributed to sea-ice change in autumn.

A similar pattern of winter negative SAT anomalies over Eurasia is apparent for autumn EsCB, but the anomalies are relatively insignificant and spatially restricted when compared with the Pan-Arctic and BKL (**Figure 3C**). The positive PCH anomalies occur in the stratosphere but lack statistical significance, which implies the absence of stratospheric processes (**Figures 4C**, **5C**). Chen and Wu (2018) found significant stratospheric PCH responses over the mid–high latitudes in response to EsCB sea-ice loss in September–October on interannual timescales, but these PCH anomalies reach lower troposphere in March rather than in winter. Another significant cold SAT anomaly occurs over Alaska, and this coldness is associated with weakening of the Aleutian low possibly related to persistent EsCB sea-ice loss (**Figures 2C**, **3C**).

On the interdecadal timescale, autumn sea-ice loss in these subregions is connected with significant cooling over large parts of Eurasia and North America, and the correlations are statistically stronger than the unfiltered results (**Figures 3A–C**). This suggests that, in decadal periods of autumn sea-ice loss (gain), low (high) temperature anomalies are likely to occur over midlatitude land areas. In addition, it is interesting to note that lower-than-normal SAT anomalies are found over North America for all regional SIC indices and over the Eurasian midlatitudes for EsCB (**Figures 3D–F**), which disappear in the unfiltered results. This discrepancy implies that Arctic sea-ice loss has some physical linkage with North American coldness on interdecadal rather than interannual timescales, as well as the autumn EsCB-winter Eurasian SAT linkage. Reasons for this closer linkage are probably the stronger negative NAO phase and the enhanced Siberian high that stretch into North America (**Figures 4D–F**). Furthermore, the downward wave propagation to troposphere is significantly enhanced. In particular, the EsCB-related PCH anomalies display significant positive anomalies and propagate into the lower troposphere in early February (**Figures 5D–F**). These intensified circulation situations provide favorable conditions for the occurrence of cold temperatures in the Northern Hemisphere midlatitudes.

In conclusion, there is a dynamic relationship between autumn sea-ice loss in different regions and wintertime atmospheric circulation and attendant midlatitude coldness, mainly through stratospheric pathways. Specifically, the BKL sea-ice variation is closely related to the Eurasian midlatitude coldness on both interannual and interdecadal timescales, but to the North American coldness on the interdecadal timescale only. The EsCB sea-ice is connected with midlatitude coldness in Eurasia and North America on the interdecadal timescale.

Winter Sea Ice–Related Temperature and Circulation

Winter sea-ice has a different effect on wintertime atmospheric circulation relative to autumn sea-ice. As for winter Pan-Arctic and BKL sea-ice loss, cold anomalies in the Eurasian midlatitude are quite a lot weaker and lack statistical significance. Meanwhile, broad and significant Arctic warming is evident in regions of sea-ice loss (**Figures 3G,H**). Winter sea-ice loss corresponds to a weak positive phase of NAO pattern over the North Atlantic regions, which is different to the autumn sea-ice–related negative NAO pattern. The main positive anomaly centers are situated over Siberia and the North Atlantic, with the Siberian high relatively weaker in magnitude and more zonally orientated when compared with autumn sea-ice-related circulation anomalies (**Figures 4G,H**). That is the reason why low temperatures occur over Northeast China along the eastern margin of the high pressure. In cases of BKL sea-ice loss, the expansion of Davis Strait sea-ice is conducive to the anomalous low pressure over Greenland-northern North America and the anomalous high pressure over North Atlantic (Dai et al., 2019). In addition, the weak positive NAO pattern is very likely attributed to the strengthened and significant stratospheric polar vortex in early winter (**Figures 5G,H**). The stratospheric process associated with winter sea-ice loss differs from that with autumn sea-ice loss. In late winter, the stratospheric process is characterized by a weakened polar vortex, weak downward propagation in late January and obvious upward propagation of tropospheric waves in February. This weak stratospheric process related with winter sea-ice loss is different from the robust stratospheric process in Zhang et al. (2018), since their focus is sea-ice loss in November–December, while our focus is December–February. These results suggest that the tropospheric pathway may play a major role in the impacts of winter sea-ice change on Eurasian climate, while stratospheric pathway play a minor role.

In comparison, the winter Ber is linked to significant cooling over eastern North America and evident warming over the Aleutian region of sea-ice loss (**Figure 3I**), consistent with previous results (Kug et al., 2015; Screen, 2017A). In the troposphere, there is a clear wave train downstream of the Bering Sea, dynamically connected with an anomalous high over Alaska, which plays a vital role in linking the reduction in Ber sea-ice to the cold conditions in eastern North America (**Figure 4I**). This result is in agreement with Iida et al. (2020) that winter Bering sea-ice loss can affect wintertime North American cold anomalies by changing the Alaska Oscillation, the dominant mode over the highlatitude North Pacific. In the stratosphere, there is insignificant downward propagation of the positive PCH response that emerges in late December and early February (**Figure 5I**). Likewise, the stratospheric pathway is less important in the linkage between the winter Ber and the cold conditions in North American.

On the interdecadal timescale, the Eurasian midlatitude cold temperature is statistically insignificant; and furthermore, in turn, overall warming is apparent over the Arctic with penetration into northern Eurasia. Conversely, the North

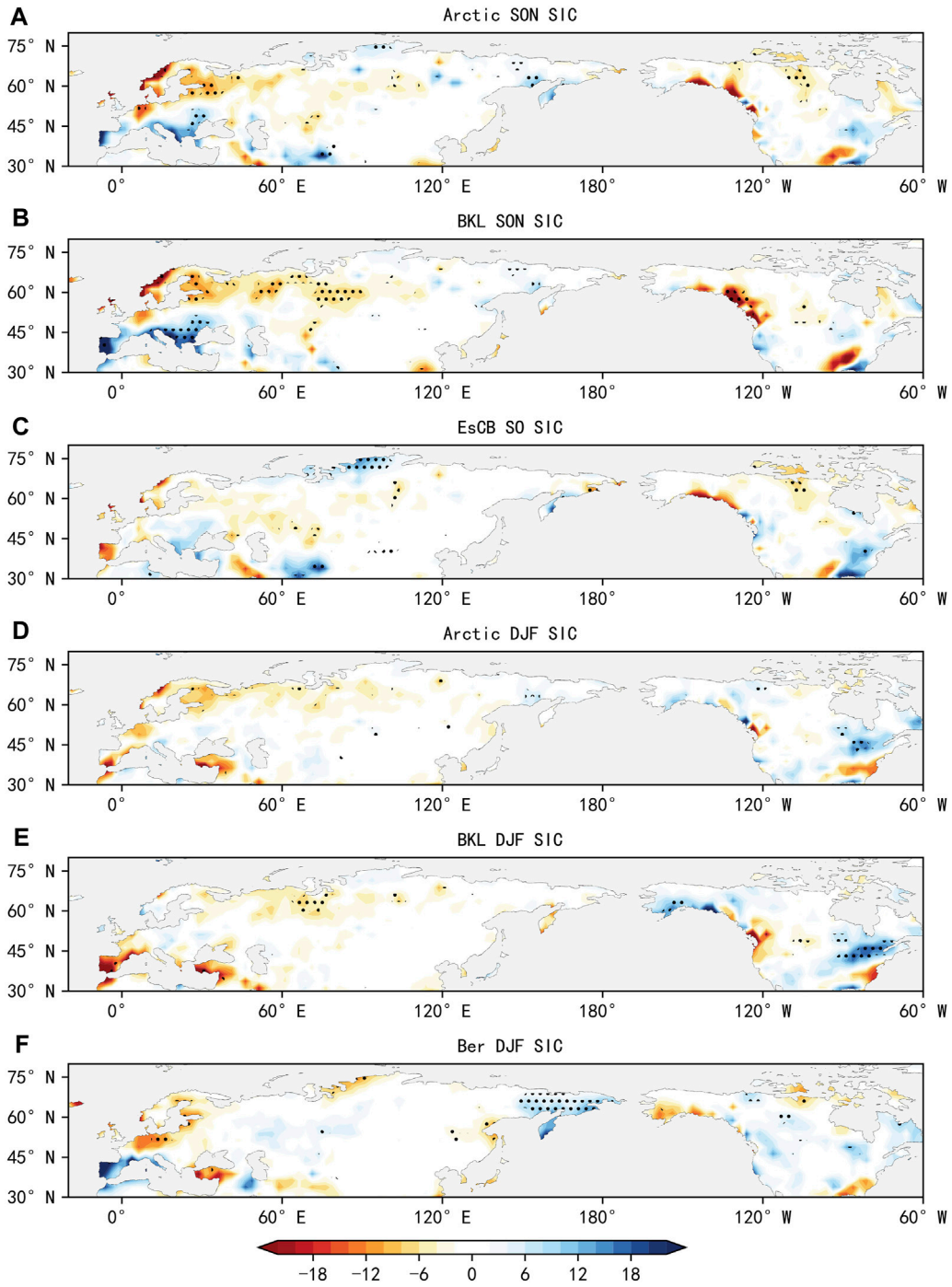

FIGURE 6 | As **Figures 3A–C** and **Figures 3G–I** but for monthly mean precipitation over land (unit: mm).

American midlatitude cold temperature is robust (**Figures 3J,K**). This indicates that in decades with Pan-Arctic and BKL sea-ice loss (gain) in winter, the highlatitude Eurasia tend to be warmer (colder) and the midlatitude Eurasian cold conditions tend to be milder (warmer) and the midlatitude North America tend to be colder (warmer), contrary to autumn sea-ice loss. The Siberian high shifts southwards in position and the positive NAO pattern is more apparent when compared with that associated with autumn sea-ice change (**Figures 4J,K**). The southerly winds along the western margin of the Siberian high guide warm air to the Arctic and Eurasian highlatitude regions; and meanwhile, warm advection along the eastern margin transports warm air from the open oceans to the Eurasian highlatitudes, leading to the

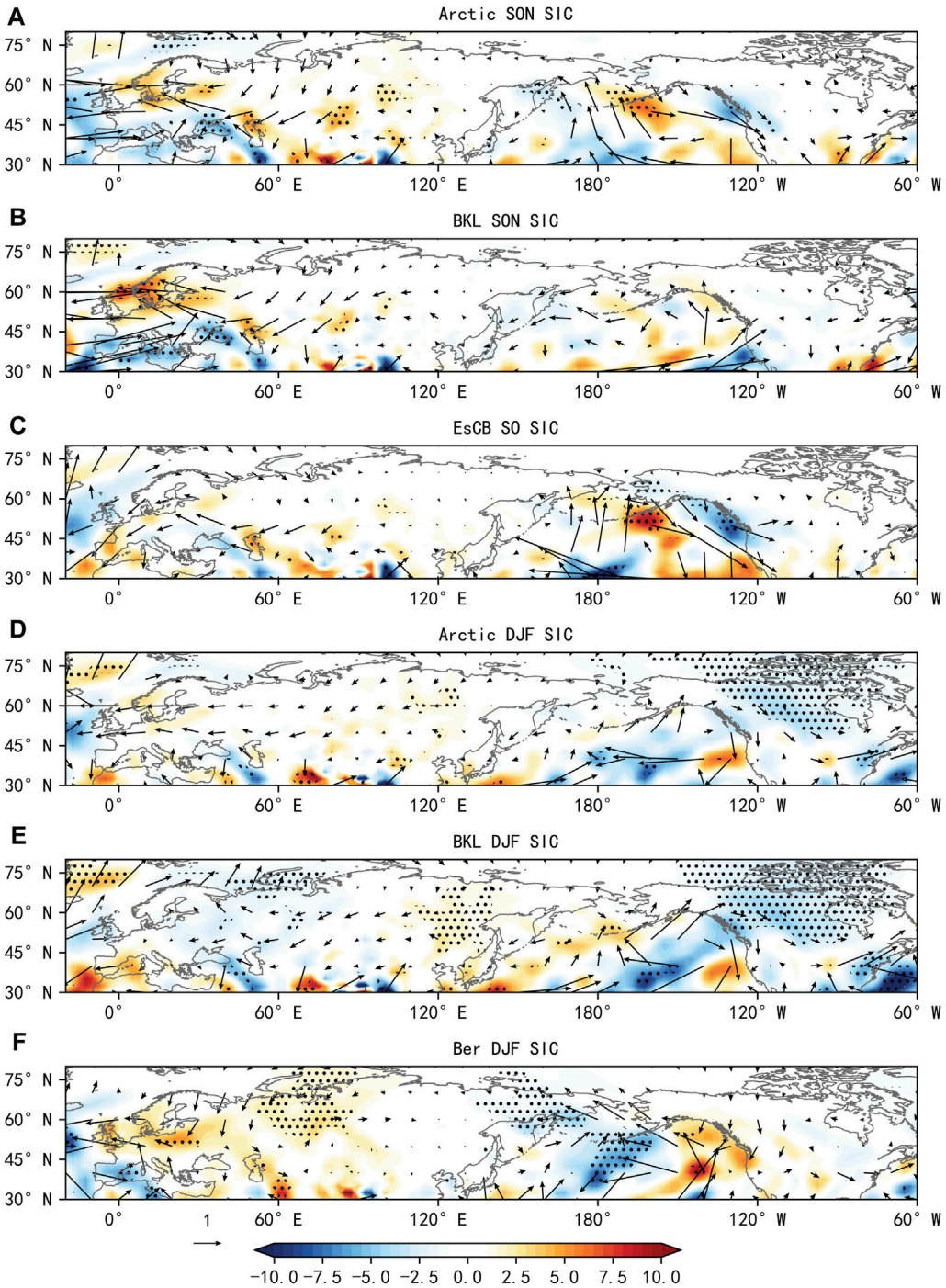

FIGURE 7 | As in **Figure 6** but for 1,000–500-hPa cumulative moisture transport fluxes [vectors; units: g (m s)$^{-1}$] and associated divergence [shading; units: g (m^2 s)$^{-1}$].

warm highlatitude Eurasia. Furthermore, significantly negative PCH anomalies are overwhelmingly found throughout the troposphere and stratosphere, leading to the positive NAO pattern and cold North America. Therefore, it can be concluded that the Eurasian highlatitude warming and weakened midlatitude cooling is dynamically linked to winter sea-ice loss in BKL, mainly through tropospheric rather than stratospheric pathways.

As for Ber, there is significant SAT warming in central Eurasia and Alaska and insignificant warming over North America (**Figure 3L**). The latter warming is contrary to the unfiltered cooling over North America, indicating that the impacts of Ber

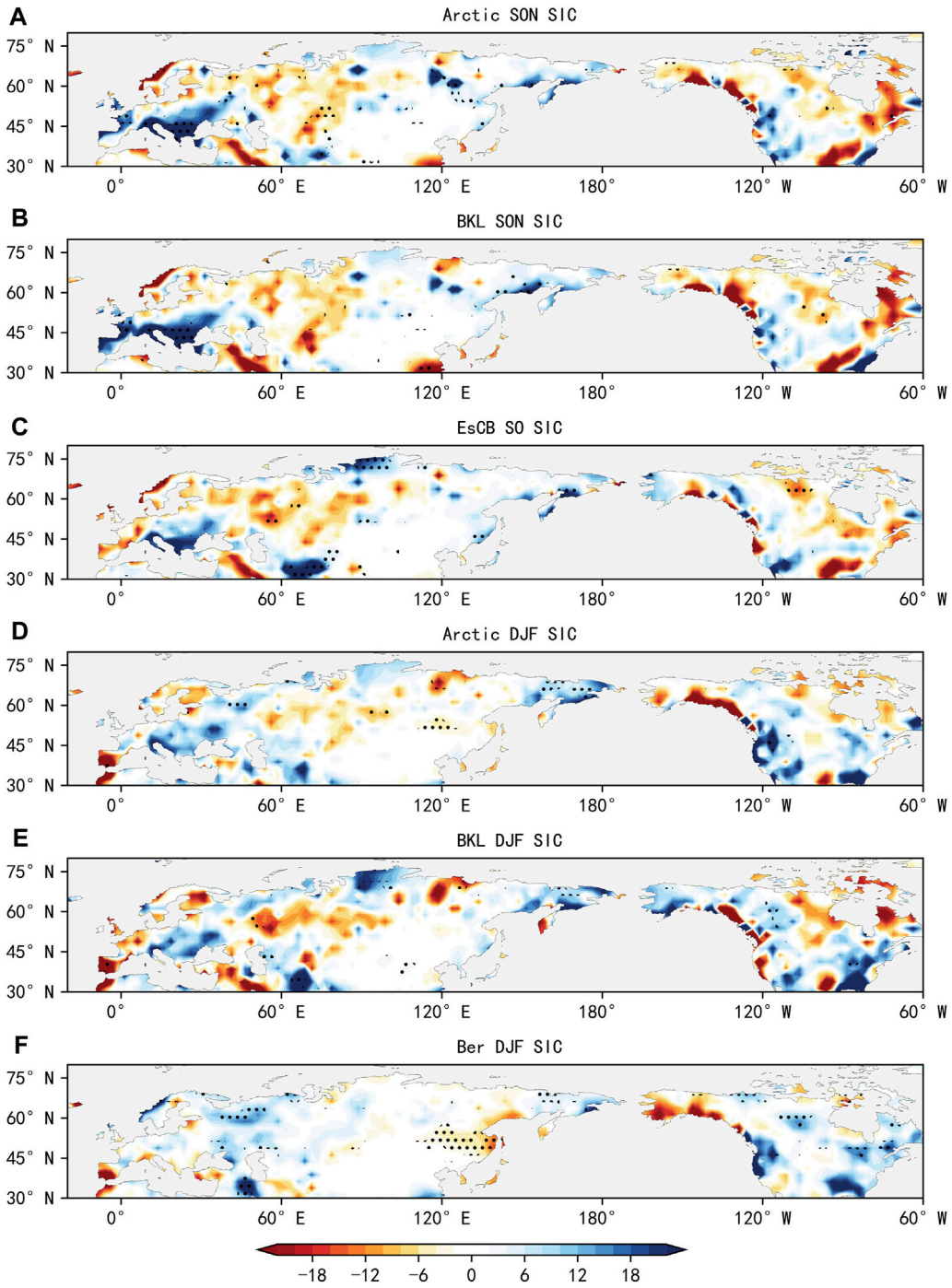

FIGURE 8 | As in **Figure 6** but for the interdecadal component of precipitation.

sea-ice on North American cooling possibly exist at the interannual timescale (figure not shown) rather than the interdecadal timescale. A circumglobal-scale teleconnection wave train, with high pressure anomalies over East Asia, a strengthened Aleutian low, and weakened high-pressure anomalies over Alaska (**Figure 4L**), is favorable for the occurrence of warm temperatures over central Eurasia. In addition, the low pressure in the Aleutian region is contrary to autumn sea-ice-induced high anomalies, which implies that atmospheric circulation dominates the Bering Sea and that the southerly winds guide warm air northwards to the Bering Sea and hence ice loss happens there. The stratospheric pathway, however, has little impact on the wintertime climate (**Figure 5L**).

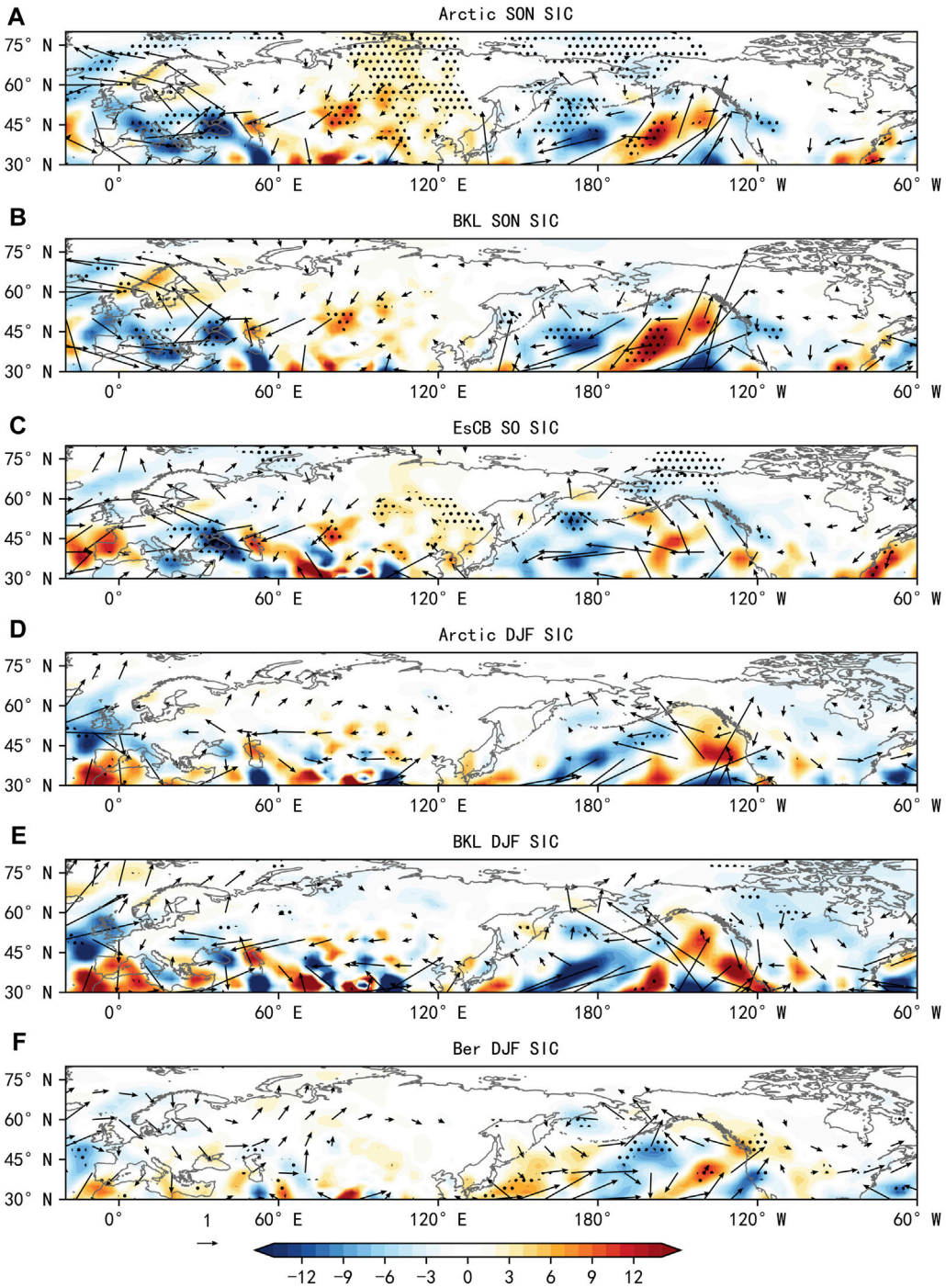

FIGURE 9 | As in **Figure 7** but for the interdecadal component of moisture transport fluxes and associated divergence.

Generally speaking, the winter BKL sea-ice loss (gain) is linked to an enhanced (a weakened) Siberian high and lower (higher) temperatures in the highlatitudes of Eurasia. In contrast, the winter sea-ice loss (gain) in Ber is linked to a large-scale teleconnection wave train downstream of the Bering Sea, with higher (lower) than normal temperature in North America on the interannual timescale and in central Eurasia on the interdecadal timescale.

Precipitation and Moisture Transport

In addition to temperature, large-scale circulation anomalies associated with Arctic sea-ice variation also affect precipitation. On the one hand, strengthening of the Siberian high caused by melting of Arctic sea-ice changes the precipitation pattern in the midlatitudes (Gong and Ho, 2002). On the other hand, the expansion of the Arctic open

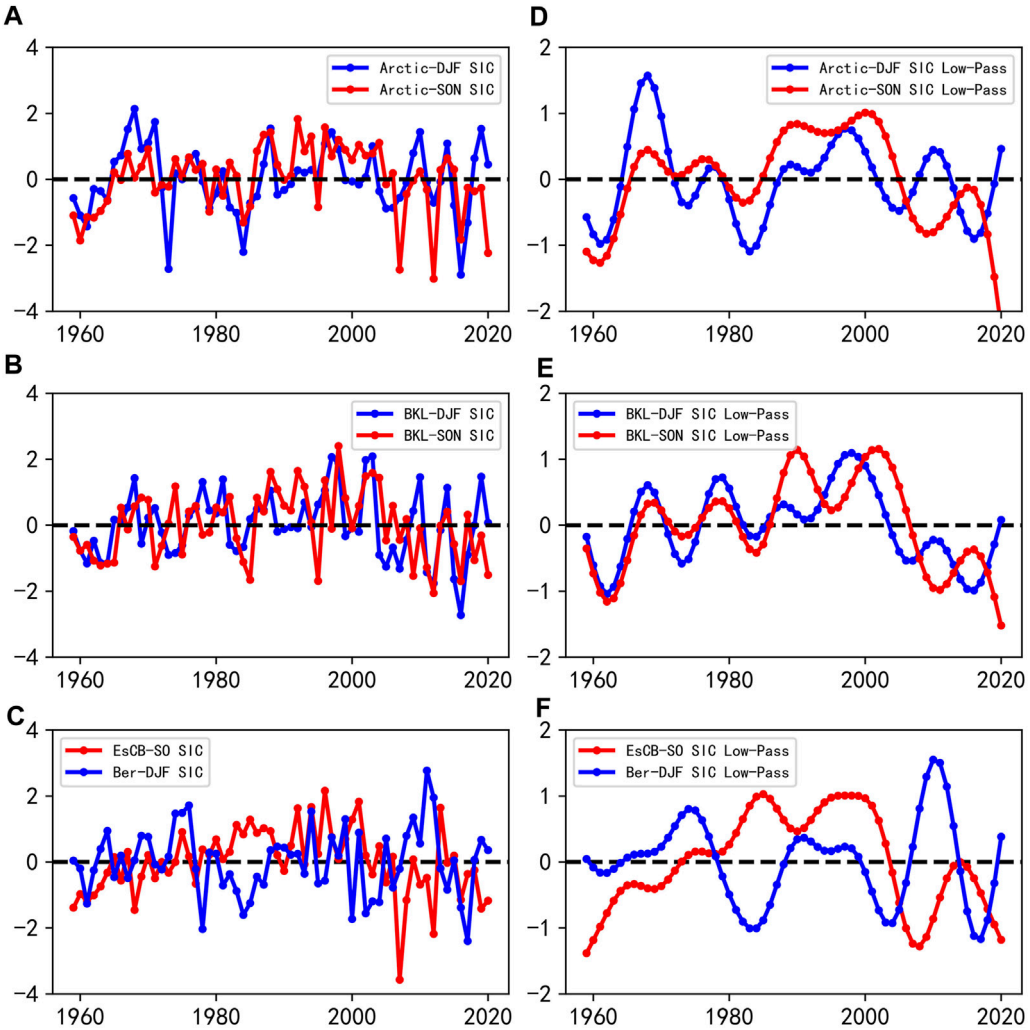

FIGURE 10 | As in **Figure 1** but for the period from 1959 to 2020.

ocean also provides water vapor conditions for precipitation over the continent (Ben et al., 2016). **Figures 6–9** show the wintertime precipitation and large-scale moisture flux anomalies regressed upon the sea-ice in different regions and seasons.

In terms of autumn Pan-Arctic and BKL sea-ice loss, a meridional dipole precipitation anomaly pattern can be found in the Northern Hemisphere mid–high-latitudes, which shows more precipitation over the midlatitudes, such as in southern Europe, and little precipitation at highlatitudes, such as northwestern Eurasia and northeastern Canada (**Figures 6A,B**). This dipole pattern is mainly affected by the anomalous anticyclone over Siberia and the Canadian Archipelago, which gives rise to apparent water vapor divergence over Eurasian highlatitudes and northeastern Canada, leading to a deficit in precipitation over these regions. Meanwhile, the anomalous anticyclone over the North Atlantic–Europe region converges water vapor flux from the Atlantic and Eurasia (**Figures 7A,B**), resulting in increased precipitation over southern Europe. This wintertime precipitation pattern is similar to that in Li and Wang (2012), who applied the autumn Kara–Laptev sea-ice index during 1982–2010 for regression. For EsCB, due to the weak circulation anomalies, water vapor flux and precipitation anomalies are broadly weak (**Figures 6C**, **7C**).

On the interdecadal timescale, the precipitation anomalies related to autumn sea-ice loss in the three regions show similar dipole patterns, but with stronger precipitation in magnitude and a southward extension of the deficit in precipitation in central Eurasia. This dipole pattern is due to the meridional enhancement and expansion of Siberia–North America high pressure anomalies, which facilitate an increased frequency of cold and dry air into Siberia and North America. Meanwhile, the negative precipitation anomalies over northeast Canada are spreading towards southeast Canada. Moreover, the anomalous cyclone located in the northeast Atlantic–Europe region is strengthened, relative to the unfiltered results, and facilitates water vapor transport from the Atlantic and

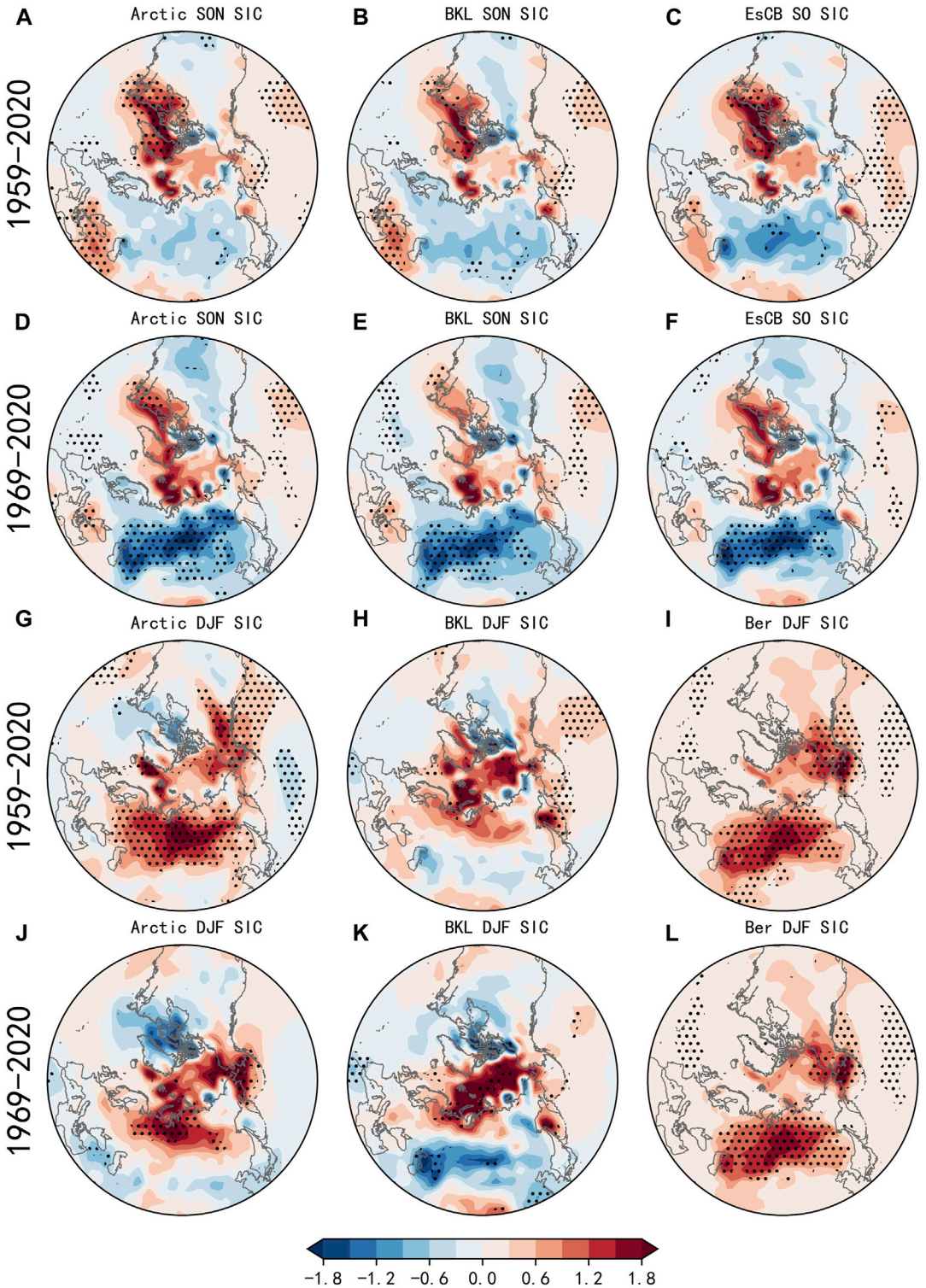

FIGURE 11 | As in **Figure 3** but for interdecadal component of sea-ice indices and surface air temperature during 1959–2020 [**(A–C)** and **(G–I)**] and 1969–2020 [**(D–F)** and **(J–L)**].

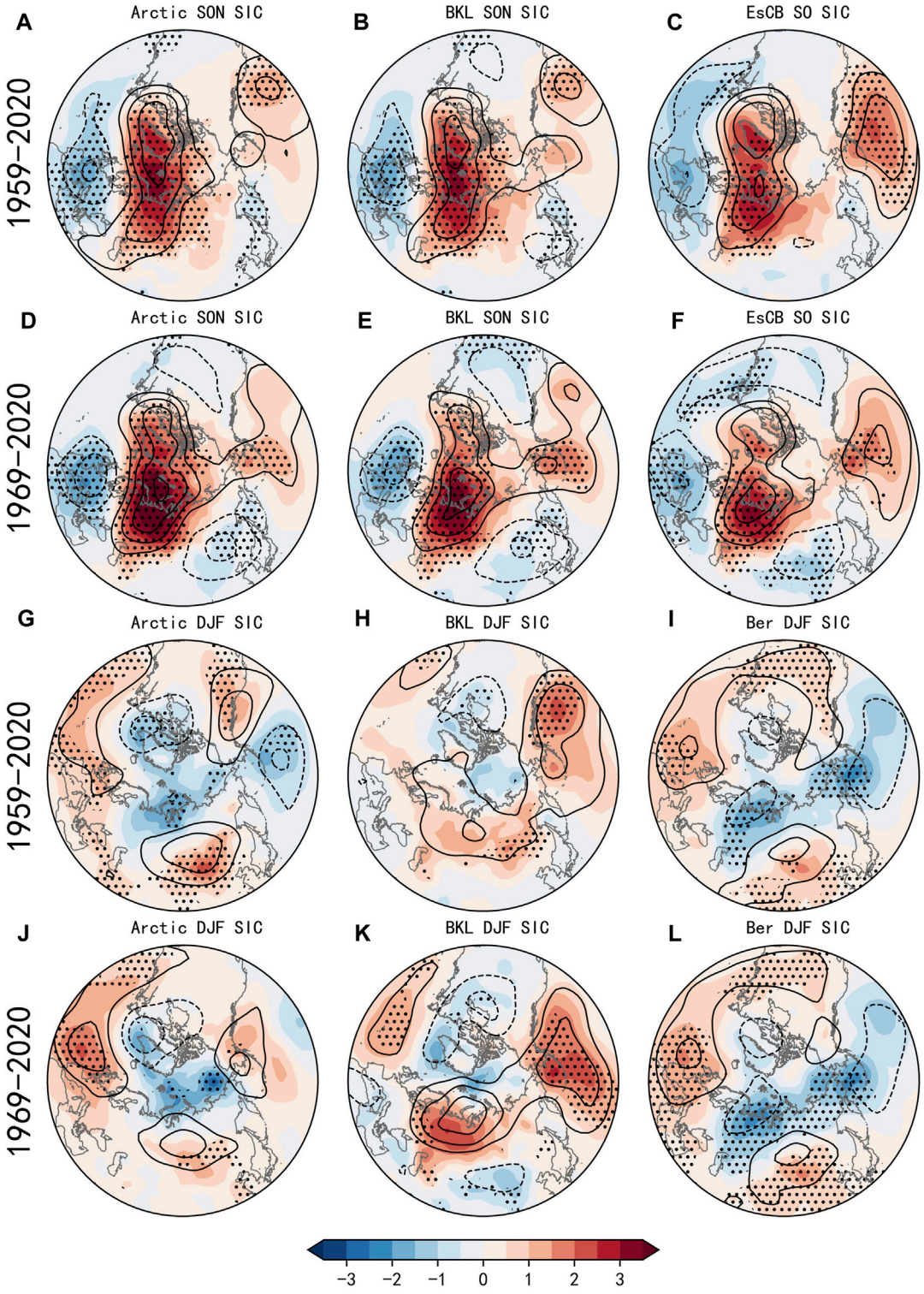

FIGURE 12 | As in **Figure 4** but for interdecadal sea-ice loss during 1959–2020 [**(A–C)** and **(G–L)**] and 1969–2020 [**(D–F)** and **(J–L)**].

Mediterranean (**Figures 8A–C**; **Figures9A–C**). Therefore, the dipole pattern is strengthened in intensity, and the area influenced is enlarged to nearby regions.

For the winter Pan-Arctic and BKL sea-ice loss, insufficient precipitation is generally observed in Eurasia, which corresponds to the more extensive Siberian high and accompanies a divergence

in moisture transport. The anomalous low pressure in northern North America is favorable for the convergence of water vapor and excessive precipitation over the northeastern United States (**Figures 6D,E**; **Figures 7D,E**). For the winter Ber, the moisture flux and precipitation anomalies over both continents are weak. However, the Alaskan high pressure and melting Ber sea-ice facilitate water vapor convergence in the Far East, contributing to increased precipitation there (**Figures 6F**, **7F**).

On the interdecadal timescale, the main difference for the Pan-Arctic and BKL is the north–south tripole pattern of precipitation over the Eurasian continent, with high snowfall around the Arctic and in southern Europe and low snowfall in the midlatitudes. This is because the anomalous Siberian high moves southwards, which leads to the southward displacement of the dipole pattern identified in the unfiltered results. In addition, the high snowfall around the Arctic can be attributed to the increased area of open water, and the Siberian high transports more water vapor from BKL to the Eurasian highlatitudes. However, the cause of the increase in precipitation over southern Europe is different to that in the unfiltered results **Figures 3A-C**. The high pressure anomaly over western Europe and the westerly winds carry water vapor from the North Atlantic to southern Europe. In North America, the low pressure over northeastern North America and the high pressure over the Aleutian region appear to guide water vapor from the Arctic *via* the northerly winds, resulting in more precipitation over northwestern and southeastern North America (**Figures 8D,E**; **Figures 9D,E**). For the Bering Sea, due to the anticyclonic circulation near the Barents Sea, the water vapor from the Arctic Ocean and Europe converges in eastern Europe, leading to abundant precipitation there. Northeast China is located at the eastern margin of the anomalous Eurasian high, which is controlled by the dry current from the northern continent and hence dominated by reduced precipitation. Similar to the Pan-Arctic and BKL, the low pressure over northern North America and the high pressure over the northern Atlantic facilitate water vapor convergence in northern and central North America, with moisture sources from the Arctic, North America and North Atlantic (**Figures 8F**, **9F**).

To conclude, changes in precipitation are dynamically consistent with large-scale atmospheric circulation and temperature. The precipitation patterns associated with autumn sea-ice change on interdecadal timescales resemble those in the unfiltered results, which display a north–south dipole pattern over the Northern Hemisphere. For winter sea-ice change, a north–south tripole pattern is identifiable for BKL, and excessive European precipitation is apparent for Ber.

CONCLUSION AND DISCUSSION

The interdecadal linkage between the wintertime Northern Hemisphere climate and sea-ice in different regions and seasons is analyzed in this paper. The results can be summarized as follows:

The Pan-Arctic and BKL sea-ice, irrespective of seasonality, display similar relationships with large-scale atmospheric circulation, near-surface air temperature, and precipitation anomalies. The WACC mode of wintertime temperature is dynamically consistent with the sea-ice loss in both autumn and winter. Autumn sea-ice loss can affect the wintertime climate in the midlatitudes through stratospheric pathways, which generally leads to a negative NAO phase with an anomalous high over the Arctic and continental highlatitudes. These anomalous circulations appear to induce severe cold events in the midlatitudes, albeit still controversially, and a north–south dipole precipitation pattern over Northern Hemisphere continents. However, wintertime sea-ice loss affects the climate mainly through tropospheric pathways. Significant warming is observed over the Arctic and extends to highlatitudes, whereas mild coldness is found in the midlatitudes. For precipitation, there is a meridional "less-more-less" tripole pattern over the Eurasian continent and abundant precipitation over North America.

The atmospheric circulation and climate anomalies associated with autumn EsCB shows similarity to those with Pan-Arctic and BKL on the interdecadal timescale, but large difference on the interannual timescale. For winter, however, the Ber-related circulation and climate anomalies differ from those of the Pan-Arctic and BKL. There are low pressure centers over Siberia and northeastern North America and hence positive precipitation anomalies there, and high pressure over East Asia and hence strong central Eurasian warming.

The present study focuses on the interdecadal relationship between the Arctic and midlatitudes during the 1979–2020 period. Given that the periodism of Arctic sea-ice indices is shorter than 20 years, it appears reasonable to conduct interdecadal analysis using 40-year dataset. To further verify the interdecadal variations of sea-ice on longer timescale, we extend the period of dataset to 1959 and 1969, respectively. **Figures 10–12** show the Arctic sea-ice indices and associated SAT, and SLP and 500-hPa geopotential height anomalies. Prior to 1979, there is relatively heavy than average sea-ice in diverse regions, and high persistence of sea-ice anomalies between autumn and winter (**Figure 10**). The temperature and circulation anomalies during the 1969–2020 and 1979–2020 periods are similar in spatial pattern and magnitude, particularly for the robust Eurasian cooling (**Figure 11**). The main difference is the disappearance of significant cold anomalies over North America, which is caused by the stronger low pressure anomalies over North America (**Figure 12**). For the 1959–2020 period, the spatial patterns remain similar, but the magnitudes largely reduce and lack statistical significance. This is because the NAO pattern and Siberian high are relatively weaker, in companion with the weakened East Asian trough, which is conducive to cold-air outbreaks into the midlatitudes (**Figure 12**). Another reason for the differences between different periods, is the lack of sea-ice data until the satellite era. Before sea-ice can be seen from satellites, rather coarse indicators of the sea-ice have been monitored and higher spatial resolution sea-ice data can be acquired for recent three decades (Rayner et al., 2003; Coon et al., 2007).

Another question worthy of discussion is the nonstationary relationship betweensea-ice and wintertime climate in long-term timescales. In this study, comparing dataset of long period to short period, this interdecadal linkage begins to attenuate and lacks statistical significance. For the 1850–2099 period, Kolstad and Screen (2019) discovered evidence of nonstationarity in the relationship between autumn sea-ice and the winter NAO, which implicates that the recently intimate ice-NAO relationship is unstable. Furthermore, recent studies reported that weakened positive anomaly of Siberian High after the mid-1990s is induced by lesser Kara-Laptev sea-ice loss, and that enhanced spring AO after the late-1990s is caused by larger interannual variability of Laptev-eastern Siberian-Beaufort sea ice (Chen et al., 2019; 2020B). These results implicate that the circulation anomalies caused by sea-ice change are strongly dependent upon the analysis period and the location of sea-ice loss.

These findings have important implications for seasonal and interdecadal forecasting in the future, especially in the context of ongoing sea-ice loss. However, some regional precipitation anomalies still cannot be explained by mid–high-latitude circulation anomalies; for example, the precipitation anomalies over southeastern North America where there are complex tropical-extratropical interactions. Previous studies have also demonstrated that precipitation inland is strongly influenced by climate change (Lin and Zhou, 2015; Zhao et al., 2019) and El Niño–Southern Oscillation (ENSO) (Zhou and Wu, 2010), amongst other factors. Furthermore, recent studies have indicated that wintertime Arctic sea-ice anomalies can also have a significant impact on tropical climate systems, including the ENSO and Intertropical Convergence Zone, through large-scale atmospheric wave trains and equatorial warm Kelvin wave and monotonic temperature increase in deep ocean, respectively. (e.g., Wang et al., 2018; Chen et al., 2020A). Therefore, sensitivity experiments are needed to isolate the individual effect of Arctic sea-ice. Furthermore, it is important to note that statistical association does not guarantee causality. As such, to further demonstrate the part of the midlatitude climate anomalies caused by sea-ice change in distinct geographical regions and seasons, coupled model simulations are required, which is the next step for our group's research (Kim et al., 2014; Screen, 2017a).

DATA AVAILABILITY STATEMENT

The original contributions presented in the study are included in the article/Supplementary Material, further inquiries can be directed to the corresponding author.

AUTHOR CONTRIBUTIONS

XH and RZ conceived the study and wrote the manuscript. SD and ZZ provided critical feedback and helped shape the research and manuscript. All authors contributed to the article and approved the submitted version.

FUNDING

RZ was supported by the National Key Research and Development Program of China (Grants 2016YFA0601500 and 2019YFC1509105), National Natural Science Foundation of China (Grants 41790472 and 42075016), and Shanghai Pujiang Program (Grant 2020PJD004).

REFERENCES

Ayarzagüena, B., and Screen, J. A. (2016). Future Arctic Sea Ice Loss Reduces Severity of Cold Air Outbreaks in Midlatitudes. *Geophys. Res. Lett.* 43, 2801–2809. doi:10.1002/2016GL068092

Ben, G. K., Kopec, X., Michel, F. A., and Posmentier, E. S. (2016). Influence of Sea Ice on Arctic Precipitation. *Proc. Natl. Acad. Sci. U S A.* 113, 46–51. doi:10.1073/pnas.1504633113

Chen, S., Wu, R., and Chen, W. (2019). Enhanced Impact of Arctic Sea Ice Change during Boreal Autumn on the Following spring Arctic Oscillation since the Mid-1990s. *Clim. Dyn.* 53, 5607–5621. doi:10.1007/s00382-019-04886-y

Chen, S., and Wu, R. (2018). Impacts of Early Autumn Arctic Sea Ice Concentration on Subsequent spring Eurasian Surface Air Temperature Variations. *Clim. Dyn.* 51, 2523–2542. doi:10.1007/s00382-017-4026-x

Chen, S., Wu, R., Chen, W., and Yu, B. (2020a). Influence of winter Arctic Sea Ice Concentration Change on the El Niño-Southern Oscillation in the Following winter. *Clim. Dyn.* 54, 741–757. doi:10.1007/s00382-019-05027-1

Chen, S., Wu, R., Cheng, W., and Yu, B. (2020b). Weakened Impact of Autumn Arctic Sea Ice Concentration Change on the Subsequent winter Siberian High Variation Around the Late-1990s. *Int. J. Climatol* 41, 2700–2717. doi:10.1002/joc.6875

Cohen, J., Screen, J. A., Furtado, J. C., Barlow, M., Whittleston, D., Coumou, D., et al. (2014). Recent Arctic Amplification and Extreme Mid-latitude Weather. *Nat. Geosci* 7, 627–637. doi:10.1038/ngeo2234

Cohen, J., Zhang, X., and Francis, J. (2020). Divergent Consensuses on Arctic Amplification Influence on Midlatitude Severe winter Weather. *Nat. Clim. Chang* 10, 20–29. doi:10.1038/s41558-019-0662-y

Coon, M., Kwok, R., Levy, G., Pruis, M., Schreyer, H., and Sulsky, D. (2007). Arctic Ice Dynamics Joint Experiment (AIDJEX) Assumptions Revisited and Found Inadequate. *J. Geophys. Res.* 112 (C11), C11S90. doi:10.1029/2005JC003393

Dai, H., Fan, K., and Liu, J. (2019). Month-to-Month Variability of Winter Temperature over Northeast China Linked to Sea Ice over the Davis Strait-Baffin Bay and the Barents-Kara Sea. *J. Clim.* 32, 6365–6384. doi:10.1175/JCLI-D-18-0804.1

Davis, R. (1976). Predictability of Sea Surface Temperature and Sea Level Pressure Anomalies over the North Pacific Ocean. *J. Phys. Oceanography* 6, 249–266. doi:10.1175/1520-0485(1976)006,0249:POSSTA.2.0.CO;2

Ding, S., Wu, B., and Chen, W. (2020). Dominant Characteristics of Early Autumn Arctic Sea Ice Variability and its Impact on Winter Eurasian Climate. *J. Clim.* 34 (5), 1–67.

Ding, S., and Wu, B. (2021). Linkage between Autumn Sea Ice Loss and Ensuing spring Eurasian Temperature. *Clim. Dyn*. doi:10.1007/s00382-021-05839-0

Francis, J. A., and Vavrus, S. J. (2012). Evidence Linking Arctic Amplification to Extreme Weather in Mid-latitudes. *Geophys. Res. Lett.* 39, a–n. doi:10.1029/2012GL051000

Gong, D.-Y., and Ho, C.-H. (2002). The Siberian High and Climate Change over Middle to High Latitude Asia. *Theor. Appl. Climatology* 72, 1–9. doi:10.1007/s007040200008

Honda, M., Inoue, J., and Yamane, S. (2009). Influence of Low Arctic Sea-ice Minima on Anomalously Cold Eurasian winters. *Geophys. Res. Lett.* 36, L08707. doi:10.1029/2008GL037079

Iida, M., Sugimoto, S., and Suga, T. (2020). Severe Cold Winter in North America Linked to Bering Sea Ice Loss. *J. Clim.* 33, 8069–8085. doi:10.1175/JCLI-D-19-0994.1

Kalnay, E., Kanamitsu, M., Kistler, R., Collins, W., Deaven, D., Gandin, L., et al. (1996). The NCEP/NCAR 40-year Reanalysis Project. *Bull. Amer. Meteorol. Soc.* 77, 437–470.

Kim, B.-M., Son, S.-W., Min, S.-K., Jeong, J.-H., Kim, S.-J., Zhang, X., et al. (2014). Weakening of the Stratospheric Polar Vortex by Arctic Sea-Ice Loss. *Nat. Commun.* 5, 4646. doi:10.1038/ncomms5646

Kolstad, E. W., and Screen, J. A. (2019). Nonstationary Relationship between Autumn Arctic Sea Ice and the winter North Atlantic Oscillation. *Geophys. Res. Lett.* 46, 7583–7591. doi:10.1029/2019GL083059

Kug, J.-S., Jeong, J.-H., Jang, Y.-S. Min., Kim, B.-M., Folland, C. K., Min, S.-K., et al. (2015). Two Distinct Influences of Arctic Warming on Cold winters over North America and East Asia. *Nat. Geosci* 8, 759–762. doi:10.1038/NGEO2517

Li, C., Stevens, B., and Marotzke, J. (2015). Eurasian winter Cooling in the Warming Hiatus of 1998-2012. *Geophys. Res. Lett.* 42, 8131–8139. doi:10.1002/2015GL065327

Li, F., and Wang, H. (2012). Autumn Sea Ice Cover, Winter Northern Hemisphere Annular Mode, and Winter Precipitation in Eurasia. *J. Clim.* 26, 3968–3981. doi:10.1175/JCLI-D-12-00380.1

Lin, R., and Zhou, T. (2015). Reproducibility and Future Projections of the Precipitation Structure in East Asia in Four Chinese GCMs that Participated in the CMIP5 Experiments. *Chin. J. Atmos. Sci.* 39, 338–356. doi:10.3878/j.issn.1006-9895.1407.14110

Liu, N., Lin, L., Kong, B., Wang, Y., Zhang, Z., and Chen, H. (2016). Association between Arctic Autumn Sea Ice Concentration and Early winter Precipitation in China. *Acta Oceanol. Sin.* 35, 73–78. doi:10.1007/s13131-016-0860-7

Ma, J., Wang, H., and Zhang, Y. (2012). Will Boreal winter Precipitation over China Increase in the Future? an AGCM Simulation under Summer "Ice-free Arctic" Conditions. *Chin. Sci. Bull.* 57, 921–926. doi:10.1007/s11434-011-4925-x

Mori, M., Kosaka, Y., Watanabe, M., Nakamura, H., and Kimoto, M. (2019). A Reconciled Estimate of the Influence of Arctic Sea-Ice Loss on Recent Eurasian Cooling. *Nat. Clim Change* 9, 123–129. doi:10.1038/s41558-018-0379-3

Mori, M. M., Shiogama, H., Inoue, J., and Kimoto, M. (2014). Robust Arctic Sea-Ice Influence on the Frequent Eurasian Cold winters in Past Decades. *Nat. Geosci* 7, 869–873. doi:10.1038/NGEO2277

Nakamura, T., Yamazaki, K., Iwamoto, K., Honda, M., Miyoshi, Y., Ogawa, Y., et al. (2016). The Stratospheric Pathway for Arctic Impacts on Midlatitude Climate. *Geophys. Res. Lett.* 43, 3494–3501. doi:10.1002/2016GL068330

Nakamura, T., Yamazaki, K., Iwamoto, K., Honda, M., Miyoshi, Y., and Ukita, J. (2014). A Negative Phase Shift of the winter AO/NAO Due to the Recent Arctic Sea-Ice Reduction in Late Autumn. *J. Geophys. Res. Atmos.* 120, 3209–3227. doi:10.1002/2014JD022848

Pedersen, R. A., Cvijanovic, I., Langen, P. L., and Vinther, B. M. (2016). The Impact of Regional Arctic Sea Ice Loss on Atmospheric Circulation and the NAO. *J. Clim.* 29, 889–902. doi:10.1175/JCLI-D-15-0315.1

Peings, Y., and Magnusdottir, G. (2014). Response of the Wintertime Northern Hemisphere Atmospheric Circulation to Current and Projected Arctic Sea Ice Decline: A Numerical Study with CAM5. *J. Clim.* 27, 244–264. doi:10.1175/JCLI-D-13-00272.1

Peings, Y., and Magnusdottir, Y. G. (2015). Role of Sea Surface Temperature, Arctic Sea Ice and Siberian Snow in Forcing the Atmospheric Circulation in winter of 2012-2013. *Clim. Dyn.* 45, 1181–1206. doi:10.1007/s00382-014-2368-1

Rayner, N. A., Parker, D. E., Horton, E. B., and Folland, A. (2003). Global Analyses of Sea Surface Temperature, Sea Ice, and Night marine Air Temperature since the Late Nineteenth century. *J. Geophys. Res.* 108, 4407. doi:10.1029/2002JD002670

Screen, J. A. (2017a). Far-flung Effects of Arctic Warming. *Nat. Geosci* 10, 253–254. doi:10.1038/ngeo2924

Screen, J. A. (2017b). Simulated Atmospheric Response to Regional and Pan-Arctic Sea Ice Loss. *J. Clim.* 30, 3945–3962. doi:10.1175/JCLI-D-16-0197.1

Selesnick, I. W., and Burrus, C. S. (1998). Generalized Digital Butterworth Filter Design. *IEEE Trans. Signal. Process.* 46 (6), 1688–1694. doi:10.1109/78.678493

Song, L., Wang, L., Chen, W., and Zhang, Y. (2016). Intraseasonal Variation of the Strength of the East Asian Trough and its Climatic Impacts in Boreal winter. *J. Clim.* 29, 2557–2577. doi:10.1175/JCLI-D-14-00834.1

Sun, J., and Wang, H. (2012). Changes of the Connection between the Summer North Atlantic Oscillation and the East Asian Summer Rainfall. *J. Geophys. Res.* 117, a–n. doi:10.1029/2012JD017482

Sun, L., Deser, C., and Tomas, R. A. (2015). Mechanisms of Stratospheric and Tropospheric Circulation Response to Projected Arctic Sea Ice Loss*. *J. Clim.* 28, 7824–7845. doi:10.1175/JCLI-D-15-0169.1

Sun, L., Perlwitz, J., and Hoerling, M. (2016). What Caused the Recent "Warm Arctic, Cold Continents" Trend Pattern in winter Temperatures?. *Geophys. Res. Lett.* 43, 5345–5352. doi:10.1002/2016gl069024

Takaya, K., and Nakamura, H. (2005). Mechanisms of Intraseasonal Amplification of the Cold Siberian High. *J. Atmos. Sci.* 62, 4423–4440. doi:10.1175/JAS3629.1

Trenberth, K. E. (1999). Atmospheric Moisture Recycling: Role of Advection and Local Evaporation. *J. Clim.* 12, 1368–1381. doi:10.1175/1520-0442(1999)012<1368:AMRROA>2.0.CO;2

Van Oldenborgh, G. J., Haarsma, R., De Vries, H., and Allen, M. R. (2015). Cold Extremes in North America vs. Mild Weather in Europe: The Winter of 2013-14 in the Context of a Warming World. *Bull. Amer. Meteorol. Soc.* 96, 707–714. doi:10.1175/BAMS-D-14-00036.1

Wang, K., Deser, C., Sun, L., and Tomas, R. A. (2018). Fast Response of the Tropics to an Abrupt Loss of Arctic Sea Ice *via* Ocean Dynamics. *Geophys. Res. Lett.* 45, 4264–4272. doi:10.1029/2018GL077325

Wang, S., Nath, D., and Chen, W. (2021). Nonstationary Relationship between Sea Ice over Kara–Laptev Seas during August–September and Ural Blocking in the Following winter. *Int. J. Climatol.* 41 (Suppl. 1), E1608–E1622. doi:10.1002/joc.6794E1622

WMO Regional Climate Centres (2012). *Cold Spell in Europe and Asia in Late winter 2011/2012. Issued by WMO Regional Climate Centres: RA II (Asia): Tokyo Climate Centre, Japan Meteorological Agency (JMA). RA VI (Europe): Pilot Regional Climate Centre, node on Climate Monitoring (RCC-CM), Lead Centre Deutscher Wetterdienst (DWD), Germany*. WMO Regional Climate Centres, 20. available at: http://reliefweb.int/sites/reliefweb.int/files/resources/dwd_2012- _report.pdf.

Wu, B., Su, J., and Zhang, R. (2011). Effects of Autumn-winter Arctic Sea Ice on winter Siberian High. *Chin. Sci. Bull.* 56, 3220–3228. doi:10.1007/s11434-011-4696-4

Wu, B., Yang, K., and Francis, J. A. (2017). A Cold Event in Asia during January-February 2012 and its Possible Association with Arctic Sea Ice Loss. *J. Clim.* 30, 7971–7990. doi:10.1175/JCLI-D-16-0115.1

Xie, P., and Arkin, P. A. (1997). Global Precipitation: A 17-year Monthly Analysis Based on Gauge Observations, Satellite Estimates, and Numerical Model Outputs. *Bull. Amer. Meteorol. Soc.* 78, 2539–2558. doi:10.1175/1520-0477(1997)078<2539:GPAYMA>2.0.CO;2

Zhang, P., Wu, Y., Simpson, I. R., Smith, K. L., Zhang, X., De, B., et al. (2018). A Stratospheric Pathway Linking a Colder Siberia to Barents-Kara Sea Sea Ice Loss. *Sci. Adv.* 4, eaat6025. doi:10.1126/sciadv.aat6025

Zhang, R. N., and Screen, J. A. (2021). Diverse Eurasian winter Temperature Responses to Barents-Kara Sea Ice Anomalies of Different Magnitudes and Seasonality. *Geophys. Res. Lett.* 48, e2021GL092726. doi:10.1029/2021gl092726

Zhang, R., Zhang, R., and Dai, G. (2021). Intraseasonal Contributions of Arctic Sea-Ice Loss and Pacific Decadal Oscillation to a century Cold Event during Early 2020/21 winter. *Clim. Dyn.*. doi:10.1007/s00382-021-05931-5

Zhao, Y., Xiao, D., and Pai, H. (2019). Projection and Application for Future Climate in china by CMIP5 Climate Model. *Meteorol. Sci. Technol.* 47, 608–621. doi:10.1002/joc.5409

Zhou, L.-T., and Wu, R. (2010). Respective Impacts of the East Asian winter Monsoon and ENSO on winter Rainfall in China. *J. Geophys. Res.* 115, D02107. doi:10.1029/2009JD012502

Conflict of Interest: The authors declare that the research was conducted in the absence of any commercial or financial relationships that could be construed as a potential conflict of interest.

Publisher's Note: All claims expressed in this article are solely those of the authors and do not necessarily represent those of their affiliated organizations, or those of the publisher, the editors and the reviewers. Any product that may be evaluated in this article, or claim that may be made by its manufacturer, is not guaranteed or endorsed by the publisher.

frontiers in Earth Science

ORIGINAL RESEARCH
published: 21 September 2021
doi: 10.3389/feart.2021.742331

A Statistical Hydrological Model for Yangtze River Watershed Based on Stepwise Cluster Analysis

Feng Wang[1,2], *Guohe Huang*[1]*, *Yongping Li*[1], *Jinliang Xu*[3], *Guoqing Wang*[4], *Jianyun Zhang*[4], *Ruixin Duan*[1] *and Jiayan Ren*[1]

[1]State Key Joint Laboratory of Environmental Simulation and Pollution Control, China-Canada Center for Energy, Environment and Ecology Research, UR-BNU, School of Environment, Beijing Normal University, Beijing, China, [2]Sino-Canada Resources and Environmental Research Academy, North China Electric Power University, Beijing, China, [3]Key Laboratory of Power Station Energy Transfer Conversion and System, North China Electric Power University, Ministry of Education, Beijing, China, [4]State Key Laboratory of Hydrology-Water Resources and Hydraulic Engineering, Nanjing Hydraulic Research Institute, Nanjing, China

Streamflow prediction is one of the most important topics in operational hydrology. The responses of runoffs are different among watersheds due to the diversity of climatic conditions as well as watershed characteristics. In this study, a stepwise cluster analysis hydrological (SCAH) model is developed to reveal the nonlinear and dynamic rainfall-runoff relationship. The proposed approach is applied to predict the runoffs with regional climatic conditions in Yichang station, Hankou station, and Datong station over the Yangtze River Watershed, China. The main conclusions are: 1) the performances of SCAH in both deterministic and probabilistic modeling are notable.; 2) the SCAH is insensitive to the parameter *p* in SCAH with robust cluster-tree structure; 3) in terms of the case study in the Yangtze River watershed, it can be inferred that the water resource in the lower reaches of the Yangtze River is seriously affected by incoming water from the upper reaches according to the strong correlations. This study has indicated that the developed statistical hydrological model SCAH approach can characterize such hydrological processes complicated with nonlinear and dynamic relationships, and provide satisfactory predictions. Flexible data requirements, quick calibration, and reliable performances make SCAH an appealing tool in revealing rainfall-runoff relationships.

Keywords: stepwise cluster analysis hydrological model, streamflow prediction, statistical hydrological, yangtze river watershed, climate change

OPEN ACCESS

Edited by:
Shan Zhao,
Shandong University, China

Reviewed by:
Mei Xuefei,
East China Normal University, China
Huaiwei Sun,
Huazhong University of Science and Technology, China

***Correspondence:**
Guohe Huang
huangg@uregina.ca

Specialty section:
This article was submitted to Hydrosphere, a section of the journal Frontiers in Earth Science

Received: *16 July 2021*
Accepted: *06 September 2021*
Published: *21 September 2021*

Citation:
Wang F, Huang G, Li Y, Xu J, Wang G, Zhang J, Duan R and Ren J (2021) A Statistical Hydrological Model for Yangtze River Watershed Based on Stepwise Cluster Analysis. Front. Earth Sci. 9:742331. doi: 10.3389/feart.2021.742331

HIGHLIGHTS:

- A stepwise cluster analysis hydrological model (SCAH) was proposed.
- The proposed SCAH is applied in three stations runoff simulation in the Yangtze River watershed.
- Both deterministic and probabilistic predictions are generated in the proposed SCAH.

INTRODUCTION

Streamflow prediction is one of the most important topics in operational hydrology, which can provide valuable information for water resource allocation, hydropower generation, flood risk management, irrigation, and agricultural crop forecasting (Fan et al., 2015). A crucial task is to select

and develop an advanced forecasting model which can effectively model hydrological processes and provide accurate prediction (Liu et al., 2016). The task is complicated by the many complexities in hydrological systems such as extensive nonlinearities, temporal-spatial variations, interactions, and uncertainties (Solomatine and Ostfeld, 2008; Cheng et al., 2016). During the past decades, great effort has been applied to this issue and a series of hydrological models have been developed to improve hydrologic prediction (Xie et al., 2020; Wang et al., 2021c). These hydrological models primarily include process-based and data-driven models (Li et al., 2015). The process-based models represent the runoff generating mechanisms realistically based on the inherent mass and energy conservation laws in the water cycle system. The main drawback of such models is that the expression of physical processes is often oversimplified, and many uncertainties such as model structure (and/or parameter) uncertainties exist (Bhadra et al., 2009; Zhang et al., 2016). Another drawback is that the process-based models mainly rely on the parameterization process and cannot reflect the mapping between independent (i.e., explanatory, boundary input) and dependent (i.e., response, output) variables in the hydrologic system (Wang et al., 2021a). In comparison, the data-driven models are able to capture this mapping, which involves the analysis of boundary input and the corresponding response time series rather than the physical process (Solomatine and Ostfeld, 2008). Due to the flexible data requirements, quick calibration, and reliable performance, data-driven models have been proven to be effective for streamflow forecasting (Fan et al., 2016). Nonparametric statistical techniques mainly including statistical regression, artificial intelligence, and machine learning methods have been commonly used as practical tools to calculate surface runoff.

However, previous data-driven models still suffer from several difficulties in reflecting the inherently complicated relationships within the environmental process (Wang et al., 2021b). A number of statistic models such as multiple linear regression, autoregressive, and autoregressive integrated moving average cannot reflect nonlinear relationships between predictors (e.g., climatic factors) and responses (e.g., streamflow) (Solomatine and Ostfeld, 2008; Ordieres-Meré et al., 2020). Besides, it can hardly fit the observations very well with nonlinear relationships in the water cycle (Fan et al., 2020; Li et al., 2020). The artificial intelligence-based models may suffer from a few deficiencies such as getting trapped in local optimum, overfitting, subjectivity in the choice of model parameters, and the components of its complex structure (Wang et al., 2020). As for machine-learning models, such as random forest (Sun et al., 2016), the reliability and development of these models met many obstacles stemming from a lack of thorough understanding of the underlying processes (Gaume and Gosset, 2003; Solomatine and Ostfeld, 2008; Li et al., 2015). To solve the above problems, one potential approach is to extend innovative and advanced multivariate statistical methods to reflect the complicated environmental processes with nonlinear and dynamic characteristics (Li et al., 2015; Yu et al., 2020). Stepwise cluster analysis is an improved multivariate analysis tool, which can handle nonlinear and discrete relationships between predictors and predictands firstly introduced by (Huang, 1992). Therefore, as the extension of previous studies, the objective of this study is to develop a stepwise cluster analysis hydrological (SCAH) approach to reveal the nonlinear and dynamic rainfall-runoff relationship. Then the developed SCAH will be applied at Yichang station, Hankou station, and Datong station within the Yangtze River Watershed, China, to demonstrate the applicability of the proposed model.

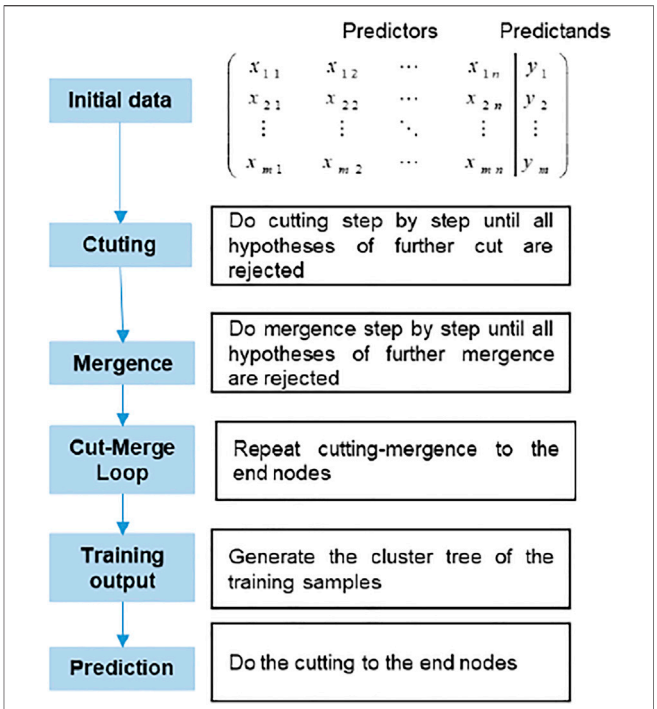

FIGURE 1 | The framework of SCAH.

FRAMEWORK OF STEPWISE CLUSTER ANALYSIS HYDROLOGICAL MODEL

In this study, the SCAH model framework was proposed and used for runoff prediction. The framework of this study is presented in **Figure 1**. Firstly, the correlations between streamflow and climatic conditions are analyzed to screen out potentially significant climatic variables. The runoffs with the selected climatic variables are simulated by the proposed SCAH model in which multiple dependent variables are taken into account. As a kind of nonparametric statistical method, stepwise cluster analysis was firstly proposed by (Huang, 1992). In stepwise cluster analysis, the sample sets of response variables are derived into new sets through cutting or merging actions based on given criteria, and cluster trees are built during the process (Duan et al., 2021). The structures of cluster trees reflect the inherent relationships between the explanatory and response variables. With the advantage of capturing discrete and nonlinear relationships between explanatory and response variables,

stepwise cluster analysis has received much attention for environmental issues such as air quality prediction (Huang, 1992), process control (Huang et al., 2006), climate projections (Wang et al., 2013), stream flow prediction (Cheng et al., 2016; Zhuang et al., 2016), groundwater simulation (Han et al., 2016), and ecosystem analysis and prediction (Sun et al., 2018). This previous researcher has indicated that the stepwise cluster analysis approach can characterize environmental processes with complicated nonlinear and dynamic relationships and provide satisfactory predictions.

According to the theory of multivariate analysis of variance, the sample sets of predictors and predictands are divided into new sets through a series of cutting and merging processes (Wang et al., 2013; Li et al., 2015). As shown in **Figure 1**, several main steps are included in SCAH: 1) Select predictors and predictands and prepare the training matrix; 2) Do cutting actions step by step until all hypotheses of further cuts are rejected; 3) Do merging actions until all hypotheses of further merges are rejected; 4) Repeat cutting-merging to the end nodes where hypotheses of further cutting are accepted; 5) generate the cluster tree of the training samples; 6) Do prediction according to the generated cluster tree.

According to (Huang, 1992), the cutting and merging criterion is an F test based on the theory of Wilks' likelihood ratio criterion. For example, assume a cluster $V_{m\times n}$, which contains m samples of n dimension predictors. The cluster $V_{m\times n}$ can be cut into two sub-clusters $V^1_{\alpha\times n}$ and $V^2_{\beta\times n}$, where $\alpha+\beta=m$. The value of Wilks' statistic Λ can be calculated as follows:

$$\Lambda=\frac{|W|}{|W+B|} \tag{1}$$

where W is the within-groups sums of squares and cross products matrix; B is the between-group sums of squares and cross products. $|W|$ and $|W+B|$ indicate the determinants of matrixes. The smaller the Λ value is, the larger the difference between the sub-clusters of $V^1_{\alpha\times n}$ and $V^2_{\beta\times n}$ is.

$$W=\sum_{i=1}^{p}\left(V^1_{\alpha\times n}-\overline{V}^1_{\alpha\times n}\right)^T\left(V^1_{\alpha\times n}-\overline{V}^1_{\alpha\times n}\right)+\sum_{i=1}^{q}\left(V^2_{\beta\times n}-\overline{V}^2_{\beta\times n}\right)^T\left(V^2_{\beta\times n}-\overline{V}^2_{\beta\times n}\right) \tag{2}$$

$$B=\frac{\alpha\beta}{\alpha+\beta}\left(\overline{V}^1_{\alpha\times n}-\overline{V}^2_{\beta\times n}\right)^T\left(\overline{V}^1_{\alpha\times n}-\overline{V}^2_{\beta\times n}\right) \tag{3}$$

$\overline{V}^1_{\alpha\times n}$ and $\overline{V}^1_{\beta\times n}$ are the sample means of sub-clusters $V^1_{\alpha\times n}$ and $V^2_{\beta\times n}$, respectively:

$$\overline{V}^1_{\alpha\times n}=\frac{1}{\alpha}\sum_{i=1}^{p}V^1_{\alpha\times n} \tag{4}$$

$$\overline{V}^2_{\beta\times n}=\frac{1}{\beta}\sum_{i=1}^{p}V^2_{\beta\times n} \tag{5}$$

The cutting point is optimal, if and only if the value of Λ is minimal (Huang, 1992). On the contrary, sub-clusters $V^1_{\alpha\times n}$ and $V^2_{\beta\times n}$ cannot be cut, if the Λ value is very large, but may be merged into a new cluster. By Rao's F approximation (Rao et al., 1973), we have the R-statistic as following:

$$R=\frac{1-\Lambda^{1/S}}{\Lambda^{1/S}}\frac{ZS-P(K-1)/2+1}{P(K-1)} \tag{6}$$

where K is the number of groups and P is the number of predictors. Z and S can be calculated as follows:

$$Z=m-1-(P+K)/2 \tag{7}$$

$$S=\frac{P^2\times(K-1)^2-4}{P^2+(K-1)^2-5} \tag{8}$$

Here, $K=2$ (two sub-clusters $V^1_{\alpha\times n}$ and$V^2_{\beta\times n}$) and the R-statistic will be an exact F-variate:

$$F(P,m-P-1)=\frac{1-\Lambda}{\Lambda}\times\frac{m-P-1}{P} \tag{9}$$

Therefore, the criteria for cutting and merging clusters becomes to conduct a number of F tests (Rao et al., 1973). For example, the F test could be used to identify whether sub-clusters $V^1_{\alpha\times n}$ and $V^2_{\beta\times n}$ are significantly different. Cluster $V_{p\times n}$ can be cut into two sub-clusters $V^1_{\alpha\times n}$ and $V^2_{\beta\times n}$ if $F(P,m-P-1)$ is larger than $F_{p-cutting}$. The p-cutting is the significance level of cutting, which can be set according to the demand. The default is 0.05. On the other hand, the F test could also be used to identify whether any two of the generated sub-clusters are significantly similar. For two clusters $V^i_{\alpha\times n}$ and $V^j_{\beta\times n}$ with samples of α' and β', if $F(P,\alpha'+\beta'-P-1)$ is smaller than $F_{p-merging}$, the two clusters can be merged into a new cluster. The p-merging is the significance level of merging, which can be set according to the demand. The default is 0.05. Repeat cutting-merging until no cluster can be further cut and no clusters can be further merged. After the cutting-merging loop, a cluster tree with a series of nodes (i.e., intermediate nodes and end nodes) is built for prediction. For a more detailed description of the SCA method, refer to the authors' previous work by (Huang, 1992; Huang et al., 2006; Cheng et al., 2016; Fan et al., 2016). The main advantage of SCAH is the capability of modeling variations of multiple dependent variables ys (e.g., runoffs over multiple catchments in this study) with independent variables xs. Beyond that, this method can identify dominant independent variables for ys, adapt to highly nonlinear xs-ys relationships due to non-functional assumptions, reveal the equifinality in xs-ys relationships, and reveal the interactions of xs in impacting ys.

Five statistical coefficients, including Nash–Sutcliffe efficiency (NSE) (Nash and Sutcliffe, 1970), Pearson correlation coefficient (COR), Mean Absolute Error (MAE), Root Mean Squared Error (RMSE), and Percent BIAS (PBIAS) (Gupta et al., 1999) are used to evaluate the performance of the SCAH model in the Yangtze River watershed. Let N be the total number of observations (or predictions); $Q_{obs,i}$ the observed value, $Q_{sim,i}$ the estimated value, $\overline{Q}_{obs}$ and $\overline{Q}_{sim}$ the mean of all observed and estimated, respectively. The NSE, COR, MAE, RMSE, and PBIAS are presented as:

$$\mathrm{NSE}=1-\frac{\sum_{i=1}^{N}\left(Q_{obs,i}-Q_{sim,i}\right)^2}{\sum_{i=1}^{N}\left(Q_{obs,i}-\overline{Q}_{obs}\right)^2} \tag{10}$$

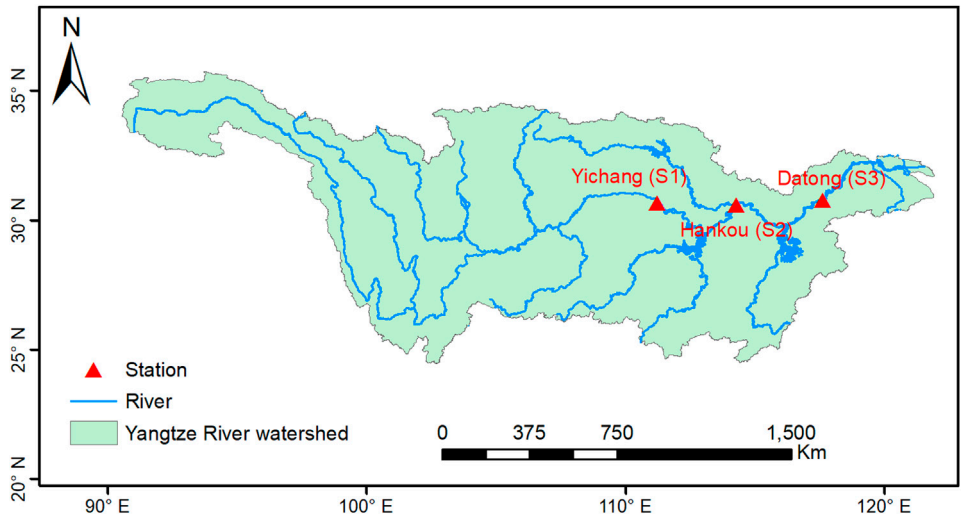

FIGURE 2 | The Yangtze River watershed.

$$COR = \frac{\sum_{i=1}^{N}(Q_{obs,i} - \overline{Q}_{obs})(Q_{sim,i} - \overline{Q}_{sim})}{\sqrt{\sum_{i=1}^{N}(Q_{obs,i} - \overline{Q}_{obs})^2}\sqrt{\sum_{i=1}^{N}(Q_{sim,i} - \overline{Q}_{sim})^2}} \quad (11)$$

$$MAE = \frac{1}{N}\sum_{i=1}^{N}|Q_{obs,i} - Q_{sim,i}| \quad (12)$$

$$RMSE = \sqrt{\frac{1}{N}\sum_{i=1}^{N}(Q_{obs,i} - Q_{sim,i})^2} \quad (13)$$

$$PBIAS = \frac{\sum_{i=1}^{N}(Q_{obs,i} - Q_{sim,i})}{\sum_{i=1}^{N}(Q_{obs,i})} \times 100 \quad (14)$$

Values of the NSE coefficient can range from negative infinity to 1. NSE coefficients greater than 0.75 are considered "good," whereas values between 0.75 and 0.5 are considered as "satisfactory" (Moriasi et al., 2007). The COR value is a measure of the linear correlation between the observed and simulated values. MAE and RMSE are used to describe average model-performance error (Willmott and Matsuura, 2005). PBIAS indicates whether the simulated value is larger or smaller compared to the corresponding observed value. Model underestimated the value with PBIAS larger than 0, and overestimated opposite.

To better evaluate the model performance under uncertainties, the relative error of the interval solution (REIS) of sample i are proposed by (Li et al., 2015):

$$REIS(\%) = \begin{cases} \frac{Q_{i,sim}^{max} - Q_{i,obs}}{Q_{i,obs}} * 100, & if \quad Q_{i,sim}^{max} < Q_{i,obs} \\ 0, & if \quad Q_{i,sim}^{min} < Q_{i,obs} < Q_{i,sim}^{max} \\ \frac{Q_{i,sim}^{min} - Q_{i,obs}}{Q_{i,obs}} * 100, & if \quad Q_{i,obs} < Q_{i,sim}^{min} \end{cases} \quad (15)$$

where $Q_{i,sim}^{min}$ and $Q_{i,sim}^{max}$ are the minimum and maximum simulated flow of the sample i in the corresponding end node, respectively.

Therefore the mean relative error of the interval solution (MREIS) can be defined as:

$$MREIS(\%) = \frac{1}{N}\sum_{i=1}^{N}|REIS(\%)| \quad (16)$$

The ratio of observations falling into the interval solution (RF) can be defined as

$$RF(\%) = \frac{1}{N}\sum_{i=1}^{N} nreis_i$$
$$nreis_i = \begin{cases} 1, & if \; Q_{i,sim}^{min} < Q_{i,obs} < Q_{i,sim}^{max} \\ 0, & otherwise \end{cases} \quad (17)$$

OVERVIEW OF THE STUDY AREA

A case study within the Yangtze River watershed (24°30′–35°45′N and 90°33′–122°25′E) in south China (**Figure 2**) is applied to demonstrate the applicability of the proposed model. As the third-longest river in the world and the longest in China, the Yangtze is 6,300 km long with a basin area of 1.8 million km^2 (Hayashi et al., 2004; Ma et al., 2016). The main section of the basin is located in a subtropical warm-wet zone heavily affected by both East and South Asian monsoon activities. The southern part of the basin is near to tropical climates and the northern part is close to the temperate zone. The annual mean temperature in the southern and northern parts are 19 and 15°C, respectively (Xie et al., 2020). Owing to great topographic variability, annual precipitation varies greatly in different sections of the Yangtze River with a range of 300–2,000 mm and appears to increase from northwest to southeast. Affected by summer southwest monsoon and southeast monsoon, the precipitation has noticeable seasonal

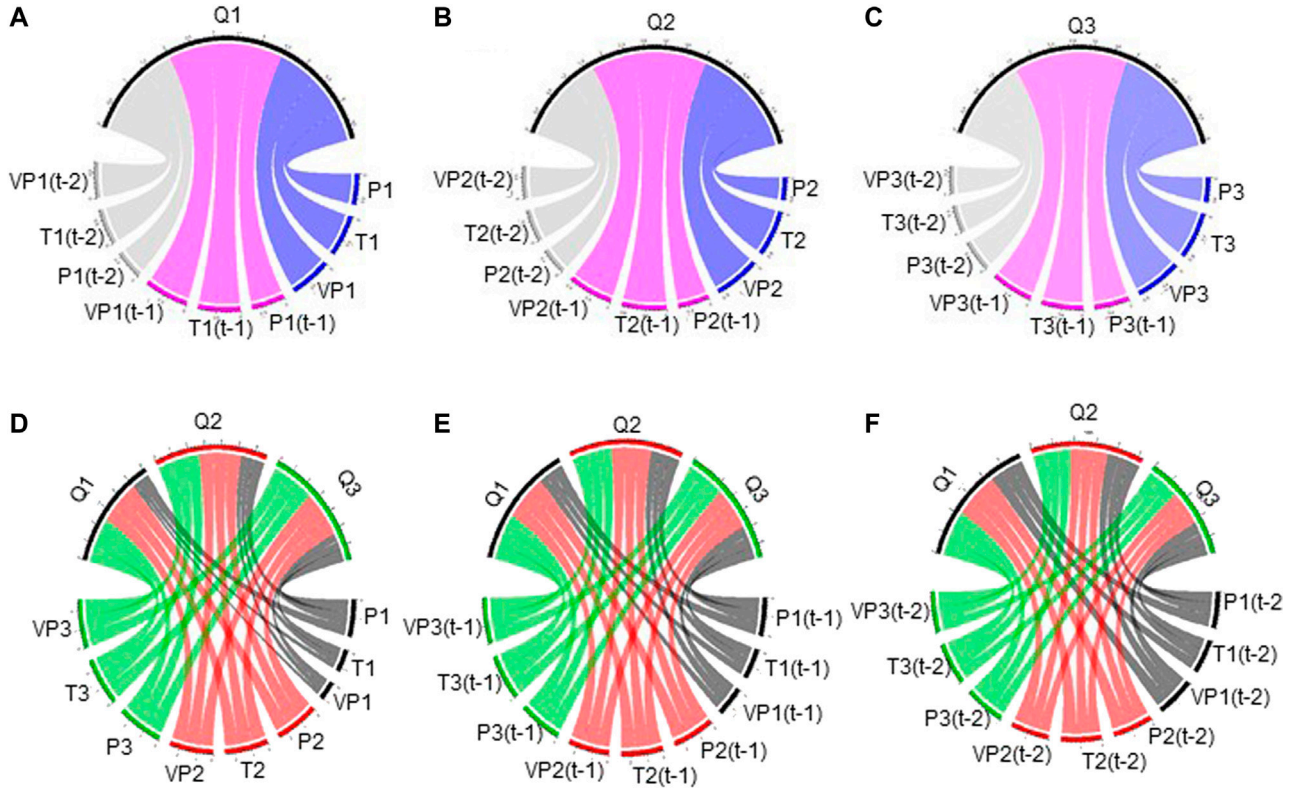

FIGURE 3 | The correlation between predictors and streamflow. streamflow.[Note: **(A)**, **(B)**, and **(C)** present the correlation between predictors in different month ahead and stream. **(D–F)** present the correlation between predictors and streams between different stations. Predictors are defined in **Table 2**].

and regional variations, with most of the precipitation reaching its peak from April to October (Zhang et al., 2019). It is reported that summer precipitation and rainstorm frequency have increased in the past few decades (Chaudhuri et al., 2020). By the 2080s, the annual mean precipitation is expected to increase in the range of 5.33–15.29% under different scenarios (Huang et al., 2011).

The Yangtze River spans nearly one-fifth of mainland China, traverses three economic zones in eastern, central, and western China, and crosses nineteen provinces of the country all told. As one of the most densely populated and economically developed areas in China, the Yangtze River Basin has experienced a booming economy over the last decade and constituted over 40% of gross domestic product (GDP) (Chen et al., 2017). In addition to urbanization, the Yangtze River Basin is a favorable location for agriculture, which accounts for 25% of the total cultivated land area in China (Kong et al., 2018). As the primary water source, the Yangtze River is supporting the ever-growing socio-economic development in the Yangtze River basin and northern China. Inevitably, rapid urbanization and global climatic change are accompanied by many social, economic, environmental, and resource issues. Many issues such as water resource allocation, urban flooding risk management, reservoir operation, soil erosion control, and environmental protection are associated with precise streamflow predictions. According to the Development and Planning Outline of the Yangtze River Economic Belt, issued by the National Development and Reform Commission (NDRC, 2016), the processes of urbanization and industrialization will continue to gain momentum in the next 2 decades. Therefore, precise streamflow prediction is essential in this region which helps practitioners and policymakers make more comprehensive management and targeted policy decision of water resources.

Three streamflow stations, namely Yichang station, Hankou station, and Datong station in the Yangtze River watershed are here studied, which represent the upper, middle, and lower reaches (Zhang et al., 2006). The changes of water level and streamflow of these three gauging stations represent the fundamental principles of the whole Yangtze River Catchment. Runoff data came from https://www.bafg.de/GRDC/EN/02_srvcs/21_tmsrs/stationMaps.html?nn =201566. Climatic data are obtained from the national meteorological stations closest to hydrologic stations. The time periods of all data series are dated from 1965 to 1984. The data has not been extended beyond 1990 in order to preserve the stationarity of the data, since rapid economic development and large-scale land uses have taken place in China since 1990.

RESULT ANALYSES

Correlation Analysis of Predictors

Previous reports have shown that the inclusion of additional antecedent meteorological variables, such as precipitation and

TABLE 1 | The correlation between predictors and streamflow.

Logogram	Climate variables	Q1	Q2	Q3
v1	P1	0.61	0.69	0.70
v2	T1	0.30	0.44	0.49
v3	VP1	0.21	0.37	0.46
v4	P1(t-1)	0.83	0.86	0.87
v5	T1(t-1)	0.83	0.87	0.87
v6	VP1(t-1)	0.84	0.88	0.87
v7	P1(t-2)	0.85	0.88	0.87
v8	T1(t-2)	0.84	0.87	0.87
v9	VP1(t-2)	0.85	0.88	0.87
v10	P2	0.69	0.71	0.69
v11	T2	0.48	0.59	0.64
v12	VP2	0.44	0.59	0.66
v13	P2(t-1)	0.88	0.85	0.80
v14	T2(t-1)	0.89	0.85	0.81
v15	VP2(t-1)	0.88	0.84	0.79
v16	P2(t-2)	0.90	0.85	0.79
v17	T2(t-2)	0.90	0.85	0.80
v18	VP2(t-2)	0.89	0.84	0.79
v19	P3	0.58	0.54	0.51
v20	T3	0.49	0.50	0.52
v21	VP3	0.61	0.58	0.59
v22	P3(t-1)	0.71	0.61	0.54
v23	T3(t-1)	0.72	0.62	0.55
v24	VP3(t-1)	0.69	0.58	0.51
v25	P3(t-2)	0.71	0.61	0.53
v26	T3(t-2)	0.72	0.62	0.54
v27	VP3(t-2)	0.70	0.60	0.52

TABLE 2 | Abbreviations and descriptions of predictors and predicated factors in SCAM.

Abbreviations	Descriptions
Q	Streamflow
P	Precipitation
T	mean Temperature
VP	Vapor Pressure
P(t-1)	Precipitation in 1 month ahead
T (t-1)	mean Temperature in 1 month ahead
VP (t-1)	Vapor Pressure in 1 month ahead
P(t-2)	Precipitation in 2 months ahead
T(t-2)	mean Temperature in 2 months ahead
VP(t-2)	Vapor Pressure in 2 months ahead

Note: Q1, Q2, and Q3 present the stream in Yichang station (S1), Hankou station (S2), and Datong station (S3) respectively in this research. The other predictors are equally prescriptive.

temperature, in the statistical hydrological model increased streamflow forecast skill (Fan et al., 2016; Slater and Villarini, 2017). Therefore, in this study, meteorological variables for the current month, 1 month ahead, and 2 months ahead are used as predictors. The correlation coefficients between monthly streamflow and potential predictors are provided in **Figure 3** and the corresponding values are supported in **Table 1**. From **Figures 3A–C**, it can be found that there are strong correlations (ranging from 0.51 to 0.91) between the antecedent meteorological variables and stream. For example, in station S1 (Yichang), temperature and vapor pressure 1 month ahead are the most correlated variables to monthly streamflow, with the highest correlation coefficient (i.e., 0.88 and 0.90). This result indicates a delay in the response of streamflow to meteorological variables. This may be related to the spatial variation of meteorological variables and the confluence time in the basin. The correlations between meteorological variables and streams between different stations are presented in **Figures 3D–F**, and . Strong correlations (ranging from 0.37 to 0.90) of monthly streamflow with the meteorological variables in surrounding stations are found. It is worth noting that there are strong correlations (greater than 0.86) between antecedent meteorological variables in Yichang station and the streamflow in Hankou and Datong stations. Similar results are thrown up between antecedent meteorological variables in Hankou station and the streamflow in Datong station. This may be related to the geographical location of the three stations. As shown in **Figure 1**, Yichang station, Hankou station, and Datong station are located in the upper, middle, and lower reaches of the Yangtze River respectively. Depending on the size and the topography of these basins, it takes days to months for the upstream precipitation to reach the downstream hydrological station through runoff generation and river confluence in the basin. Therefore, the strongest correlation is delayed in time. At the same time, according to the strong correlations, it can be inferred that the water resource in the lower reaches of the Yangtze River is seriously affected by incoming water from the upper reaches.

Deterministic Prediction

The SCAH model is calibrated with the data from 1956 to 1975 and validated with the data from 1976 to 1985 in the Yangtze River watershed, using the abovementioned predictors. In detail, SCAH is established for only one predicted variable (i.e., streamflow for a particular station), calibrated using each station flow, and applied for the stream prediction of that station. A default significance level of 0.05 is chosen in SCAH since a 95% confidence level is acceptable for statistical testing. The generated cluster trees obtained from SCAH are presented in **Figure 4**. According to the generated cluster trees, streamflow of Yichang station, Hankou station, and Datong station could be predicted through forcing the predictors into three cluster trees respectively.

Figure 5 shows the simulated and observed time series of monthly flow in three streamflow gauge stations during calibration and validation periods. The results show a good agreement of the observed and forecast hydrographs for SCAH, with slight under-prediction on some days (e.g., flood peak). The performance criteria of SCAH for the three stations are shown in **Table 3**. According to the five statistical coefficients, both the two schemes yielded acceptable simulation in all three stations. This result is consistent with previous studies (Fan et al., 2015; Li et al., 2015; Fan et al., 2016; Zhuang et al., 2016) which indicated that stepwise cluster analysis can provide reliable and efficient flow prediction. In the calibration period, measured and simulated monthly stream flows have a good match using the two schemes. The NSEs are larger than 0.94 and the CORs are larger than 0.96 with a slight difference between the three stations (**Table 3**). The difference between the two schemes is negligible in the calibration period. However, there are notable

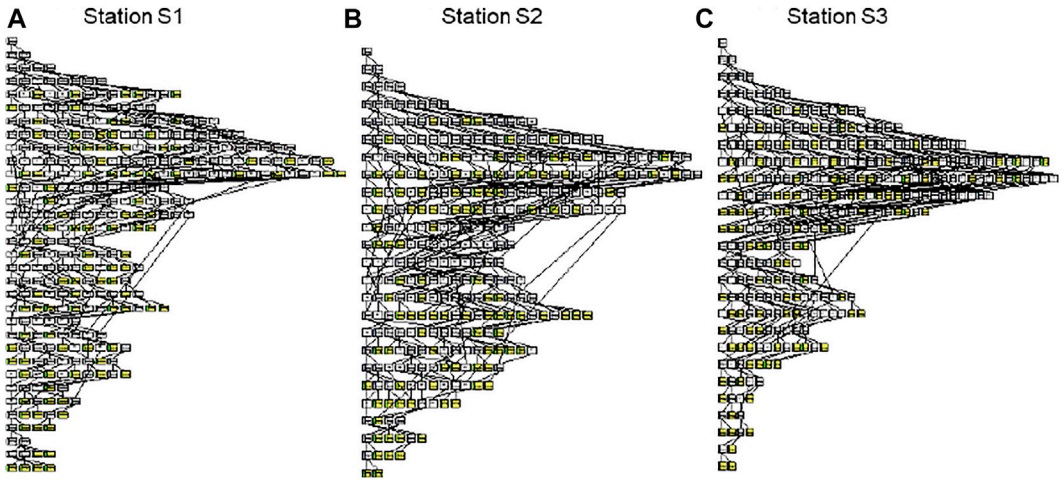

FIGURE 4 | SCAH model cluster tree for **(A)** Station S1, **(B)** Station S2, and **(C)** Station S3. (p = 0.05 and yellow boxes indicate end nodes; Stations S1, S2, and S3 represent Yichang station, Hankou station, and Datong station).

different performances observed between the three stations as well as the two schemes in the validation period. On the whole, the SCAH performs "good" (NSE >0.75) in three stations. In detail, using a single-site calibration approach, SCAH overestimates verification period runoff on S2 and S3 stations (**Figure 5**), with PBAIS <−3. The NSE ranges from 0.70 to 0.82, and COR varies from 0.84 to 0.90 across the three stations (**Table 3**). The lower average simulation error in SCAH can be observed through the lower MAE and RMSE values. Even both of the three stations which overestimated the streamflow during the validation period had negative PBIAS. The absolute PBIAS increased in the validation period, especially for station S3 (Datong station) where the absolute PBIAS increased from 0.14 to 4.78. The high NSE and COR, as well as the low MAE, RMSE, and PBAIS clearly indicate the superior hydrologic simulation of SCAH. This means that SCAH can reflect a comprehensive rainfall-runoff relationship, which considers the nonlinear and dynamic relationships between climate information and streamflow.

Table 4 presents the SCAH model performance (NSE, COR, MAE, RMSE, and PBIAS) for Yichang station, Hankou station, and Datong station under different p levels for calibration and validation periods. It can be found that model representation of SCAH is sensitive to the p level. In the calibration period, as the p level rises, the model performance of SCAH tends to increase with increased NSE and COR values and decreased MAE and RMSE values; while SCAH has the best model performance when the p level equals 0.01 in the validation period. In detail, when $p = 0.01$, NSE and MAE values in station S1 are 0.90 and 1.61 in calibration and 0.83 and 2.18 invalidation respectively. When $p = 0.10$, the corresponding values are 0.99 and 0.28 in calibration and 0.80 and 2.47 in the validation respectively. This is because the higher p level means lower threshold values for cutting processes, leads to more cut actions, and corresponds to more leaf nodes (as shown in **Table 4**) and less variation in each leaf node, resulting in fewer deviations between predictions and observations in the calibration period. While in the validation period, the over-segmentation of leaf nodes did not lead to more accurate prediction results. In contrast, the deviation predictions and observations actually increased. Results also show that the sensitivity of different statistical indicators to p level is different, and PBIAS is the most sensitive indicator. COR and RMSE share similar trends with NSE and MAE, respectively. Therefore, the SCAH is suggested for monthly runoff prediction with a robust structural tree and better validation performance in terms of the five statistical coefficients with the three p levels evaluated in this study.

Probabilistic Predictions

In the aforementioned study, the future deterministic prediction of streamflow was estimated using the mean value of the samples in the corresponding end node of the derived cluster tree. In fact, the proposed SCAH approach can also generate more results such as interval forecasting results (Fan et al., 2015; Li et al., 2015; Fan et al., 2016) using the maximum and minimum flow values of the end node, which can reflect uncertainties. The comparison of the forecasted intervals obtained through SCAH and observed monthly flow are presented in **Figure 6**. Through **Figure 6**, it can be seen that the forecasted intervals of SCAH can catch the fluctuations of actual monthly flow during the calibration period. Nearly all the observations are covered by the forecasting intervals. Moreover, the predicted intervals of SCAH are relatively large, especially for some peaks. During the validation period (**Figures 6D–F**), the forecasted intervals can generally cover the main part of observations in this period, except for some underestimates during high streamflow periods. This is because the prediction was conducted using a twenty-year training tree, which might not cover all the possible precipitation-runoff relationships, especially for the stream peak periods. Comparatively speaking, more observations are covered by the forecasting intervals obtained by SCAH with wider forecasted intervals. Generally, the results show an overall good agreement between observed data and predicted intervals.

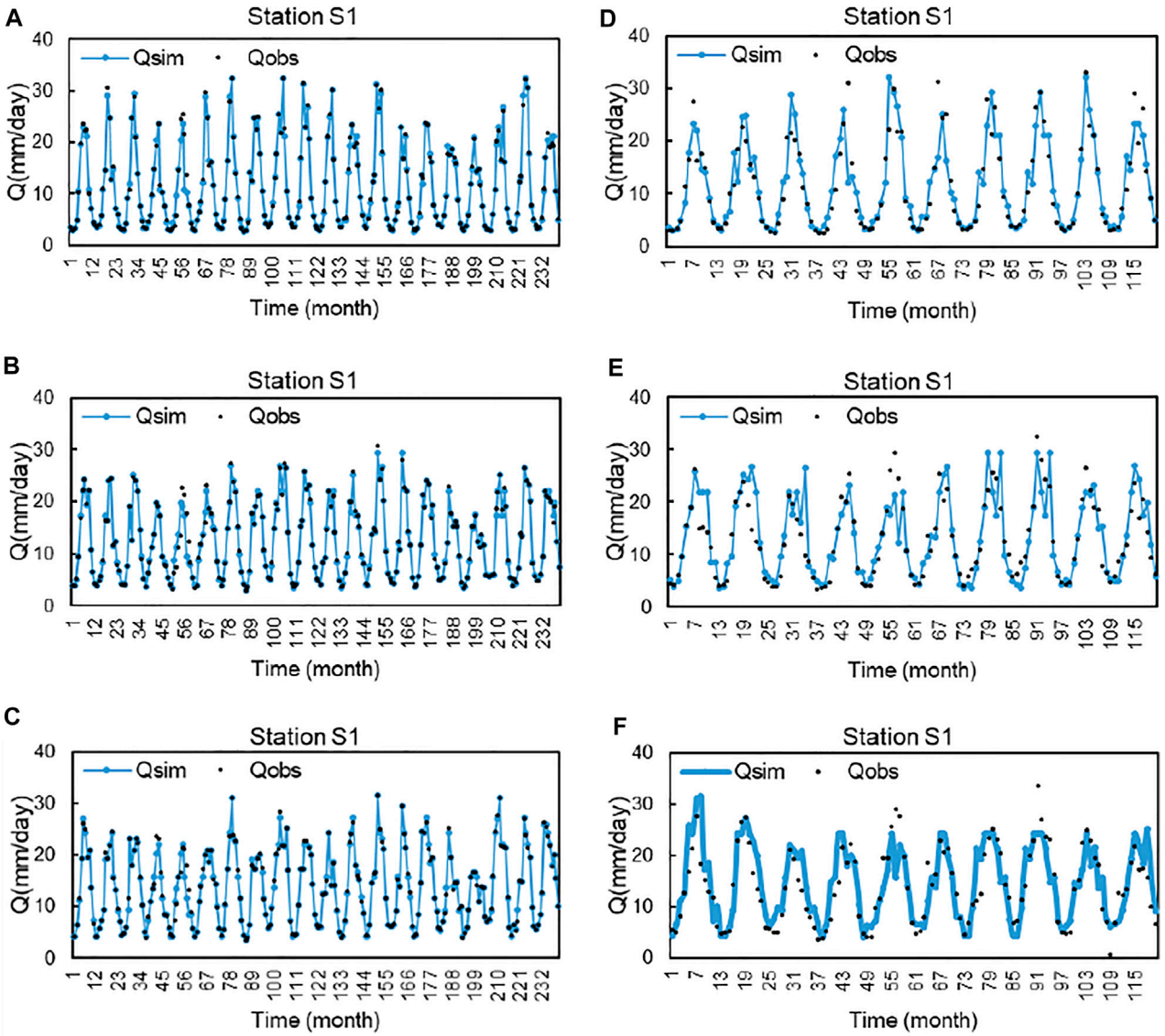

FIGURE 5 | Comparison of streamflow simulated by SCAH (the blue lines) with measurement values (the black circle) in the Yangtze River watershed. (Note: the first column presents the calibration period and the second column presents the validation period. Station S1, S2, and S3 represent Yichang station, Hankou station, and Datong station).

TABLE 3 | Model performance of SCAH in Yangtze River watershed. (Note: Stations S1, S2, and S3 represent Yichang station, Hankou station, and Datong station).

Station		S1	S2	S3
Calibration period	NSE	0.99	0.98	0.99
	COR	0.99	0.99	0.99
	MAE	0.28	0.27	0.29
	RMSE	0.84	0.89	0.81
	PBIAS	0.46	0.16	0.14
Validation period	NSE	0.80	0.74	0.70
	COR	0.90	0.88	0.85
	MAE	2.48	2.66	2.91
	RMSE	3.85	3.77	4.03
	PBIAS	−2.97	−2.16	−4.78

The performance of SCAH (REIS, MREIS, and RF) for the calibration and validation periods using two calibration strategies are presented in **Figure 7** and **Figure 8**. In the calibration period, the proportions of samples with absolute REIS smaller than 5% in thethree stations are 95.42, 96.25, and 97.92%, respectively for SCAH in Yichang station, Hankou station, and Datong station. As presented in **Figure 8**, the MREIS in the three stations are 1.15, 1.09, and 0.70%, respectively for SCAH during the calibration period. Moreover, among the 240 samples used for calibration, there are more than 226 samples where the observation value falls into its corresponding stream-flow interval estimated by the two calibration strategy, accounting for more than 94% of the total samples. On the whole, SCAH shows an insignificant performance in the calibration period. However, in the

TABLE 4 | Model performance of SCAH under different p levels. (Note: S1, S2, and S3 represent Yichang station, Hankou station, and Datong station).

Station		S1			S2			S3		
		$p = 0.01$	$p = 0.05$	$p = 0.10$	$p = 0.01$	$p = 0.05$	$p = 0.10$	$p = 0.01$	$p = 0.05$	$p = 0.10$
calibration	NSE	0.90	0.96	0.99	0.92	0.97	0.98	0.98	0.97	0.99
	COR	0.95	0.98	0.99	0.96	0.98	0.99	0.99	0.99	0.99
	MAE	1.61	0.89	0.28	1.38	0.66	0.27	0.27	0.64	0.29
	RMSE	2.66	1.60	0.84	2.00	1.32	0.89	0.89	1.18	0.81
	PBIAS	0.22	0.30	0.46	0.08	0.85	0.16	0.16	0.13	0.14
validation	NSE	0.83	0.80	0.80	0.79	0.70	0.74	0.74	0.62	0.70
	COR	0.91	0.89	0.90	0.89	0.86	0.88	0.88	0.85	0.85
	MAE	2.18	2.53	2.48	2.39	2.84	2.66	2.66	3.36	2.91
	RMSE	3.50	3.83	3.85	3.42	4.02	3.77	3.77	4.49	4.03
	PBIAS	−0.90	−0.69	−2.97	−0.01	−3.32	−2.16	−2.16	−5.65	−4.78

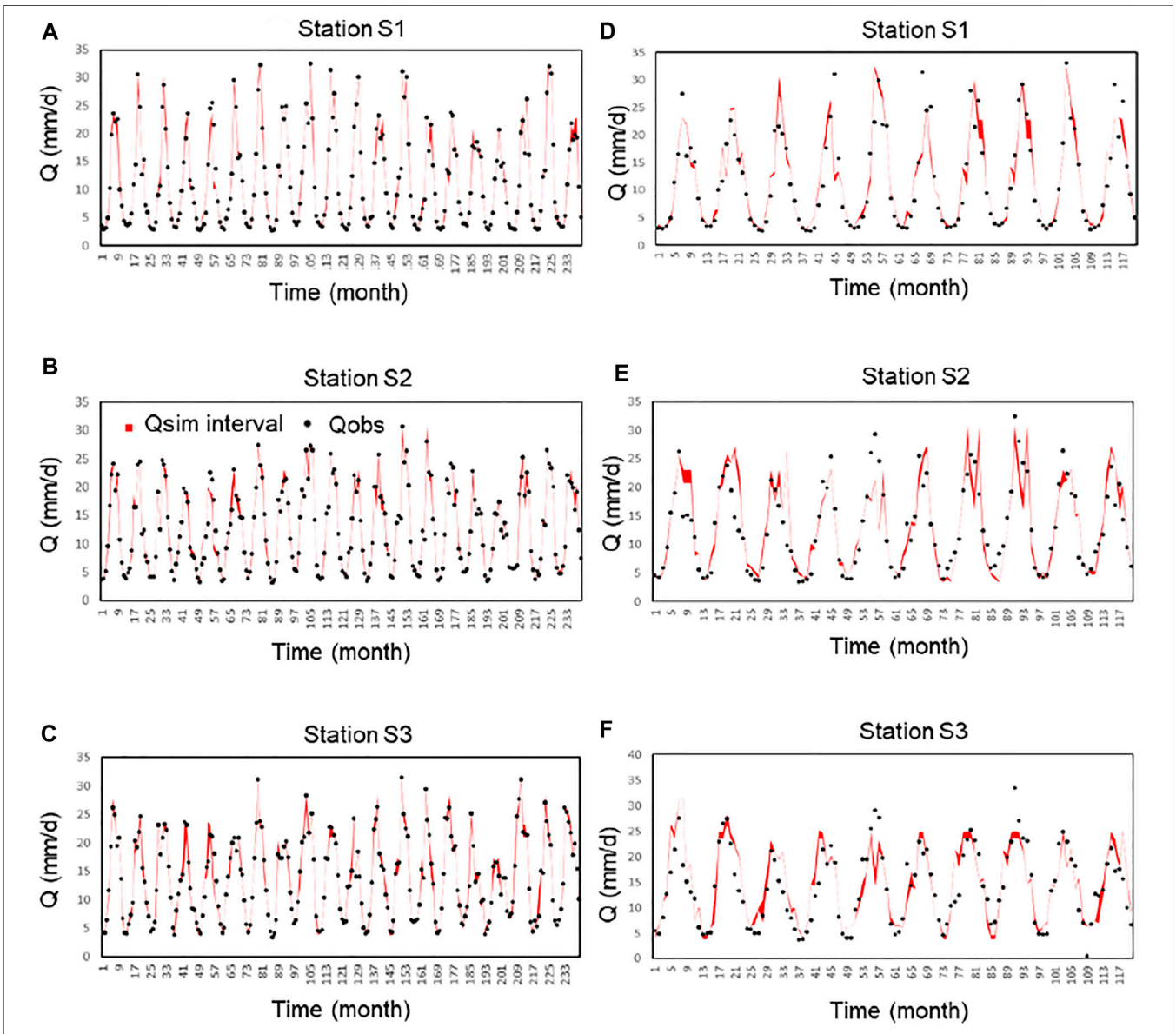

FIGURE 6 | Comparison of forecasted intervals versus observed monthly flow using SCAH (the red areas) with measurement values (the black circle) in the Yangtze River watershed. (Note: the first column presents the calibration period and the second column presents the validation period. Station S1, S2, and S3 represent Yichang station, Hankou station, and Datong station).

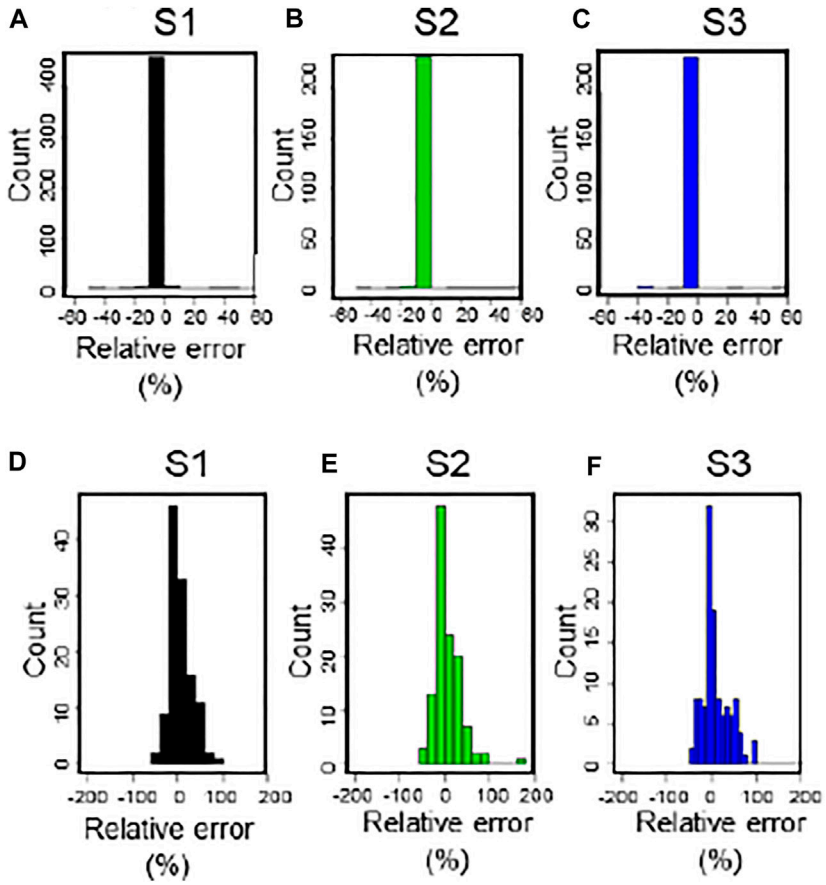

FIGURE 7 | Histograms of REIS for the calibration period [i.e., **(A–C)**] and validation period [i.e., **(D–F)**]. (Note: S1, S2, and S3 represent Yichang station, Hankou station, and Datong station).

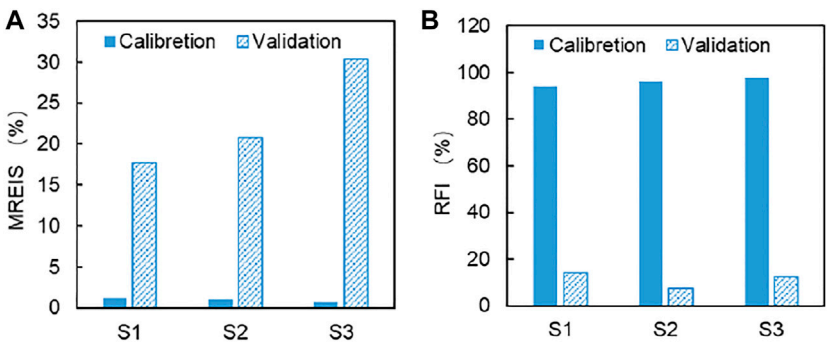

FIGURE 8 | The performance (MREIS and RF) of SCAH for the calibration and validation periods. (Note: S1, S2, and S3 represent Yichang station, Hankou station, and Datong station).

validation period, the proportions of samples with the absolute REIS smaller than 5% in Yichang station, Hankou station, and Datong station are 26.67, 20.83, and 28.33%, respectively. The MREIS in these three stations is 10.24, 11.73, and 21.69%, respectively. Moreover, SCAH can improve the ratio of observations falling into the interval solution. The RFs in the three stations are only 14.2, 7.50, and 12.5%, respectively for the SCAH in the three stations. The above results are sufficient to illustrate the advantages of SCAH to predict streamflow probability.

CONCLUSION

Streamflow prediction is one of the most important topics in operational hydrology. The responses of runoffs are different among watersheds due to the diversity of climatic conditions as well as watershed characteristics. In this study, to characterize the hydrological process complicated with nonlinear and dynamic relationships, SCAH was developed and applied to predict the runoffs with regional climatic conditions over the Yangtze River watershed, China. The main conclusions are specified as follows: First, the performances of SCAH in both deterministic and probabilistic modeling are notable. Flexible data requirements, quick calibration, and reliable performances make SCAH an appealing tool in revealing rainfall-runoff relationships. Second, the SCAH is insensitive to p levels in monthly runoff prediction with a robust structural tree and good validation performance in terms of the five statistical coefficients evaluated in this study. Third, in terms of the case study of the Yangtze River watershed, it can be inferred that the water resources in the lower reaches of the Yangtze River are seriously affected by incoming water from the upper reaches according to the strong correlations.

The responses of runoffs may be different among watersheds due to the diversity of climatic conditions as well as watershed characteristics. This study has indicated that the developed SCAH approach can characterize such hydrological processes with complicated nonlinear and dynamic relationships and provide satisfactory predictions. This study provides a statistical hydrological model to simulate streamflow considering the nonlinear and dynamic relationships. On the other hand, a series of extensions, improvements, or applications can be conducted in future studies based on this study. For instance, considering multiple response variables may reflect the complex interaction and nonlinear relationship between climatic variables and streamflow in the environmental process. Although the proposed model has been applied to three watersheds in the Yangtze River watershed, including upper, middle, and lower reaches, results presented in this paper may be updated as more datasets (cases) become available and included. Our analysis can be strengthened by focusing on more catchments where more data are available. An obvious future step will also be the inclusion of the global catchments, rather than just in China where the available hydrologic data are very limited owing to data licensing issues.

DATA AVAILABILITY STATEMENT

The original contributions presented in the study are included in the article/Supplementary Material, further inquiries can be directed to the corresponding author.

AUTHOR CONTRIBUTIONS

GH: Conceptualization, supervision; YL: investigation; JX: review, revision, supervision; GW: funding acquisition; JZ: project administration; RD: review and editing; JR: visualization; All authors have read and agreed to the published version of the manuscript.

FUNDING

This research was supported by the National Key Research and Development Plan (2016YFA0601502) and the Natural Sciences Foundation (U2040212). All data used in this paper are available from https://www.bafg.de/GRDC/EN/02_srvcs/21_tmsrs/stationMaps.html?nn=201566 and http://data.cma.cn/. All computations are conducted in R and the related codes are available from the authors upon request.

REFERENCES

Bhadra, A., Bandyopadhyay, A., Singh, R., and Raghuwanshi, N. S. (2009). Rainfall-Runoff Modeling: Comparison of Two Approaches with Different Data Requirements. *Water Resour. Manage.* 24 (1), 37–62. doi:10.1007/s11269-009-9436-z

Chaudhuri, S., Roy, M., Roy, M., and Jain, A. (2020). Appraisal of WaSH (Water-Sanitation-Hygiene) Infrastructure Using a Composite Index, Spatial Algorithms and Sociodemographic Correlates in Rural India. *J. Env Inform.* 35 (1). doi:10.3808/jei.201800398

Chen, Y., Zhang, S., Huang, D., Li, B.-L., Liu, J., Liu, W., et al. (2017). The Development of China's Yangtze River Economic Belt: How to Make it in a green Way?. *Sci. Bull.* 62 (9), 648–651. doi:10.1016/j.scib.2017.04.009

Cheng, G., Dong, C., Huang, G., Baetz, B. W., and Han, J. (2016). Discrete Principal-Monotonicity Inference for Hydro-System Analysis under Irregular Nonlinearities, Data Uncertainties, and Multivariate Dependencies. Part I: Methodology Development. *Hydrol. Process.* 30 (23), 4255–4272. doi:10.1002/hyp.10909

D. N. Moriasi, D. N., J. G. Arnold, J. G., M. W. Van Liew, M. W., R. L. Bingner, R. L., R. D. Harmel, R. D., and T. L. Veith, T. L. (2007). Model Evaluation Guidelines for Systematic Quantification of Accuracy in Watershed Simulations. *Trans. ASABE* 50 (3), 885–900. doi:10.13031/2013.23153

Duan, R., Huang, G., Li, Y., Zhou, X., Ren, J., and Tian, C. (2021). Stepwise Clustering Future Meteorological Drought Projection and Multi-Level Factorial Analysis under Climate Change: A Case Study of the Pearl River Basin, China. *Environ. Res.* 196, 110368. doi:10.1016/j.envres.2020.110368

Fan, Y., Huang, K., Huang, G., Li, Y., and Wang, F. (2020). An Uncertainty Partition Approach for Inferring Interactive Hydrologic Risks. *Hydrol. Earth Syst. Sci.* 24 (9), 4601–4624. doi:10.5194/hess-24-4601-2020

Fan, Y. R., Huang, G. H., Li, Y. P., Wang, X. Q., and Li, Z. (2016). Probabilistic Prediction for Monthly Streamflow through Coupling Stepwise Cluster Analysis and Quantile Regression Methods. *Water Resour. Manage.* 30 (14), 5313–5331. doi:10.1007/s11269-016-1489-1

Fan, Y. R., Huang, W., Huang, G. H., Li, Z., Li, Y. P., Wang, X. Q., et al. (2015). A Stepwise-Cluster Forecasting Approach for Monthly Streamflows Based on Climate Teleconnections. *Stoch Environ. Res. Risk Assess.* 29 (6), 1557–1569. doi:10.1007/s00477-015-1048-y

Gaume, E., and Gosset, R. (2003). Over-parameterisation, a Major Obstacle to the Use of Artificial Neural Networks in Hydrology?. *Hydrol. Earth Syst. Sci.* 7 (5), 693–706. doi:10.5194/hess-7-693-2003

Gupta, H. V., Sorooshian, S., and Yapo, P. O. (1999). Status of Automatic Calibration for Hydrologic Models: Comparison with Multilevel Expert Calibration. *J. Hydrol. Eng.* 4 (2), 135–143. doi:10.1061/(ASCE)1084-0699

Han, J.-C., Huang, Y., Li, Z., Zhao, C., Cheng, G., and Huang, P. (2016). Groundwater Level Prediction Using a SOM-Aided Stepwise Cluster

Inference Model. *J. Environ. Manag.* 182, 308–321. doi:10.1016/j.jenvman.2016.07.069

Hayashi, S., Murakami, S., Watanabe, M., and Bao-Hua, X. (2004). HSPF Simulation of Runoff and Sediment Loads in the Upper Changjiang River Basin, China. *J. Environ. Eng.* 130 (7), 801–815. doi:10.1061/(ASCE)0733-9372

Huang, G. (1992). A Stepwise Cluster Analysis Method for Predicting Air Quality in an Urban Environment. *Atmos. Environ. B. Urban Atmosphere* 26 (3), 349–357. doi:10.1016/0957-1272(92)90010-P

Huang, G. H., Huang, Y. F., Wang, G. Q., and Xiao, H. N. (2006). Development of a Forecasting System for Supporting Remediation Design and Process Control Based on NAPL-Biodegradation Simulation and Stepwise-Cluster Analysis. *Water Resour. Res.* 42 (6). doi:10.1029/2005WR004006

Huang, J., Zhang, J., Zhang, Z., Xu, C., Wang, B., and Yao, J. (2011). Estimation of Future Precipitation Change in the Yangtze River basin by Using Statistical Downscaling Method. *Stoch Environ. Res. Risk Assess.* 25 (6), 781–792. doi:10.1007/s00477-010-0441-9

Kong, L., Zheng, H., Rao, E., Xiao, Y., Ouyang, Z., and Li, C. (2018). Evaluating Indirect and Direct Effects of Eco-Restoration Policy on Soil Conservation Service in Yangtze River Basin. *Sci. total Environ.* 631-632, 887–894. doi:10.1016/j.scitotenv.2018.03.117

Li, Z., Huang, G., Han, J., Wang, X., Fan, Y., Cheng, G., et al. (2015). Development of a Stepwise-Clustered Hydrological Inference Model. *J. Hydrol. Eng.* 20 (10), 04015008. doi:10.1061/(ASCE)HE.1943-5584.0001165

Li, Z., Li, J. J., and Shi, X. P. (2020). A Two-Stage Multisite and Multivariate Weather Generator. *J. Environ. Inform.* 35 (2), 148–159. doi:10.3808/jei.201900424

Liu, Y., Guo, J., Sun, H., Zhang, W., Wang, Y., and Zhou, J. (2016). Multiobjective Optimal Algorithm for Automatic Calibration of Daily Streamflow Forecasting Model. *Math. Probl. Eng.*. doi:10.1155/2016/8215308

Ma, M., Ren, L., Singh, V. P., Yuan, F., Chen, L., Yang, X., et al. (2016). Hydrologic Model-Based Palmer Indices for Drought Characterization in the Yellow River basin, China. *Stoch Environ. Res. Risk Assess.* 30 (5), 1401–1420. doi:10.1007/s00477-015-1136-z

Nash, J. E., and Sutcliffe, J. V. (1970). River Flow Forecasting through Conceptual Models Part I - A Discussion of Principles. *J. Hydrol.* 10 (3), 282–290. doi:10.1016/0022-1694(70)90255-6

Ordieres-Meré, J., Ouarzazi, J., El Johra, B., and Gong, B. (2020). Predicting Ground Level Ozone in Marrakesh by Machine-Learning Techniques. *J. Environ. Inform.* 36 (2), 93–106. doi:10.3808/jei.202000437

Rao, C. R., Rao, C. R., Statistiker, M., Rao, C. R., and Rao, C. R. (1973). *Linear Statistical Inference and its Applications, 2.* New York: Wiley. doi:10.1112/jlms/s1-42.1.382b

Slater, L., and Villarini, G. (2017). Evaluating the Drivers of Seasonal Streamflow in the U.S. Midwest. *Water* 9 (9), 695. doi:10.3390/w9090695

Solomatine, D. P., and Ostfeld, A. (2008). Data-driven Modelling: Some Past Experiences and New Approaches. *J. hydroinformatics* 10 (1), 3–22. doi:10.2166/hydro.2008.015

Sun, H., Gui, D., Yan, B., Liu, Y., Liao, W., Zhu, Y., et al. (2016). Assessing the Potential of Random forest Method for Estimating Solar Radiation Using Air Pollution index. *Energ. Convers. Manage.* 119, 121–129. doi:10.1016/j.enconman.2016.04.051

Sun, J., Li, Y. P., Gao, P. P., Suo, C., and Xia, B. C. (2018). Analyzing Urban Ecosystem Variation in the City of Dongguan: A Stepwise Cluster Modeling Approach. *Environ. Res.* 166, 276–289. doi:10.1016/j.envres.2018.06.009

Wang, F., Huang, G., Cheng, G., and Li, Y. (2021b). Multi-level Factorial Analysis for Ensemble Data-Driven Hydrological Prediction. *Adv. Water Resour.* 153, 103948. doi:10.1016/j.advwatres.2021.103948

Wang, F., Huang, G. H., Cheng, G. H., and Li, Y. P. (2021a). Impacts of Climate Variations on Non-stationarity of Streamflow over Canada. *Environ. Res.* 197, 111118. doi:10.1016/j.envres.2021.111118

Wang, F., Huang, G. H., Fan, Y., and Li, Y. P. (2021c). Development of Clustered Polynomial Chaos Expansion Model for Stochastic Hydrological Prediction. *J. Hydrol.* 595, 126022. doi:10.1016/j.jhydrol.2021.126022

Wang, F., Huang, G. H., Fan, Y., and Li, Y. P. (2020). Robust Subsampling ANOVA Methods for Sensitivity Analysis of Water Resource and Environmental Models. *Water Resour. Manage.* 34 (10), 3199–3217. doi:10.1007/s11269-020-02608-2

Wang, X., Huang, G., Lin, Q., Nie, X., Cheng, G., Fan, Y., et al. (2013). A Stepwise Cluster Analysis Approach for Downscaled Climate Projection - A Canadian Case Study. *Environ. Model. Softw.* 49, 141–151. doi:10.1016/j.envsoft.2013.08.006

Willmott, C., and Matsuura, K. (2005). Advantages of the Mean Absolute Error (MAE) over the Root Mean Square Error (RMSE) in Assessing Average Model Performance. *Clim. Res.* 30 (1), 79–82. doi:10.3354/cr030079

Xie, W. P., Yang, J., Yang, J. S., Yao, R. J., and Wang, X. P. (2020). Impact Study of Impoundment of the Three Gorges Reservoir on Salt-Water Dynamics and Soil Salinity in the Yangtze River Estuary. *J. Environ. Inform.* 36 (1). doi:10.3808/jei.202000432

Yu, B. Y., Wu, P., Wu, P., Sui, J., Ni, J., and Whitcombe, T. (2020). Variation of Runoff and Sediment Transport in the Huai River - A Case Study. *J. Environ. Inform.* 35 (2). doi:10.3808/jei.202000429

Zhang, J., Li, Y., Huang, G., Chen, X., and Bao, A. (2016). Assessment of Parameter Uncertainty in Hydrological Model Using a Markov-Chain-Monte-Carlo-Based Multilevel-Factorial-Analysis Method. *J. Hydrol.* 538, 471–486. doi:10.1016/j.jhydrol.2016.04.044

Zhang, Q., Liu, C., Xu, C.-y., Xu, Y., and Jiang, T. (2006). Observed Trends of Annual Maximum Water Level and Streamflow during Past 130 Years in the Yangtze River basin, China. *J. Hydrol.* 324 (1-4), 255–265. doi:10.1016/j.jhydrol.2005.09.023

Zhang, Y., Sun, A., Sun, H., Gui, D., Xue, J., Liao, W., et al. (2019). Error Adjustment of TMPA Satellite Precipitation Estimates and Assessment of Their Hydrological Utility in the Middle and Upper Yangtze River Basin, China. *Atmos. Res.* 216, 52–64. doi:10.1016/j.atmosres.2018.09.021

Zhuang, X. W., Li, Y. P., Huang, G. H., and Wang, X. Q. (2016). A Hybrid Factorial Stepwise-Cluster Analysis Method for Streamflow Simulation - a Case Study in Northwestern China. *Hydrological Sci. J.* 61 (15), 2775–2788. doi:10.1080/02626667.2015.1125482

Conflict of Interest: The authors declare that the research was conducted in the absence of any commercial or financial relationships that could be construed as a potential conflict of interest.

Publisher's Note: All claims expressed in this article are solely those of the authors and do not necessarily represent those of their affiliated organizations, or those of the publisher, the editors and the reviewers. Any product that may be evaluated in this article, or claim that may be made by its manufacturer, is not guaranteed or endorsed by the publisher.

frontiers in Earth Science

ORIGINAL RESEARCH
published: 27 September 2021
doi: 10.3389/feart.2021.742840

Long-Term Maximum and Minimum Temperature Projections Over Metro Vancouver, Canada

Chuyin Tian[1], Guohe Huang[1,2], Yanli Liu[3], Denghua Yan[4], Feng Wang[2] and Ruixin Duan[2]*

[1]Faculty of Engineering and Applied Science, University of Regina, Regina, SK, Canada, [2]State Key Joint Laboratory of Environmental Simulation and Pollution Control, China-Canada Center for Energy, Environment and Ecology Research, School of Environment, UR-BNU, Beijing Normal University, Beijing, China, [3]State Key Laboratory of Hydrology—Water Resources and Hydraulic Engineering, Nanjing Hydraulic Research Institute, Nanjing, China, [4]China Institute of Water Resources and Hydropower Research, Beijing, China

Evident climate change has been observed and projected in observation records and General Circulation Models (GCMs), respectively. This change is expected to reshape current seasonal variability; the degree varies between regions. High-resolution climate projections are thereby necessary to support further regional impact assessment. In this study, a gated recurrent unit-based recurrent neural network statistical downscaling model is developed to project future temperature change (both daily maximum temperature and minimum temperature) over Metro Vancouver, Canada. Three indexes (i.e., coefficient of determinant, root mean square error, and correlation coefficient) are estimated for model validation, indicating the developed model's competitive ability to simulate the regional climatology of Metro Vancouver. Monthly comparisons between simulation and observation also highlight the effectiveness of the proposed downscaling method. The projected results (under one model set-up, WRF-MPI-ESM-LR, RCP 8.5) show that both maximum and minimum temperature will consistently increase between 2,035 and 2,100 over the 12 selected meteorological stations. By the end of this century, the daily maximum temperature and minimum temperature are expected to increase by an average of 2.91°C and 2.98°C. Nevertheless, with trivial increases in summer and significant rises in winter and spring, the seasonal variability will be reduced substantially, which indicates less energy requirement over Metro Vancouver. This is quite favorable for Metro Vancouver to switch from fossil fuel-based energy sources to renewable and clean forms of energy. Further, the cold extremes' frequency of minimum temperature will be reduced as expected; however, despite evident warming trend, the hot extremes of maximum temperature will become less frequent.

Keywords: climate change, statistical downscaling, regional climate model, long-term projection, recurrent neural network

OPEN ACCESS

Edited by:
Shan Zhao,
Shandong University, China

Reviewed by:
Ashok Kumar Jaswal,
India Meteorological Department, India
Eduardo Zorita,
Helmholtz Centre for Materials and Coastal Research (HZG), Germany
Chenglong Zhang,
China Agricultural University, China
Mo Li,
Northeast Agricultural University, China

****Correspondence:***
Guohe Huang
huangg@uregina.ca

Specialty section:
This article was submitted to Atmospheric Science, a section of the journal Frontiers in Earth Science

Received: *16 July 2021*
Accepted: *14 September 2021*
Published: *27 September 2021*

Citation:
Tian C, Huang G, Liu Y, Yan D, Wang F and Duan R (2021) Long-Term Maximum and Minimum Temperature Projections Over Metro Vancouver, Canada. Front. Earth Sci. 9:742840. doi: 10.3389/feart.2021.742840

INTRODUCTION

Distinct impacts of climate change on Canada are being observed. The increasing rate of temperature over Canada is near twice the global rate (Canada in a Changing Climate, 2019). The relevant mitigation and adaptation measures are thereby required to be updated. The first step is to generate suitable climate projections over selected study regions. Global climate models (GCMs) have been

widely used to conduct large-scale climate change impact assessment through their coarse-scale climate projections (100–300 km resolution) (Wang et al., 2015; Tian et al., 2020). However, it is also necessary to evaluate the impacts of climate change at regional levels to understand their interrelationships with larger-scale socioeconomic processes and geographical features (Pérez et al., 2014; Jury et al., 2015; Notaro et al., 2015). To advance the representation of local climate, downscaling techniques are critical for obtaining high-resolution climate projections *via* handling the spatial mismatch between GCMs and regional climatology (Hessami et al., 2008; Roberts et al., 2019; Shrestha and Wang, 2020).

Previous studies have been conducted to develop a wide range of downscaling algorithms which can be divided into two categories: dynamic and statistical downscaling (Hewitson and Crane, 1996; Yu et al., 2020). Regional Climate Models (RCMs), the representative dynamic downscaling approach, could downscale the climate data from GCMs or continental reanalysis data through physical mechanisms. More importantly, dynamic downscaling can generate out-of-sample data that previously were not observed for climate projections (Feser et al., 2011). However, it would become difficult to obtain high-resolution climate data through RCMs with limited time or computation resources. By contrast, by building the statistical relationship between coarse-scale atmospheric variables and locally observed climate data, statistical downscaling could quickly generate a great number of possible outcomes under moderate computation requirements (Wilby et al., 2004; Li et al., 2020).

Diverse studies aimed at using statistical downscaling algorithms to support climate change impact assessments. Wang et al. (2013) developed a statistical downscaling software, SCADS, for downscaling climate projection based on stepwise cluster analysis. An application of this software was presented to generate 10 km-resolution daily temperature and monthly precipitation projections in Toronto, ON, Canada. Bechler et al. (2015) proposed a spatial hybrid downscaling (SHD) algorithm to overcome the defect that statistical downscaling cannot well capture the extreme behavior and features of spatial structures. To further display the superiority of the proposed method, the authors applied it to the French Mediterranean basin where extreme events occurred frequently. In addition, Chen et al. (2012) provided a thorough evaluation of different downscaling methods and hydrological models with two reanalysis data, suggesting that some widely used evaluation criteria were not effective to evaluate certain downscaling approaches. GIS-based statistical downscaling methods were also common tools for handling the GCM's poor simulation of local climatology. Ashiq et al. (2010) utilized various interpolation models within the GIS environment to downscale PRECIS precipitation data, which filled the gap in the lack of credible precipitation data for Pakistan. In detail, inverse distance weighted, local polynomial interpolation, and radial basis functions were combined as deterministic methods. The core of selected geostatistical models was ordinary kriging and its extension which relies on the spatial autocorrelation in models. Moreover, multidimensional GCM ensembles were downscaled statistically with a GIS-based downscaling environment by Gharbia et al. (2016a). Temperature, rainfall, wind speed, solar radiation, and relative humidity were projected at a finer spatial resolution applying the proposed method. Gharbia et al. (2016b) also provided the performance assessment for multi-GCM ensemble based on statistically downscaled fine-scale data through the GIS platform. Compared to a single GCM, GCMs ensemble in downscaling climate variables could effectively reflect the uncertainty, and consequently provide more reliable climate projections for further impact assessment studies.

Deep learning techniques, especially, recurrent neural network (RNN), have been widely used in modeling sequence dependencies that exist in many fields (e.g., image processing, and language translate) (Le et al., 2020; Westermann et al., 2020). Nevertheless, few applications could be found in climate downscaling field. Moreover, since vanishing/exploding gradient problems are inevitable in naïve RNN, gated recurrent unit (GRU) technique is also applied in this study. On the other hand, owing to complex microclimate system of Metro Vancouver (MV), limited studies can be found regarding its high-resolution regional climate projections.

Thus, this study will focus on MV, where thirteen of British Columbia's thirty most populous municipalities are located. This area is experiencing evident climate change with increasing daytime and nighttime temperatures, particularly in winter, following by consequential fewer winter days with ice or frost. In addition, motivated by the success of RNN in capturing complex non-linear relationships between time-dependent data (LeCun et al., 2015), a GRU-based RNN statistical downscaling method followed by Tian et al. will be developed to generate temperature projections (both daily maximum temperature and minimum temperature) for further impact assessment of MV. Details of the case study area and developed downscaling method are given in the next section.

OVERVIEW OF THE STUDY SYSTEM

MV is bordered by fold mountain ridges to the north, the Pacific Ocean to the west, and the semi-arid Fraser Valley to the east, which results in a complicated microclimate system with growing urban heat island effects (Hay and Oke, 1976; Oke, 1976). As one of the most developed regions in the province of British Columbia (BC), Canada, MV is committed to becoming a carbon-neutral region by 2050 (Arcand et al., 2018). Switching from fossil fuel-based energy sources to renewable and clean forms of energy is consequently essential to decarbonize MV's energy system (Zeng et al., 2011). Nevertheless, evident global warming has been changing the weather patterns. For example, it may increase the summer hot days of MV. Measures such as redesign of provincial energy infrastructures are needed for mitigation and adaptation under climate change (Metro Vancouver, 2018). Therefore, it is desired that high-resolution climate projections representing local climate features of MV be generated to support further impact assessment under climate change.

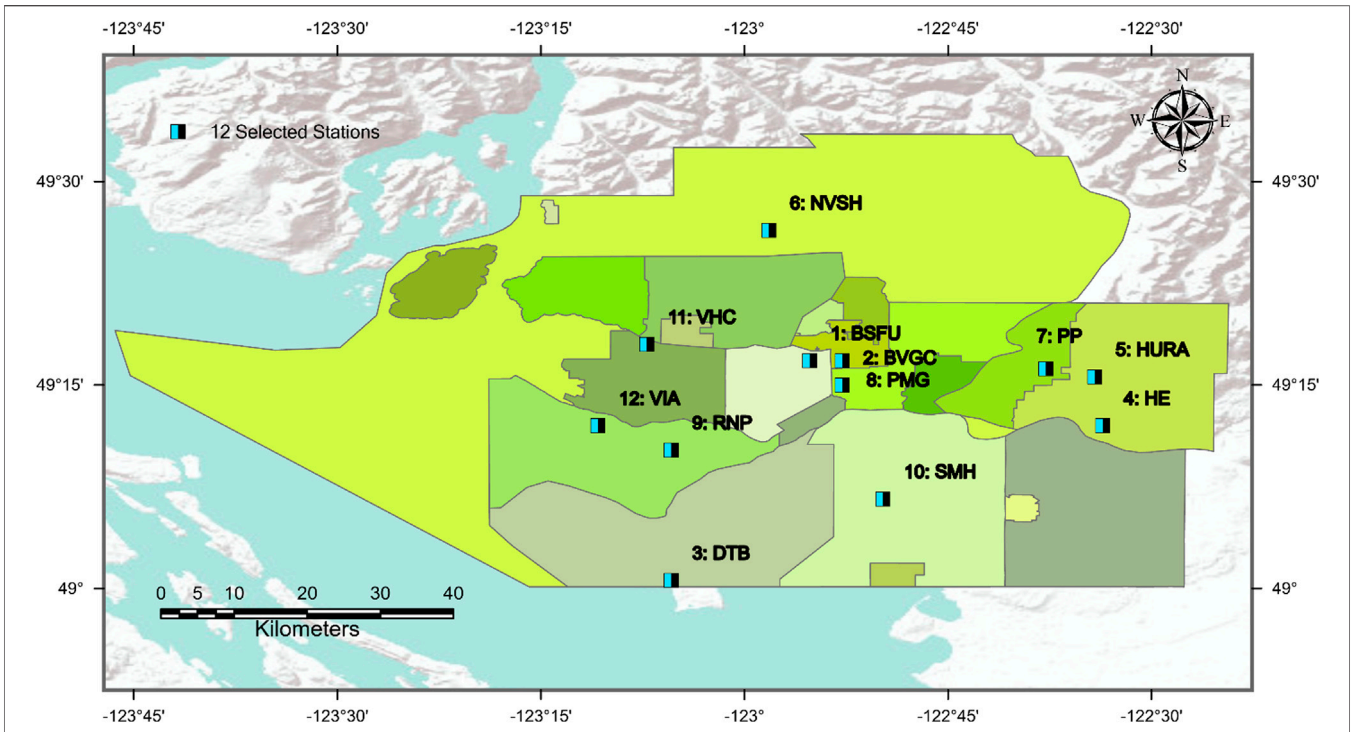

FIGURE 1 | The spatial distribution of 12 selected meteorological stations.

TABLE 1 | Original performance of RCM outputs and validation results (all monthly data between 1996 and 2005) of the developed downscaling model.

		Original data (RCM)			Downscaled data		
		R^2	r	RMSE (°C)	R^2	r	RMSE (°C)
BURNABY SIMON FRASER U (BSFU)	max	0.74	0.93	2.93	0.89	0.95	1.93
	min	0.71	0.84	3.86	0.87	0.96	1.56
BURQUITLAM VANCOUVER GOLF COURSE (BVGC)	max	0.66	0.93	3.67	0.93	0.96	1.68
	min	0.56	0.92	2.96	0.92	0.96	1.28
DELTA TSAWWASSEN BEACH (DTB)	max	0.37	0.92	4.29	0.95	0.97	1.26
	min	0.84	0.93	1.65	0.9	0.95	1.33
HANEY EAST (HE)	max	0.57	0.83	4.21	0.93	0.96	1.75
	min	0.55	0.87	3.1	0.85	0.92	1.81
HANEY UBC RF ADMIN (HURA)	max	0.57	0.94	4.21	0.92	0.97	1.83
	min	0.37	0.89	3.51	0.86	0.93	1.68
N VAN SEYMOUR HATCHERY (NVSH)	max	0.63	0.94	4.09	0.97	0.98	1.21
	min	0.35	0.92	3.04	0.96	0.98	1.02
PITT POLDER (PP)	max	0.4	0.93	5.09	0.91	0.97	1.99
	min	0.64	0.98	2.57	0.99	0.99	0.44
PORT MOODY GLENAYRE (PMG)	max	0.72	0.93	3.22	0.91	0.96	1.85
	min	0.47	0.96	2.82	0.99	0.99	0.06
RICHMOND NATURE PARK (RNP)	max	0.13	0.91	5.77	0.92	0.97	1.76
	min	0.71	0.92	2.48	0.9	0.95	1.49
SURREY MUNICIPAL HALL (SMH)	max	0.75	0.96	3.03	0.98	0.99	0.81
	min	0.69	0.97	0.98	0.98	0.99	0.18
VANCOUVER HARBOUR CS (VHC)	max	0.23	0.92	4.91	0.9	0.95	1.78
	min	0.83	0.94	1.74	0.92	0.96	1.16
VANCOUVER INTL A (VIA)	max	0.39	0.93	4.36	0.93	0.97	1.43
	min	0.81	0.94	1.99	0.93	0.96	1.25

To undertake high-resolution climate projections, 12 high-quality meteorological stations are selected, as shown in **Figure 1**. Daily minimum and maximum temperature observations at these stations are obtained from Environment and Climate Change Canada, representing the realistic climate of MV (Historical data). Temperature simulation from RCMs displays poor

performances compared to these observations (**Table 1**). Thus, to combine the advantages of dynamical and statistical downscaling, in this study, RCM outputs (25 km × 25 km), both historical and projected, are selected to support the developed downscaling work. The outputs (WRF-MPI-ESM-LR) are acquired from the NA-CORDEX where climate projections cover most of North America (Mearns et al., 2017). NA-CORDEX is the North American component of the international CORDEX (Coordinated Regional Downscaling Experiment) program which has been providing global coordination of regional climate downscaling for improved regional climate change adaptation and impact assessment. The selected historical RCM simulations are driven by the ERA-Interim historical reanalysis; future projections are driven by a GCM (MPI-ESM-LR) using representative concentration pathways 8.5 (RCP 8.5). With the local-scale observations over MV, the GRU-based RNN statistical downscaling model (detailed information is displayed in the next section) will be developed to correct/downscale gridded simulations (daily maximum/minimum temperature) from the selected RCM. The time series is divided into two time slots, i.e., 1986–1995 for calibration, and 1996–2005 for validation.

GATED RECURRENT UNIT-BASED RECURRENT NEURAL NETWORK DOWNSCALING MODEL

Deep learning with multiple hidden layers is employed to represent complex functions in a series of fields (e.g., image analysis, language analysis, and runoff prediction) (Ordieres-Meré et al., 2020). Recurrent neural network (RNN, first developed by Hopfield (2018)), as a class of deep learning, has been applied to capture complex non-linear relationships, especially for time-dependent data as it allows forward and backward connections among time steps. It is found that with acceptable correlation, RNN performs better ability to capture the non-linear relationship than some traditional data-driven models. Considering the complicated non-linear relationship that exists between relatively coarse-scale simulation and realistic temperature observations, RNN statistical downscaling model followed by Tian et al. (2021) is developed for generating high-resolution temperature projections for MV. The minimum and maximum temperature projections from RCM will be downscaled, respectively.

RNN basically consists of the input layer, multiple hidden layers, and the output layer, as expressed in **Eq. 1**. Since the superiority of back propagation arithmetic (Li et al., 2010), RNN models can display impressive memory ability to store information from the last time step, and then decide the current outputs combined with the current outputs. However, when the time steps are large, the deeper layer is, the easier would the error of partial derivative accumulate. Specifically, the gradient will get quite small, leading to the weight in larger time steps becoming constant, which is generally known as the vanishing gradient problem. By contrast, substantial updates of

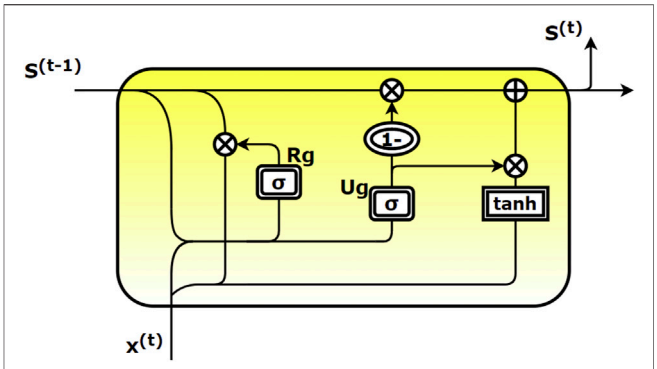

FIGURE 2 | Neuron network of GRU.

weights in antecedent time steps, i.e., exploding gradient, will also significantly impact the accuracy of RNN training.

$$y = \left\langle \sum_{i=1}^{m} x_i W_i + b \right\rangle \tag{1}$$

where angle brackets denote an activation function; x_i is the input variable; W_i is the vector of weight assigned to corresponding input variable; b is the bias term.

Gated recurrent unit (GRU) technique is developed to handle the above-mentioned vanishing/exploding gradient problem. Different from a typical RNN, a reset gate and update gate are added in the hidden block (as shown in **Figure 2**), which aimed to forget the unnecessary state/input from the last/current time step. Thus, it can effectively avoid the vanishing/exploding gradient problem, and meanwhile, make the computation simpler. Albeit the application of GRU-based RNN in statistical downscaling is still in infancy, it has been demonstrated to perform better capability to capture time-dependent relationships with limited correlation between simulation and observation (LeCun et al., 2015). In detail, the GRU-based RNN can be represented as follows:

$$Ug_u = \langle W_u \cdot x^{(t)} + U_u \cdot S^{(t-1)} + b_u \rangle \tag{2}$$

$$Rg_r = \langle W_r \cdot x^{(t)} + U_r \cdot S^{(t-1)} + b_r \rangle \tag{3}$$

$$\widehat{S}^{(t)} = \tanh\langle W_s \cdot x^{(t)} + U_s \cdot \left(Rg_r \times S^{(t-1)}\right) + b_s \rangle \tag{4}$$

$$S^{(t)} = Ug_u \widehat{S}^{(t)} + \left(1 - Ug_u\right) S^{(t-1)} \tag{5}$$

where W and U are related weights; Ug_u is the update gate aimed to learn long-term dependency relationship between coarse-scale RCM simulation and temperature observation, which is determined by both hidden state from the last time step $S^{(t-1)}$ and the present input $x^{(t)}$; Rg_r is the reset gate applying the activate function of sigmoid to the linear transformations of $x^{(t)}$ and $S^{(t-1)}$, which is used to capture short-term dependency relationship between time-dependent data; $\widehat{S}^{(t)}$ and $S^{(t)}$ are the candidate state and final cell state, respectively; $\widehat{S}^{(t)}$ is generated by the current input and the reset gate employing activation function of tanh; $S^{(t)}$ considers both last final cell state and candidate state. The parameters in the update/reset gate range from 0 to 1;

estimated values are used to determine whether the last state should be updated/reset.

In addition, to avoid over-fitting, dropout technique is applied in this study. Specifically, certain probabilities will be assigned in k neurons of a certain layer; in this way, relevant parameters will not be updated within each training iteration. That is, the final cell state would not be overly reliant on certain neurons of the hidden layer. The detailed structure and model settings can refer to Tian et al. (2021). Besides, three model evaluation criteria, i.e., determinant coefficient (R^2), root mean square error (RMSE), and correlation coefficient (r), are used to evaluate the GRU-based RNN statistical downscaling.

RESULTS AND DISCUSSION

Validation Results

To validate the calibrated GRU-based RNN downscaling model, the daily maximum and minimum temperatures in the baseline period (i.e., 1985–2005) are generated *via* the proposed downscaling model. The produced temperature values are then compared with meteorological observations at 12 selected stations of MV. The R^2, RMSE, and r are calculated as indexes to characterize the downscaling capability of the developed approach. The validation results of monthly maximum and minimum temperature for observation and simulated values at the 12 weather stations are displayed in **Table 1**. Also, temperature observations are compared to the original outputs from RCM, indicating the necessity of downscaling work.

It is quite clear that for maximum temperature, most of the R-squared coefficients over the 12 meteorological stations are higher than 0.88. The highest value could be achieved at 0.98 (SMH station), while the lowest value is obtained at BSFU station (0.89). The overall performance of the presented downscaling model for maximum temperature is stabilized with the average R-square value being 0.93. Compared to the outputs of RCM, the other two indexes (r and RMSE) also suggest the good downscaling capability of the developed model. For instance, the value of RMSE at VHC station could be decreased from 4.91–*to* 1.78. However, the performance for minimum temperature varies relatively greatly at the 12 stations, which is not as satisfactory as that for maximum temperature. Though the highest value could be reached as high as 0.99 (PP station and PMG station, corresponding to 0.64 and 0.47 of original RCM outputs, respectively), the lowest R^2 is only 0.85 for HE station. Moreover, another two stations display relatively poor performance with the values being lower than 0.88 (0.87 of BSFU and 0.86 of HURA). Alpine and coastal areas have been one of the challenges in climate simulation for both GCM and RCM. Despite a few stations are not quite ideal and competitive with previous studies of other regions, compared to RCM outputs, prominent improvements could be found in all the indexes after employing the developed GRU-based RNN downscaling model. Therefore, the overall performance of the calibrated model could still be competitive.

To further investigate the performance of the presented downscaling model, the monthly means of maximum and minimum temperature are compared between the simulated outputs and the observed temperature data. As displayed in **Figures 3**, **4**, apart from few stations (e.g., HE and PMG stations) showing evident under- or overestimate compared to observations, most of the simulated temperature could well fit with the monthly variation of observations, especially for the stations with high R^2/RMSE values (e.g., PP and SMH stations). In other words, the proposed downscaling model is able to well capture the overall seasonal and spatial patterns of MV. This further affirms its acceptable performance in simulating both maximum and minimum temperature at 12 selected weather stations. In addition, to filter out potential effect of annual cycle on the performance of the developed downscaling model, seasonal (i.e., spring, summer, autumn, and summer) validation is undertaken to further indicate the model's effectiveness (see **Supplementary Tables S1–S4**). Despite with relatively poor performance in winter owing to quite limited correlation between RCM simulations and observations, significant improvement could be found for most of the stations compared to validation results of original RCM outputs, which suggests that the developed downscaling model is able to correct RCM seasonal errors. Therefore, albeit complex microclimate resulting in limited researches regarding the downscaling work at MV, the developed GRU-based RNN downscaling model is demonstrated to be effective to downscale the daily maximum and minimum temperature of MV.

Projections of Future Daily Temperature

High-resolution temperature projections for MV are obtained from 2035 to 2100 by downscaling the 25 km outputs from WRF under RCP 8.5 scenarios with the validated GRU-based RNN downscaling model. The trend analysis in daily maximum and minimum temperature is then applied to understand future changing tendency across the selected 12 stations of MV under RCP 8.5 scenario. It should be noted that p-value < 0.01 (α = 0.01) suggests that the future temperature performs a statistically significant tendency during 2035–2100. **Figure 5** displays the downscaled projections of daily maximum temperature, and future tendencies of 12 weather stations which are estimated by Sen's slope estimator (Dong et al., 2021; Song et al., 2021). It can be seen that all stations show consistent and remarkable warming trends with all of the probability values being less than 0.0001. The trend at each station also tells a different story owing to the spatial pattern of MV. The most significant increasing trend is projected to warm by approximately 0.0037°C per month for NVSH station, which means that NVSH station would increase ~2.9°C by 2100. Also, the coastal station (e.g., DTB station) shows a similar warming trend (0.0036°C per month), taking second place among 12 meteorological stations. One may be easy to ignore is that both coastal (DTB and SMH stations) and inland stations (NVSH and PP stations) display significant warming trends in the next 65 years, which further highlights the complex climate context of MV. By contrast, the estimated warming trends at stations in highly urbanized regions such as VIA station (City of Richmond, 0.0025°C per month) and VHC station (City of

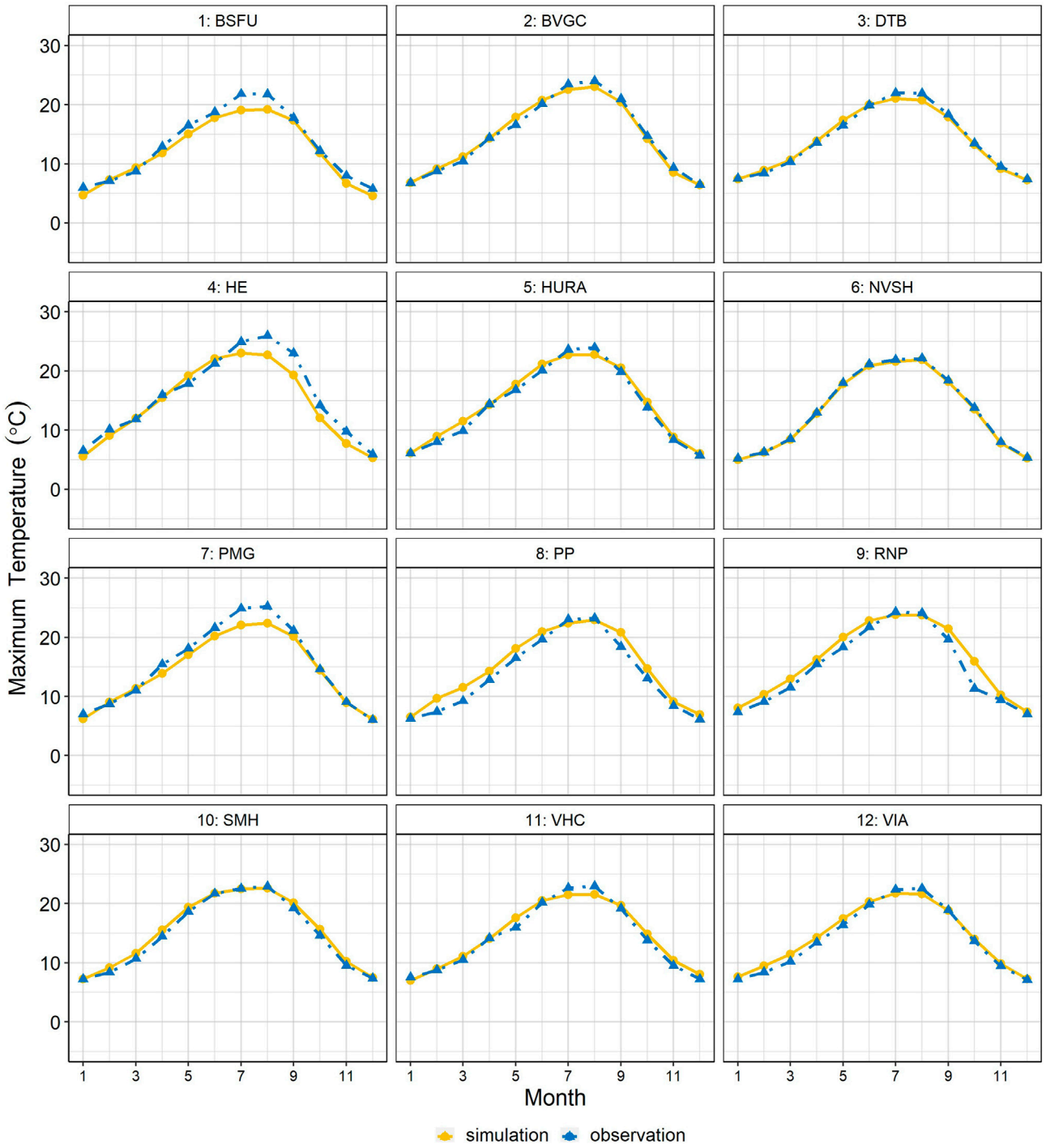

FIGURE 3 | Monthly comparisons between maximum temperature simulation and observation.

Vancouver, 0.0019°C per month) are not the most significant as expected. In addition, the lowest warming tendency is estimated at BSFU station located in City of Burnaby. Compared to varying warming trends for maximum temperature, the degree of daily minimum temperature increasing is more consistent as shown in **Figure 6**. Similarly, the hypothesis testing indicates that 12 meteorological stations will have significant changes in the next 65 years. Instead of displaying relatively different warming trends for the maximum temperature, the trends of minimum temperature ranges at a comparatively lower level (from 0.0022°C to 0.0031°C per month). City of Richmond and City of Vancouver remains at

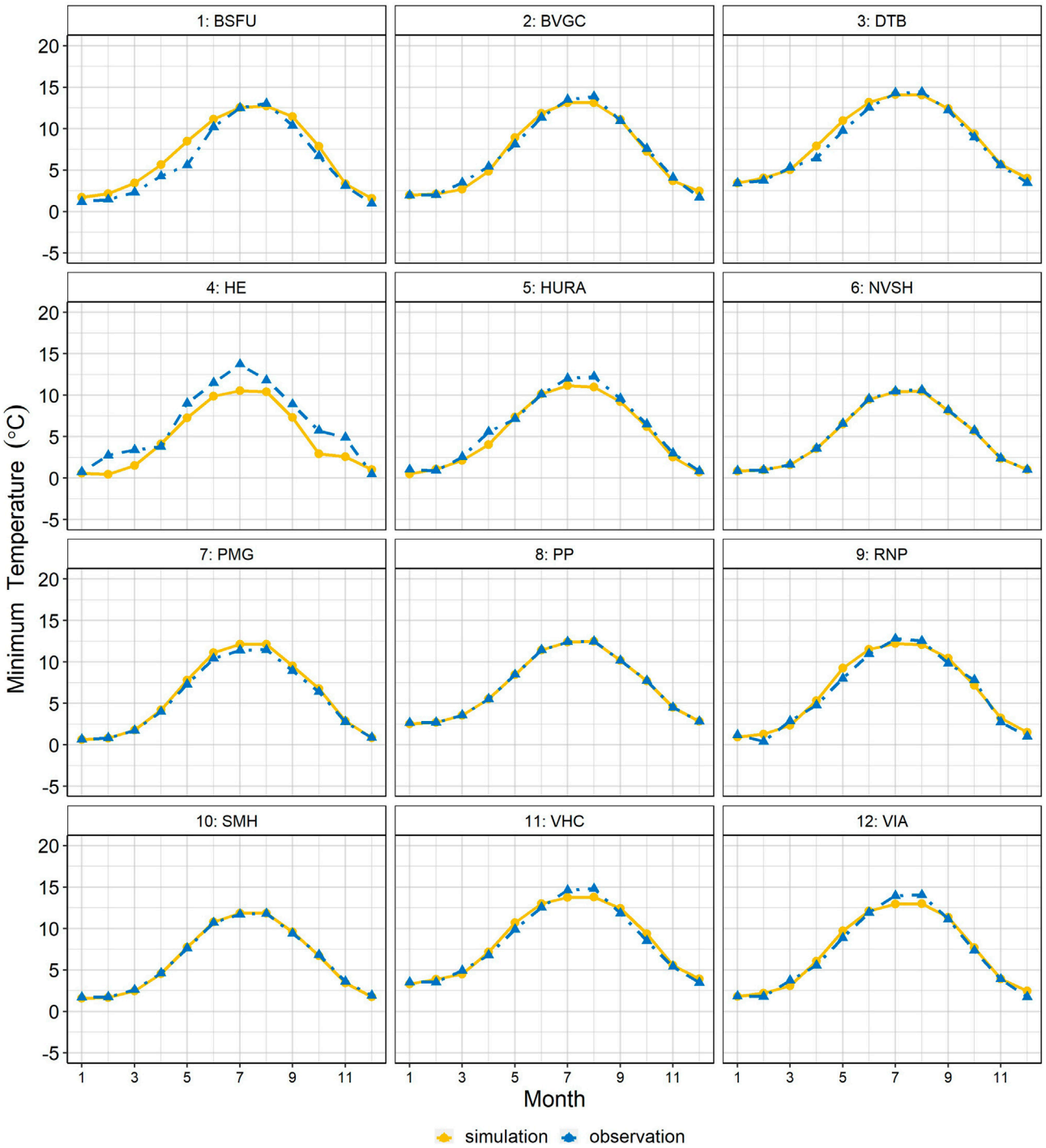

FIGURE 4 | Monthly comparisons between minimum temperature simulation and observation.

the middle level of the warming trend, with the same trend value of 0.0024°C per month. On the other hand, a much more significant warming trend (0.0026°C per month) is displayed in the minimum temperature over BSFU station, in comparison with its maximum temperature. Furthermore, similar to the pattern of maximum temperature, both coastal and inland stations (DTB and NVSH) display consistently noticeable warming tendency; the minimum temperature would increase by 2.34°C to the end of this century. Despite less variability of trend values, the average value for monthly minimum temperature could still be as high as 0.0027°C per month for the whole MV region.

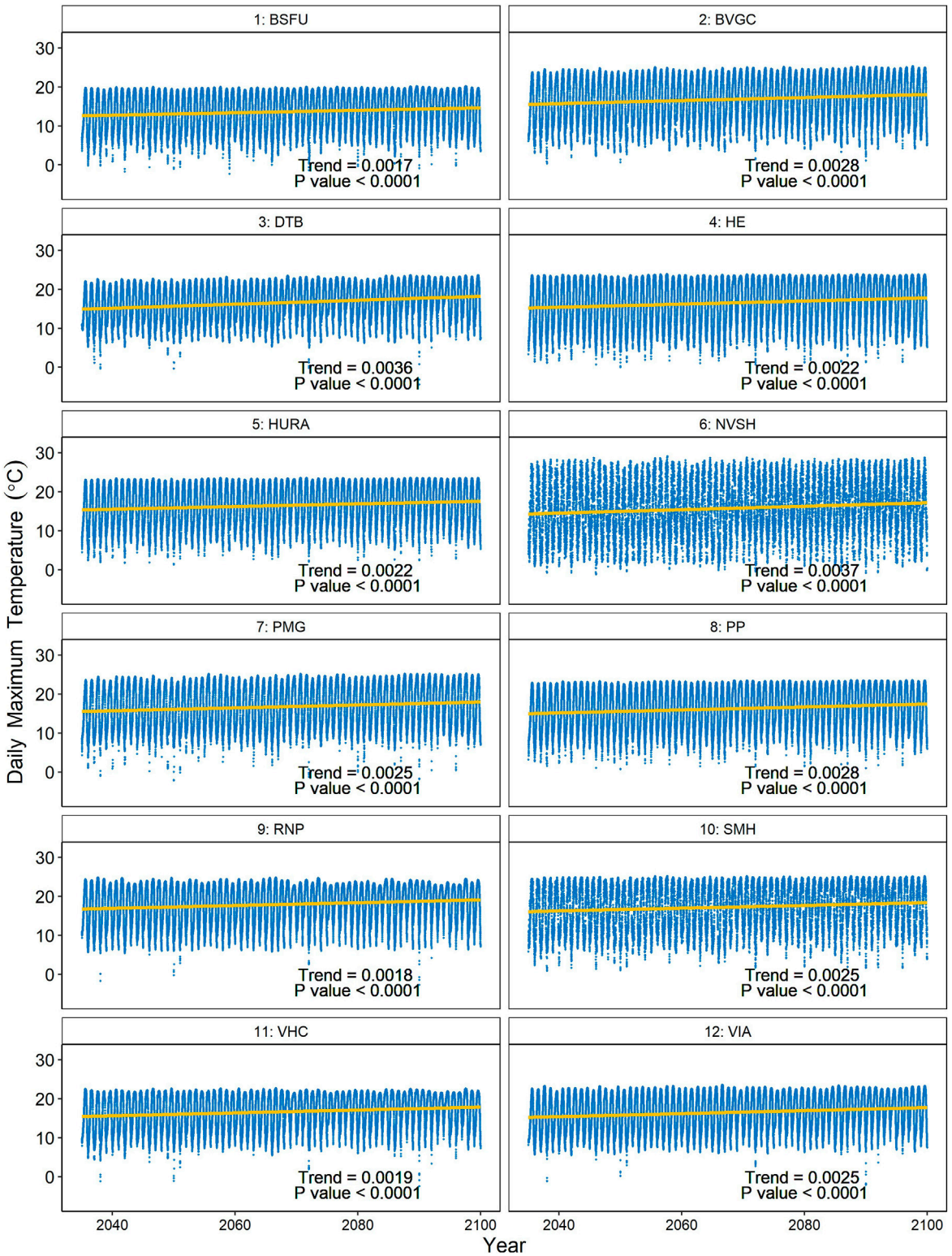

FIGURE 5 | Projected trends of daily maximum temperature between 2035 and 2100.

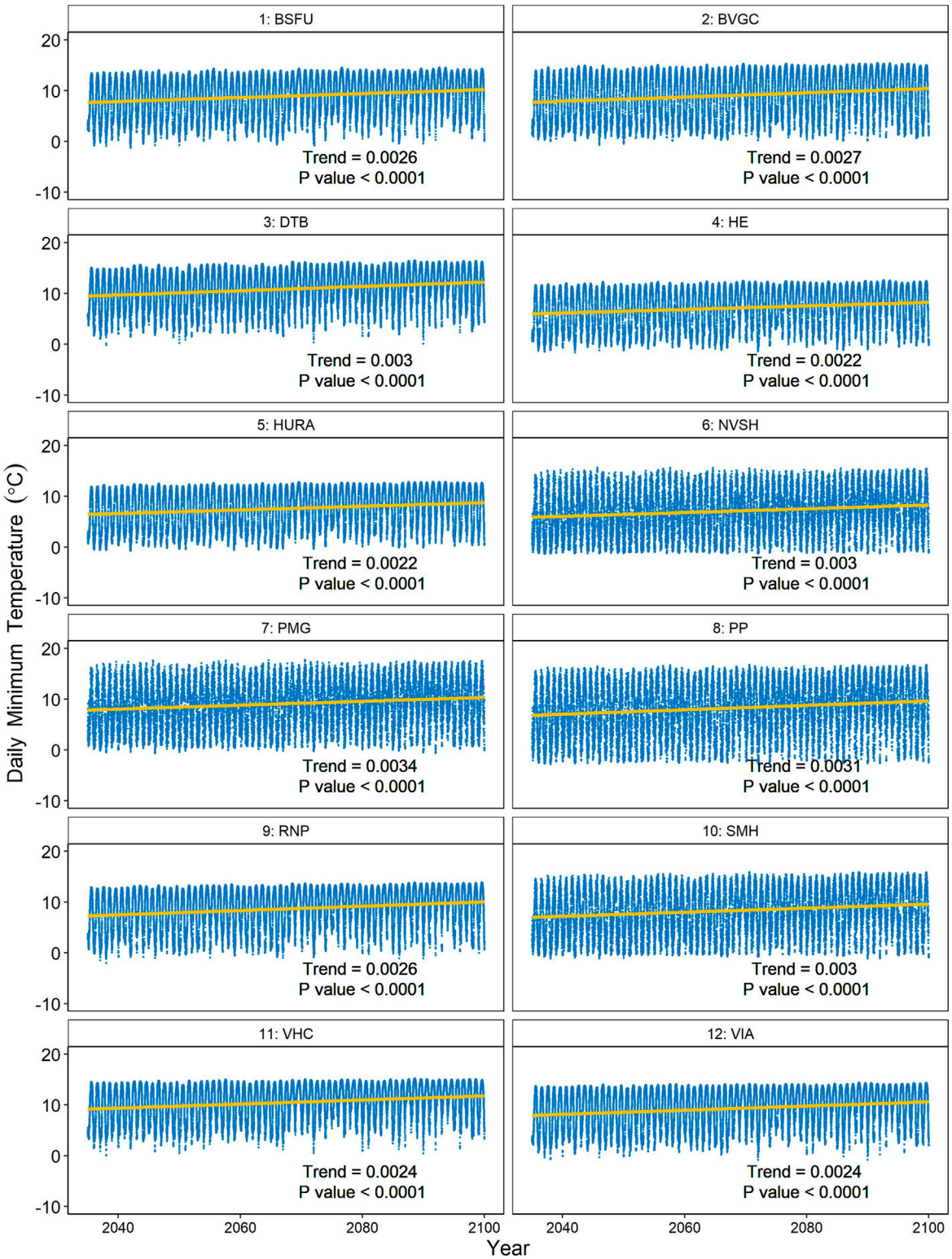

FIGURE 6 | Projected trends of daily minimum temperature between 2035 and 2100.

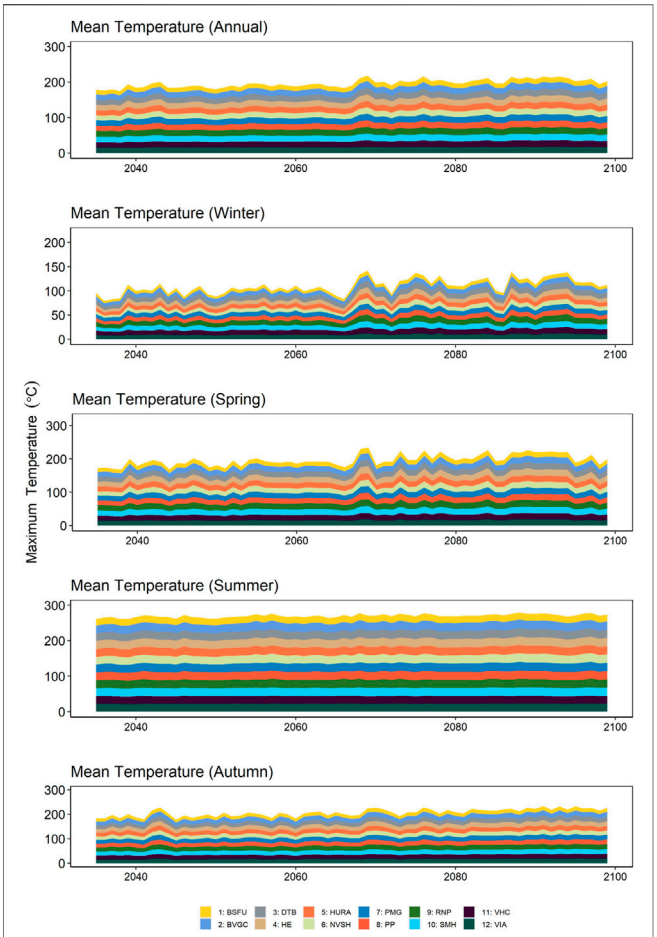

FIGURE 7 | Annual and seasonal time series of projected daily maximum temperature between 2035 and 2100.

Further, **Figures 7**, **8** present projected time series of maximum and minimum temperature at annual and seasonal time scales over the 12 weather stations from 2035 to 2100. For both plots, it is quite clear that all 4 seasonal time series display increasing temporal patterns from 2035 to the end of this century, which further confirms mentioned trend analysis. Interestingly, the increasing tendency in summer is not quite significant as expected, especially for maximum temperature. This suggests that even under RCP 8.5 scenario, the frequency of extreme hot events would not increase substantially, which seems good news for MV. On the other hand, it can be seen that winter and spring time scales have more predominant temporal variability. Considering these two patterns, MV is projected to experience less seasonal temperature variability under the global warming trend. Besides, maximum temperature values fluctuate between 2035 and 2060 with a relatively significant peak between 2060 and 2080, and continuously undulate with an overall increasing tendency instead of a constantly rising trend. Specifically, the patterns of HURA and VIA stations are relatively notable. Moreover, consistent plunges across 12 stations could be found in the wintertime series around 2065. By contrast, projected mean values on annual and autumn's time scales display successive warming trends with little temporal variability. Accordant with the results of trend analysis, the maximum temperatures of NVSH and DTB stations increase consistently with constant notable crawling. As for the minimum temperature plot (**Figure 8**), it displays similar overall patterns with that for maximum temperature. The difference is, more evident fluctuations between 2035 and 2060 are shown in winter and spring. Besides, there are sharper increases between 2060 and 2070 compared to that of maximum temperature. The annual warming tendency is not as pronounced as that for maximum temperature but more consistent, which further demonstrates the comparison in previous trend indexes.

To better explore future changes of projected temperature in the 12 meteorological stations, the future projections of daily maximum and minimum temperature are divided into three periods (the 2030s, 2050s, and 2080s, i.e., 2035–2054, 2055–2074, and 2075–2100). The projected climate changes are calculated based on the mean temperature of three periods under RCP 8.5 as well as that of the 20 years baseline, i.e., historical periods from 1985 to 2005. The projections of changes in daily maximum and minimum temperature under

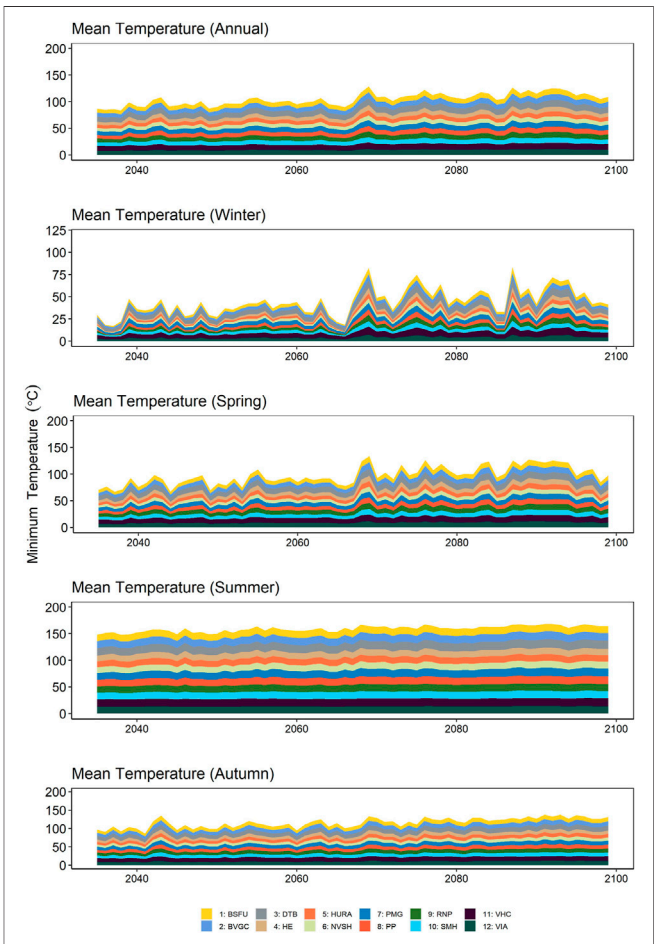

FIGURE 8 | Annual and seasonal time series of projected daily minimum temperature between 2035 and 2100.

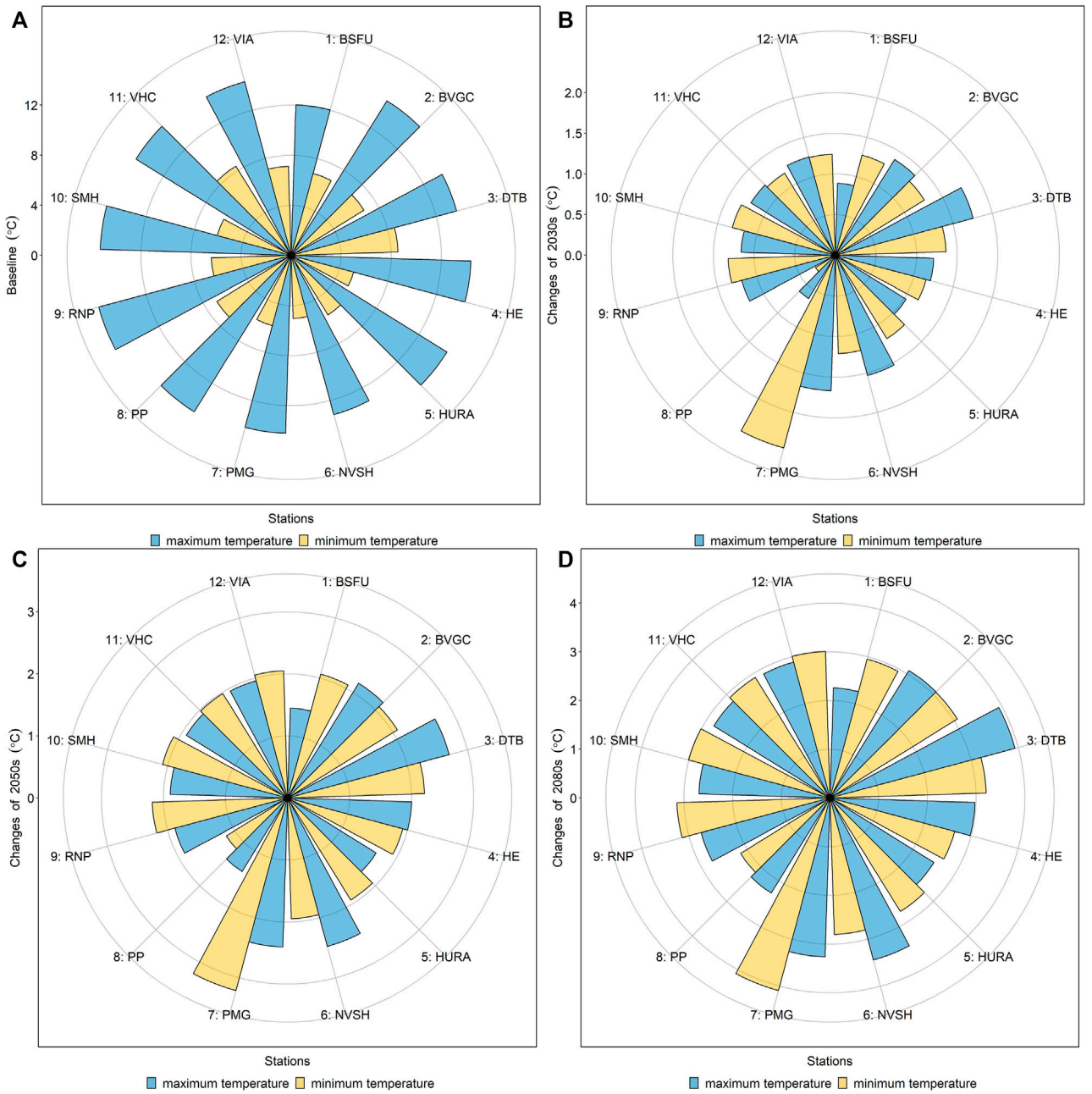

FIGURE 9 | Baseline temperature **(A)** and projected changes over 2030s **(B)**, 2050s **(C)**, and 2080s **(D)**.

RCP 8.5 scenario could be further analyzed at the 12 selected weather stations.

Figure 9 depicts the baseline simulated maximum and minimum temperature, as well as future annual temperature changes of 12 selected stations for the 2030, 2050, and 2080 s under RCP 8.5. RNP and SMH stations (located at City of Richmond and City of Surrey, respectively) show the highest maximum temperature during the baseline period; while for the minimum temperature, VHC and DTB (located at City of Vancouver and District of Delta, respectively) are the top two stations. As for the future changes, the results suggest that the simulated annual maximum temperature changes would increase consistently across the 12 weather stations from the near term to the end of this century. Instead of RNP and SMH stations, the changes in the annual maximum temperature for District of Delta (DTB station) and City of Coquitlam (PMG station) are the most significant, with change values being 1.76°C and 1.67°C in the 2030s, 2.69°C and 2.40°C in the 2050s, as well as 3.93°C and 3.26°C to the end of this century. These cities would face more serious positive changes in maximum temperature, which may increase

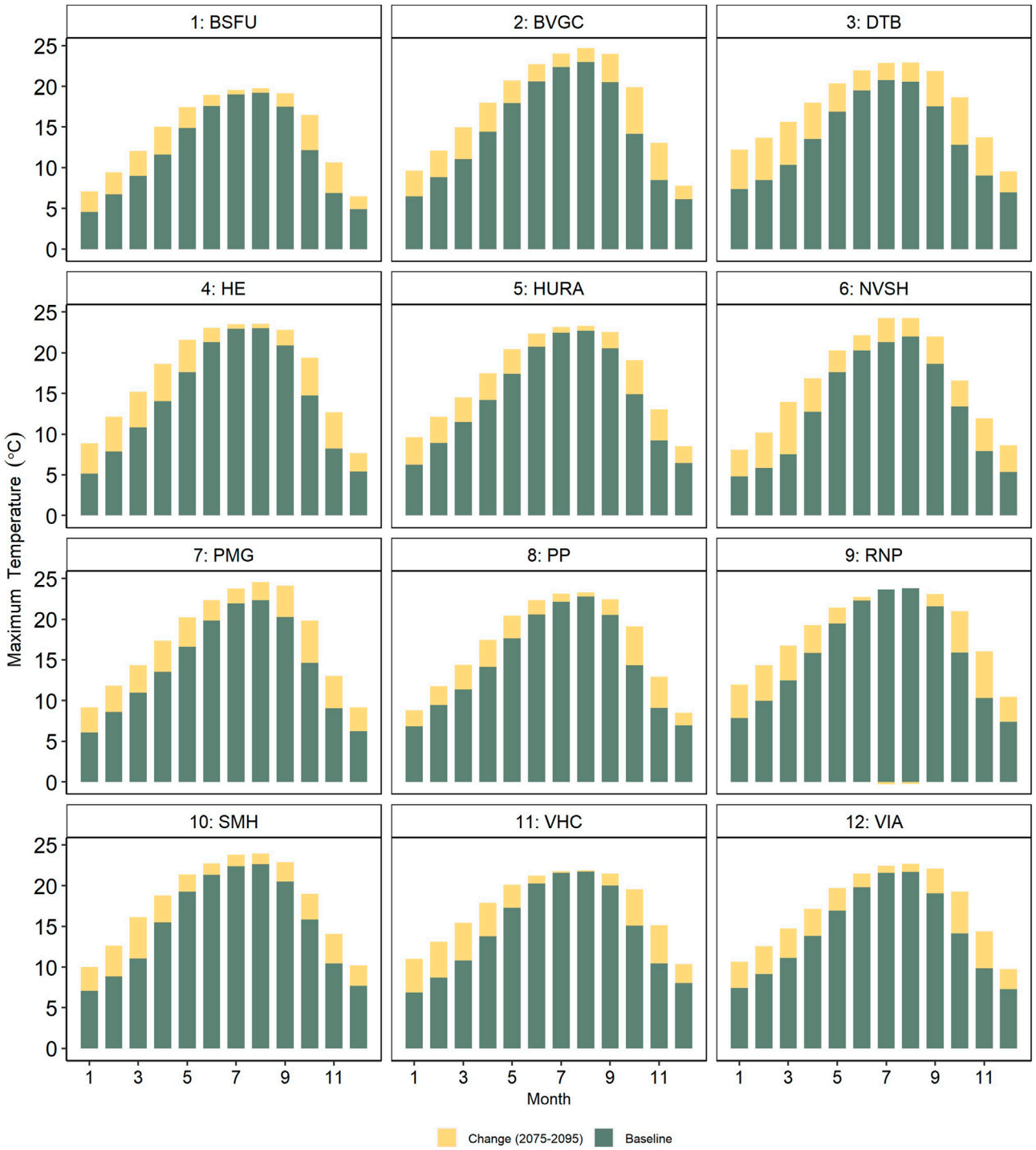

FIGURE 10 | Monthly baseline and projected changes of 2075–2095 for maximum temperature.

the cooling requirement of buildings within summer. In addition, NVSH station ranks third and also reveals conspicuous positive changes. The projected change of its maximum temperature would be 1.53°C in the near term, 2.48°C in the 2050s, and 3.44°C in the 2080s, respectively. It is interesting that even if some stations (e.g., VIA and VHC stations) display relatively gentle increasing rates in previous trend analysis, considerable positive change will still occur. In particular, to the end of this century, almost half of the selected stations will increase by ~3°C in comparison with the baseline maximum temperature. Potential impacts from positive changes under the high radiative value of RCP 8.5 still have to be faced in the future. For the minimum

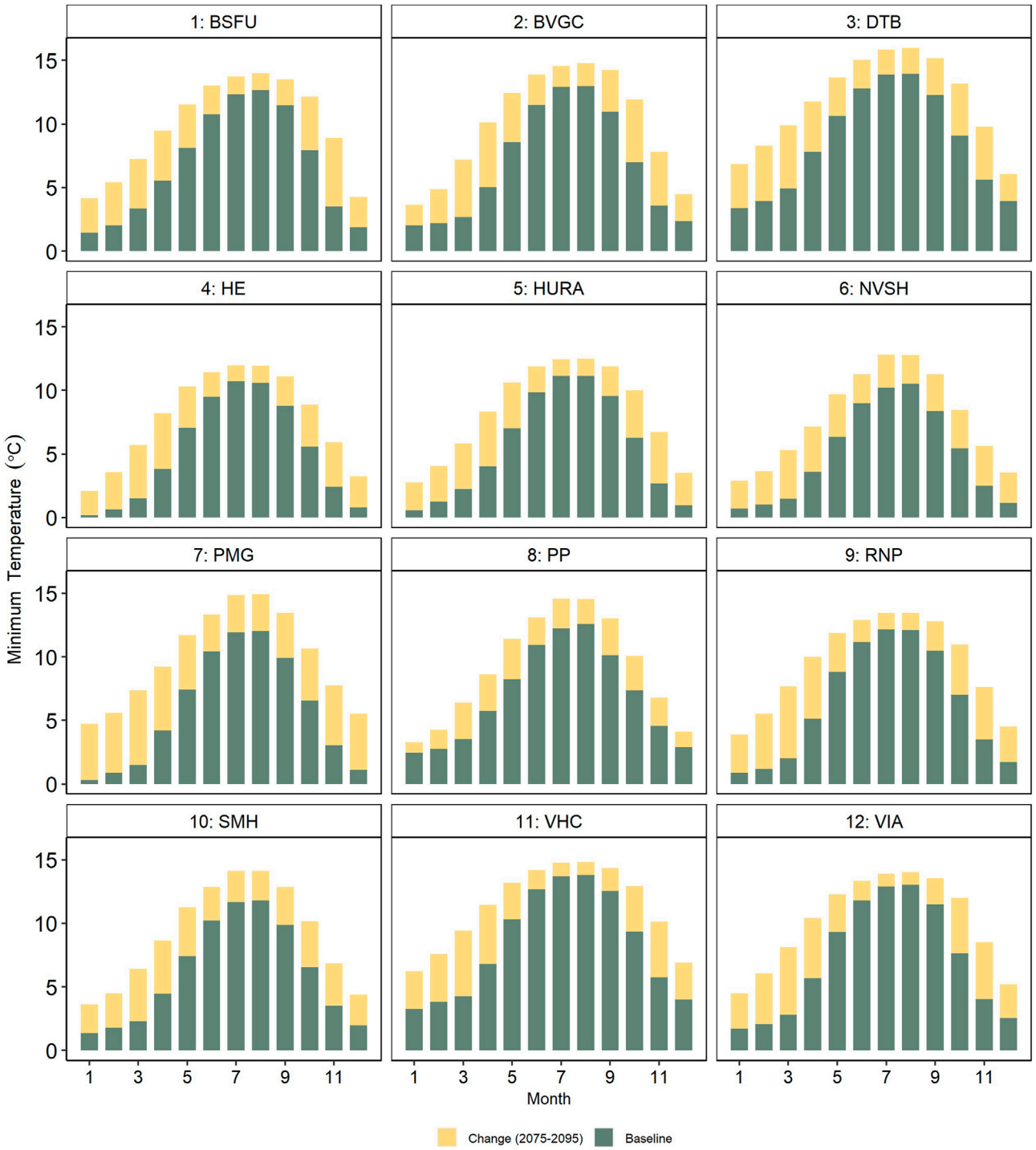

FIGURE 11 | Monthly baseline and projected changes of 2075–2095 for minimum temperature.

temperature, similar to patterns of the maximum temperature, the entire MV region (12 stations) displays an obvious rising tendency from the 2030s–2080s. Even for the least positive change of PP station located in District of Pitt Meadows would increase from 0.29°C in the 2030s to 1.16°C in the 2050s, and then continue to as high as 2.16°C in the 2080s. The greatest warming in the minimum temperature still occurs in the PMG station (City of Coquitlam); by the 2080s, the changes could reach as high as 4.09°C relative to the historical baseline. Moreover, one of the highly urbanized cities, City of Richmond, shows quite a bit increase compared to historical climate. The positive change could reach 3.14°C at the end of this century. This

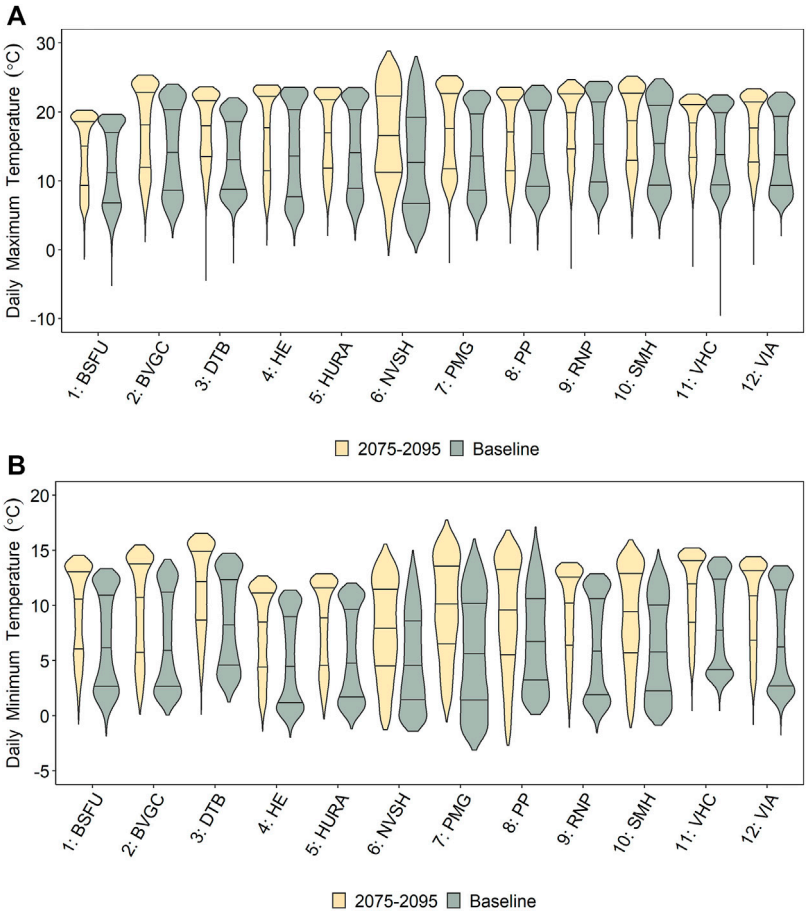

FIGURE 12 | Frequency distributions of daily maximum **(A)** and minimum **(B)** temperature between 2075 and 2095.

may cause by the relatively lower minimum temperature in the historical baseline. Comparatively, it is interesting to note that in many stations, the rises of minimum temperature are greater than those of maximum temperature, indicating the daily temperature range of these stations is projected to become narrow under RCP 8.5 scenario.

Comparatively, the annual minimum temperature shows more apparent spatial variability especially in the 2030s where the highest positive change (PMG station) could achieve at more than 8 times of the least increase relative to the baseline. Albeit less spatial pattern is found for the annual minimum temperature, the rising amplitude compared to historical climate is commensurate with that for annual maximum temperature in most stations. Overall, such a continuous rising tendency may raise the temperature of MV by 2.28°C by the end of this century. Both coastal and inland cities are likely to have a pronounced climate warming trend. Unexpectedly, under RCP 8.5 scenario, i.e., scenario for long-term high energy requirement and GHG emissions without any climate adaptation policies, highly urbanized cities with developed economy will not experience more frequent hot extremes. By contrast, evident increases are displayed in the projected minimum temperature, narrowing the daily temperature difference in these stations.

To understand temperature projections' temporal changes over MV, monthly maximum and minimum temperature changes are calculated for the specific period, i.e., from 2075 to 2095. **Figure 10** displays monthly baseline maximum temperature and specific changes of 2,075–2,095 at the 12 meteorological. It is clear that positive changes are shown in almost every month; especially, all the 12 weather stations consistently have significant increases in January/February/March (the average change of all stations in these 3 months could reach as high as 2.99°C). The mere exception to this is that few changes could be found in July and August for most of the stations, which further demonstrates the concluded stable state during the summer period. The results also show that for most stations, changes of the maximum temperature in spring and winter are greater than those in autumn and summer. For instance, in City of Surrey (SMH station), the positive change values of winter and spring are 2.75°C and 3.52°C, while those for spring and summer would be only 2.03°C and 1.38°C, respectively. The highest positive change would be 6.47°C of NVSH station in March rather than 3.39°C of PMG station. Most of the increases in maximum temperature for PMG and DTB stations are contributed by winter and spring. Stations with relatively moderate warming trends such as VIA station also

perform considerable increases in all months with the largest increase of 5.16°C occurring in October and an average positive change of 2.91°C. As for the monthly minimum temperature under RCP 8.5 scenario shown in **Figure 11**, it can be seen that compared to the increases in monthly maximum temperature, more significant rises in winter and spring are displayed in monthly minimum temperature for most of the selected stations. More specifically, the average value in winter would be 4.73°C, while that for maximum temperature in **Figure 10** is only at 2.97°C. In addition, evident increases could also be found in July and August, which is consistent with previous findings. PMG stations show the most remarkable positive changes in nearly every month, causing the highest increases in the aforementioned annual mean. Overall, as shown in these two figures, it is quite clear that under RCP 8.5 scenario, the monthly variability will be substantially reduced across all the weather stations. The difference between the maximum and minimum temperature will also be narrowed to the end of this century. The results are consistent with previous conclusions.

Figure 12 displays the ~20 years distributions (baseline period and 2075–2095, respectively) of 12 meteorological stations. Despite the annual increases of extreme maximum temperature are not significant at most of the stations as mentioned before, the frequency of relatively lower temperature is reduced evidently since "violin" distributions of all the stations get to top-heavy. Moreover, as shown in this figure, the hot extreme's frequency would not increase substantially, which is consistent with the above-mentioned analysis. Furthermore, since NVSH station shows the most significant warming trend from 2035 to 2100, the frequency of higher and lower temperatures seems to interchange in 2075–2095, compared to the baseline period, which is different from other stations. For daily minimum temperature, there are four stations (i.e., NVSH, PMG, PP, and SMH stations) displaying similar patterns, which further highlights more notable rises in comparison with maximum temperature. In addition, top-heavy "violin" distributions are more common in **Figure 12B**; the frequency of cold extreme will experience massive declines.

CONCLUSION

In this study, a GRU-based RNN downscaling approach was developed to tackle the spatial mismatch between coarse-scale climate simulation and regional climatology for improving the representation of local future climate across MV. The complex microclimate systems under the context of the alpine and coastal areas are usually difficult to be simulated by GCMs and even RCMs. The proposed downscaling model was demonstrated (by three indexes, namely, R^2, RMSE, and r) to perform competitive ability to capture the regional climatology of MV. The effectiveness was further highlighted by the monthly comparison, indicating that the GRU-based RNN downscaling model could well simulate the MV's overall seasonal and spatial patterns.

The presented downscaling approach was then applied to generate regional high-resolution climate projections of the maximum and minimum temperature from 2,035 to 2,100 under RCP 8.5. Trend analysis in the next 65 years was first conducted by Sen's slope algorithm, which disclosed that both maximum and minimum temperature would consistently increase over the 12 selected weather stations. Both coastal and inland regions may experience more significant successive warming in the future, which revealing the complex microclimate of MV. These results were accordant with annual and seasonal analysis for temporal patterns. Furthermore, the future temperature changes were analyzed to better understand the potential impacts of climate change on MV under a high RCP scenario. It was indicated that the entire MV (12 stations) displayed obvious gradually increasing positive changes from the 2030s–2080s relative to the baseline climate of each station. In addition, both annual maximum and minimum temperature shows apparent spatial variability, especially by the 2080s. More importantly, it can be also found that with negligible increases in summer (e.g., RNP and VHC stations) and notable rises in winter and spring, the seasonal temperature variability would be reduced substantially. Further, surprisingly, despite evident warming trends, the hot extremes of maximum temperature will become less frequent. On the other hand, the cold extreme's frequency of minimum temperature will be reduced as expected.

Overall, the presented GRU-based RNN downscaling approach could effectively capture the statistical relationship between RCM outputs and realistic climatology, and consequently combine advantages of both dynamic and statistical methods. Thus, maximum and minimum temperature projections could provide effective support for further regional impact assessment in MV. However, notwithstanding it can reflect local climate features based on dynamical downscaling (RCM outputs), the systematic errors in the simulated fields hidden within RCMs would be transferred into the statistical downscaling process, which may cause relatively poor performance of some station's validation (especially in winter) in this study. Besides, a wide range of factors (e.g., input data, model selection, and parameter setup) may result in multiple uncertainties, which would impact the robustness of a single GCM/RCM model. Future research is thereby desirable to introduce multiple GCM/RCM ensembles and further investigate the inherent uncertainties to advance the performance of the proposed downscaling approach.

DATA AVAILABILITY STATEMENT

The raw data supporting the conclusion of this article will be made available by the authors, without undue reservation.

AUTHOR CONTRIBUTIONS

CT: Conceptualization, Methodology, Software, Data curation, Formal analysis, Writing—original draft. GH: Supervision, Project administration, Funding acquisition, Resources. YL: Guidance, Writing—review and editing. DY: Guidance,

Writing—review and editing. FW: Software, Writing—review. RD: Software, Writing—review.

FUNDING

This research was supported by the National Key Research and Development Plan (2016YFA0601502), Canada Research Chair Program, Natural Science and Engineering Research Council of Canada, Western Economic Diversification (15269), and MITACS.

SUPPLEMENTARY MATERIAL

The Supplementary Material for this article can be found online at: https://www.frontiersin.org/articles/10.3389/feart.2021.742840/full#supplementary-material

REFERENCES

Arcand, A., Wiebe, R., McIntyre, J., and Bougas, C. (2018). "Metropolitan Outlook 1: Economic Insights into 13 Canadian Metropolitan Economies," in Ottawa: Conference Board of Canada. Available at: https://www.conferenceboard.ca/e-library/abstract.aspx?did=9923.

Ashiq, M. W., Zhao, C., Ni, J., and Akhtar, M. (2010). GIS-based High-Resolution Spatial Interpolation of Precipitation in Mountain-plain Areas of Upper Pakistan for Regional Climate Change Impact Studies. *Theor. Appl. Climatol.* 99, 239–253. doi:10.1007/s00704-009-0140-y

Bechler, A., Vrac, M., and Bel, L. (2015). A Spatial Hybrid Approach for Downscaling of Extreme Precipitation fields. *J. Geophys. Res. Atmos.* 120, 4534–4550. doi:10.1002/2014JD022558

Bush, E., and Lemmen, D. S. (Editors) (2019). *Canada's Changing Climate Report*. Ottawa, ON: Government of Canada, 444. Available at: https://www.nrcan.gc.ca/sites/www.nrcan.gc.ca/files/energy/Climate-change/pdf/CCCR_FULLREPORT-EN-FINAL.pdf

Chen, H., Xu, C.-Y., and Guo, S. (2012). Comparison and Evaluation of Multiple GCMs, Statistical Downscaling and Hydrological Models in the Study of Climate Change Impacts on Runoff. *J. Hydrol.* 434-435, 36–45. doi:10.1016/j.jhydrol.2012.02.040

Dong, C., Huang, G., and Cheng, G. (2021). Offshore Wind Can Power Canada. *Energy* 236, 121422. doi:10.1016/j.energy.2021.121422

Feser, F., Rockel, B., von Storch, H., Winterfeldt, J., and Zahn, M. (2011). Regional Climate Models Add Value to Global Model Data: a Review and Selected Examples. *Bull. Am. Meteorol. Soc.* 92, 1181–1192. doi:10.1175/2011bams3061.1

Gharbia, S. S., Gill, L., Johnston, P., and Pilla, F. (2016a). Multi-GCM Ensembles Performance for Climate Projection on a GIS Platform. *Model. Earth Syst. Environ.* 2, 1–21. doi:10.1007/s40808-016-0154-2

Gharbia, S. S., Johnston, P., Gill, L., and Pilla, F. (2016b). Using GIS Based Algorithms for GCMs' Performance Evaluation. *Proc. 18th Mediterr. Electrotech. Conf. Intell. Effic. Technol. Serv. Citizen, MELECON* 2016, 1–6. doi:10.1109/MELCON.2016.7495476

Hay, J. E., and Oke, T. R. (1976). *The Climate of Vancouver*. Canada: Tantalus Research Vancouver.

Hessami, M., Gachon, P., Ouarda, T. B. M. J., and St-Hilaire, A. (2008). Automated Regression-Based Statistical Downscaling Tool. *Environ. Model. Softw.* 23, 813–834. doi:10.1016/j.envsoft.2007.10.004

Hewitson, B., and Crane, R. (1996). Climate Downscaling: Techniques and Application. *Clim. Res.* 7, 85–95. doi:10.3354/cr007085

Hopfield, J. J. (2018). Neural Networks and Physical Systems with Emergent Collective Computational Abilities. *Proc. Natl. Acad. Sci. U S A.* 79, 2554–2558. doi:10.1073/pnas.79.8.2554

Jury, M. W., Prein, A. F., Truhetz, H., and Gobiet, A. (2015). Evaluation of CMIP5 Models in the Context of Dynamical Downscaling over Europe. *J. Clim.* 28, 5575–5582. doi:10.1175/jcli-d-14-00430.1

Le, H. V., Bui, Q. T., Bui, D. T., Tran, H. H., and Hoang, N. D. (2020). A Hybrid Intelligence System Based on Relevance Vector Machines and Imperialist Competitive Optimization for Modelling Forest Fire Danger Using GIS. *J. Environ. Inform.* 36, 43–57. doi:10.3808/jei.201800404

LeCun, Y., Bengio, Y., and Hinton, G. (2015). Deep Learning. *Nature* 521, 436–444. doi:10.1038/nature14539

Li, Y. F., Li, Y. P., Huang, G. H., and Chen, X. (2010). Energy and Environmental Systems Planning under Uncertainty-An Inexact Fuzzy-Stochastic Programming Approach. *Appl. Energ.* 87, 3189–3211. doi:10.1016/j.apenergy.2010.02.030

Li, Z., Li, J. J., and Shi, X. P. (2020). A Two-Stage Multisite and Multivariate Weather Generator. *J. Environ. Inform.* 35.

Mearns, L. O., McGinnis, S., Korytina, D., Arritt, R., Biner, S., Bukovsky, M., et al. (2017). *The NA-CORDEX Dataset, Version 1.0. NCAR Clim. Data Gateway*. Boulder, Colorado: Boulder North Am. CORDEX Progr.

Metro Vancouver (2018). Climate 2050 Strategic Framework: Energy. Available at: http://www.metrovancouver.org/services/air-quality/AirQualityPublications/C2050-IssueAreaSummary-Energy.pdf#search=generating energy from waste.1

Notaro, M., Bennington, V., and Lofgren, B. (2015). Dynamical Downscaling-Based Projections of Great Lakes Water Levels*+. *J. Clim.* 28, 9721–9745. doi:10.1175/jcli-d-14-00847.1

Oke, T. R. (1976). The Distinction between Canopy and Boundary-layer Urban Heat Islands. *Atmosphere* 14, 268–277. doi:10.1080/00046973.1976.9648422

Ordieres-Meré, J., Ouarzazi, J., El Johra, B., and Gong, B. (2020). Predicting Ground Level Ozone in Marrakesh by Machine-Learning Techniques. *J. Environ. Inform.* 36, 93–106. doi:10.3808/jei.202000437

Pérez, J. C., Díaz, J. P., González, A., Expósito, J., Rivera-López, F., and Taima, D. (2014). Evaluation of WRF Parameterizations for Dynamical Downscaling in the Canary Islands. *J. Clim.* 27, 5611–5631. doi:10.1175/jcli-d-13-00458.1

Roberts, J. L., Tozer, C. R., Ho, M., Kiem, A. S., Vance, T. R., Jong, L M., et al. (2019). Reconciling Unevenly Sampled Paleoclimate Proxies: a Gaussian Kernel Correlation Multiproxy Reconstruction. *J. Environ. Inform.* 1–10. doi:10.3808/jei.201900420

Shrestha, N. K., and Wang, J. (2020). Water Quality Management of a Cold Climate Region Watershed in Changing Climate. *J. Environ. Inform.* 35, 56–80. doi:10.3808/jei.201900407

Song, P., Huang, G., An, C., Xin, X., Zhang, P., Chen, X., et al. (2021). Exploring the Decentralized Treatment of Sulfamethoxazole-Contained Poultry Wastewater through Vertical-Flow Multi-Soil-Layering Systems in Rural Communities. *Water Res.* 188, 116480. doi:10.1016/j.watres.2020.116480

Tian, C., Huang, G., Lu, C., Zhou, X., and Duan, R. (2021). Development of Enthalpy-Based Climate Indicators for Characterizing Building Cooling and Heating Energy Demand under Climate Change. *Renew. Sustain. Energ. Rev.* 143, 110799. doi:10.1016/j.rser.2021.110799

Tian, C., Huang, G., and Xie, Y. (2020). Systematic Evaluation for Hydropower Exploitation Rationality in Hydro-Dominant Area: A Case Study of Sichuan Province, China. *Renew. Energ.*

Wang, X., Huang, G., Lin, Q., Nie, X., Cheng, G., Fan, Y., et al. (2013). A Stepwise Cluster Analysis Approach for Downscaled Climate Projection - A Canadian Case Study. *Environ. Model. Softw.* 49, 141–151. doi:10.1016/j.envsoft.2013.08.006

Wang, X., Huang, G., Lin, Q., Nie, X., and Liu, J. (2015). High-resolution Temperature and Precipitation Projections over Ontario, Canada: A Coupled Dynamical-Statistical Approach. *Q.J.R. Meteorol. Soc.* 141, 1137–1146. doi:10.1002/qj.2421

Westermann, P., Welzel, M., and Evins, R. (2020). Using a Deep Temporal Convolutional Network as a Building Energy Surrogate Model that Spans Multiple Climate Zones. *Appl. Energ.* 278, 115563. doi:10.1016/j.apenergy.2020.115563

Wilby, R. L., Charles, S. P., Zorita, E., Timbal, B., Whetton, P., and Mearns, L. O. (2004). Guidelines for Use of Climate Scenarios Developed from Statistical Downscaling Methods. Supporting material of the Intergovernmental Panel on Climate Change. Available from the DDC of IPCC TGCIA, 27. Available at: https://www.ipcc-data.org/guidelines/dgm_no2_v1_09_2004.pdf

Yu, B. Y., Wu, P., Sui, J., Ni, J., and Whitcombe, T. (2020). Variation of Runoff and Sediment Transport in the Huai River–A Case Study. *J. Environ. Inf.* 35 (2), 138–147. doi:10.3808/jei.202000429

Zeng, Y., Cai, Y., Huang, G., and Dai, J. (2011). A Review on Optimization Modeling of Energy Systems Planning and GHG Emission Mitigation under Uncertainty. *Energies* 4, 1624–1656. doi:10.3390/en4101624

Conflict of Interest: The authors declare that the research was conducted in the absence of any commercial or financial relationships that could be construed as a potential conflict of interest.

frontiers in Earth Science

ORIGINAL RESEARCH
published: 29 September 2021
doi: 10.3389/feart.2021.759534

Changes in and Modelling of Hydrological Process for a Semi-Arid Catchment in the Context of Human Disturbance

Yue Liu[1,2,3], *Jianyun Zhang*[1,2,3,4], *Qinli Yang*[5], *Xiong Zhou*[6] *and Guoqing Wang*[1,2,3,4]*

[1]College of Hydrology and Water Resources, Hohai University, Nanjing, China, [2]Yangtze Institute for Conservation and Development, Nanjing, China, [3]Research Center for Climate Change, Ministry of Water Resources, Nanjing, China, [4]State Key Laboratory of Hydrology–Water Resources and Hydraulic Engineering, Nanjing Hydraulic Research Institute, Nanjing, China, [5]School of Resources and Environment, University of Electronic Science and Technology of China, Chengdu, China, [6]China-Canada Center for Energy, Environment and Ecology Research, UofR-BNU, Beijing Normal University, Beijing, China

Hydrological modelling is of critical importance to flood control. However, flood forecasting in semi-arid region is a great challenge to hydrologists, particularly in a changing environment. Taking the Zhulong River catchment located in north China as a case, the performance of GR4J model for hydrological modelling was investigated based on the analysis for changes in hydrological process of three periods defined as natural period (1967–1979), moderate human impact period (1980–1996) and intensive human impact period (1997–2015). Results show that 1) the annual precipitation and temperature of the catchment both presented upward trends, while the annual observed runoff exhibited a significant downward trend in the time span from 1967 to 2015; 2) the correlations between runoff and precipitation were comparatively higher on both monthly and annual scales in natural period than those in human disturbed periods; 3) both annual runoff and daily peak discharge in human disturbed periods decreased relative to those in natural period due to the environmental changes; 4) the GR4J model performed well for runoff simulations in natural period but gradually lost its applicability with the intensification of human activities. It is essential to improve the accuracy of hydrological modelling under a changing environment in further studies.

Keywords: the Zhulong River catchment, semi-arid catchment, human activities, hydrological process, GR4J model, hydrological modelling

OPEN ACCESS

Edited by:
Yulei Xie,
Guangdong University of Technology, China

Reviewed by:
Qin Guanghua,
Sichuan University, China
Shuangyan Jin,
Institute of Yellow River Hydrology and Water Resources, China

***Correspondence:**
Guoqing Wang
gqwang@nhri.cn

Specialty section:
This article was submitted to Hydrosphere, a section of the journal Frontiers in Earth Science

Received: *16 August 2021*
Accepted: *14 September 2021*
Published: *29 September 2021*

Citation:
Liu Y, Zhang J, Yang Q, Zhou X and Wang G (2021) Changes in and Modelling of Hydrological Process for a Semi-Arid Catchment in the Context of Human Disturbance. Front. Earth Sci. 9:759534. doi: 10.3389/feart.2021.759534

INTRODUCTION

The evolution of water cycle under the changing environment is a very complex process, which has been an important issue in the "Panta Rhei-Everything Flows" project (2013–2022) of IHAS (International Association of Hydrological Science) (Montanari et al., 2013). Climate change and human activities are two main driving factors affecting water cycle process under the changing environment (Wang et al., 2020). In the context of global warming, the temporal and spatial distribution of precipitation, evaporation and runoff have changed significantly (Dai et al., 2018; Charles et al., 2020). While human activities have changed the hydrological process in a basin by means of urban expansion, water extraction, water conservancy project construction and so on (Song et al., 2013; Liang et al., 2020). The acceleration of urbanization has not only changed underlying

surface of the basin, but also changed runoff yield and confluence laws as well as groundwater recharge conditions (Wang et al., 2018). The development of industrial and agricultural production has caused a substantial increase in water resources consumption, which results in corresponding changes in surface runoff, dry season runoff and groundwater level (Leng et al., 2015; Yang P. et al., 2017). The construction of water conservancy projects can effectively reduce discharge in high flow seasons and increase discharge in low flow seasons to a certain extent (Wang et al., 2019; Varentsova et al., 2020).

Hydrological models are mathematical models constructed to simulate hydrological cycles and describe hydrophysical processes. They are essential means to study the laws of hydrology and nature (Xu, 2010; Krysanova et al., 2020) and effective tools to solve practical problems, e.g., hydrological forecasting, water resources management, and water conservancy project planning and design (Musuuza et al., 2020; Thatch et al., 2020; Turner et al., 2020). Liu et al. (2019) applied the VIC model to forecast the annual maximum floods and annual first floods in the YarlungZangbo River based on precipitation and temperature data, and provided an early warning with extended lead time. Maier and Dietrich (2016) investigated the application of SWAT model for the development of water saving irrigation control strategies in Northern Germany and showed a future increase of irrigation demand in humid regions. Du et al. (2016) adopted the Xinanjiang model to simulate inflows of reservoirs and flood hydrographs of all sub-catchments in the Ganjiang River basin and established simple reservoir operation rules for calculating outflows.

Previous studies have shown that most of the hydrological models can simulate streamflow processes well in humid and semi-humid regions, but hydrological modelling in arid and semi-arid regions has always been a great challenge to hydrologists, particularly under the changing environment (Molina-Navarro et al., 2016; Bugan et al., 2020). The GR4J model, as a lumped conceptual model, has been widely applied in various climate regions of the world because of its distinctive characteristics in principle and structure (Boumenni et al., 2017; Sezen and Partal, 2019). Zeng et al. (2019) investigated the predictive ability and robustness of the GR4J model with time-varying parameters under changing environments and improved the performance of streamflow simulations in Wei River Basin. Ghimire et al. (2020) used a range of hydrological modelling approaches for flow simulation and forecasting in the Ayeyarwady Basin and revealed that the GR4J model performed best in simulations and yielded the least biases in daily flow forecasting. Grigg and Hughes (2018) implied a modified GR4J model in a forested headwater catchment in southwest Australia and improved the predictions for catchments with significant changes in vegetation cover.

Studies on changes in hydrological sequence and simulation under the changing environment for large size rivers, e.g., the Amazon River (Jahfer et al., 2020), Yangtze River (Sun et al., 2019), Yellow River (Huo et al., 2020) have attracted sufficient attentions from river managers and state authorities. However, regional flooding and water shortage issues have been increasingly serious during the past decades due to global warming and increasing water demand (Wilkinson et al., 2019; Omer et al., 2020), and attention to these issues should be paid as well. The Daqing River is an important tributary of Hai River, and the Beijing-Tianjin-Hebei region in Daqing River basin is the political, cultural and technological center of China, as well as an important engine for the country's economic development (Li et al., 2016). Since the 1980s, human activities have caused significant changes in the underlying surface of this basin, and runoff has decreased severely. However, the rapid development of Daqing River basin increases the demand for water resources, resulting in prominent problem of water shortage (Cui et al., 2019). It is therefore of great significance to investigate variation characteristics of hydrological series and hydrological modelling under such an changing environment to support water resources management and flood control of the Daqing River basin. Taking the Zhulong River catchment, an agricultural catchment in the Daqing River basin as a case, the main objectives of the paper are to investigate changes in hydrological process in different periods and to test performance of the GR4J model for extension of the model application to catchments in semi-arid regions.

DATA AND METHOD

Study Catchment and Data Sources

The Zhulong River is in southern branch of the Daqing River in Hai River basin, and consists of three tributaries: the Sha, Ci and Mengliang rivers. It stretches from Taihang Mountains in the west to Baiyang Lake in the north, crossing 14 counties and cities in Shanxi and Hebei provinces. The Beiguocun hydrometric station (east longitude 115°23′E, north latitude 38°19′N) is the control station of Zhulong River, covering a drainage area of 8,550 km^2. The main channel is 261.3 km long, with a longitudinal slope 2.5‰ and an average basin width 88.5 km. Terrain of the catchment is high in the northwest and low in the southeast. The upper reaches are covered by forested mountains, middle reaches are mainly undulating hills, and lower reaches are dominated by flat plains (**Figure 1**). The Zhulong River catchment is in the temperate semi-arid continental monsoon climate zone with an annual average temperature of 12.2°C. It has a mean annual precipitation of 523.0 mm which is extremely uneven with more than 80% concentrated in flood season. There are three large reservoirs in the catchment - Wangkuai, Koutou and Hengshanling reservoirs which are located on the Sha river, Sha river's tributary Gao river and Ci river, respectively. Each of the three reservoirs has a storage capacity of more than 100 million m^3, among which the Wangkuai Reservoir has the largest capacity, about 1.39 billion m^3. The control area of these reservoirs accounts for 51% of the total catchment, with main functions flood control and irrigation, as well as power generation and aquaculture.

Taking the Zhulong River catchment controlled by Beiguocun Hydrological Station as a study area, the DEM elevation data with a resolution of 30 m were obtained from the ASTER GDEM data set (http://www.gscloud.cn). The daily runoff data from 1967 to 2015 were extracted from the Hydrological Yearbook issued by the Ministry of Water Resources, China. Daily precipitation and

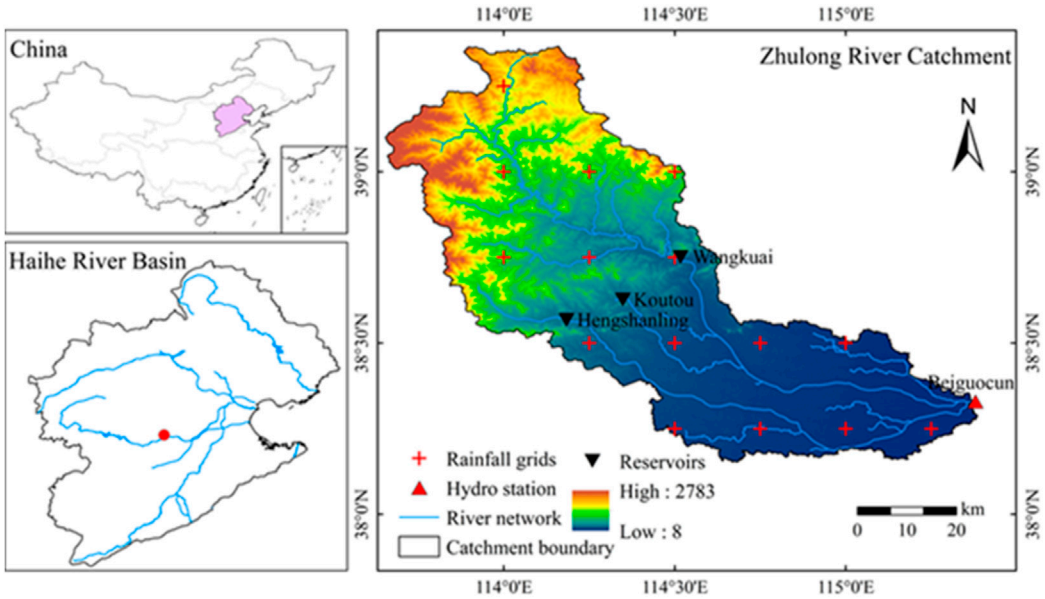

FIGURE 1 | The terrain, drainage and stations distribution of the Zhulong River catchment.

daily average air temperature over 1967–2015 were collected from the China Meteorological Administration (CMA, http://cdc.cma.gov.cn). The evaporation was calculated using Penman's formula based on the daily data set of surface climate from CMA, then the data of precipitation, runoff and evaporation were compiled and processed as inputs to drive the hydrological model.

Methodologies

Research Framework

Based on the study catchment and collected data sets, this paper investigated the variation trends of hydrometeorological variables (precipitation, temperature and runoff) from 1967 to 2015 by using Mann-Kendall rank test. Based on date sequence segment of streamflow, relationships between runoff and precipitation as well as hydrological processes under a same precipitation condition were investigated for different segmented periods. Finally, the GR4J model was applied to simulate daily and monthly discharge for periods with different degrees of human disturbance to reveal the impact of environmental changes on hydrological modelling. The research framework is shown in **Figure 2**.

Mann-Kendall Rank Test

The Mann-Kendall rank test is a nonparametric method to evaluate trends in time series of climate and hydrological elements (Mann, 1945; Kendall, 1955). The method can effectively distinguish whether a certain time series is in a natural fluctuation or a certain trend without a specific distribution test and has been widely applied all over the world (Caloiero, 2017; Hu et al., 2020). The standardized statistic Z_{MK} of the time series is defined (Yang Z. et al., 2017), with a positive value representing an upward trend, while a negative one indicating a downward trend. If $|Z_{MK}| < Z_{\alpha/2}$, the trend was not significant. For a significance level $\alpha = 5\%$, then $Z_{\alpha/2} = 1.96$.

GR4J Model

The GR4J model is a conceptual lumped hydrological model, proposed by French researchers (Oliveira et al., 1999). It has been verified in more than 400 regions with different climatic conditions after continuous improvement and development by hydrological scholars (Perrin et al., 2003; Moine et al., 2008). So far, the model has been widely used in water resources management, flood forecasting, and low flow forecasting in global catchments (Dhemi et al., 2010; Aufar and Sitanggang, 2020). The GR4J model is divided into two modules: production store and routing store, and both of them are calculated by a nonlinear reservoir. The main calculation process is shown in **Figure 3**.

When calibrating the model, the value ranges of model parameters are determined, then different parameter sets are selected to run the model, and objective functions are calculated to reflect pros and cons of simulation results until the optimal. In order to better reflect the effect of hydrological model on runoff simulations, the Nash Sutcliffe Efficiency (NSE) and Relative Error (RE) are selected to describe the degree of agreement between simulated discharge series and observed one (Nash and Sutcliffe, 1970).

RESULTS AND DISCUSSION

Variability of Annual Runoff in the Context of Intensive Human Activities

Precipitation and temperature are the most significant meteorological elements affecting the variations of runoff. The long-term variations of annual precipitation, air temperature over the catchment and the observed runoff at the Beiguocun hydrometric station during 1967–2015 are shown in **Figure 4**. The variation trends of annual precipitation, temperature and runoff were tested by using Mann-Kendall rank test and

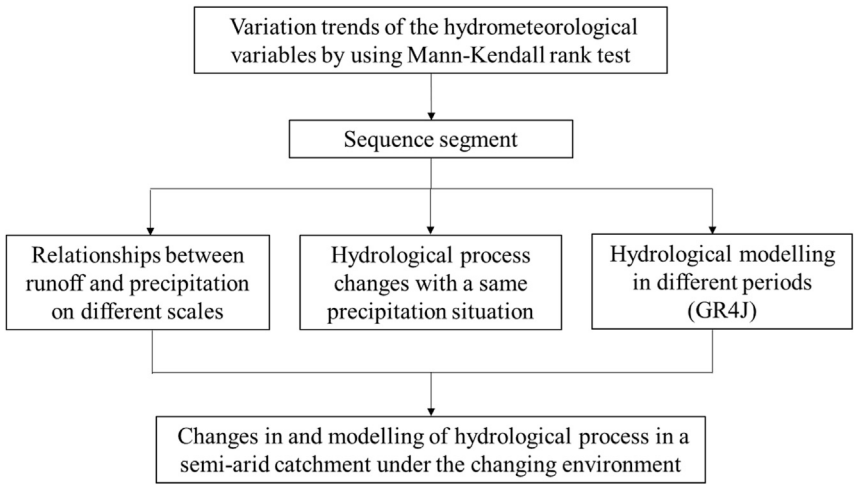

FIGURE 2 | Research framework.

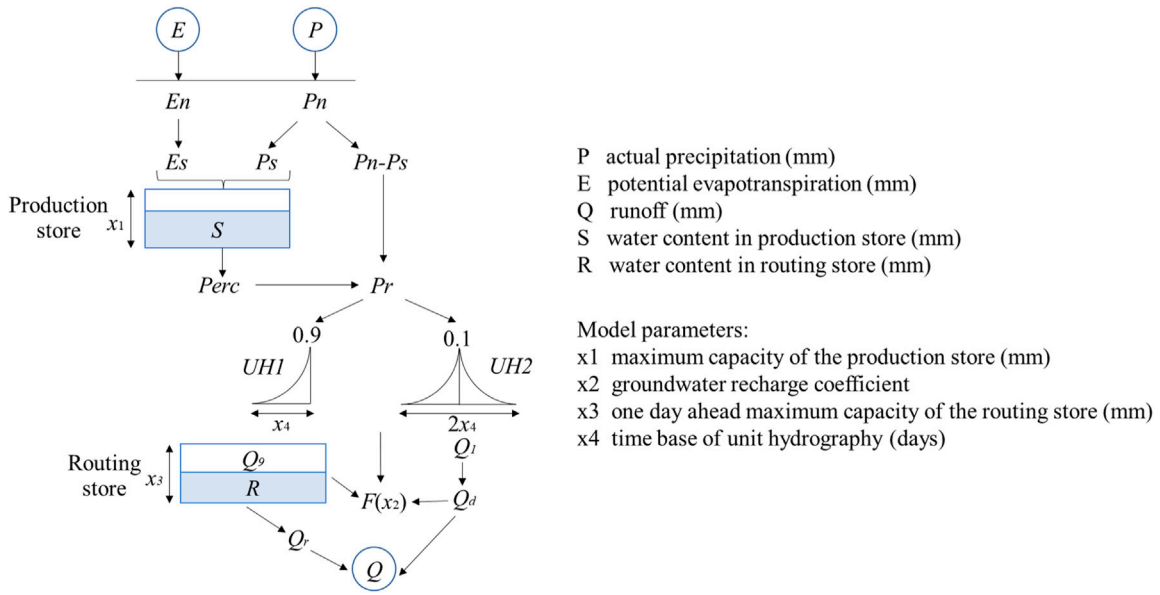

FIGURE 3 | Structure of the GR4J model (Oliveira et al., 1999).

summarized in **Table 1**, in which slope coefficient (S) illustrates the magnitude of upward or downward trend of a series.

Figure 4 and **Table 1** show that the annual temperature series exhibited a significant upward trend with a linear rising rate of 0.29°C/10 years, while annual precipitation series presented a slight upward trend (10.39 mm/10 years). Although the climate was getting warmer and wetter in the Zhulong River catchment during 1967–2015, the observed runoff series exhibited a significant downward trend with a linear decline rate of 9.21 mm/10 years probably due to the influence of human activities. According to the records in the local year book series, numerous water conservancy projects have been constructed successively in the Zhulong River catchment since 1970s for supporting industrial and agricultural development (Zheng et al., 2020). The continuous increase in water supply led to a decline in runoff series because of pumping water from the stream (Li et al., 2019). According to the degree of human activities disturbance and long-time variations of runoff, the research sequence is divided into three periods: the natural period of 1967–1979 in which the catchment kept a natural state with limited human activities; the moderate human impact period of 1980–1996 in which water conservancy projects were in operation and human activities was gradually intensified; the intensive human impact period of 1997–2015 in

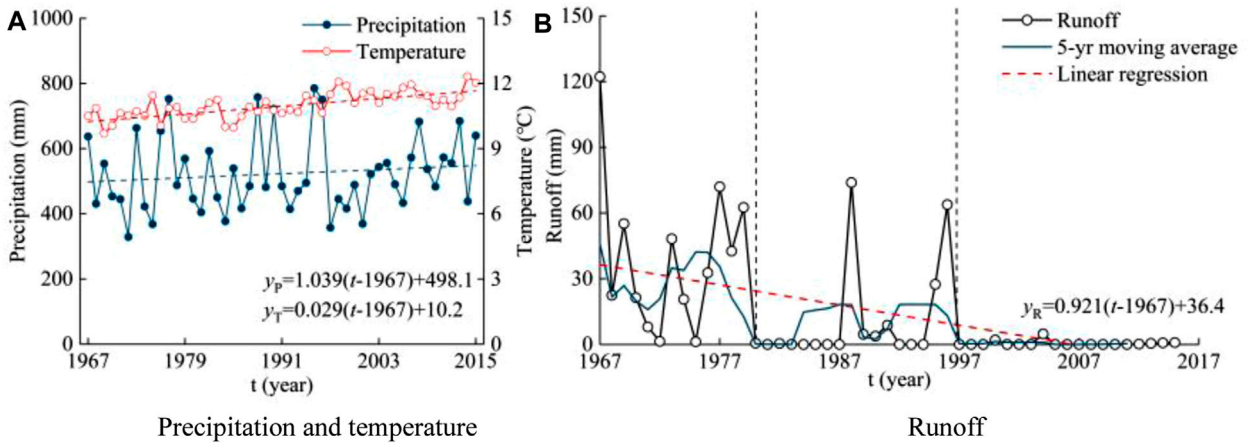

FIGURE 4 | Long-term variations of annual precipitation, air temperature over the Zhulong River catchment **(A)** and observed runoff at the Beiguocun hydrometric station **(B)** during 1967–2015.

TABLE 1 | Trend test results of annual precipitation, temperature and runoff during 1967–2015.

Elements	S	Trend	ZMK	Significance
Annual precipitation	1.039 mm/year	↑	1.302	No
Annual temperature	0.029°C/year	↑	4.973	Yes
Annual runoff	–0.921 mm/year	↓	-5.260	Yes

which, industry and agriculture were both highly developed, and human activities had a strong and stable impact.

Relationships Between Runoff and Precipitation in Different Periods

In order to analyze the relationships between runoff and precipitation in the Zhulong River catchment under a changing environment, the runoff-precipitation scatter plots of the three periods on monthly and annual scales are shown in **Figure 5**. The average seasonal distribution of observed runoff in the three periods is shown in **Figure 6**.

Figure 5 shows that correlations between runoff and precipitation in natural period was higher than those in periods with human disturbance, the correlation decreased with the intensification of human activities. The runoff-precipitation scattered points moved downward with the passage of time, which meant that the runoff generated by a same magnitude of precipitation decreased continuously. **Figure 6** shows that runoff concentrated in flood season from July to October for all the three periods. In natural period, runoff in flood season accounts for 76% of the annual total. Monthly runoff in human disturbed periods was much lower than that in natural period, particularly for the intensive human impact period. For August, runoff in moderate and intensive human impact periods decreased by 60.0 and 99.5% relative to that in natural period.

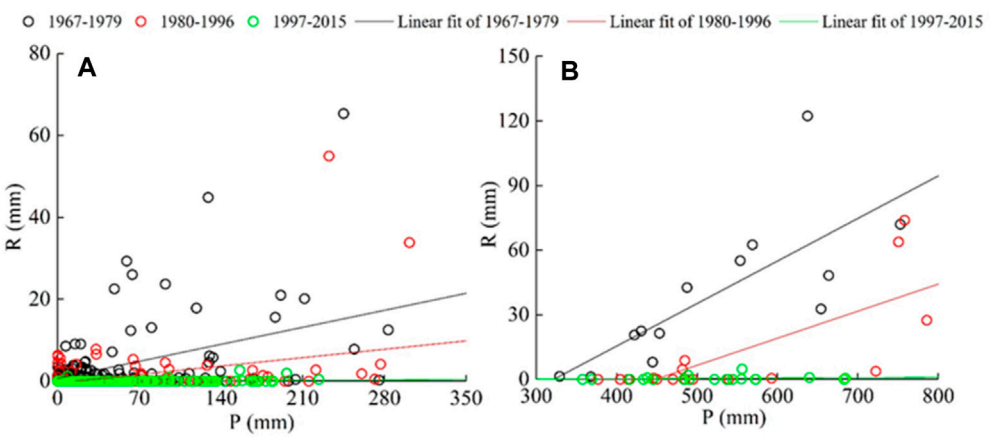

FIGURE 5 | Relationships between runoff and precipitation on monthly **(A)** and annual **(B)** scales of the Zhulong River catchment during 1967–2015.

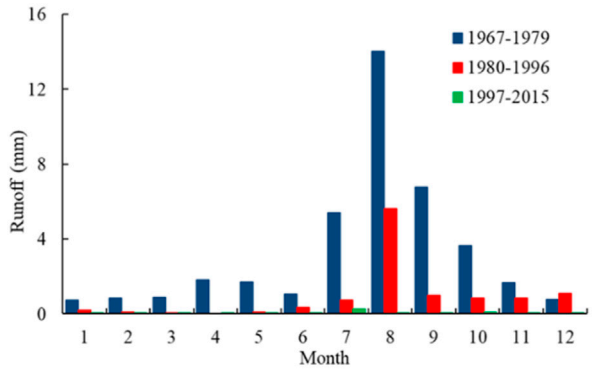

FIGURE 6 | The average seasonal distributions of observed runoff in the Zhulong River catchment during 1967–2015.

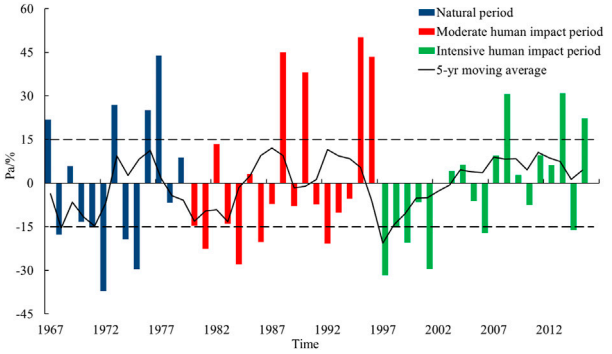

FIGURE 7 | The percentage of precipitation anomalies during 1967–2015 in the Zhulong River catchment.

Changes in Daily Discharge Process for Typical Years With a Same Precipitation Situation

Human activities have not only changed the correlation between runoff and precipitation, but also altered the process of runoff yield and confluence. In different periods and under different intensities of human activities, the runoff processes are different even with a same precipitation situation. Research years are classified according to the percentage of precipitation anomalies (Kasei et al., 2010) from 1967 to 2015 (**Figure 7**), into wet years (PA > 15%), normal years (-15% < PA < 15%) and dry years (PA < -15%) (Zhu et al., 2019). There are four wet years, five normal years and four dry years in natural period, four wet years, nine normal years and four dry years in moderate human impact period, three wet years, 11 normal years and five dry years in intensive human impact period. Then typical wet, normal and dry years are selected based on the classification results in different periods to compare daily discharge processes, as is shown in **Figure 8** (wet years are 1977, 1996, and 2013; normal years are 1978, 1991, and 2010; dry years are 1974, 1986, and 1999). The hydrological element information of typical years is shown in **Table 2**.

Figure 8 shows that the precipitation could always generated runoff in natural period, no matter in the wet year, normal year or dry year. During the moderate human impact period, the discharge process occurred only in wet and normal years. The flow ran dry for most time in intensive human impact period except for a certain runoff in the wet year. The peak discharge of typical years decreased with the intensification of human activities even under the same precipitation situation. The peak discharge of the wet year in natural period is 653 m^3/s, it drops to 378 m^3/s in moderate human impact period and 3.74 m^3/s in intensive human impact period. In natural period, precipitation in dry season could produce obvious discharge (from January to June in 1974, 1977, and 1978), but the flow in dry season was almost zero in human disturbed periods and discharge processes tended to rise and fall steeply. Statistical results in **Table 2** shows that the runoff of typical years varied greatly in different periods even though there was little difference in annual precipitation. Compared with the natural period, runoff in moderate and intensive human impact period decreased by 11.4 and 99.3% for wet years, 79.4 and 100% for normal years, 100 and 100% for dry years, respectively. Human activities had a greater impact in normal and dry years.

Hydrological Modelling for the Zhulong River Catchment in Natural and Human Disturbed Periods

In order to evaluate the performance of streamflow simulation in the Zhulong River catchment under the complex changing environment, data series of the three periods were segmented into calibration and verification periods. Then the GR4J model was applied to simulate daily and monthly discharge. The performance of GR4J model in the Zhulong River catchment is presented in **Table 3**. Daily and monthly observed and simulated discharge is shown in **Figure 9**.

Tables 3 and **Figure 9** show that the GR4J model could perform well in natural period (1967–1979) with daily and monthly NSEs of calibration period reaching 0.62 and 0.82, respectively, the REs were controlled within 5% on both scales. Additionally, the daily and monthly NSEs of verification period could reach 0.58 and 0.79, respectively, the REs were controlled within 20%. However, performance of the model was not satisfactory in human disturbed periods, with NSEs no greater than 0.3 during the moderate human impact period (1980–1996) and even less than zero during the intensive human impact period (1997–2015). Furthermore, the REs fluctuated with large amplitude and all exceeded 100% for both calibration and verification periods. During the moderate human impact period, the GR4J model could simulate a few flood peaks when precipitation and runoff were high enough, and discharge in the rest time was always over simulated. The observed discharge mostly approached zero during the intensive human impact period, meaning that the runoff had very little response to precipitation. This demonstrated that the GR4J model could not depict the laws of runoff yield and confluence any more under the complex changing environment. In **Figure 9**, most of the simulated peaks were smaller than observed ones in flood season during the natural period, which was more obvious on daily scale. This phenomenon also occurred in moderate human impact period even when there were only a few peaks being simulated. The main reason is that the Zhulong River is located

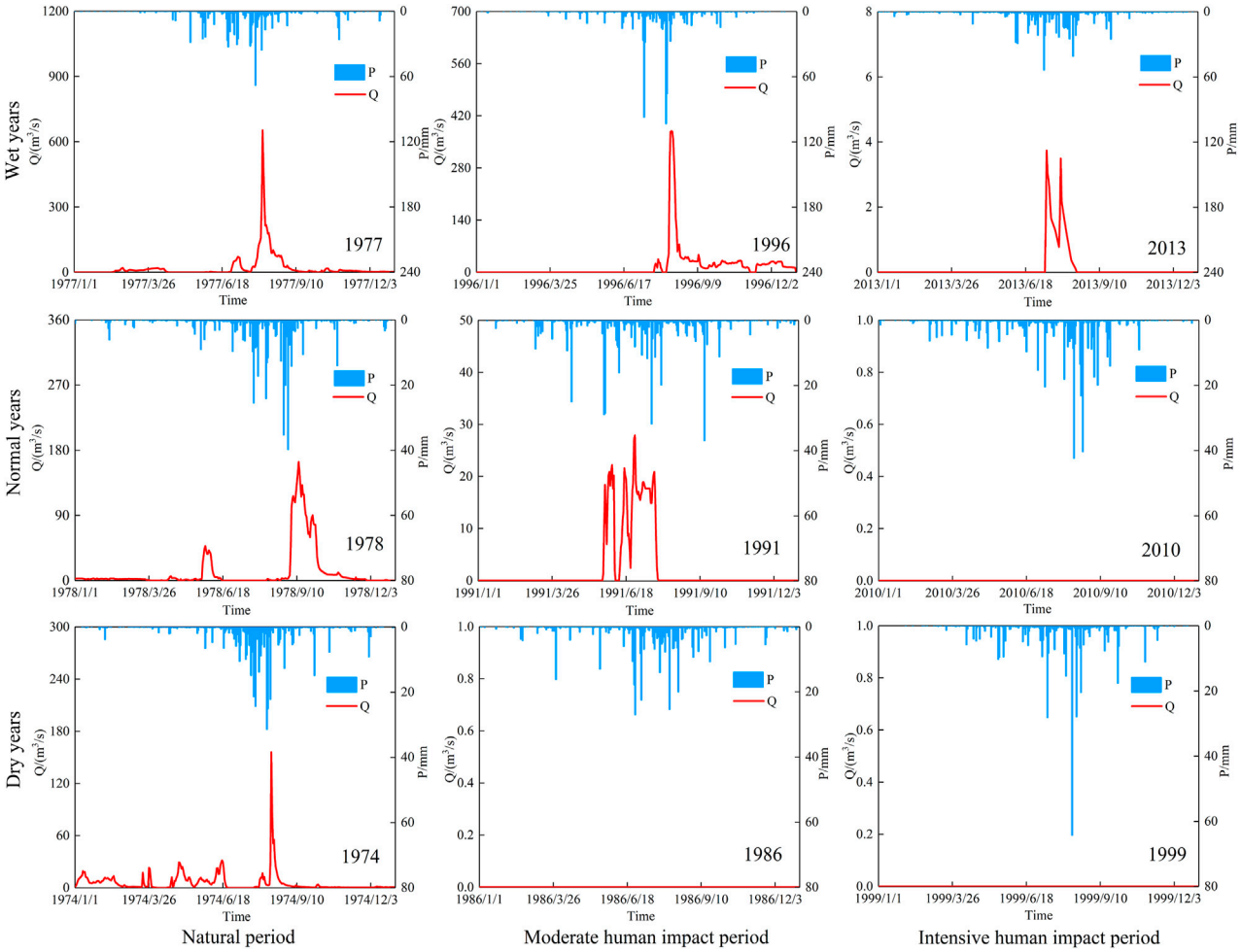

FIGURE 8 | Daily discharge processes for typical years with a same precipitation situation in different periods.

TABLE 2 | Hydrological element information of typical years in different periods.

Periods	Wet years			Normal years			Dry years		
	Year	P (mm)	R (mm)	Year	P (mm)	R (mm)	Year	P (mm)	R (mm)
Natural period	1977	752.7	72.0	1978	487.5	42.7	1974	422.1	20.6
Moderate human impact period	1996	750.5	63.8	1991	484.8	8.8	1986	416.5	0
Intensive human impact period	2013	684.4	0.5	2010	483.4	0	1999	416	0

TABLE 3 | Performance measurements of the GR4J model for daily and monthly discharge simulations in the Zhulong River catchment.

Periods	Time	Scale	Calibration period		Validation period	
			NSE	RE (%)	NSE	RE (%)
Natural period	1967–1975	Daily	0.62	4.1	0.58	18.3
	1976–1979	Monthly	0.82	4.1	0.79	18.3
Moderate human impact period	1980–1990	Daily	0.11	361.9	0.22	149.0
	1991–1996	Monthly	0.11	361.9	−0.15	149.0
Intensive human impact period	1997–2010	Daily	−30.67	1,345.7	−739.02	2014.6
	2011–2015	Monthly	−13.80	1,345.7	−606.25	2014.6

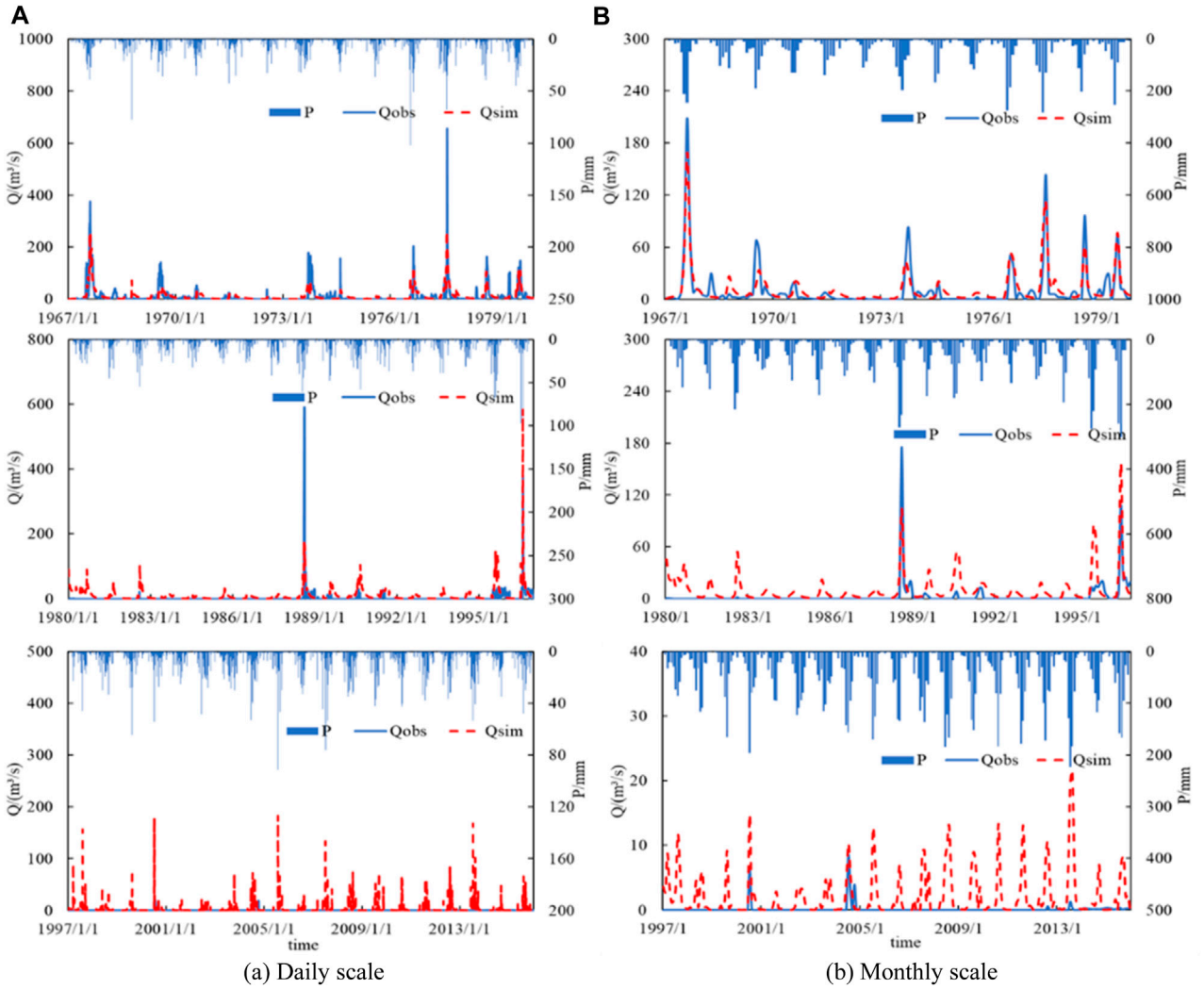

FIGURE 9 | Daily **(A)** and monthly **(B)** simulated and observed discharge (m³/s) during the three periods in the Zhulong River catchment.

in the semi-arid area, and runoff generation mechanism is dominated by the excess infiltration. While the GR4J, as a lumped hydrological model, cannot capture the changes in high intensity rainfall events accurately, resulting in smaller simulated peaks. All in all, the GR4J model may be useful for investigating streamflow simulations in the Zhulong River catchment during the natural period but gradually loses its applicability with the intensification of human activities.

DISCUSSION

Climate change and human activities are two dominant factors affecting the hydrological cycle. Climate change affects the total amount of water resources and their spatial and temporal distribution mainly through variations of precipitation and temperature. The impacts of human activities on runoff can be divided into direct ones caused by water resources development and utilization and indirect ones caused by changes in the underlying surface of the catchment. With upward trends in annual precipitation and temperature from 1967 to 2015, human activities might be a main reason for runoff decrease in the Zhulong River catchment.

Since the late 1960s, a number of large and small reservoirs (Wangkuai Reservoir and so on) have been successively established in the Zhulong River catchment. The reservoir regulation not only ensures water demand for industrial and agricultural development, but also affects the fluctuation of natural runoff. The inflow changes of Wangkuai Reservoir during 1967–2015 is shown in **Figure 10**.

Figure 10 shows that although the Wangkuai reservoir is located in the upstream of Zhulong River and its controlled area only accounts for 44% of the total catchment, the inflow of the reservoir during 1967–2015 is always larger than that of Beiguocun hydrometric station. The reservoir plays a crucial part in regulating natural discharge of the catchment, with flood control in high flow years and water storage in low flow years, the regulation in low flow years is more significant in the Zhulong River catchment. During the intensive human impact period (1997–2015), when flow of the catchment always ran dry,

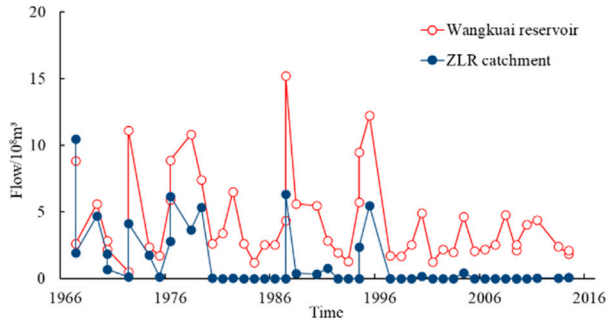

FIGURE 10 | Variations of annual flow (10^8 m^3) in the Wangkuai reservoir and Beiguocun hydrometric station.

the stored water in reservoirs ensured normal production and life of this area. As one of the main agricultural areas in North China Plain, the Zhulong River catchment is mainly covered by farmland and grassland. During the study period, with decrease of runoff in this catchment, water area shrank gradually, resulting in the changes of agricultural production structure (paddy field area decreased while dry land area increased). Meanwhile, with the acceleration of urbanization, impervious area (urban and rural land) in this catchment increased significantly, shortening the confluence time of runoff.

With the influence of human activities, the contradiction between supply and demand of water resources in the Zhulong River catchment and even the whole Hai River basin gradually intensified. The annual water resources and water consumption of Hai River basin during the intensive human impact period (1997–2015) show that although industrial structure has been optimized and water use efficiency has been improved since the 21th century, the amount of water resources is always less than water consumption, with years in this period mostly normal and low flow years except for a high flow year 2012. Since 2003, water for natural environment has been included into the statistical category of water resources in China, and has grown at a rate of 170 million m^3 per year in Hai River basin, which further exacerbates water stress in this area. During the intensive human impact period, the Hai River basin cannot achieve self-sufficiency in water resources, and it meets the daily needs of production and life mainly through inter-basin water transfer projects (the Yellow River Diversion Project and South-to-North Water Diversion Project), the Zhulong River catchment is the same. In general, the influence of human activities on runoff in the Zhulong River catchment is mainly reflected in reservoir regulation, land use change and water resources utilization. In addition, due to severe shortage of water resources, groundwater in this area has been seriously overexploited, which results in a decline in groundwater level, as well as a reduction of runoff in this catchment.

The influence of human activities on runoff was limited during the natural period, so the GR4J model could capture main features of hydrological processes and obtain a good simulation accuracy for the Zhulong River catchment. However, the intensification of human activities affects not only hydrological regimes, but also hydrological modelling, as it complicates the regional water cycle process. Tests of challenges to hydrological modelling in semi-arid catchments under the changing environment should be enhanced in further studies.

CONCLUSION

The annual precipitation and temperature both presented upward tends by Mann-Kendall rank test, with rising rates 10.39 mm/10 years and 0.29°C/10 years respectively, while the annual runoff exhibited a significant downward trend with a decline rate of 9.21 mm/10 years probably due to the influence of human activities. According to the degree of human disturbance and long-time variations of runoff, the research sequence was divided into three periods (natural period from 1967 to 1979, moderate human impact period from 1980 to 1996 and intensive human impact period from 1997 to 2015) to investigate the changes in hydrological process and hydrological modelling under the changing environment.

Correlations between runoff and precipitation in natural period were higher than those in periods with human disturbance on monthly and annual scales. The correlation decreased with the intensification of human activities. Runoff concentrated in flood season from July to October for all the three periods. Monthly runoff in human disturbed periods was much lower than that in natural period, particularly for the intensive human impact period. Both annual runoff and peak discharge in human disturbed periods decreased relative to those in natural period with a same precipitation situation due to the environmental changes. Human activities had a greater impact in normal and dry years.

The GR4J model performed well for streamflow simulations in the Zhulong River catchment during the natural period. However, the model's performance was not satisfactory in periods with human disturbance. During the moderate human impact period, the GR4J model could still catch several flood peaks, but when came to the intensive human impact period, the model completely lost its applicability.

Changes of underlying surface have altered the confluence process in the catchment, and human activities like water resources utilization and water conservancy projects have a more significant and direct effect on runoff reduction, which presents more challenges for hydrological simulations in semi-arid areas. It also raises higher requirements for hydrological models to quickly assess water resources under the changing environment with complex human disturbance.

DATA AVAILABILITY STATEMENT

The original contributions presented in the study are included in the article/supplementary material, further inquiries can be directed to the corresponding author.

AUTHOR CONTRIBUTIONS

JZ and GW designed the study and analyzed results and improved the manuscript. YL performed calculations and drafted the paper. XZ collected hydro-meteorological data, and QY reviewed the document and edited the final version.

FUNDING

Project supported by the National Key Research and Development Program of China (No.2016YFA0601501), the National Natural Science Foundation of China (Grant Nos 41830863, 51879162, 51609242, 52079026, 51779146, 41601025) and The Belt and Road Fund on Water and Sustainability of the State Key Laboratory of Hydrology-Water Resources and Hydraulic Engineering (Grant No. 2019nkzd02).

REFERENCES

Aufar, Y., and Sitanggang, I. S. (2020). Parameter Optimization of Rainfall-Runoff Model GR4J Using Particle Swarm Optimization on Planting Calendar. *Int. J. Adv. Sci. Eng. Inf. Tech.* 10 (6), 2575–2581. doi:10.18517/ijaseit.10.6.9110

Boumenni, H., Bachnou, A., and Alaa, N. E. (2017). The Rainfall-Runoff Model GR4J Optimization of Parameter by Genetic Algorithms and Gauss-Newton Method: Application for the Watershed Ourika (High Atlas, Morocco). *Arab J. Geosci.* 10 (15), 343. doi:10.1007/s12517-017-3086-x

Bugan, R., García, C. L., Jovanovic, N., Teich, I., Fink, M., and Dzikiti, S. (2020). Estimating Evapotranspiration in a Semi-arid Catchment: A Comparison of Hydrological Modelling and Remote-Sensing Approaches. *Water SA* 46 (2), 158–170. doi:10.17159/wsa/2020.v46.i2.8231

Charles, S. P., Chiew, F. H. S., Potter, N. J., Zheng, H., Fu, G., and Zhang, L. (2020). Impact of Downscaled Rainfall Biases on Projected Runoff Changes. *Hydrol. Earth Syst. Sci.* 24 (6), 2981–2997. doi:10.5194/hess-24-2981-2020

Cui, H., Xiao, W., Zhou, Y., Hou, B., Lu, F., and Pei, M. (2019). Spatial and Temporal Variations in Vegetation Cover and Responses to Climatic Variables in the Daqing River Basin, North China. *J. Coastal Res.* 93 (sp1), 450–459. doi:10.2112/si93-059.1

Dai, A., Zhao, T., and Chen, J. (2018). Climate Change and Drought: a Precipitation and Evaporation Perspective. *Curr. Clim. Change Rep.* 4 (3), 301–312. doi:10.1007/s40641-018-0101-6

Dhemi, H., Muljana, W., and Munajat, C. M. (2010). "Rainfall-Runoff Modeling of Citarum Hulu River Basin by Using GR4J," in Paper presented at the World Congress on Engineering, London, June 30–July 2, 2010.

Du, J., Zheng, D., Xu, Y., Hu, S., and Xu, C. (2016). Evaluating Functions of Reservoirs′ Storage Capacities and Locations on Daily Peak Attenuation for Ganjiang River Basin Using Xinanjiang Model. *Chin. Geogr. Sci.* 26 (6), 789–802. doi:10.1007/s11769-016-0838-6

Ghimire, U., Agarwal, A., Shrestha, N. K., Daggupati, P., Srinivasan, G., and Than, H. H. (2020). Applicability of Lumped Hydrological Models in a Data-Constrained River Basin of Asia. *J. Hydrol. Eng.* 25 (8), 05020018. doi:10.1061/(ASCE)HE.1943-5584.0001950

Grigg, A. H., and Hughes, J. D. (2018). Nonstationarity Driven by Multidecadal Change in Catchment Groundwater Storage: A Test of Modifications to a Common Rainfall-Run-Off Model. *Hydrol. Process.* 32 (24), 3675–3688. doi:10.1002/hyp.13282

Hou, B., Jiang, C., and Sun, O. J. (2020). Differential Changes in Precipitation and Runoff Discharge during 1958-2017 in the Headwater Region of Yellow River of China. *J. Geogr. Sci.* 30 (9), 1401–1418. doi:10.1007/s11442-020-1789-5

Hu, Z., Liu, S., Zhong, G., Lin, H., and Zhou, Z. (2020). Modified Mann-Kendall Trend Test for Hydrological Time Series under the Scaling Hypothesis and its Application. *Hydrol. Sci. J.* 65 (14), 2419–2438. doi:10.1080/02626667.2020.1810253

Jahfer, S., Vinayachandran, P. N., and Nanjundiah, R. S. (2020). The Role of Amazon River Runoff on the Multidecadal Variability of the Atlantic ITCZ. *Environ. Res. Lett.* 15 (5), 054013. doi:10.1088/1748-9326/ab7c8a

Kasei, R., Diekkrüger, B., and Leemhuis, C. (2010). Drought Frequency in the Volta Basin of West Africa. *Sustain. Sci.* 5 (1), 89–97. doi:10.1007/s11625-009-0101-5

Kendall, M. G. (1955). Rank Correlation Methods. *Br. J. Psychol.* 25 (1), 86–91.

Krysanova, V., Hattermann, F. F., and Kundzewicz, Z. W. (2020). How Evaluation of Hydrological Models Influences Results of Climate Impact Assessment-An Editorial. *Climatic Change* 163, 1121–1141. doi:10.1007/s10584-020-02927-8

Leng, G., Tang, Q., Huang, M., and Leung, L.-y. R. (2015). A Comparative Analysis of the Impacts of Climate Change and Irrigation on Land Surface and Subsurface Hydrology in the North China Plain. *Reg. Environ. Change* 15 (2), 251–263. doi:10.1007/s10113-014-0640-x

Li, J., Ma, Q., Tian, Y., Lei, Y., Zhang, T., and Feng, P. (2019). Flood Scaling under Nonstationarity in Daqinghe River basin, China. *Nat. Hazards* 98 (2), 675–696. doi:10.1007/s11069-019-03724-y

Li, J., Sun, H., and Feng, P. (2016). How to Update Design Floods after the Construction of Small Reservoirs and Check Dams: A Case Study from the Daqinghe River basin, China. *J. Earth Syst. Sci.* 125 (4), 795–808. doi:10.1007/s12040-016-0688-8

Liang, S. Q., Wang, W. S., Zhang, D., Li, Y. Q., and Wang, G. Q. (2020). Quantifying the Impacts of Climate Change and Human Activities on Runoff Variation: Case Study of the Upstream of Minjiang River, China. *J. Hydrol. Eng.* 25 (9). doi:10.1061/(ASCE)HE.1943-5584.0001980

Liu, L., Xu, Y. P., Pan, S. L., and Bai, Z. X. (2019). Potential Application of Hydrological Ensemble Prediction in Forecasting Floods and its Components over the Yarlung Zangbo River basin, China. *Hydrol. Earth Syst. Sci.* 23 (8), 3335–3352. doi:10.5194/hess-23-3335-2019

Maier, N., and Dietrich, J. (2016). Using SWAT for Strategic Planning of Basin Scale Irrigation Control Policies: a Case Study from a Humid Region in Northern Germany. *Water Resour. Manage.* 30 (9), 3285–3298. doi:10.1007/s11269-016-1348-0

Mann, H. B. (1945). Nonparametric Tests against Trend. *Econometrica* 13 (3), 245–259. doi:10.2307/1907187

Moine, N. L., Andreassian, V., and Mathevet, T. (2008). Confronting Surface- and Groundwater Balances on the La Rochefoucauld-Touvre Karstic System (Charente, France). *Water Resour. Res.* 44 (3), 893–897. doi:10.1029/2007wr005984

Molina-Navarro, E., Hallack-Alegría, M., Martínez-Pérez, S., Ramírez-Hernández, J., Mungaray-Moctezuma, A., and Sastre-Merlín, A. (2016). Hydrological Modeling and Climate Change Impacts in an Agricultural Semiarid Region. Case Study: Guadalupe River basin, Mexico. *Agric. Water Manage.* 175, 29–42. doi:10.1016/j.agwat.2015.10.029

Montanari, A., Young, G., Savenije, H. H. G., Hughes, D., Wagener, T., Ren, L. L., et al. (2013). "Panta Rhei-Everything Flows": Change in Hydrology and Society-The IAHS Scientific Decade 2013-2022. *Hydrol. Sci. J.* 58 (6), 1256–1275. doi:10.1080/02626667.2013.809088

Musuuza, J. L., Gustafsson, D., Pimentel, R., Crochemore, L., and Pechlivanidis, I. (2020). Impact of Satellite and *In Situ* Data Assimilation on Hydrological Predictions. *Remote Sensing* 12 (5), 811. doi:10.3390/rs12050811

Nash, J. E., and Sutcliffe, J. V. (1970). River Flow Forecasting through Conceptual Models Part I - A Discussion of Principles. *J. Hydrol.* 10, 282–290. doi:10.1016/0022-1694(70)90255-6

Oliveira, N. D., Yang, X. L., Makhlouf, Z., and Michel, C. (1999). GR3J: a Daily Watershed Model with Three Free Parameters. *Hydrol. Sci. J.* 44 (2), 263–277.

Omer, A., Elagib, N. A., Zhuguo, M., Saleem, F., and Mohammed, A. (2020). Water Scarcity in the Yellow River Basin under Future Climate Change and Human Activities. *Sci. Total Environ.* 749, 141446. doi:10.1016/j.scitotenv.2020.141446

Perrin, C., Michel, C., and Andreassian, V. (2003). Improvement of a Parsimonious Model for Streamflow Simulation. *J. Hydrol.* 279 (1-4), 275–289. doi:10.1016/s0022-1694(03)00225-7

Sezen, C., and Partal, T. (2019). The Utilization of a GR4J Model and Wavelet-Based Artificial Neural Network for Rainfall-Runoff Modelling. *Water Sci. Technol.* 19 (5-6), 1295–1304. doi:10.2166/ws.2018.189

Song, X. M., Zhang, J. Y., Zhan, C. S., and Liu, C. Q. (2013). Review for Impacts of Climate Change and Human Activities on Water Cycle. *J. Hydraulic Eng.* 44 (7), 779–190. (in Chinese).

Sun, F., Mejia, A., Zeng, P., and Che, Y. (2019). Projecting Meteorological, Hydrological and Agricultural Droughts for the Yangtze River basin. *Sci. Total Environ.* 696, 134076. doi:10.1016/j.scitotenv.2019.134076

Thatch, L. M., Gilbert, J. M., and Maxwell, R. M. (2020). Integrated Hydrologic Modeling to Untangle the Impacts of Water Management during Drought. *Groundwater* 58 (3), 377–391. doi:10.1111/gwat.12995

Caloiero, T. (2017). Trend of Monthly Temperature and Daily Extreme Temperature during 1951–2012 in New Zealand. *Theor. Appl. Climatology* 129 (1-2), 111–127. doi:10.1007/s00704-016-1764-3

Turner, S. W. D., Doering, K., and Voisin, N. (2020). Data-Driven Reservoir Simulation in a Large-Scale Hydrological and Water Resource Model. *Water Resour. Res.*. Available at: https://agupubs.onlinelibrary.wiley.com/doi/epdf/10.1029/2020WR027902.

Varentsova, N. A., Kireeva, M. B., Frolova, N. L., Kharlamov, M. A., Ilich, V. P., and Sazonov, A. A. (2020). Forecasting Water Inflow into the Tsimlyansk Reservoir during Spring Flood under Current Climate Conditions: Problems and Reproducibility. *Water Resour.* 47 (6), 953–967. doi:10.1134/s0097807820060159

Wang, H., Mei, C., Liu, J., and Shao, W. (2018). A New Strategy for Integrated Urban Water Management in China: Sponge City. *Sci. China Technol. Sci.* 61 (3), 317–329. doi:10.1007/s11431-017-9170-5

Wang, W., Zhang, Y., and Tang, Q. (2020). Impact Assessment of Climate Change and Human Activities on Streamflow Signatures in the Yellow River Basin Using the Budyko Hypothesis and Derived Differential Equation. *J. Hydrol.* 591, 125460. doi:10.1016/J.JHYDROL.2020.125460

Wang, Y. X., Li, J. Z., Zhang, T., and Wang, B. (2019). Changes in Drought Propagation under the Regulation of Reservoirs and Water Diversion. *Theor. Appl. Climatol.* 138 (1-2), 701–711. doi:10.1007/s00704-019-02839-3

Wilkinson, M. E., Addy, S., Quinn, P. F., and Stutter, M. (2019). Natural Flood Management: Small-Scale Progress and Larger-Scale Challenges. *Scottish Geograph. J.* 135 (1-2), 23–32. doi:10.1080/14702541.2019.1610571

Xu, Z. X. (2010). Hydrological Models: Past, Present and Future. *Beijing Norm. Univ.* 46, 278–289.

Yang, P., Xia, J., Zhang, Y., and Hong, S. (2017). Temporal and Spatial Variations of Precipitation in Northwest China during 1960-2013. *Atmos. Res.* 183, 283–295. doi:10.1016/j.atmosres.2016.09.014

Yang, Z., Zhou, Y., Wenninger, J., Uhlenbrook, S., Wang, X., and Wan, L. (2017). Groundwater and Surface-Water Interactions and Impacts of Human Activities in the Hailiutu Catchment, Northwest China. *Hydrogeol J.* 25 (5), 1341–1355. doi:10.1007/s10040-017-1541-0

Zeng, L., Xiong, L., Liu, D., Chen, J., and Kim, J.-S. (2019). Improving Parameter Transferability of GR4J Model under Changing Environments Considering Nonstationarity. *Water* 11 (10), 2029. doi:10.3390/w11102029

Zheng, X. T., Cheng, W. Q., Liu, Y. Y., Pang, L. J., Guo, W. Y., and Ran, H. D. (2020). Inflow Runoff Evolution and Analysis of Their Influencing Factors under Connection of Wangkuai and Xidayang Reservoirs. *Water Resour. Power* 38 (3), 21–24. (in Chinese).

Zhu, N., Xu, J., Li, K., Luo, Y., Yang, D., and Zhou, C. (2019). Spatiotemporal Change of Plum Rains in the Yangtze River Delta and its Relation with EASM, ENSO, and PDO during the Period of 1960-2012. *Atmosphere* 10 (5), 258. doi:10.3390/atmos10050258

Conflict of Interest: The authors declare that the research was conducted in the absence of any commercial or financial relationships that could be construed as a potential conflict of interest.

Publisher's Note: All claims expressed in this article are solely those of the authors and do not necessarily represent those of their affiliated organizations, or those of the publisher, the editors and the reviewers. Any product that may be evaluated in this article, or claim that may be made by its manufacturer, is not guaranteed or endorsed by the publisher.

frontiers in Earth Science

ORIGINAL RESEARCH
published: 04 October 2021
doi: 10.3389/feart.2021.751969

Characteristics of Precipitation During Meiyu and Huang-Huai Rainy Seasons in Anhui Province of China

Yuliang Zhou, Ping Zhou, Yuliang Zhang, Chengguo Wu, Juliang Jin, Yi Cui and Shaowei Ning*

College of Civil Engineering, Hefei University of Technology, Hefei, China

Based on the spatial distribution characteristics of the summer monsoon rain belt, Anhui Province of China is divided into three regions, namely, the south of the Yangtze River region (SYA), the Yangtze-Huai region (YHA), and the north of the Huaihe region (NHA). The western Pacific subtropical high (WPSH) ridge and the number of regional rainy days are adopted to identify the onset and ending dates of Meiyu and Huang-Huai rainy seasons during 1957–2020, using China's national standard on "Meiyu monitoring indices." Then precipitation characteristics of these three regions during Meiyu and Huang-Huai rainy seasons are investigated. Finally, the return periods of the precipitation during the northward movement of summer monsoon over Anhui Province are calculated. The results show that there are 7 years without the occurrence of Huang-Huai rainy season, but 8 years with the occurrence of two Meiyu periods and 5 years with two Huang-Huai rainy periods. Thus, there is only one Meiyu period and one Huang-Huai rainy period in the rest 49 years. For the first Meiyu period during 1957–2020, the average onset and ending dates are 14th June and 10th July, respectively, while the corresponding precipitation presents a decreasing tendency from south to north regions in Anhui Province. For the first Huang-Huai rainy period during 1957–2020, the average onset and ending dates are 10th July and 23rd July, respectively, and the corresponding precipitation shows an increasing tendency from south to north regions. For the northward movement of summer monsoon over Anhui Province, the average onset and ending dates are 14th June and 25th July, respectively, and the corresponding precipitation in NHA is close to that in YHA, but less than that in SYA. Annual precipitation in SYA, YHA, and NHA are 999.5, 1010.6, and 618.7 mm, respectively, during the northward movement of summer monsoon over Anhui Province in 2020, and the corresponding return periods are 56.0, 161.6, and 29.2 years, respectively.

Keywords: precipitation characteristics, Meiyu, Huang-Huai rainy season, return period, subtropical high ridge, Anhui Province

OPEN ACCESS

Edited by:
Yulei Xie,
Guangdong University of Technology, China

Reviewed by:
Qinghua Luan,
Hebei University of Engineering, China
Zilong Wang,
Northeast Agricultural University, China
Zhenxing Zhang,
University of Illinois at Urbana-Champaign, United States

****Correspondence:***
Ping Zhou
chaohupingping@126.com

Specialty section:
This article was submitted to Hydrosphere, a section of the journal Frontiers in Earth Science

Received: *02 August 2021*
Accepted: *23 August 2021*
Published: *04 October 2021*

Citation:
Zhou Y, Zhou P, Zhang Y, Wu C, Jin J, Cui Y and Ning S (2021) Characteristics of Precipitation During Meiyu and Huang-Huai Rainy Seasons in Anhui Province of China. Front. Earth Sci. 9:751969. doi: 10.3389/feart.2021.751969

INTRODUCTION

East Asian summer monsoon (EASM) is the most important as well as the specific climate phenomenon over East Asia (Huang et al., 2015; Bombardi et al., 2017; Xu et al., 2021). Summer precipitation in the Eastern Monsoon Region of China (EMRC) is dominated by EASM, resulting in a relatively high occurrence frequency of severe disasters, such as floods and

droughts (Xia et al., 2017; Yang et al., 2020). Anhui Province is located across both the eastern monsoon region and the north-south climate transition zone of China. Affected by the weather systems at low and mid-to-high latitudes, the precipitation characteristics in Anhui Province are complicated to identify. Recently, severe droughts and floods have occurred in Anhui Province, especially the consecutive drought over the region of the Yangtze-Huaihe River Basin in 2019, and the floods over the Yangtze River Basin and the Huaihe River Basin in 2020. Therefore, a thorough understanding of precipitation characteristics during the period of the northward movement of summer monsoon over Anhui Province is needed for disasters forecast and prevention.

Previous studies about regional precipitation typically focus on the statistical analysis of the temporal and spatial distribution of extreme precipitation in terms of the trend, abrupt change, and the return period with various time scales for administrative convenience, such as day, month, and season (Wang and Xu, 2002; Ye, 2012; Tang and Chen, 2015; Wang et al., 2015; Ding et al., 2016; Huang et al., 2020). However, there is seldom research focusing on process characteristics of precipitation from the perspective of the large-scale weather systems (Sun and Zhu, 2013; Zhang et al., 2019; Zhang et al., 2020). Precipitation resulted from summer monsoon and typhoons is the two most dominant components of precipitation in flood season in Anhui Province. The variation of summer monsoon precipitation is relatively smaller than that of typhoon precipitation. Thus the summer monsoon precipitation characteristics, including the onset, ending dates, and precipitation amounts during the period of the northward movement of summer monsoon affecting Anhui Province are the scientific and reasonable basis for phase division of scheduling scheme of reservoir, and it also can provide support for the determination of time step for the run theory-based drought process identification with clear physical meaning. Then the issues related to the widely applied monthly precipitation drought index may be solved. The monthly precipitation drought index may not completely reflect precipitation process associated with a large-scale weather system longer than 1 month, which does not begin on the first day nor end on the last day of a month.

Obviously, reservoir operation for flood control and drought relief is strongly subjected to precipitation associated with the large-scale weather systems. The period from the onset of Meiyu season to the end of the Huang-Huai rainy season is the main stage of the summer monsoon main rain belt affecting Anhui Province. The associated precipitation is the most important component of summer precipitation and determines the precipitation characteristics in the flooding season (Water Resources Department of Anhui Province, 1998; Wang et al., 2018) as well as the regional drought and flood pattern. So this study aims, and would be the first, to uncover the characteristics of precipitation during Meiyu and Huang-Huai rainy seasons in Anhui Province based on the synoptic indices, so as to provide data support for the schedule of reservoir operation and flood/drought disasters prevention.

During Meiyu season, the precipitation in Anhui Province mainly lies in the south of the Yangtze River region in Anhui Province (SYA) and Yangtze-Huai region in Anhui Province (YHA), while there is little precipitation in the north of Huaihe region in Anhui Province (NHA) (Liang et al., 2007; Ninomiya, 2009). During the Huang-Huai rainy season, the precipitation mainly concentrates in the NHA region, while SYA and YHA are controlled by the northwest Pacific subtropical high (hereinafter, SH) pressure zone with very little precipitation.

Therefore, according to the distribution characteristics of the summer monsoon rain belt, Anhui Province can be divided into three regions, namely, SYA, YHA, and NHA. Zhou et al. (2021) analyzed the characteristics of precipitation during Meiyu season in three regions of Anhui Province. However, they have not studied the precipitation during Huang-Huai rainy season, which may be the most important component of summer precipitation in NHA. In light of this, firstly in this study, Meiyu season and the Huang-Huai rainy season in Anhui Province were identified for the above three regions each year. Following that, the temporal and spatial distribution characteristics of precipitation were analyzed from the perspective of large-scale weather processes. The trend variation and the return period of the precipitation during the period of the northward movement of summer monsoon affecting Anhui Province were also specified. The analysis results can provide scientific support for the planning, design, and operation management of the regional water conservancy project, rational use of regional water resources, and decision making on countermeasure for flood and drought disasters mitigation.

The rest of this article is organized as follows. In the section "*Materials and Methods*," the methods for identifying the characteristics of Meiyu season and Huang-Huai rainy seasons are presented. In the section "*Results and Discussion*," the precipitation characteristics of Meiyu and Huang-Huai rainy seasons during 1957–2020 in terms of the duration, onset and ending dates, total amount, and return periods are derived, especially for the year 2020 with severe flood. *Conclusion* is the last section.

MATERIALS AND METHODS

Identification Methods of Meiyu and Huang-Huai Rainy Seasons

Meiyu is a unique weather and climate phenomenon that occurs over China's Yangtze-Huai River valley, the southern part of the Korean Peninsula, and mid-south regions in Japan from mid-June to early-to-mid July (Ge et al., 2008; Wang, 2020). Generally, Meiyu season is determined by the consecutive summer monsoon precipitation resulting from the move of SH, whose ridge surpasses 20°N for the first northward jump in mid-June, then stagnates at 20–25°N over the above regions (Liang et al., 2007; Zhang, 2007; Ge et al., 2008; Liu and Ding, 2008; Liu et al., 2012; Wang et al., 2018). Following that, in the mid July, the SH ridge surpasses 25°N for the second northward jump, then stagnates at 25–30°N over the region between the Huang River and the Huai River Basin. Correspondingly, the summer monsoon main rain belt forms the so-called Huang-Huai rainy season. Apart from SH, the central location and the range of the main rain belt of the

summer monsoon are also affected by other climatic factors, such as the South Asian high, East Asian congestion, and the Indian monsoon (Liang et al., 2007). In previous studies, the proposed thresholds and criteria for identifying Meiyu season and Huang-Huai rainy season are typically different from each other until the implementation of the "Meiyu monitoring indices (GB/T 33671-2017)" from the National Standard of China in 2017 (National Climate Center of the China Meteorological Administration et al., 2017; Zhao et al., 2018).

Based on the "Meiyu monitoring indices (GB/T 33671-2017)" (National Climate Center of the China Meteorological Administration et al., 2017), this study uses the position of the SH ridge (National Climate Center of the China Meteorological Administration, 2016) and the length of rainy days as the indices to identify the characteristics of Meiyu season and Huang-Huai rainy seasons; that is, the first rainy day when the SH ridge exceeds 19°N for 5 consecutive days is defined as the starting time of Meiyu season. The first day when the SH ridge exceeds 25°N for 5 consecutive days is regarded as the earliest possible ending date of Meiyu season, and the first day when the SH ridge exceeds 27°N for 5 consecutive days is regarded as the latest possible ending date of Meiyu season. If the precipitation in the north of the Huaihe region in Anhui Province suddenly increases or shifts from a non-rainy day to a rainy day while the precipitation in the south of the Yangtze River region of Anhui Province decreases or shifts from a rainy day to a non-rainy day, this day is characterized as the beginning date of Huang-Huai rainy season and the previous day is regarded as the ending date of Meiyu season. When the SH ridge exceeds 30°N for 5 consecutive days, the day before the occurrence of non-rainy days in the north of the Huaihe region is defined as the ending date of Huang-Huai rainy season. If the first 5 days of the SH ridge exceeding 30°N are all non-rainy days, then the last rainy day before the SH ridge that reaches 30°N is regarded as the ending date of Huang-Huai rainy season. If the SH ridge does not exceed 30°N for 5 consecutive days, that is, the SH ridge does not cross 30°N and withdraw southward, the last rainy day before the SH ridge reaching the northernmost tip is taken as the ending date of Huang-Huai rainy season. Generally, after Huang-Huai rainy season, the SH ridge jumps north again and North China and Northeast China would enter the rainy season. However, after the end of Huang-Huai rainy season, if the SH ridge does not immediately jump northward, but first moves southward, such a climatic process leads to the second Meiyu season. After that, the SH ridge jumps northward again or withdraws southward. Under the condition of the jumping northward again, the date that fulfills the conditions for ending the Huang-Huai rainy season is considered as the ending date of the second Huang-Huai rainy season.

Data

According to "Meiyu monitoring indices (GB/T 33671-2017)" (National Climate Center of the China Meteorological Administration et al., 2017) and "Monitoring Indices of Northwest Pacific Subtropical High (QX/T 304-2015)" (National Climate Center of the China Meteorological Administration, 2016), the processes of Meiyu and Huang-Huai rainy seasons are identified mainly according to the atmospheric circulation conditions and meteorological elements. The SH ridge is mainly adopted as an atmospheric circulation element, and the rainy periods, rainy days, and temperature are represented as meteorological elements. The position of the SH ridge refers to the average position of the ridge of SH on each meridian within 110–130°E. Regional rainy days are specified when more than 1/3 of the regional stations have daily precipitation amount more than 0.1 mm and the average daily precipitation amount of all the stations in the region exceeds 2.0 mm. The upper-air circulation data used to calculate the SH ridge are the daily average 500 hPa geopotential height and zonal wind speed in the NCEP/NCAR reanalysis data of the United States. The data used to determine the regional rainy days is the daily precipitation of the observation stations in Anhui Province during 1957–2020.

So the required data to identify Meiyu and Huang-Huai rainy processes is obtained as follows: the upper-air circulation data adopts the daily average 500 hPa geopotential height and the zonal wind speed. The data can be freely downloaded from the NCEP/NCAR reanalysis project's webpage: https://psl.noaa.gov/data/gridded/data.ncep.reanalysis.html. The meteorological data including daily precipitation and average temperature are obtained from 15 observation stations in Anhui Province during 1957–2020, which is provided by the China Meteorological Data Network (http://data.cma.cn). Other related data of precipitation, flood, and drought disasters are collected from the National Hydrological Annual Report provided by Information Center, Ministry of Water Resources, PRC. (http://xxzx.mwr.gov.cn/xxgk/gbjb/sqnb).

RESULTS AND DISCUSSION

Identification of Meiyu and Huang-Huai Rainy Seasons in Anhui Province

Provided by the China Meteorological Data Network, Anqing (the station has no data during 2017–2020, which is replaced by Ma'anshan station), Ningguo, and Tunxi stations are the representative stations for the SYA region. The six stations including Chaohu, Hefei, Chuzhou, Lu'an, Huoshan, and Shouxian are representative stations for the YHA region. Five stations in Fuyang, Bengbu, Bozhou, Suzhou, and Dangshan are the representative stations for the NHA region. All of the above stations are shown in **Figure 1** (Zhou et al., 2021).

The onset and ending dates of Meiyu and Huang-Huai rainy seasons are identified by the position of the SH ridge and the rainy days as listed in **Supplementary Appendix Table A1** in Appendix.

Supplementary Appendix Table A1 shows the following: 1) During 1957–2020, there are 7 years without the occurrence of Huang-Huai rainy season (only with Meiyu season), which are 1968, 1982, 1999, 2014, 2015, 2016, and 2018. At the end of Meiyu season, the SH ridge surpassed 30°N directly in 1968, 1982, 1999, and 2018. Differently, Meiyu season of 2014 ended on 17th July, and the SH ridge was located among 27–30°N on 18th and 19th July (precipitation amount in SYA, YHA, and NHA was 3.5, 0.0, 6.2 mm, respectively). On 20th July, the SH ridge jumped

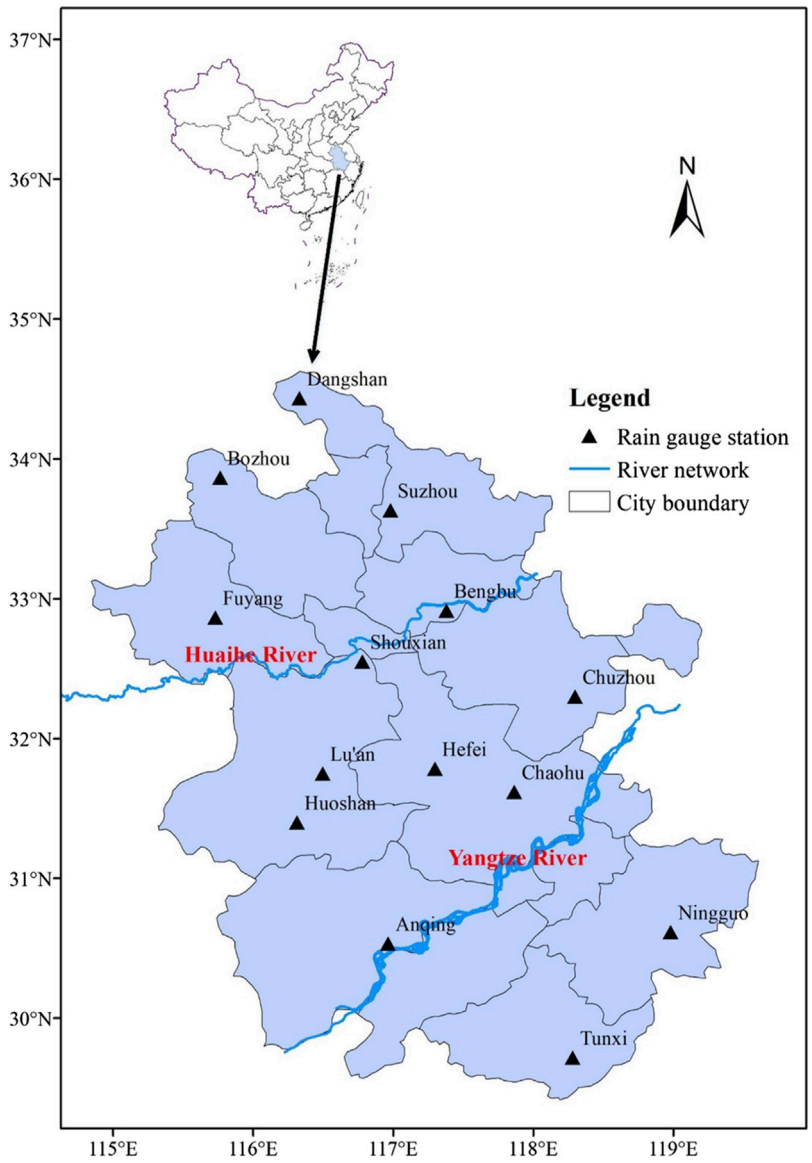

FIGURE 1 | Location of rain gauge stations in Anhui Province.

northward over 30°N. Meiyu season in 2015 ended on 26th July. Only on 27th July, the SH ridge was located at 27–30°N (the daily precipitation amount in SYA, YHA, and NHA was 0.0, 0.1, and 6.2 mm, respectively), and the SH ridge jumped northward over 30°N after 27th July. Meiyu season of 2016 ended on 22nd July. The SH ridge was located at 27–30°N on 23rd and 24th July (there was no precipitation in SYA, YHA, and NHA). After that, the SH ridge jumped northward over 30°N. 2) For the 5 years of 1957, 1973, 1977, 1998, and 2009, the SH ridge first laid in the typical range of the SH ridge during Meiyu season, then moved northward–southward–northward to the typical range of the SH ridge during Huang-Huai rainy season, Meiyu season, and Huang-Huai rainy season, respectively. 3) In 1964, 1985, and 2012, the SH ridge successively laid in the typical range of the SH ridge during Meiyu season, Huang-Huai season, and Meiyu season. The SH ridge did not stably surpass 30°N in 1985 and 2012. In 1964, the SH ridge quickly jumped northward and surpassed 30°N after the second Meiyu season. 4) The length of Meiyu and Huang-Huai rainy season exceeded 5 days in most of the recorded years, except for the years of 1964, 1979, 2005, 2009, and 2012. 5) The northward movement of the summer monsoon started in June and ended before the late July in most of the recorded years, except for the following starting time: May 18, 1991; May 27, 2001, and July 9, 1982. In addition, there were 14 years with the summer monsoon ending in August, 10 of them before the start of autumn, while 4 of them in mid-August (they were August 18, 1957; August 14, 1974; August 18, 1998, and August 13, 2020).

To distinguish the rainy periods dominated by the SH ridge in the same range at different stages, the period when the SH ridge is first located in the typical range of the SH ridge during Meiyu

TABLE 1 | Characteristics of Meiyu and Huang-Huai rainy season during 1957–2020 in Anhui Province.

Stage	Average time	Average duration/d	Shortest duration/d	Longest duration/d	Earliest onset	Latest onset	Earliest ending date	Latest ending date
I	6.14–7.10	27.0	3.0 (2012)	56.0 (1991)	5.18 (1991)	7.09 (1982)	6.15 (1961)	7.31 (1987)
II	7.10–7.23	14.4	3.0 (1979, 2005)	32.0 (1988)	6.16 (1961)	8.01 (1987)	7.01 (1964)	8.14 (1974)
III					5.18 (1991)	7.09 (1982)	6.15 (1961)	8.13 (1957)
IV					6.16 (1961)	8.01 (1987)	7.01 (1964)	8.18 (1957, 1998)
W	6.14–7.25	42.0	19.0 (1982)	69.0 (2011)	5.18 (1991)	7.09 (1982)	7.01 (1964)	8.18 (1957, 1998)

Note: The time corresponding to II *in the table is the statistical value of 58 years when the Huang-Huai rainy season is not empty; the number before "( )" in the shortest, longest, earliest, and latest column are characteristic values, and the number in "( )" is the year corresponding to the extreme value.*

season is specified as the narrowly defined Meiyu season. The period when the SH ridge is first located in the typical range of the SH ridge during Huang-Huai rainy season is specified as the narrowly defined Huang-Huai rainy season. The period when the SH ridge lies in the typical range of the SH ridge corresponding to Meiyu season is defined as the broadly defined Meiyu season. The period when the SH ridge lies in the typical range of the SH ridge corresponding to the Huang-Huai rainy season is defined as the broadly defined Huang-Huai rainy season. The broadly defined Meiyu season includes the narrowly defined Meiyu season, and the broadly defined Huang-Huai rainy season includes the narrowly defined Huang-Huai rainy season. If the SH ridge does not move southward to the SH ridge range corresponding to the Meiyu season after the second northward jump, the broadly defined Meiyu season is the same as the narrowly defined Meiyu season. If the SH ridge does not move southward after the second northward jump, or does not jump northward again after the southward movement to the SH ridge range corresponding to the Huang-Huai rainy season, the broadly defined Huang-Huai rainy season is the same as the narrowly defined Huang-Huai rainy season. During 1957–2020, there are 8 years with the occurrence of the second Meiyu season, and 5 years among them with the second Huang-Huai rainy season. Therefore, there are 8 years in which the broadly defined Meiyu season is different from the narrowly defined Meiyu season, and 5 years in which the broadly defined and narrowly defined Huang-Huai rainy seasons are different. Except for 7 years with only a narrowly defined Meiyu season and 8 years with the second Meiyu season, in the rest 49 years there are one narrowly defined Meiyu season and one Huang-Huai rainy season.

Precipitation Characteristics for Meiyu and Huang-Huai Rainy Seasons

The timing characteristics of Meiyu and Huang-Huai rainy seasons are shown in **Table 1**, including the following five stages of summer monsoon in Anhui Province: the narrowly defined Meiyu (stage I), the narrowly defined Huang-Huai rainy season (stage II), the broadly defined Meiyu season (stage III), the broadly defined Huang-Huai rainy season (stage IV), and the whole period of northward movement of summer monsoon (stage W).

It can be seen from **Table 1** that the average duration of the narrowly defined Meiyu season in 64 years is 27.0 days, and the average duration of the narrowly defined Huang-Huai rainy season in 57 years is 14.2 days. Therefore, the 64 years' average duration of the narrowly defined Huang-Huai rainy season, including the 7-years empty Huang-Huai rainy season, is 12.8 days. Furthermore, it can be seen that the average duration of the period from the onset of Meiyu season to the ending date of the first Huang-Huai rainy season is 39.8 days, which is close to the multiyear average duration of 42.0 days for the northward movement of summer monsoon affecting Anhui Province. In terms of multiyear average, the duration of broadly defined Meiyu season and narrowly defined Meiyu season, as well as broadly defined Huang-Huai rainy season and narrowly defined Huang-Huai rainy season are almost the same. The duration of Meiyu season and Huang-Huai rainy season vary significantly from year to year. The shortest is only 3 days and the longest is 56 days. The shortest duration of Huang-Huai rainy season is 3 days, and the longest is 32 days. The shortest duration of the northward movement of summer monsoon affecting Anhui Province is 19 days, while the longest is 69 days. The earliest onset is 18th May and the latest ending date is 18th August. The characteristics of precipitation at various stages of the northward movement of summer monsoon affecting Anhui Province are shown in **Table 2**.

It can be seen from **Table 2** that in the narrowly defined Meiyu season (i.e., stage I), the 64 years average precipitation amount during this stage decreases from south to north regions in Anhui Province. The precipitation amount in NHA is less than that in SYA or YHA, and the precipitation amount in NHA is only about 1/2 of that in SYA. Specifically, as shown in **Supplementary Appendix Table A1**, in the 64 years' narrowly defined Meiyu season, there are 46 years in which the precipitation amount in NHA is lower than that in SYA and YHA. In 1976, 1981, 2017, and 2018, the precipitation amount in NHA is lower than that in SYA but slightly higher than that in YHA. In 1962, 1968, 1972, 1982, and 2003, the precipitation amount in NHA is lower than that in YHA but higher than that in SYA (in which, the precipitation amount in NHA during this stage in 1968 and 1972 is close to that in YHA). The precipitation amount in NHA during this stage is higher than that in YHA and SYA in 1958, 1963, 1965, 1967, 1979, 2000, 2005, 2006, and 2007. Among them, the main rain belt during Meiyu season in 2007 laid in the Huaihe River Basin and, consequently, heavy floods occurred along the Huaihe River; while 1958, 1965, 2000, and 2005 are empty Meiyu years, the precipitation amount in SYA and YHA is very low and less than that in NHA; in 1963 and 1979, the precipitation

TABLE 2 | Statistical characteristics of precipitation in SYA, YHA, and NHA during 1957–2020 over Meiyu and Huang-Huai rainy seasons.

Stage	Average value			Minimum value			Maximum value		
	SYA	YHA	NHA	SYA	YHA	NHA	SYA	YHA	NHA
I	346.1	239.6	169.3	10.5 (1958)	33.3 (1958)	2.8 (2012)	1022.4 (1999)	955.0 (1991)	549.5 (2007)
II	30.3	55.2	109.2	0	0	0	200.3 (1981)	243.1 (1974)	478.7 (1965)
III	361.8	248.5	173.2	10.5 (1958)	33.3 (1958)	9.3 (1988)	1022.4 (1999)	955.0 (1991)	549.5 (2007)
IV	31.4	67.2	112.8	0	0	0	200.3 (1981)	243.1 (1974)	478.7 (1965)
W	393.2	315.6	286.0	33.0 (1958)	72.3 (2001)	48.3 (2014)	1022.8 (1996)	1010.6 (2020)	670.2 (1965)

Note: The numbers in "( )" in the table are the year corresponding to the extreme value.

amount in SYA, YHA, and NHA during Meiyu season are very close to each other, and the precipitation amount during Meiyu season in SYA is very close to that in NHA in 1967; in 2006, the main rain belts during Meiyu season laid in SYA, NHA, and the region of south of the Huaihe River (including SYA and YHA) successively, and heavy rainfall occurred when the main rain belt laid in NHA. **Supplementary Appendix Table A1** and **Table 2** show that the spatial distribution characteristics of precipitation during Meiyu season in Anhui Province are consistent with the national Meiyu regionalization: SYA belongs to the Meiyu region in the middle and lower reaches of the Yangtze River, YHA belongs to the Yangtze-Huai Meiyu region, and the Huaihe River in Anhui Province almost overlaps with the northern boundary of China's Meiyu region (National Climate Center of the China Meteorological Administration et al., 2017).

Table 2 shows that during the narrowly defined Huang-Huai rainy season (stage II), the 64-year average precipitation amount during this stage increases from south to north regions in Anhui Province, and the precipitation amount in NHA is significantly higher than that in SYA and YHA. At this stage, the average precipitation amount in NHA is 109.2 mm, which is about twice of that in YHA and 3.5 times of that in SYA. Specifically, **Supplementary Appendix Table A1** shows that there are 7 years with empty Huang-Huai rainy season and 50 years with the precipitation amount in NHA greater than that in SYA and YHA. In 1960, 1971, 1985, and 1986, the precipitation amount in NHA is lower than that in YHA but significantly higher than that in SYA. In 1981, 2006, and 2011, the precipitation amount in NHA is lower than that in SYA. Among these years, the precipitation amount in NHA during Huang-Huai rainy season in 2006 and 2011 is close to that in SYA but less than that in YHA. During Huang-Huai rainy season in 1981, the precipitation in SYA and YHA results from the typhoon; thus, the precipitation amount is significantly higher than that in NHA.

Table 2 shows that the 64-year average precipitation amount from the beginning of the narrowly defined Meiyu season to the end of the narrowly defined Huang-Huai rainy season in SYA, YHA, and NHA is 376.4, 294.8, and 278.5 mm, respectively, and these values are close to 393.2, 315.6, and 286.0 mm for the 64-year average precipitation amount during the period of the summer monsoon moving northward in the three regions of Anhui Province. Therefore, the multiyear average precipitation amount in YHA and that in NHA from the narrowly defined Meiyu season to the narrowly defined Huang-Huai rainy season are close to each other but less than that of SYA. In addition, there is little difference in the average precipitation amount between the broadly defined and the narrowly defined Meiyu seasons or the broadly defined and the narrowly defined Huang-Huai rainy seasons. The precipitation amount in the narrowly defined Meiyu season varies from year to year. The minimum precipitation amount during Meiyu season in SYA, YHA, and NHA is less than 50 mm. The maximum precipitation amount during Meiyu season in SYA, YHA, and NHA is greater than 500 mm. Among them, the precipitation amount in SYA and YHA is close to each other, that is, above 1000 mm, while precipitation amount in NHA is only about 1/2 of that in SYA and YHA. The precipitation amount in the narrowly defined Huang-Huai rainy season varies greatly from year to year. Except for the years with empty Huang-Huai rainy season, the minimum precipitation amount at this stage in SYA is only 0.1 mm and to in NHA is less than 10 mm. The maximum precipitation amount during Huang-Huai rainy season in SYA, YHA, and NHA is also different. The maximum precipitation amount in SYA is less than 150 mm (except for 200.3 mm in 1981 under the influence of typhoon), but the maximum value in YHA is close to 250 mm, and the maximum value in NHA is close to 500 mm.

According to the daily precipitation amount series during 1957–2020, the average precipitation amount in SYA, YHA, and NHA from June to July for 64 years is 453.5, 341.0, and 317.8 mm, respectively. Therefore, when summer monsoon moves northward, the average precipitation amount in SYA, YHA, NHA is 393.2, 315.6, and 286.0 mm, respectively, accounting for 87, 93, and 90% of the precipitation from June to July, respectively. The results show that the precipitation from June to July in Anhui Province is mainly formed by the frontal rain belt resulting from the summer monsoon.

Stage III is different from stage I in 8 years and stage IV is different from stage II in 5 years. The years in which the dates and precipitation of stage III, I, IV, and II are different are shown in **Table 3**.

Table 3 shows that the second period of Meiyu season begins in July, with the largest average precipitation amount in SYA, successively followed by YHA and NHA, while the 8-year average duration of the period is 10.3 days. All the second periods of Huang-Huai rainy season start after mid July, with the largest average precipitation amount in NHA, successively followed by

TABLE 3 | Dates and precipitation of the second period of Meiyu and Huang-Huai rainy seasons in SYA, YHA, and NHA during 1957–2020.

Year	Second period of Meiyu season					Second period of Huang-Huai rainy season				
	Date	Duration/d	Precipitation/mm			Date	Duration/d	Precipitation/mm		
			SYA	YHA	NHA			SYA	YHA	NHA
1957	7.26–8.13	19	216.0	155.7	40.4	8.14–8.18	5	0.3	24.1	24.0
1973	7.19–7.28	10	62.9	35.8	28.8	7.29–8.03	6	34.7	30.9	40.6
1977	7.12–7.17	6	110.8	27.7	5.3	7.18–7.25	8	30.1	82.9	89.5
1998	7.13–8.02	9	206.7	121.0	96.3	8.03–8.18	16	18.6	90.6	182.7
2009	7.24–7.31	21	135.5	45.6	12.3	8.01–8.04	4	16.0	8.8	2.6
1964	7.18–7.21	4	54.6	32.7	25.0					
1985	7.18–7.26	8	76.2	68.8	22.2					
2012	7.09–7.17	9	145.4	81.7	17.2					
Mean value		10.3	126.0	71.1	30.9	Mean value	7.8	19.9	47.5	67.9

YHA and SYA, while the 5-year average duration of the period is 7.8 days.

Return Period of Precipitation During Meiyu and Huang-Huai Rainy Seasons

According to the precipitation amount during Meiyu and Huang-Huai rainy seasons in SYA, YHA, and NHA in **Supplementary Appendix Table A1**, the frequency analysis of the precipitation amount corresponding to the northward movement of summer monsoon affecting Anhui Province in these three regions is analyzed. In 1996, 1999, and 2020, the precipitation amount during Meiyu and Huang-Huai rainy seasons in SYA is 1022.8, 1022.4, and 999.5 mm, respectively. The historical floods in China, since 1840 (Luo, 2006), and the precipitation during the extreme Meiyu events years (e.g., 1954) in the Yangtze-Huai Meiyu region are used for comparison and analysis (Water Resources Department of Anhui Province., 1998; Wang and Xu, 2002; Luo, 2006; Zhang, 2007; Ding et al., 2016; Information Center of the Ministry of Water Resources, 1983–2020). The precipitation during Meiyu and Huang-Huai rainy seasons of these 3 years are higher than the corresponding precipitation in the years with severe flood occurred in the Yangtze River Basin, such as in 1896 and 1931, but slightly lower than that of 1954 with the largest flood in history in the basin (according to the daily precipitation records in the Tunxi Station, the precipitation amount in this period is 1185.0 mm, which is the largest ever recorded). Therefore, the precipitation amount during this period of the above 3 years can be considered as the second, third, and fourth largest values since 1840.

The precipitation amount during Meiyu and Huang-Huai rainy seasons in YHA in 1991 and 2020 is 959.8 and 1010.6 mm, respectively. These two values are higher than that during this period in the years with severe flood occurred in the Huaihe River Basin, such as in 1921, 1931, and 1954 (Luo, 2006). Among which, according to the daily precipitation records of the representative stations in YHA (Chuzhou, Huoshan, and Hefei stations), the precipitation amount during this period of 1954 is 849.2 mm, which is far less than the abovementioned 2 years. Therefore, the precipitation amount of these 2 years during this period can be considered as the first and second extreme values since 1840.

The precipitation during Meiyu and Huang-Huai rainy seasons from 1957 to 2020 in NHA is a continuous time series without extraordinary value. According to the records (Information Center of the Ministry of Water Resources, 1983; Luo, 2006), the precipitation amount during this period in 1954 reaches the maximum value since 1840. According to the daily precipitation series of the representative stations in NHA (Suzhou, Bozhou, and Fuyang stations), the precipitation during this period of 1954 is 819.2 mm. Consequently, the return period of the precipitation during this period in 1954 is about 181 years.

The P-III curve is used to fit the frequency of precipitation during Meiyu and Huang-Huai rainy seasons in SYA, YHA, and NHA, respectively. The fitting results are shown in **Figure 2**.

It can be seen from **Figure 2** that the P-III curve can well fit the empirical frequency points. The mean value, coefficient of variation, and coefficient of skew of the precipitation during Meiyu and Huang-Huai rainy seasons in SYA are 381.3 mm, 0.59, and 1.28, respectively. The three coefficients of the P-III curve in YHA are 295.5 mm, 0.63, and 1.65, respectively. The three coefficients of the P-III curve in NHA are 286.0 mm, 0.53, and 1.14 respectively. Based on these parameters of the frequency curve, it can be obtained that the precipitation amount during this period with the return period of 180 years in SYA is 1201.9 mm. It is slightly higher than the maximum value of 1185.0 mm at the Tunxi station over 181 years since 1840. The precipitation amount during this period with the return period of 180 years in NHA is 821.9 mm, which is also very close to the maximum value of 819.2 mm in this region over 181 years since 1840. It demonstrates that the P-III curve is suitable to be taken as the frequency curve of precipitation during this period in Anhui Province. Precipitation under different return periods in SYA, YHA, and NHA are given in **Table 4**.

According to P-III curve and their parameter values, the return periods of 63.9, 63.8, and 56.0 years are specified for the precipitation of 1022.8, 1022.4, and 999.5 mm during Meiyu and Huang-Huai rainy seasons in SYA in 1996, 1999, and 2020, respectively. The return periods corresponding to the precipitation of 959.8 and 1010.6 mm in the year of 1991 and 2020 in YHA are 118.6 and 161.6 years, respectively. The return periods for the precipitation of 670.2, 612.9, and 618.7 mm in

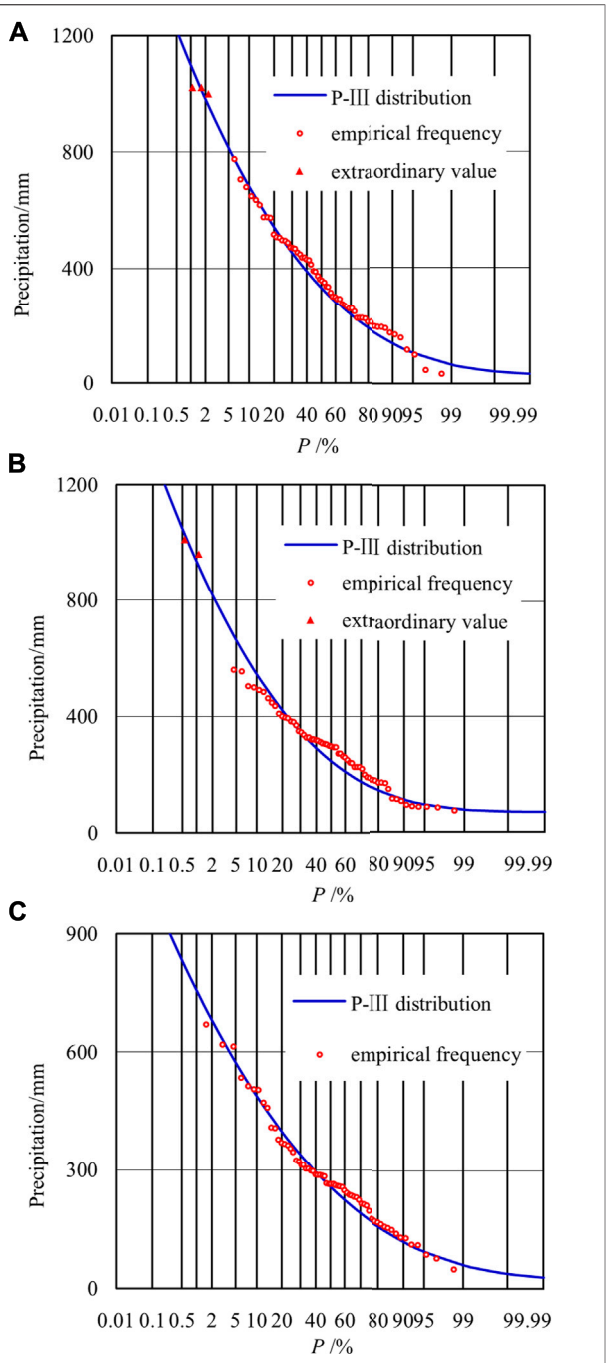

FIGURE 2 | Frequency curve of precipitation during Meiyu and Huang-Huai rainy seasons from 1957 to 2020 in **(A)** SYA, **(B)** YHA, and **(C)** NHA.

TABLE 4 | Precipitation during Meiyu and Huang-Huai rainy seasons in SYA, YHA, and NHA for some typical return periods (unit: mm).

Return period/a	100	50	30	20	10	5	3	2
SYA	1100.9	979.4	888.0	813.6	682.6	543.7	432.9	334.6
YHA	931.5	816.3	730.6	661.7	542.4	419.8	325.9	246.9
NHA	757.9	680.5	622.0	574.2	489.4	398.3	324.5	257.9

NHA in the year of 1965, 2007, and 2020 are 45.7, 27.8, and 29.2 years, respectively.

CONCLUSION

Based on the position of the SH ridge and the regional rainy days as the indices, Meiyu and Huang-Huai rainy seasons during 1957–2020 are identified. The precipitation characteristics of Meiyu and Huang-Huai rainy seasons in SYA, YHA, and NHA are analyzed, respectively. The return period of precipitation in the above three regions are specified when the summer monsoon moves northward over Anhui Province. The main conclusions are given as follows:

1) The 64-year average precipitation amount during Meiyu season in Anhui Province decreases from south to north regions. The 64-year average precipitation amount of the first period of Meiyu season in SYA, YHA, and NHA is 346.1, 239.6, and 169.3 mm, respectively. The 64-year average precipitation amount during Huang-Huai rainy season in Anhui Province increases from south to north regions. The three regional precipitations in the first period of Huang-Huai rainy season are 30.3, 55.2, and 109.2 mm, respectively.
2) With the northward movement of summer monsoon over Anhui Province, the 64-year average precipitation in YHA and NHA is close to each other, but less than that in SYA. The average precipitation amount in these three regions is 393.2, 315.6, and 286.0 mm, respectively, and it varies from year to year. The precipitation amount in SYA, YHA, and NHA during this period accounts for 87, 93, and 90% of the precipitation amount during June-July, respectively, implying that the precipitation during June-July is formed by the frontal rain belt resulting from the northward movement of summer monsoon.
3) The average duration of the first period of Meiyu season is 27.0 days from 14th June to 10th July. The first Huang-Huai rainy season mainly starts from 10th July to 23rd July with duration of 14.4 days. The northward movement of summer monsoon over Anhui Province mainly starts from 14th June to 25th July with duration of 42.0 days. The onset and ending dates of Meiyu season, Huang-Huai rainy season, and the northward movement of summer monsoon over Anhui Province vary greatly from year to year. Particularly, there are 8 years with the occurrence of a second period of Meiyu season, and 5 years with a second Huang-Huai rainy season out of 64 years.
4) The return periods corresponding to the precipitation of 1022.8 mm at 1996, 1022.4 mm at 1999, and 999.5 mm at 2020 in SYA are 63.9, 63.8, and 56.0 years, respectively, which are lower than the return period of the precipitation in 1954. The return periods of the precipitation of 959.8 mm at 1991 and 1010.6 mm at 2020 in YHA are 118.6 and 161.6 years, respectively. It is higher than the return period of precipitation during this period in 1954. The return periods corresponding to the precipitation of 670.2 mm at 1965, 612.9 mm at 2007, and 618.7 mm at 2020 in NHA are 45.7, 27.8, and 29.2 years, respectively. It is also lower than the return period of precipitation during this period in 1954.

DATA AVAILABILITY STATEMENT

Publicly available datasets were analyzed in this study. This data can be found here: http://data.cma.cn, https://psl.noaa.gov/data/gridded/data.ncep.reanalysis.html.

AUTHOR CONTRIBUTIONS

YZ and JJ designed the research. PZ, YZ, CW, YC, and SN performed the research. YZ and YZ wrote the manuscript. All the authors contributed to the article and approved the submitted version.

FUNDING

This work was supported by the National Key Research and Development Project of China (Grant No. 2017YFC1502403) and the National Natural Science Foundation of China (Grant Nos 51779067 and 51709071).

SUPPLEMENTARY MATERIAL

The Supplementary Material for this article can be found online at: https://www.frontiersin.org/articles/10.3389/feart.2021.751969/full#supplementary-material

REFERENCES

Bombardi, R. J., Pegion, K. V., Kinter, J. L., Cash, B. A., and Adams, J. M. (2017). Sub-seasonal Predictability of the Onset and Demise of the Rainy Season over Monsoonal Regions. *Front. Earth Sci.* 5, 14. doi:10.3389/feart.2017.00014

Ding, J. L., Wang, H., Dong, Z. R., and Wang, F. W. (2016). Characteristics of Extreme Precipitation in Anhui from 1960 to 2013. *J. Arid Meteorol.* 34 (2), 252–260. doi:10.11755/j.issn.1006-7639(2016)-02-0252

Ge, Q., Guo, X., Zheng, J., and Hao, Z. (2008). Meiyu in the Middle and Lower Reaches of the Yangtze River since 1736. *Chin. Sci. Bull.* 53 (1), 107–114. doi:10.1007/s11434-007-0440-5

Huang, D.-Q., Zhu, J., Zhang, Y.-C., Huang, Y., and Kuang, X.-Y. (2015). Assessment of Summer Monsoon Precipitation Derived from Five Reanalysis Datasets over East Asia. *Q.J.R. Meteorol. Soc.* 142 (694), 108–119. doi:10.1002/qj.2634

Huang, J. P., Zhang, G. L., Yu, H. P., Wang, S. S., Guan, X. D., and Ren, Y. (2020). Characteristics of Climate Change in the Yellow River basin during Recent 40 Years. *J. Hydraul. Eng.* 51 (9), 1048–1058. doi:10.13243/j.cnki.slxb.20200603

Information Center of the Ministry of Water Resources (1983). *National Hydrological Annual Report*. Beijing: China Water & Power Press.

Lee, S.-E., and Seo, K.-H. (2013). The Development of a Statistical Forecast Model for Changma. *Weather Forecast.* 28 (6), 1304–1321. doi:10.1175/WAF-D-13-00003.1

Liang, P., Tang, X., Ke, X. X., and He, J. H. (2007). Review of Study on Influencing Factors of China Meiyu. *J. Meteorol. Sci.* 27 (4), 464–471. doi:10.3969/j.issn.1009-0827.2007.04.018

Liu, D., He, J., Yao, Y., and Qi, L. (2012). Characteristics and Evolution of Atmospheric Circulation Patterns during Meiyu over the Jianghuai valley. *Asia-pacific J. Atmos. Sci.* 48 (2), 145–152. doi:10.1007/s13143-012-0014-6

Liu, Y., and Ding, Y. (2008). Teleconnection between the Indian Summer Monsoon Onset and the Meiyu over the Yangtze River Valley. *Sci. China Ser. D-earth Sci.* 51 (7), 1021–1035. doi:10.1007/s11430-008-0073-9

Luo, C. Z. (2006). *A Compilation of Survey Data on the Historical Floods in China*. Beijing: China Bookstore press.

National Climate Center of the China Meteorological Administration (2017). *Climate Center of Shanghai, Climate Center of Wuhan, Climate Center of Anhui, Climate Center of Jiangsu, Meteorological Bureau of Yangzhou. Meiyu Monitoring Indices (GB/T 33671-2017)*. Beijing: China Standard Press.

National Climate Center of the China Meteorological Administration (2016). *Monitoring Indices of Northwest Pacific Subtropical High (QX/T 304-2015)*. Beijing: China Meteorological Press.

Ninomiya, K. (2009). Characteristics of Precipitation in the Meiyu-Baiu Season in the CMIP3 20th Century Climate Simulations Kozo NINOMIYA. *J. Meteorol. Soc. Jpn.* 87 (4), 829–843. doi:10.2151/jssj.87.82910.2151/jmsj.87.829

Sun, Y., and Zhu, W. J. (2013). Rainstorm Characteristics during Meiyu Period in Jiangsu and its Effect on Water Levels of Lower Reaches of the Changjiang River. *Sci. Geogr. Sin.* 33 (2), 238–243. doi:10.13249/j.cnki.sgs.2013.02.23810.5846/stxb201206120844

Tang, Y. H., and Chen, X. H. (2015). Multi-scale Spatio-Temporal Characteristics and Influence of Precipitation Variation in Zhujiang River basin during the Last 50 Years. *Sci. Geogr. Sin.* 35 (4), 476–482. doi:10.1007/s11589-011-0776-4

Wang, J. (2020). Relationships between Jianghuai Meiyu Anomaly and the Collaborative Evolution of Wave Trains in the Upper and Lower Troposphere in Mid-july of 2020. *Front. Earth Sci.* 8, 597930. doi:10.3389/feart.2020.597930

Wang, J., Zhou, Y. L., Zhou, P., and Jin, J. L. (2018). Study on the Spatial Characteristics of Plum rains in Anhui Province Based on Set Pair Analysis. *Water Resour. Power* 36 (11), 1–4.

Wang, S. C., Cheng, X. F., and Yang, W. W. (2015). Characteristics of Rainfall in Chaohu basin in the Last 56 Years and Their Influences on Droughts and Floods. *Res. Soil Water Conserv* 22 (3), 289–294. doi:10.13869/j.cnki.rswc.2015.03.052

Wang, X. R., and Xu, M. (2002). Some Statistical Characteristics of Summer Precipitation in Anhui Province. *J. Anhui Normal Univ. (Nat Sci. Ed.* 25 (3), 281–285. doi:10.14182/j.cnki.1001-2443.2002.03.020

Water Resources Department of Anhui Province (1998). *Flood and Drought Disasters in Anhui*. Beijing: China Water & Power Press.

Xia, J., Duan, Q.-Y., Luo, Y., Xie, Z.-H., Liu, Z.-Y., and Mo, X.-G. (2017). Climate Change and Water Resources: Case Study of Eastern Monsoon Region of China. *Adv. Clim. Change Res.* 8 (2), 63–67. doi:10.1016/j.accre.2017.03.007

Xu, B., Chen, H., Gao, C., Zeng, G., and Huang, Q. (2021). Abnormal Change in spring Snowmelt over Eurasia and its Linkage to the East Asian Summer Monsoon: the Hydrological Effect of Snow Cover. *Front. Earth Sci.* 8, 594656. doi:10.3389/feart.2020.594656

Yang, W., Yang, H., and Yang, D. (2020). Classifying Floods by Quantifying Driver Contributions in the Eastern Monsoon Region of China. *J. Hydrol.* 585, 124767. doi:10.1016/j.jhydrol.2020.124767

Ye, Z. W. (2012). Precipitation Change in Flood Season and its Relationship with EASM in the Hongze lake Catchments in Recent 60 Years. *Sci. Geogr. Sin.* 32 (11), 1358–1363. doi:10.13249/j.cnki.sgs.2012.011.135810.1556/oh.2012.34m

Zhang, J., Zhou, X., Jiang, S., Tu, L., and Liu, X. (2020). Monsoon Precipitation, Economy and Wars in Ancient China. *Front. Earth Sci.* 8, 317. doi:10.3389/feart.2020.00317

Zhang, Y. (2007). Extremely Heavy Meiyu over the Yangtze and Huaihe Valleies in 1931. *Adv. Water Sci.* 18 (1), 8–16. doi:10.14042/j.cnki.32.1309.2007.01.002

Zhang, Y., Li, T. J., Li, J. Y., and Zhong, D. Y. (2019). Influence of the Westerlies and the South Asia Monsoon on Water Vapor Transport and Precipitation in the Three-River Headwaters Region during the Rainy Season. *Adv. Water Sci.* 30 (3), 348–358. doi:10.14042/j.cnki.32.1309.2019.03.005

Zhao, J. H., Chen, L. J., and Xiong, K. G. (2018). Climate Characteristics and Influential Systems of Meiyu to the South of the Yangtze River Based on the New Monitoring Rules. *Acta Meteorol. Sin.* 76 (5), 680–698. doi:10.11676/qxxb2018.025

Zhou, Y., Zuo, Y., Zhang, Y., Jin, J., Zhou, P., Wu, C., et al. (2021). Identification and Characteristics Analysis of Meiyu in Anhui Province

Based on the National Standard of Meiyu Monitoring Indices. *Hydrol. Res.* doi:10.2166/nh.2021.042

Conflict of Interest: The authors declare that the research was conducted in the absence of any commercial or financial relationships that could be construed as a potential conflict of interest.

Publisher's Note: All claims expressed in this article are solely those of the authors and do not necessarily represent those of their affiliated organizations, or those of the publisher, the editors, and the reviewers. Any product that may be evaluated in this article, or claim that may be made by its manufacturer, is not guaranteed or endorsed by the publisher.

frontiers in Earth Science

ORIGINAL RESEARCH
published: 12 October 2021
doi: 10.3389/feart.2021.747429

Impact of Climate Change on Water Availability in Water Source Areas of the South-to-North Water Diversion Project in China

*Cuiping Qiao[1], Zhongrui Ning[2,3,4], Yan Wang[3,4,5], Jinqiu Sun[3,4,5], Qianguo Lin[6] and Guoqing Wang[2,3,4,5]**

[1]North China University of Water Resources and Electric Power, Zhengzhou, China, [2]College of Hydrology and Water Resources, Hohai University, Nanjing, China, [3]Yangtze Institute for Conservation and Development, Nanjing, China, [4]Research Center for Climate Change, Ministry of Water Resources, Nanjing, China, [5]State Key Laboratory of Hydrology-Water Resources and Hydraulic Engineering, Nanjing Hydraulic Research Institute, Nanjing, China, [6]College of Environmental Science and Engineering, North China Electric Power University, Beijing, China

The South-to-North Water Diversion project (SNWD project) is a mega water project designed to help solve water shortages in North China. The project's management and operation are highly influenced by runoff change induced by climate change in the water source areas. It is important to understand water availability from the source areas in the context of global warming to optimize the project's regulation. Based on the projections of nine GCMs, the future runoff in the water source areas of the three diversion routes was simulated by using a grid-based model RCCC-WBM (Water Balance Model developed by Research Center for Climate Change). Results show that temperature will rise by about 1.5°C in the near future (2035, defined as 2026–2045) and 2.0°C in the far future (2050, defined as 2041–2060) relative to the baseline period of 1956–2000. Although GCM projections of precipitation are highly uncertain, the projected precipitation will likely increase for all three water source areas. As a result of climate change, the simulated runoff in the water source areas of the SNWD project will likely increase slightly by less than 3% relative to the baseline period for the near and far future. However, due to the large dispersion and uncertainty of GCM projections, a high degree of attention should be paid to the climate-induced risk of water supply under extreme situations, particularly for the middle route of the SNWD project.

Keywords: climate change, water resources, South-to-North Water Diversion Project, water source areas, GCM projections, RCCC-WBM

OPEN ACCESS

Edited by:
Xander Wang,
University of Prince Edward Island, Canada

Reviewed by:
Caihong Hu,
Zhengzhou University, China
Chuanzhe Li,
China Institute of Water Resources and Hydropower Research, China

****Correspondence:***
Guoqing Wang
gqwang@nhri.cn

Specialty section:
This article was submitted to Interdisciplinary Climate Studies, a section of the journal Frontiers in Earth Science

Received: *26 July 2021*
Accepted: *07 September 2021*
Published: *12 October 2021*

Citation:
Qiao C, Ning Z, Wang Y, Sun J, Lin Q and Wang G (2021) Impact of Climate Change on Water Availability in Water Source Areas of the South-to-North Water Diversion Project in China. Front. Earth Sci. 9:747429. doi: 10.3389/feart.2021.747429

INTRODUCTION

Water is the most direct and vulnerable sector influenced by climate change (Zhang and Wang, 2007; IPCC, 2008, 2013, 2021). China faces shortages in water sources due to a huge population (Liu et al., 2019). Uneven spatiotemporal distribution of water resources further exacerbates water scarcity in many arid regions (Hoekstra, 2014; Cosgrove and Loucks, 2015; Montanari et al., 2015). How much water is available in the context of global warming has been attracting tremendous attention from various arms of the central government, local communities, and river basin managers (Kundzewicz et al., 2018; Lu et al., 2019; Luo et al., 2019).

Studies show that only 10% of the total renewable water resources are currently used by people, and nearly 80% of the world's population is exposed to high levels of threat to water security (Oki and Kanae, 2006; Vörösmarty et al., 2010). Both climate change and human activities add complexity to the formation, migration, and transformation mechanisms of water resources by altering hydrological cycles, thereby aggravating water scarcity and water conflicts among different socioeconomic sectors (Haddeland et al., 2014; Liu et al., 2017; Tang et al., 2019). Because of the critical importance of water to socioeconomic development, climate change and its impacts on water resources have been investigated in previous studies (Wang et al., 2017; Liu et al., 2018; Bao et al., 2019; Sun et al., 2019). Regional and global hydrologic models combined with global climate model projections have been widely used to assess changes in water resources induced by climate change (Sivakumar, 2011; Schewe et al., 2013; Wang et al., 2012, 2017). The Xin'anjiang model which is based on the saturation excess mechanism has been mostly applied to humid catchments (Yuan et al., 2016; Zhang et al., 2019), while infiltration excess-based watershed models (e.g., GR4J model, SIMHYD model, etc.) have been used for assessing climate change impacts in arid catchments (Jones et al., 2006; Trudel et al., 2017). Land surface models (e.g., VIC model, CAS-LSM model, etc.) are mainly applied to large scale regions or applied at continental scale for hydrological modeling and climate change study (Wang et al., 2012; Wang et al., 2020). Due to the lack of observations, hydrological models with physical interpretation and simple model structure have attracted more interest and been applied in climate change study (Wang et al., 2014; Shahid et al., 2017). Compared with some of the well-known hydrological models (e.g., Xin'anjiang model, Tank model, etc.), simple models (e.g., RCCC-WBM) have advantages of easier understanding, fewer model parameters, more feasible transferability to the poorly gauged areas, etc. (Guan et al., 2019). The projected climate change impacts showed that water cycles have undergone considerable changes in the context of global warming, and such changes have altered water resource distribution in time and space (Bierkens, 2015; Mehran et al., 2017). Available water resources in the eastern monsoon region of China are decreasing and extreme hydrological events are occurring more frequently (Duan and Phillips, 2010; Xia et al., 2017), which increases the vulnerability of water resources and adds extra pressure on the security of water supplies, particularly in arid and semi-arid areas (Wang and Zhang, 2015; Jin et al., 2020).

China suffers from water shortages due to its large population and extremely low per capita water volume, accounting for less than one-third of the world average (CREEI, 2014; Liu et al., 2019). Conditions are particularly severe in the country's northern regions, where half of the population and two-thirds of the nation's farmland are located, but where there is only one-fifth of its water resources (Liu and Zheng, 2002; Liu and Xia, 2004). To alleviate water scarcity and maintain socioeconomic development in northern China, the central government has embarked on a strategic and ambitious infrastructure project known as the South-to-North Water Diversion project (SNWD project; Zhang, 2009; Zhao et al., 2017). The project is designed to transfer 44.8 km^3 of water per year from the water-abundant Yangtze River to the Huang-Huai-Hai region via its eastern, middle, and western routes, at a total cost of about US$62 billion (Stone and Jia, 2006; Liu et al., 2012; Yan and Chen, 2013; Long et al., 2020). By the end of 2018, the eastern route had brought an accumulated 3.1 billion m^3 of water to Shandong and the middle route had brought an accumulated 17.8 billion m^3 of water (http://nsbd.mwr.gov.cn; Yin et al., 2020). It has been observed that streamflow into the Danjiangkou Reservoir, the headwater source in the middle route of the SNWD project, has continuously decreased since the 1980s (Liu et al., 2012; Sun et al., 2014; She et al., 2017), negatively affecting the water supply of the middle route of the SNWD project. Using a climate elasticity method, Liu et al. (2012) concluded that the climatic variation (indicated by precipitation and potential evapotranspiration) was responsible for 84.1–90.1% of the stream decline. She et al. (2017) also showed that the sharp decrease in annual runoff from the Danjiangkou Reservoir is mainly influenced by the decrease in annual precipitation. While climate change affects the water availability of the water source area, it also affects the encounter probability of flood and drought between the water source areas and the water receiving areas (Chen and Xie, 2012; Liu et al., 2015; Xia et al., 2017).

Climate change will be one of the major challenges to the management and operation of the SNWD project, as water resources are sensitive to climate change and variability (Wang et al., 2012, 2017). With the expectation that water supplies will only become tighter in the future (Rodell et al., 2018; Pokhrel et al., 2021), it is essential to understand water availability in water source areas under climate change for the efficient and reasonable allocation of water resources by the SNWD project. However, previous studies on the SNWD project mainly focused on the historical variation of stream flow, so there are limited studies on future water availability of water source areas of the SNWD project, particularly for all three source areas together (Su et al., 2016; Yu et al., 2017). The objective of this study is to investigate future climate changes in the three water source areas and the extent to which the stream flow will change in the coming decades relative to the design period (1956–2000) of the SNWD project and finally to support the project operation practices and revisions of the second phase plan.

DATA SOURCES AND METHODOLOGY

Study Areas and Data Sources

The SNWD project approved by China's State Council in 2002 is a national strategic project that transfers water from the Yangtze River to the Huai River, Yellow River, and Hai River to solve water shortages in North China. The project was designed with three water diversion routes among which the eastern route and the middle route have been constructed and in use since 2013 and 2014, respectively, while the western route is still in the planning stages. Based on the project planning, the water source areas of the project consist of the upper Yangtze River for the western route with a drainage area of 299,087 km^2, the middle and upper

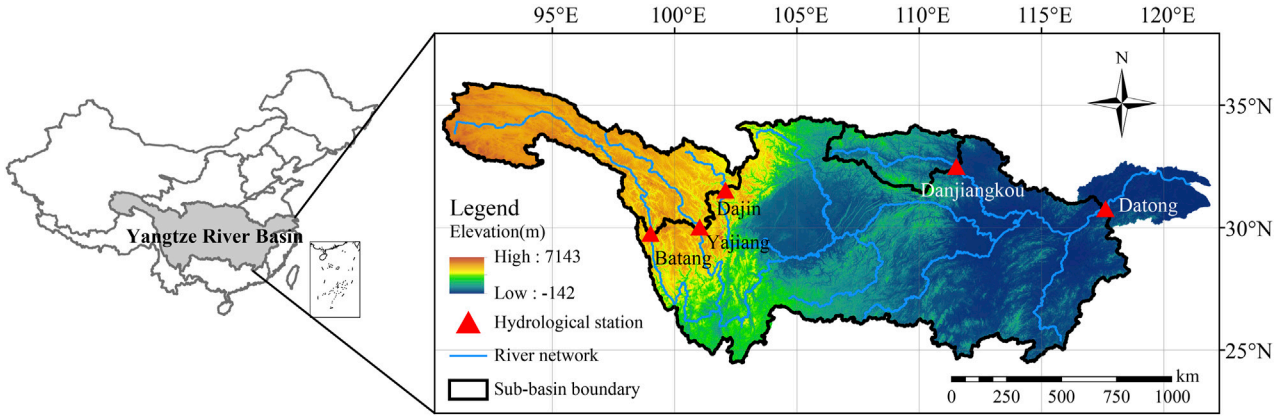

FIGURE 1 | Water source areas, river systems, and locations of key hydrometric stations of the South-to-North Water Diversion Project in the Yangtze River basin.

TABLE 1 | Overview of nine GCMs used in this study.

Nos.	GCMs	Country and developer	Resolution	Nos.	GCMs	Country and developer	Resolution
1	BCC-CSM1	China, BCC	2.8° × 2.8°	6	FIO-ESM	China, FIO	2.8° × 2.8°
2	CNRM-CM5	France, CNRM-CERFACS	1.4° × 1.4°	7	GFDL-ESM2M	America, GFDL	2.0° × 2.5°
3	CSIRO-MK3	Australia, CSIRO	1.9° × 1.9°	8	GISS-E2-H	America, GISS	2.0° × 2.5°
4	FGOALS-G2	China, LASG-CESS	3.0° × 2.8°	9	MIROC-ESM	Japan, CCSR/NIES/FRCGC	2.8° × 2.8°
5	CCSM4	America, NCAR	0.9° × 1.3°	-	-	-	-

Han River for the mid-route with a drainage area of 94,784 km^2, and the area (1,705,383 km^2) above Datong hydrometric station for the eastern route, which covers almost the entire Yangtze River basin. The water source areas of the project, major river systems of the Yangtze River, and locations of key hydrometric stations controlling water source areas are shown in **Figure 1**.

The daily grid meteorological data over the Yangtze River basin with a spatial resolution of 0.25° and 1951–2020 data series were collected from the China Meteorological Administration (CMA). The daily observed discharge data at five hydrometric stations which control drainage source areas of the SNWD project, shown in **Figure 1**, were collected from the Hydrology Bureau of the Ministry of Water Resources (MWR). These hydro-meteorological data were used to calibrate hydrological models for climate change impact assessment.

The SNWD project was designed by using the 1956–2000 data series. In order to understand the future climate changes relative to those in the design period, we defined two future periods as follows: near future (NF) from 2026 to 2045, and far future (FF) from 2041 to 2060. The future climate scenarios were downloaded from https://www.wcrp-climate.org/wgcm-cmip/wgcm-cmip6. As both the high-emission scenarios, e.g., SSP5-8.5, and the low-emission scenarios, e.g., SSP1-2.6, consider extreme emission pathways, the medium-emission scenarios, e.g., SSP2-4.5, will probably occur in the future. We therefore only used climate change projections under the SSP2-4.5 scenario in this study. Based on simulation performance to the past variation of climate variables and consideration of GCM independence (Xin et al., 2020; Zhao et al., 2021), nine GCMs were selected and used in this study (**Table 1**). The nine GCM projections under the SSP2-4.5 scenario were downscaled to a 0.25° grid by using a LARS-WG statistical downscaling method (Hassan et al., 2014). The data series of the projected climate scenarios are from 1901 to 2099.

RCCC-WBM

In this study, the RCCC-WBM (Water Balance Model developed by the Research Center for Climate Change) was applied to the study areas for climate change impact assessment. The model is a conceptual hydrological model that considers the three runoff components of surface flow, underground flow, and snowmelt flow. The model inputs include monthly precipitation, pan evaporation, and temperature. The model has been applied to hundreds of catchments worldwide (Wang et al., 2014; Guan et al., 2019). The model structure is shown in **Figure 2**.

Based on the RCCC-WBM, we developed a grid-based model covering the entire Yangtze River basin, which was divided into 1,812 grid cells with a spatial resolution of 0.25°. The RCCC-WBM is employed to calculate runoff yield in each grid cell. For a catchment that covers numerous grid cells, the flow routing scheme in the VIC (Variable Infiltration Capacity) model was referenced in the model flow concentrating from grid cells to catchment outlet (Wang et al., 2012, 2014).

The RCCC-WBM has four parameters that need to be calibrated by comparing the simulated and recorded discharge series. The Nash and Sutcliffe efficiency criterion (NSE) and the

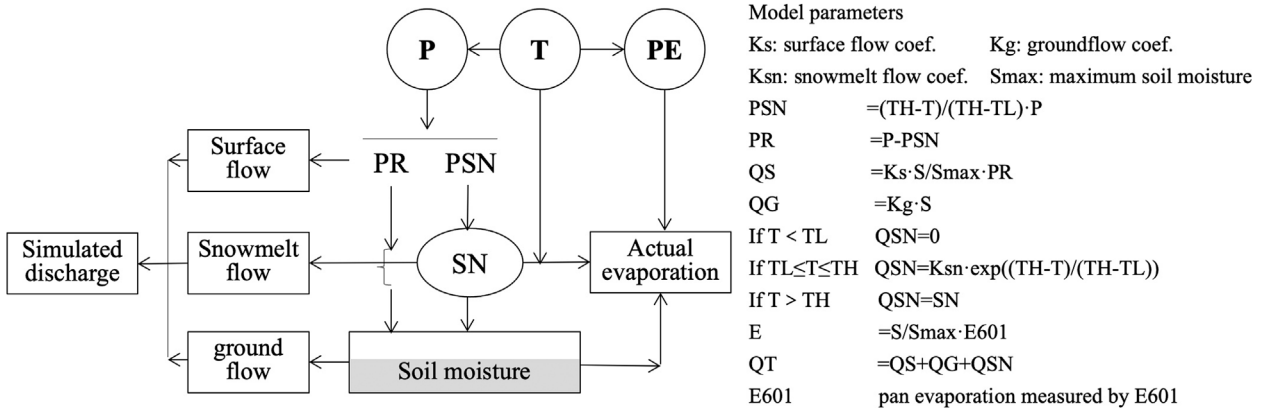

FIGURE 2 | The model structure and principle of the RCCC-WBM.

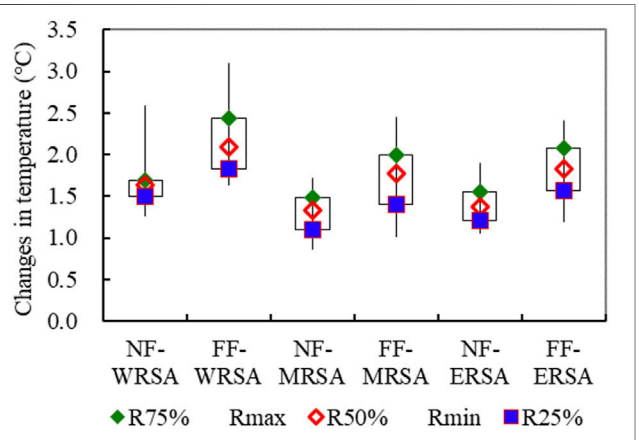

FIGURE 3 | Temperature changes in two periods of near future (NF) and far future (FF) relative to baseline of 1956–2000 for all three source areas of the South-to-North Water Diversion Project (WRSA, MRSA, and ERSA denote the western route source area, the middle route source area, and the eastern route source area, respectively; same as **Figure 4** and **Figure 7**).

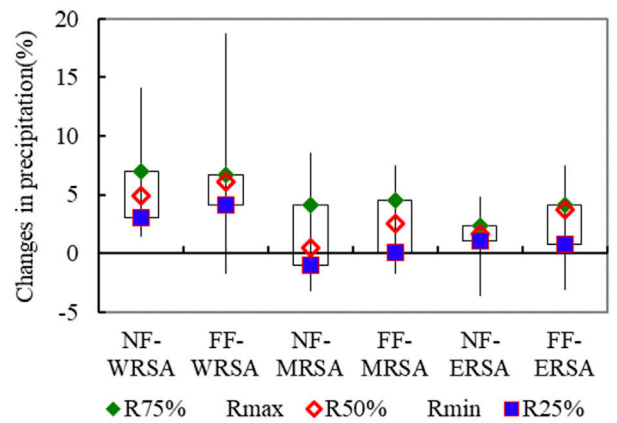

FIGURE 4 | Precipitation changes in two periods of near future (NF) and far future (FF) relative to baseline of 1956–2000 for all three source areas of the South-to-North Water Diversion Project.

relative error of volumetric fit (RE), which describe the fitting performance of the simulated discharge to the recorded discharge, are employed as the objective functions to calibrate the model (Nash and Sutcliffe, 1970; Moriasi et al., 2007; Gupta et al., 2009).

RESULTS AND DISCUSSION

Changes in Temperature and Precipitation for Water Source Areas

Taking 1956–2000 as a baseline period, changes in temperature in the near and far future relative to the baseline period for all three source areas, i.e., the western route source area (WRSA), middle route source area (MRSA), and eastern route source area (ERSA), of the SNWD project were investigated (**Figure 3**).

Figure 3 shows that the nine GCMs all projected that temperatures will continue to rise in the near future and far future although they projected different rise ranges. In the near future of 2026–2045, temperature will rise by 1.64°C [1.27°C, 2.58°C], 1.33°C [0.87°C, 1.71°C], and 1.37°C [1.06°C, 1.89°C] for WRSA, MRSA, and ERSA, respectively. However, temperature will rise higher in the far future of 2041–2060. On average, temperature would rise by 2.09°C, 1.78°C, and 1.82°C, respectively, with ranges of [1.64°C, 3.09°C], [1.02°C, 2.44°C], and [1.19°C, 2.41°C] for the three water source areas.

Temperature is a thermal driver of the hydrological cycle, and temperature rise could reduce runoff yield by increasing catchment evaporation. According to IPCC, there is high confidence that global mean evaporation increases with global warming, with evaporation increasing by 1–3% for every 1°C increase in temperature (IPCC, 2021). Previous studies indicate that a 1°C rise in temperature might lead to an approximately 5% decrease in runoff for humid areas (IPCC, 2008; Wang et al.,

TABLE 2 | Discharge simulation results for the five hydrometric stations within source areas of the South-to-North Water Diversion Project.

Source areas	Stations	Model calibration			Model validation		
		Data series	NSE-v (%)	Re-v (%)	Data series	NSE-v (%)	Re-v (%)
Western route	Dajin	1957–1989	83.7	−1.1	1990–2000	85.1	−0.2
	Yajiang	1956–1989	86.6	−1.9	1990–2000	89.3	2.1
	Batang	1960–1989	83.3	0.4	1990–2000	74.6	−0.7
Middle route	Danjiangkou	1956–1989	81.5	1.7	1990–2000	73.0	0.4
Eastern route	Datong	1956–1989	90.6	−0.8	1990–2000	87.4	0.3

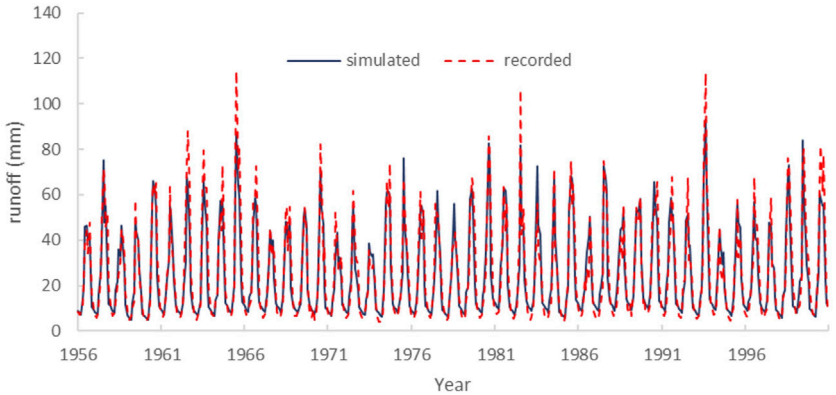

FIGURE 5 | Monthly recorded and simulated runoff at the Yajiang station during 1956–2000.

2016). Changes in temperature will definitely influence water availability in the water source area of the SNWD project.

Figure 4 shows changes in precipitation during the coming periods of the near future and far future relative to the baseline period. The figure indicates that precipitation projections have a higher uncertainty than that of temperature as a GCM might project decrease in precipitation while another one might project precipitation increase. For the WRSA, all GCMs project that precipitation in near future will increase by 4.9% with a range of [1.43%, 14.1%], and most of the GCM projections show a 6.06% precipitation increase in the far future on average with a range of [−1.68%, 18.77%]. For the MRSA, more than half of the GCMs projected that precipitation will increase by 0.45% [−3.23%, 8.61%] in the near future and 2.54% [−1.77%, 7.5%] in the far future. For the ERSA, most of the GCMs projected that precipitation will increase by 1.63% [−3.62%, 4.84%] in the near future and 3.71% [−3.13%, 7.45%] in the far future.

According to the definition of uncertainty by the IPCC (IPCC, 2013), precipitation in the WRSA will almost certainly increase in the near future and will very likely increase in the far future, while precipitation in both the MRSA and ERSA is likely to increase in both the near and far future. Increases in precipitation for the source areas could increase runoff yield and will no doubt benefit implementation of the SNWD project.

Model Calibration and Discharge Simulation

A suitable hydrological model is essential to quantify the impact of climate change on water resources. Within the source areas of the SNWD project, there are daily discharges available at five hydrometric stations with a data series length of over 30 years. The grid meteorological data were used to drive the grid-based model RCCC-WBM for discharge simulation. Simulation results are given in **Table 2**. The monthly recorded and simulated discharges at the Yajiang hydrometric station were compared, as shown in **Figure 5**.

Table 2 shows that the grid-based model RCCC-WBM performs well in the discharge simulation for all five catchments. The NSEs in both calibration and validation periods are above 0.7, while the REs in the periods are limited in the range of ±2.0%. **Figure 5** indicates that the monthly recorded and simulated runoff series at the Yajiang station for 1956–2000 matched well, which is in accordance with the results in **Table 2**. **Table 2** and **Figure 5** both sufficiently illustrate that the RCCC-WBM is qualified for simulating runoff under the future climate change scenarios.

By using the downscaled grid climate scenarios of nine GCMs to drive the grid-based model RCCC-WBM, monthly runoff yield series for grid cells were simulated for 1951–2090. The catchment average annual runoff yields of the three source areas of the SNWD project over the period were then calculated based on the areal weighted method. The 9-GCM-based annual runoff simulations for the three source areas and the simulation-based median runoff series over the period of 1951–2090 are shown in **Figure 6**. **Figure 6** shows that the nine simulated annual runoff series all exhibited a natural fluctuation with no significant variation trends. However, the range of runoff variability in the coming decades becomes larger than that in the past.

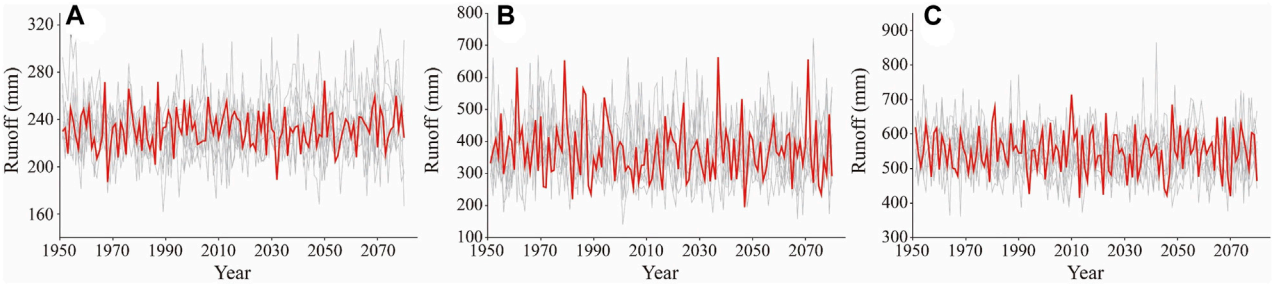

FIGURE 6 | The simulated annual runoff series (gray lines) of the nine GCMs and the simulation-based median runoff series (red line) during 1951–2090 for all three source areas of the South-to-North Water Diversion project (**(A–C)** denote source areas of the western route, the middle route, and the eastern route, respectively).

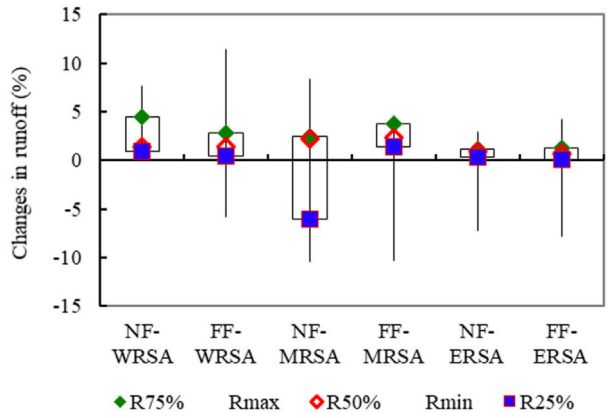

FIGURE 7 | Runoff changes in two periods of near future (NF) and far future (FF) relative to the baseline period of 1956–2000 for all three source areas of the South-to-North Water Diversion Project.

Changes in Runoff for the Three Water Diversion Areas

Runoff changes in the near future and far future relative to the baseline period of 1956–2000 were investigated based on the simulated runoff over the period of 1951–2090 under the nine GCM scenarios for all three source areas (**Figure 7**).

Figure 7 indicates that for the WRSA, all GCMs project that runoff in the near future will increase by 1.42% with a range of [0.29%, 7.69%], and most of the GCMs project a 1.36% runoff increase in the far future on average with a range of [−5.84%, 11.40%]. The projected runoff in the WRSA will very likely increase in both the near and far future. For the MRSA, over 50% of the GCMs project that runoff will increase by 2.25% [−10.48%, 8.31%] in the near future and 2.35% [−10.27%, 4.60%] in the far future. Although more than half of the GCMs project runoff in the middle route source area will increase in the future, we also find that the projected runoff might decrease by > 10% in extreme conditions. Attention to the risk of runoff reduction induced by climate change should be given in the practical operation of the middle route sub-project. For the ERSA, most of the nine GCMs project runoff will increase in the near future with the exception of the GISS-E2-R which projects runoff will decrease by −7.3%. The GISS-E2-R and GFDL-ESM2G project annual runoff will decrease by −7.8% and −7.0% in far future while the other seven GCMs project annual runoff will increase by [0.1%, 4.2%]. On average, the median GCM project runoff will increase by 0.88% in the near future and 0.7% in the far future. In general, the projected runoff in the eastern route source area will likely increase in the coming decades, which could support operation of the eastern route sub-project.

DISCUSSION

Both changes in temperature and precipitation could affect regional water resources by altering hydrological cycles. Global land surface temperature rose by 0.85°C during the period 1880–2012 (IPCC, 2013) while temperatures in China rose by 0.9°C in the same period. Temperatures in China have risen particularly fast during recent decades (1956–2012), increasing at a rate of 0.25°C/10a, which is higher than the global average (Qin et al., 2012). The variation of the projected temperature over the three source areas in this study are in accordance with the previous studies, which will continue to rise in the future (Tao et al., 2011). However, the projected increase in temperature in this study is approximately 0.33°C/10a, which is much higher than that in the past (Huang et al., 2014). The projected regional average precipitation over the three source areas will likely increase in the rapid warming situation although several GCMs project a certain decrease in precipitation. Most previous studies support the findings although there is great uncertainty in precipitation projections (Zhang et al., 2010; Guo et al., 2012).

Numerous studies have indicated that the precipitation in the Yangtze River basin will increase in the coming decades, and, as a result, stream flow will probably increase (Bian et al., 2017; Yu et al., 2017; Lu et al., 2018), which is in accordance with the findings in this study. However, Gu et al. (2015) found that annual runoff at the Panzhihua station in the upper Yangtze River basin during 2011–2040 may decrease by 1.2–3.5% compared to that in 1970–1999, which is counter to the conclusions drawn in this study. The discrepancy might result from differences in the baseline period, future periods, GCMs, and the study catchments

selected. Although inflow to the Danjiangkou Reservoir decreased in the past (Liu et al., 2012; Sun et al., 2014), the projected runoff will likely increase by 2% in the coming decades. The hydrological regime is shifting to benefit the operation of the SNWD project due to climate change.

SUMMARY AND CONCLUSIONS

In the context of global warming, temperatures in the source areas of the SNWD project will continue to rise. Relative to the baseline period (1956–2000), temperatures will rise by about 1.5°C and 2.0°C in the near future (2026–2045) and the far future (2041–2060). Precipitation will likely increase for all three source areas although GCM projections are quite dispersed and uncertain.

The grid-based model RCCC-WBM performs well for discharges in the study areas. The simulated runoff is associated with GCM projections. According to the nine GCMs, the median runoff will likely increase by less than 3% relative to the baseline for all three source areas of the SNWD project, which could guarantee the security of water supply to some extent. However, attention should be paid to the risk to water supply induced by extreme climate change conditions when the project operates in practice.

DATA AVAILABILITY STATEMENT

The raw data supporting the conclusions of this article will be made available by the authors, without undue reservation.

AUTHOR CONTRIBUTIONS

CQ: conceptualization and methodology. GW and JQ: data curation and model. ZN: formal analysis and visualization. YW and GW: writing and editing the manuscript. QL: discussion and suggestions for data analysis.

FUNDING

This research was financially supported by the National Key Research and Development Programs of China (Grants 2016YFA0601500, 2017YFA0605002, and 2017YFC0404602), the National Natural Science Foundation of China (Grant nos. 41830863, 51879162, 51609242, 51779146, and 41601025), and the State Key Laboratory of Hydrology-Water Resources and Hydraulic Engineering (Grant no. 2019nkzd02).

REFERENCES

Bao, Z., Zhang, J., Wang, G., Chen, Q., Guan, T., Yan, X., et al. (2019). The Impact of Climate Variability and Land Use/Cover Change on the Water Balance in the Middle Yellow River Basin, China. *J. Hydrol.* 577, 123942. doi:10.1016/j.jhydrol.2019.123942

Bian, H., Lü, H., Sadeghi, A., Zhu, Y., Yu, Z., Ouyang, F., et al. (2017). Assessment on the Effect of Climate Change on Streamflow in the Source Region of the Yangtze River, China. *Water.* 9, 70. doi:10.3390/w9010070

Bierkens, M. F. P. (2015). Global Hydrology 2015: State, Trends, and Directions. *Water Resour. Res.* 51, 4923–4947. doi:10.1002/2015WR017173

Chen, F., and Xie, Z. (2012). Effects of Climate Change on Synchronous-Asynchronous Encounter Probability of Rich-Poor Precipitation Between Water Source Area and Water Receiving Areas in the Middle Route of South-To-North Water Transfer Project. *Clim. Environ. Res.* 17 (2), 139–148. doi:10.3878/j.isn.1006-9585.2011.10097

China Renewable Energy Engineering Institute (CREEI) (2014). *Ministry of Water Resources. Water Resources Assessment and its Development & Utilization in China*. Beijing: China Hydropower Press.

Cosgrove, W. J., and Loucks, D. P. (2015). Water Management: Current and Future Challenges and Research Directions. *Water Resour. Res.* 51, 4823–4839. doi:10.1002/2014WR016869

Duan, Q., and Phillips, T. J. (2010). Bayesian Estimation of Local Signal and Noise in Multimodel Simulations of Climate Change. *J. Geophys. Res.* 115, D18123. doi:10.1029/2009JD013654

Gu, H., Yu, Z., Wang, G., Wang, J., Ju, Q., Yang, C., et al. (2015). Impact of Climate Change on Hydrological Extremes in the Yangtze River Basin, China. *Stoch. Environ. Res. Risk Assess.* 29, 693–707. doi:10.1007/s00477-014-0957-5

Guan, X., Zhang, J., Elmahdi, A., Li, X., Liu, J., Liu, Y., et al. (2019). The Capacity of the Hydrological Modeling for Water Resource Assessment Under the Changing Environment in Semi-Arid River Basins in China. *Water.* 11 (7), 1328. doi:10.3390/w11071328

Guo, J., Chen, H., Xu, C.-Y., Guo, S., and Guo, J. (2012). Prediction of Variability of Precipitation in the Yangtze River Basin Under the Climate Change Conditions Based on Automated Statistical Downscaling. *Stoch. Environ. Res. Risk Assess.* 26 (2), 157–176. doi:10.1007/s00477-011-0464-x

Gupta, H. V., Kling, H., Yilmaz, K. K., and Martinez, G. F. (2009). Decomposition of the Mean Squared Error and NSE Performance Criteria: Implications for Improving Hydrological Modelling. *J. Hydrol.* 377, 80–91. doi:10.1016/j.jhydrol.2009.08.003

Haddeland, I., Heinke, J., Biemans, H., Eisner, S., Flörke, M., Hanasaki, N., et al. (2014). Global Water Resources Affected by Human Interventions and Climate Change. *Proc. Natl. Acad. Sci. USA.* 111 (9), 3251–3256. doi:10.1073/pnas.1222475110

Hassan, Z., Shamsudin, S., and Harun, S. (2014). Application of SDSM and LARS-WG for Simulating and Downscaling of Rainfall and Temperature. *Theor. Appl. Climatol.* 116, 243–257. doi:10.1007/s00704-013-0951-8

Hoekstra, A. Y. (2014). Water Scarcity Challenges to Business. *Nat. Clim Change.* 4 (5), 318–320. doi:10.1038/nclimate2214

Huang, X., Cai, X., Yang, P., and Zhao, J. (2014). Climate Change Trend Analysis in Western Route of South-To-North Water Diversion Project. *South-To-North Water Transf. Water Sci. Technol.* 12 (3), 5–9. doi:10.13476/j.cnki.nsbdqk.2014.03.002

IPCC (2008). *Climate Change and Water*. Cambridge and New York: Cambridge University Press.

IPCC (2013). *Climate Change 2013: The Physical Science Basis*. Cambridge and New York: Cambridge University Press.

IPCC (2021). *Climate Change 2021: The Physical Science Basis*. Cambridge and New York: Cambridge University Press.

Jin, J., Wang, G., Zhang, J., Yang, Q., Liu, C., Liu, Y., et al. (2020). Impacts of Climate Change on Hydrology in the Yellow River Source Region, China. *J. Water Clim. Chang.* 11, 916–930. doi:10.2166/wcc.2018.085

Jones, R. N., Chiew, F. H. S., Boughton, W. C., and Zhang, L. (2006). Estimating the Sensitivity of Mean Annual Runoff to Climate Change Using Selected Hydrological Models. *Adv. Water Resour.* 29 (10), 1419–1429. doi:10.1016/j.advwatres.2005.11.001

Kundzewicz, Z. W., Krysanova, V., Benestad, R. E., Hov, Ø., Piniewski, M., and Piniewski, I. M. (2018). Uncertainty in Climate Change Impacts on Water Resources. *Environ. Sci. Pol.* 79, 1–8. doi:10.1016/j.envsci.2017.10.008

Liu, C., and Xia, J. (2004). Water Problems and Hydrological Research in the Yellow River and the Huai and Hai River Basins of China. *Hydrol. Process.* 18, 2197–2210. doi:10.1002/hyp.5524

Liu, C., and Zheng, H. (2002). South-to-North Water Transfer Schemes for China. *Int. J. Water Resour. Development.* 18, 453–471. doi:10.1080/0790062022000006934

Liu, J., Bao, Z., Liu, C., Wang, G., Liu, Y., Wang, J., et al. (2019). Change Law and Cause Analysis of Water Resources and Water Consumption in China in Past 20 Years. *Hydro-science Eng.* 4, 31–41. doi:10.16198/j.cnki.1009-640x.2019.04.005

Liu, J., Yang, H., Gosling, S. N., Kummu, M., Flörke, M., Pfister, S., et al. (2017). Water Scarcity Assessments in the Past, Present, and Future. *Earth's Future.* 5 (6), 545–559. doi:10.1002/2016ef000518

Liu, X., Liu, C., Luo, Y., Zhang, M., and Xia, J. (2012). Dramatic Decrease in Streamflow from the Headwater Source in the Central Route of China's Water Diversion Project: Climatic Variation or Human Influence? *J. Geophys. Res.* 117, a–n. doi:10.1029/2011JD016879

Liu, X., Luo, Y., Yang, T., Liang, K., Zhang, M., and Liu, C. (2015). Investigation of the Probability of Concurrent Drought Events Between the Water Source and Destination Regions of China's Water Diversion Project. *Geophys. Res. Lett.* 42, 8424–8431. doi:10.1002/2015GL065904

Liu, Y., Zhang, J., Wang, G., Wang, G., Jin, J., Liu, C., et al. (2020). How Do Natural Climate Variability, Anthropogenic Climate and Basin Underlying Surface Change Affect Streamflows? A Three-Source Attribution Framework and Application. *J. Hydro-environment Res.* 28, 57–66. doi:10.1016/j.jher.2018.08.005

Long, D., Yang, W., Scanlon, B. R., Zhao, J., Liu, D., Burek, P., et al. (2020). South-to-North Water Diversion Stabilizing Beijing's Groundwater Levels. *Nat. Commun.* 11, 3665. doi:10.1038/s41467-020-17428-6

Lu, S., Bai, X., Li, W., and Wang, N. (2019). Impacts of Climate Change on Water Resources and Grain Production. *Technol. Forecast. Soc. Change.* 143, 76–84. doi:10.1016/j.techfore.2019.01.015

Lu, W., Wang, W., Shao, Q., Yu, Z., Hao, Z., Xing, W., et al. (2018). Hydrological Projections of Future Climate Change Over the Source Region of Yellow River and Yangtze River in the Tibetan Plateau: A Comprehensive Assessment by Coupling RegCM4 and VIC Model. *Hydrological Process.* 32 (13), 2096–2117. doi:10.1002/hyp.13145

Luo, M., Liu, T., Meng, F., Duan, Y., Bao, A., Xing, W., et al. (2019). Identifying Climate Change Impacts on Water Resources in Xinjiang, China. *Sci. Total Environ.* 676, 613–626. doi:10.1016/j.scitotenv.2019.04.297

Mehran, A., AghaKouchak, A., Nakhjiri, N., Stewardson, M. J., Peel, M. C., Phillips, T. J., et al. (2017). Compounding Impacts of Human-Induced Water Stress and Climate Change on Water Availability. *Sci. Rep.* 7, 6282. doi:10.1038/s41598-017-06765-0

Montanari, A., Bahr, J., Blöschl, G., Cai, X., Mackay, D. S., Michalak, A. M., et al. (2015). Fifty Years ofWater Resources Research: Legacy and Perspectives for the Science of Hydrology. *Water Resour. Res.* 51 (9), 6797–6803. doi:10.1002/2015wr017998

Moriasi, D. N., Arnold, J. G., Van Liew, M. W., Bingner, R. L., Harmel, R. D., and Veith, T. L. (2007). Model Evaluation Guidelines for Systematic Quantification of Accuracy in Watershed Simulations. *Trans.ASABE.* 50, 885–900. doi:10.13031/2013.23153

Nash, J. E., and Sutcliffe, J. V. (1970). River Flow Forecasting Through Conceptual Models Part I - A Discussion of Principles. *J. Hydrol.* 10 (3), 282–290. doi:10.1016/0022-1694(70)90255-6

Oki, T., and Kanae, S. (2006). Global Hydrological Cycles and World Water Resources. *Science.* 313 (5790), 1068–1072. doi:10.1126/science.1128845

Pokhrel, Y., Felfelani, F., Satoh, Y., Boulange, J., Burek, P., Gädeke, A., et al. (2021). Global Terrestrial Water Storage and Drought Severity Under Climate Change. *Nat. Clim. Chang.* 11, 226–233. doi:10.1038/s41558-020-00972-w

Qin, D., Ding, Y., and Mu, M. (2012). *Climate and Environment Evolution: 2012.* Beijing: Meteorology Press.

Rodell, M., Famiglietti, J. S., Wiese, D. N., Reager, J. T., Beaudoing, H. K., Landerer, F. W., et al. (2018). Emerging Trends in Global Freshwater Availability. *Nature.* 557, 651–659. doi:10.1038/s41586-018-0123-1

Schewe, J., Heinke, J., Gerten, D., Haddeland, I., Arnell, N. W., Clark, D. B., et al. (2013). Multimodel Assessment of Water Scarcity Under Climate Change. *Proc. Natl. Acad. Sci. USA.* 111 (9), 3245–3250. doi:10.1073/pnas.1222460110

Shahid, M., Cong, Z., and Zhang, D. (2017). Understanding the Impacts of Climate Change and Human Activities on Streamflow: a Case Study of the Soan River Basin, pakistan. *Theor. Appl. Climatol.* 134, 205. doi:10.1007/s00704-017-2269-4

She, D., Xia, J., Shao, Q., Taylor, J. A., Zhang, L., Zhang, X., et al. (2017). Advanced Investigation on the Change in the Streamflow into the Water Source of the Middle Route of China's Water Diversion Project. *J. Geophys. Res. Atmos.* 122, 6950–6961. doi:10.1002/2016JD025702

Sivakumar, B. (2011). Global Climate Change and its Impacts on Water Resources Planning and Management: Assessment and Challenges. *Stoch. Environ. Res. Risk Assess.* 25, 583–600. doi:10.1007/s00477-010-0423-y

Stone, R., and Jia, H. (2006). HYDROENGINEERING: Going Against the Flow. *Science.* 313, 1034–1037. doi:10.1126/science.313.5790.1034

Su, B., Huang, J., Zeng, X., Gao, C., and Jiang, T. (2016). Impacts of Climate Change on Streamflow in the Upper Yangtze River Basin. *Climatic Change.* 141 (3), 533–546. doi:10.1007/s10584-016-1852-5

Sun, L., Wang, Y.-Y., Zhang, J.-Y., Yang, Q.-L., Bao, Z.-X., Guan, X.-X., et al. (2019). Impact of Environmental Change on Runoff in a Transitional basin: Tao River Basin from the Tibetan Plateau to the Loess Plateau, China. *Adv. Clim. Change Res.* 10 (4), 214–224. doi:10.1016/j.accre.2020.02.002

Sun, Y., Tian, F., Yang, L., and Hu, H. (2014). Exploring the Spatial Variability of Contributions From Climate Variation and Change in Catchment Properties to Streamflow Decrease in a Mesoscale Basin by Three Different Methods. *J. Hydrol.* 508, 170–180. doi:10.1016/j.jhydrol.2013.11.004

Tang, Q., Liu, X., Li, Z., Zhang, X., Yu, Q., et al. (2019). Integrated Water Systems Model for Terrestrial Water Cycle Simulation. *Adv. Earth Sci.* 34 (2), 115–123. doi:10.11867/j.issn.1001-8166.2019.02.0115

Tao, H., Gemmer, M., Jiang, J., Lai, X., and Zhang, Z. (2011). Assessment of CMIP3 Climate Models and Projected Changes of Precipitation and Temperature in the Yangtze River Basin, China. *Climatic Change.* 111 (3-4), 737–751. doi:10.1007/s10584-011-0144-3

Trudel, M., Doucet-Généreux, P.-L., and Leconte, R. (2017). Assessing River Low-Flow Uncertainties Related to Hydrological Model Calibration and Structure Under Climate Change Conditions. *Climate.* 5 (1), 19. doi:10.3390/cli5010019

Vörösmarty, C. J., McIntyre, P. B., Gessner, M. O., Dudgeon, D., Prusevich, A., Green, P., et al. (2010). Global Threats to Human Water Security and River Biodiversity. *Nature.* 467 (7315), 555–561. doi:10.1038/nature09440

Wang, G., Zhang, J., Xu, Y., Bao, Z., and Yang, X. (2017). Estimation of Future Water Resources of Xiangjiang River Basin With VIC Model Under Multiple Climate Scenarios. *Water Sci. Eng.* 10, 87–96. doi:10.1016/j.wse.2017.06.003

Wang, G., Zhang, J., Jin, J., Liu, Y., He, R., Bao, Z., et al. (2014). Regional Calibration of a Water Balance Model for Estimating Stream Flow in Ungauged Areas of the Yellow River Basin. *Quat. Int.* 336, 65–72. doi:10.1016/j.quaint.2013.08.051

Wang, G., Zhang, J., Jin, J., Pagano, T. C., Calow, R., Bao, Z., et al. (2012). Assessing Water Resources in China Using PRECIS Projections and VIC Model. *Hydrol. Earth Syst. Sci. Discuss.* 8, 7293–7317. doi:10.5194/hessd-8-7293-2011

Wang, G., and Zhang, J. (2015). Variation of Water Resources in the Huang-Huai-Hai Areas and Adaptive Strategies to Climate Change. *Quat. Int.* 380-381, 180–186. doi:10.1016/j.quaint.2015.02.005

Wang, G., Zhang, J., He, R., Liu, C., Ma, T., Bao, Z., et al. (2016). Runoff Sensitivity to Climate Change for Hydro-Climatically Different Catchments in China. *Stoch. Environ. Res. Risk Assess.* 31 (4), 1011–1021. doi:10.1007/s00477-016-1218-6

Wang, Y., Xie, Z., Jia, B., Wang, L., Li, R., Liu, B., et al. (2020). Sensitivity of Snow Simulations to Different Atmospheric Forcing Data Sets in the Land Surface Model CAS-LSM. *J. Geophys. Res. Atmos.* 125, e2019JD032001. doi:10.1029/2019JD032001

Xia, J., Duan, Q.-Y., Luo, Y., Xie, Z.-H., Liu, Z.-Y., and Mo, X.-G. (2017). Climate Change and Water Resources: Case Study of Eastern Monsoon Region of China. *Adv. Clim. Change Res.* 8, 63–67. doi:10.1016/j.accre.2017.03.007

Xin, X., Wu, T., Zhang, J., Yao, J., and Fang, Y. (2020). Comparison of Cmip6 and Cmip5 Simulations of Precipitation in China and the East Asian Summer Monsoon. *Int. J. Climatol.* 40 (15), 6423–6440. doi:10.1002/joc.6590

Yan, B., and Chen, L. (2013). Coincidence Probability of Precipitation for the Middle Route of South-To-North Water Transfer Project in China. *J. Hydrol.* 499, 19–26. doi:10.1016/j.jhydrol.2013.06.040

Yin, Y., Wang, L., Wang, Z., Tang, Q., Piao, S., Chen, D., et al. (2020). Quantifying Water Scarcity in Northern China Within the Context of Climatic and Societal

Changes and South-to-North Water Diversion. *Earth's Future.* 8, 1–17. doi:10.1029/2020EF001492

Yu, Z., Gu, H., Wang, J., Xia, J., and Lu, B. (2017). Effect of Projected Climate Change on the Hydrological Regime of the Yangtze River basin, china. *Stoch. Environ. Res. Risk Assess.* 32 (1), 1–16. doi:10.1007/s00477-017-1391-2

Yuan, F., Tung, Y.-K., and Ren, L. (2016). Projection of Future Streamflow Changes of the Pearl River Basin in China Using Two Delta-Change Methods. *Hydrol. Res.* 47 (1), 217–238. doi:10.2166/nh.2015.159

Zhang, H., Wang, B., Liu, D. L., Zhang, M., Feng, P., Cheng, L., et al. (2019). Impacts of Future Climate Change on Water Resource Availability of Eastern Australia: A Case Study of the Manning River basin. *J. Hydrol.* 573, 49–59. doi:10.1016/j.jhydrol.2019.03.067

Zhang, J., and Wang, G. (2007). *Impact of Climate Change on Hydrology and Water Resources*. Beijing: Science Press.

Zhang, L., Qin, L., Hu, Z., and Zeng, S. (2010). Simulated Hydrologic Responses to Climate Change of Water Source Area in the Middle Route of South-To-North Water Transfer Project. *J. Hydraul. Eng.* 41 (11), 1261–1271. doi:10.13243/j.cnki.slxb.2010.11.001

Zhang, Q. (2009). The South-To-North Water Transfer Project of China: Environmental Implications and Monitoring Strategy. *J. Am. Water Resour. Assoc.* 45 (5), 1238–1247. doi:10.1111/j.1752-1688.2009.00357.x

Zhao, M., Su, B., Jiang, T., Wang, A., and Tao, H. (2021). Simulation and Projection of Precipitation in the Upper Yellow River Basin by CMIP6 Multi-Model Ensemble[J]. *Plateau Meteorology.* 40 (3), 547–558. doi:10.7522/j.issn.1000-0534.2020.00066

Zhao, Z.-Y., Zuo, J., and Zillante, G. (2017). Transformation of Water Resource Management: a Case Study of the South-To-North Water Diversion Project. *J. Clean. Prod.* 163, 136–145. doi:10.1016/j.jclepro.2015.08.066

Conflict of Interest: The authors declare that the research was conducted in the absence of any commercial or financial relationships that could be construed as a potential conflict of interest.

Publisher's Note: All claims expressed in this article are solely those of the authors and do not necessarily represent those of their affiliated organizations, or those of the publisher, the editors, and the reviewers. Any product that may be evaluated in this article, or claim that may be made by its manufacturer, is not guaranteed or endorsed by the publisher.

frontiers in Earth Science

ORIGINAL RESEARCH
published: 19 October 2021
doi: 10.3389/feart.2021.745185

Detection, Attribution, and Future Response of Global Soil Moisture in Summer

Liang Qiao[1,2], *Zhiyan Zuo*[1,3]*, *Dong Xiao*[2] *and Lulei Bu*[1,2]

[1]Department of Atmospheric and Oceanic Sciences/Institute of Atmospheric Sciences, Fudan University, Shanghai, China, [2]State Key Laboratory of Severe Weather, Chinese Academy of Meteorological Sciences, Beijing, China, [3]Collaborative Innovation Center on Forecast and Evaluation of Meteorological Disasters, Nanjing University of Information Science and Technology, Nanjing, China

Soil moisture variations and its relevant feedbacks (e.g., soil moisture–temperature and soil moisture–precipitation) have a crucial impact on the climate system. This study uses reanalysis and Coupled Model Intercomparison Project phase 6 simulations datasets to detect, attribute, and project soil moisture variations. The effect of anthropogenic forcings [greenhouse gases (GHG), anthropogenic aerosols (AA), and land use (LU) change] on soil moisture is much larger than that of the natural forcing. Soil moisture shows a drying trend at a global scale, which is mainly attributed to GHG forcing. The effects of external forcings vary with the regions significantly. Over eastern South America, GHG, AA, and natural forcings make soil dry, while LU forcing makes the soil wet. Over severely drying Europe, all the external forcings including GHG, AA, LU, and natural forcing exhibit drying effect. The optimal fingerprint method detection results show that some of GHG, AA, LU, and natural signals can be detected in soil moisture variations in some regions such as Europe. The soil will keep drying in all scenarios over most parts of the globe except Sahel and parts of mid-latitudes of Asia. With the increase of anthropogenic emissions, the variation of global soil moisture will be more extreme, especially in hotspots where the land–atmosphere coupling is intensive. The drying trend of soil moisture will be much larger on the surface than in middle and deep layers in the future, and this phenomenon will be more severe under the high-emission scenario. It may be affected by increased evaporation and the effect of carbon dioxide fertilization caused by global warming.

Keywords: detection and attribution, soil moisture, future scenario, drying trend, anthropogenic forcings

OPEN ACCESS

Edited by:
Yulei Xie,
Guangdong University of Technology, China

Reviewed by:
Weili Duan,
Xinjiang Institute of Ecology and Geography (CAS), China
Ling Ji,
Beijing Institute of Technology, China

***Correspondence:**
Zhiyan Zuo
zuozhy@fudan.edu.cn

Specialty section:
This article was submitted to Hydrosphere, a section of the journal Frontiers in Earth Science

Received: *21 July 2021*
Accepted: *14 September 2021*
Published: *19 October 2021*

Citation:
Qiao L, Zuo Z, Xiao D and Bu L (2021) Detection, Attribution, and Future Response of Global Soil Moisture in Summer. Front. Earth Sci. 9:745185. doi: 10.3389/feart.2021.745185

INTRODUCTION

As an essential parameter of the land surface process and the climate system, soil moisture affects surface air temperature, atmospheric humidity, precipitation, stability of the atmospheric boundary layer, and atmospheric circulation by influencing the surface evapotranspiration, surface albedo, soil heat capacity, and vegetation growth conditions (Delworth and Manabe, 1988; Zuo and Zhang, 2016; Liu et al., 2017). Furthermore, soil moisture plays an important role in the energy, water, and biochemical cycles in the climate system (Sellers et al., 1997; Seneviratne et al., 2010; Zhang et al., 2016). Zhang and Zuo (2011) found that spring soil moisture significantly impacts the East Asian summer monsoon and the precipitation in East China by changing the surface thermal conditions. The abnormal soil moisture affects evaporation and temperature, causing an anomalous land–sea

temperature difference, that affecting the East Asian summer monsoon circulation. Berg et al. (2017) indicated that soil moisture is essential for the mean circulation and precipitation of the West African monsoon. On the one hand, anomalous soil moisture changes evaporation and transpiration, resulting in anomalous land–ocean thermal contrast. On the other hand, the anomaly of surface evaporation changes the meridional temperature gradients and causes large-scale circulation changes, affecting West African monsoon circulation and precipitation.

With global warming, the land–atmosphere coupling is strengthened, reinforcing the influence of soil moisture on the land surface process and climate change (Zhang et al., 2011; Vogel et al., 2017; Zhou et al., 2019a). Seneviratne et al. (2006) reported that the feedback of summer soil moisture on the atmosphere would increase the temperature and climate variability in Eastern and Central Europe. With the increase of greenhouse gases concentrations, this region will become a new land–atmosphere coupling hotspot. Through the land–atmosphere interaction experiment, Berg et al. (2014) suggested that soil moisture is crucial for the coupling of land surface and atmosphere. Soil moisture controls the partitioning of available energy between the sensible and latent heat flux, which makes the soil moisture dynamics enhance temperature uncertainty over the hotspots of land–atmosphere coupling. Li et al. (2019) used the CCSM-WRF model to study the temperature variation in summer over East Asia and proposed that the feedback of soil moisture caused the mean temperature in summer to increase by 0.15°C, with key regions appearing over the northern Tibetan Plateau, the Sichuan Basin, and the middle and lower reaches of the Yangtze River during 2071–2100 under the RCP8.5 scenario.

In recent decades, based on satellites, observations, and model simulations, soil moisture has become drier in many regions. Dorigo et al. (2012) used a multi-satellite surface soil moisture dataset and found the subtle drying trends in the southern United States, central South America, central Eurasia, northern Africa and the Middle East, Mongolia and northeastern China, northern Siberia, and Western Australia. The result is also confirmed in GLDAS and ERA-Interim datasets. Zhou et al. (2019a) used the Coupled Model Intercomparison Project phase 5 (CMIP5) models and deduced that the land–atmosphere feedback greatly exacerbated the concurrent soil and atmospheric drought. The frequency and intensity of both soil drought and atmospheric aridity enhanced by land–atmosphere feedback are projected to increase in the 21st century.

With soil moisture drying, soil moisture and temperature interaction have increased and intensified extreme high temperature and heatwave events. Liu et al. (2020) analyzed the mechanism of heatwave in Europe and concluded that although heatwaves are initially triggered by abnormal atmospheric circulation, the strong coupling between soil moisture and temperature further strengthened the heatwaves. Meanwhile, land cover plays a key role in determining the occurrence and intensity of coupling between soil moisture and temperature. Based on the reconstruction of tree rings for the past 260 years, Zhang et al. (2020) revealed an abrupt shift to hotter and drier climate over inland East Asia. Persistent soil moisture deficit enhances land–atmosphere coupling, which intensifies land surface warming and soil moisture drying.

In summary, the soil moisture variation in summer, especially in hotspots of land–atmosphere coupling, has a great impact on climate change and extreme climate events, and its relevant feedbacks (e.g., soil moisture–temperature and soil moisture–precipitation) are prerequisite for reproducing historical trends and ensuring fitness for future projections. Therefore, the detection and attribution of soil moisture variation are essential and urgent. At present, the analysis of soil moisture variation tends to focus on precipitation, temperature, and atmospheric circulation (Zuo and Zhang, 2007; Meng and Quiring, 2010; Wei et al., 2016). Cheng et al. (2015) concluded that the soil moisture in East Asia showed a drying trend through the GLDAS dataset, which is significant in northeast China, north China, Mongolia, and Russia near Lake Baikal. The drying trend of soil moisture is mainly driven by the decreasing precipitation and is enhanced almost twofold by increasing temperatures. Chen et al. (2016) detected a significant decreased trend in surface soil moisture in eastern China by the satellite product and attributed the decreasing trend to precipitation/potential evapotranspiration. However, few studies have detected and attributed the effects of external forcings on soil moisture variation. Coupled Model Intercomparison Project phase 6 (CMIP6) is initiated and organized by the World Climate Research Program Coupling Simulation Working Group. CMIP6 provides climate simulation data to the global science community by designing the standards of climate model experiments and setting the shared data format (Eyring et al., 2016; Zhou et al., 2019b). CMIP6 contains many well-designed experiments, and most of the climate models participate in the experiments designed by CMIP6. Therefore, this study used the CMIP6 model experiments to detect and attribute the external forcings on soil moisture variation in summer, and to analyze the future changes of soil moisture under different emission scenarios. This study will provide a more profound understanding for the anthropogenic effects on soil moisture variation. Data, models, and methods are explained in *Data and Methods*; results and analysis are provided in *Results*; the discussion and summary are presented in *Discussion and Summary*.

DATA AND METHODS

Data

Reanalysis datasets are selected to replace observation data in the analysis of soil moisture attribution because soil moisture lacks long time period and spatially continuous observation data. European Centre for Medium-Range Weather Forecasts Reanalysis v5 (ERA5) and Global Land Data Assimilation System Noah 2.0 (GLDAS-Noah 2.0) reanalysis datasets are selected for this study, and experts have widely recognized them in previous studies (Bi et al., 2016; Cheng et al., 2019; Deng et al., 2020). ERA5 derives from the European Centre for Medium-Range Weather Forecasts, and incorporates soil

TABLE 1 | CMIP6 models (first column), latitude grid points (second column), longitude grid points (third column), and number of mrsos (moisture in the upper portion of the soil column) members (fourth and after column) in different experiments. HIST is all forcing simulation experiment—GHG, AA, NAT, and LU—is only considering greenhouse gases, anthropogenic aerosols, natural, and land use forcing experiment, respectively.

Model	Lat	Lon	HIST	GHG	AA	NAT	LU
ACCESS-CM2	144	192	2	3	3	3	—
ACCESS-ESM1-5	145	192	3	3	3	3	—
BCC-CSM2-MR	160	320	3	3	3	3	1
BCC-ESM1	64	128	3	—	—	—	—
CAMS-CSM1-0	160	320	1	—	—	—	—
CanESM5	64	128	25	50	30	50	9
CAS-ESM2-0	128	256	4	—	—	—	—
CESM2	192	288	11	3	2	3	3
CESM2-WACCM	192	288	3	—	—	—	—
CMCC-ESM2	192	288	—	—	—	—	1
CNRM-CM6-1	128	256	30	9	10	10	—
CNRM-CM6-1-HR	360	720	1	—	—	—	—
E3SM-1-0	180	360	5	—	—	—	—
E3SM-1-1-ECA	180	360	1	—	—	—	—
EC-Earth3-Veg	256	512	3	—	—	—	1
FIO-ESM-2-0	192	288	3	—	—	—	—
GFDL-CM4	180	288	1	—	—	3	—
GFDL-ESM4	180	288	—	1	2	1	1
GISS-E2-1-G	90	144	12	10	15	20	—
GISS-E2-1-G-CC	90	144	1	—	—	—	—
GISS-E2-1-H	90	144	10	—	—	—	—
IPSL-CM6A-LR	143	144	32	10	9	10	4
MIROC6	128	256	10	3	3	3	1
MPI-ESM-1-2-HAM	96	192	2	—	—	—	—
MPI-ESM1-2-HR	192	384	10	—	—	—	—
MPI-ESM1-2-LR	96	192	10	—	—	—	1
MRI-ESM2-0	160	320	5	5	5	5	—
NorESM2-LM	96	144	3	—	—	—	1
NorESM2-MM	192	288	1	—	—	—	—
UKESM1-0-LL	144	192	—	—	—	—	4
CMIP6-MMEM	160	320	195	100	85	114	27

moisture data from *in situ* observations of the global SYNOP network and satellite remote sensing data (Hersbach et al., 2020). The spatial resolution of ERA5 is 0.25°*0.25°, and the soil is divided into four vertical layers, with the ranges of 0–7, 7–28, 28–100, and 100–289 cm. GLDAS-Noah 2.0 derives from the National Aeronautics and Space Administration; it is based on the satellite and observation data and uses the offline land surface model of NOAH to provide output using land surface variables. The spatial resolution of GLDAS is 0.25° *0.25°, and the soil is divided into four vertical layers, with the ranges of 0–10, 10–40, 40–100, and 100–200 cm.

In order to analyze the detection and attribution of global soil moisture variation in summer, all forcing simulation (historical) experiment, detection and attribution experiment, preindustrial control (CTRL) experiment, land use experiment, and scenario experiment in CMIP6 models are used. The selected soil moisture variables are moisture in the upper portion of the soil column (mrsos) and total water content of the soil layer (mrsol). The purpose of the historical experiment is to reproduce the simulation of historical climate changes since 1850. The purpose of the detection and attribution experiment is to evaluate the impact on the climate by only considering specific external forcings. The experiments considering greenhouse gases (GHG), anthropogenic aerosols (AA), and natural forcing are selected in the detection and attribution experiment. In order to obtain the impact of land use (LU) forcing on the climate, the difference between historical and hist-noLu experiments (a model experiment to keep land use at the preindustrial level in 1850) is calculated. The CTRL experiment, also known as the preindustrial reference experiment, is the result of setting the external forcings before the industrial revolution in 1850. The CTRL experiment mainly reflects the internal variability of the climate. The scenario experiment reflects future climate (2015–2100) under different shared socioeconomic pathways (SSP). SSP1-2.6, SSP2-4.5, and SSP5-8.5 are selected as low-, medium-, and high-emission scenarios, respectively, to evaluate soil moisture variation in the future. Monthly summer data from 1979 to 2014 are selected for soil moisture detection and attribution. June, July, and August are regarded as summer in the Northern Hemisphere, while December, January, and February are regarded as summer in the Southern Hemisphere. The CMIP6 models, the number of model members, and the spatial resolution of model in this study are shown in **Tables 1**, **2**, **3**.

The depths of soil layer that most datasets have are chosen under the premise of considering the physical meaning in order to unify the thickness of the soil layers in different models and reanalysis datasets. Three depths of 10 cm, 100 cm, and 200 cm are selected as shallow, middle, and deep layers, respectively. The shallow soil moisture (10 cm) directly affects evaporation, so it is

TABLE 2 | Same as **Table 1**, but for mrsol (total water content of the soil layer).

Model	Lat	Lon	HIST	GHG	AA	NAT	LU
ACCESS-CM2	144	192	2	—	—	—	—
ACCESS-ESM1-5	145	192	3	—	—	—	3
BCC-CSM2-MR	160	320	3	3	3	3	1
BCC-ESM1	64	128	3	—	—	—	—
CanESM5	64	128	25	50	30	50	10
CESM2	192	288	11	3	2	3	3
CESM2-FV2	96	144	3	—	—	—	—
CESM2-WACCM	192	288	3	—	—	—	—
CESM2-WACCM-FV2	96	144	3	—	—	—	—
CMCC-ESM2	192	288	—	—	—	—	1
CNRM-CM6-1	128	256	28	—	—	—	—
CNRM-CM6-1-HR	360	720	1	—	—	—	—
CNRM-ESM2-1	128	256	10	—	—	—	—
EC-Earth3-Veg	256	512	3	—	—	—	1
GFDL-ESM4	180	288	1	—	—	—	1
GISS-E2-1-G	90	144	19	—	10	20	—
GISS-E2-1-G-CC	90	144	1	—	—	—	—
GISS-E2-1-H	90	144	10	—	—	—	—
HadGEM3-GC31-LL	144	192	4	4	4	4	—
IPSL-CM6A-LR	143	144	32	10	—	10	4
MIROC6	128	256	50	3	3	3	—
MPI-ESM-1-2-HAM	96	192	2	—	—	—	—
MPI-ESM1-2-HR	192	384	10	—	—	—	—
MPI-ESM1-2-LR	96	192	10	—	—	—	1
MRI-ESM2-0	160	320	6	5	5	5	—
NorESM2-LM	96	144	3	3	3	2	1
NorESM2-MM	192	288	1	—	—	—	—
UKESM1-0-LL	144	192	—	—	—	—	4
CMIP6-MMEM	160	320	247	81	60	100	30

TABLE 3 | List of CMIP6 pi-control experiment used to estimate internal climate variability in this research. The first and fourth columns include model names, the second and fifth columns include the total years of mrsos (moisture in the upper portion of the soil column) in pi-control experiment, and the third and sixth columns include the total years of mrsol (total water content of the soil layer) in pi-control experiment.

Model	Mrsos	Mrsol	Model	Mrsos	Mrsol
ACCESS-CM2	500	500	EC-Earth3-CC	505	—
ACCESS-ESM1-5	900	900	EC-Earth3-Veg-LR	501	501
AWI-ESM-1-1-LR	100	100	EC-Earth3-Veg	500	188
BCC-CSM2-MR	600	600	EC-Earth3	1,105	1,000
BCC-ESM1	451	451	GFDL-CM4	500	—
CAMS-CSM1-0	500	—	GFDL-ESM4	500	—
CanESM5-CanOE	501	501	GISS-E2-1-G	851	882
CanESM5	1,000	2,051	GISS-E2-1-H	1,102	301
CESM2-FV2	500	500	GISS-E2-2-G	151	151
CESM2-WACCM	500	499	HadGEM3-GC31-LL	—	500
CESM2-WACCM-FV2	—	500	IPSL-CM6A-LR	2,250	1,950
CESM2	1,200	1,200	MIROC6	800	800
CMCC-CM2-SR5	500	500	MPI-ESM-1-2-HAM	780	780
CMCC-ESM2	500	—	MPI-ESM1-2-HR	500	500
CNRM-CM6-1	500	—	MPI-ESM1-2-LR	1,100	1,100
E3SM-1-0	500	—	MRI-ESM2-0	701	952
E3SM-1-1-ECA	251	—	NorESM2-LM	170	—
E3SM-1-1	251	—	TaiESM1	100	100
EC-Earth3-AerChem	311	308	UKESM1-0-LL	1,880	1,880
			SUM	23,561	20,195

the most direct and essential part of the land surface process. Middle soil moisture (100 cm) is often the depth where plant roots are concentrated, and vegetation cover plays a significant role in land–atmosphere interaction and ecology. For the deep layer (200 cm), all models and reanalysis datasets have reached a depth of at least 200 cm. Meanwhile, the deeper the layer, the more genuine the reflection of soil moisture memory and soil hydrological processes (Hagemann and Stacke, 2015). The linear difference method (Liu et al., 2014; Zhang et al., 2018) is used to unify the datasets with inconsistent thickness, and the unit is uniformly converted into kg/m^2.

Methods

For trend analysis, the least square method of linear regression is used to analyze soil moisture variation. In the attribution of soil moisture variation, the spatial distribution of soil moisture trends shows that separately considering GHG forcing, AA forcing, natural forcing, and LU forcing are used for analysis. The multi-model ensemble mean (MMEM) is used to express the results of the CMIP6 model simulation, which can reduce the uncertainty caused by the initial disturbance and the model difference.

The optimal fingerprint is a method to detect the attribution of external forcing signals to climate change by eliminating internal climate variability noise. Many experts have adopted the optimal fingerprint method to realize the attribution analysis of climate change (Hegerl et al., 1997; Allen and Stott, 2003; Sun et al., 2014). In this study, the optimal fingerprint method of total least squares generalized regression is used to detect the attribution of soil moisture variation. This method splits the observations (y) into the external forcings (X) as "signals" and the internal climate variability (ε) as "noise": $y = X\beta+\varepsilon$. In the formula, β is the scaling factor of the external forcing, and X comes from CMIP6 detection and attribution experiments. If the scaling factor is significantly greater than zero (the lower limit of the 90% confidence interval of the scaling factor is greater than zero), it means that the response of the external forcing can be detected in the observation. If the scaling factor is greater than (less than) 1, then the external forcing is considered to underestimate (overestimate) the observed response.

1979 to 2014 (36 years in total) is divided into six segments of the same length (6 consecutive years). The mean value during the 6 year period will reduce the variability and noise in the signal and observation. The internal climate variability is obtained from CTRL experiment. A total of 23,561 years of CTRL experiment from 36 climate models of mrsos are divided into non-overlapping consecutive 36 years, with a total of 626 segments. Furthermore, a total of 20,195 years of CTRL experiment from 28 climate models of mrsol are divided into non-overlapping consecutive 36 years, with a total of 538 segments. The specific models of CTRL experiment are shown in **Table 3**. The segments of internal climate variability are divided into two groups with same numbers. One group is used for the optimal fingerprint method, and another is used for the residual consistency test. The residual consistency test estimates whether the residual after removing the external forcing signal from the observation is consistent with the internal climate variability (Allen and Tett, 1999; Allen and Stott, 2003). This study uses one signal to separately detect whether external forcings are included in soil moisture variation.

RESULTS

The trends (1979–2014) of shallow, middle, and deep soil moisture of three datasets of ERA5, GLDAS, and CMIP6-MMEM, respectively, in summer are compared (**Figure 1**). The results show that global soil moisture is mainly a drying

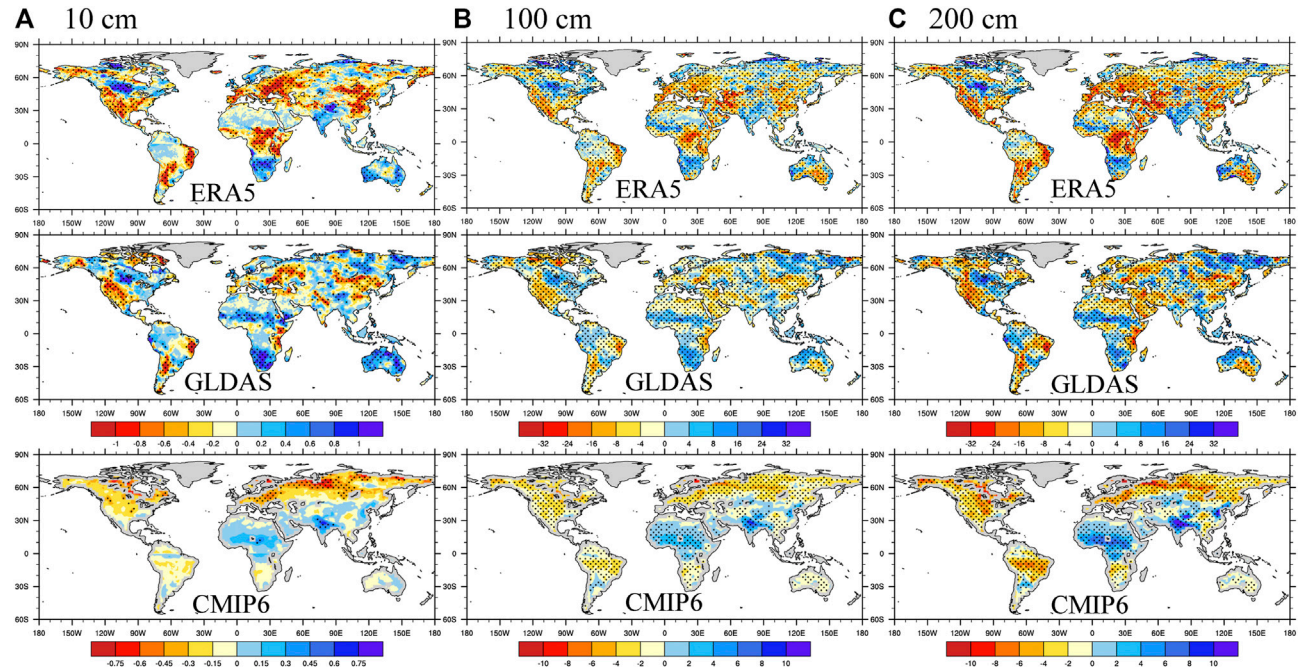

FIGURE 1 | Spatial distribution of the soil moisture trend (kg/m^2/decade, 1979–2014) in different datasets in summer (the Northern Hemisphere is averaged in June, July, and August, and the Southern Hemisphere is averaged in December, January, and February). **(A)**, **(B)**, and **(C)** Shallow (10 cm), middle (100 cm), and deep (200 cm) soil moisture, respectively. Black dots indicate where a given area passes the 90% significance test.

trend in summer, and the extent of the drying region is more prominent in CMIP6-MMEM than in ERA5 and GLDAS. This result is similar to Cheng and Huang (2016) viewpoint. They reported that global soil moisture is dominated by negative trends, especially in transitional regions between dry and wet climates. Affected by the range of soil moisture values at different depths, the drying trend of shallow soil moisture is the weakest, followed by the middle soil moisture, and the trend of deep soil moisture being the largest. For the same dataset, the spatial distribution of soil moisture trend at different depths is consistent, indicating that the soil moisture of each layer changes together. In general, the three datasets have consistent trends in most regions. For example, the soil moisture exhibits the drying trend in southwestern North America, eastern South America, Europe, mid-latitudes of East Asia, and the Indo-China Peninsula. Meanwhile, soil moisture exhibits the wetting trend in the Indian subcontinent and Sahel. However, in some small regions, the soil moisture trend is not consistent in different datasets. For instance, in northern North America and southern Africa, soil moisture exhibits mainly the wetting trend in reanalysis datasets, while CMIP6-MMEM exhibits mainly the drying trend, and in Central Africa, soil moisture exhibits mainly the drying trend in ERA5, while GLDAS and CMIP6-MMEM exhibit mainly the wetting trend. The trend of the reanalysis datasets is greater than that of CMIP6-MMEM, which is mainly affected by the MMEM method averaging multiple members and models. Because soil moisture is an unconventional observation element, there are some divergences inevitably among different datasets. These divergences are often influenced by land surface models on hydrological process simulation (Zampieri et al., 2012; Clark et al., 2015). However, the soil moisture trend of selected reanalysis datasets and CMIP6-MMEM is consistent in most regions.

In order to evaluate the stability of climatological soil moisture in summer, the spatial distribution of the standard deviation (1979–2014) of soil moisture in summer is analyzed (**Figure 2**). The standard deviation of soil moisture is generally tiny in extremely arid and humid regions, such as the Sahara Desert, West Asia, Amazon rainforest, and mid-latitudes of East Asia. For extremely arid regions, due to the slight rainfall, the land surface is in a state of drought for a long time, and the variability of soil moisture is naturally tiny. There is much precipitation in summer and the surface water is sufficient for the humid area, so the soil moisture is usually saturated. Regions with high standard deviations are mainly in Europe, mid-latitude of Asia, central South America, eastern North America, Indian subcontinent, Sahel, and southern Africa. These regions are often located in transition zones between humid and arid regions, or regions where rainy and dry seasons occur alternatively, which makes the soil moisture variability relatively large.

The regions where soil moisture has the most significant impact on land–atmosphere interaction are generally located in the dry–wet transition regions. Soil moisture is high in humid regions, which have enough water on the surface to evaporate so that evaporation is not affected by soil moisture, but mainly affected by energy in humid regions. However, soil moisture in arid areas is too low to meet the demand for evaporation. In the dry–wet transition regions, soil moisture

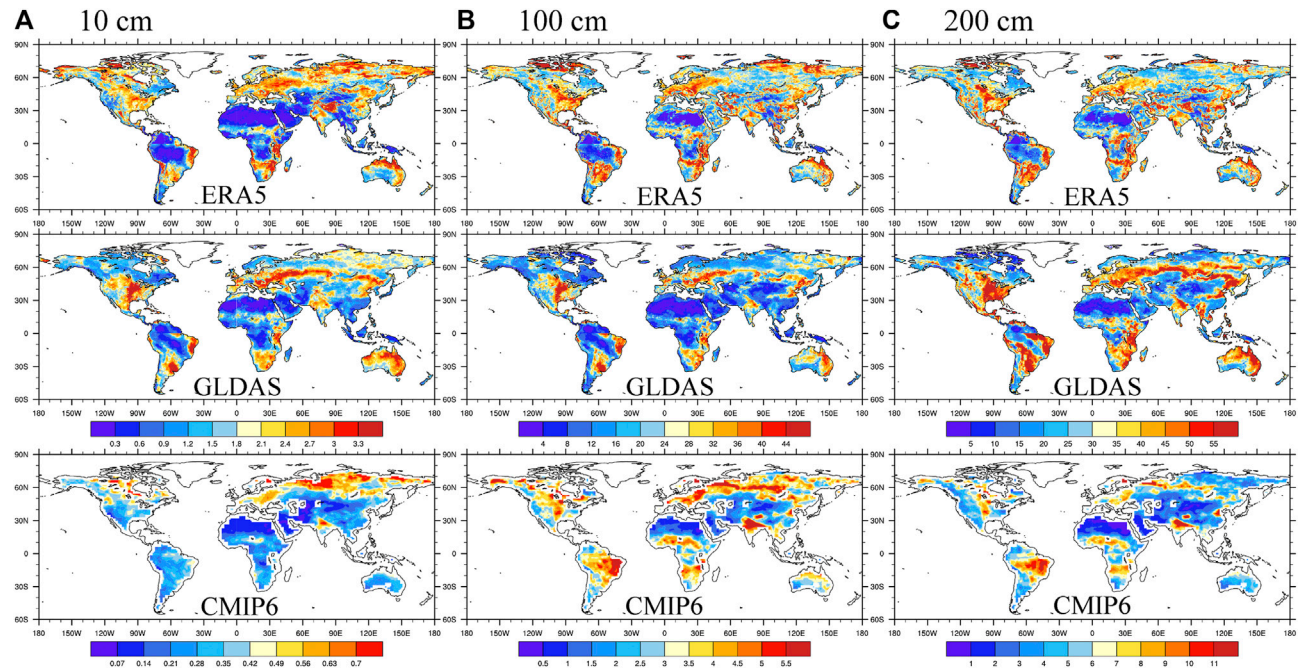

FIGURE 2 | Same as **Figure 1**, but for standard deviation (kg/m^2) of soil moisture.

plays a decisive role in evaporation, which in turn affects the energy distribution of surface net radiation between sensible and latent heat flux, affecting the energy and water cycle between land and atmosphere. Therefore, when selecting the study regions, the hotspots of the land–atmosphere coupling in the dry–wet transition regions are taken as the primary study regions. When performing detection and attribution analysis, an essential prerequisite is whether the model can simulate the soil moisture variation. Therefore, based on the above analysis, the global average and five hotspots of land–atmosphere coupling with the same trend are selected to conduct the detection and attribution analysis of soil moisture in summer. The five regions are mid-latitudes of East Asia (M-EA: 40–55°N, 90–135°E), Europe (36–58°N, 0–40°E), Sahel (15–20°N, 18°W–38°E), Western North America (W-NA: 22–35°N, 98–118°E), and the Eastern South America (E-SA, 2–22°S, 35–60°W).

The global average and five selected hotspots of soil moisture time series are analyzed (**Figure 3**). Results show that the global average is the drying trend in the reanalysis datasets and CMIP6 models, and the drying trend is weaker than that of hotspots, which is mainly affected by the global average. The soil moisture is the drying trend in the M-EA, Europe, the W-NA, and the E-SA, and the trend is wetting only in Sahel. It is the same as previous results through the spatial trend distribution (**Figure 1**). The trends of shallow, middle, and deep soil moisture in global average and selected hotspots are consistent with different reanalysis datasets and CMIP6 models, indicating that the CMIP6 models can simulate the soil moisture trend well in these regions, which lays the foundation for the subsequent detection and attribution of soil moisture variation. Comparing the time series of different regions, soil moisture in Europe has the most remarkable drying trend, and the deep soil moisture of ERA5 reached 13.48 kg/m^2/decade, followed by the W-NA and the E-SA.

The single forcing effect on the soil moisture trend is analyzed through the CMIP6 detection and attribution experiment, land use experiment, and historical experiment. **Figure 4** shows the spatial distribution of shallow, middle, and deep soil moisture trends in summer considering only the GHG, AA, natural, and LU forcing, respectively. The trend of shallow soil moisture has only passed the significance test in a few regions, while the trends of middle and deep soil moisture have passed the significance test in most regions; this may be due to the smaller value range of shallow soil moisture, which leads to the shallow soil moisture variation being smaller. On the whole, the spatial distribution of the soil moisture trend at different depths under every single forcing is basically the same, which means that the regional trend can extend from surface to deep layers. The GHG forcing makes the soil moisture significantly dry in high latitudes of the Northern Hemisphere, northern South America, and Western Europe. The wetting trend is relatively weaker than the drying trend, and the distribution range is small. The wetting trend mainly occurs in southern South America, central Africa, and parts of the mid-latitudes of Asia. The AA forcing causes a significant drying trend in Europe, high latitudes of Asia, and eastern South America. The soil moisture in middle and deep layers shows a strong drying trend, which is distributed in a belt around 60°N from Europe to East Asia. Meanwhile, soil moisture has a strong wetting trend in Sahel, Tibet Plateau, and Northeast China. The influence of natural forcing on soil moisture is generally weaker than that of other external forcings, but some regions in the middle and deep layers have passed the significance

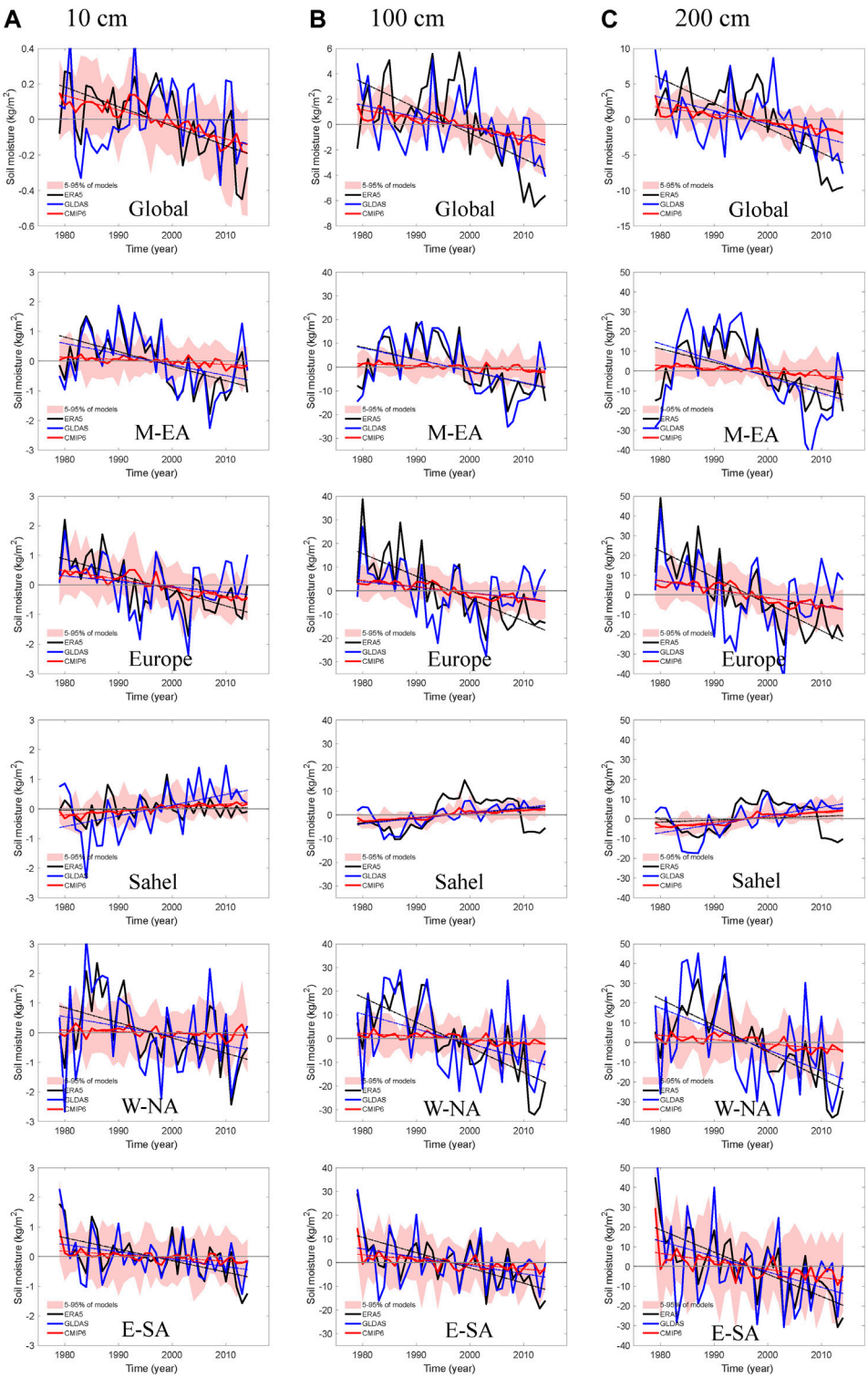

FIGURE 3 | Time series of soil moisture (kg/m^2, 1979–2014) in the global average and selected hotspots. The solid black line is ERA5, the solid blue line is GLDAS, the solid red line is CMIP6-MMEM, the corresponding dotted line is the trend line, and the pink shade is the range of 5–95% of all CMIP6 models. The M-EA is mid-latitudes of East Asia, the W-NA is Western North America, and the E-SA is Eastern South America.

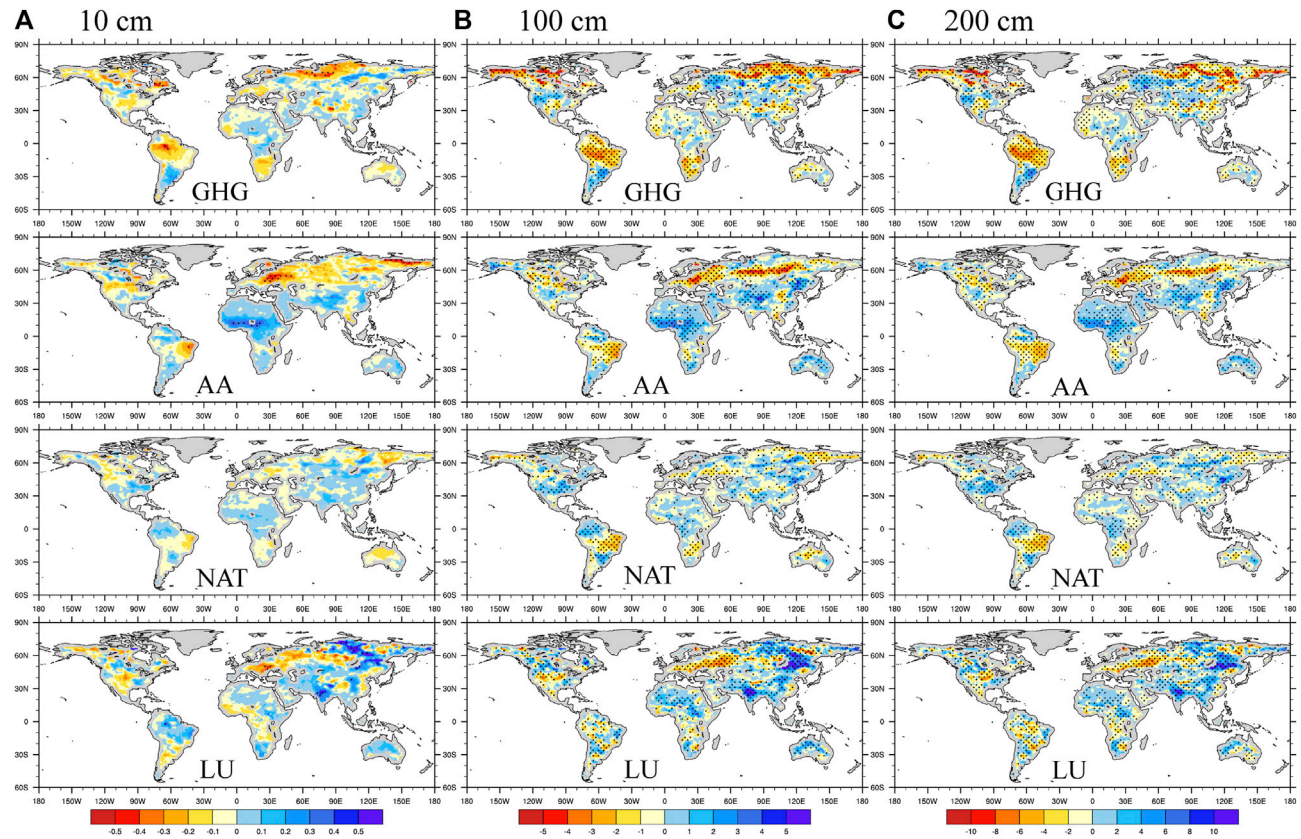

FIGURE 4 | Spatial distribution of the soil moisture trend (kg/m^2/decade, 1979–2014) from CMIP6 experiments (the experiment only considering greenhouse gases (GHG) forcing, the experiment only considering anthropogenic aerosols (AA) forcing, the experiment only considering natural (NAT) forcing, and the experiment only considering land use (LU) forcing). **(A)**, **(B)**, and **(C)** Shallow (10 cm), middle (100 cm), and deep (200 cm) soil moisture, respectively. Black dots indicate where a given area passes the 90% significance test.

test. Under the LU forcing effect, the drying trend is most pronounced in Europe, and the wetting trend occurs in northeast China, the eastern Mongolian plateau, and the Indian subcontinent.

Based on the external forcing experiment, the soil moisture trend is mainly affected by GHG, AA, and LU forcings, and the natural forcing effect is very small. The attribution characteristics of soil moisture variation are similar to the research results of Gu et al. (2019). They suggested that the anthropogenic climate change signal is detectable in global soil moisture drying. However, these external forcings do not produce a consistent global effect on soil moisture like surface air temperature (e.g., GHG forcing has a warming effect globally and AA forcing has a cooling effect in most parts of the world). The effects of external forcings on soil moisture have significant regional divergences. For instance, in the M-EA, the effect of GHG forcing is a drying trend, while the effect of AA and LU forcings is a wetting trend. In the E-SA, the GHG and AA forcings make soil moisture dry, while the LU forcing makes soil moisture wet. However, some regions have the same trend under different forcings. For example, in Western Europe, GHG, AA, natural, and LU forcings all make soil moisture dry, while it is opposite in Sahel.

Furthermore, the optimal fingerprint method is used to detect whether the external forcing signals are contained in the soil moisture variation. **Figure 5** shows the scaling factors of different external forcings. Overall, scaling factors in some regions have a wide range of 90% confidence interval, which makes some forcing signals undetectable. At the same time, the wide range of confidence interval also indicates that the internal climate variability also plays a role in the soil moisture variation (Zhang et al., 2007; Zhou et al., 2020). On the global average, the signals of all forcings and GHG forcing can be detected in soil moisture variation of ERA5 and GLDAS at different depths, except in shallow soil moisture of GLDAS. The scaling factors of AA, natural, and LU forcings are too large or even negative, which indicates that these external forcings have little effect on soil moisture variation. In Europe, the signals of all forcings and AA forcing can basically be detected in ERA5 and GLDAS at different depths, but some lower limits of the 90% confidence interval of scaling factors are less than 0. Meanwhile, the signal of GHG can only be detected in the shallow soil moisture. In Sahel, all forcings and AA forcing signals can be detected in GLDAS, and LU forcing signals can also be detected in the middle and deep layers, but the scaling factor is large. Only the signals of all forcings and LU forcing on middle and deep soil moisture

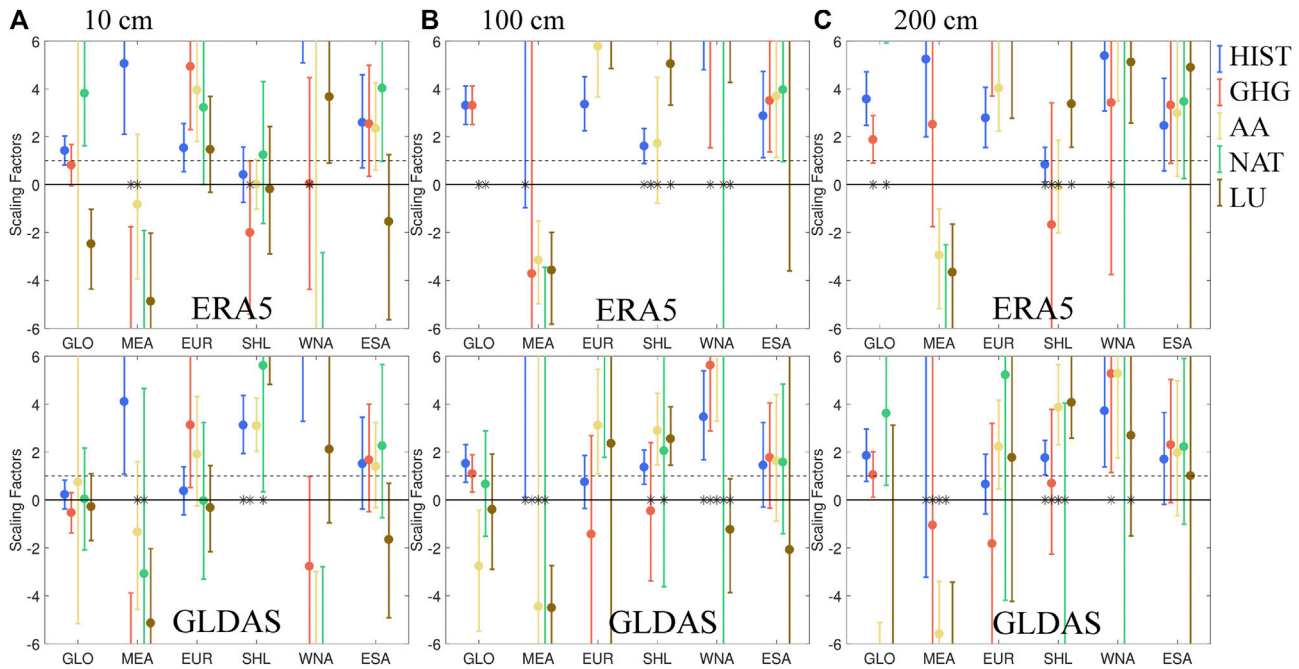

FIGURE 5 | Scaling factors through the optimal fingerprint method over global average (GLO), mid-latitudes of East Asia (MEA), Europe (EUR), African Sahel (SHL), Western North America (WNA), and Eastern South America (ESA). The blue dot is the scaling factor of the all forcing (HIST) signal, the red dot is the scaling factor of the greenhouse gase (GHG) forcing signal, the yellow dot is the scaling factor of the anthropogenic aerosol (AA) forcing signal, the green dot is the scaling factor of the natural (NAT) forcing signal, and the brown dot is the scaling factor of the land use (LU) forcing signal. The corresponding extension line is the 90% confidence interval of the scaling factor. **(A)**, **(B)**, and **(C)** Shallow (10 cm), middle (100 cm), and deep (200 cm) soil moisture, respectively.

variation can be detected in ERA5. In the E-SA, except LU forcing, other forcing signals can be detected at different soil layers in ERA5 and GLDAS, but the confidence interval of some scaling factors contains the value of 0 in GLDAS. In the M-EA, the scaling factors of each forcing are either too large or less than 0, and it is hard to detect the impact on soil moisture variation. The detection of results by the optimal fingerprint method of the W-NA is similar to that of the M-EA. However, some forcing signals of deep soil moisture can be detected in the M-EA and the W-NA, but the scaling factors are too large. In the residual consistency test, the test result is obviously related to the regions. In the three regions of the M-EA, the W-NA, and Sahel, most of the forcing signals failed in the residual consistency test, and the detection results of the optimal fingerprint method are also poor in these three regions.

Based on the detection results of the optimal fingerprint method, some external forcing signals cannot be detected in some regions. On the one hand, it means that soil moisture variation is complicated, and the internal climate variability has a significant impact on soil moisture variation. On the other hand, this may be related to the shorter time period. However, it still confirms that GHG, AA, and LU forcings can be detected in some regions, and natural forcing plays a minor role in soil moisture variation.

According to the above analysis, anthropogenic forcings (GHG, AA, and LU) have a significant impact on soil moisture variation, especially in hotspots. Furthermore, through the CMIP6 scenario experiment, a low-emission scenario (SSP1-2.6), a medium-emission scenario (SSP2-4.5), and a high-emission scenario (SSP5-8.5) are selected to analyze the soil moisture variation in the future. **Figure 6** shows the soil moisture time series of global and hotspots' average in the past and different scenarios. Combined with **Table 4**, the global average and selected hotspots will become drier in the future except for Sahel. The soil moisture of Sahel shows a significant wetter tendency in the high-emission scenario, but soil moisture under low-emission and medium-emission scenarios almost has no trend. On global average, with the increase of anthropogenic emission, the drying trend of soil moisture will increase in all layers, and there are similar phenomena in the M-EA, Europe, the W-NA, and the E-SA. The above analysis shows that with the increase of anthropogenic emission, the trend of soil moisture will also increase (soil moisture in areas with drying trend will become drier and in areas with wetting trend will become wetter), which will exacerbate climate instability. In the first half of the 21st century, the divergences of soil moisture variation in different emission scenarios are not significant, but in the second half of the 21st century, the variation will increase among low-, medium-, and high-emission scenarios. The drying trends of shallow, middle, and deep soil moisture in Europe are the severest. Before 2040, the divergence among low-, medium-, and high-emission scenarios is minor, and then the divergence starts to increase, especially under the high-emission scenario. In the M-EA, the soil moisture almost has the same drying trend in the medium- and high-emission scenarios. Meanwhile, there is nearly no significant trend in the

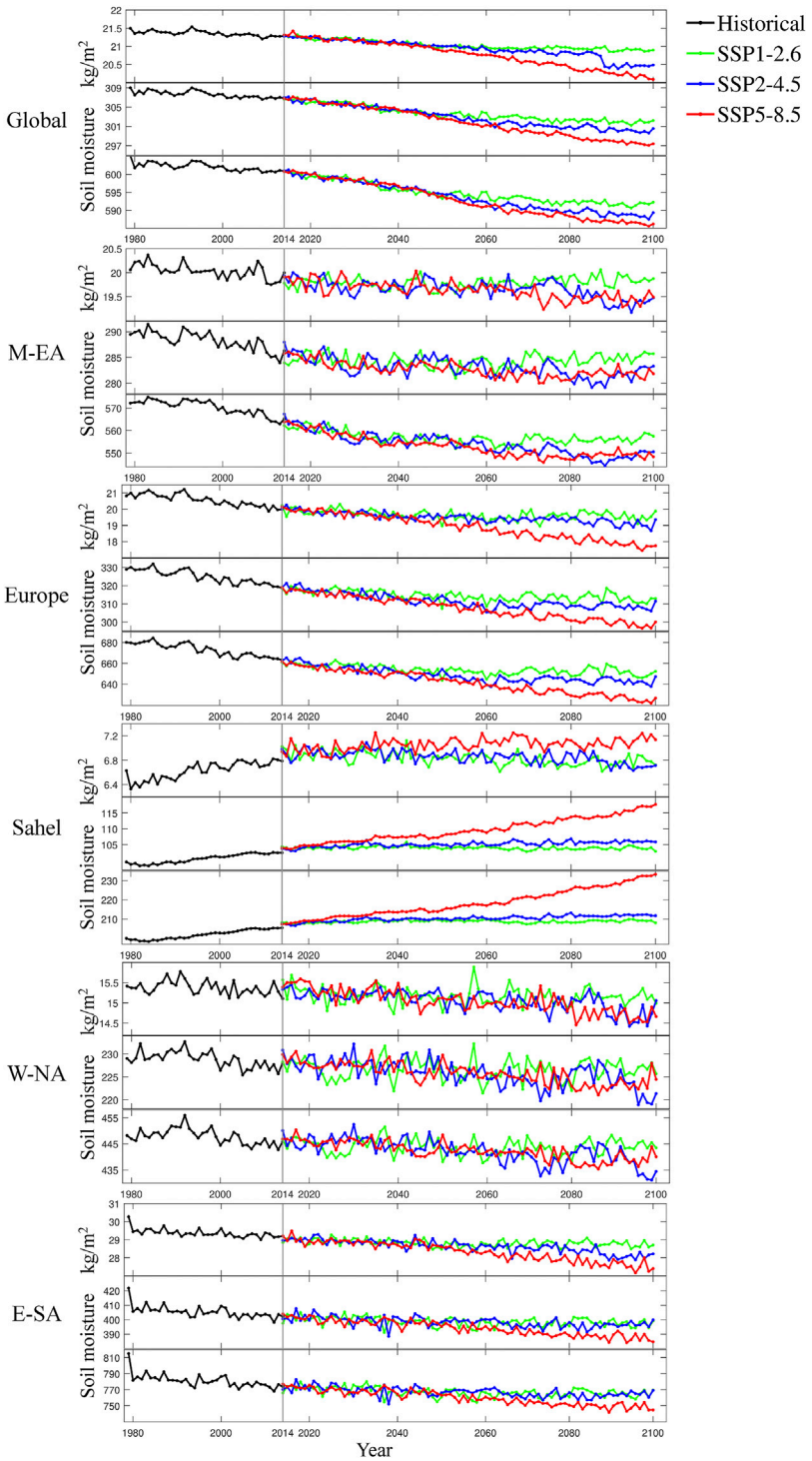

FIGURE 6 | Time series of soil moisture (kg/m^2) in the global average and selected hotspots in historical (black line, 1979–2014) and different emission scenarios [SSP1-2.6 (green line), SSP2-4.5 (blue line), and SSP5-8.5 (red line), 2015–2100]. The M-EA is mid-latitudes of East Asia, the W-NA is Western North America, and the E-SA is Eastern South America.

TABLE 4 | Soil moisture trend (kg/m2/decade, 2015–2100) of global average and selected hotspots under different emission scenarios in the future. The M-EA is mid-latitudes of East Asia, the W-NA is Western North America, and the E-SA is Eastern South America.

Depth (cm)	Scenario	Global	M-EA	Europe	Sahel	W-NA	E-SA
10	SSP1-2.6	−0.046	0.011	−0.044	−0.023	−0.014	−0.028
10	SSP2-4.5	−0.094	−0.044	−0.104	−0.025	−0.063	−0.114
10	SSP5-8.5	−0.148	−0.054	−0.302	0.018	−0.091	−0.204
100	SSP1-2.6	−0.592	0.075	−0.641	−0.050	−0.067	−0.458
100	SSP2-4.5	−0.872	−0.481	−1.307	0.246	−0.732	−0.738
100	SSP5-8.5	−1.260	−0.423	−2.493	1.500	−0.693	−1.922
200	SSP1-2.6	−1.102	−0.559	−1.054	0.080	−0.121	−1.019
200	SSP2-4.5	−1.597	−1.759	−2.345	0.497	−1.283	−1.317
200	SSP5-8.5	−1.956	−1.682	−4.377	2.868	−1.100	−3.409

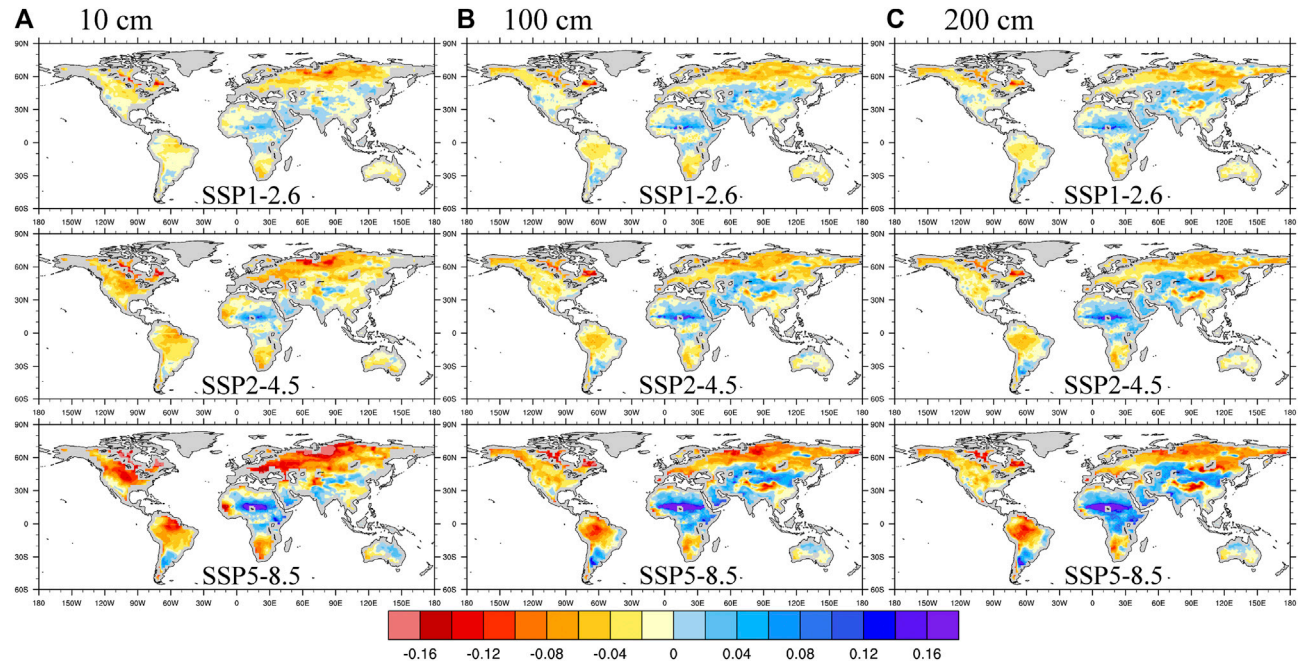

FIGURE 7 | Distribution of the ratio of the difference of soil moisture (kg/m^2) in different emission scenarios. The ratio of the difference between future (2081–2100) and historical (1995–2014) climatological soil moisture [the ratio = (future–historical)/historical]. **(A)**, **(B)**, and **(C)** Shallow (10 cm), middle (100 cm), and deep (200 cm) soil moisture, respectively.

low-emission scenario, which indicates that the M-EA is more sensitive to anthropogenic emission, and the medium-emission can also cause a similar drying trend as the high-emission scenario. The W-NA has similar variation characteristics as that of the M-EA.

Furthermore, the distribution of future changes of soil moisture is analyzed. **Figure 7** shows the distribution of the ratio, which is calculated by dividing the difference between future (2081–2100) and historical (1995–2014) climatological soil moisture by historical climatology [the ratio = (future–historical)/historical]. Overall, soil moisture in most parts of the world has a drying trend under different future scenarios, but wetting trend mainly appears in Sahel and parts of mid-latitudes of Asia. This spatial pattern is basically consistent with the pattern caused by GHG forcing on soil moisture variation, which means that with the emission of GHG increase in the future, the GHG forcing effect on soil moisture will be more intense. In most regions, future soil moisture changes have such characteristics that as anthropogenic emission increases, the soil moisture trend will also increase (the regions with drying trend will be drier and the regions with wetting trend will be wetter). The results in the study of Joo et al. (2020) also confirmed this viewpoint. In addition to the hotspots analyzed above, the soil moisture changes in the Tibet Plateau, high latitudes of the Northern Hemisphere, northern South America, and northern North America are also very significant. It means that as anthropogenic emissions increase, soil moisture and climate anomalies will become more unstable and serious. In the regions with a drying trend, the trend of soil moisture in the surface layer is drier than that of middle and deep

layers. On the contrary, the regions with a wetting trend of soil moisture will become wetter with the depth increase, and the space range with a wetting trend in the deep layer will expand. The reason for the severe drying trend of surface soil moisture is that the increased GHG concentration leads to global warming and evaporation increasing. The surface soil moisture is directly affected by the enhancement of evaporation, which makes the surface soil moisture drier. For the wetting trend in deep layers, due to the increase of carbon dioxide concentration on vegetation fertilization, water use efficiency of vegetation increases, leading to the root zone layer (middle and deep layers) becoming wetter (Mankin et al., 2017; Dai et al., 2018).

DISCUSSION AND SUMMARY

The reanalysis (ERA5 and GLDAS) and CMIP6 data are used in this study to detect and attribute global soil moisture variation in summer. Also, the soil moisture responses to different scenarios are analyzed. From a global perspective, soil moisture shows mainly a drying trend in most regions, and it will become much drier with the increase of anthropogenic emission in the future. The detection and attribution results show that the global drying trend is mainly affected by GHG forcing. In different datasets, soil moisture appears to exhibit consistently a drying trend in Europe, southwestern North America, eastern South America, mid-latitudes of East Asia, and the Indo-China Peninsula; however, Indian subcontinent and Sahel show a wetting trend.

In most parts of the world, the soil moisture variations in shallow, middle, and deep layers are consistent. In the regions with a drying trend, the surface layer will become drier than the middle and deep layers in the future, while in wetting regions, the deep soil moisture will become wetter than those of surface and middle layers, and this phenomenon will be more severe with the increase of anthropogenic emission. The surface layer will get when drier affected by the increased evaporation caused by global warming, and the wetting trend is being more severe in the deep layer, which is affected by the effect of carbon dioxide fertilization (Mankin et al., 2017; Dai et al., 2018).

Both the spatial distribution of the detection and attribution experiment, and the detection results of the optimal fingerprint method show that the soil moisture variation is mainly affected by anthropogenic forcings (GHG, AA, and LU), while natural forcing is relatively minor. Different external forcings have diverse influence on soil moisture variation in different regions. For example, all external forcings make soil moisture drier in Europe, while in the M-EA, AA and LU forcings show a wetting trend on soil moisture, and the GHG forcing shows a drying trend.

The variability of soil moisture in hotspots of land–atmosphere coupling is significant, and with the increase of anthropogenic emission, the soil moisture trend will be more extreme (the regions with drying trend will become drier and the regions with wetting trend will become wetter) in the future. Meanwhile, the divergence under different emission scenarios will be amplified in the second half of the 21st century. These characteristics of soil moisture variation will lead to more severe climate instability and being more prone to extreme climate events in the future.

DATA AVAILABILITY STATEMENT

The original contributions presented in the study are included in the article/Supplementary Material; further inquiries can be directed to the corresponding author.

AUTHOR CONTRIBUTIONS

ZZ and DX conceived and designed the research; LQ and LB processed the data; LQ analyzed the data and wrote the manuscript; and ZZ, DX, LQ, and LB reviewed the paper.

FUNDING

This work was supported by the National Key Research and Development Program (Grant No. 2016YFA0601502) and the National Natural Science Foundation of China (Grant Nos. 41822503, 41375092, and 42005056).

REFERENCES

Allen, M. R., and Stott, P. A. (2003). Estimating Signal Amplitudes in Optimal Fingerprinting, Part I: Theory. *Clim. Dyn.* 21, 477–491. doi:10.1007/s00382-003-0313-9

Allen, M. R., and Tett, S. F. B. (1999). Checking for Model Consistency in Optimal Fingerprinting. *Clim. Dyn.* 15 (6), 419–434. doi:10.1007/s003820050291

Berg, A., Lintner, B. R., Findell, K. L., Malyshev, S., Loikith, P. C., and Gentine, P. (2014). Impact of Soil Moisture-Atmosphere Interactions on Surface Temperature Distribution. *J. Clim.* 27 (21), 7976–7993. doi:10.1175/jcli-d-13-00591.1

Berg, A., Sheffield, J., and Milly, P. C. D. (2017). Divergent Surface and Total Soil Moisture Projections under Global Warming. *Geophys. Res. Lett.* 44, 236–244. doi:10.1002/2016GL071921

Bi, H., Ma, J., Zheng, W., and Zeng, J. (2016). Comparison of Soil Moisture in GLDAS Model Simulations and *In Situ* Observations over the Tibetan Plateau. *J. Geophys. Res. Atmos.* 121, 2658–2678. doi:10.1002/2015JD024131

Chen, X., Su, Y., Liao, J., Shang, J., Dong, T., and Wang, C. (2016). Detecting Significant Decreasing Trends of Land Surface Soil Moisture in Eastern China during the Past Three Decades (1979–2010). *J. Geophys. Res. Atmos.* 121, 5177–5192. doi:10.1002/2015JD024676

Cheng, S., and Huang, J. (2016). Enhanced Soil Moisture Drying in Transitional Regions under a Warming Climate. *J. Geophys. Res. Atmos.* 121, 2542–2555. doi:10.1002/2015JD024559

Cheng, S., Guan, X., Huang, J., Ji, F., and Guo, R. (2015). Long-term Trend and Variability of Soil Moisture over East Asia. *J. Geophys. Res. Atmos.* 120, 8658–8670. doi:10.1002/2015JD023206

Cheng, M., Zhong, L., Ma, Y., Zou, M., Ge, N., Wang, X., et al. (2019). A Study on the Assessment of Multi-Source Satellite Soil Moisture Products and Reanalysis Data for the Tibetan Plateau. *Remote Sens.* 11, 1196. doi:10.3390/rs11101196

Clark, M. P., Fan, Y., Lawrence, D. M., Adam, J. C., Bolster, D., Gochis, D. J., et al. (2015). Improving the Representation of Hydrologic Processes in Earth System Models. *Water Resour. Res.* 51, 5929–5956. doi:10.1002/2015WR017096

Dai, A., Zhao, T., and Chen, J. (2018). Climate Change and Drought: a Precipitation and Evaporation Perspective. *Curr. Clim. Change Rep.* 4, 301–312. doi:10.1007/s40641-018-0101-6

Delworth, T. L., and Manabe, S. (1988). The Influence of Potential Evaporation on the Variabilities of Simulated Soil Wetness and Climate. *J. Clim.* 1 (5), 523–547. doi:10.1175/1520-0442(1988)001<0523:tiopeo>2.0.co;2

Deng, M., Meng, X., Li, Z., Lyv, Y., Lei, H., Zhao, L., et al. (2020). Responses of Soil Moisture to Regional Climate Change over the Three Rivers Source Region on the Tibetan Plateau. *Int. J. Climatol.* 40, 2403–2417. doi:10.1002/joc.6341

Dorigo, W., de Jeu, R., Chung, D., Parinussa, R., Liu, Y., Wagner, W., et al. (2012). Evaluating Global Trends (1988–2010) in Harmonized Multi-Satellite Surface Soil Moisture. *Geophys. Res. Lett.* 39, L18405. doi:10.1029/2012GL052988

Eyring, V., Bony, S., Meehl, G., Seniror, C., Stevens, B., Stouffer, R., et al. (2016). Overview of the Coupled Model Intercomparison Project Phase 6 (Cmip6) Experimental Design and Organization. *Geosci. Model. Dev.* 9, 1937–2016. doi:10.5194/gmd-9-1937-2016

Gu, X., Zhang, Q., Li, J., Singh, V. P., Liu, J., Sun, P., et al. (2019). Attribution of Global Soil Moisture Drying to Human Activities: A Quantitative Viewpoint. *Geophys. Res. Lett.* 46, 2573–2582. doi:10.1029/2018GL080768

Hagemann, S., and Stacke, T. (2015). Impact of the Soil Hydrology Scheme on Simulated Soil Moisture Memory. *Clim. Dyn.* 44, 1731–1750. doi:10.1007/s00382-014-2221-6

Hegerl, G. C., Hasselmann, K., Cubasch, U., Mitchell, J., Roeckner, E., Voes, R., et al. (1997). Multi-fingerprint Detection and Attribution Analysis of Greenhouse Gas, Greenhouse Gas-Plus-Aerosol and Solar Forced Climate Change. *Clim. Dyn.* 13, 613–634. doi:10.1007/s003820050186

Hersbach, H., Bell, B., Berrisford, P., Hirahara, S., Horanyi, A., Munoz-Sabater, J., et al. (2020). The ERA5 Global Reanalysis. *Q. J. R. Meteorol. Soc.* 146 (730), 1999–2049. doi:10.1002/qj.3803

Joo, J., Jeong, S., Zheng, C., Park, C., Park, H., and Kim, H. (2020). Emergence of Significant Soil Moisture Depletion in the Near Future. *Environ. Res. Lett.* 15 (12), 124048. doi:10.1088/1748-9326/abc6d2

Li, K., Zhang, J., Yang, K., and Wu, L. (2019). The Role of Soil Moisture Feedbacks in Future Summer Temperature Change over East Asia. *J. Geophys. Res. Atmos.* 124, 12034–12056. doi:10.1029/2018JD029670

Liu, L., Zhang, R., and Zuo, Z. (2014). Intercomparison of spring Soil Moisture Among Multiple Reanalysis Data Sets over Eastern China. *J. Geophys. Res. Atmos.* 119, 54–64. doi:10.1002/2013JD020940

Liu, L., Zhang, R., and Zuo, Z. (2017). Effect of Spring Precipitation on Summer Precipitation in Eastern China: Role of Soil Moisture. *J. Clim.* 30, 9183–9194. doi:10.1175/jcli-d-17-0028.1

Liu, X., He, B., Guo, L., Huang, L., and Chen, D. (2020). Similarities and Differences in the Mechanisms Causing the European Summer Heatwaves in 2003, 2010, and 2018. *Earth's Future* 8, e2019EF001386. doi:10.1029/2019EF001386

Mankin, J. S., Smerdon, J. E., Cook, B. I., Williams, A. P., and Seager, R. (2017). The Curious Case of Projected Twenty-First-Century Drying but Greening in the American West. *J. Clim.* 30 (21), 8689–8710. doi:10.1175/jcli-d-17-0213.1

Meng, L., and Quiring, S. M. (2010). Observational Relationship of Sea Surface Temperatures and Precedent Soil Moisture with Summer Precipitation in the U.S. Great Plains. *Int. J. Climatol.* 30, 884–893. doi:10.1002/joc.1941

Sellers, P. J., Dickinson, R. E., Randall, D. A., Betts, A. K., Hall, F. G., Berry, J., et al. (1997). Modeling the Exchanges of Energy, Water, and Carbon between Continents and the Atmosphere. *Science* 275 (5299), 502–509. doi:10.1126/science.275.5299.502

Seneviratne, S., Lüthi, D., Litschi, M., and Schar, C. (2006). Land–atmosphere Coupling and Climate Change in Europe. *Nature* 443, 205–209. doi:10.1038/nature05095

Seneviratne, S. I., Thierry, C., Edouard, L., Martin, H., Eric, B., Irene, L., et al. (2010). Investigating Soil Moisture–Climate Interactions in a Changing Climate: A Review. *Earth Sci. Rev.* 99 (3–4), 125–161. doi:10.1016/j.earscirev.2010.02.004

Sun, Y., Zhang, X., Zwiers, F. W., Song, L., Wan, H., Hu, T., et al. (2014). Rapid Increase in the Risk of Extreme Summer Heat in Eastern China. *Nat. Clim. Change* 4, 1082–1085. doi:10.1038/nclimate2410

Vogel, M. M., Orth, R., Cheruy, F., Hagemann, S., Lorenz, R., van den Hurk, et al. (2017). Regional Amplification of Projected Changes in Extreme Temperatures Strongly Controlled by Soil Moisture-Temperature Feedbacks. *Geophys. Res. Lett.* 44, 1511–1519. doi:10.1002/2016GL071235

Wei, J., Su, H., and Yang, Z. L. (2016). Impact of Moisture Flux Convergence and Soil Moisture on Precipitation: a Case Study for the Southern United States with Implications for the globe. *Clim. Dyn.* 46, 467–481. doi:10.1007/s00382-015-2593-2

Zampieri, M., Serpetzoglou, E., Anagnostou, E. N., Nikolopoulos, E. I., and Papadopoulos, A. (2012). Improving the Representation of River–Groundwater Interactions in Land Surface Modeling at the Regional Scale: Observational Evidence and Parameterization Applied in the Community Land Model. *J. Hydrol.* 420–421, 72–86. doi:10.1016/j.jhydrol.2011.11.041

Zhang, R., and Zuo, Z. (2011). Impact of Spring Soil Moisture on Surface Energy Balance and Summer Monsoon Circulation over East Asia and Precipitation in East China. *J. Clim.* 24 (13), 3309–3322. doi:10.1175/2011jcli4084.1

Zhang, X., Zwiers, F., Hegerl, G., Lambert, F., Gillett, N., Solomon, S., et al. (2007). Detection of Human Influence on Twentieth-century Precipitation Trends. *Nature* 448, 461–465. doi:10.1038/nature06025

Zhang, J., Wu, L., and Dong, W. (2011). Land-atmosphere Coupling and Summer Climate Variability over East Asia. *J. Geophys. Res.* 116, D05117. doi:10.1029/2010JD014714

Zhang, R., Liu, L., and Zuo, Z. (2016). Variation of Soil Moisture over China and Their Influences on Chinese Climate. *Chin. J. Nat.* 38 (5), 313–319. doi:10.1007/978-981-10-2338-5_31

Zhang, G., Li, J., Rong, X., Xin, Y., Li, J., Chen, H., et al. (2018). An Assessment of CAMS-CSM in Simulating Land–Atmosphere Heat and Water Exchanges. *J. Meteorol. Res.* 32 (6), 862–880. doi:10.1007/s13351-018-8055-0

Zhang, P., Jeong, J. H., Yoon, J. H., Kim, H., Wang, S. Y., Linderholm, H. W., et al. (2020). Abrupt Shift to Hotter and Drier Climate over Inner East Asia beyond the Tipping point. *Science* 27, 1095–1099. doi:10.1126/science.abb3368

Zhou, S., Williams, A. P., Berg, A. M., Cook, B. I., Zhang, Y., Hagemann, S., et al. (2019a). Land–atmosphere Feedbacks Exacerbate Concurrent Soil Drought and Atmospheric Aridity. *Proc. Natl. Acad. Sci. Sep.* 116 (38), 18848–18853. doi:10.1073/pnas.1904955116

Zhou, T., Zou, L., and Chen, X. (2019b). Commentary on the Coupled Model Intercomparison Project Phase 6 (CMIP6). *Clim. Change Res.* 15 (5), 445–456. doi:10.12006/j.issn.1673-1719.2019.193

Zhou, T., Zhang, W., Zhang, L., Zhang, X., Qian, Y., Peng, D., et al. (2020). The Dynamic and Thermodynamic Processes Dominating the Reduction of Global Land Monsoon Precipitation Driven by Anthropogenic Aerosols Emission. *Sci. China Earth Sci.* 63, 919–933. doi:10.1007/s11430-019-9613-9

Zuo, Z., and Zhang, R. (2007). The spring Soil Moisture and the Summer Rainfall in Eastern China. *Chin. Sci. Bull.* 52, 3310–3312. doi:10.1007/s11434-007-0442-3

Zuo, Z., and Zhang, R. (2016). Influence of Soil Moisture in Eastern china on the East Asian Summer Monsoon. *Adv. Atmos. Sci.* 33, 151–163. doi:10.1007/s00376-015-5024-8

Conflict of Interest: The authors declare that the research was conducted in the absence of any commercial or financial relationships that could be construed as a potential conflict of interest.

Publisher's Note: All claims expressed in this article are solely those of the authors and do not necessarily represent those of their affiliated organizations, or those of the publisher, the editors, and the reviewers. Any product that may be evaluated in this article, or claim that may be made by its manufacturer, is not guaranteed or endorsed by the publisher.

frontiers in Earth Science

ORIGINAL RESEARCH
published: 20 October 2021
doi: 10.3389/feart.2021.752425

Quantitative Estimation on Contribution of Climate Changes and Watershed Characteristic Changes to Decreasing Streamflow in a Typical Basin of Yellow River

Xizhi Lv[1], Shanshan Liu[2], Shaopeng Li[1], Yongxin Ni[1], Tianling Qin[2] and Qiufen Zhang[1]*

[1]Henan Key Laboratory of Yellow Basin Ecological Protection and Restoration, Yellow River Institute of Hydraulic Research, Zhengzhou, China, [2]State Key Laboratory of Simulation and Regulation of Water Cycle in River Basin, China Institute of Water Resources and Hydropower Research, Beijing, China

OPEN ACCESS

Edited by:
Yulei Xie,
Guangdong University of Technology, China

Reviewed by:
Yiping Wu,
Xi'an Jiaotong University, China
Henian Wang,
Chinese Academy of Forestry, China
Zhe Yuan,
Changjiang River Scientific Research Institute (CRSRI), China

***Correspondence:**
Tianling Qin
qintl@iwhr.com

Specialty section:
This article was submitted to Hydrosphere, a section of the journal Frontiers in Earth Science

Received: *03 August 2021*
Accepted: *14 September 2021*
Published: *20 October 2021*

Citation:
Lv X, Liu S, Li S, Ni Y, Qin T and Zhang Q (2021) Quantitative Estimation on Contribution of Climate Changes and Watershed Characteristic Changes to Decreasing Streamflow in a Typical Basin of Yellow River. Front. Earth Sci. 9:752425. doi: 10.3389/feart.2021.752425

Climate changes and underlying surface of the watershed have affected the evolution of streamflow to a different degree. It is of great significance to quantitatively evaluate main drivers of streamflow change for development, utilization, and planning management of water resources. In this study, the Huangshui River basin, a typical basin of the Qinghai-Tibetan Plateau, China, was chosen as the research area. Huangshui is the largest first-class tributary in the upstream of the Yellow River. Based on the Budyko hypothesis, streamflow and meteorological datasets from 1958 to 2017 were used to quantitatively assess the relative contributions of changes in climate and watershed characteristics to streamflow change in research area. The results show that the streamflow of Huangshui River basin shows an insignificant decreasing trend; the sensitivity coefficients of streamflow to precipitation, potential evapotranspiration, and watershed characteristic parameter are 0.5502, −0.1055, and −183.2007, respectively. That is, 1 unit increase in precipitation would induce an increase of 0.5502 units in streamflow, and 1 unit increase in potential evapotranspiration would induce a decrease of 0.1055 units in streamflow, and an increase of 1 unit in the watershed characteristic coefficient would induce a decrease of 183.2007 units in streamflow. The streamflow decreased by 20.48 mm (13.59%) during the change period (1994–2017) compared with that during the reference period (1958–1993), which can be attributed to watershed characteristic changes (accounting for 73.64%) and climate change (accounting for 24.48%). Watershed characteristic changes exert a dominant influence upon the reduction of streamflow in the Huangshui River basin.

Keywords: streamflow, Budyko hypothesis, climate changes, underlying surface, Huangshui River basin, climate changes

INTRODUCTION

As a significant part of the hydrological process, streamflow in many basins of the world is experiencing a decreasing trend, which is particularly evident in the Haihe River, Huaihe River, Songhuajiang River, Liaohe River, and Hanjiang River of China, and streamflow variability is generally influenced by climate change and anthropogenic activities (Wang et al., 2013; Zhang et al., 2015; Kong et al., 2016). Climate changes, such as precipitation and potential evaporation changes caused by increasing temperature, may have a crucial impact on streamflow (Huo et al., 2008). Human activities, including irrigation, land use changes, reservoir, and other hydraulic engineering, can result in significant hydrological alterations. Previous studies showed human activities are the primary driving factor of streamflow variability (Wang et al., 2012; Zhan et al., 2013). Due to the increases in human activities caused by rapid growth of economy and population in lots of places, the demand for water resources has been increased sharply over the past decades, and the decreasing trend of streamflow will continue (Velpuri and Senay, 2013). Situations of water shortage recorded have increased rapidly around the world. Recently, extreme hydrological events including floods, drought, and heavy rainfall have been reported more frequently in a changing environment (Thompson, 2012; Zhao et al., 2019). Understanding the evolution of streamflow and quantifying the individual impacts of climate change and human activities on streamflow are crucial to managers and policy-makers for sustainable water resources/basin management. Simultaneously, they are essential for the sustainable use of water resources and development of regional economics.

Researchers initially analyze components, annual and inter-annual changes of streamflow, and the correlations with climatic factors (Li and Tang, 1981; You, 1995). With the strengthening of human activities, researchers gradually consider the impact of human activities to streamflow, but it is limited to qualitative explanation (Tang, 1995; Xu, 1995; Wang et al., 2021). The sensitivity analysis of climate on streamflow is reported more frequently recently, and generally the sensitivity coefficient of streamflow to precipitation is greater than potential evaporation in many regions (Wang and Yu, 2015). Latest studies focus on quantitative assessments of runoff changes, including climate change and human activities/land use changes, and indicate that human activities are the dominant factor for runoff variability in most of the world's rivers (Wang et al., 2012; Wang et al., 2013; Lv et al., 2019; Hu et al., 2020; Liu, 2020). Vegetation condition is the most representative factor of human activities in some areas, such as the Loess Plateau of China, the effect of vegetation was deeply conducted (Zhao et al., 2010; Li et al., 2019; Sun et al., 2020). However, the sensitivity analyses of streamflow to climatic and no-climatic factors are still rare in present studies.

In order to assess the hydrological response in a changing environment, over the past years, two primary methods have been applied to separate the effects of climate change and human activities on streamflow variability: hydrologic model and statistical methods. Hydrological models, such as SWAT model (Zhang et al., 2012), Xinanjiang model (Jiang et al., 2007), and GBHM model (Xu et al., 2013), are very useful to investigate streamflow evolution, and the models require numbers of high-quality recorded datasets as the input in order to ensure accuracy. Simultaneously, the modeling results have some uncertainties caused by the shortcomings from model structure, parameters, and scale problem. By contrast, statistical methods, including the cumulative anomaly curve method (Ran et al., 2010) and time trend method (Wei and Zhang, 2010), are comparatively simple, but lack a clear physical mechanism and so provide generalized relationships. In addition, catchment experiments also are powerful tools for assessing the impact of vegetation on the water balance (Costa et al., 2003); nevertheless, they are applied to small catchments due to the limiting conditions.

Numerous methods have been proposed to study the hydrological cycle process, and among them, hydrological modeling method has been widely used in different regions of the world. However, as these process-based models are complex combinations of scientific hypotheses, their results are highly dependent on the embedded hypotheses and often vary greatly among models (Beer et al., 2010; Yang et al., 2015). Additionally, they also require major efforts on model calibration and have uncertainties in the structure and parameters of the model (Wang and Yu, 2015). The advantage of using the Budyko framework lies in its ability to analytically separate the impacts of mean climate conditions and catchment properties on hydrological partitioning (Roderick & Farquhar, 2011; Wang & Hejazi, 2011; Liu and McVicar, 2012; Xu et al., 2014; Liang et al., 2015).

The Budyko framework demonstrates the long-term physical distribution between precipitation, evaporation, and streamflow. Due to the efforts and contributions of subsequent researchers, the original Budyko equation (Budyko, 1974) has developed into many forms, such as Fu (1981), Mezentsev–Choudhury–Yang (Mezentsev, 1955; Choudhury, 1999; Zhang et al., 2001; Yang et al., 2008; Wang and Tang, 2014), which all have one parameter (ω) related to the characteristics of watershed (e.g., soils, topography, vegetation, and land use types). Among the above equations, Fu equation is considered to be the most widely concerned and applied equation in the world. The parameter (ω) can be calculated according to the method in literature (Lv et al., 2019). Additionally, based on the Budyko framework, the climate sensitivity method initially proposed by Schaake (1990), which is very similar to other sensitivity (Milly and Dunne, 2002), has been also adopted to estimate the effects of climate change with continuous extension and improvement (Fu et al., 2007). Researchers believe that the sensitivity method is more credible than other statistical methods because of including basic physical processes. Over the last studies, the climate elasticity approach has been widely used to investigate climate- and human-induced streamflow variability and furthermore analyze the major driving factor of change (Ma et al., 2010).

The Huangshui River basin is the important water-producing area of the upper catchment of the Yellow River, and streamflow in this region has showed a reducing trend recently (Huo et al., 2008). However, quantitatively assessing the sensitivities and relative contributions of streamflow to different factors

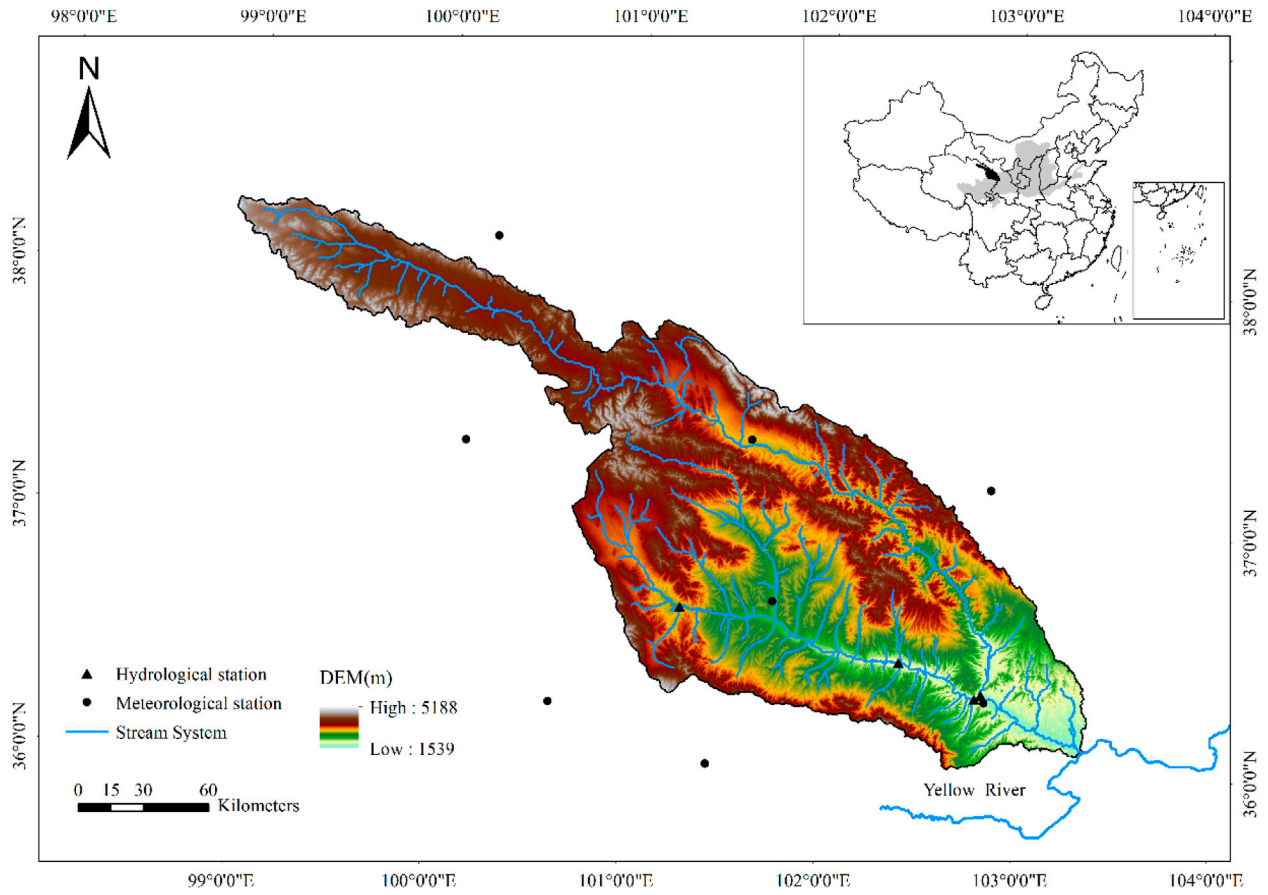

FIGURE 1 | Location of the Huangshui River basin and hydrological and meteorological stations.

(climatic and no-climatic factors) for the whole basin have not been reported. The major purposes of this study are to 1) explore the temporal trends and change point of annual streamflow; 2) obtain the sensitivity coefficients of streamflow to precipitation, potential evaporation, and watershed characteristic; and 3) quantitatively separate the impacts of climate change and watershed characteristic change to streamflow changes in the Huangshui River basin.

STUDY AREA

The Huangshui River is the largest first-level tributary on the left bank of the upper Yellow River (**Figure 1**), which primarily includes the main stream and the tributary Datong River. Its main river length is 374 km, and the drainage area of the catchments is 32863 km^2 (36°02′–38°20′N, 98°54′–103°24′E). The Huangshui River basin is located in the transitional zone between the Qinghai-Tibetan Plateau and the Loess Plateau. The whole basin is shaped like leaves, narrow in the east and wide in the west. The topography of the basin is high in the northwest and low in the southeast. The basin is at an altitude of 1500–5200 m and belongs to a continental climate; alpine and drought are the climatic characteristics of this area, and the basin is one of the regions which is frequently influenced by East Asian Monsoon, South Asian Monsoon, and Plateau Monsoon. The average mean temperature is 0.6–7.9°C, the average maximum temperature is 34.7°C, the average minimum temperature is −32.6°C, the average mean evaporation is 800–1500 mm, and the average mean precipitation is 300–500 mm. The precipitation shows obvious season variation, and more than 70% occurs between June and September due to the southeast monsoon from the Bay of Bengal. The annual runoff is about 44.5 billion m^3, which mainly comes from the mixed supplies of snowmelt and precipitation. The soil and vegetation are significantly different in different regions of the basin due to the comprehensive influence of terrain, altitude, climate, and soil parent material. The main soil-forming parent materials are the tertiary red soil and the quaternary loess.

RESEARCH METHODS

The Budyko Hypothesis

Budyko (1974) believed that on a long time, the actual evapotranspiration of the basin was determined by a balance between the land surface water supply conditions (precipitation) and atmospheric evaporation requirements (net radiation or

potential evapotranspiration) and put forward the general form of a balanced relationship:

$$\frac{E}{P} = f(E_0 / P), \tag{1}$$

where E is the actual evapotranspiration (mm); P is the mean annual precipitation (mm); E_0 is the mean annual potential evapotranspiration (mm).

Following the Budyko hypothesis, according to the physical meaning of watershed hydrometeorology, Baopu Fu (1981) analyzed and deduced the form of Budyko hypothesis curve and provided another form of analytical expression:

$$\frac{E}{P} = 1 + \frac{E_0}{P} - \left[1 + \left(\frac{E_0}{P}\right)^{\omega}\right]^{1/\omega}, \tag{2}$$

where ω is a non-dimensional parameter of the watershed underlying characteristic, which is related to the land use, soil, vegetation, topography, and other characteristics.

Therefore, taking the underlying surface factors of the watershed, Budyko hypothesis was developed into a new form of expression:

$$\frac{E}{P} = f\left(\frac{E_0}{P}, \omega\right) \tag{3}$$

Sensitivity Analysis of Influencing Factors of Water Watershed Runoff

Based on the water balance equation ($P = E + Q$) for a long period, combined with **Eq. 2**, there is

$$Q = \left[P^{\omega} + E_0^{\omega}\right]^{1/\omega} - E_0. \tag{4}$$

Based on the definition of the sensitivity coefficient, combined with **Eq. 4**, the calculation formulas of sensitivity coefficients of Q to P, E_0, ω can be obtained as follows:

$$\frac{\partial Q}{\partial P} = \left[1 + \left(\frac{E_0}{P}\right)^{\omega}\right]^{(1/\omega-1)} \tag{5}$$

$$\frac{\partial Q}{\partial E_0} = \left[1 + \left(\frac{P}{E_0}\right)^{\omega}\right]^{(1/\omega-1)} - 1 \tag{6}$$

$$\frac{\partial Q}{\partial \omega} = \left[P^{\omega} + E_0^{\omega}\right] \cdot \left[\left(-\frac{1}{\omega^2}\right) \cdot \ln\left(P^{\omega} + E_0^{\omega}\right) + \frac{1}{\omega} \cdot \frac{1}{P^{\omega} + E_0^{\omega}} \cdot \left(\ln P \cdot P^{\omega} + \ln E_0 \cdot E_0^{\omega}\right)\right], \tag{7}$$

where ω is calculated using the least squares method.

Estimating the Contribution of Climate and Watershed Characteristic Variabilities to Streamflow

Perturbations in precipitation, potential evaporation, and watershed characteristic will result in changes of water balances. Therefore, it can be suggested that the mean annual streamflow change was caused by climate and watershed characteristic variabilities, and this can be expressed as the following:

$$\Delta Q_{climate} = \frac{\partial Q}{\partial P} \cdot \Delta P + \frac{\partial Q}{\partial E_0} \cdot \Delta E_0 \tag{8}$$

$$\Delta Q_{watershed} = \frac{\partial Q}{\partial \omega} \cdot \Delta \omega \tag{9}$$

$$\Delta Q = \overline{Q_2} - \overline{Q_1}, \tag{10}$$

where ΔP, ΔE_0, and $\Delta \omega$ denote changes in streamflow, potential evaporation, and watershed characteristic, respectively; $\overline{Q_1}$, $\overline{Q_1}$ denote mean annual streamflow in the reference and change period, respectively.

Therefore, the contribution rates of climate and watershed characteristic variabilities can be determined in the following expression:

$$I_{\text{climate}} = \frac{\Delta Q_{\text{climate}}}{\Delta Q} \times 100\% \tag{11}$$

$$I_{\text{watershed}} = \frac{\Delta Q_{\text{watershed}}}{\Delta Q} \times 100\% \tag{12}$$

The Mann–Kendall Test

1) The Mann–Kendall trend test

The Mann–Kendall trend test, recommended by the World Meteorological Organization and widely used to detect varying trends in hydro-climatic time series (Wang and Yu, 2015), is adopted in this study. The test statistics is as follows:

$$Z = \begin{cases} \dfrac{S-1}{\sqrt{Var(S)}}, & S > 0 \\ 0, & S = 0 \\ \dfrac{S+1}{\sqrt{Var(S)}}, & S < 0 \end{cases}, \tag{13}$$

where

$$S = \sum_{i=1}^{n-1} \sum_{j=i+1}^{n} \operatorname{sgn}\left(x_j - x_i\right) \tag{14}$$

$$\operatorname{sgn}\left(x_j - x_i\right) = \begin{cases} +1, & x_j > x_i \\ 0, & x_j = x_i \\ -1, & x_j < x_i \end{cases} \tag{15}$$

$$Var(S) = \frac{n(n-1)(2n+5)}{18}, \tag{16}$$

where x_i and x_j denote two simple variables from a time series data ($x_1, x_2, x_3 \ldots, x_n$); n is the data size; Z and S stand for a test statistic, respectively.

Under the significance level of α, the null hypothesis of no trend is rejected if $|Z| > Z_{(1-\alpha/2)}$, where $Z_{(1-\alpha/2)}$ denotes the critical value obtained from the standard normal distribution tables. A positive Z value indicates an upward trend and vice versa. In this study, $\alpha = 0.05$.

2) The Mann–Kendall change-point analysis

The test statistic S_k is calculated as follows:

$$S_k = \sum_{i=1}^{k} \sum_{j=1}^{i-1} r_{ij} \, (k = 2, 3, 4, \ldots, n) \tag{17}$$

$$r_{ij} = \begin{cases} 1, x_i > x_j \\ 0, x_i \le x_j \end{cases} (1 \le j \le i) \quad (18)$$

Then, the statistics index UF_k is calculated as follows:

$$UF_k = \frac{S_k - E(S_k)}{\sqrt{Var(S_k)}} (k = 1, 2, 3, ..., n), \quad (19)$$

where

$$E(S_k) = \frac{k(k-1)}{4} \quad (20)$$

$$Var(S_k) = \frac{k(k-1)(2k+5)}{72} \quad (21)$$

Another statistics index UB_k is obtained using the same procedure shown above but with an adverse time series. The two lines of UF_k and UB_k may make an intersection point at a certain significance level, and then the point will be identified as the abrupt point.

Precipitation-Streamflow Double Cumulative Curve

Double cumulative curve (Huo et al., 2008) is the most intuitive and widely used method in time series analysis, and it is adopted to determine the time and degree when watershed characteristic begins to significantly influence streamflow in this study. When it is primarily affected by precipitation, the double cumulative curve is a straight line; when other factors such as the underlying surface of the watershed are significantly affected, the curve will shift and have a break point. The degree of curve deviation indicates the impact intensity of the underlying surface of the watershed. The precipitation-streamflow double cumulative curve can be defined by

$$\sum Q = a \sum P + b \quad (22)$$

$$\Delta Q_{dcc} = \sum Q_{dcc} - \sum Q, \quad (23)$$

where $\sum Q$, $\sum P$, $\sum Q_{dcc}$, and ΔQ_{dcc} denote cumulative streamflow, cumulative precipitation, simulated cumulative streamflow, and cumulative streamflow by watershed characteristic, respectively; a and b denote fixed parameters.

DATA

This study utilized annual runoff data from China Hydrology Yearbook. The observed series cover the period from 1958 to 2017. Meteorological data from eight weather stations within and around the research area were provided by the National Climate Center of China Meteorological Administration (http: //www.data.cma.cn/) (**Table 1**). All the meteorological data series with daily temperature, relative humidity, wind speed, sunshine duration, and precipitation were also from 1958 to 2017, and the potential evapotranspiration was calculated by Penman–Monteith formula (Allen et al., 1998). The NDVI dataset used in this study is NASA Global Inventory Monitoring and Modeling Systems Normalized Difference Vegetation Index third dataset (GIMMS NDVI 3 g) and it is the longest NDVI time series so far, with a period of from 1982 to 2015, a spatial resolution of 1/12°, and a temporal interval of 15 days (Ni et al., 2020), and it is confirmed that the dataset can provide high-quality data for places from mid to high latitudes. Annual NDVI values are obtained by using maximum value composite method (Zhang et al., 2013).

RESULTS

Characteristics of Streamflow Variability in the Huangshui River Basin

The Mann–Kendall trend test of annual streamflow for Huangshui River basin was summarized in **Figure 2**. The results showed that the statistical test value (Z) was −1.59, and its absolute value ($|Z|$) was less than 1.96, indicating that the annual streamflow of the Huangshui River basin exhibited an insignificant downward trend at the 0.05 significance level.

The Mann–Kendall mutation test was performed on the streamflow data, as is showed in **Figure 2**. It can be noted that, before 1987, although the UF and UB lines had several intersections, however, there was no obvious abrupt point. After 1987, lines of UF and UB crossed in 1993, and the intersection point was within the critical lines of ±1.96 (0.05 significance level). Therefore, the abrupt change point of annual streamflow in the Huangshui River basin was in 1993. Furthermore, the data series from 1958 to 2017 can be split into two periods: the reference period (1958–1993) and the change period (1994–2017).

It was clearly seen that compared with the reference period, the mean annual streamflow in the change period decreased from 150.71 to 130.23 mm (**Figure 3**). It is concluded that the annual streamflow reduced by 20.48 mm (13.59%).

Sensitivity of Watershed Streamflow to Climatic Factors and Watershed Characteristic

Based on the annual data series of 1958–2017 in the Huangshui River basin, values of the mean annual precipitation, the mean annual streamflow, and the mean potential evapotranspiration were 418.81, 142.52, and 833.28mm, respectively. Further, watershed characteristic parameter (ω) calculated on the basis of **Eq. 4** was 1.7306.

These data obtained previously were used in **Eq. 5**, **Eq. 6**, and **Eq. 7**; the sensitivity coefficients of streamflow to precipitation, potential evapotranspiration, and watershed characteristic parameter were $\partial Q/\partial P$ = 0.5502, $\partial Q/\partial E_0$ = −0.1055, and $\partial Q/\partial \omega$ = −183.2007, respectively. That means that every unit increase in precipitation, potential evapotranspiration, and watershed characteristic parameter will lead to the streamflow change by 0.5502, −0.1055, and −183.2007 units. Thus, it is suggested that the streamflow change is positively related to precipitation, and it is negatively related to potential evapotranspiration and watershed characteristic. Meanwhile, among climate factors, streamflow becomes more sensitive to change in precipitation

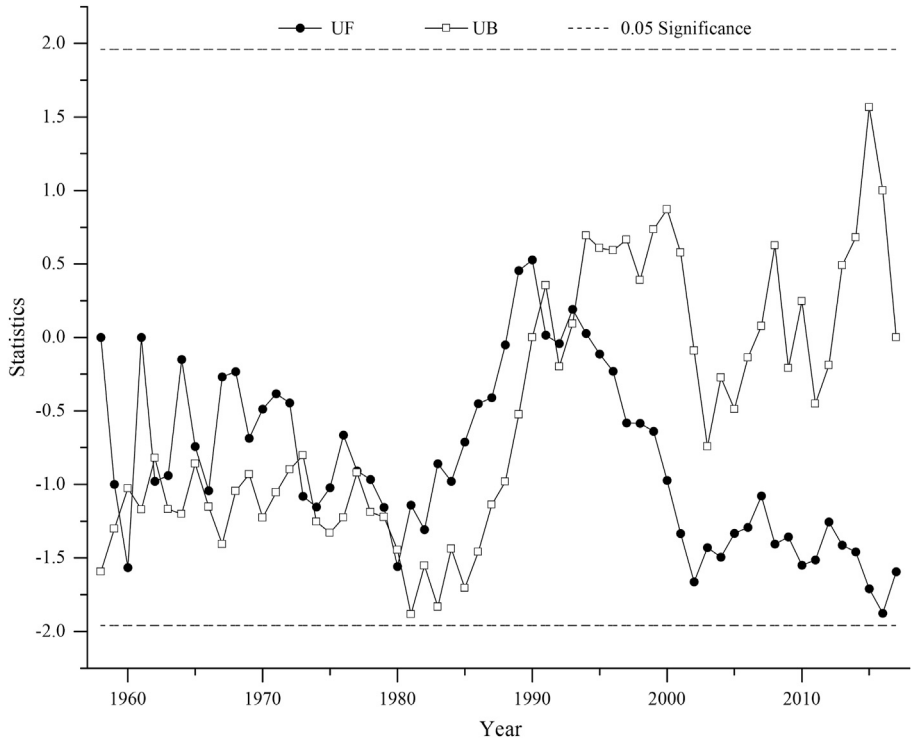

FIGURE 2 | Mann–Kendall change-point detection in time series of annual streamflow.

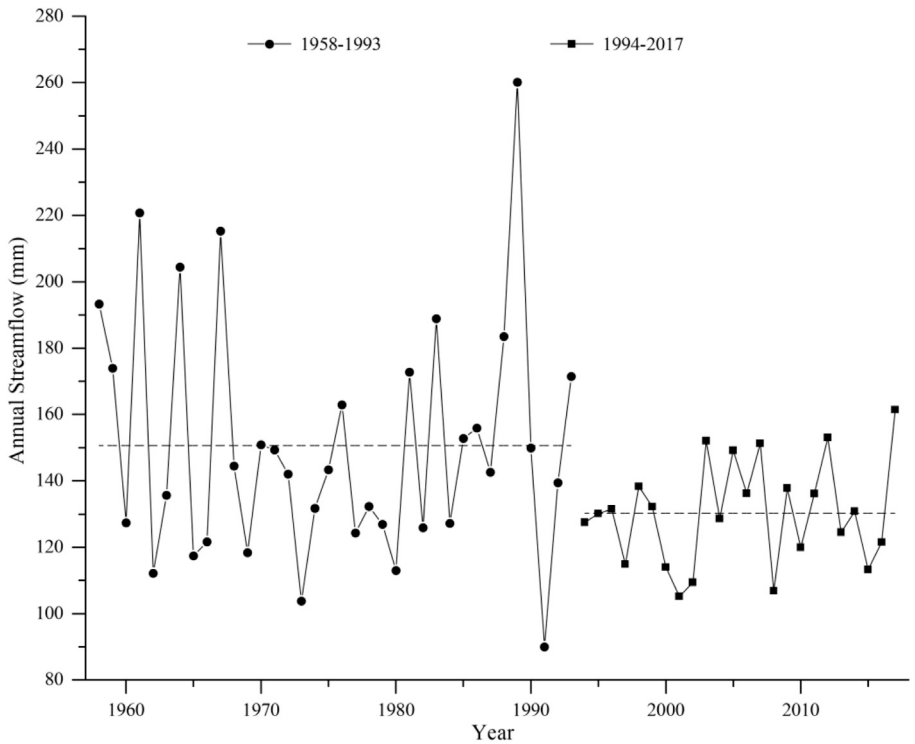

FIGURE 3 | Annual streamflow comparison of reference period and change period in the Huangshui River basin.

TABLE 1 | The overview of hydrological and meteorological stations in the Huangshui River basin.

ID	Station	Type	Longitude	Latitude	Altitude/m
1	Qilian	Meteorological station	100.25	38.18	2,787
2	Minhe		102.08	36.03	1,814
3	Guide		101.37	36.02	2,273
4	Xining		101.75	36.73	2,295
5	Gonghe		100.62	36.27	2,835
6	Gangcha		100.13	37.00	1,330
7	Menyuan		101.62	37.38	1,285
8	Wuqiaoling		102.87	37.20	3,045
1	Huangyuan	Hydrological station	101.27	36.68	2,619
2	Ledu		102.42	36.48	1,971
3	Minhe		102.80	36.33	1,779
4	Jijiabao		102.78	36.32	1,818

TABLE 2 | The changes of streamflow and meteorological and watershed characteristic parameter in two periods.

Period	*Q*/mm	*P*/mm	E_0/mm	ω
1958–1993	150.71	411.65	836.46	1.6412
1994–2017	130.23	429.56	828.51	1.8153
1958–2017	142.52	418.81	833.28	1.7306
Change/△	−20.48	17.91	−7.95	0.1741

TABLE 3 | Relative contribution rates of climate change and watershed characteristic changes to streamflow variability.

Project	$\triangle Q$	$\triangle Q_{climate}$	$\triangle Q_{watershed}$	Error
Influence quantity/mm	−20.48	10.69	−31.90	0.73
Contribution rate/%	100	24.68	73.64	1.68

than that in potential evapotranspiration. The results also suggest that watershed characteristic changes play a more important role than climate changes on streamflow variability in the Huangshui River basin.

Attribution Analysis of Streamflow Changes in the Huangshui River Basin

Based on the data provided from the Huangshui River basin in period of 1958–2017, the mean annual streamflow, the mean annual precipitation, and the mean annual potential evapotranspiration in the reference period (1958–1993) and the change period (1994–2017) were calculated, respectively. Further, watershed characteristic parameter (ω) can be also calculated on the basis of **Eq. 4**. The results are shown in **Table 2**. During two periods, P and ω increase from 411.65 to 429.56 mm and from 1.6412 to 1.8153, respectively, while E_0 decreases from 836.46 to 828.51 mm, conversely.

The effects of climate changes and watershed characteristic changes on the streamflow amount were 10.69 mm and −31.90 mm, respectively, calculated by **Eq. 8–12**. The impacts of climate and watershed characteristic changes on streamflow are summarized in **Table 3**. The watershed characteristic changes should be principally responsible for streamflow change, which led to a large streamflow decrease of 31.90 mm and contributes 73.64% of the total streamflow change, while climate-induced streamflow change only accounted for 24.68%.

Double Cumulative Curve Verification

As shown in **Figure 4**, the slope of the curve changed abruptly in 1993, which is consistent with the Mann–Kendall test result and the division of the study period in this study. That means that underlying surface of the watershed has significant impact on the streamflow of the Huangshui River basin after 1993.

Figure 4 also shows that the correlation equation of cumulative streamflow and cumulative precipitation in the period of 1958–1993 was $\sum Q = 0.3729$, $\sum P$–14.669, the correlation coefficient R^2 was 0.9977, the time series N was 60 years, and the confidence level was 0.001.

The cumulative simulated streamflow in the change period was obtained by using the correlation equation on the basis of cumulative precipitation in the same period. Thus, further, the values of simulated streamflow are calculated during the change period. During the changing period (1994–2017), the observed mean streamflow is 130.23 mm, while the simulated mean streamflow is 160.19 mm (**Figure 5**). Therefore, the underlying surface of watershed is estimated to have resulted in a 29.96 mm change of the basin.

DISCUSSION

Attribution Analysis of Streamflow Variability

In spite of slowly upward trend in annual precipitation and slightly downward trend in annual potential evaporation, slightly decreasing trend in annual streamflow can be found for the Huangshui River basin. That infers, streamflow is affected by other factors (primary human activities) in addition to climate change. Huangshui River Basin plays an important role in politics, economy, culture and transportation in Qinghai Province, China. Due to the needs of water supply and development, many water retaining structures (such as reservoirs) have been built in this region, which reduces the streamflow of Huangshui River and its tributaries directly to different degrees and changes spatiotemporal distribution of

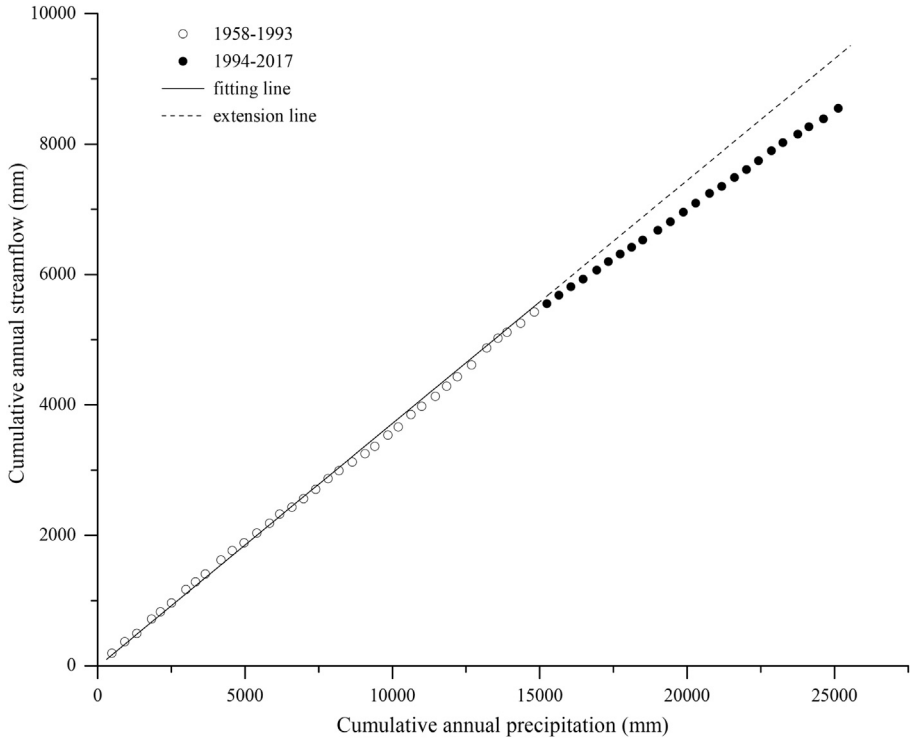

FIGURE 4 | Double mass curve analysis between streamflow and precipitation.

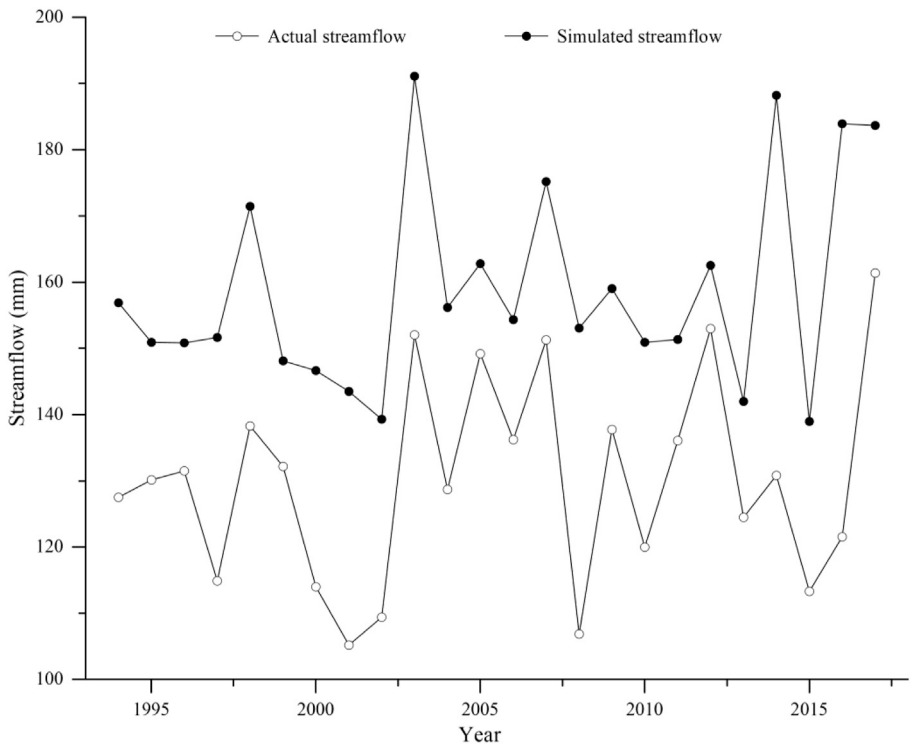

FIGURE 5 | Double cumulative curve comparison of simulated values and observed values in the changed period.

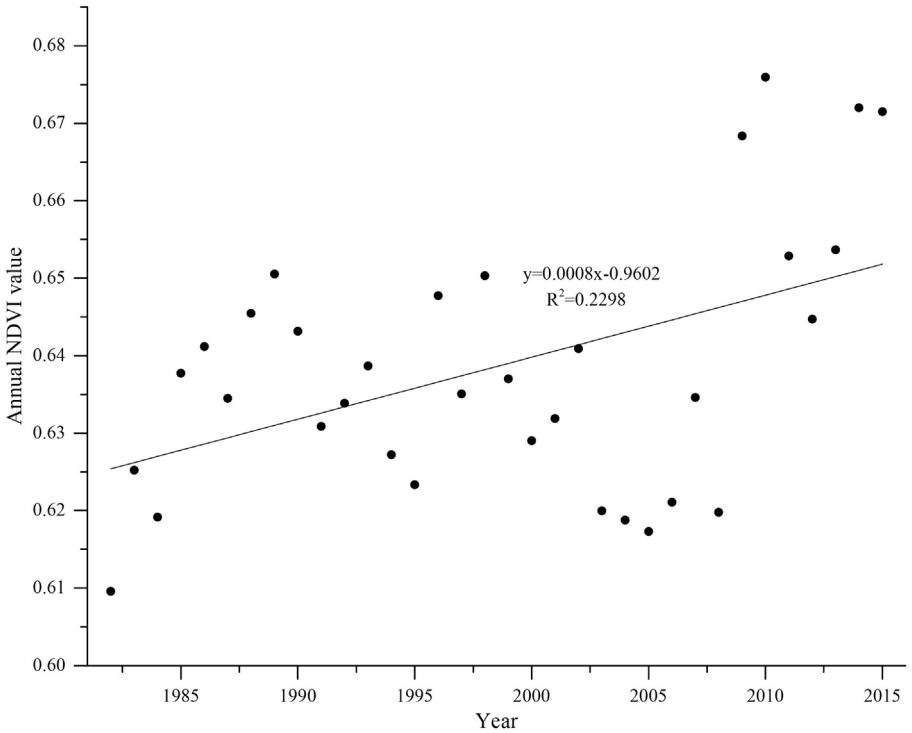

FIGURE 6 | Change trend of annual NDVI in the Huangshui River basin from 1982 to 2015.

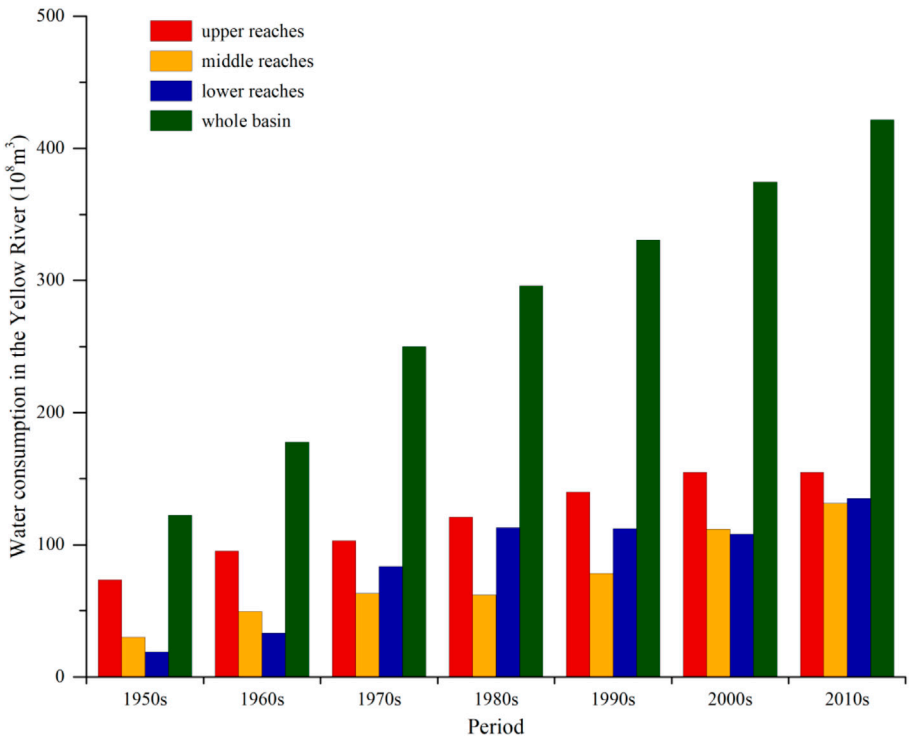

FIGURE 7 | Water consumption in the Yellow River basin during different periods since 1950s.

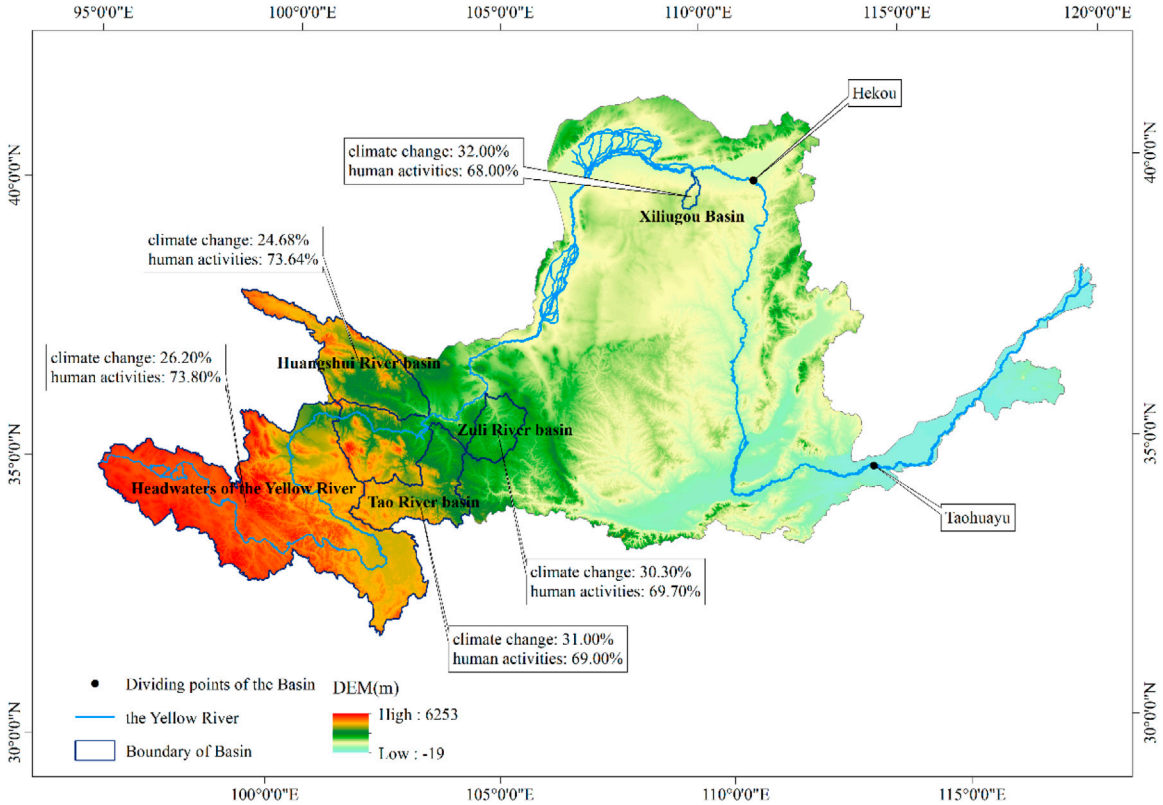

FIGURE 8 | The map focusing on observed impacts of the hydrological response in the **upper** Yellow River.

streamflow. Researchers believe that reservoirs with large storage capacity could lead to the strengthening of evaporation and river channel leakage, which also reduces streamflow to some degree (Feng et al., 2020). In addition, owing to serious soil and water loss in the middle and lower reaches of the basin, soil and water conservations have gradually covered this area since the 1970s, including terraced fields, afforestation and grass-planting, and warping dam. Vegetation is the most important land use type in Huangshui basin, with a proportion of more than 85%, and the proportion of other land use types is small. As seen in **Figure 6**, the vegetation coverage of this region during 1982–2015 has improved dramatically, and annual mean NDVI has increased gradually at a rate of 0.0008/year (range from 0.6094 in 1982 to 0.6716 in 2015). Therefore, the increase in vegetation coverage could improve the soil structure and result in the enhancing of evaporation and infiltration and more water is trapped in the soil, leading to streamflow decline in the basin outlet through intercepting more precipitation (Xu, 2011; Qiu et al., 2021).

Climate change and human activities are generally considered as the two primary factors of streamflow variation, and the effects of them to streamflow are significantly different in different catchments. Studies have shown that the decrease in precipitation caused by climate change is the main reason for the decrease in the runoff of the Congo River in Africa (Noel and Saiers, 2017); however, for the Colorado River in the United States, the impact of human activities on runoff changes is slightly greater than climate change (Shi et al., 2019). In the mainstream area of the Yangtze basin, the increase in precipitation caused by climate change is the main reason for the streamflow variability in the upper reaches of the basin, and human activities are the main factor in runoff change for the lower reaches of the basin, mainly including the reduction of lake area and the hardening of the ground caused by urbanization (Wang et al., 2013). For the tributaries of the Haihe River, human activities are the main factors for declining streamflow in Luanhe River catchment, Chaohe River catchment, and Zhanghe River catchment, while climate change is the main driver leading to decreasing streamflow in the Huto River catchment, and increasing water demand should be responsible for streamflow variability in the whole basin (Wang et al., 2013). Streamflow of the Yellow River basin shows a significantly downward trend, which is primarily caused by human activities. As shown in **Figure 7**, compared with 1950s, in the early 21st century, the water consumption of the upper reaches and whole basin of the Yellow River basin has increased by approximately two and three times, respectively. Research indicates that agricultural irrigation accounted for more than 50% of the Yellow River runoff during the same period. In addition, in order to control serious soil and water loss, large-scale soil and water conservation projects have been constructed in the upper and middle reaches of the Yellow River since the 1970s, but it also reduces the runoff generation capacity of the basin.

In order to further understand streamflow variability of the upper Yellow River, this study compares attributions of streamflow in the headwaters of the Yellow River basin

(HYRB) (Zheng et al., 2009), the Tao River basin (Sun et al., 2019), the Zuli River basin (Deng, 2001), and the Xiliugou basin (Yao et al., 2015) of the upper Yellow River. The contributions of runoff change in the above studies were quantitatively evaluated by using the double mass curves method, climate elasticity method, RCC-WBM model, and SWAT model, and the results are listed in **Figure 8**. Research in the HYRB indicates that the contribution rates of climate change and human activities to streamflow variability were 26.20 and 73.80%, respectively, which is extremely similar to the conclusions of this study (climate changes account for 24.68% and watershed characteristic changes account for 73.64%). These results suggest that the sensitivity analysis method based on Budyko theory is used to investigate the river basin streamflow evolution is feasible, and the results are accurate. Besides, these also indicate related human activities have tremendous influences on the slow decline in streamflow for the entire upper Yellow River.

Cause-Effect of Changing Point

In this study, the streamflow of Huangshui River basin showed a change point in 1993, which was very similar with other researches in the upper reaches of the Yellow River. After studying climate change in northwest China where the Huangshui River basin is located, some researchers believe that the abrupt changes of surface wind speed and mean annual temperature in the past 44 years (1960–2003) are in 1990 and 1994, and the region experiences a period of lower surface wind speed after 1990 and a warmer period after 1994, respectively (Wang et al., 2007), and researchers believe that obvious changes of extreme maximum and minimum temperatures in Hexi Corridor of northwest China are in 1996 and 1993, and the subsequent climate is all warmer (Li et al., 2015).

Uncertainties

It is essential that there are some uncertainties in the assessment of climate change and human activities on basin drainage. This study assumes that climate and watershed characteristic changes are independent of each other. Nevertheless, these two factors are interacting in an exceedingly complicated way, even in the reference period (Wang et al., 2019). In addition, we analyze streamflow variability and estimate climate and watershed-characteristic-induced to streamflow variability, but the values (**Table 2** and **3**) show only average values during the reference and change period and lack consideration of range or change of the values. Moreover, the change of present permafrost in an alpine basin significantly complicated the hydrological processes due to climate warming, and we do not consider the extent of its impact (Fang et al., 2019). In fact, watershed characteristic parameter (ω) includes both climate-induced and watershed-characteristic-induced variabilities, and attribution analysis in this study overestimates the effect of watershed characteristic on streamflow variability (Xu et al., 2014). The spatiotemporal distribution of meteorological stations is not considered in the Budyko framework, and it is possible to have another type of error in quantitative assessment/analysis (Shahid et al., 2018). In the future research, these uncertainties need be paid more attention.

CONCLUSION

Based on the Budyko framework, this study assessed relative contributions of climate and watershed characteristic changes on streamflow in the Huangshui River basin. The main conclusions are as follows:

1) From 1958 to 2017, the annual streamflow of Huangshui River basin showed an insignificant downward trend. The streamflow series had a change point in 1993, and thus the streamflow reference period was set to 1958–1993, and the change period was 1994–2017. In the change period, the streamflow decreased by 20.48 mm (13.59%) compared with the reference period.
2) Sensitivity coefficients of streamflow to precipitation, potential evapotranspiration, and watershed characteristic parameter in Huangshui River basin are 0.5502, −0.1055, and −183.2007, respectively. It shows that an increase in precipitation by 1 unit will induce an increase of 0.5502 units in streamflow, and an increase in potential evapotranspiration by 1 unit will induce a decrease of 0.1055 units in streamflow, and an increase in the watershed characteristic parameter by 1 unit will induce a decrease of 183.2007 units in streamflow.
3) During the change period (1994–2017), the streamflow change in the Huangshui River basin is mainly caused by the watershed underlying surface change, and its contribution rate is 77.64%, and the impact of climate changes on runoff is only 24.68%.

DATA AVAILABILITY STATEMENT

The original contributions presented in the study are included in the article/Supplementary Material; further inquiries can be directed to the corresponding author.

AUTHOR CONTRIBUTIONS

XL wrote the original draft of this manuscript. TQ and SSL designed the manuscript. SPL and YN undertook the analysis of data. QZ revised the manuscript.

FUNDING

This study was financially supported by the National Key Research and Development Project (No. 2017YFA0605004), State Key Laboratory Fund (IWHR-SKL-KF201903), National Natural Sciences Foundation of China (51979118), and Central Nonprofit Research Institutions Basic Scientific Research Special Fund (HKY-JBYW-2019-01). All experiments were in compliance with the current laws of the country in which they were performed.

ACKNOWLEDGMENTS

The authors thank the data observers for their hard work.

REFERENCES

Beer, C., Reichstein, M., Tomelleri, E., Ciais, P., Jung, M., Carvalhais, N., et al. (2010). Terrestrial Gross Carbon Dioxide Uptake: Global Distribution and Covariation with Climate. *Science* 329 (5993), 834–838. doi:10.1126/science.1184984

Budyko, M. I. (1974). *Climate and Life*. Academic Press.

Choudhury, B. J. (1999). Evaluation of an Empirical Equation for Annual Evaporation Using Field Observations and Results from a Biophysical Model. *J. Hydrol.* 216 (1-2), 99–110. doi:10.1016/S0022-1694(98)00293-5

Costa, M. H., Botta, A., and Cardille, J. A. (2003). Effects of Large-Scale Changes in Land Cover on the Discharge of the Tocantins River, Southeastern Amazonia. *J. Hydrol.* 283 (1-4), 206–217. doi:10.1016/S0022-1694(03)00267-1

Deng, J. L. (2001). Trend and Mutation Analysis of Spatial and Temporal Distribution on Runoff and Sediment in Zulihe River Basin. *J. China Hydrol.* 21 (2), 47–50.

Fang, J., Li, G., Rubinato, M., Ma, G., Zhou, J., Jia, G., et al. (2019). Analysis of Long-Term Water Level Variations in Qinghai Lake in China. *Water* 11 (10), 2136–2156. doi:10.3390/w11102136

Feng, J., Zhao, G., Mu, X., Tian, P., and Tian, X. (2020). Analysis on Runoff Regime in Middle Yellow River and its Driving Factors. *J. Hydroelectric Eng.* 39 (8), 90–103.

Fu, B. P. (1981). On the Calculation of the Evaporation from Land Surface. *Scientia atmosoherica sinica* 5 (1), 25–33.

Fu, G., Charles, S. P., and Chiew, F. H. S. (2007). A Two-Parameter Climate Elasticity of Streamflow index to Assess Climate Change Effects on Annual Streamflow. *Water Resour. Res.* 43 (11), 2578–2584. doi:10.1029/2007WR005890

Hu, J., Wu, Y., Wang, L., Sun, P., Zhao, F., Jin, Z., et al. (2021). Impacts of Land-Use Conversions on the Water Cycle in a Typical Watershed in the Southern Chinese Loess Plateau. *J. Hydrol.* 593, 125741. doi:10.1016/j.jhydrol.2020.125741

Huo, Z., Feng, S., Kang, S., Li, W., and Chen, S. (2008). Effect of Climate Changes and Water-related Human Activities on Annual Stream Flows of the Shiyang River basin in Arid north-west China. *Hydrol. Process.* 22, 3155–3167. doi:10.1002/hyp.6900

Jiang, T., Chen, Y. D., Xu, C.-y., Chen, X., Chen, X., and Singh, V. P. (2007). Comparison of Hydrological Impacts of Climate Change Simulated by Six Hydrological Models in the Dongjiang Basin, South China. *J. Hydrol.* 336, 316–333. doi:10.1016/j.jhydrol.2007.01.010

Kong, D., Miao, C., Wu, J., and Duan, Q. (2016). Impact Assessment of Climate Change and Human Activities on Net Runoff in the Yellow River Basin from 1951 to 2012. *Ecol. Eng.* 91, 566–573. doi:10.1016/j.ecoleng.2016.02.023

Li, H., Gao, Z., Wang, S., and Wang, H. (2015). Extreme Temperature Variation of Hexi Corridor in Recent 60 Years. *Arid Land Geogr.* 38 (1), 1–9.

Li, X., and Tang, Q. (1981). An Analysis on Annual Runoff of West Sichuan and north Yunnan. *Acta Geographica Sinica* 36 (1), 90–100.

Li, Y., Mao, D., Feng, A., and Schillerberg, T. (2019). Will Human-Induced Vegetation Regreening Continually Decrease Runoff in the Loess Plateau of China. *Forests* 10 (10), 906–925. doi:10.3390/f10100906

Liang, W., Bai, D., Jin, Z., You, Y., Li, J., and Yang, Y. (2015). A Study on the Streamflow Change and its Relationship with Climate Change and Ecological Restoration Measures in a Sediment Concentrated Region in the Loess Plateau, China. *Water Resour. Manage.* 29 (11), 4045–4060. doi:10.1007/s11269-015-1044-5

Liu, Q., and Mcvicar, T. R. (2012). Assessing Climate Change Induced Modification of Penman Potential Evaporation and Runoff Sensitivity in a Large Water-Limited basin. *J. Hydrol.* 464-465, 352–362. doi:10.1016/j.jhydrol.2012.07.032

Liu, X. (2020). Quantitative Attribution of Runoff and Sediment Load Change in Huangshui River. *Yellow River* 42 (1), 6–10.

Lv, X., Zuo, Z., Ni, Y., Sun, J., and Wang, H. (2019). The Effects of Climate and Catchment Characteristic Change on Streamflow in a Typical Tributary of the Yellow River. *Sci. Rep.* 9, 1–10. doi:10.1038/s41598-019-51115-x

Ma, H., Yang, D., Tan, S. K., Gao, B., and Hu, Q. (2010). Impact of Climate Variability and Human Activity on Streamflow Decrease in the Miyun Reservoir Catchment. *J. Hydrol.* 389 (3-4), 317–324. doi:10.1016/j.jhydrol.2010.06.010

Mezentsev, V. S. (1955). More on the Calculation of Average Total Evaporation. *Meteorol. Gidrol* 5, 24–26.

Milly, P. C. D., and Dunne, K. A. (2002). Macroscale Water Fluxes 2. Water and Energy Supply Control of Their Interannual Variability. *Water Resour. Res.* 38 (10), 24-1–24-9. doi:10.1029/2001WR000760

Ni, Y., Zhou, Y., and Fan, J. (2020). Characterizing Spatiotemporal Pattern of Vegetation Greenness Breakpoints on Tibetan Plateau Using GIMMS NDVI3g Dataset. *IEEE Access* 8, 56518–56527. doi:10.1109/ACCESS.2020.2982661

Noel, A., and Saiers, J. (2017). Simulated Hydrologic Response to Projected Changes in Precipitation and Temperature in the Congo River basin. *Hydrol. Earth Syst. Sci.* 21, 4115–4130. doi:10.5194/hess-21-4115-2017

Qiu, L., Wu, Y., Shi, Z., Yu, M., Zhao, F., and Guan, Y. (2021). Quantifying Spatiotemporal Variations in Soil Moisture Driven by Vegetation Restoration on the Loess Plateau of China. *J. Hydrol.* 600. doi:10.1016/j.jhydrol.2021.126580

Ran, L., Wang, S., and Fan, X. (2010). Channel Change at Toudaoguai Station and its Responses to the Operation of Upstream Reservoirs in the Upper Yellow River. *J. Geogr. Sci.* 20 (2), 231–247. doi:10.1007/s11442-010-0231-9

Roderick, M. L., and Farquhar, G. D. (2011). A Simple Framework for Relating Variations in Runoff to Variations in Climatic Conditions and Catchment Properties. *Water Resour. Res.* 47 (12), 667–671. doi:10.1029/2010WR009826

Schaake, J. C. (1990). From Climate to Flow. *Clim. Change US Water Resour.*, 177–206.

Shahid, M., Cong, Z., and Zhang, D. (2018). Understanding the Impacts of Climate Change and Human Activities on Streamflow: a Case Study of the Soan River basin, Pakistan. *Theor. Appl. Climatology* 134 (1-2), 205–219. doi:10.1007/s00704-017-2269-4

Shi, X., Qin, T., Nie, H., Weng, B., and He, S. (2019). Changes in Major Global River Discharges Directed into the Ocean. *Ijerph* 16, 1469. doi:10.3390/ijerph16081469

Sun, L., Wang, Y.-Y., Zhang, J.-Y., Yang, Q.-L., Bao, Z.-X., Guan, X.-X., et al. (2019). Impact of Environmental Change on Runoff in a Transitional basin: Tao River Basin from the Tibetan Plateau to the Loess Plateau, China. *Adv. Clim. Change Res.* 10 (4), 214–224. doi:10.1016/j.accre.2020.02.002

Sun, P., Wu, Y., Wei, X., Sivakumar, B., Qiu, L., Mu, X., et al. (2020). Quantifying the Contributions of Climate Variation, Land Use Change, and Engineering Measures for Dramatic Reduction in Streamflow and Sediment in a Typical Loess Watershed, China. *Ecol. Eng.* 142. doi:10.1016/j.ecoleng.2019.105611

Tang, Y. (1995). On Human Action Influence on the Runoff in Luanhe River basin. *J. Shaanxi Normal Univ. (Natural Sci. Edition)* 23 (2), 125126. doi:10.15983/j.cnki.jsnu.1995.02.035

Thompson, J. R. (2012). Modelling the Impacts of Climate Change on upland Catchments in Southwest Scotland Using MIKE SHE and the UKCP09 Probabilistic Projections. *Hydrol. Res.* 43 (4), 507–530. doi:10.2166/nh.2012.105

Velpuri, N. M., and Senay, G. B. (2013). Analysis of Long-Term Trends (1950-2009) in Precipitation, Runoff and Runoff Coefficient in Major Urban Watersheds in the United States. *Environ. Res. Lett.* 8 (2), 024020–024026. doi:10.1088/1748-9326/8/2/024020

Wang, D., and Hejazi, M. (2011). Quantifying the Relative Contribution of the Climate and Direct Human Impacts on Mean Annual Streamflow in the Contiguous United States. *Water Resour. Res.* 47 (10), 411. doi:10.1029/2010WR010283

Wang, D., and Tang, Y. (2014). A One-Parameter Budyko Model for Water Balance Captures Emergent Behavior in Darwinian Hydrologic Models. *Geophys. Res. Lett.* 41 (13), 4569–4577. doi:10.1002/2014GL060509

Wang, F., Duan, K., Fu, S., Gou, F., Liang, W., Yan, J., et al. (2019). Partitioning Climate and Human Contributions to Changes in Mean Annual Streamflow Based on the Budyko Complementary Relationship in the Loess Plateau, China. *Sci. Total Environ.* 665, 579–590. doi:10.1016/j.scitotenv.2019.01.386

Wang, H., Lv, X., and Zhang, M. (2021). Sensitivity and Attribution Analysis Based on the Budyko Hypothesis for Streamflow Change in the Baiyangdian Catchment, China. *Ecol. Indicators* 121, 107221. doi:10.1016/j.ecolind.2020.107221

Wang, H., and Yu, X. (2015). Sensitivity Analysis of Climate on Streamflow in north China. *Theor. Appl. Climatol* 119, 391–399. doi:10.1007/s00704-014-1289-6

Wang, H., and Yu, X. (2015). Sensitivity Analysis of Climate on Streamflow in north China. *Theor. Appl. Climatol.* 119 (1-2), 391–399. doi:10.1007/s00704-014-1289-6

Wang, P., Yang, J., Zhang, Q., He, J., Wang, D., and Lu, D. (2007). Climate Change Characteristic of Northeast China in Recent Half century. *Adv. Earth Sci.* 22 (6), 649–656.

Wang, S., Yan, M., Yan, Y., Shi, C., and He, L. (2012). Contributions of Climate Change and Human Activities to the Changes in Runoff Increment in Different Sections of the Yellow River. *Quat. Int.* 282, 66–77. doi:10.1016/j.quaint.2012.07.011

Wang, W., Shao, Q., Yang, T., Peng, S., Xing, W., Sun, F., et al. (2013). Quantitative Assessment of the Impact of Climate Variability and Human Activities on Runoff Changes: a Case Study in Four Catchments of the Haihe River basin, China. *Hydrol. Process.* 27 (8), 1158–1174. doi:10.1002/hyp.9299

Wang, Y., Ding, Y., Ye, B., Liu, F., Wang, J., and Wang, J. (2013). Contributions of Climate and Human Activities to Changes in Runoff of the Yellow and Yangtze Rivers from 1950 to 2008. *Sci. China Earth Sci.* 56, 1398–1412. doi:10.1007/s11430-012-4505-1

Wei, X., and Zhang, M. (2010). Quantifying Streamflow Change Caused by forest Disturbance at a Large Spatial Scale: A Single Watershed Study. *Water Resour. Res.* 46 (12), 439–445. doi:10.1029/2010WR009250

Xu, J. (1995). A Comparative Study of the Zonal Differences in River Runoff and Human Influence in China. *Geographical Res.* 14 (3), 33–42.

Xu, J. (2011). Variation in Annual Runoff of the Wudinghe River as Influenced by Climate Change and Human Activity. *Quat. Int.* 244 (2), 230–237. doi:10.1016/j.quaint.2010.09.014

Xu, X., Yang, D., Yang, H., and Lei, H. (2014). Attribution Analysis Based on the Budyko Hypothesis for Detecting the Dominant Cause of Runoff Decline in Haihe basin. *J. Hydrol.* 510, 530–540. doi:10.1016/j.jhydrol.2013.12.052

Xu, X., Yang, H., Yang, D., and Ma, H. (2013). Assessing the Impacts of Climate Variability and Human Activities on Annual Runoff in the Luan River basin, China. *Hydrol. Res.* 44 (5), 940–952. doi:10.2166/nh.2013.144

Yang, H., Yang, D., Lei, Z., and Sun, F. (2008). New Analytical Derivation of the Mean Annual Water-Energy Balance Equation. *Water Resour. Res.* 44 (3), 893–897. doi:10.1029/2007WR006135

Yang, Y., Donohue, R. J., McVicar, T. R., and Roderick, M. L. (2015). An Analytical Model for Relating Global Terrestrial Carbon Assimilation with Climate and Surface Conditions Using a Rate Limitation Framework. *Geophys. Res. Lett.* 42, 9825–9835. doi:10.1002/2015GL066835

Yao, H., Shi, C., Shao, W., Bai, J., and Yang, H. (2015). Impacts of Climate Change and Human Activities on Runoff and Sediment Load of the Xiliugou basin in the Upper Yellow River. *Adv. Meteorology* 2015, 1–12. doi:10.1155/2015/481713

You, P. (1995). Surface Water Resources and Runoff Composition in the Tarim River Basin. *Arid Land Geogr.* 18 (2), 29–35. doi:10.13826/j.cnki.cn65-1103/x.1995.02.005

Zhan, C., Niu, C., Song, X., and Xu, C. (2013). The Impacts of Climate Variability and Human Activities on Streamflow in Bai River basin, Northern China. *Hydrol. Res.* 44 (5), 875–885. doi:10.2166/nh.2012.146

Zhang, B., Wu, P., Zhao, X., Wang, Y., and Gao, X. (2013). Changes in Vegetation Condition in Areas with Different Gradients (1980-2010) on the Loess Plateau, China. *Environ. Earth Sci.* 68 (8), 2427–2438. doi:10.1007/s12665-012-1927-1

Zhang, L., Dawes, W. R., and Walker, G. R. (2001). Response of Mean Annual Evapotranspiration to Vegetation Changes at Catchment Scale. *Water Resour. Res.* 37 (3), 701–708. doi:10.1029/2000WR900325

Zhang, M., Wei, X., Sun, P., and Liu, S. (2012). The Effect of forest Harvesting and Climatic Variability on Runoff in a Large Watershed: The Case Study in the Upper Minjiang River of Yangtze River basin. *J. Hydrol.* 464-465, 1–11. doi:10.1016/j.jhydrol.2012.05.050

Zhang, S., Yang, D., Yang, H., and Lei, H. (2015). Analysis of the Dominant Causes for Runoff Reduction in Five Major Basins over China during 1960-2010. *Adv. Water Sci.* 26 (5), 605–613. doi:10.14042/j.cnki.32.1309.2015.05.001

Zhao, F., Zhang, L., Xu, Z., and Scott, D. F. (2010). Evaluation of Methods for Estimating the Effects of Vegetation Change and Climate Variability on Streamflow. *Water Resour. Res.* 46 (3), 742–750. doi:10.1029/2009WR007702

Zhao, Y., Yang, N., Wei, Y., Hu, B., Cao, Q., Tong, K., et al. (2019). Eight Hundred Years of Drought and Flood Disasters and Precipitation Sequence Reconstruction in Wuzhou City, Southwest China. *Water* 11 (2), 219. doi:10.3390/w11020219

Zheng, H., Zhang, L., Zhu, R., Liu, C., Sato, Y., and Fukushima, Y. (2009). Responses of Streamflow to Climate and Land Surface Change in the Headwaters of the Yellow River Basin. *Water Resour. Res.* 45 (7), 641–648. doi:10.1029/2007wr006665

Conflict of Interest: The authors declare that the research was conducted in the absence of any commercial or financial relationships that could be construed as a potential conflict of interest.

frontiers in Environmental Science

ORIGINAL RESEARCH
published: 25 October 2021
doi: 10.3389/fenvs.2021.742901

Risk Assessment of Dam-Breach Flood Under Extreme Storm Events

Xiajing Lin[1], *Guohe Huang*[1,2]*, *Guoqing Wang*[3], *Denghua Yan*[4] *and Xiong Zhou*[2]

[1]*Faculty of Engineering and Applied Science, University of Regina, Regina, SK, Canada,* [2]*State Key Joint Laboratory of Environmental Simulation and Pollution Control, China-Canada Center for Energy, Environment and Ecology Research, UR-BNU, School of Environment, Beijing Normal University, Beijing, China,* [3]*State Key Laboratory of Hydrology-Water Resources and Hydraulic Engineering, Nanjing Hydraulic Research Institute, Nanjing, China,* [4]*China Institute of Water Resources and Hydropower Research, Beijing, China*

In recent years, as a result of increasingly intensive rainfall events, the associated water erosion and corrosion have led to the increase in breach risk of aging dams in the United States. In this study, a hydrodynamic model was used to the inundation simulation under three hypothetical extreme precipitation-induced homogeneous concrete dam-breach scenarios. All hydraulic variables, including water depth, flow velocity, and flood arriving time over separated nine cross-sections in the Catawba River, were calculated. The hypothetical simulation results illustrate that the impact of Hurricane Florence's rainfall is far more severe over the downstream of hydraulic facilities than that of the Once-in-a-century storm rainfall event. Although Hurricane Florence's rainfall observed in Wilmington had not historically happened near the MI Dam site, the river basin has a higher probability to be attacked by such storm rainfall if more extreme weather events would be generated under future warming conditions. Besides, the time for floodwaters to reach cross-section 6 under the Hurricane Gustav scenario is shorter than that under the Once-in-a-century rainfall scenario, making the downstream be inundated in short minutes. Since the probability can be quantitatively evaluated, it is of great worth assessing the risk of dam-break floods in coastal cities where human lives are at a vulnerable stage.

Keywords: dam failure, inundation mapping, extreme storm events, flood vulnerability, heavy rainfall

OPEN ACCESS

Edited by:
Shan Zhao,
Shandong University, China

Reviewed by:
Lvyang Xiong,
China Agricultural University, China
Yanhu He,
Guangdong University of Technology, China

***Correspondence:**
Guohe Huang
huangg@uregina.ca

Specialty section:
This article was submitted to Environmental Informatics and Remote Sensing, a section of the journal Frontiers in Environmental Science

Received: *16 July 2021*
Accepted: *21 September 2021*
Published: *25 October 2021*

Citation:
Lin X, Huang G, Wang G, Yan D and Zhou X (2021) Risk Assessment of Dam-Breach Flood Under Extreme Storm Events. Front. Environ. Sci. 9:742901. doi: 10.3389/fenvs.2021.742901

INTRODUCTION

Heretofore, about 87,000 dams have been built in the United States, which control 600,000 miles (970,000 km) of rivers (**Figure 1**) (Infrastructure Report Card, 2017). However, most dams in the United States have been built for nearly 100 years or even more, and thousands of dams have been listed as high-risk dams, all of which are facing the risk of failure (Chen and Hossain, 2019). Such man-made structures are more likely to fail when they become older, as they will not be able to withstand today's warmer climate and associated extreme weather events (Mallakpour et al., 2019). For instance, extreme rainfall events, such as hurricanes, tropical cyclones, and typhoon-induced precipitation, may attribute to dam failures and lead to devastating inundation disasters (Hill and Lackmann, 2011). Such dam failures including overtopping and piping failures frequently occurred when the accumulated floods came from the high stage level of the river. The inundation disasters caused by those hydrological failures

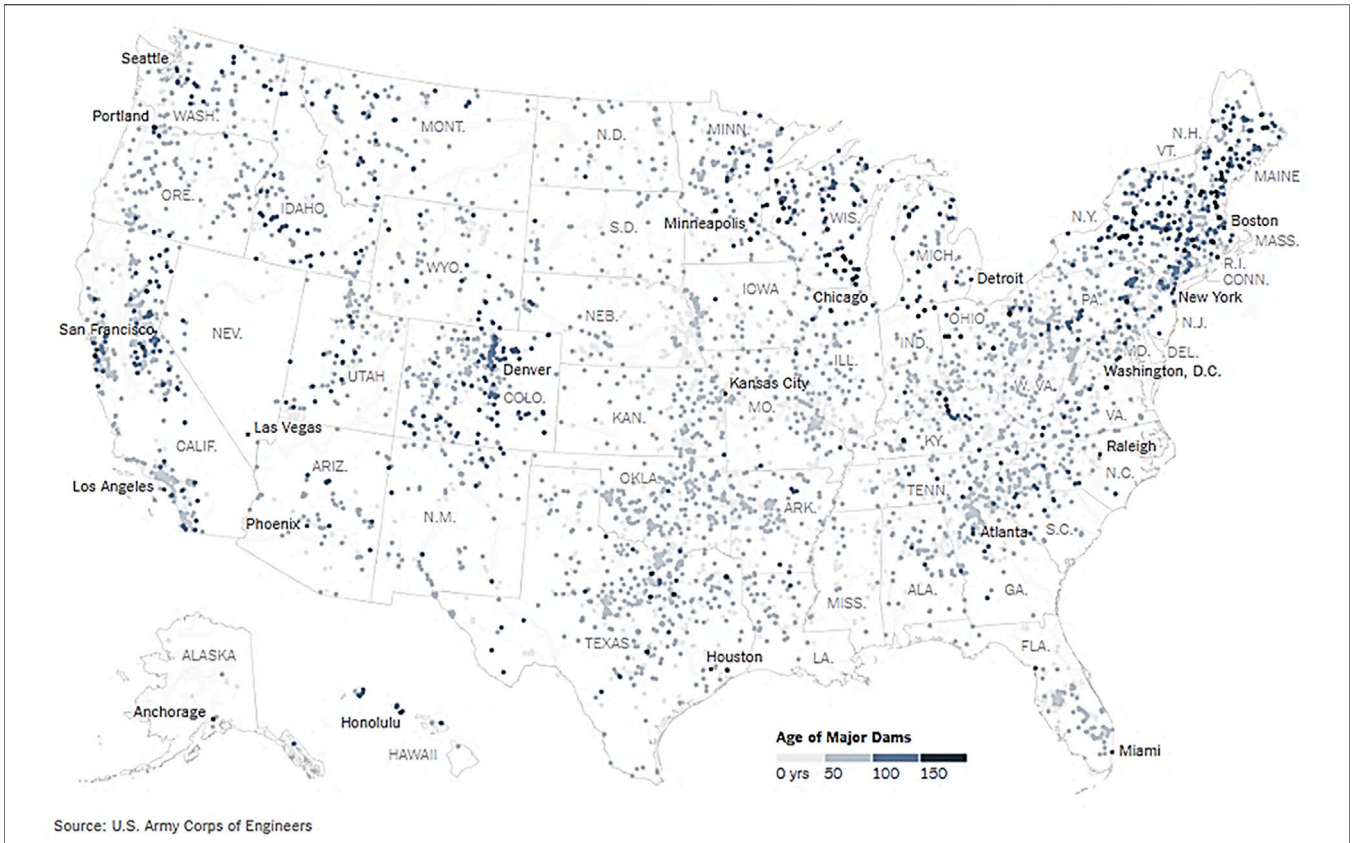

FIGURE 1 | America's aging dams and distribution (data source: https://www.nytimes.com).

are short in duration, fast in speed, and large in flow, and its harm to the protection area is far greater than that of the general flood. Therefore, analyzing the dam breach flood vulnerability under extreme storm events is of vital importance.

The dam breach simulations were challenging due to the accuracy of extreme flood estimates and time step definition (Chaudhuri et al., 2020; Yu et al., 2020). Various multidimensional hydrodynamic models, thus, have been designed to simulate extreme events through evaluating flood timing and inundation areas. Models such as HEC-RAS, DAMBRK, FLO-2D, and MIKE are commonly used when it comes to deal with hypothetical dam-breach events. Yang et al. developed a three-dimensional river flood plain on the national river system in southern Canada (Yang et al., 2006). The HEC-RAS model was used to simulate the flood by generating the plane diagram of six differently designed storm events with return periods of 100, 50, 25, 10, 5, and 2 years (Yang et al., 2006). Lodhi et al. conducted a proposed dam breach flood simulation under series of scenarios over River Yamuna, India (Lodhi and Agrawal, 2012). The hydrological DAMBRK model and ArcGIS were adopted for mapping the flood inundated areas in the downstream of the dam site (Lodhi and Agrawal, 2012). The authors used the deterministic method to calculate the possible maximum flood (PMF) based on a 1000-year recurrence period under various dam failure scenarios. Ganiyu et al. carried out a hypothetical dam-breach case study in Asa Dam, Nigeria, through assessing the flood hazard along the approximately 12 km river channel by using the HEC-RAS and HEC-GeoRAS models. The unsteady flow simulation was modeled with Once-in-a-century 24-h flow event data based on the digital terrain model from USGS (Ganiyu, 2018).

Despite previous studies involving the risk of extreme rainfall/flood events with different return periods, they have been examined in various watersheds in the United States by using the hydrodynamic models; few studies have been conducted to assess the flood risk to specific dams in consideration of hurricane event–induced rainfall. As an extension of the previous research, the overall objective of this study was to evaluate the dam-break floodwater hydrograph and routing through the downstream valley and floodplain. In detail, the two-dimensional dam-breach inundation simulation and downstream vulnerability assessment under three extreme storm rainfall scenarios were conducted. The inundation depths, resulting damages to the downstream communities, and potential affecting areas over the watershed were comprehensively evaluated. The hypothetical dam-breach scenarios of the Mountain Island dam (MI Dam, MI Lake, North Carolina (NC), United States) were analyzed using the HEC-RAS model in conjunction with the ArcGIS pro.

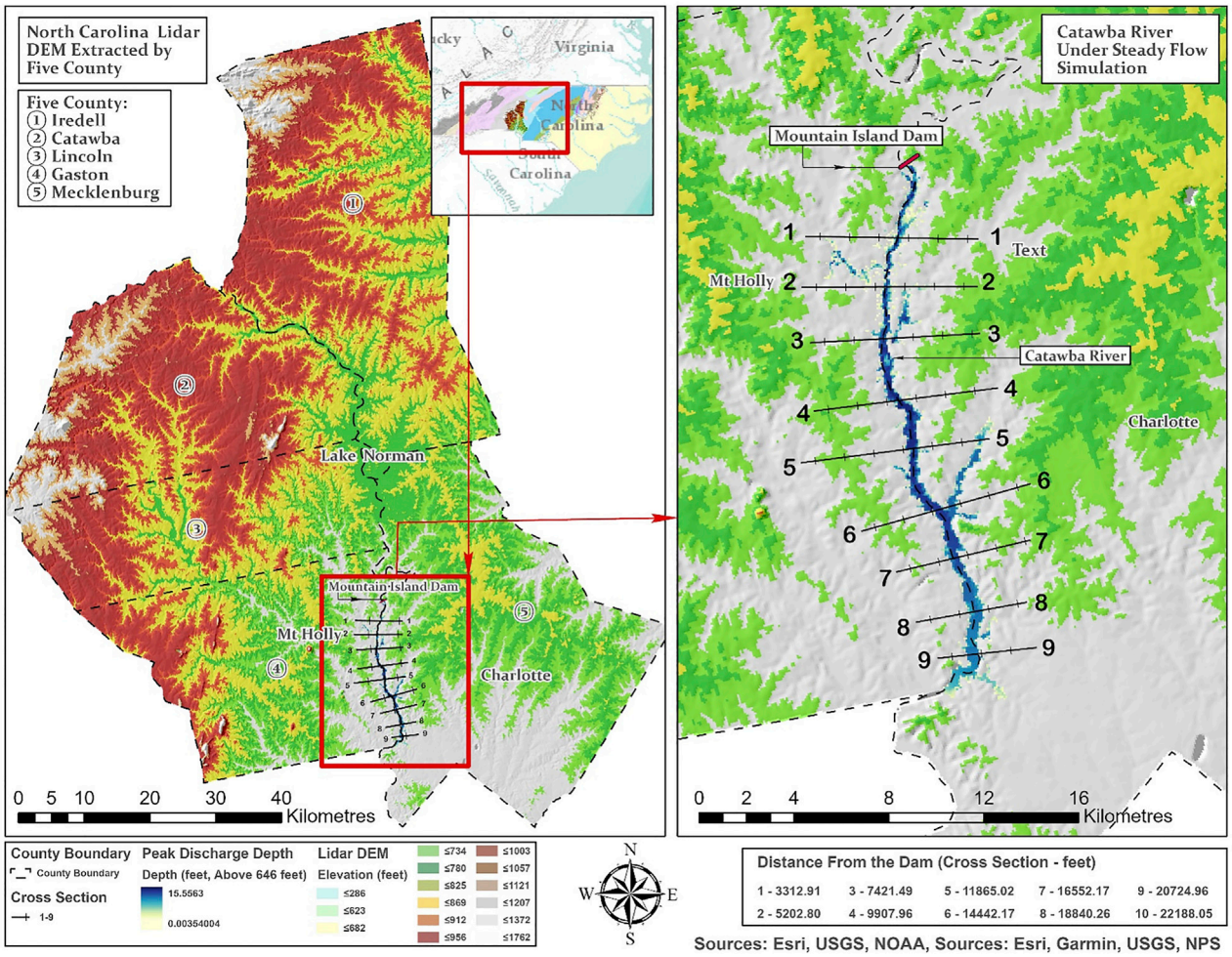

FIGURE 2 | Study area.

MATERIALS AND METHODS

Study Area

It is identified that 168 high-hazard dams have been found in poor or unsatisfactory condition in North Carolina as climate change induces rainstorms to be generated more frequently and put those dams under the dangerous state (Dalesio, 2019). As recorded, at least 18 dams failed in NC as floodwaters from Hurricane Matthew and Hurricane Florence attacked the inland. The water levels at MI Lake have been rising in recent years, especially during heavy rain seasons. Since the construction year of the MI dam (1924) was much earlier than that of the Cowans Ford dam (1963), its flood controlling capacity is significantly inadequate to meet the peak discharge coming from the upstream. It poses a great threat to the safety of life and property of the residents along the river, especially when the extreme storms attack inland.

In this study, we propose various hypothetical dam-breach scenarios over the high-risk dam which is the MI Dam in MI Lake. MI Lake, with a water area of 112 km^2, is a large sub-lake of the Catawba River in North Carolina, United States. The flows of MI Lake into Catawba River are governed by the releases from the MI Dam on MI Lake, with over 85% of the total inflow to the reservoir coming from Lake Norman regulated by Cowans Ford Dam (Dalesio, 2019). The terrain distribution of this study area is shown in **Figure 2**, and the generated nine cross-sections are shown in **Figure 3** for further discussion.

Hydrodynamic Model

The risk analysis of dam-break flood is considered as a more urgent topic with the development of social economy, as the population and social wealth are more concentrated in the lower reaches of the reservoir (Bales et al., 2001; Mohsin and Muhammad Umar, 2013; Balogun and Ganiyu, 2017). However, the occurrence of the dam break and the formation of the associated flood are unsteady and unpredictable, which poses threat to the safety of life (Asnaashari et al., 2014; Derdous et al., 2015). In fact, the computational simulation procedure of dam-break flood is complicated as it is necessary to calculate the maximum peak discharge and flood process at the dam site, as well as the flood evolution process and inundation

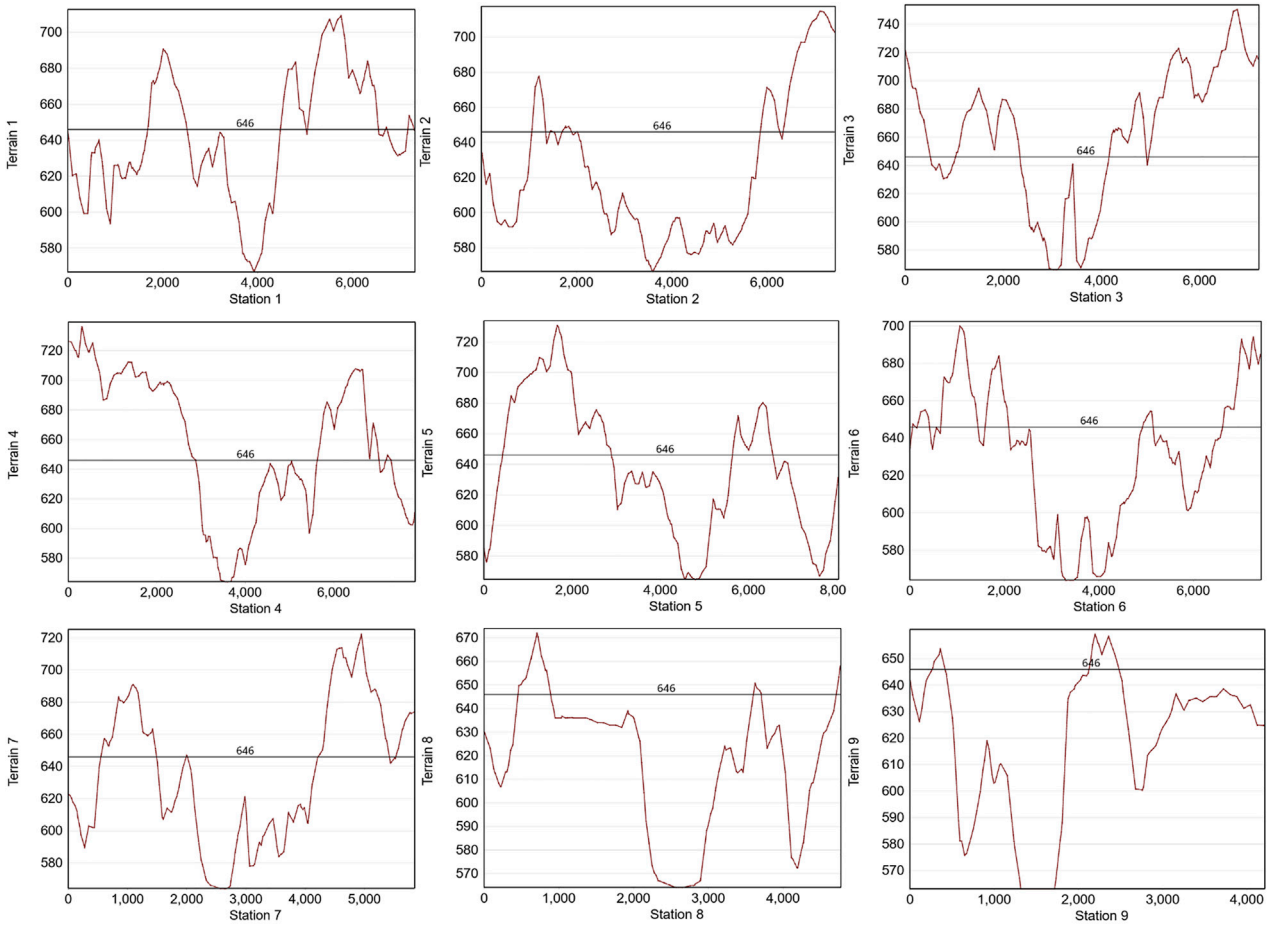

FIGURE 3 | Terrain over cross-sections 1–9

situation in the downstream of the dam. Therefore, numerical hydrodynamic models have been considered for evaluating the dam-break flood and stream routing, and we mainly assess the performance of the HEC-RAS model in this case study.

A hydrodynamic model is mainly composed of the upper and lower boundary conditions, initial conditions, calculation area, and other parts, which are interrelated to form a whole model. It is very interesting to calculate the grid with the two-dimensional model of RAS. It is specially stated in the HEC-RAS official manual that its calculation grid uses a kind of technology called "subgrid." The hydraulic characteristics such as elevation–wet cycle, elevation–roughness, and elevation–cross-section area can be extracted by the edge of each cell grid and then be integrated into the calculation (Brunner et al., 2016). Most of the cell grids of hydrodynamic models can only extract the elevation of the endpoint, the center points, and interpolate the plane in a single grid. The spatial scale of the grid has thus become the main sensitive factor (Brunner et al., 2016). However, HEC-RAS can extract more terrain details within the same scale grid, which is less sensitive to spatial step size. Hence, HEC-RAS ensures the accuracy of the results in the case of large-scale spatial grids and enables the interior of a single grid to be partially submerged, which saves quantities of computational time.

The HEC-RAS two-dimensional model computations currently consist of only two equations, the complete shallow water equation and the diffusion wave equation, which is simplified from the former and omits the inertial action, turbulence, and Coriolis effect. The diffusion wave hypothesis is subjected only to gravity, friction, and water pressure (Brunner et al., 2016). The diffusion wave equation has a fast convergence rate, small error, and narrow application range. However, the diffusion wave equation is hardly used in dam-break flood simulation. In addition, there are many conditions under which diffusion wave equations cannot be used, and the RAS manual explains more details in the scope of its application (Brunner et al., 2016).

The hydrodynamic simulation of dam break is generally divided into two methods: integral method and stepwise method. The integral method is to couple the dam-break model with the hydrodynamic model. The whole model simulates the dam-break process to solve the flow process of the breach, and simultaneously calculate the corresponding

downstream flood evolution in the same time step. Such models generally require separate models of reservoirs and dams. At this point, the upper boundary condition of the integral model is usually the reservoir inflow or the upstream channel of the reservoir. The stepwise method separates dam-break simulation from flood evolution. The process of simulating and calculating the flow rate of the dam break is completed externally. It is imported as the condition of the upper boundary, which should be located at the dam site, which does not depend on specific model functions.

In this case study, the hypothetical dam-break flood simulation adopts the integral method. The model elements are divided into the reservoir, dam, and downstream influence area. There are no tributaries and downstream reservoirs, and the downstream impact area is simulated with a single two-dimensional grid.

Data Source

When the interpolated surface is generated from elevation points, both the MIKE and TELEMAC hydrodynamic models can read the elevation point format, and the elevation can then be assigned to the computational grid. However, HEC-RAS currently does not have this capability and can only read the interpolated/ completed topographic surface data, which means that no missing values are allowed before input to HEC-RAS. This would directly lead to a computational failure (Brunner et al., 2016).

The spatial radar mapping of SRTM30 and SRTM90 has a large scale of topographic data with low accuracy. The spatial resolution of DEM is generally around 30 m with a small number of missing values, especially in some places such as river channels and embankments. However, the losses can be very severe. At this point, another type of data source lays the foundation for more accurate simulation of RAS. This is a high-resolution DEM generated from point cloud data scanned by a LiDAR system, which has extremely high accuracy. The spatial resolution of the DEMs generated by the LiDAR system for the river and its banks is currently about 1 m. In fact, the "subgrid" technology in HEC-RAS is prepared for this high-resolution DEM. In the general hydrodynamic model, in order to better fit the terrain in the high-resolution DEM, the computational grid space ratio is set to be relatively small, which will significantly prolong the simulation time. The "subgrid" technique of HEC-RAS achieves similar terrain fitting effect in large-scale grid.

Satellite Images, Terrain Data, and Hydrological Boundary Conditions

The satellite images and land cover of North Carolina were obtained from USGS, and the coordinate system for the NC region was acquired from EPSG (number at 32,119). The hydrological and climate station observations and historical/ real-time runoff datasets were retrieved from USGS at https://waterwatch.usgs.gov. The daily precipitation reanalysis is from the North American Regional Reanalysis (NARR,https://www.ncdc.noaa.gov/data-access/model-data/model-datasets/north-american-regional-reanalysis-narr). The interpolated high-resolution Lidar DEM (20 foot) was attained from North Carolina One Map (https://www.nconemap.gov) and used as the geometric raster input data for HEC-RAS simulation. The precipitation records of three designed extreme storm scenarios were regarded as the input boundary conditions.

Dam Parameters

The MI Dam parameters were retrieved from the website at http://mountain-island.lakesonline.com/Dam/3AE5F61F-AD60-4BA4-B6B5-189EA16B095F/.

Simulation Process

In this case, the homogeneous concrete dam will be arranged downstream. The HEC-RAS hydrodynamic model will be used to create an inundation map under the overtopped dam failure scenarios. The initial water level of the reservoir is 96 ft (elevation 646 ft). The flowchart of idealized overtopped dam-break simulations under extreme precipitation scenarios is shown in **Figure 4**. Here, four separate steps have been conducted for the dam-break flood simulation in HEC-RAS and ArcGIS pro, including preprocessing, reservoir modeling, dam modeling, and boundary and initial conditions setting. The idealized dam-break case 2D model validation results are shown in **Table 1**.

First Step: Preprocessing. Landsat images were loaded to confirm the location of reservoir and dam in the preprocessing step. Lidar DEMs (20 ft) provided by the NC one mapping organization were incorporated with the North Carolina coordinate system (EPSG32119.prj) in HEC-RAS. A new geometric 2D model was then created in the raster map associated with the raster elements (MI dam, Catawba River basin, MI Lake inundation area, Cowans Ford dam). The generated river topography by interpolation based on river segments, is allowed to be modified in RAS. Land-use maps in the raster format were introduced on the maps, and roughness manning's n values were assigned by the land type (**Table 2**).

First Step: Reservoir Modeling. The dam and reservoir element layers are created in the RAS Mapper as two-dimensional connections, storage areas, and two-dimensional flow area geometric input data. According to the relationship between reservoir characteristic water level (dead water level, normal water level, designed flood level, and checked flood level) and corresponding storage capacity, the elevation—volume curve (water level—storage capacity) of the reservoir is fitted with a quadratic curve. The reference equation is as follows (Brunner et al., 2016):

$$W = P_1 (H - H_r)^2 + P_2 (H - H_r) + P_3,$$

where W is the storage capacity; P_1, P_2, and P_3 are the coefficients of quadratic function; h is the characteristic water level; and H_r is the dead water level.

Third Step: Dam Modeling. The SA/2D regional connection cell modeling is performed by giving the dam connections between each reservoir and setting the weir embankment Cd = 1.44. The dam breach modeling is performed in the diffuse top

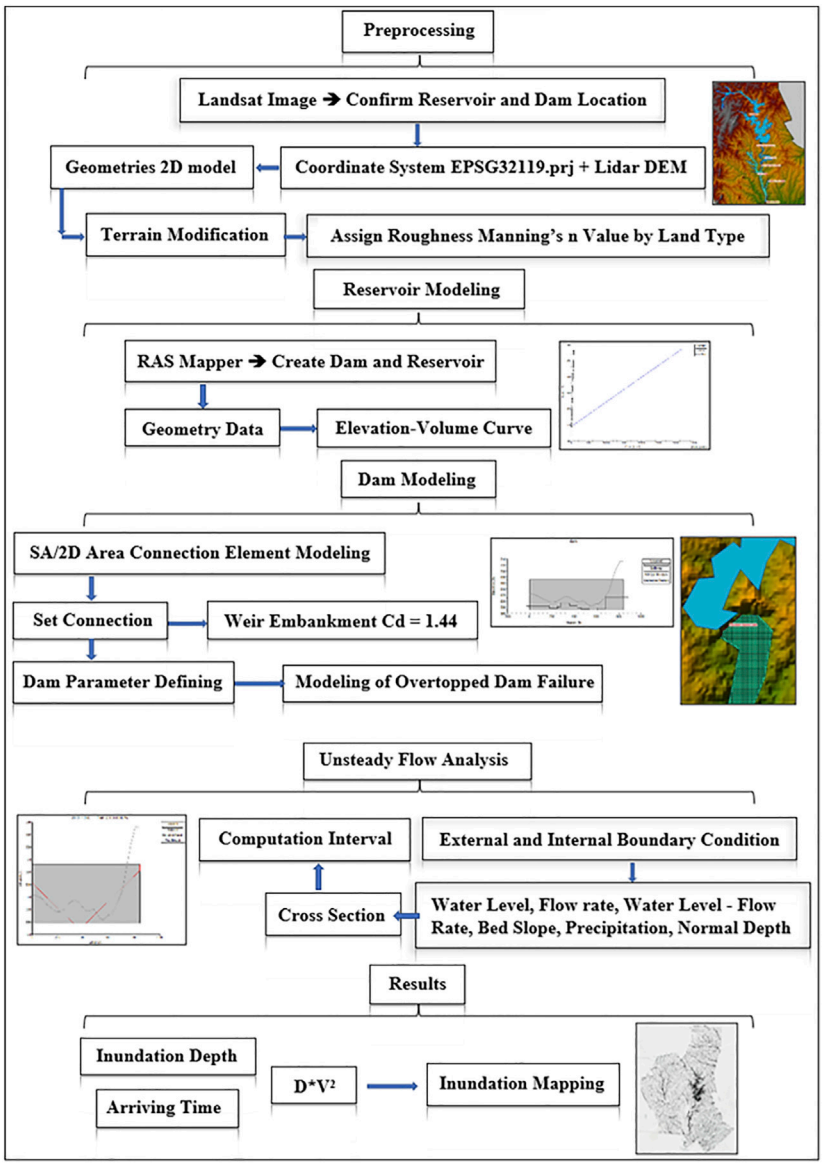

FIGURE 4 | Flowchart of dam-break flood simulation.

TABLE 1 | Water depth goodness-of-fit statistics for the idealized dam-break case (Balogun and Ganiyu, 2017).

Time (seconds)	10	20	30
ME (10^3 m)	−6.01	−4.68	−2.97
NME (%)	−0.06	−0.05	−0.03
MAE (10^2 m)	2.00	3.13	4.18
NMAE (%)	0.20	0.31	0.42
RMSE (meter)	0.128	0.163	0.190
NRMSE (%)	1.28	1.63	0.9
R^2	0.99683	0.99372	0.98909

mode (overtopping failure). The dam parameters were set to include the breach bottom elevation, pool elevation, pool volume, inlet, bottom elevation, bottom width, and left- and right-side slopes H:V. The diffuse top failure mode is calculated according to the Von Thun & Gillete Function (Brunner et al., 2016).

Last Step: Unsteady Flow Analysis. The unsteady flow (non-constant flow) analysis was performed under external and internal boundary conditions, including water level, flow velocity, water level flow rate, streambed slope, precipitation, and normal depth at each cross-section. The calculation interval was set to 1 min. Non-constant flow simulations were performed based on the incompressible flow assumption. The differential form of the mass continuity equation is as follows (Brunner et al., 2016):

$$\frac{\partial H}{\partial t} + \frac{\partial (hu)}{\partial x} + \frac{\partial (hv)}{\partial y} + q = 0,$$

TABLE 2 | Manning's *n* values for various land covers (Balogun and Ganiyu, 2017).

NLCDX1 value	Normal Manning's n value	Allowable range of n values	Land cover definition
11	0.04	0.025–0.05	Open water
21	0.04	0.03–0.05	Developed, open space
22	0.100	0.08–0.12	Developed, low intensity
23	0.080	0.06–0.14	Developed, medium intensity
24	0.150	0.12–0.20	Developed, high intensity
31	0.025	0.023–0.030	Barren land (rock/sand/clay)
41	0.160	0.10–0.16	Deciduous forest
42	0.160	0.10–0.16	Evergreen forest
43	0.160	0.10–0.16	Mixed forest
52	0.100	0.07–0.16	Shrub/scrub
71	0.035	0.025–0.050	Grassland/herbaceous
81	0.030	0.025–0.050	Pasture/hay
82	0.035	0.025–0.050	Cultivated crops
90	0.120	0.045–0.15	Woody wetlands
95	0.070	0.05–0.085	Emergent herbaceous wetlands

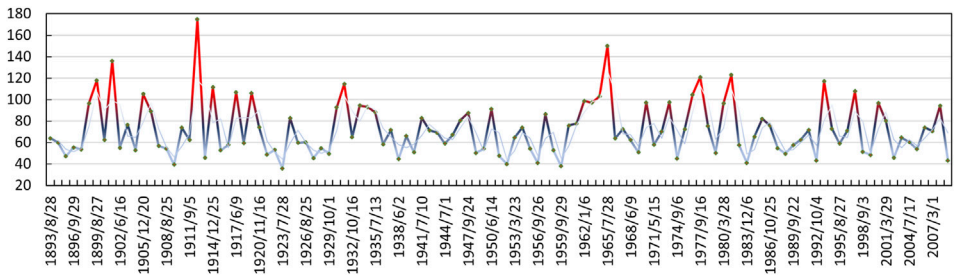

FIGURE 5 | Highest rainfall record (mm) by each year in Charlotte City of North Carolina.

where t is the time, u and v are the velocities in two dimension, and q is the sink flux term.

RESULTS

Dam Failure Scenarios

Once-in-a-Century Storm Rainfall Induced Dam Break Flood Scenario

The intensity–duration–frequency curve (IDF curve) is an engineering mathematical function based on time series, which links rainfall intensity (inches/hour) with its duration (minutes) and frequency (return period). The IDF curves are frequently used in the civil engineering of hydrological flood forecast and urban drainage design, especially as an evaluation index for the flood resistance capacity of the dam (Wang et al., 2014). Here, the IDF curves are obtained through the frequency analysis of historically observed meteorological station precipitation.

The empirical plotting position approach (Dettinger et al., 2018) was applied to measure the 2-, 10-, and 50-year historical 6-h storm rainfall events by computing the P (probability)-T (return period) relationship associated with each rainfall volume by the corresponding duration. The Once-in-a-century storm rainfall intensity can be obtained in every minute by a linear relationship with the larger exceedance probability. The historical annual maximum daily precipitation records during 1983–2009 are shown in **Figure 5**. The computed 6-h extreme rainfall distribution, accumulated storm rainfall depth, and storm rainfall intensity corresponding to each return period are shown in **Figure 6**.

Hurricane Rainfall Induced Dam Break Flooding Scenarios

Figure 7A,B are the daily cumulative rainfall distributions in North and South Carolina and surrounding states provided by the NOAA NCEP multisensor stage IV precision dataset. The distribution of the spiral rain belt of a hurricane can be clearly observed. The area where the hurricane eye meets the eyewall is generally affected by high-intensity rainfall. During this period, the upstream and downstream of the river in the coastal area will be scoured by a rainstorm to a large extent, and the streamflow diversion would force those aging dams to bear a doubly stressful time caused by the rising flood stage on both sides. Therefore, the dam is more likely to suffer from an overtopping risk. To explore the spatial and temporal distributions of two hurricane rainfall events in NC province more clearly, the gridded average daily precipitation reanalysis data (0.125° × 0.125°) on Sep.13 ~ 18, 2018 and Aug.25 ~ 28, 2008 were extracted. The NetCDF format

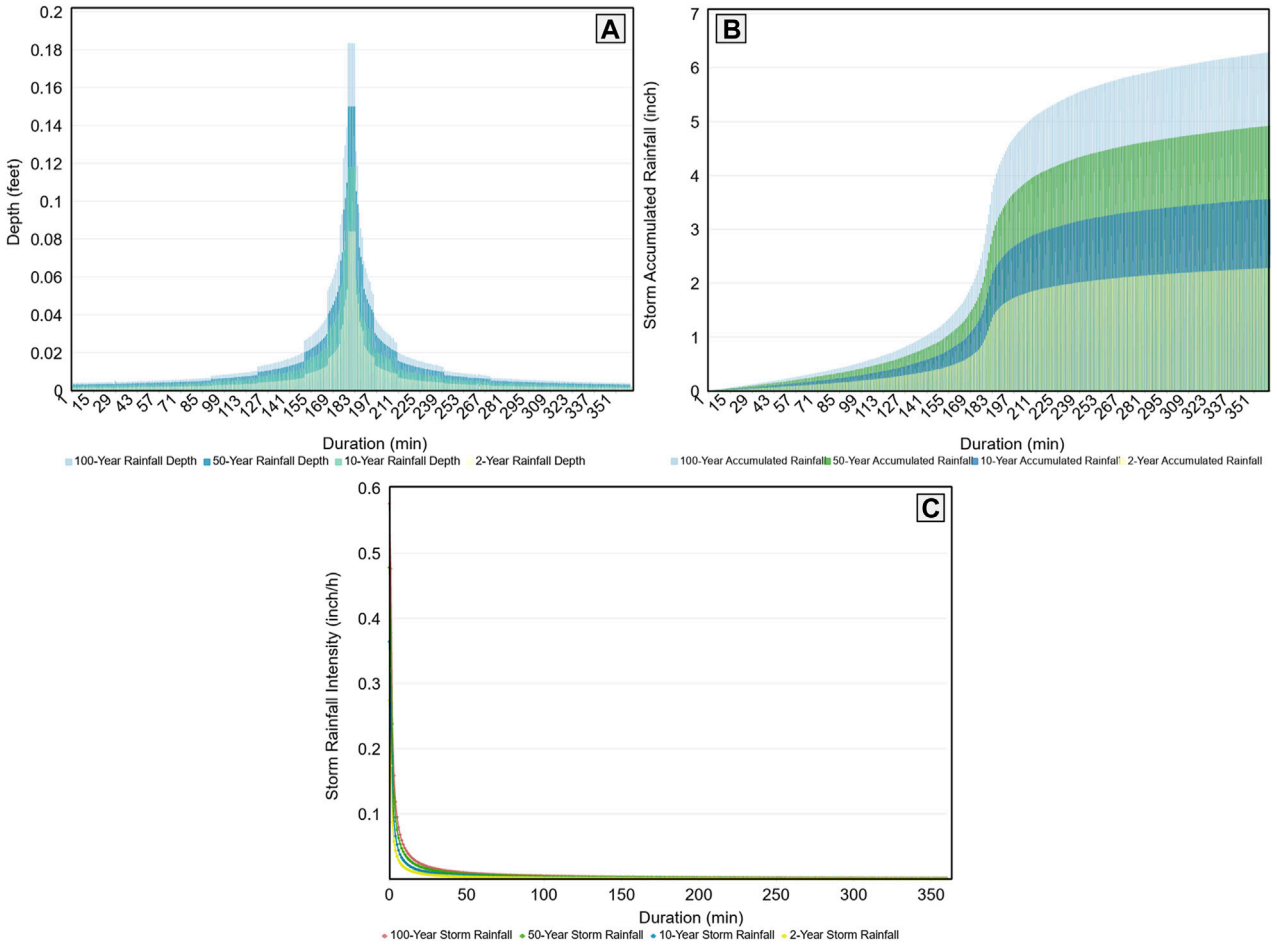

FIGURE 6 | (A) 6-hour storm rainfall depth by different return periods; **(B)** 6-hour storm accumulated rainfall depth by different return periods; **(C)** 6-hour storm rainfall intensity–duration–frequency curve.

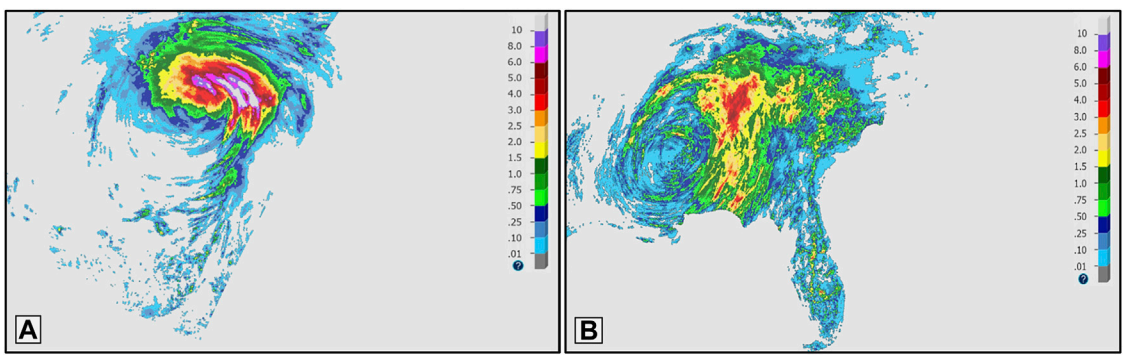

FIGURE 7 | (A) Daily precipitation distribution in North and South Carolina and surrounding states during Hurricane Florence on Sep. 16, 2018 and **(B)** Hurricane Gustav on Aug. 26, 2008 (data source: NOAA NCEP Multi-sensor Stage IV precipitation analysis).

was then transformed into a raster in order to create the contour plot of precipitation on each day (**Figure 8**). The rainfall events caused by two serious hurricanes in the history of the United States are considered as the inducers of dam break. The frequency of rainfall and the location of two landing hurricanes are different in time and space.

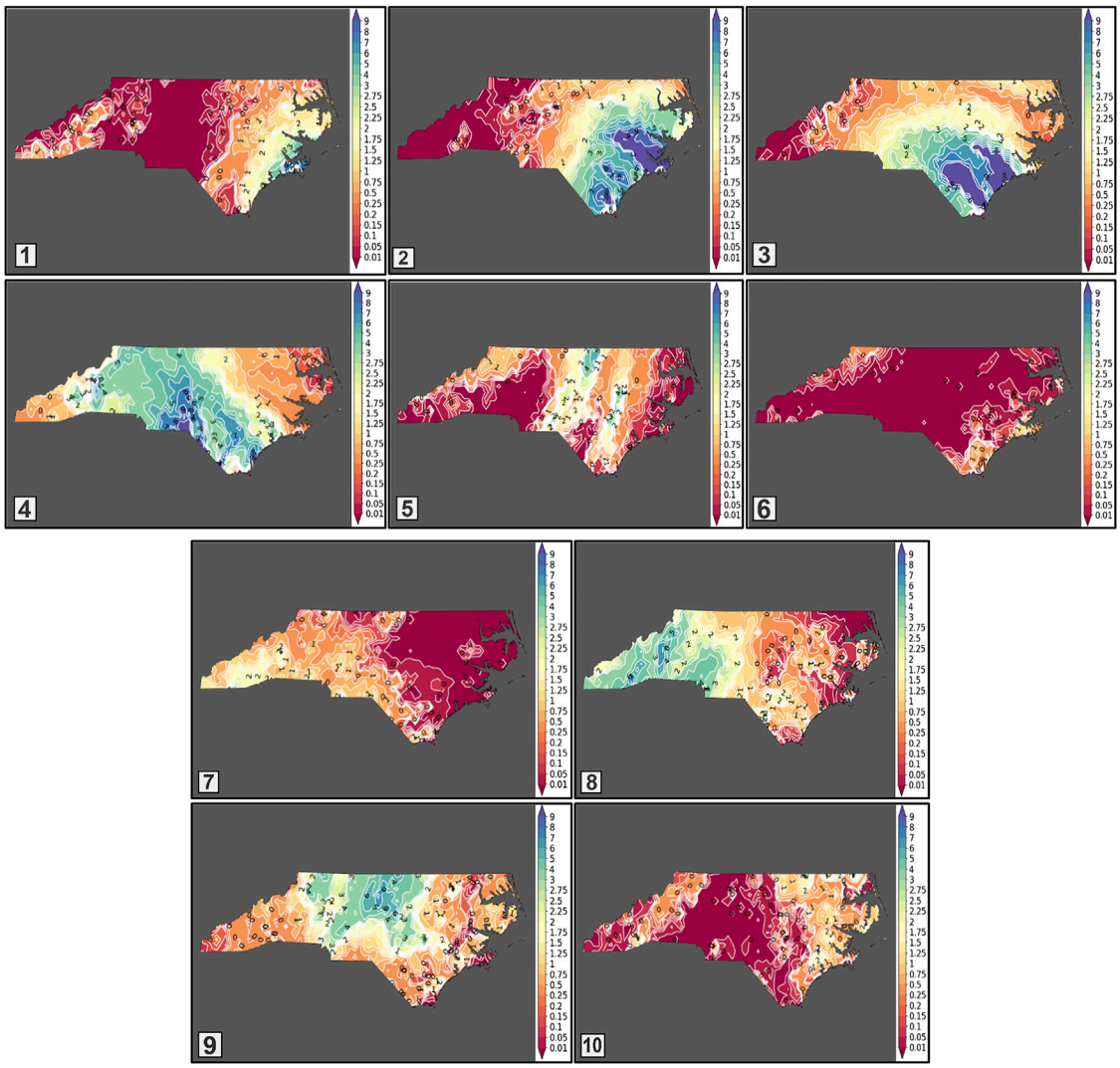

FIGURE 8 | Contour plot of reanalysis daily precipitation (inches) in North Carolina during Hurricane Florence on Sep.13–18 2018 (No.1 ~ 6) and Hurricane Gustav on Aug.25–28 2008 (No.7 ~ 10).

Hurricane Florence (Sep.13 ~ 18, 2018) landed in Wilmington on the eastern part of North Carolina and led to the power plant of Wilmington to be breached by devastating floodwaters. MI Lake and Catawba River were not seriously affected by Hurricane Florence; thus, the old dam survived from the disastrous events. However, according to the rainfall observation recorded in the meteorological station of Charlotte City, the 3-day accumulated rainfall brought by Hurricane Gustav (Aug.26, 2008) was considered as the historical heaviest precipitation event at KCLT Charlotte observation, yet it was not brought to any dam breach. The rainfall brought by Hurricane Florence (**Figure 9**, No.1) in Wilmington was observed as a type of intensive neutral rainfall, while Hurricane Gustav in Charlotte observation was a transient high-intensity storm (**Figure 9**, No.2).

To some extent, the accumulated rainfall brought by Hurricane Gustav is higher than that of Hurricane Florence in Charlotte City but not as serious as in Wilmington City. However, it could not be sure that such a level of hurricane-induced rainfall in Wilmington would not occur in Charlotte City under the impact of climate change on hurricane intensity. Therefore, it is essential to explore the risk of dam failure exposed to such an extreme situation (Hurricane Florence rainfall in Wilmington) in the area near the dam site.

Simulation Results

This study mainly focuses on the influence of the MI dam-break flood on Charlotte City and Mount Holly, which are 5,202.8 ft and 11,865.02 ft away from the downstream of the dam. It is assumed that the formation time of the gap is 2 h, and the breaking process starts to spread from the center point. When the water level exceeds the dam crest elevation of 647.5 ft, the dam break begins. The downstream boundary condition is set to the level of peak discharge water depth.

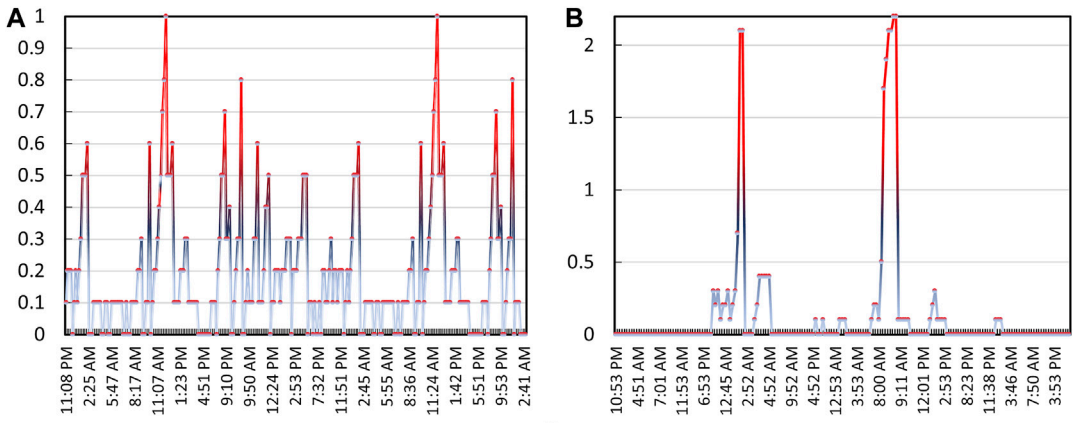

FIGURE 9 | (A) Hurricane Florence precipitation observation (inches) of Wilmington weather station; **(B)** top three-day heaviest rainfall at KCLT record in Charlotte City (Hurricane Gustav).

In the simulation of hydrodynamic systems using the HEC-RAS model, it is usually necessary to assume that the water surface profile is a steady, gradually varied water flow case. The second assumption is that a dam failure event is a hypothetical case. Typically, a reasonable modeling approach might be to assume that the roughness coefficient is of twice the normal Manning's n value and then transition to a normal roughness factor in the downstream valley from the dam site. Under this roughness coefficient condition, turbulent flow, sediment, and debris transport due to the dam breach are expected to be reduced.

In response to the three extreme scenarios of heavy rainfall, the upstream dam (Cowans Ford dam) was considered as the unsteady input flow under its maximum discharge situation. The simulated dam breach happened at the MI dam, with its upstream inflow (MI Lake) and downstream outflow (Catawba River) affected by the extreme storm precipitation scenarios. The inundation maps under three extreme scenarios in different periods and all hydraulic variables including water depth, flow velocity, and flood arriving time over separated nine cross-sections in the Catawba River are shown in the following results.

Once-in-a-Century Storm Rainfall Induced Dam-Break Flood Scenario

The formation of extremely intensive discharge results from the combination of an accumulated additional inflow and unsteady floodwater caused by the Once-in-a-century storm rainfall induced dam breach. By comparing the water depth of each cross-section simulated when the upstream dam was drained by the peak discharge, the dam-break flood caused by the Once-in-a-century rainfall event shows an abnormal water level over the central river channel. Affected by the dynamic variations of surface topography, it takes 60 min for the peak discharge to reach section 6, and the water depth in this cross-section is nearly three times the maximum drainage depth (**Figure 10**). It is noteworthy to observe that the safety of life and property of residents would be severely affected by the floodwater in cross-section 2 although it is nearly 3,000 ft away from the river center. After 90 min of dam failure, it is potentially dangerous that the water level of **sections 1**–6 in the center of the river remains over 25 ft, while 150 min after the dam break, flows through cross-**sections 1**–6 moderately level off and transit to the area below cross-section 7. However, low-lying areas in the range of 3,000 m from the river channel at cross-section 7 remain flooded.

Hurricane Florence Rainfall Induced Dam-Break Flooding Scenario

Affected by Hurricane Florence's intensive neutral rainfall, the water level in the channel center will remain significantly high for a long period of time. The velocity (**Figure 11**, D^*V^2 (60 min)) observed in the hurricane storm rainfall induced dam-break flood was faster than that of the flood observed in the Once-in-a-century storm rainfall event (**Figure 10**, D^*V^2 (60 min)). Within 60 min, the latter illustrated that the floodwater has reached the cross-section 8, while the former is still at the cross-section 6. In **Figure 11**, under the influence of continuous rainfall, the central water level of the channel at cross-sections 2–4 tends to continuously rise during this breaking period. Within 150 min after the break, the water depth of the second station exceeds 55 ft, and the water depth of the fifth station is over 60 ft in the low-lying area 4,000 ft away from the center of the river. The central floodwater at cross-sections 7–8 is fast-moving, yet the water level is falling at 150 min. Possibly due to the significant gap in terrain difference between the river outlet and the downstream flow area, the speed of flood discharge is consequently faster. Additionally, the floodwater depth contributed from the accumulated rainfall of Hurricane Florence exceeds 6 times the flood level caused by the peak discharge situations in low-lying regions.

Hurricane Gustav Induced Dam-Break Flood Scenario

The water level in the center of the river decreases with the time of dam breach (**Figure 12**). In stations 1–6, the floodwater depth can exceed 30 ft within 60 min after the dam break. It is possibly because Hurricane Gustav is considered as a type of transient high-intensity storm and the instantaneous precipitation is comparatively higher. However, the cumulative rainfall of

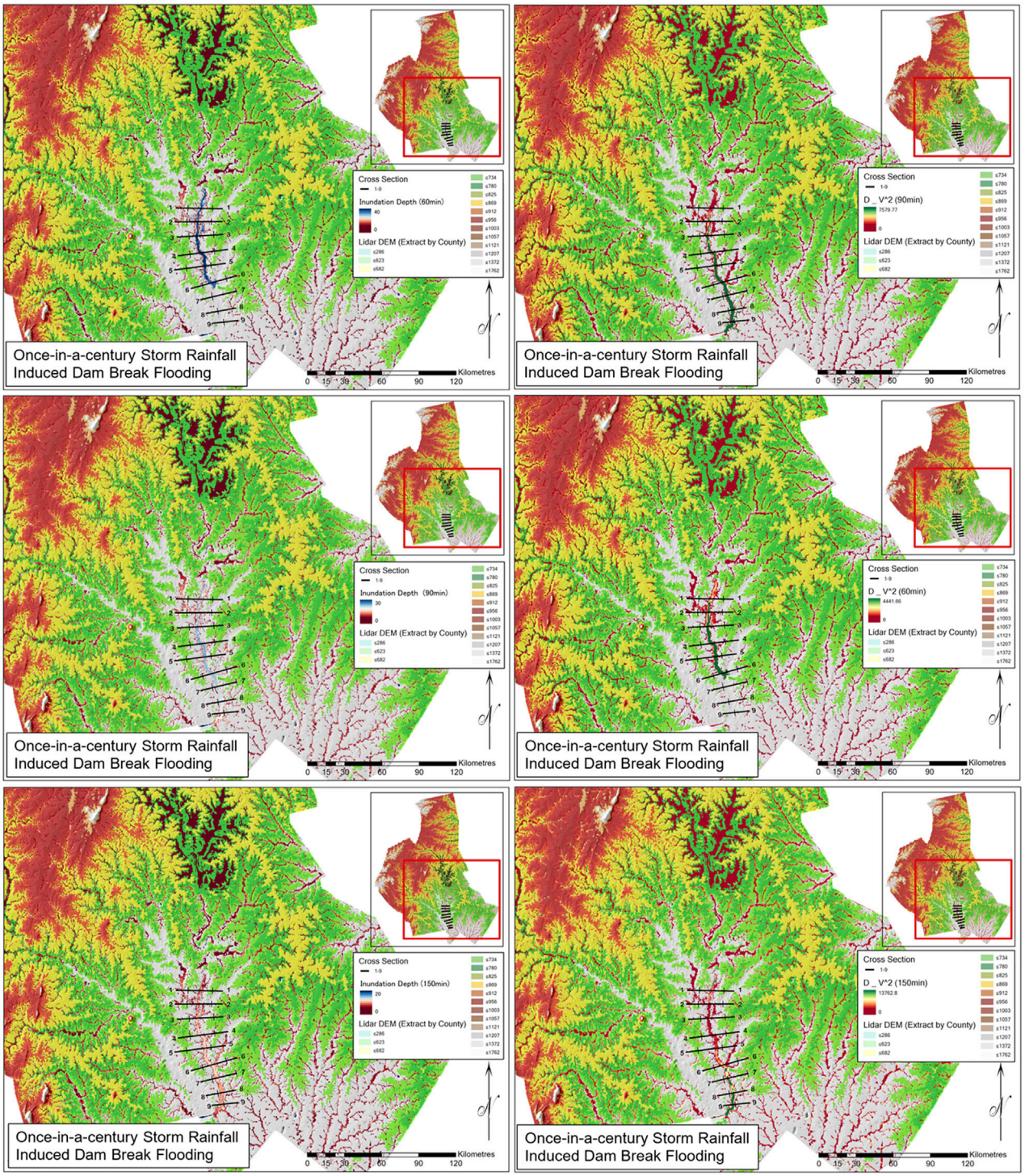

FIGURE 10 | Once-in-a-century storm rainfall induced dam-break flooding scenario.

Hurricane Gustav is relatively more than that of Hurricane Florence. The dam-break flood is greatly affected by the accumulated rainfall, and the flood discharge capacity of the MI dam is not equal to the supply of rainwater flowing into the river channel. The instantaneous rainfall is conducive to the timely drainage of the river water flowing into the downstream direction, and the excessive floodwater can be eliminated during the period of relatively sparse rainfall.

It is obvious that under the Hurricane Florence scenario, floodwater took the shortest time to reach each section

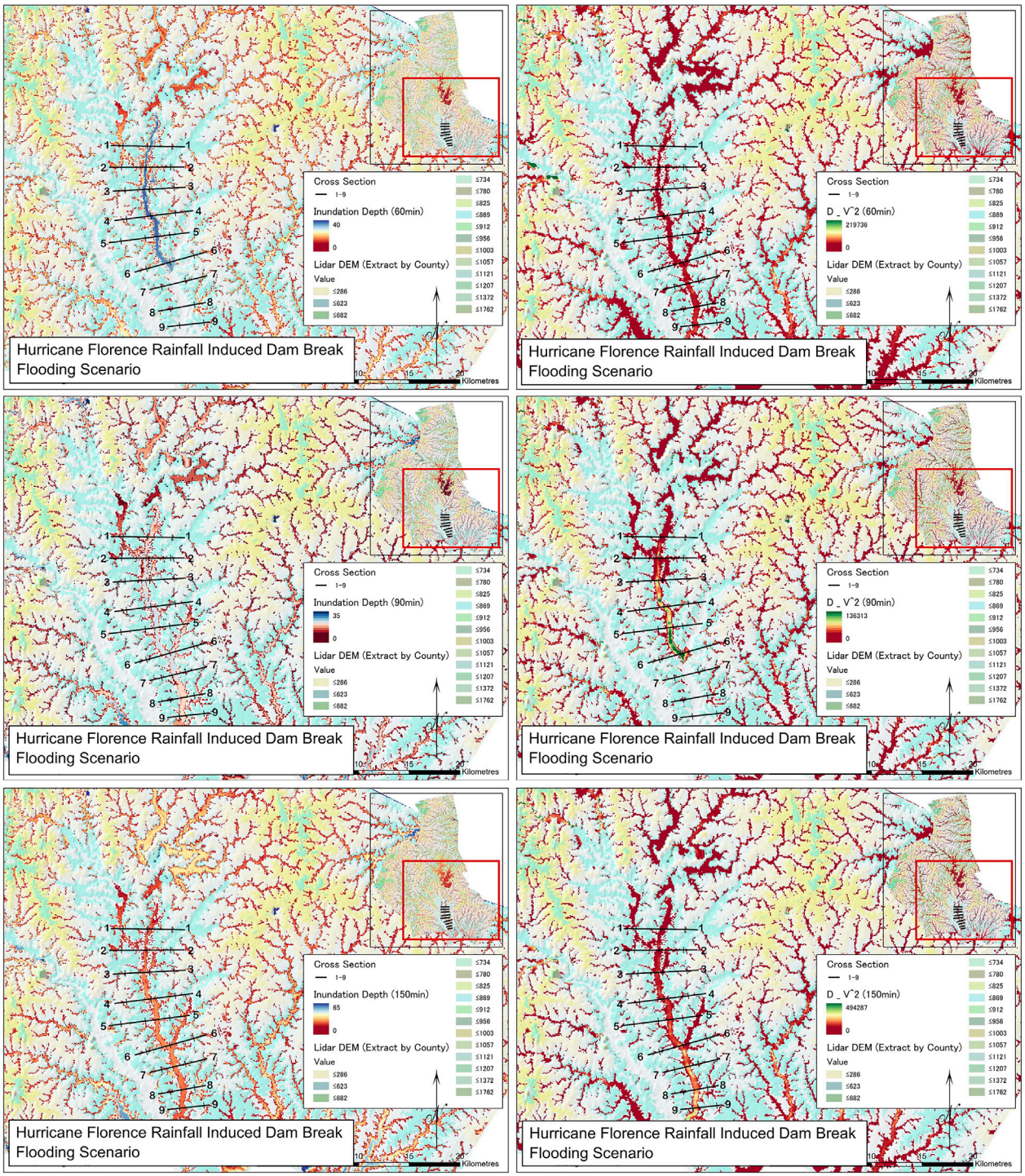

FIGURE 11 | Hurricane Florence rainfall induced dam-break flooding scenario.

compared to the other two scenarios. In the Hurricane Gustav scenario, the time for floodwaters to reach cross-section 6 is shorter than that of the Once-in-a-century rainfall event. Although Hurricane Florence's extremely heavy rainfall on Wilmington had not historically occurred near the MI dam site, it was well beyond the range of the Once-in-a-century storm intensity–duration–frequency curve. In other words, if tropical cyclones' increase in intensity is expected under future

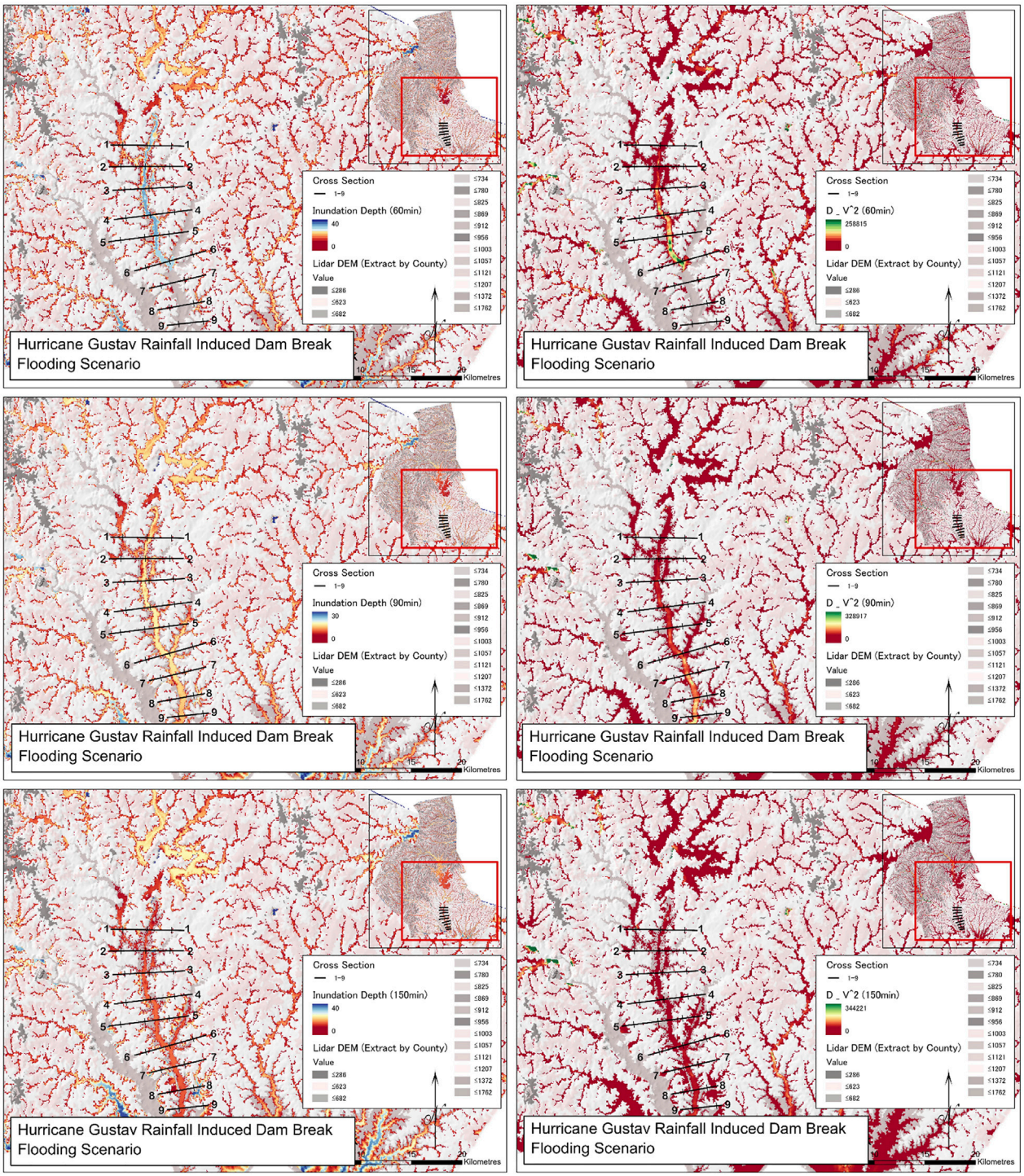

FIGURE 12 | Hurricane Gustav rainfall induced dam-break flooding scenario.

warming conditions, Hurricane Florence-induced rainfall is more likely to occur near the MI dam in the future and may generate a far more severe impact than that of the Once-in-a-century storm rainfall event. Hence, dam owners are responsible to repair and upgrade those aging dams like the MI dam ahead of time, while people living on the downstream side of the dam should be evacuated in advance when such intensive hurricanes attacked near the dam.

DISCUSSION

Three hypothetical dam-break scenarios were proposed based on historical extreme rainfall events including Once-in-a-century storm rainfall and two devastating hurricane events. The presumption was that the proposed dam would collapse. However, the occurrence of dam break and the formation of floodwaters are unsteady and unpredictable in the real world. In the face of extreme events, the relationship between rainfall and runoff can be calculated to assess the probability of dam failure risk based on the severity degree of rainfall (Mallakpour et al., 2019; Chaudhuri et al., 2020; Yu et al., 2020). It is recommended that the prediction results of downscaling gridded RCM data (regional climate model) can be used to evaluate the trend of future extreme rainfall events and the possibility of dam failure (Tryhorn and Degaetano, 2011; Wang et al., 2013; Moeini and Soltani-nezhad, 2020). Additionally, stronger storms in warmer climates should be taken into consideration as the IDF (intensity–duration–frequency) curve varies and the dam failure risk would be simultaneously changed in the future. In other words, the future climate information is recommended to be incorporated in the dam failure probability evaluation (Aerts and Botzen, 2011; Dottori et al., 2016).

CONCLUSION

Most modern dams are built to resist natural disasters such as floods, landslides, and seepage, and some dams are built for irrigation and water supply. A number of older dams built more than 50 years ago were not designed to modern standards, most of which have already shown signs of degradation (erosion, aging, and disrepair). In recent years, as a result of the increasingly intensive extreme rainfall events associated with dam failure caused by the water erosion and inadequate maintenance, the breach risk of aging dams continues to be dramatically increased in the United States. The risk of dam failure predominantly derives from the high stage level of the river, which leads to overtopping and piping failures (Li et al., 2008; He et al., 2018; Shrestha and Wang, 2020).

In this case study, a hydrodynamic model was applied to the inundation simulation of three types of extreme precipitation-induced homogeneous concrete dam breach. The inundation maps of the three extreme scenarios in different time periods and all hydraulic variables including water depth, flow velocity, and flood arriving time over separated nine cross-sections in the Catawba River were calculated. The hypothetical simulation results illustrate that the impact of Hurricane Florence's rainfall is far more severe over the downstream of hydraulic facilities than that of the Once-in-a-century storm rainfall event. Although Hurricane Florence's rainfall observed in Wilmington had not historically happened near the MI dam site, the river basin has a higher probability to be attacked by such storm rainfall if more extreme weather events would be generated as previously predicted under future warming conditions. Besides, the time for floodwaters to reach cross-section 6 under the Hurricane Gustav scenario is shorter than that under the Once-in-a-century rainfall scenario, making the downstream be inundated in short minutes. Therefore, dam owners are responsible for maintaining the dams they have built in the past and are legally and morally responsible for all the effects of a dam collapse. Since the probability can be quantitatively evaluated, it is of great worth to assess the risk of dam-break flood in coastal cities where human lives are at a vulnerable stage.

DATA AVAILABILITY STATEMENT

The original contributions presented in the study are included in the article/Supplementary Material; further inquiries can be directed to the corresponding author.

AUTHOR CONTRIBUTIONS

Conceptualization, XJ and GH; methodology, XJ; software, XJ; validation, XJ, GQ, and DH; formal analysis, GQ; investigation, DH; resources, XJ; data curation, XJ; writing—original draft preparation, XJ; writing—review and editing, GH and XZ; visualization, XJ; supervision, GH; project administration, GH; funding acquisition, GH.

FUNDING

This research was supported by the National Key Research and Development Plan (2016YFC0502800), Natural Sciences Foundation (U2040212), Canada Research Chair Program, Natural Science and Engineering Research Council of Canada, Western Economic Diversification (15269), and MITACS.

ACKNOWLEDGMENTS

We are also very grateful for the helpful inputs from the editor and reviewers.

REFERENCES

Aerts, J. C. J. H., and Botzen, W. J. W. (2011). Climate Change Impacts on Pricing Long-Term Flood Insurance: a Comprehensive Study for the Netherlands. *Glob. Environ. Change* 21 (3), 1045–1060. doi:10.1016/j.gloenvcha.2011.04.005

Asnaashari, A., Meredith, D., and Scruton, M. (2014). "Dam Breach Inundation Analysis Using HEC-RAS and GIS - Two Case Studies in British Columbia, Canada," in Canadian Dam Association Annual Conference, October, 2014 Conference - Banff Alberta.

Dalesio, E. P. (2019). N Carolina No. 2 in risky dams where failure could kill. Retrieved from: https://apnews.com/article/9214fb55444f4369999d0d9d23505fea

Bales, J. D., Sarver, K. M., and Giorgino, M. J. (2001). Mountain Island Lake, North Carolina; Analysis of Ambient Conditions and Simulation of Hydrodynamics, Constituent Transport, and Water-Quality Characteristics, 1996–97: U.S. *Geol. Surv. Water Resour. Invest. Rep. 2001* 4138, 85. doi:10.3133/wri014138

Balogun, O., and Ganiyu, H. (2017). Development of Inundation Map for Hypothetical ASA Dam Break Using HEC-RAS and ArcGIS. *Arid Zone J. Eng.* 13 (6), 831–839.

Chaudhuri, S., Roy, M., and Jain, A. (2020). Appraisal of WaSH (Water-Sanitation-Hygiene) Infrastructure Using a Composite Index, Spatial Algorithms and Sociodemographic Correlates in Rural India. *J. Environ. Inform.* 35 (1), 1–22. doi:10.3808/jei.201800398

Chen, X., and Hossain, F. (2019). Understanding Future Safety of Dams in a Changing Climate. *Bull. Am. Meteorol. Soc.* 100, 1395–1404. doi:10.1175/bams-d-17-0150.1

Derdous, O., Djemili, L., Bouchehed, H., and Tachi, S. E. (2015). A GIS Based Approach for the Prediction of the Dam Break Flood hazard - A Case Study of Zardezas Reservoir "Skikda, Algeria". *J. Water Land Develop.* 27 (1), 15–20. doi:10.1515/jwld-2015-0020

Dettinger, M., Ralph, F., and Rutz, J. (2018). Empirical Return Periods of the Most Intense Vapor Transports during Historical Atmospheric River Landfalls on the US West Coast. *J. Hydrometeorol.* 19. 1363–1377. doi:10.1175/jhm-d-17-0247.1

Dottori, F., Salamon, P., Bianchi, A., Alfieri, L., and Hirpa, F. A. (2016). Development and Evaluation of a Framework for Global Flood hazard Mapping. *Adv. Water Resour.* 94, 7–102. doi:10.1016/j.advwatres.2016.05.002

Ganiyu, H. (2018). Study and Analysis of Asa River Hypothetical Dam Break Using HEC-RAS. *Agric. Bioresour. Biomed. Food Environ. Water Resour. Eng.* 36, 1.

He, Y., Gui, Z., Su, C., Chen, X., Chen, D., Lin, K., et al. (2018). Response of Sediment Load to Hydrological Change in the Upstream Part of the Lancang-Mekong River over the Past 50 Years. *Water* 10 (7), 888. doi:10.3390/w10070888

Brunner, G. W.; Institute for Water Resources (U.S.); Hydrologic Engineering Center (U.S.) (2016). *HEC-RAS river analysis system: Hydraulic reference manual. Davis, CA: US Army Corps of Engineers, Institute for Water Resources*. Hydrologic Engineering Center.

Hill, K. A., and Lackmann, G. M. (2011). The Impact of Future Climate Change on TC Intensity and Structure: A Downscaling Approach. *J. Clim.* 24, 4644–4661. doi:10.1175/2011jcli3761.1

Infrastructure Report Card (2017). Dams. Retrieved February 21, 2017.

Li, Y. P., Huang, G. H., Yang, Z. F., and Nie, S. L. (2008). IFMP: Interval-Fuzzy Multistage Programming for Water Resources Management under Uncertainty. *Resour. Conser. Recycl.* 52 (5), 800–812. doi:10.1016/j.resconrec.2007.11.007

Lodhi, M., and Agrawal, D. (2012). Dam-break Flood Simulation under Various Likely Scenarios and Mapping Using GIS: Case of a Proposed Dam on River Yamuna, India. *J. Mountain Sci.* 9, 10. doi:10.1007/s11629-012-2148-5

Mallakpour, I., AghaKouchak, A., and Sadegh, M. (2019). Climate-Induced Changes in the Risk of Hydrological Failure of Major Dams in California. *Geophys. Res. Lett.* 46, 2130–2139. doi:10.1029/2018gl081888

Moeini, R., and Soltani-nezhad, M. (2020). Extension of the Constrained Gravitational Search Algorithm for Solving Multi-Reservoir Operation Optimization Problem. *J. Environ. Inform.* 36 (2), 70–81. doi:10.3808/jei.202000434

Mohsin, J. B., and Muhammad Umar, R. Q. (2013). Landslide Dam and Subsequent Dam-Break Flood Estimation Using HEC-RAS Model in Northern Pakistan. *Nat. Hazards* 65 (1), 241–254. doi:10.1007/s11069-012-0361-8

Shrestha, N. K., and Wang, J. (2020). Water Quality Management of a Cold Climate Region Watershed in Changing Climate. *J. Environ. Inform.* 35 (1), 56–80. doi:10.3808/jei.201900407

Tryhorn, L., and Degaetano, A. (2011). A Comparison of Techniques for Downscaling Extreme Precipitation over the Northeastern United States. *Int. J. Climatol.* 31, 1975–1989. doi:10.1002/joc.2208

Wang, X., Huang, G., and Liu, J. (2014). Projected Increases in Intensity and Frequency of Rainfall Extremes through a Regional Climate Modeling Approach. *J. Geophys. Res. Atmos.* 119, 10. doi:10.1002/2014jd022564

Wang, X., Huang, G., Lin, Q., Nie, X., Cheng, G., Fan, Y., et al. (2013). A Stepwise Cluster Analysis Approach for Downscaled Climate Projection - A Canadian Case Study. *Environ. Model. Softw.* 49, 141–151. doi:10.1016/j.envsoft.2013.08.006

Yang, J., Townsend, R. D., and Daneshfar, B. (2006). Applying the HEC-RAS Model and GIS Techniques in River Network Floodplain Delineation. *Can. J. Civ. Eng.* 33, 19–28. doi:10.1139/l05-102

Yu, B. Y., Wu, P., Sui, J., Ni, J., and Whitcombe, T. (2020). Variation of Runoff and Sediment Transport in the Huai River–A Case Study. *J. Environ. Inform.* 35 (2), 138–147. doi:10.3808/jei.202000429

Conflict of Interest: The authors declare that the research was conducted in the absence of any commercial or financial relationships that could be construed as a potential conflict of interest.

Publisher's Note: All claims expressed in this article are solely those of the authors and do not necessarily represent those of their affiliated organizations, or those of the publisher, the editors, and the reviewers. Any product that may be evaluated in this article, or claim that may be made by its manufacturer, is not guaranteed or endorsed by the publisher.

frontiers in Earth Science

ORIGINAL RESEARCH
published: 29 October 2021
doi: 10.3389/feart.2021.751974

Evaluation of the Ability of CMIP6 Global Climate Models to Simulate Precipitation in the Yellow River Basin, China

Lin Wang[1,2], *Jianyun Zhang*[1,2,3], *Zhangkang Shu*[1,2], *Yan Wang*[1,2,3], *Zhenxin Bao*[1,2,3], *Cuishan Liu*[1,2,3], *Xiong Zhou*[4] *and Guoqing Wang*[1,2,3]*

[1]State Key Laboratory of Hydrology-Water Resources and Hydraulic Engineering, Nanjing Hydraulic Research Institute, Nanjing, China, [2]Research Center for Climate Change, Nanjing, China, [3]Yangtze Institute for Conservation and Development, Nanjing, China, [4]China-Canada Center for Energy, Environment and Ecology Research, UofR-BNU, Beijing Normal University, Beijing, China

Choosing an appropriate GCM (Global Climate Model, GCM) is of great significance for the simulation of the hydrological cycle over a basin under future climate scenarios. In this study, the Rank Score Method (RS) with eight indicators were applied to comprehensively evaluate the suitability of 19 GCMs issued in the Sixth Global Atmosphere and Coupled Model Intercomparison Project (CMIP6) to the Yellow River Basin (YRB). The results indicated that: 1) The GCMs perform differently in simulating precipitation over the YRB with the top six GCMs ranking from MRI-ESM2-0, ACCESS-CM2, CNRM-CM6-1, CNRM-ESM2-1, FGOALS-f3-L, to MPI-ESM1-2-HR. 2) Most GCMs overestimated the precipitation, and poorly simulated the phase distribution of extremes mainly due to overstimulation of wet season span and precipitation amount in the season, although all GCMs could capture decadal feature of annual precipitation. Meanwhile, it is also found that most GCMs underestimated summer precipitation and overestimated spring precipitation. 3) The GCMs well simulated the spatial distribution of annual precipitation, with an overestimation in the source area, and an underestimation in the northern part of the middle reaches of YRB.

Keywords: CMIP6, climate model, precipitation simulation, comprehensive assessment, the yellow river basin

OPEN ACCESS

Edited by:
Shan Zhao,
Shandong University, China

Reviewed by:
Brian Ayugi,
Nanjing University of Information Science and Technology, China
Chunhui Li,
Beijing Normal University, China

***Correspondence:**
Guoqing Wang
gqwang@nhri.cn

Specialty section:
This article was submitted to Interdisciplinary Climate Studies, a section of the journal Frontiers in Earth Science

Received: *02 August 2021*
Accepted: *12 October 2021*
Published: *29 October 2021*

Citation:
Wang L, Zhang J, Shu Z, Wang Y, Bao Z, Liu C, Zhou X and Wang G (2021) Evaluation of the Ability of CMIP6 Global Climate Models to Simulate Precipitation in the Yellow River Basin, China. Front. Earth Sci. 9:751974. doi: 10.3389/feart.2021.751974

INTRODUCTION

With the further intensification of global climate change, the hydrological cycle processes have been significantly affected. The Sixth Intergovernmental Panel on Climate Change (IPCC) Assessment Report of group 1 showed that in 2015–2100, the global warming trend will be even more significant, climate change will intensify in all regions, and extremely high temperature and precipitation events will become more frequent (Masson-Delmotte et al., 2021). Therefore, analyzing the changes in the hydrological process of the basin, and simulating the change of hydrological elements under future climate scenarios are of great significance for the management and planning of water resources in the basin (Reboita et al., 2019). The Global Climate Models (GCMs) in a series of Global Atmosphere and Coupled Model Intercomparison Projects (CMIPs) developed by the World Climate Change Research Program (WCRP) are effective tools for predicting future climate change, and have been widely used to study the impact of climate change on the processes of the hydrological cycle (Stouffer et al., 2017; Zhang and Chen, 2021). Some

studies have noted that the models in the CMIP could well simulate the variation of various climate elements on a large scale (Fu et al., 2021; Zhu et al., 2021). However, due to the differences in simulation mechanisms, initial condition setting, parameterization scheme setting, spatial resolution and so on of each model, the performance of GCMs in various regions is quite different (Song Y. H. et al., 2021; You et al., 2021). Therefore, assessing the regional applicability of GCMs is of great importance for further research on the impact of climate change on the regional hydrological cycle.

A growing body of research has evaluated the applicability of the GCMs in the CMIPs to various regions. Chen et al. (2020) compared the ability of CMIP6 and CMIP5 models to simulate the global extreme climates, and found that the simulated results of CMIP6 models were usually closer to the observations than that of the CMIP5 for most regions, especially for temperature simulations. Iqbal et al. (2021) evaluated the precipitation simulation capability of 35 GCMs in the CMIP6 in Southeast Asia, and the results indicated that most GCMs could well simulate the precipitation change in the region. Khan et al. (2021) used Bayesian models to averagely evaluate the applicability of the 13 GCMs in the CMIP5 over the Indus River Basin, and the results showed that the optimal models for simulating temperature and precipitation were not consistent. Therefore, due to the good applicability of the GCMs in the CMIP6 and the uncertainty of the models, it is necessary to conduct a regional climate model evaluation. Zhu et al. (2021) analyzed the extreme climate predictions of China when global warming was 1.5°C, 2°C, and 3°C higher than the industrialization (1861–1900) period based on the latest (CMIP6) simulations, and compared them with the simulation results of the CMIP5. The evaluation showed that the GCMs in the CMIP6 performed better than those in the CMIP5, especially in simulating extreme precipitation. Yang et al. (2021) assessed the performance of 20 coupled GCMs in the CMIP6 in simulating temperature and precipitation in China, and found that the GCMs in the CMIP6 could reproduce the spatial distributions of temperature and precipitation. Dabang et al. (2020) compared the simulation ability of GCMs in the CMIP5 and CMIP6 in terms of temperature and precipitation in China from 1961 to 2005, and the results indicated that the current GCMs in the CMIP6 simulated lower temperatures and higher precipitation across the country compared with the CMIP5 models, but with little improvement in interannual temperature and winter monsoon. Overall, the CMIP models could well simulate the regional precipitation in China, despite some overestimations.

The Yellow River is the mother river of China. The river basin suffers from frequent droughts, floods and has been severely affected by climate change. Exploring the changes in the hydrological processes of the Yellow River Basin under future climate scenarios could promote the sustainable development of the basin (Niu et al., 2021). At present, most studies evaluating the performance of GCMs have been conducted for large research areas, such as China or the world, but relatively few studies have been conducted over basin-scales, such as the Yellow River Basin, where the simulation capabilities of GCMs in spatial and temporal have not been comprehensively considered (Yang et al., 2018; Zhou and Han, 2018). The CMIP6 is the latest global atmospheric and coupled model intercomparison plan proposed by the WCRP and has the largest number of participating models, the most complete design of scientific experiments, and the largest simulated data in more than 20 years of the CMIP (Song Z. et al., 2021). The urgent problem is how to choose a suitable model for the study area from a large number of model data. The objective of this work is to evaluate the abilities of the 19 GCMs in the CMIP6 to simulate precipitation in the Yellow River Basin, and select suitable GCMs with better simulation abilities to provide a basis and reference for the hydrological cycle process in response to the future climate change, water resources planning and management in the basin.

STUDY AREA AND DATA DESCRIPTION

Study Area

The Yellow River is the second-longest river in China, is located between 96°25′—118°75′E and 32°75′—41°75′N, has a drainage area of 79.5 × 104 km^2 and with a total river length of 5,464 km. The terrain of the Yellow River Basin is high in the west and low in the east, which is dominated by mountains in the middle and upper reaches of the Yellow River, and the middle and lower reaches are dominated by plains and hills, forming the three-level ladder from upper down to lower down (**Figure 1**). The annual precipitation in most parts of the basin is between 200 and 650 mm, with more than 650 mm in the southern and lower reaches of the middle and upper reaches. In particular, the northern slope of the southern Qinling Mountains generally has 700–1,000 mm in precipitation, while the inland areas of northwest Ningxia and Inner Mongolia have less than 150 mm. Those elements significantly affect the climate of different regions in the basin, with large annual and seasonal variations in the climatic elements, hence the frequent droughts and floods (Song S. et al., 2021; Xu et al., 2021).

Data Description

The observed data of precipitation over the Yellow River Basin applied in this paper comes from the CN05.1 data set, which was provided by the National Meteorological Center in China. The data set covers the years 1961–2018 with a spatial resolution of 0.25° × 0.25°, with good consistency and applicability (Pang et al., 2021; Shu et al., 2021). Considering the integrity of stimulated data, we chose the data to form the 19 GCMs in the CMIP6, which were obtained from the official website of CMIP6 (https://esgfnode.llnl.gov/projects/cmip6). The specific model information is shown in **Table 1**, and all the models are at daily resolution. Because the resolution of each model and the observed data is different, the bilinear interpolation method was used to interpolate to the resolution of 0.5° × 0.5° to facilitate comparison. After the interception, there are 317 grids in the Yellow River Basin, as shown in **Table 1**. The data series from 1961 to 2014 were selected for evaluation and analysis.

TABLE 1 | Basic information of the GCMs of the CMIP6 used in this study. The "lon" means longitude, the "lat" means latitude, the "lon × lat" means the spatial resolution of each model.

Number	Model	Country	Atmospheric resolution (lon × lat)
1	ACCESS-CM2	Australia	1.875° × 1.25°
2	ACCESS-ESM1-5	Australia	1.875° × 1.25°
3	BCC-CSM2-MR	China	1.125° × 1.125°
4	CMCC-CM2-SR5	Italy	1.25° × 0.9375°
5	CNRM-CM6-1	France	1.40625° × 1.40625°
6	CNRM-ESM2-1	France	1.40625° × 1.40625°
7	FGOALS-f3-L	China	1.25° × 1°
8	FGOALS-g3	China	2° × 2.25°
9	GFDL-CM4	the United States	1.25° × 1°
10	GFDL-ESM4	the United States	1.25° × 1°
11	IITM-ESM	Russia	1.875° × 1.904°
12	INM-CM4-8	Russia	2° × 1.5°
13	MIROC-ES2L	Japan	2.8125° × 2.7893°
14	MIROC6	Japan	1.40625° × 1.40625°
15	MPI-ESM1-2-HR	Germany	0.9375° × 0.935°
16	MPI-ESM1-2-LR	Germany	1.875° × 1.8652°
17	MRI-ESM2-0	Japan	1.125° × 1.125°
18	NESM3	China	1.875° × 1.865°
19	NorESM2-LM	Norway	2.5° × 1.89474°

TABLE 2 | Statistical indices and evaluation methods applied in this study.

Scale	Climatic characteristics	Method	Index
Temporal	Climate average	Multi-year average precipitation	MAE
	Inter-year variability	Coefficient of Variation	MAE
	Trend	Modified Mann-Kendall test Z	MAE
	Trend slope	Modified Mann-Kendall test β	MAE
	Correlation	Temporal correlation coefficient Rt	COR
Spatial	Correlation	Spatial correlation coefficient Rs	COR
	Inter-year change mode-1	The first modal from the Empirical Orthogonal Function (EOF1)	COR
	Inter-year change mode-2	The second modal from the Empirical Orthogonal Function (EOF2)	COR

MAE means the Mean Absolute Error, the COR means the Correlation coefficient.

METHODOLOGY

The ability of the different GCMs to reproduce the properties of those observed at the study area was assessed using eight statistical indices. The evaluated indices and methods were shown in **Table 2**.

For the simulation ability on the temporal scale, the average annual precipitation and the coefficient of variation were used to evaluate the mean state and the inter-annual variability. In addition, the Modified Mann-Kendall (MMK) method was used to test the long-term change trend of the series, then the correlation coefficient method was used to calculate the temporal correlation coefficient, and evaluate the correlation between the observations and the simulated series (Hamed and Rao, 1998). In addition to using the spatial correlation coefficient to judge the spatial correlation between the observations and the simulations, the Empirical Orthogonal Function modal decomposition (EOF) method was applied to comprehensively evaluate the spatial modal simulation ability of the GCMs (Sang et al., 2021). Finally, combining the above eight indicators, the Rank Scoring (RS) method was used to evaluate the ability of the 19 GCMs to simulate the precipitation in the Yellow River Basin.

1) The method for calculating the Mean Absolute Error (MAE) is:

$$MAE = |X_s - X_o| \tag{1}$$

Where$X_s$is the simulated value of the climatic characteristic quantity, and $X_o$is the observed value of the climatic characteristic quantity. The closer the MAE value is to zero, the more accurate the model is.

2) Correlation coefficient (COR) is calculated as:

$$COR = \frac{\sum_{i=1}^{n}\left(X_{o,i} - \overline{X_o}\right)\left(X_{s,i} - \overline{X_s}\right)}{\sqrt{\sum_{i=1}^{n}\left(X_{o,i} - \overline{X_o}\right)^2} \cdot \sqrt{\sum_{i=1}^{n}\left(X_{s,i} - \overline{X_s}\right)^2}} \tag{2}$$

When calculating the temporal correlation coefficient, $X_{s,i}$ and $X_{o,i}$are the simulated and observed values at the i-th time point respectively, and n is the total length of the sequence. When calculating the spatial correlation coefficient between the simulated value of each climate characteristic quantity and the observed value in the Yellow River Basin, $X_{s,i}$ and $X_{o,i}$ are the simulated value and observed value of the climate characteristic

TABLE 3 | Statistical indices values and RS total scores of precipitation simulated by 19 GCMs. The models and indicators in bold were the relatively better ones in the table, and the indicators in bold were performed best in each category.

Model	Mean	cv	z	B	rt	Rs	EOF1	EOF2	RS
Observed	466.1	0.12	0.22	1.29	—	—	—	—	—
ACCESS-CM2	646.7	**0.12**	**0.15**	0.39	0.01	0.77	**0.16**	**0.13**	**7.79**
ACCESSES-M1-5	721.6	0.10	−0.28	−0.51	−0.05	0.77	−0.18	−0.05	6.38
BCC-CSM2-MR	683.4	0.11	0.46	0.93	**0.14**	0.64	−0.08	−0.15	6.16
CMCC-CM2-SR5	1,083.1	0.10	−1.17	−0.99	0.01	0.69	−0.09	0.08	4.52
CNRM-CM6-1	**509.2**	0.11	**0.29**	0.47	-0.02	0.77	0.06	0.11	**7.63**
CNRM-ESM2-1	**502.1**	0.13	**0.37**	0.73	−0.05	0.76	**0.16**	0.03	**7.09**
FGOALS-f3-L	**483.8**	0.13	0.08	0.15	0.03	0.57	0.09	0.03	**6.81**
FGOALS-g3	586.0	0.10	0.00	0.01	−0.19	0.73	−0.15	−0.26	6.49
GFDL-CM4	574.3	0.13	−0.29	−0.63	0.01	0.74	−0.23	−0.16	6.54
GFDL-ESM4	578.5	**0.12**	−0.96	−1.90	**0.16**	**0.78**	0.00	0.07	6.08
IITM-ESM	791.6	0.09	−0.01	−0.01	−0.02	0.69	−0.04	−0.09	5.41
INM-CM4-8	1,068.7	0.10	−0.39	−1.49	0.12	0.66	0.10	0.10	4.49
MIROC-ES2L	957.7	0.06	−0.22	−0.38	0.02	0.68	−0.05	−0.14	4.43
MIROC6	832.2	0.09	−0.19	−0.27	−0.03	0.66	**0.17**	**0.22**	5.22
MPI-ESM1-2-HR	603.9	**0.12**	0.71	1.55	−0.06	**0.80**	0.11	0.07	**6.99**
MPI-ESM1-2-LR	785.1	0.11	0.28	0.74	0.08	0.67	0.03	0.11	5.90
MRI-ESM2-0	503.6	0.14	−0.18	−0.29	**0.18**	**0.80**	**0.23**	**0.17**	**7.83**
NESM3	879.3	0.09	−0.19	−0.55	0.08	0.65	−0.16	−0.10	4.78
NorESM2-LM	982.6	0.11	0.39	1.29	−0.08	0.72	−0.04	0.06	5.03

quantity of the i-th grid point in the basin respectively, and n is the number of grids (Alves et al., 2018). The model performance is better the closer the COR values are to 1.

3) The advantage of the RS method is that it gives a unified evaluation result for different evaluation indicators, and can also analyze a single feature value, which makes the evaluation result more intuitive and objective, so it is more conducive to comprehensive evaluation. This method first calculates the degree of fitness between the simulated sequence and the observed sequence of various statistical feature values, then assigns a score of 0–10 to each model according to the degree of fitness, which can be effectively applied to different regions (Shiru and Chung, 2021). The calculation method is as follows:

$$RS_k(T) = \begin{cases} \left(1 - \dfrac{T_k - T_{\min}}{T_{\max} - T_{\min}}\right) \times 10; & T = MAE \\ \left(\dfrac{T_k - T_{\min}}{T_{\max} - T_{\min}}\right) \times 10; & T = COR \end{cases} \quad (3)$$

Where $RS_k(T)$ is the score value of the climate characteristic quantity T of the k-th model. T_k, $T_{\min}$ and $T_{\max}$ are the calculated values of the climatic characteristic quantity T of the k-th model, and the minimum and maximum values of the climatic characteristic quantity of all models. The range of RS is 0–10. The higher the score, the better the simulation ability of the climate model in this region.

RESULTS AND DISCUSSION

Comprehensive Evaluation for the Stimulated Ability of GCMs

The RS scores of each index and total scores of 19 GCMs were shown in **Table 3**.

It can be seen that the simulation capabilities of the 19 GCMs were quite different. The highest RS score was 7.83 (MRI-ESM2-0) and the lowest was 4.52 (CMCC-CMA-SR5). The models with relatively higher scores were MRI-ESM2-0 (7.83), ACCESS-CM2 (7.79), CNRM-CM6-1 (7.63), CNRM-ESM2-1 (7.09), MPI-ESM1-2-HR (6.99) and FGOALS-f3-L (6.81) (**Figure 2**). The results showed that no model performs well for each indicator. Each GCM had better or poorer performance indicators than others, which indicated the necessity of a comprehensive evaluation of indicators.

The average annual precipitation of observation in the Yellow River Basin was 466.1 mm, while those of the 19 GCMs ranged from 483.8 to 1,083.1 mm. Therefore, all models overestimated the average annual precipitation. The closest simulated value was from FGOALS-f3-L (483.8 mm), while the greatest overestimation was from model CMCC-CM2-SR5 at 1,083.1 mm. Previous studies noted that most climate models overstimulated the precipitation in the basin, a factor related to that was the more convective precipitation simulated by the GCMs (Zhou and Han, 2018). For the inter-annual variability, there was little difference between the models. It showed that the spatial variation of the simulated annual precipitation in most GCMs was close to the observation in terms of the coefficient of variation. In addition, the precipitation of the basin from 1961 to 2014 showed an insignificant increase trend ($Z<\pm1.96$), and nine models that could simulate the increasing trend. However, the Z value of the best scored MRI-ESM2-0 was −0.18, which failed to simulate the increasing trend of the observation. But the better performance of other climatic characteristics made up for the lack of trend simulation, which showed that quantitative assessment of the sensitivity of climate characteristics is a problem that needs further research (Yazdandoost et al., 2020). Finally, in terms of spatial and temporal correlation, though almost all of the GCMs showed highly spatial correlation, they performed badly on temporal correlation, with 8 GCMs showing negative correlation, implying a large deviation between the simulated value and the observation (**Figure 3**). For example, the

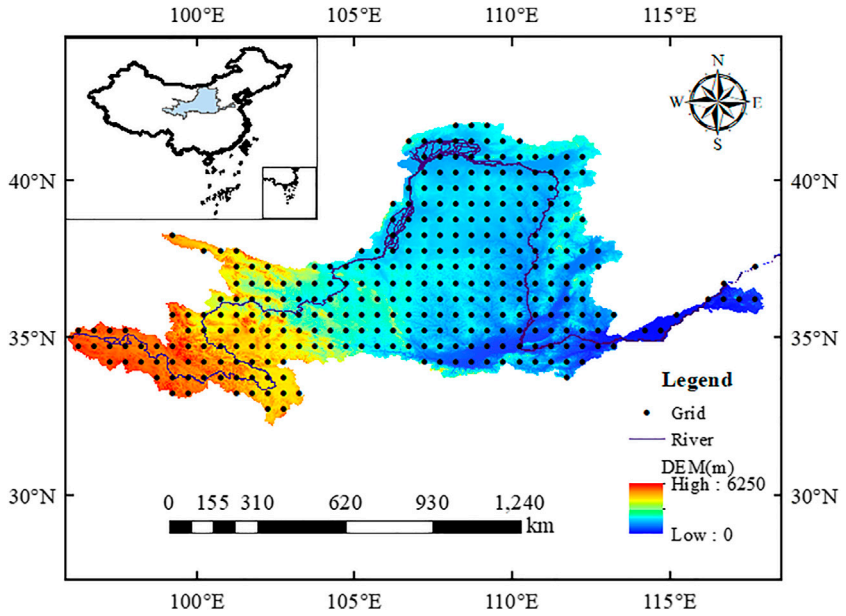

FIGURE 1 | Meteorological grid and river system of the Yellow River Basin.

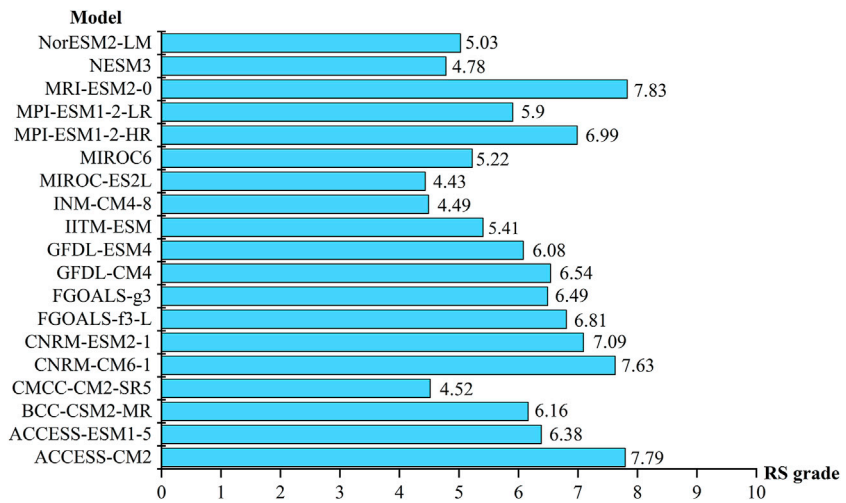

FIGURE 2 | RS scores of the 19 GCMs in CMIP6.

precipitation stimulated by MRI-ESM2 0 at 32.75°N 102.75°E was 1,418.1 mm, while the observed precipitation over this grid was 848.37 mm, so there is a significant deviation between the simulation and the observation.

Simulation of Temporal Characteristic

Simulation of Annual Precipitation

The ability of the different GCMs to reproduce the properties of those observed at the study area was assessed using eight statistical indices. The evaluated indices and methods were shown in Table.

Table indicated that the annual precipitation in the Yellow River Basin showed an insignificant increase from 1961 to 2014. The maximum precipitation occurred in 1964 (597.7 mm), and the minimum precipitation was in 1965 (342.2 mm). **Figure 4** showed the annual precipitation change of the six models with higher scores. Almost all of the models could simulate the inter-annual change of precipitation in the basin. However, not only the annual precipitation in the Yellow River Basin was overestimated, but the simulation value of peak and valley also lagged. Moreover, the peak value was obviously overestimated, and the valley value was underestimated, which is related to the

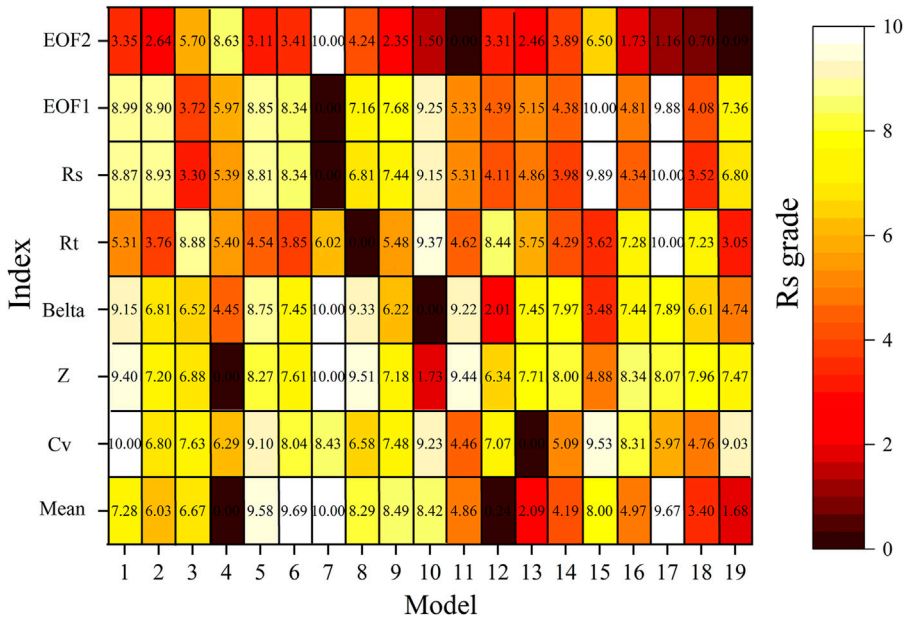

FIGURE 3 | Comparison of the RS scores of the eight indicators over the 19 GCMs, 1–19 are the 19 CMIP6 models listed in **Table 1**: ACCESS-CM2, ACCESS-ESM1-5, BCC-CSM2-MR, CMCC-CM2-SR5, CNRM-CM6-1, CNRM-ESM2-1, FGOALS-f3-L, FGOALS-g3, GFDL-CM4, GFDL-ESM4, IITM-ESM, INM-CM4-8, MIROC-ES2L, MIROC6, MPI-ESM1-2-HR, MPI-ESM1-2-LR, MRI-ESM2 0, NESM3, NorESM2-LM.

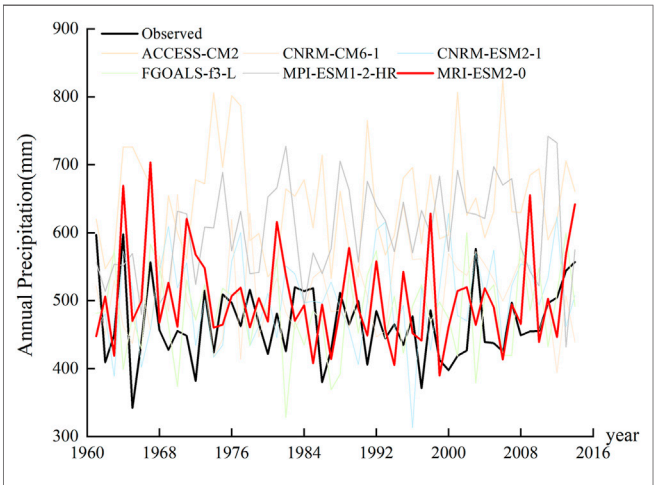

FIGURE 4 | Annual precipitation of the six higher-scoring GCMs and the observed data. The red line denotes the GCM with the highest score in the comprehensive evaluation.

uncertainty of the climate model and the resolution of the data (Orlowsky and Seneviratne, 2013). For example, the highest scored MRI-ESM2-0's simulated annual precipitation in 1964 was 669.3 mm, and the simulated annual precipitation in 1965 appeared to be 470.1 mm (**Table 4**), which was the closest to the observed data among the six optimal models. It also had the least hysteresis impact, so the GCMs ranked high by the RS method were seen to have better abilities in replicating the historical variation of inter-year precipitation in the Yellow River Basin.

In order to compare the uncertainty of the simulated annual precipitation in the Yellow River Basin between the GCMs, the uncertainty interval of the annual precipitation stimulated by 19 GCMs and six higher-scoring models were calculated with absolute deviations (**Figure 5**). Among them, the range of the simulated annual precipitation of the 19 models was 313.2–1,391.5 mm, while that of the six higher-scoring models was 313.2–818.4 mm, which indicated that the higher-scoring GCMs significantly reduced the uncertainty of simulated precipitation in the Yellow River Basin.

Simulation of the Seasonal Pattern

The maximum monthly precipitation of observed data in the basin from 1961 to 2014 occurred in July (102.2 mm), but it occurred in August in the six models. The maximum monthly precipitation in the basin was overestimated by 113.2 mm by ACCESS-CM2, 110.4 mm by CNRM-CM6-1, and 107.43 mm by CNRM-ESM2-1. However, the other three models underestimated it: FGOALS-f3-L by 91.3 mm, MPI-ESM1-2-HR by 91.4 mm, and MRI-ESM2-0 by 82.5 mm (**Figure 6**). On the other hand, the minimum monthly precipitation of observation occurred in December with 3.2 mm, but the six models all predicted it to occur in January with higher precipitation than observation. Therefore, the GCMs offer poor simulations of the phase distribution of the monthly extreme precipitation. Furthermore, the wet season in the Yellow River Basin is from May to September, and the dry season is from October to April, the monthly average precipitation was 38.8mm, which was consistent with previous research conclusions (Cui, 2008). Although most GCMs in the CMIP6 could simulate the intra-year variation of wet and dry

TABLE 4 | Annual precipitation of six higher-scoring GCMs and observed precipitation from 1964 to 1965.

Model *P* (mm)	Observed	ACCESS-CM2	CNRM-CM6-1	CNRM-ESM2-1	FGOALS-f3-L	MPI-ESM1-2-HR	MRI-ESM2-0
1964	597.7	726.0	462.7	573.0	399.2	551.4	669.3
1965	342.2	726.2	437.2	519.2	478.2	569.4	470.1

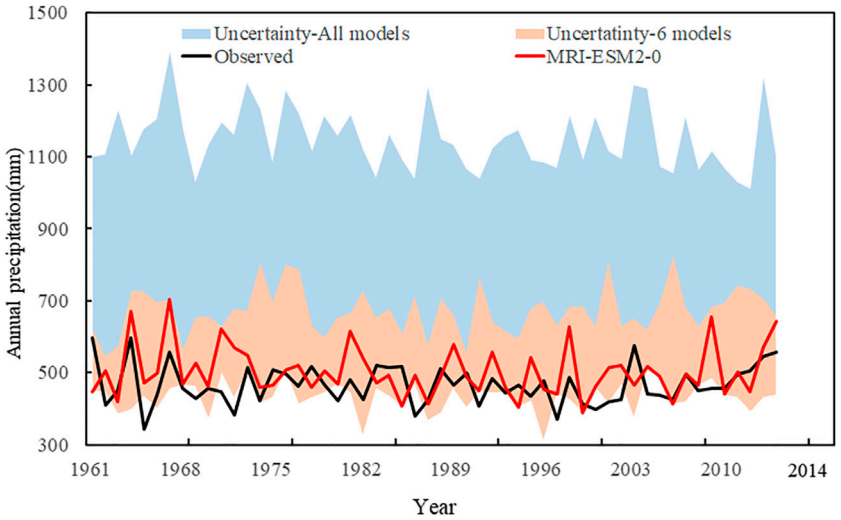

FIGURE 5 | Uncertainty interval of stimulated annual precipitation from the 19 GCMs and the six higher-scoring models. The black line is the annual precipitation change of the observed precipitation, and the red line is the annual precipitation change simulated by the GCM with the highest score.

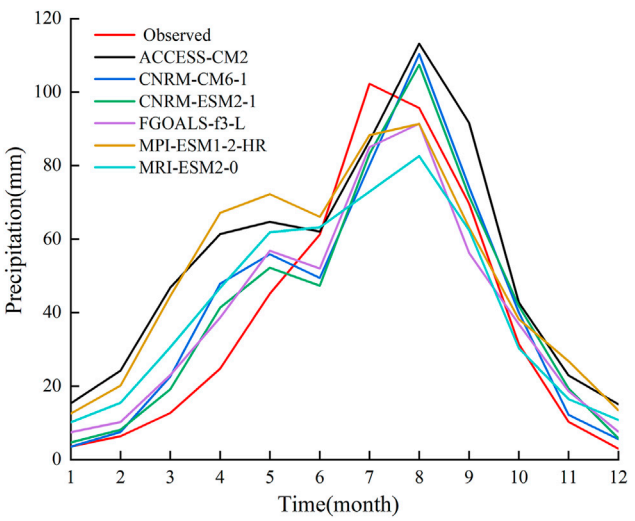

FIGURE 6 | Distribution of the intra-year precipitation from the simulated data of six higher-scoring GCMs and observed data.

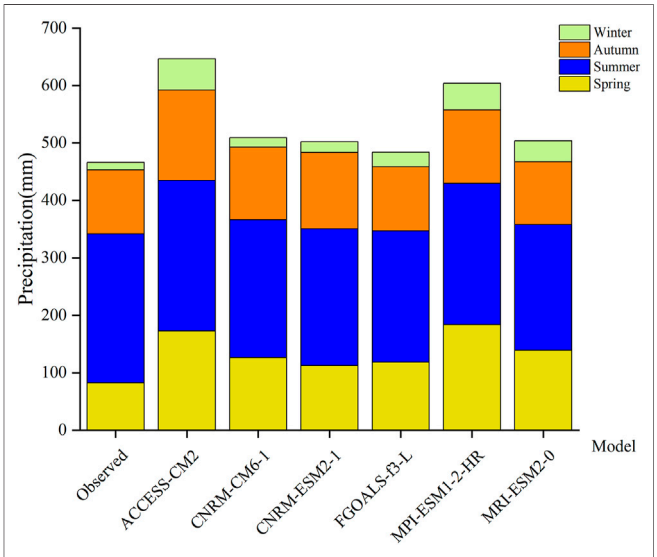

FIGURE 7 | Seasonal precipitation of the observation and simulation from the six higher-scoring GCMs, spring is from March to May, summer is from June to August, autumn is from September to November, and winter is from December to February.

seasons in the Yellow River Basin, the wet season simulated by the six models except FGOALS-f3-L was April to September, and the monthly average precipitation was higher than the observed data, so the wet season simulated by most GCMs was too long and the precipitation during the period was overestimated.

The observed precipitation indicated that the summer precipitation in the Yellow River Basin was the most abundant, which could reach 259.1 mm, accounting for 55%

TABLE 5 | Maximum and minimum average annual precipitation of the grids simulated by the observed and the six higher-scoring GCMs over the Yellow River Basin.

Model	Observed	ACCESS-CM2	CNRM-CM6-1	CNRM-ESM2-1	FGOALS-f3-L	MPI-ESM1-2-HR	MRI-ESM2-0
P_{max} (mm)	831.3	1859.0	1,611.6	1,580.4	921.2	1,697.3	703.4
P_{min} (mm)	157.8	135.2	76.7	71.6	114.9	111.3	389.5

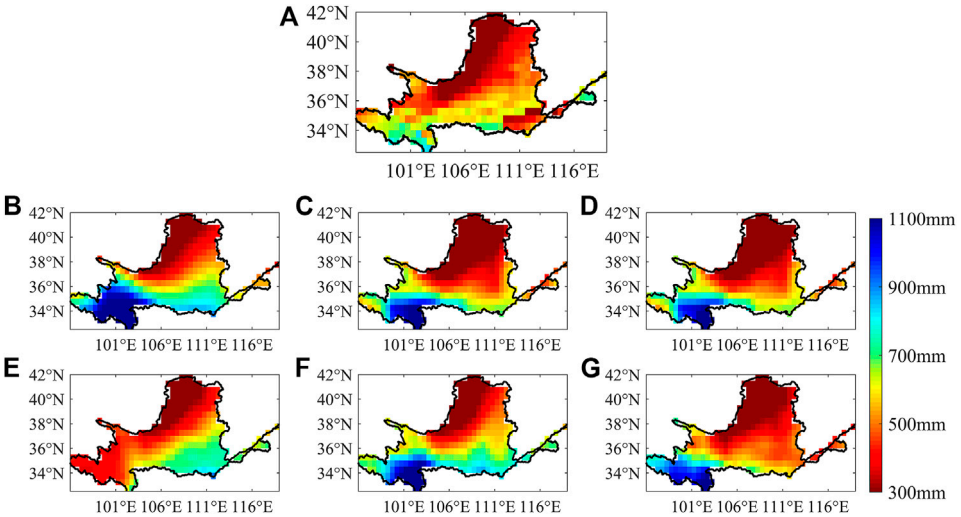

FIGURE 8 | Spatial distribution of average annual precipitation from the observation and six higher-scoring GCMs. Panels **(A–G)** are the observed data, ACCESS-CM2, CNRM-CM6 -1, CNRM-ESM2-1, FGOALS-f3-L, MPI-ESM1-2-HR, MRI-ESM2-0, respectively.

of the annual precipitation. The winter precipitation was insufficient, only 12.9 mm, accounting for 3% of the annual precipitation. In general, the six higher-scoring GCMs could simulate the seasonal characteristics of the basin with abundant summer precipitation and less precipitation in winter. However, except for the summer precipitation simulated by the ACCESS-CM2 l (261.9 mm), which was slightly higher than the observed data, that simulated by the other five models were lower than observed. Among them, the summer precipitation simulated by the MRI-ESM2-0 model was the lowest of 218.7 mm, indicating that most GCMs in the CMIP6 underestimated the summer precipitation in the basin (**Figure 7**).

The observed autumn precipitation (111.42 mm) was also higher than the spring precipitation (82.6 mm) in the Yellow River Basin. While the CNRM-ESM2-1 model could simulate the changes of the spring and autumn precipitation, the precipitation in spring simulated by the other five models was higher than that in autumn. Some studies concluded that the wet season was from May to September in the Yellow River Basin, with the highest precipitation in summer, and the precipitation in autumn was significantly higher than that in spring (Li et al., 2016; Yuan et al., 2016). Therefore, the GCMs could not well simulate the changes of precipitation in the basin in spring and autumn, and obviously overestimated the precipitation in spring and underestimated it in summer.

Simulation of Spatial Characteristic

Spatial Distribution Characteristics of Precipitation

The average annual precipitation in the Yellow River Basin decreases from south to north, the maximum grid average annual precipitation is 831.4 mm while the minimum is 157.8 mm (**Table 5**). **Figure 8** indicated that the GCMs could well simulate the spatial distribution characteristics of the annual precipitation in the Yellow River Basin. However, they all overestimated the maximum precipitation, and underestimated the minimum precipitation, especially overestimated the precipitation in the source area of the Yellow River.

In order to further analyze the ability of the 6 GCMs to replicate the spatial distribution of average annual precipitation in the Yellow River Basin, this paper calculated the relative deviation of the average annual precipitation from the six higher-scoring GCMs and observed data (**Figure 9**). The results indicated that except for the CNRM-ESM2-1, which underestimated the average annual precipitation in the source area of the Yellow River, the other five models significantly overestimated it. Besides that, the six models all underestimated the precipitation in the northern part of the middle reaches of the Yellow River Basin, and there was also a significant underestimation in the lower reaches of the basin. Therefore, the GCMs had large uncertainties in the simulation of the spatial distribution of the precipitation in the Yellow River Basin. Xu et al. (2010) assessed the uncertainty in the impacts of climate change on river discharge in the Yangtze and Yellow

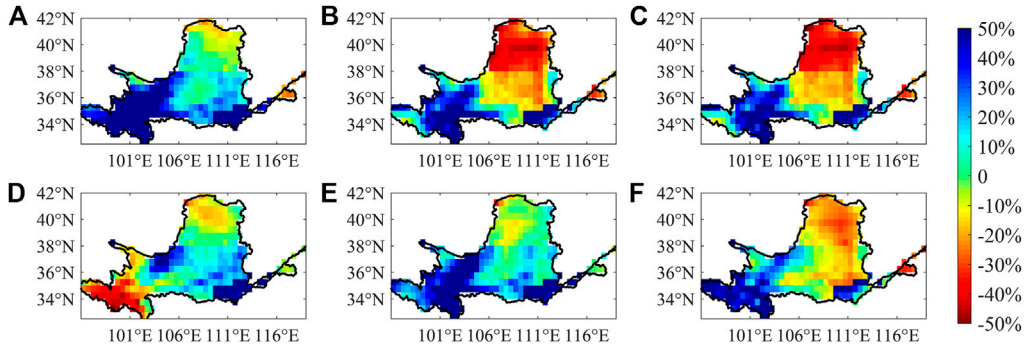

FIGURE 9 | Deviation of the spatial distribution of the average annual precipitation in the Yellow River Basin simulated by six higher-scoring GCMs. Panels **(A–F)** are ACCESS-CM2, CNRM-CM6 -1, CNRM-ESM2-1, FGOALS-f3-L, MPI-ESM1-2-HR, MRI-ESM2-0.

River Basins, and found that the precipitation in the Yellow River Basin simulated by the GCMs was obviously affected by regional climate characteristics. The climatic conditions of the basin from the source region to the lower reaches are very complex, which increases the uncertainty of climate model simulations (Bao and Feng, 2014).

Spatial Distribution Characteristics of Precipitation Modalities

The spatial distribution of the first mode and the second mode was obtained by the EOF decomposition of the observed average annual precipitation in the Yellow River Basin (**Figures 10A**, **11A**). The cumulative explained variance of the first and second modes of the average annual precipitation in the Yellow River Basin was 98.48%, which could almost explain the spatial and temporal variability of the basin. On the one hand, the explained variance of the first mode was 97.89% and the mode over the whole basin showed a consistent trend. The EOF1 of the whole basin was a positive signal, the maximum variability was located in the northern part of the middle reaches, which decreases from the north to the south over the Yellow River Basin. The explained variance of the second mode of the average annual precipitation in the Yellow River Basin was 0.52%, which was represented by the characteristic of east-west antiphase bounded by the middle part of the Yellow River. Among them, the negative signal was from the source of the Yellow River to the middle reaches, and the positive signal was from the middle reaches to the lower reaches of the basin. Liu and Zheng (2002) and Hao et al. (2010) used the EOF method to study the spatial pattern of precipitation in the Yellow River Basin under the impact of climate change, and the results noted that the spatial structure of precipitation in the Yellow River Basin could be divided into four types: "total consistency", "north-south", "west-east" and "complex" due to the particularity of geographical location and climatic conditions. Therefore, the spatial modal distribution characteristics of the average annual precipitation in the Yellow River Basin obtained in this paper were reasonable. The GCMs could well simulate the spatial variation of the EOF mode of the average annual precipitation in the Yellow River Basin, and the explained variance was higher than the observed data, so there was an over-fitting phenomenon (**Figure 10**). In addition, the six higher-scoring GCMs could simulate the spatial characteristics of the first mode and the second mode in the basin (**Figure 11**). However, most GCMs overestimated the simulated variability of the first mode in the northern part of the basin and the second mode in the source region of the Yellow River. Of the GCMs, the CNRM-CM6-1 had the best simulation effect on the spatial characteristics of the first and second modes of the average annual precipitation in the basin. The explained variance, in this case, was closest to the observed data, and the phenomenon of overestimating the modal variability was not very significant.

DISCUSSION AND CONCLUSIONS

Discussion

This study comprehensively evaluated the ability of 19 GCMs from the CMIP6 to simulate the properties of precipitation in the Yellow River Basin, and provided a basis of model selection for research on the hydrological cycle under future climate scenarios in the Yellow River Basin. Woldemeskel et al. (2014) found that different models have great differences in the precipitation simulation capabilities over basin scales, and choosing the better model helps reduce the uncertainty of model simulation. Therefore, this research is of great significance to the prediction of future flood disasters and sustainable development of the Yellow River Basin. In this study, we found that the GCMs in the CMIP6 showed an obvious zoning phenomenon when simulating the spatial distribution of precipitation in the basin. The average annual precipitation in the source area of the Yellow River was overestimated, and underestimated in the middle reaches of the river. This is related to the sophisticated topographical characteristics of the Yellow River Basin. The basin spans the Qinghai-Tibet Plateau, the Loess Plateau, the Guanzhong Plain, the Hetao and the Yinchuan Plain, so the underlying surface and topography of the basin are complex. Such complicated topographical conditions significantly affect the climatic characteristics of the Yellow River Basin.

At present, it is difficult for GCMs to accurately simulate the climate characteristics of the Yellow River Basin, and the

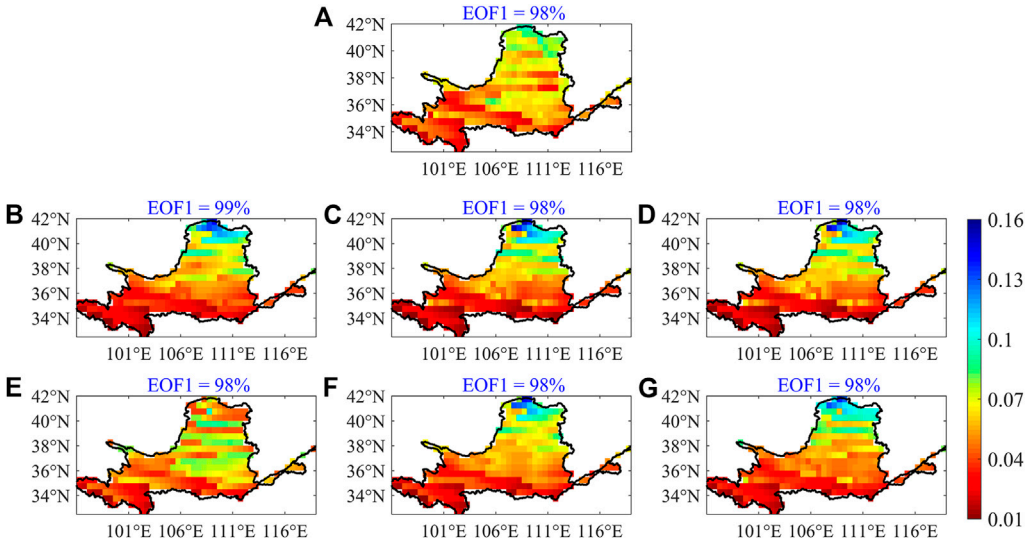

FIGURE 10 | Spatial distribution of the first EOF mode (EOF1) of the average annual precipitation from observation and six higher-scoring GCMs. Panels **(A–G)** are the observed data, ACCESS-CM2, CNRM-CM6 -1, CNRM-ESM2-1, FGOALS-f3-L, MPI-ESM1-2-HR, MRI-ESM2-0.

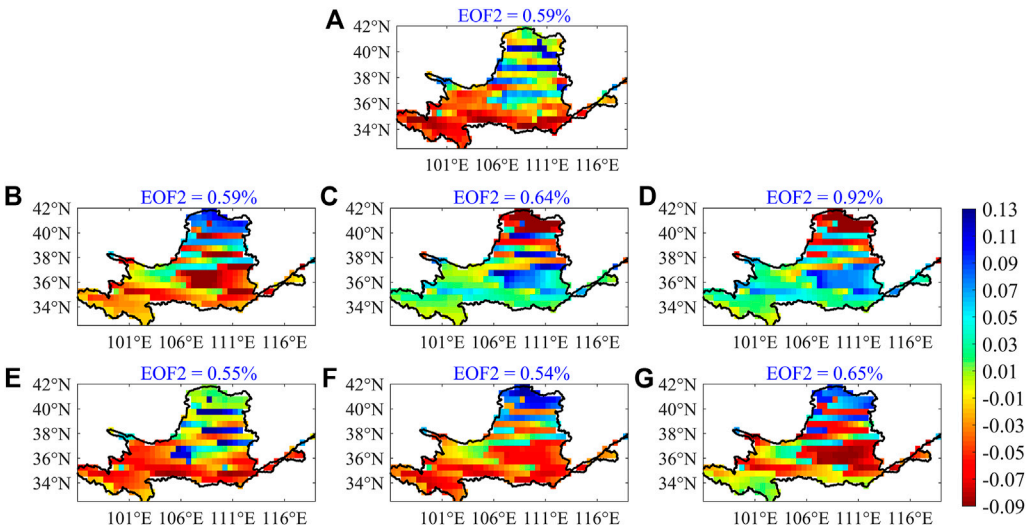

FIGURE 11 | Spatial distribution of the second EOF mode (EOF2) of the average annual precipitation from observation and six higher-scoring GCMs. Panels **(A–G)** are the observed data, ACCESS-CM2, CNRM-CM6 -1, CNRM-ESM2-1, FGOALS-f3-L, MPI-ESM1-2-HR, MRI-ESM2-0.

resolution of most GCMs in the CMIP6 is still relatively coarse (Hui et al., 2015). Therefore, one urgent problem is how to improve the simulation capabilities of GCMs. In order to better simulate and predict future climate changes in the Yellow River Basin, dynamic or statistical downscaling methods could be used for the GCMs selected in this paper. Besides that, the downscale data could be corrected by the bias correction technology, then it could drive the hydrological models, and explore the impact of future climate changes on the hydrological processes in the Yellow River Basin (Zhao et al., 2019). For hydrological models, it is necessary to use meteorological data with a high resolution, so the multiple models could be considered to drive the hydrological models separately and then aggregated to improve simulation accuracy. Hamlet et al. (2020) found that the multi-model ensemble average enables the simulation errors of different climate models (including the simulation errors of spatial distribution) to offset each other, with a better simulation effect. The simulation capacity will increase as the set of samples increases, but it will gradually stabilize after reaching a certain number of samples. And due to the frequent occurrence of droughts and floods in the Yellow River Basin, combining different climate and land-use scenarios to predict the changes of future extreme drought and flood disasters in the Yellow River Basin is a direction worth studying.

Conclusion

Based on the simulated precipitation data of 19 GCMs in the CMIP6 and the observed data of the Yellow River Basin from 1961 to 2014, this paper selected eight indicators and combined them with the RS method. The ability of the GCMs in the CMIP6 to simulate the temporal and spatial variations of precipitation in the Yellow River Basin was comprehensively evaluated, the conclusions are as follow:

1) The GCMs differed greatly in their ability to simulate precipitation in the Yellow River Basin. The top six GCMs ranking are: MRI-ESM2-0, ACCESS-CM2, CNRM-CM6-1, CNRM-ESM2-1, FGOALS- f3-L, MPI-ESM1-2-HR.
2) Most GCMs overestimated the annual precipitation and poorly simulate the phase distribution of the extremes, although they could simulate the variation of intra-year precipitation. Meanwhile, it also found that the wet season simulated by most GCMs was too long, the precipitation was also overestimated during this period. Most GCMs in the CMIP6 could simulate the variation of precipitation in summer and winter, but they underestimated the summer precipitation and overestimated the spring precipitation in the Yellow River Basin.
3) All GCMs could well simulate the spatial distribution of the annual precipitation over the basin, but there was a significant overestimation phenomenon in the source area, and an underestimation in the northern part of the middle reaches.
4) The GCMs in the CMIP6 performed well in simulating the spatial variation of modal in the Yellow River Basin, the simulation ability of CNRM-CM6-1 was the best. But most models overestimated the simulation variability of the first mode in the northern part of the basin and the second mode in the source area of the Yellow River.

DATA AVAILABILITY STATEMENT

The datasets presented in this study can be found in online repositories. The names of the repository/repositories and accession number(s) can be found below: https://esgf-node.llnl.gov/search/cmip6/.

AUTHOR CONTRIBUTIONS

LW: writing original draft. JZ and ZS: discussion and suggestions for data anaysis. YW: Grammar modification and polishing. ZB and CL: formal analysis and visualization. XZ: conceptualization and methodology. GW: data curation and software.

FUNDING

This research has been financially supported by National Key Research and Development Programs of China (Grants: 2016YFA0601500, 2017YFA0605002, 2017YFC0404602), and the National Natural Science Foundation of China (grant nos. 41830863, 51879162, 51609242, 51779146, 41601025), and the State Key Laboratory of Hydrology-Water Resources and Hydraulic Engineering (grant no. 2019nkzd02).

ACKNOWLEDGMENTS

Thanks for the CMIP6 model data provided by the CMIP6 official website, thanks for the CN05 grid point precipitation data provided by the China National Climate Center, thanks for all the co-authors for their efforts in this paper, and thanks for the editorial department and reviewers for their support and help in this paper.

REFERENCES

Alves, J. M. B., Vasconcelos Junior, F. C., Chaves, R. R., Silva, E. M., Servain, J., Costa, A. A., et al. (2018). Evaluation of the AR4 CMIP3 and the AR5 CMIP5 Model and Projections for Precipitation in Northeast Brazil. *Front. Earth Sci.* 4, 44. doi:10.3389/feart.2016.00044

Bao, J., and Feng, J. (2014). "Evaluation of the Water Vapor Transport over the Yellow River Basin in CMIP5 Models," in Egu General Assembly Conference.

Chen, H., Sun, J., Lin, W., and Xu, H. (2020). Comparison of CMIP6 and CMIP5 Models in Simulating Climate Extremes. *Sci. Bull.* 65 (17), 1415–1418. doi:10.1016/j.scib.2020.05.015

Fu, Y., Lin, Z., and Wang, T. (2021). Simulated Relationship between Wintertime ENSO and East Asian Summer Rainfall: From CMIP3 to CMIP6. *Adv. Atmos. Sci.* 38 (2), 221–236. doi:10.1007/s00376-020-0147-y

Hamed, K. H., and Rao, A. R. (1998). A. Modified Mann-kendall Trend Test for Autocorrelated Data. *J. Hydrol.* 204 (1-4), 182–196. doi:10.1016/S0022-1694(97)00125-X

Hamlet, A. F., Byun, K., Robeson, S. M., Widhalm, M., and Baldwin, M. (2020). Impacts of Climate Change on the State of Indiana: Ensemble Future Projections Based on Statistical Downscaling. *Clim. Change* 163 (4), 1881–1895. doi:10.1007/s10584-018-2309-9

Hao, X., Ouyang, X., Xie, S., Shi, S., Linli, L. I., and Luo, L. (2010). The Spatial and Temporal Structure of Precipitation in the Yellow River Basin. *Prog. Geogr.* 23 (2), 65–69. doi:10.1007/BF02873097

Hui, P., Tang, J., Wang, S., Wu, J., and Kang, Y. (2014). Future Climate Projection under IPCC A1B Scenario in the Source Region of Yellow River with Complex Topography Using RegCM3. *J. Geophys. Res. Atmos.* 119 (19), 11,205–11,222. doi:10.1002/2014JD021992

Iqbal, Z., Shahid, S., Ahmed, K., Ismail, T., Ziarh, G. F., Chung, E.-S., et al. (2021). Evaluation of CMIP6 GCM Rainfall in mainland Southeast Asia. *Atmos. Res.* 254 (1), 105525. doi:10.1016/j.atmosres.2021.105525

Jiang, D., Hu, D., Tian, Z., Lang, X., and Lang (2020). Differences between CMIP6 and CMIP5 Models in Simulating Climate over China and the East Asian Monsoon. *Adv. Atmos. Sci.* 37 (10), 1102–1118. doi:10.1007/s00376-020-2034-y

Khan, F., Pilz, J., and Ali, S. (2021). Evaluation of CMIP5 Models and Ensemble Climate Projections Using a Bayesian Approach: A Case Study of the Upper Indus Basin, Pakistan. *Environ. Ecol. Stat.* 28, 383–404. doi:10.1007/s10651-021-00490-8

Li, Q., Yang, M., Wan, G., and Wang, X. (2016). Spatial and Temporal Precipitation Variability in the Source Region of the Yellow River. *Environ. Earth Sci.* 75 (7), 594. 591-594.514. doi:10.1007/s12665-016-5583-8

Liu, C., and Zheng, H. (2002). *Distribution Pattern of Precipitation and its Evolution Characters in the Yellow River Basin, China*.

Liu, Q., Yang, Z., and Cui, B. (2008). Spatial and Temporal Variability of Annual Precipitation during 1961-2006 in Yellow River Basin, China. *J. Hydrol.* 361 (3-4), 330–338. doi:10.1016/j.jhydrol.2008.08.002

Masson-Delmotte, V., Zhai, P., Pirani, A., Connors, S. L., Péan, C., Berger, S., et al. (Editors) (2021). "IPCC, 2021: Summary for Policymakers," *Climate Change 2021: The Physical Science Basis.Contribution of Working Group I to the Sixth*

Assessment Report of the Intergovernmental Panel on ClimateChange (Cambridge University Press).

Niu, Z., Feng, L., Chen, X., and Yi, X. (2021). Evaluation and Future Projection of Extreme Climate Events in the Yellow River Basin and Yangtze River Basin in China Using Ensembled CMIP5 Models Data. *Ijerph* 18 (11), 6029. doi:10.3390/ijerph18116029

Orlowsky, B., and Seneviratne, S. I. (2013). Elusive Drought: Uncertainty in Observed Trends and Short- and Long-Term CMIP5 Projections. *Hydrol. Earth Syst. Sci.* 17 (5), 1765–1781. doi:10.5194/hess-17-1765-2013

Pang, G., Wang, X., Chen, D., Yang, M., and Liu, L. (2021). Evaluation of a Climate Simulation over the Yellow River Basin Based on a Regional Climate Model (REMO) within the CORDEX. *Atmos. Res.* 254 (4), 105522. doi:10.1016/j.atmosres.2021.105522

Reboita, M. S., Ambrizzi, T., Silva, B. A., Pinheiro, R. F., and da Rocha, R. P. (2019). The South Atlantic Subtropical Anticyclone: Present and Future Climate. *Front. Earth Sci.* 7, 1–22. doi:10.3389/feart.2019.00008

Sang, Y., Ren, H.-L., Shi, X., Xu, X., and Chen, H. (2021). Improvement of Soil Moisture Simulation in Eurasia by the Beijing Climate Center Climate System Model from CMIP5 to CMIP6. *Adv. Atmos. Sci.* 38, 237–252. doi:10.1007/s00376-020-0167-7

Shiru, M. S., and Chung, E.-S. (2021). Performance Evaluation of CMIP6 Global Climate Models for Selecting Models for Climate Projection over Nigeria. *Theor. Appl. Climatol.* 146, 599–615. doi:10.1007/s00704-021-03746-2

Shu, Z., Zhang, J., Jin, J., Wang, L., Wang, G., Wang, J., et al. (2021). Evaluation and Application of Quantitative Precipitation Forecast Products for Mainland China Based on TIGGE Multimodel Data. *J. Hydrometeorol.* 22, 1199–1219. doi:10.1175/JHM-D-20-0004.1

Song, S., Singh, V. P., Song, X., and Kang, Y. (2021a). A Probability Distribution for Hydrological Drought Duration. *J. Hydrol.* 599, 12647. doi:10.1016/j.jhydrol.2021.126479

Song, Y. H., Chung, E. S., and Shahid, S. (2021b). Spatiotemporal Differences and Uncertainties in Projections of Precipitation and Temperature in South Korea from CMIP6 and CMIP5 General Circulation Model S. *Int. J. Climatol.* doi:10.1002/joc.7159

Song, Z., Xia, J., She, D., Li, L., Hu, C., and Hong, S. (2021c). Assessment of Meteorological Drought Change in the 21st Century Based on CMIP6 Multi-Model Ensemble Projections over Mainland China. *J. Hydrol.* 601, 126643. doi:10.1016/j.jhydrol.2021.126643

Stouffer, R. J., Eyring, V., Meehl, G. A., Bony, S., Senior, C., Stevens, B., et al. (2017). CMIP5 Scientific Gaps And Recommendations For CMIP6. *Bull. Am. Meteorol. Soc.* 98 (1), 95–105. doi:10.1175/BAMS-D-15-00013.1

Woldemeskel, F. M., Sharma, A., Sivakumar, B., and Mehrotra, R. (2014). A Framework to Quantify GCM Uncertainties for Use in Impact Assessment Studies. *J. Hydrol.* 519, 1453–1465. doi:10.1016/j.jhydrol.2014.09.025

Xu, H., Taylor, R. G., and Xu, Y. (2010). Quantifying Uncertainty in the Impacts of Climate Change on River Discharge in Sub-catchments of the Yangtze and Yellow River Basins, China. *Hydrol. Earth Syst. Sci.* 15 (1), 333–344. doi:10.5194/hess-15-333-2011

Xu, Z., Zhang, S., and Yang, X. (2021). Water and Sediment Yield Response to Extreme Rainfall Events in a Complex Large River basin: A Case Study of the Yellow River Basin, China. *J. Hydrol.* 597 (2), 126183. doi:10.1016/j.jhydrol.2021.126183

Yang, X., Zheng, W., Ren, L., Zhang, M., Wang, Y., Liu, Y., et al. (2018). Potential Impact of Climate Change to the Future Streamflow of Yellow River Basin Based on CMIP5 Data. *Proc. IAHS* 376, 97–104. doi:10.5194/piahs-376-97-2018

Yang, X., Zhou, B., Xu, Y., and Han, Z. (2021). CMIP6 Evaluation and Projection of Temperature and Precipitation over China. *Adv. Atmos. Sci.* 38 (5), 817–830. doi:10.1007/s00376-021-0351-4

Yazdandoost, F., Moradian, S., Izadi, A., and Aghakouchak, A. (2021). Evaluation of CMIP6 Precipitation Simulations across Different Climatic Zones: Uncertainty and Model Intercomparison. *Atmos. Res.* 250, 105369. doi:10.1016/j.atmosres.2020.105369

You, Q., Cai, Z., Wu, F., Jiang, Z., Pepin, N., and Shen, S. S. P. (2021). Temperature Dataset of CMIP6 Models over China: Evaluation, Trend and Uncertainty. *Clim. Dyn.* 57, 17–35. doi:10.1007/s00382-021-05691-2

Yuan, F., Berndtsson, R., Uvo, C. B., Zhang, L., and Jiang, P. (2016). Summer Precipitation Prediction in the Source Region of the Yellow River Using Climate Indices. *Hydrol. Res.* 47, 847–856. doi:10.2166/nh.2015.062

Zhang, S., and Chen, J. (2021). Uncertainty in Projection of Climate Extremes: A Comparison of CMIP5 and CMIP6. *J. Meteorol. Res.* 35 (4), 646–662. doi:10.1007/s13351-021-1012-3

Zhao, F., Shuo-Ben, B. I., Xing-Yu, L. I., Wei-Ting, W. U., and Jiang, T. T. (2019). Spatial Characteristics of Drought/flood Disasters Based on EOF and REOF in the Middle and Lower Reaches of the Yellow River from 1470 to 1911. *Arid Land Geogr.* 42 (4), 799–809.

Zheng, H., and Liu, C. (2004). On Evolution Modes of Water Resources in the Yellow River Basin[J]. *Acta Geographica Sinica* 59 (2), 267–273.

Zhou, W. C., and Han, Z. Y. (2018). Assessing CMIP5 Climate Simulations and Objective Selection of Models over the Yellow River Basin. *J. Meteorol. Environ.* 34 (06), 42–55.

Zhu, H., Jiang, Z., and Li, L. (2021). Projection of Climate Extremes in China, an Incremental Exercise from CMIP5 to CMIP6. *Sci. Bull.* doi:10.1016/j.scib.2021.07.026

Conflict of Interest: The authors declare that the research was conducted in the absence of any commercial or financial relationships that could be construed as a potential conflict of interest.

Publisher's Note: All claims expressed in this article are solely those of the authors and do not necessarily represent those of their affiliated organizations, or those of the publisher, the editors and the reviewers. Any product that may be evaluated in this article, or claim that may be made by its manufacturer, is not guaranteed or endorsed by the publisher.

frontiers in Earth Science

ORIGINAL RESEARCH
published: 19 November 2021
doi: 10.3389/feart.2021.756943

Summertime Moisture Sources and Transportation Pathways for China and Associated Atmospheric Circulation Patterns

Ruonan Zhang[1,2]*, *QuCheng Chu*[3], *Zhiyan Zuo*[1,2] and *Yanjun Qi*[4]

[1]Department of Atmospheric and Oceanic Sciences, Institute of Atmospheric Sciences, Fudan University, Shanghai, China, [2]Innovation Center of Ocean and Atmosphere System, Zhuhai Fudan Innovation Research Institute, Zhuhai, China, [3]State Key Laboratory of Satellite Ocean Environment Dynamics, Second Institute of Oceanography, Ministry of Natural Resources, Hangzhou, China, [4]Chinese Acadamy of Meteorological Science, Beijing, China

Based on the Lagrangian particle dispersion model, HYSPLIT 4.9, this study analyzed the summertime atmospheric moisture sources and transportation pathways affecting six subregions across China. The sources were: Midlatitude Westerly (MLW), Siberian-Arctic regions (SibArc), Okhotsk Sea (OKS), Indian Ocean (IO), South China Sea (SCS), Pacific Ocean (PO), and China Mainland (CN). Furthermore, the relative contributions of these seven moisture sources to summertime precipitation in China were quantitatively assessed. Results showed that the CN precipitation source dominates the interannual and interdecadal variation of precipitation in most subregions, except Southwest and South China. The Northeast China vortex and Pacific–Japan (PJ) teleconnection, which transport water vapor from the MLW, OKS and PO sources, are crucial atmospheric systems and patterns for the variation of precipitation in Northeast China. The interannual variation of precipitation in Northwest and North China is mainly dominated by mid–high-latitude Eurasian wave trains, which provide the necessary dynamical conditions and associated moisture transport from the MLW and SibArc sources. In addition, an enhanced western North Pacific subtropical high (WNPSH) accompanied by the East Asian–western North Pacific summer monsoon and PJ teleconnection, transports extra moisture to North China from the SCS and PO sources, as well to the Yangtze River Valley and South China. The Indian summer monsoon (ISM) is also critically important for the interdecadal change in precipitation over the Yangtze River Valley and South China, *via* the southwesterly branch of moisture transport from the IO source. The interdecadal changes in precipitation over Southwest China are determined by the IO and SCS sources, *via* enhanced WNPSH coupling with a weakened ISM. These results suggest that the interdecadal and interannual variations of moisture sources contribute to the attendant variation of summertime precipitation in China *via* large-scale circulation regimes in both the mid–high and lower latitudes.

Keywords: moisture source, atmospheric wave trains, east asian summer monsoon, Pacific-Japan teleconnection, Indian summer monsoon

OPEN ACCESS

Edited by:
Xander Wang,
University of Prince Edward Island, Canada

Reviewed by:
Shaobo Qiao,
Sun Yat-sen University, China
Yanju Liu,
National Climate Center, China

***Correspondence:**
Ruonan Zhang
rn_zhang@fudan.edu.cn

Specialty section:
This article was submitted to Interdisciplinary Climate Studies, a section of the journal Frontiers in Earth Science

Received: *11 August 2021*
Accepted: *20 October 2021*
Published: *19 November 2021*

Citation:
Zhang R, Chu Q, Zuo Z and Qi Y (2021) Summertime Moisture Sources and Transportation Pathways for China and Associated Atmospheric Circulation Patterns. Front. Earth Sci. 9:756943. doi: 10.3389/feart.2021.756943

INTRODUCTION

Interannual and interdecadal variations of summer precipitation over China are fundamentally controlled by water vapor transport (Zhou and Yu, 2005; Zhao et al., 2007; Sun and Wang, 2011; Zhu et al., 2011), dynamically associated with large-scale atmospheric circulation in both the lower and mid–high latitudes. The major atmospheric circulation regimes affecting the East Asian moisture pathways include the East Asian summer monsoon, western North Pacific subtropical high (WNPSH), Indian summer monsoon (ISM), midlatitude westerly (MLW), and Arctic Oscillation. Specifically, the subtropical high and summer monsoon transport water vapor from the South China Sea and western Pacific through southwesterly and southeasterly moisture branches to yield precipitation over eastern China (Wang and Chen, 2012; Sun and Wang, 2014a, 2014b). The ISM is critical for summertime precipitation over Southwest China (Tian and Fan, 2013) and the semiarid regions of China (Yatagai and Yasunari, 1995), mainly through the southwesterly branch of the moisture pathway that transports water vapor from the Indian Ocean. The MLW, which transports moisture from the Eurasian continent, has an impact on the westerly branch of moisture supply to South China during summer (Simmonds et al., 1999) and to northern China during winter (Gong et al., 2001; Zhou, 2011). In high-latitude regions, Arctic sea-ice loss and the North Atlantic Oscillation have additional influence on the moisture transport over Northwest China (Liu et al., 2012; Li and Wang, 2013; Zhang and Zhou, 2015; Hua et al., 2017) and North China (Zhang et al., 2018) through large-scale Eurasian wave trains. Besides these large-scale atmospheric regimes, local evapotranspiration is another crucial source of atmospheric moisture, which accounts for approximately 9.6% of total rainfall as estimated by the global annual mean recycling (Trenberth, 1999). Numaguti (1999) demonstrated that most of the summertime precipitation over the Eurasian continent is supplied by evaporation from the continental surface. Considering the complex regime of atmospheric water vapor transport over China (Zhou and Yu, 2005), the atmospheric sources are thus differing in distinct subregions of China. Although past studies have identified various moisture sources of regional precipitation, they do not provide a complete picture of affecting factors in both the lower and mid–high latitudes.

Typically, two types of numerical models are employed to simulate the atmospheric water cycle and to trace the trajectories of air parcels. One is the conventional Eulerian method, which diagnoses local sources of precipitable moisture over a fixed region and concerns the temporal variation of a fixed air parcel. Its disadvantage is its lack of a reasonable "source–receptor" linkage between the possible moisture source and the target precipitation regions. Given this deficiency, another effective method is the Lagrangian numerical model, which traces the origins of atmospheric water and the trajectories of specific air parcels over time. The most commonly used model is the Flexible Particle Dispersion Model (Stohl and James, 2005), which has been extensively employed to study the global water cycle (Gimeno et al., 2010; Chen et al., 2012; Chen et al., 2013; Viste and Sorteberg, 2013; Drumond et al., 2011; Sun and Wang, 2014a, Sun and Wang, 2014b). However, besides this model, the Hybrid Single-Particle Lagrangian Integrated Trajectory Model (HYSPLIT; Draxler and Hess, 1998) is helpful in studying global water vapor transport processes. For instance, Jiang et al. (2013); Jiang et al. (2017) utilized HYSPLIT to investigate water vapor transport characteristics over the Yangtze–Huaihe River valley during the mei-yu period and decadal changes in North China precipitation during the rainy season. Chen and Luo (2018) analyzed the sources and pathways of South China precipitation during the pre-summer rainy season. Chu et al. (2019) identified the role of moisture sources and transportation pathways in the variation of precipitation over East China and its linkage to tropical sea surface temperature. In the present study, HYSPLIT is employed to simulate the atmospheric moisture sources and physical pathways of summertime precipitation in six subregions across China.

Regionally speaking, most studies emphasize the moisture sources of summertime precipitation over East China (Sun and Wang, 2014b; Chu et al., 2019) and the semiarid grasslands (Yatagai and Yasunari, 1995; Huang et al., 2011; Sun and Wang, 2014a), whilst a complete picture of the moisture sources for precipitation over has yet to be thoroughly examined. Furthermore, elucidation of the possible mechanisms involved in regional precipitation variations has tended to focus on the tropical ocean and large-scale circulation systems, such as the East Asian and Indian summer monsoons and the MLW. Considering the complex atmosphere–ocean and tropics–extratropics interactions, however, current understanding of the atmospheric circulation regimes affecting subregional precipitation remains vague. Therefore, the aim of the present study was to quantitatively investigate the Northern Hemisphere atmospheric moisture sources for precipitation over the whole of China and their relative contributions to summertime precipitation over distinct subregions. Moreover, the critical atmospheric regimes acting as atmospheric bridges linking the moisture sources to the target precipitation regions were also examined.

DATA AND METHODS

Version 4.9 of HYSPLIT9, a Lagrangian particle dispersion model, was employed to trace air parcel trajectories before the air parcels arrived in target regions (Draxler and Hess, 1998). The 6-hourly and monthly geopotential height, horizontal and vertical wind, 2-m temperature, sea surface temperature, evaporation, precipitable water, and precipitation during 1979–2017, at a resolution of $1^{\circ} \times 1^{\circ}$, from the ERA-Interim reanalysis, were used as input data for the HYSPLIT model.

The air parcels in the middle and lower troposphere (500 m, 1,000 m, 1,500 m, 2,000 m, 2,500 m, 3,000 m, and 3,500 m) within a 10-day period (the average lifespan for atmospheric moisture; Trenberth et al., 2011) were selected to trace the trajectories at an acceptable accuracy. Given that HYSPLIT 4.9 may result in a disordering of water vapor trajectories, the K-means clustering

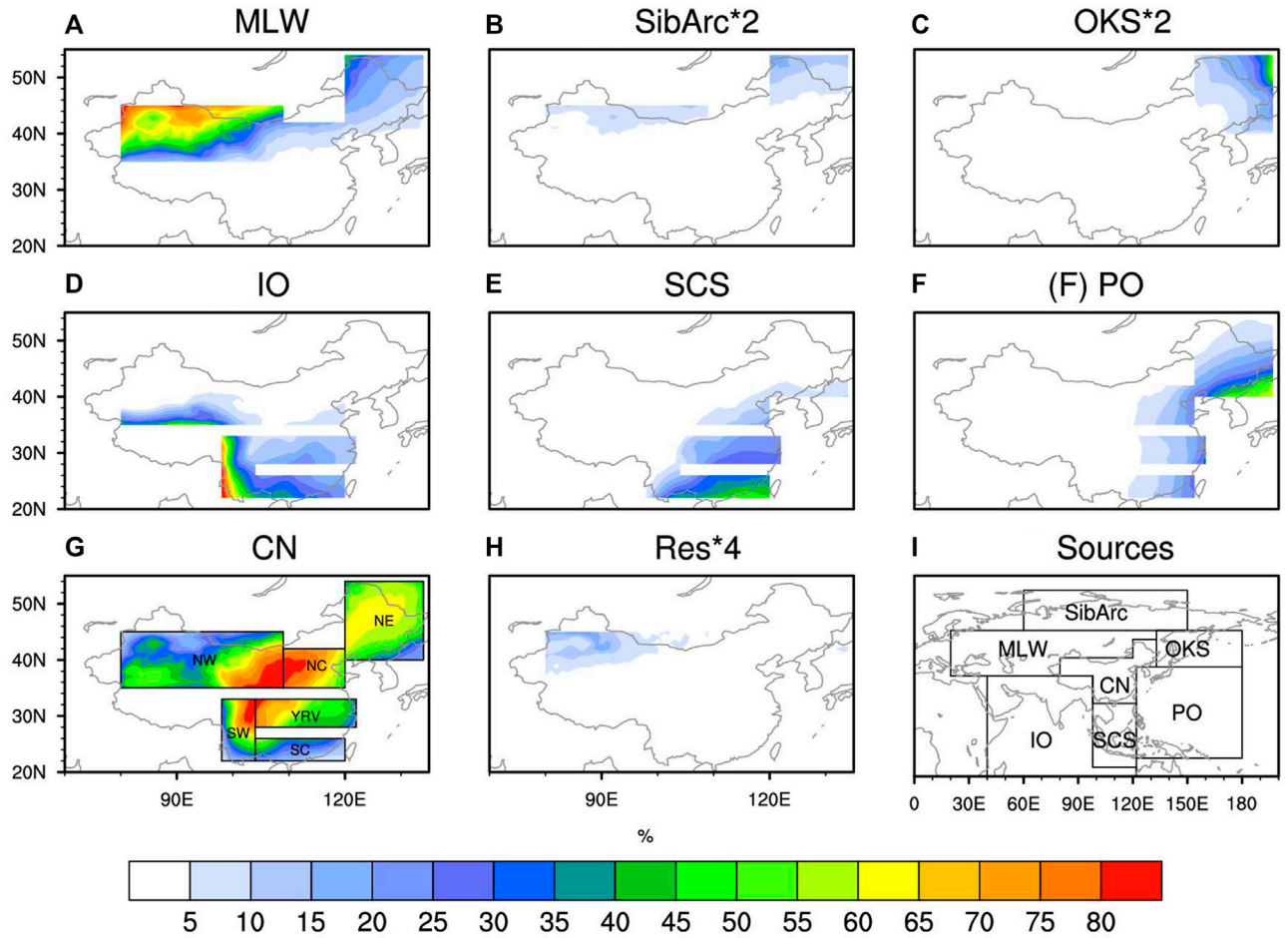

FIGURE 1 | Contribution rates (%) of seven moisture sources to summer precipitation over China: **(A)** MLW, **(B)** SibArc, **(C)** OKS, **(D)** IO, **(E)** SCS, **(F)** PO, **(G)** CN, and **(H)** residual. The magnitudes of the SibArc and OKS sources are doubled, and the residual source is quadrupled. The specific geographical division of sources is shown in **(I)**.

method was additionally used to cluster the trajectories (Chu et al., 2019). Several studies have expanded the usage of Lagrangian models and proposed the "moisture source attribution method (Sodemann and Stohl, 2009)" and "areal source–receptor attribution method (Sun and Wang, 2014a; Sun and Wang, 2014b)" to quantitatively compute the moisture variation along the air parcel trajectories. These methods are efficient in evaluating the relative contribution of the evaporation source to the precipitation in the target location. In this study, the air parcel trajectory and precipitation data were derived from the HYSPLIT 4.9 outputs, which were then employed to quantify the relative contributions of various moisture sources and to distinct target regions (Emil et al., 2016; Chu et al., 2019). This model also has a disadvantage in that it considers only one "evaporation (uptake)-precipitation (release)" cycle within 10 days–the mean time of one atmospheric water cycle process.

Given the complex nature of affecting regimes, we focused on seven moisture source regions in the Northern Hemisphere: the MLW, Siberian-Arctic regions (SibArc), Okhotsk Sea (OKS), Indian Ocean (IO), South China Sea (SCS), Pacific Ocean (PO), and China Mainland (CN). The residual sources are labeled as Res, as shown in **Figure 1**. Thereinto, it should be noted that the water vapor carried over the South China Sea and China Mainland were calculated independently because of their influence by several moisture transport branches. In addition, six target subregions in China were selected to provide a complete picture for China as a whole: Northwest China (NW), North China (NC), Northeast China (NE), Yangtze River Valley (YRV), South China (SC), and Southwest China (SW).

To further identify the critical atmospheric patterns that affect the variations of subregional precipitation, a series of atmospheric pattern indices were defined. The metrics are shown below:

1) The Pacific–Japan (PJ) teleconnection is a dominant pattern in the Northwest Pacific and East Asian region that features an anomalous dipole of lower tropospheric circulation over the Philippine Sea and the midlatitudes around Japan (Nitta, 1987). Conventionally, the PJ index is calculated from the leading mode of 850-hPa vorticity over the Northwest Pacific

[10°–55°N, 100°–160°E (Kosaka and Nakamura, 2010)]. In this study, we defined the PJ index with a pointwise method: Z (45°N, 140°E) − Z (20°N, 140°E) − Z (60°N, 140°E), where Z denotes the 500-hPa geopotential height. This PJ index is highly correlated with the classical one, with a correlation coefficient of 0.61, suggesting its representativeness of the classical PJ pattern.

2) The East Atlantic/West Russia pattern is a prominent teleconnection pattern that affects the Eurasian climate and characterized by positive height anomalies over Europe and northern China and negative anomalies over the central North Atlantic and north of the Caspian Sea (Barnston and Livezey, 1987). Here, we defined a high-latitude Eurasian wave train index as Z (60°N, 75°E) − Z (60°N, 30°E) − Z (40°N, 135°E), and a midlatitude Eurasian wave train index as Z (60°N, 50°E) − Z (40°N, 75°E) + Z (30°N, 110°E), where Z again denotes the 500-hPa geopotential height. The correlation coefficients between the East Atlantic/West Russia index and high- and midlatitude Eurasian wave train indices are −0.12 and −0.65, respectively, suggesting a similarity between the East Atlantic/West Russia pattern and the midlatitude Eurasian wave train pattern.
3) Following Wang et al. (2001), the WNPSH index was defined as the areal-averaged 850-hPa geopotential height within 15°–25°N and 115°–150°E.
4) Following Wang and Fan (1999), the ISM index was defined as the areal-averaged 850-hPa zonal wind between (5°–15°N, 40°–80°E) and (20°–30°N, 70°–90°E)—the former minus the latter.
5) A Northeast China Vortex index was defined as the area-averaged 500-hPa geopotential height over 40°–50°N and 110°–130°E.

RESULTS

Relative Contributions of the Seven Moisture Sources

Figure 1 shows the relative contribution rates of the seven moisture sources to the climatological summer precipitation over China. The results are then further summarized in **Figure 2** as a pie chart. In addition, the moisture trajectories of air parcels 10 (8, 6, 4, and 2) days before reaching each subregion is presented in **Figure 3**. It should be noted that a fair amount of the air parcels move at high latitudes, whereas the evaporation and release of moisture are mainly cycled at relatively lower latitudes. Broadly speaking, most air parcels arriving in the three northern subregions (i.e., Northwest, North and Northeast China) originate from the CN, MLW, SibArc and OKS sources, whereas air parcels that arrive in the southern subregions (i.e., Southwest, South and Southeast China) are governed predominantly by the tropical ocean and CN sources. Specifically, the precipitation center of the MLW source is located in Northwest and Northeast China, with area-averaged contribution rates of approximately 29.4 and 14.4%, respectively (**Figures 1A**, **2A**,C). The precipitation of the SibArc and OKS sources contributes little to summertime precipitation over the whole of China (around 1–7%), and the target region is spatially confined to Northwest and Northeast China, which is located in the vicinity of the source origins (**Figures 1B,C**). The moisture trajectory of the MLW, SibArc and OKS sources can also be seen from the evolution of air parcel locations 10–2 days before reaching Northwest and Northeast China (**Figures 3A,C**). Regarding the tropical ocean sources, the IO source precipitation plays a decisive role in the precipitation of southwestern China (48.4%), with the magnitude then decreasing northeastward radically from Southwest to Northwest China, the YRV, and South China (**Figures 1D**, **2A,C–E**, **3D–F**). The SCS and PO sources precipitations have similar impacts on East China (**Figures 1E,F**, **3D–F**). The main difference is that the former makes a more prominent contribution to the precipitation of South China, with the contribution rate decreasing with latitude (**Figures 1E**, **2F**, **3F**), while the latter mainly affects the precipitation of Northeast China and the contribution rate weakens westwards from coastal to inland regions (**Figures 1**, **2C**, **3D–F**).

In addition to the six remote sources, most air parcels arriving in China are primarily dominated by the local CN source (**Figures 1G**, **2**, **3**). Notably, considering the local evaporation, the contribution rates of the CN source precipitation differ considerably among the different regions—roughly between 25.8 and 68.3%. The center of China, including the North–Northwest China, YRV and Southwest China subregions, is overwhelmingly influenced by moisture transport from surrounding areas (~80%), which arguably reflects the strong feedback of local evaporation. This finding is consistent with those of Numaguti (1999) and Sun and Wang (2014b), who attributed continental evaporation as the primary origin for continental precipitation. Technically, the contribution of the CN source appears to be overestimated, partially due to the 10-day tracing method, which considered only one process of evaporated moisture uptake, transport and release and therefore omitted any distant transport beyond 10 days. To sum up, these seven sources cumulatively account for greater than 95% of the total summertime precipitation, which may provide valuable precursors for synoptic-scale rainfall forecasts. The remaining contributions will come from residual sources across the globe, especially for the precipitation of Northwest China (**Figure 1H**).

Figure 4 shows the variations of total precipitation and relevant sources of precipitation in the different subregions of China. For each subregion, summertime precipitation shows distinct interdecadal and interannual variations. Broadly speaking, the interannual components of precipitation explain larger amounts of the total variance than the interdecadal components (**Table 1**). The precipitation of Northwest China and its CN source display a similar increasing trend from 1979, superimposed with clear interannual variations (**Figure 4A**), and their correlation coefficient is high at 0.92 (**Table 2**). Their interdecadal components explain approximately 18% of the total variance, with the remaining 82% from interannual timescales. The MLW and IO sources (i.e., the 2nd and 3rd) show clear interannual variations, accounting for 88 and 97% of the total variance, respectively. In comparison, the summertime precipitation in North–Northeast China, the YRV, and South

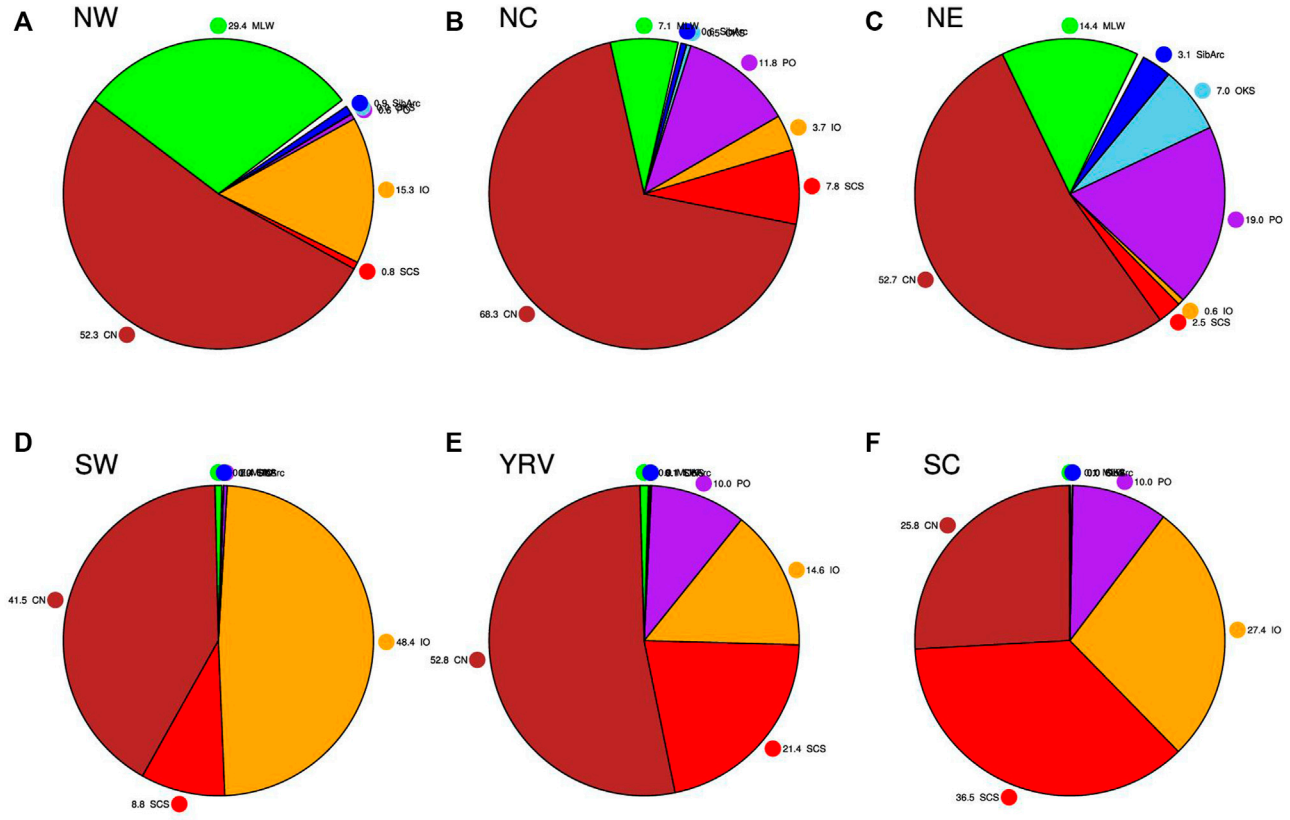

FIGURE 2 | Pie chart of the relative contributions of the seven moisture sources to total precipitation in the six subregions: **(A)** NW, **(B)** NC, **(C)** NE, **(D)** SW, **(E)** YRV, and **(F)** SC.

China show similar interdecadal variations superimposed with interannual variation, which is characterized by a consecutively southward retreat of summertime precipitation on interdecadal timescales (**Figures 4B–E**). In particular, the interdecadal component of YRV precipitation accounts for 44% of the total variance. Specifically, there is increased rainfall in Northeast China peaking in the mid-1980s, a southward displacement to North China peaking in the early 1990s, a rapid southward shift to the middle and lower YRV peaking at 1998, and then a further extension to South China peaking in the early 2000s. The decadal evolution of rain belts is consistent with the findings of previous studies (Ding et al., 2009; Zhu et al., 2011; Chu et al., 2019), which reported similar features in terms of a southward retreat. One common trait they share is the crucial role of moisture from the CN source in terms of total precipitation. For North China, around 68.3% of the total precipitation is determined by the CN moisture source, while 11.8% is determined by the PO moisture source (**Figures 2B**, **3B**). Similarly, the CN and PO moisture transport pathways account for 52.7 and 19% of the rainfall in Northeast China, respectively, and show noticeable interdecadal variations (explained variances of 24 and 12%, respectively), whilst the MLW moisture transport pathway displays evident interannual variability (explained variance of 86%). For the YRV and South China, the SCS moisture source plays a secondary and a dominant role in total rainfall, respectively, featuring similar interdecadal variations with an explained total variance of roughly 46%. In addition, the IO source makes interdecadal contributions to the rainfall in the YRV and South China (explained variance of 29 and 22%, respectively), and the PO source makes interannual contributions (93 and 99%, respectively). As for Southwest China, the interdecadal change in precipitation is distinct from the other subregions, being characterized by decreasing rainfall from 1979 and increasing rainfall since the early 2000s, and the explained variance of the interdecadal component is 15% (**Figure 4F**). Almost identical interdecadal changes are found for the SCS source, with an explained variance of 19%, whilst similar interannual variations exist for the CN and IO sources, both with an explained variance of 95%. These results suggest that the variations of summertime precipitation differ among the six subregions of China, which is fundamentally due to the significant variations in moistures source and their relative contributions.

Role of Large-Scale Atmospheric Circulation

To better understand the causes and mechanisms involved in the variations of summertime precipitation in China, we analyzed the large-scale atmospheric circulation anomalies associated with the

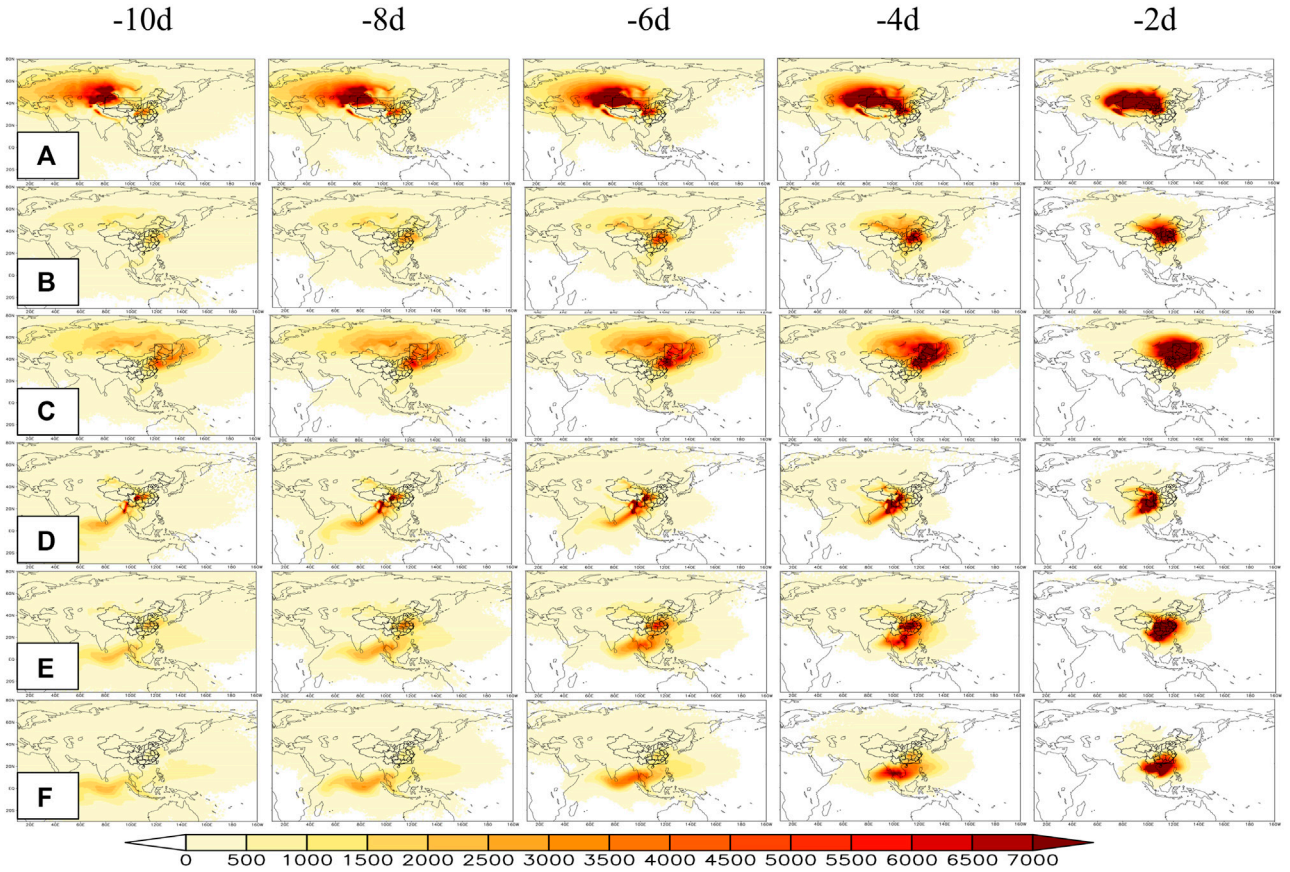

FIGURE 3 | Moisture trajectories of air parcels 10 (8, 6, 4, and 2) days before reaching the six subregions: **(A)** NW, **(B)** NC, **(C)** NE, **(D)** SW, **(E)** YRV, and **(F)** SC.

moisture sources. The key circulation patterns were identified to investigate their impacts on summertime precipitation in the different subregions. **Figures 5–10** show the water vapor flux anomalies accumulated in the lower–middle troposphere and 500-hPa geopotential height anomalies regressed on the precipitation source, and the correlation of the precipitation source anomalies with the key atmospheric circulation pattern indices.

For Northwest China (**Figure 5**), the CN, MLW, IO and SibArc sources are the four leading ones, accounting for 52.3, 29.4, 15.3 and 0.9% of the total precipitation, respectively. The circulation pattern associated with the MLW source shows an evident Eurasian wave train, with anomalously high pressure over a region covering Siberia to the Kara Sea and anomalously low pressure over the regions of North Europe and North Asia to Japan (**Figure 5B**). Such a high-latitude wave train is also apparent in the circulation pattern associated with the SibArc source (**Figure 5D**). Note that the circulation anomalies over the region from the Arctic to the North Atlantic project largely to the negative phase of the North Atlantic Oscillation, consistent with Hua et al. (2017). However, for the CN source, there is a fairly weak high-latitude wave train pattern over the Eurasian continent, and the circulation anomalies over China are insignificant (**Figure 5A**), suggesting an important contribution from local evapotranspiration. For the IO source, a similar but slightly southward-shifted wave train is identifiable over the midlatitudes extending from Europe to China and resembling the East Atlantic/West Russia pattern. Meanwhile, enhanced easterly winds are apparent over the northern India, representing an enhanced ISM (**Figure 5C**). Here, we define a high-latitude and a midlatitude wave train index, as described in *Data and Methods*. The commonality of the high-latitude and midlatitude wave trains is the cyclonic anomaly over northern China and the anticyclonic anomaly over southern China associated with the enhanced ISM. The cyclonic circulation anomaly facilitates cold-air outbreaks from high latitudes, and the anticyclonic tropospheric anomaly favors moisture transport from the tropical oceans. Therefore, the northwesterly and southwesterly branches of moisture pathways converge in Northwest China, resulting in excessive precipitation over northern and southern Northwest China, respectively (**Figures 5E–H**).

For North China (**Figure 6**), the CN, PO, MLW and SCS sources tend to be the major contributors, with contribution rates of 66.3, 11.8, 7.8 and 7.1%, respectively. The critical role of the CN source is in agreement with previous studies reporting that evaporation from the land area over and south of North China is the most important contributor (around 61.1%) to

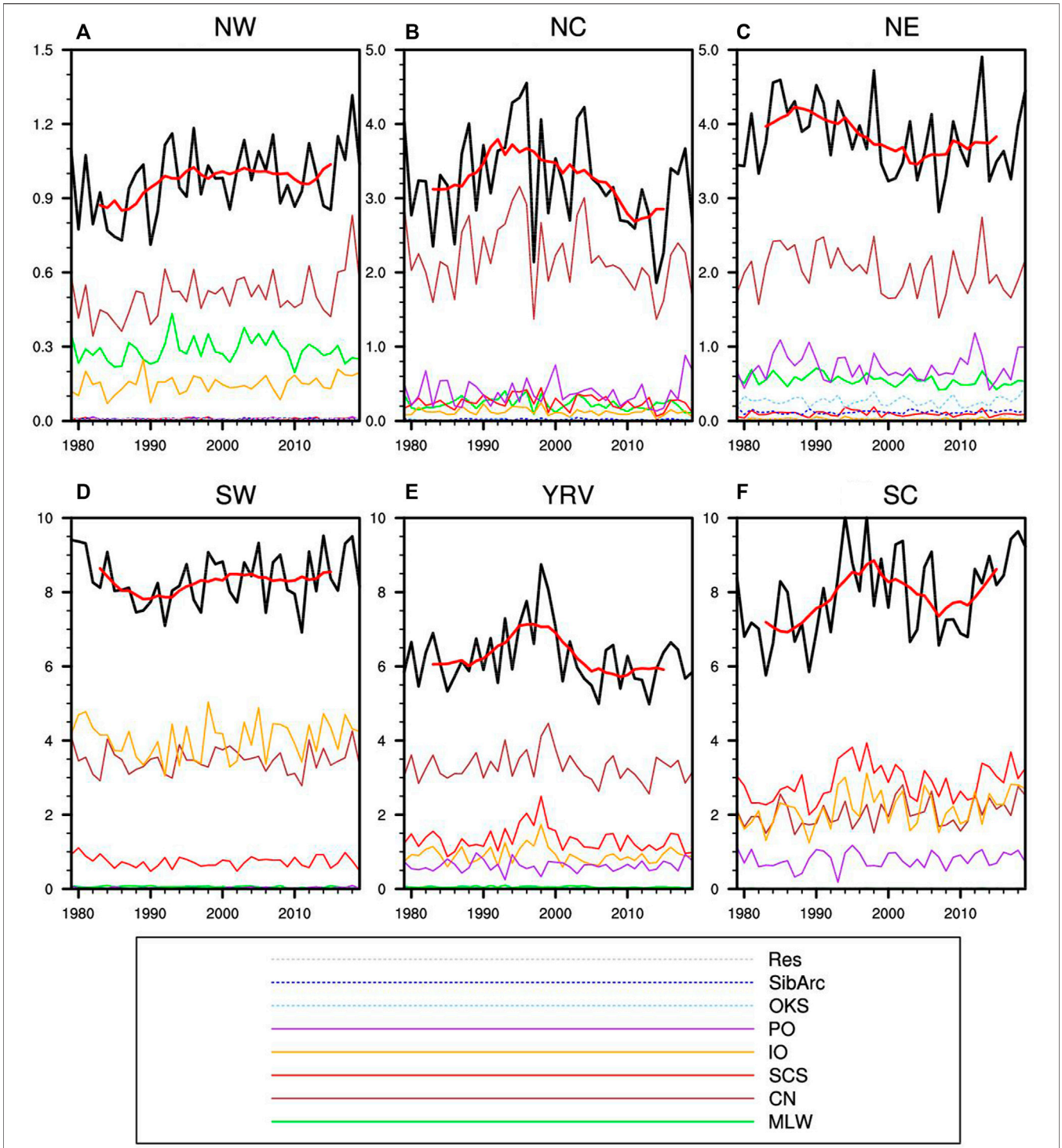

FIGURE 4 | Total precipitation (black) and the related seven moisture sources precipitation (colors) (units: mm/day) area-averaged over the six subregions: **(A)** NW, **(B)** NC, **(C)** NE, **(D)** SW, **(E)** YRV, and **(F)** SC. The thick red lines overlaid on the black lines denote the 9-year running average of the total precipitation. The green, brown, red, orange, purple, sky-blue, blue and gray lines denote the MLW, CN, SCS, IO, PO, OKS, SibArc and Res sources, respectively.

the summertime rainfall in North China (Sun and Wang, 2014; Chu et al., 2019). The circulation patterns related to the CN and MLW sources are a similar high-latitude wave train, and the anomalously low center over Northeast China will certainly lead to a uniform increase in summertime precipitation over North China (**Figures 6A,C**). In particular, the MLW source gives rise to

TABLE 1 | Explained variances of summertime total and source precipitation in different regions by the interannual and interdecadal component.

	Interannual component						Interdecadal component					
	NW	**NC**	**NE**	**YRV**	**SC**	**SW**	**NW**	**NC**	**NE**	**YRV**	**SC**	**SW**
Total	82%	68%	76%	56%	66%	85%	18%	32%	24%	44%	34%	15%
MLW	88%	90%	86%	77%	95%	77%	12%	10%	14%	23%	5%	23%
CN	83%	71%	76%	75%	89%	95%	17%	29%	24%	25%	11%	5%
SCS	91%	80%	82%	54%	54%	81%	9%	20%	18%	46%	46%	19%
IO	97%	86%	81%	71%	78%	95%	3%	14%	19%	29%	22%	5%
PO	99%	91%	88%	93%	99%	98%	1%	9%	12%	7%	1%	2%
OKS	84%	89%	98%	94%	84%	83%	16%	11%	2%	6%	16%	17%
SibArc	97%	91%	99%	91%	90%	96%	3%	9%	1%	9%	10%	4%

TABLE 2 | Correlation coefficients between total precipitation and related source precipitation in different subregions. Asterisks denote correlation coefficients exceeding the 95% confidence level.

	NW	**NC**	**NE**	**YRV**	**SC**	**SW**
MLW	0.64*	0.56*	0.65*	0.45*	0.12	−0.04
CN	0.92*	0.97*	0.92*	0.90*	0.76*	0.62*
SCS	0.53*	0.71*	0.48*	0.89*	0.80*	0.41*
IO	0.55*	0.61*	0.38*	0.84*	0.88*	0.83*
PO	0.46*	0.37*	0.63*	−0.27	0.24	0.20
OKS	0.22	0.06	0.39*	0.24	−0.16	−0.05
SibArc	0.38*	0.53*	−0.06	0.15	0.02	−0.18

a rainfall belt across North China (**Figure 6G**). Besides the CN source, the PO is the most significant source of moisture and dynamics for precipitation in North China. An apparent meridional wave train that closely resembles the positive phase of the PJ teleconnection pattern acts as an atmospheric bridge linking the PO moisture source to rainfall in North China, accompanied by cyclonic (anticyclonic) anomalies in the tropical (midlatitude) Northwest Pacific (**Figure 6B**). Such anomalously strong convective activity over the tropics tends to the promotion of a Rossby wave teleconnection in the poleward direction (Kosaka and Nakamura, 2010). The East Asian–western North Pacific monsoon (Wang et al., 2008) provides an additional source of moisture from the PO for the abundant rainfall over eastern North China (figure not shown). In addition, the SCS source is associated with an enhanced WNPSH, which brings abundant water vapor along the western margin of the subtropical high (**Figure 6D**). This finding is consistent with those of Ding et al. (2009) and Jiang et al. (2017) who reported that the southwesterly moisture transport associated with the PO and SCS sources is the dominant moisture pathway for variations of North China precipitation. In summary, the mid–high-latitude wave train, subtropical high, and PJ teleconnection are dominant circulation systems for North China precipitation.

Figure 7 shows the major circulation patterns that govern the variations of Northeast China precipitation. The CN, PO, MLW and OKS sources explain 52.7, 19, 14.4 and 7% of total rainfall, respectively. A common feature for the circulation anomalies is the prominent cyclonic anomaly over Northeast China, which can be regarded as the Northeast China vortex—the classic climate system affecting northern China. This pattern is especially evident in the circulation patterns associated with the CN, MLW and OKS sources (**Figures 7A,C,D**). It is reasonable to assume that the Northeast China vortex converges together the water vapor branches from the west (MLW source), south (CN source), and east (OKS source), and thus produces heavy rainfall over vast regions of North and Northeast China (**Figures 7E,G,H**). However, an anticyclonic circulation system associated with the PO source is identifiable over the Okhotsk Sea, reflecting the remote influence of the PJ teleconnection (**Figure 7B**). The southwesterly moisture transmission branch transports moisture from the PO along the western margin of the anticyclone and yields excessive rainfall over East China (**Figure 7F**). In addition, the precipitation over Northeast China might be influenced by the East Asian summer monsoon, which transports water vapor from the SCS source (Sun et al., 2017)—something that can also be seen in the OKS-related circulation pattern (**Figure 7D**). To sum up, summertime precipitation in northern China, including the Northwest, North and Northeast China subregions, is primarily affected by atmospheric regimes in in mid–high-latitudes, such as mid–high-latitude wave trains, the Northeast China vortex, and the PJ teleconnection. The exception is that the subtropical high has additional impacts on North China precipitation and the ISM has extra effects on Northwest China precipitation.

Considering the complex regime of atmospheric water vapor transport over northern and southern China (Zhou and Yu, 2005), the atmospheric sources of the southern subregions could be different from those of the northern subregions. Aside from North China, the YRV and South China subregions are significantly affected by the East Asian summer monsoon and subtropical high. Therefore, there will be intrinsic linkages among the summertime precipitation in these three subregions. For instance, the anomalously stronger East Asian summer monsoon brings excessive rainfall to North and South China and insufficient rainfall to the YRV. Such an out-of-phase relationship in rainfall is linked to the variability of the East Asian monsoon (Ding et al., 2009). Summertime precipitation in the YRV is predominantly controlled by the CN (52.8%), SCS (21.4%), IO (14.6%), and PO (10%) sources, which together account for approximately 98% of total precipitation (**Figure 2E**). These relative contributions of moisture sources are slightly distinct from those reported by Chu et al. (2019), partly due to the different methods used for classifying water vapor sources. In the present study, the CN precipitation source

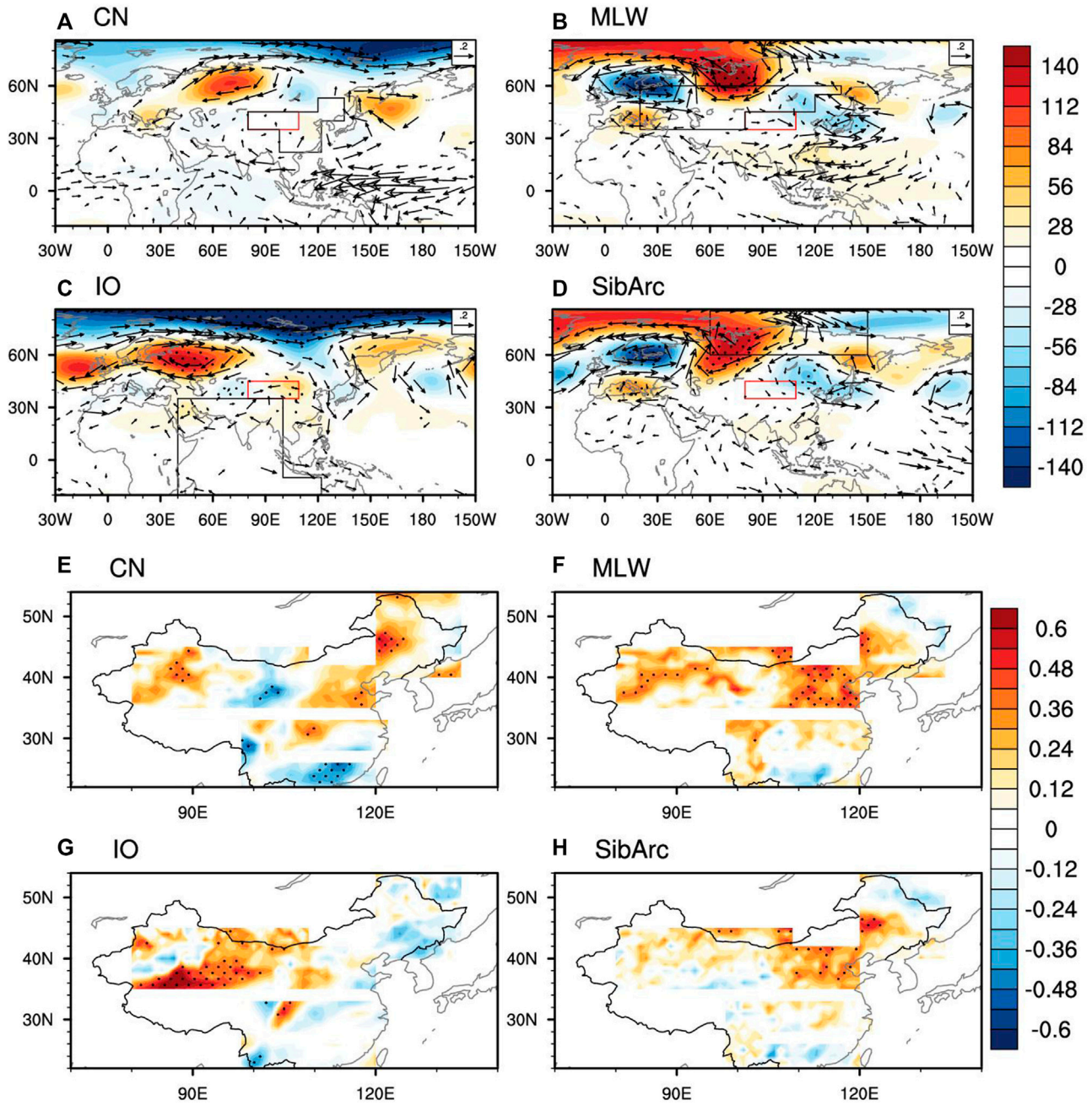

FIGURE 5 | (A–D) 500-hPa geopotential height and vertical accumulation of lower–middle tropospheric water vapor flux regressed against the CN, MLW, IO and SibArc sources of NW precipitation. Panels **(E–H)** show the correlation coefficients between the CN, MLW and SibArc moisture sources, and the high-latitude wave train index, and between the IO moisture source and the midlatitude wave train index. The red (black) box denotes the target (moisture source) region. Stippling denotes the statistical significance of regression and correlation values at the 95% confidence level.

for the YRV is controlled by southwesterly and northerly moisture branches, which transport moisture from southern China and North–Northeast China, respectively (**Figure 8A**). This suggests that, similar to North China rainfall (Sun and Wang, 2014), the YRV rainfall largely originates from the evaporation taking place over land areas, rather than oceanic factors (Wei et al., 2012). In addition, a strengthened subtropical high, along with a weakened East Asian summer monsoon (figure not shown), is the key contributor to the southwesterly moisture pathway of YRV rainfall, which carries water vapor from the SCS and IO sources (**Figures 8B,C**), consistent with the findings of Fan et al. (2008) and Wang and Chen (2012). Simultaneously, a weakened ISM is apparent alongside the strengthened subtropical high (**Figure 8C**), which corresponds to more rainfall over the

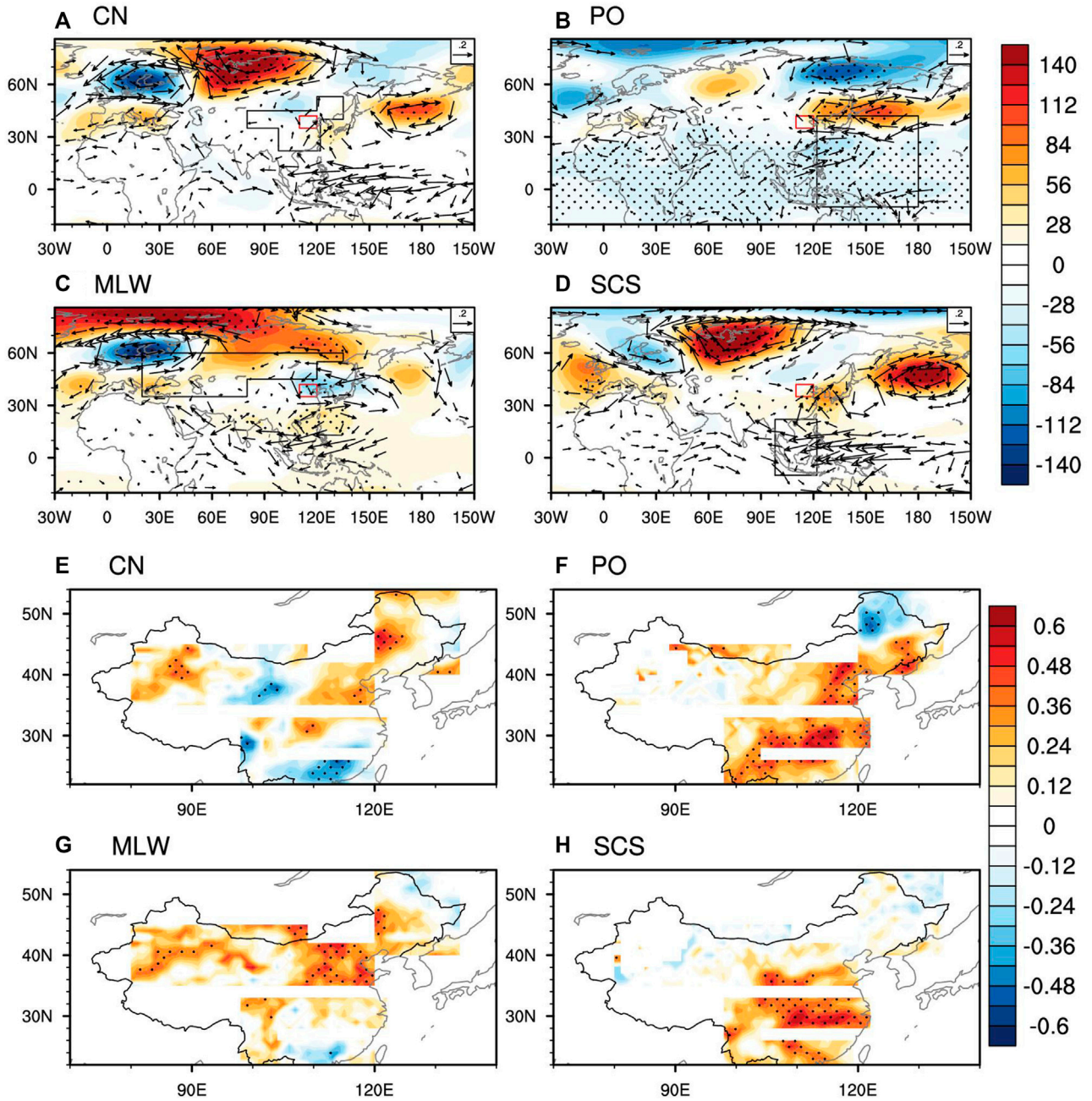

FIGURE 6 | As in **Figure 5** but for NC. Panels **(A–D)** show circulation anomalies regressed against the CN, PO, MLW and SCS moisture sources. Panels **(E–H)** show the CN and MLW source precipitation anomalies correlated with the high-latitude wave train index, the PO source with the PJ index, and the SCS source with the WNPSH index.

YRV, consistent with the conclusion in Zhang (2001). The PJ teleconnection appears to be closely linked with the PO precipitation source (**Figures 8D,H**). The aforementioned out-of-phase relationship with total precipitation is reproduced in the CN and IO precipitation sources (**Figures 8E,G**). These results indicate that the subtropical high and PJ pattern provide uniformly excessive summertime rainfall over the whole of East China, while the evaporation from land areas and the ISM provide additional information for the uneven distribution of East China rainfall.

In comparison, the precipitation in South China is dominated by the SCS, IO, CN and PO sources (**Figure 9**), with contribution rates of 36.5, 27.4, 25.8 and 10%, respectively. Note that CN is no longer the primary source for South China precipitation owing to the increased influence from the tropical oceans. Like the YRV, the precipitation in South China is affected primarily by

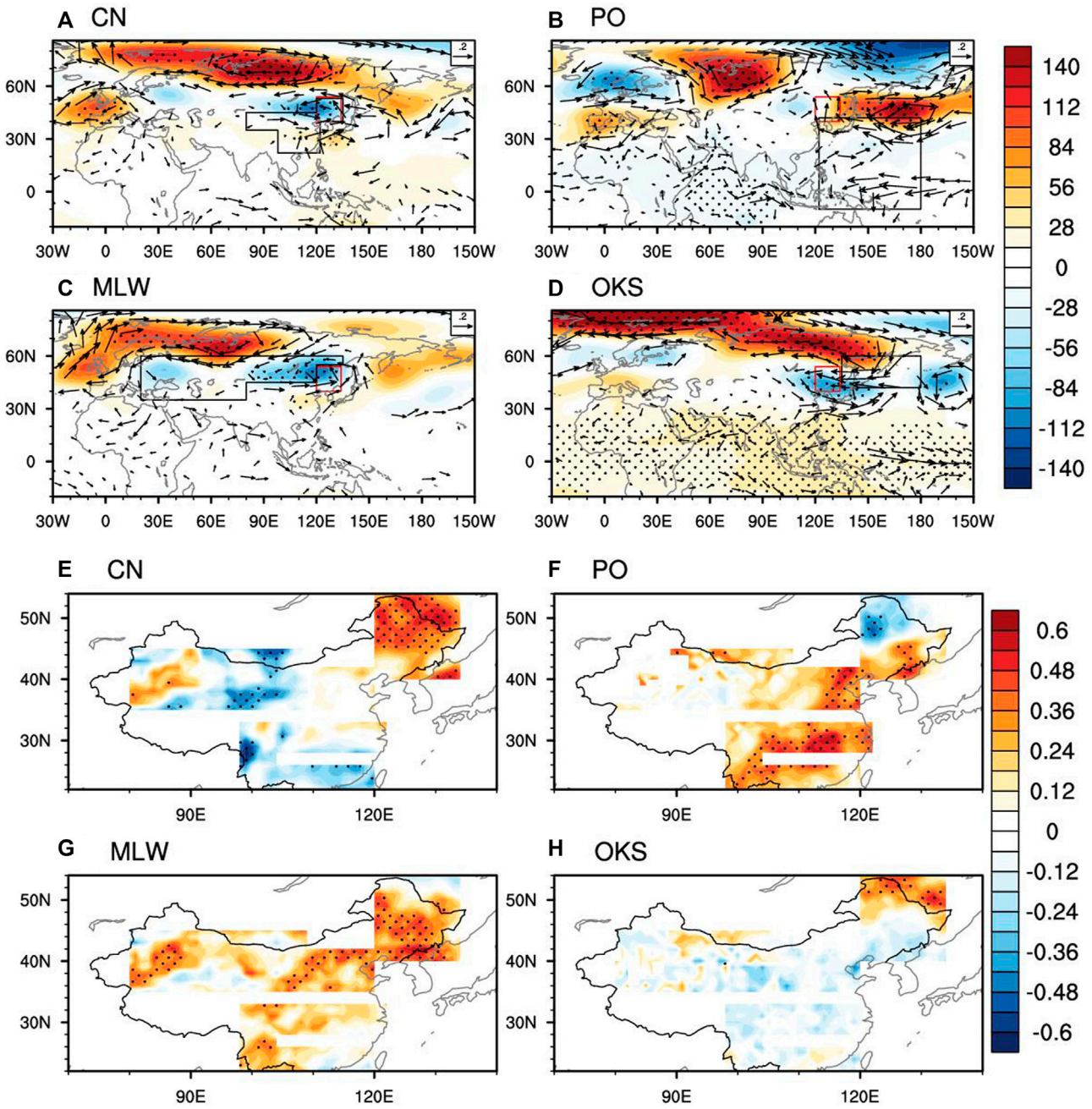

FIGURE 7 | As in **Figure 5** but for NE. Panels **(A–D)** show circulation anomalies regressed against the CN, PO, MLW and OKS moisture sources. Panels **(E–H)** show the CN, MLW and OKS source precipitation anomalies correlated with the NE vortex index, and the PO source with the PJ index.

enhanced southerly winds from the SCS source, corresponding to an intensified subtropical high (**Figure 9A**). On the contrary, a weakened subtropical high and enhanced East Asian–western North Pacific monsoon can also bring water vapor from land evaporation over the north of South China (**Figure 9C**), resulting in less rainfall over the YRV and, in turn, heavy rainfall over South China (**Figure 9G**). In addition, a weakened ISM transports water vapor from the Indian Ocean through the westerly branch of moisture pathways over northern India (**Figure 9B**), leading to excessive IO-source precipitation over western South China (**Figure 9F**). The PO source further causes spatially restricted rainfall over South China through the PJ teleconnection and the enhanced monsoon (**Figures 9D,H**). These results suggest that the moisture transport from the SCS and IO sources dominates the variation in South China precipitation (Sun and Wang, 2014; Chu et al., 2019) through a strengthened subtropical high and weakened ISM. Conversely, land evaporation from CN becomes less important, particularly

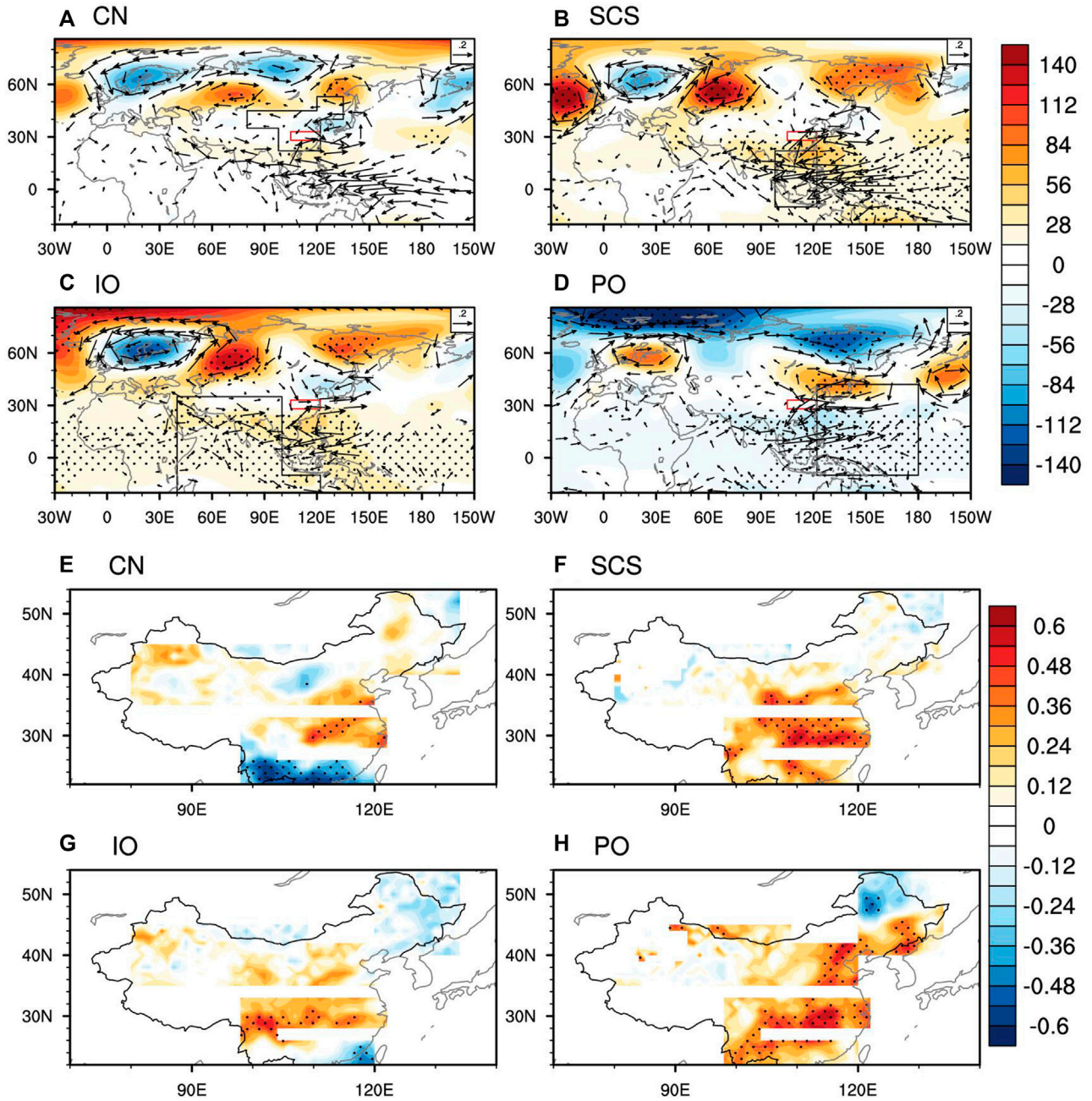

FIGURE 8 | As in **Figure 5** but for the YRV. Panels **(A–D)** show circulation anomalies regressed against the CN, SCS, IO and PO moisture sources. Panels **(E–H)** show the CN, SCS and IO source precipitation anomalies correlated with the WNPSH index, and the PO source with the PJ index.

relative to YRV and North China precipitation, with moisture contributions mainly from the YRV region or the PO through a weakened subtropical high.

The relative contributions to precipitation in Southwest China are distinct from those of other subregions in that the IO (48.4%), CN (41.5%) and SCS (8.8%) are the primary sources for Southwest China precipitation, which together explain 99.1% of the total precipitation (**Figure 10**). The amplified subtropical high, along with weakened ISM, brings water vapor from the Bay of Bengal and the Indian Ocean *via* a southwesterly pathway (**Figure 10A**). These two branches of moisture pathways result in strong convergence and hence heavy rainfall over Southwest China (**Figure 10D**). Similarly, the intensified subtropical high associated with the SCS source also transports moisture from the PO through the southeasterly moisture branch (**Figure 10C**), resulting in a belt of heavy rain

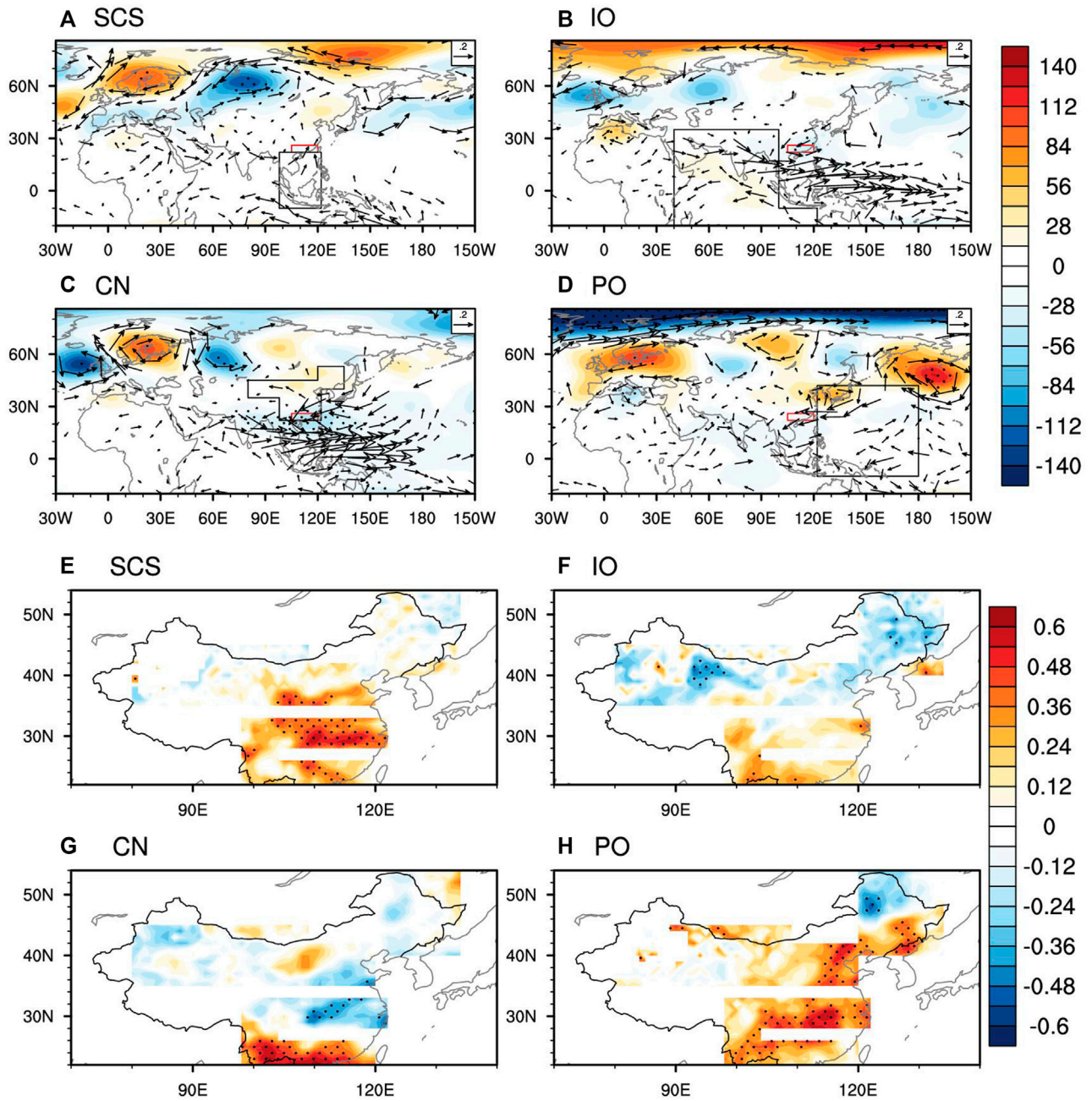

FIGURE 9 | As in **Figure 5** but for SC. Panels **(A–D)** show circulation anomalies regressed against the SCS, IO, CN and PO moisture sources. Panels **(E–H)** show the SCS source precipitation anomalies correlated with the WNPSH index, the IO source with the reversed ISM index, the CN source with the reversed WNPSH index, and the PO source with the PJ index.

over the whole of southern China and southern North China (**Figure 10F**). Conversely, the CN source is associated with a weakened subtropical high and enhanced East Asian–Western North Pacific monsoon, albeit the pattern is more zonally orientated, with the easterly winds bringing moisture transport from the evaporation over land areas (**Figure 10B**). This indicates that the heavy rainfall over South China can provide further evaporation sources for Southwest China precipitation (**Figure 10E**). To sum up, different from northern China, the three southern China subregions are primarily controlled by atmospheric circulation regimes associated with tropical ocean origins south of the mainland, such as the subtropical high, East Asian summer monsoon, and ISM.

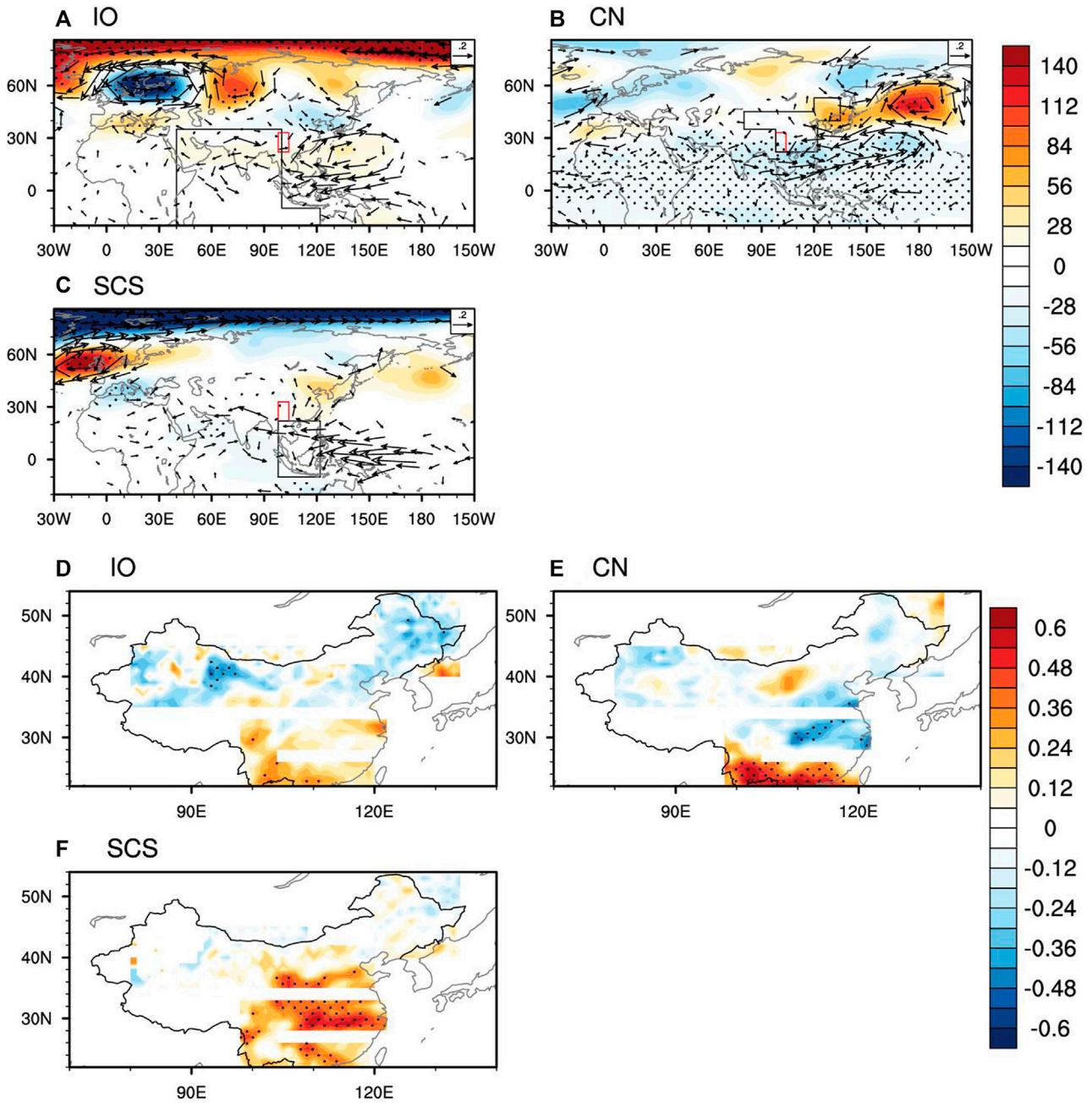

FIGURE 10 | As in **Figure 5** but for Southwest China. Panels **(A–C)** show circulation anomalies regressed against the IO, CN and SCS moisture sources. Panels **(D–F)** show the IO source precipitation anomalies correlated with the reversed ISM index, the CN source with the reversed WNPSH index, and the SCS source with the WNPSH index.

CONCLUSION

In this study, version 4.9 of the HYSPLIT model was used to quantitatively simulate the potential moisture sources (i.e., MLW, SibArc, OKS, IO, SCS, PO, and CN) and transport features for the interannual and interdecadal variation of summertime precipitation in six subregions of China. In addition, the large-scale atmospheric circulation regimes and associated mechanisms for these source–receptor linkages were further analyzed. Based on the 10-day trajectories of air parcels, the relative contributions of different moisture sources were calculated. The main results can be summarized as follows:

The CN, MLW, IO and SibArc sources of precipitation account for 52.3, 29.4, 15.3 and 0.9% of the precipitation in Northwest China, respectively, and thus the CN source dominates the increasing trend of precipitation in this region

and the MLW and IO sources govern the interannual and interdecadal variation. Mid–high-latitude wave trains are the dominant regimes for excessive rainfall over Northwest China, *via* the transport of moisture from evapotranspiration in Eurasian land areas, as well as from the Arctic and the Indian Ocean.

For North China, the precipitation originating from evapotranspiration in land areas (66.3%) is strong, in which a high-latitude wave train and the WNPSH are dynamically involved in the underlying mechanisms. The PO, MLW and SCS sources are essential for the interannual variation of summertime precipitation, with the PJ teleconnection, mid–high-latitude wave train, and East Asian summer monsoon transporting moisture *via* the easterly, westerly and southwesterly branches.

Likewise, precipitation originating from evapotranspiration over land areas is the key contributor to the variation in Northeast China precipitation. The Northeast China vortex, which transports water vapor from the CN, MLW and OKS sources, is the major regime affecting the summertime climate over Northeast China. The PJ teleconnection has an additional impact through the southeasterly branch of moisture transport from the PO. Meanwhile, the contributions from the SibArc and SCS sources can not be neglected (3.1 and 2.5%)

For the YRV, similarly, land evapotranspiration and the SCS and IO sources are the predominant moisture sources for the variation of precipitation, mainly through the southwesterly branch of moisture transport pathways *via* intensified subtropical high coupling with a weakened East Asian monsoon and ISM. The Asian monsoon appears to have opposite impacts on summertime precipitation over the YRV and South China subregions. Additionally, the PJ teleconnection contributes to the variation of summertime rainfall through the easterly branch of moisture transport from the PO.

The moisture sources for precipitation in South and Southwest China are distinct from those of the northern subregions, suggesting that tropical ocean sources are key contributors to precipitation in southern subregions, rather than the CN source. The SCS and IO sources are the major ones in terms of the interdecadal change in South China precipitation, largely due to the southerly and westerly winds associated with the subtropical high and weakened ISM. Besides, the CN source contributes to 25.8% of total rainfall, with most of the land evapotranspiration coming from the YRV region.

For Southwest China, the weakened ISM accompanying the enhanced subtropical high, associated with the IO source, leads to the convergence of water vapor over Southwest China, resulting in excessive rainfall. The second contributor would be the CN source, which transports water vapor from South China through an oppositely weakened subtropical high.

The present study builds upon some already considerable advances in understanding the source–receptor relationship between moisture sources and summertime precipitation in China at the subregional scale. Thereinto, the complex, large-scale circulation regimes responsible for these linkages can provide useful precursors for summertime climate prediction. Although this study offers some progress in elucidating the complexity of this topic through observational analysis and 10-day simulations with HYSPLIT 4.9, the precise physical processes and possible external forcings underpinning the variations of summertime precipitation remain to be comprehensively explored. These aspects should be addressed by analyzing numerical simulation results using state-of-art atmospheric or coupled models. Given that the HYSPLIT model considers only one "evaporation (uptake)-precipitation (release)" cycle, the analysis of multicycle processes may be necessary for future research, which will necessitate more computations and discussions.

DATA AVAILABILITY STATEMENT

The original contributions presented in the study are included in the article/Supplementary Material, further inquiries can be directed to the corresponding author.

AUTHOR CONTRIBUTIONS

RZ and QC conceived the study, and RZ wrote the manuscript. ZZ and YQ provided critical feedback and helped shape the research and manuscript. All authors contributed to the article and approved the submitted version.

FUNDING

RZ was supported by the National Key Research and Development Program of China (Grant 2016YFA0601500), the National Natural Science Foundation of China (Grant 42075016), and the Shanghai Pujiang Program (Grant 2020PJD004).

REFERENCES

Barnston, A. G., and Livezey, R. E. (1987). Classification, Seasonality and Persistence of Low-Frequency Atmospheric Circulation Patterns. *Mon. Wea. Rev.* 115, 1083–1126. doi:10.1175/1520-0493(1987)115<1083:csapol>2.0.co;2

Chen, B., Xu, X. D., Yang, S., and Zhang, W. (2012). On the Origin and Destination of Atmospheric Moisture and Air Mass over the Tibetan Plateau. *Theor. Appl. Climatol.* 110, 423–435. doi:10.1007/s00704-012-0641-y

Chen, Y., and Luo, Y. (2018). Analysis of Paths and Sources of Moisture for the South China Rainfall during the Presummer Rainy Season of 1979-2014. *J. Meteorol. Res.* 32, 744–757. doi:10.1007/s13351-018-8069-7

Chu, Q.-c., Zhi, R., Wang, Q.-g., and Feng, G.-l. (2019). Roles of Moisture Sources and Transport in Precipitation Variabilities during Boreal Summer over East China. *Clim. Dyn.* 53, 5437–5457. doi:10.1007/s00382-019-04877-z

Ding, Y., Sun, Y., Wang, Z., Zhu, Y., and Song, Y. (2009). Inter-decadal Variation of the Summer Precipitation in China and its Association with Decreasing Asian Summer Monsoon Part II: Possible Causes. *Int. J. Climatol.* 29 (13), 1926–1944. doi:10.1002/joc.1759

Draxler, R. R., and Hess, G. D. (1998). An Overview of the HYSPLIT_4 Modeling System of Trajectories, Dispersion, and Deposition. *Aust. Meteorol. Mag.* 47 (4), 295–308.

Drumond, A., Nieto, R., and Gimeno, L. (2011). Sources of Moisture for China and Their Variations during Drier and W-etter C-onditions in 2000–2004: a Lagrangian A-pproach. *Clim. Res.* 50, 215–225. doi:10.3354/cr01043

Emil, S. D., Amey, P., and Subimal, G. (2016). Use of Atmospheric Budget to Reduce Uncertainty in Estimated Water Availability over South Asia from Different Reanalyses. *Sci. Rep.* 6, 29664. doi:10.1038/srep29664

Fan, K., Wang, H., and Choi, Y. J. (2008). A Physically-Based Statistical Forecast Model for the Middle-Lower Reaches of the Yangtze River Valley Summer Rainfall. *Chin. Sci. Bull.* 53, 602–609. doi:10.1007/s11434-008-0083-1

Gimeno, L., Drumond, A., Nieto, R., Trigo, R. M., and Stohl, A. (2010). On the Origin of continental Precipitation. *Geophys. Res. Lett.* 37, L13804. doi:10.1029/2010gl043712

Gong, D. Y., Wang, S. W., and Zhu, J. H. (2001). East Asian winter Monsoon and Arctic Oscillation. *Geophys. Res. Lett.* 28, 2073–2076. doi:10.1029/2000GL012311

Hua, L., Zhong, L., and Ma, Z. (2017). Decadal Transition of Moisture Sources and Transport in Northwestern China during Summer from 1982 to 2010. *J. Geophys. Res. Atmos.* 122, 12522–12540. doi:10.1002/2017jd027728

Huang, G., Liu, Y., and Huang, R. (2011). The Interannual Variability of Summer Rainfall in the Arid and Semiarid Regions of Northern China and its Association with the Northern Hemisphere Circumglobal Teleconnection. *Adv. Atmos. Sci.* 28, 257–268. doi:10.1007/s00376-010-9225-x

Jiang, Z. H., Ren, W., Liu, Z. Y., and Yang, H. (2013). Analysis of Water Vapor Transport Characteristics During the Meiyu over the Yangtze Huaihe River Valley using the Lagrangian Method. *Acta. Meteorol. Sci.* 71 (2), 295–304 (in Chinese).

Jiang, Z., Jiang, S., Shi, Y., Liu, Z., Li, W., and Li, L. (2017). Impact of Moisture Source Variation on Decadal-Scale Changes of Precipitation in North China from 1951 to 2010. *J. Geophys. Res. Atmos.* 122, 600–613. doi:10.1002/2016jd025795

Kosaka, Y., and Nakamura, H. (2010). Mechanisms of Meridional Teleconnection Observed between a Summer Monsoon System and a Subtropical Anticyclone. Part I: The Pacific-Japan Pattern. *J. Clim.* 23, 5085–5108. doi:10.1175/2010jcli3413.1

Li, F., and Wang, H. (2013). Autumn Sea Ice Cover, winter Northern Hemisphere Annular Mode, and winter Precipitation in Eurasia. *J. Clim.* 26, 3968–3981. doi:10.1175/jcli-d-12-00380.1

Liu, J., Curry, J. A., Wang, H., Song, M., and Horton, R. M. (2012). Impact of Declining Arctic Sea Ice on winter Snowfall. *Proc. Natl. Acad. Sci.* 109, 4074–4079. doi:10.1073/pnas.1114910109

Nitta, T. (1987). Convective Activities in the Tropical Western Pacific and Their Impact on the Northern Hemisphere Summer Circulation. *J. Meteorol. Soc. Jpn.* 65, 373–390. doi:10.2151/jmsj1965.65.3_373

Numaguti, A. (1999). Origin and Recycling Processes of Precipitating Water over the Eurasian Continent: Experiments Using an Atmospheric General Circulation Model. *J. Geophys. Res.* 104, 1957–1972. doi:10.1029/1998jd200026

Renhe, Z. (2001). Relations of Water Vapor Transport from Indian Monsoon with that over East Asia and the Summer Rainfall in China. *Adv. Atmos. Sci.* 18, 1005–1017. doi:10.1007/BF03403519

Simmonds, I., Bi, D., and Hope, P. (1999). Atmospheric Water Vapor Flux and its Association with Rainfall overChina in Summer. *J. Clim.* 12, 1353–1367. doi:10.1175/1520-0442(1999)012<1353:awvfai>2.0.co;2

Sodemann, H., and Stohl, A. (2009). Asymmetries in the Moisture Origin of Antarctic Precipitation. *Geophys. Res. Lett.* 36, L22803. doi:10.1029/2009gl040242

Stohl, A., and James, P. (2005). A Lagrangian Analysis of the Atmospheric Branch of the Global Water Cycle. Part II: Moisture Transports between Earth's Ocean Basins and River Catchments. *J. Hydrometeorol.* 6, 961–984. doi:10.1175/Jhm470.1

Sun, B., and Wang, H. (2014b). Analysis of the Major Atmospheric Moisture Sources Affecting Three Sub-regions of East China. *Int. J. Climatol* 35 (9), 2243–2257. doi:10.1002/joc.4145

Sun, B., and Wang, H. (2014a). Moisture Sources of Semiarid Grassland in China Using the Lagrangian Particle Model FLEXPART. *J. Clim.* 27 (6), 2457–2474. doi:10.1175/jcli-d-13-00517.1

Sun, B., Zhu, Y., and Wang, H. (2011). The Recent Interdecadal and Interannual Variation of Water Vapor Transport over Eastern China. *Adv. Atmos. Sci.* 28, 1039–1048. doi:10.1007/s00376-010-0093-1

Sun, L., Shen, B., Sui, B., and Huang, B. (2017). The Infuences of East Asian Monsoon on Summer Precipitation in Northeast China. *Clim. Dyn.* 48 (5–6), 1–13.

Tian, B., and Fan, K. (2013). Factors Favorable to Frequent Extreme Precipitation in the Upper Yangtze River Valley. *Meteorol. Atmos. Phys.* 121, 189–197. doi:10.1007/s00703-013-0261-9

Trenberth, K. E. (1999). Atmospheric Moisture Recycling: Role of Advection and Local Evaporation. *J. Clim.* 12, 1368–1381. doi:10.1175/1520-0442(1999)012<1368:amrroa>2.0.co;2

Trenberth, K. E., Fasullo, J. T., and Mackaro, J. (2011). Atmospheric Moisture Transports from Ocean to Land and Global Energy Fows in Reanalyses. *J. Climate* 24 (18), 4907–4924.

Viste, E., and Sorteberg, A. (2013). Moisture Transport into the Ethiopian highlands. *Int. J. Climatol.* 33, 249–263. doi:10.1002/Joc.3409

Wang, B., and Fan, Z. (1999). Choice of South Asian Summer Monsoon Indices. *Bull. Amer. Meteorol. Soc.* 80, 629–638. doi:10.1175/1520-0477(1999)080<0629:cosasm>2.0.co;2

Wang, B., Wu, R., and Lau, K. M. (2001). Interannual Variability of the Asian Summer Monsoon: Contrasts between the Indian and the Western North Pacific-East Asian Monsoons*. *J. Clim.* 14, 4073–4090. doi:10.1175/1520-0442(2001)014<4073:ivotas>2.0.co;2

Wang, B., Wu, Z., Li, J., Liu, J., Chang, C. P., Ding, Y., et al. (2008). How to Measure the Strength of the East Asian Summer Monsoon. *J. Clim.* 21, 4449–4463. doi:10.1175/2008jcli2183.1

Wang, H. J., and Chen, H. (2012). Climate Control for southeastern China Moisture and Precipitation: Indian or East Asian Monsoon. *J. Geophys. Res. Atmos.* 117 (D12), 48–50. doi:10.1029/2012jd017734

Wei, J., Dirmeyer, P. A., Bosilovich, M. G., and Wu, R. (2012). Water Vapor Sources for Yangtze River Valley Rainfall: Climatology, Variability, and Implications for Rainfall Forecasting. *J. Geophys. Res.* 117, D05126. doi:10.1029/2011JD016902

Yatagai, A., and Yasunari, T. (1995). Interannual Variations of Summer Precipitation in the Arid/semi-Arid Regions in China and Mongolia : Their Regionality and Relation to the Asian Summer Monsoon. *J. Meteorol. Soc. Jpn.* 73, 909–923. doi:10.2151/jmsj1965.73.5_909

Zhang, L., and Zhou, T. (2015). Drought over East Asia: a Review. *J. Clim.* 28 (8), 3375–3399. doi:10.1175/jcli-d-14-00259.1

Zhang, R. N., Sun, C., and Li, W. (2018). Relationship between Summer Eurasian Teleconnection and the Interannual Variations of Arctic Sea Ice and Associated Influence on Summer Precipitation over China. *Chin. J. Geophys.* 61, 91–105. doi:10.6038/cjg2018K0755

Zhao, P., Zhang, R., Liu, J., Zhou, X., and He, J. (2007). Onset of Southwesterly Wind over Eastern China and Associated Atmospheric Circulation and Rainfall. *Clim. Dyn.* 28, 797–811. doi:10.1007/s00382-006-0212-y

Zhou, L. T. (2011). Impact of East Asian winter Monsoon on Rainfall over southeastern China and its Dynamical Process. *Int. J. Climatol.* 31, 677–686. doi:10.1002/joc.2101

Zhou, T. J., and Yu, R. C. (2005). Atmospheric Water Vapor Transport Associated with Typical Anomalous Summer Rainfall Patterns in China. *J. Geophys. Res. Atmos.* 110 (D8), 211. doi:10.1029/2004jd005413

Zhu, Y., Wang, H., Zhou, W., and Ma, J. (2011). Recent Changes in the Summer Precipitation Pattern in East China and the Background Circulation. *Clim. Dyn.* 36, 1463–1473. doi:10.1007/s00382-010-0852-9

Conflict of Interest: The authors declare that the research was conducted in the absence of any commercial or financial relationships that could be construed as a potential conflict of interest.

frontiers in Earth Science

ORIGINAL RESEARCH
published: 07 December 2021
doi: 10.3389/feart.2021.758664

Change in Extreme Precipitation Over Indochina Under Climate Change From a Lagrangian Perspective of Water Vapor

Zelun Cheng[1,2], *Zuowei Xie*[2]*, *Wei Tang*[3], *Cholaw Bueh*[2], *Yuanfa Gong*[1] and *Jie Yan*[4,5]

[1]School of Atmospheric Sciences, Chengdu University of Information Technology, Chengdu, China, [2]International Center for Climate and Environment Sciences, Institute of Atmospheric Physics, Chinese Academy of Sciences, Beijing, China, [3]China Meteorological Administration Institute for Development and Programme Design, Beijing, China, [4]State Key Laboratory of Alternate Electrical Power System with Renewable Energy Sources, School of New Energy, North China Electric Power University, Beijing, China, [5]China Huaneng Group Co., Ltd., Beijing, China

OPEN ACCESS

Edited by:
Xander Wang,
University of Prince Edward Island, Canada

Reviewed by:
Jing Ma,
Nanjing University of Information Science and Technology, China
Sushant Das,
Abdus Salam International Centre for Theoretical Physics, Italy

***Correspondence:**
Zuowei Xie
xiezuowei@mail.iap.ac.cn

Specialty section:
This article was submitted to Interdisciplinary Climate Studies, a section of the journal Frontiers in Earth Science

Received: 14 August 2021
Accepted: 08 November 2021
Published: 07 December 2021

Citation:
Cheng Z, Xie Z, Tang W, Bueh C, Gong Y and Yan J (2021) Change in Extreme Precipitation Over Indochina Under Climate Change From a Lagrangian Perspective of Water Vapor. Front. Earth Sci. 9:758664. doi: 10.3389/feart.2021.758664

The process of global warming has humidified the atmosphere and increased the occurrence of extreme-precipitation events over the Indochina Peninsula, which lies in the transition region from the South Asian monsoon to the East Asian monsoon. The annual occurrence number of days of extreme precipitation over the Indochina Peninsula exhibits a significant change in 2003, with an abnormally higher occurrence number during the period 2003–2015 than that during 1951–2002. The extreme precipitation and such decadal change are contributed by more moisture sources associated with an enhanced dipole circulation over the Indian Ocean, which could be linked to the Pacific Decadal Oscillation. The daily large-scale meteorological pattern directly associated with extreme precipitation is characterized by an enhanced dipole of the typical summer monsoon pattern, with a zonally elongated Mascarene high and a deepened monsoon trough from northern India to the South China Sea. Such an intensified dipole provides two major channels of water vapor: one along the low-level westerly jet over the Indian Ocean and the other along the gyre of monsoon trough over the South China Sea. Compared with that during the period 1951–2002, the dipole is enhanced from northern India to the Indian Ocean and weakened over the Indochina Peninsula during the period 2003–2015. Although the Lagrangian analysis shows that the trajectory of air masses is displaced southward to the Indian Ocean, the intensified low-level westerly jet increases the evaporation of water from the ocean and thus not only enhances the water channel over the Indian Ocean but also yields a parallel water channel over the Bay of Bengal. In contrast, in spite of the increased trajectory density of air masses over the South China Sea, the lingering of air mass suppresses the evaporation of water and thus provides a declined contribution to the extreme precipitation during 2003–2015.

Keywords: extreme precipitation, Indochina, Lagrangian perspective, water vapor, monsoon, PDO

INTRODUCTION

Global warming increases the frequency and intensity of extreme-precipitation events (Alexander et al., 2006; Zhang et al., 2020). The intensification of extreme precipitation is principally caused by enhancement of atmospheric moisture content, which plays an important role in the global water cycle and climate system (Bengtsson, 2010). Changes in the intensity and pathways of moisture transport lead to variabilities in rain belts and patterns (Zhou et al., 2001; Huang et al., 2011). The Indochina Peninsula is located in the Asian monsoon region, where there is abundant moisture content and thus a greater vulnerability to climate change (Ge et al., 2017). For example, Thailand encountered its worst floods due to heavy and widespread rainfall during the 2011 rainy season, which resulted in more than 800 deaths and affected 13.6 million people (Promchote et al., 2016). Thus, investigating the moisture change for extreme precipitation over the Indochina Peninsula against the background of climate change is an important topic for the atmospheric water cycle and could provide guidance for regional water resources management and natural disaster prediction (Christensen and Christense, 2003).

The Indochina Peninsula is a unique region that lies in the transition zone between the South Asian monsoon and the East Asian monsoon (Zhang et al., 2002). Therefore, water vapor is transported by the low-level westerly over the Indian Ocean and the southeasterly associated with the subtropical ridge over the North Pacific. The moisture transport for precipitation over the Indochina Peninsula exhibits an apparent intraseasonal variability (Chhin et al., 2019). Prior to the onset of the summer monsoon, water vapor for precipitation is mainly contributed by the enhancement of moisture transport from the Bay of Bengal. In contrast, water vapor for precipitation during the summer monsoon is largely provided by moisture transport from the South China Sea. Moreover, the identification of moisture sources has received an increasing attention in the analysis of both extreme precipitation and a changing hydrological cycle due to climate change (Gimeno et al., 2013; Stojanovic et al., 2021).

The variations of moisture transport to the Indochina Peninsula are directly related to atmospheric circulations embedded in the planetary-scale Asia–Australia monsoon system (Chang et al., 2005). After the 1990s, the warming of surface temperature and enhancement of convective activity in the Indochina Peninsula deepened the monsoon trough and thereby increased the moisture transport from the Bay of Bengal to the Indochina Peninsula. Meanwhile, the deepened monsoon trough was able to induce more tropical cyclone activity over the Bay of Bengal to the South China Sea (Faikura et al., 2020) and significantly increased precipitation over the Indochina Peninsula (Takahashi et al., 2015). The monsoon trough may comprise an import portion of *daily* large-scale meteorological pattern (LMP), which provides a favorable circulation pattern for triggering or intensifying synoptic processes (e.g., moisture transport) to promote the occurrence of extreme precipitation and is connected to low-frequency modes of climate variability (Grotjahn et al., 2015). Since the warming has increased the water vapor holding capacity of the atmosphere and the variability of precipitation (Zhang et al., 2021), it would be of interest to investigate how changes in moisture transport associated with the change in LMP contribute to the extreme precipitation against different climate backgrounds, taking the Pacific Decadal Oscillation (PDO) for example.

Cheng et al. (2021) found a significant upward trend in extreme precipitation over South China and the Indochina Peninsula, which they attributed to the increasing frequency of the meridional wave train over East Asia. By contrast, the reason for the upward trend in extreme precipitation over the Indochina Peninsula remains an open question. Meanwhile, much of the effort in prior studies has focused primarily on the variabilities of monsoonal precipitation and the model representation of extreme precipitation over the Indochina Peninsula (e.g., Zhang et al., 2002; Ge et al., 2021; Tang et al., 2021; Wu and Zhu, 2021). This unanswered question served as motivation for the present study, which aims to explore the change in extreme precipitation over the Indochina Peninsula from the Lagrangian perspective of water vapor transport to address two issues: the change in water vapor transport and the underlying mechanisms. To answer these two questions, we first identify the *daily* LMP responsible for extreme precipitation over the Indochina Peninsula, mainly in terms of composite 850-hPa stream function anomalies and associated moisture transport. Then, we construct LMP indices by projecting daily 850-hPa stream function anomalies onto the LMP and investigate their potential linkages with anomalous remote forcing.

The remainder of this paper is organized as follows: **Section 2** describes the data and methods. **Section 3** presents the results in terms of the changes in LMP and water vapor transport from a Lagrangian perspective and the potential influence of the PDO on extreme precipitation. **Section 4** discusses associations with weather systems of the intraseasonal variability. And finally, a summary of the study's main findings is provided in **Section 5**.

DATA AND METHODS

Data

The daily precipitation dataset comes from APHRODITE (Yatagai et al., 2012). This suite of high-resolution gridded datasets is jointly constructed by the Meteorology Institute of the Japan Meteorological Agency and the Research Institute for Humanity and Nature. They use a SphereMap-type scheme based on the rainfall distribution to interpolate Global Telecommunications System–based data from gauge observations, precompiled data by other projects or organizations, and data from individual collections to produce the gridded precipitation data. In this study, we adopt APHRO_MA_V1101 (1951–2007) and APHRO_MA_V1101EX (2007–2015) on a 0.5 × 0.5° latitude–longitude grid encompassing 15°S–55°N and 60°–155°E.

We also use the ERA5 global reanalysis dataset provided by the Copernicus Climate Change Service (Hersbach et al., 2020). The ERA5 reanalysis covers the period from 1950 to the present day. The variables used here are the *u*- and *v*-components of wind at 850, 700, and 200 hPa; total column water vapor; and vertically

integrated eastward and northward water vapor fluxes. The air parcel tracking requires data at a relatively high horizontal and vertical grid spacing. Thus, six-hourly surface pressure, 3D winds, and specific humidity on a 0.5 × 0.5° longitude–latitude grid at 32 vertical levels between 1,000 and 10 hPa are used as the input for the Lagrangian analysis tool LAGRANTO 2.0.

The monthly mean sea surface temperature (SST) data used in this study are from the Extended Reconstructed SST, version 5 (ERSST.v5), of the National Oceanic and Atmospheric Administration (NOAA; Huang et al., 2017). These data are provided on a 2 × 2° longitude–latitude grid for the period from 1854 to the present day. We also use the PDO index and Madden-Julian Oscillation (MJO) index based on outgoing longwave radiation (OMI) provided by the NOAA Physical Sciences Laboratory. The western North Pacific tropical cyclone database comes from China Meteorological Administration (Lu et al., 2021).

Following prior studies (Zhang et al., 2002; Yang and Wu, 2019), we focus on the rainy season over the Indochina Peninsula from 1 May to 31 October in the years 1951–2015. The OMI is available for the period from 1979 to 2015.

Definition and Objective Classification of Extreme Precipitation

Given the large spatial variability of the topography, we use the values based on the 95th percentile instead of fixed absolute values to define the extreme-precipitation threshold value for each grid point (Lai et al., 2020). In addition, a spatial coverage criterion of extreme precipitation is also required to remove any regional influence of the topography. Therefore, an extreme-precipitation event is identified if the number of grid points with precipitation above the threshold values is at least 5% of the total grid points (Zhao et al., 2017). Accordingly, we identified 1,428 extreme precipitation events with 2,775 days over the Indochina Peninsula to South China (Cheng et al., 2021).

To isolate the extreme-precipitation patterns, we apply self-organizing maps (SOM; Kohonen, 2001) to all extreme-precipitation events over the Indochina Peninsula to South China. It works by mapping high-dimensional data to a low-dimensional representative space with a neuronal structure (readers are referred to Supplementary Material for more details). The precipitation percentiles of 1,232 grid points in the study area on 2,775 extreme-precipitation days are input into the SOM with a specified number of nodes. The SOM is trained over 50,000 iterations, with each cycle of training adjusting the weights of the neurons until, finally, the SOM outputs the optimal neurons representing the spatial patterns (i.e., best matching units) of extreme precipitation.

As shown in Cheng et al. (2021), the SOM is repeated with the number of nodes (N) from 2 to 20 to determine the optimum number of clusters, which shows that four clusters are sufficiently different from each other (**Supplementary Figure S1**). Readers are referred to the Supplementary Material for more details. These four best-matching units are then used to determine the cluster indices of 2,775 extreme-precipitation days by finding the minimum Euclidian distance among the percentile field on each extreme-precipitation day and best-matching units. The cluster indices associated with 2,775 extreme-precipitation days are used to composite the circulations for each cluster. These four clusters are named the South China cluster, the Indochina Peninsula cluster, the Burma–Yunnan cluster, and the Southern South China–Northern Vietnam cluster according to their respective geographical distributions of cluster-mean extreme precipitation (**Supplementary Figure S2**). The current study simply adopts the Indochina Peninsula cluster of extreme precipitation with 543 days (**Figure 1**).

Running *t*-Test

We use a running t-test to detect a possible change in the series of the occurrence number of days of extreme precipitation (Fu and Wang, 1992). For time series with sample size n, the size numbers of the subsequences $x1$ and $x2$ around a certain time are n_1 and n_2, respectively. The means of each sample are $\bar{x}_1$ and $\bar{x}_2$, respectively, while the variances are s_1^2 and s_2^2. Assuming the null hypothesis (H_0) is that there is no difference between the sample means $\bar{x}_1$ and $\bar{x}_2$, the statistical quantity t_i is defined as follows:

$$t_i = \frac{\bar{x}_1 - \bar{x}_2}{s \cdot \sqrt{1/n_1 + 1/n_2}} \sim t\,(n_1 + n_2 - 2)$$

For the significance level α, if the statistic $t_i > t_\alpha$, the null hypothesis H_0 is rejected. The means of the two subsequences are significantly different, and thus, a significant change at time i is obtained.

Backward Trajectories

The Lagrangian analysis tool LAGRANTO (Sprenger and Wernli, 2015) is applied to calculate 5-day backward trajectories of air parcels associated with extreme precipitation over the Indochina Peninsula. For more details, readers are referred to Sprenger and Wernli (2015), where they can find a schematic overview of the typical steps involved in computing trajectories. The advantage of LAGRANTO, compared to other trajectory tools such as FLEXTRA and HYSPLIT, is the highly flexible definition of the trajectory's initial parcel position and height, which allows the results of each time step to be converted into trajectory density data (Schemm et al., 2017). Thus, it is a powerful Lagrangian analysis tool for the study of air mass trajectories.

Specifically, the grid points of the high-precipitation percentile area over the Indochina Peninsula are considered as initial air parcel positions, which are within the region of 10°–17°N and 98°–109°E (**Figure 1A**). The initial height for all grid points is 700 hPa, which is likely associated with the cloud for precipitation. The air parcels of these grid points are tracked backward for 5 days, starting from each of the extreme-precipitation days, which is sufficient to characterize the large-scale flow of air (Schemm et al., 2017). To exclude the overlap trajectory information for extremes, we select 128 out of 543 extreme-precipitation days such that there is no extreme-precipitation day within 5 days prior to an extreme-precipitation day. LAGRANTO provides information on air mass position along each trajectory in terms of longitude, latitude, and pressure height with the value of specific humidity. In addition,

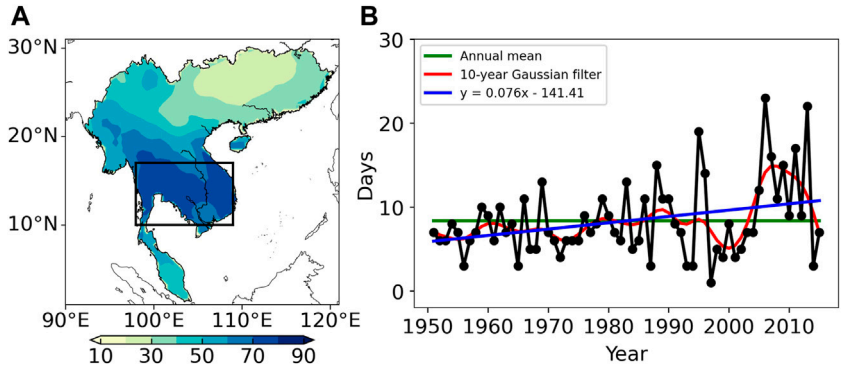

FIGURE 1 | (A) Composite precipitation percentile and **(B)** time series of the annual number of days of extreme precipitation (black), along with the decadal variability (red) and long-term trend (blue) for extreme precipitation of the Indochina Peninsula cluster, which are adopted from Figures 5B and 9C in Cheng et al. (2021), respectively. The box in **(A)** denotes the starting region of the backward trajectories.

LAGRANTO also provides a density tool that converts all the trajectories to trajectory densities on a $1^{\circ} \times 1^{\circ}$ longitude–latitude grid.

Potential Source Contribution Function Analysis

Potential source contribution function (PSCF) analysis is a method for identifying potential pollution sources based on the conditional probability function (Zeng and Hopke, 1989). The contribution of the pollution at each grid point to the pollution in the target region is calculated as the ratio of the residence time of the pollution trajectory to all trajectories. Some researchers have applied this method to investigate potential water vapor sources, which has revealed a relatively good capability of PSCF analysis in identifying moisture sources (Salamalikis et al., 2015; Meng et al., 2020). To begin with, following Wang et al. (2014), the threshold value is calculated by averaging the specific humidity along all the trajectories, which is used to determine the potential contribution of a trajectory. Then, for a grid point, the number of trajectories with the specific humidity exceeding the threshold values is counted. A larger number of counted trajectories indicates that the grid point has a high PSCF value. An area including a larger number of grid points with high PSCF values can be considered to be a potential moisture source. At the same time, in order to reduce the error of the conditional probability function that is due to the small total number of samples, a weight function $W\ (n_{ij})$ is introduced to calculate the PSCF. The formula for the PSCF and weight function is as follows (Zeng and Hpoke, 1989):

$$PSCF_{ij} = \frac{m_{ij}}{n_{ij}} \cdot W\ (n_{ij})$$

$$W\ (n_{ij}) = \begin{cases} 1.00, & 3n_{ave} < n_{ij} \\ 0.70, & 1.5n_{ave} < n_{ij} \leq 3n_{ave} \\ 0.40, & n_{ave} < n_{ij} \leq 1.5n_{ave} \\ 0.17 & n_{ij} \leq n_{ave} \end{cases}$$

where m_{ij} is the number of trajectories passing through the grid $(i,\ j)$ and exceeding the threshold in the research area; n_{ij} is the number of total trajectories in the grid $(i,\ j)$; and n_{ave} is the average number of trajectories for each point.

RESULTS

Circulation Features of Extreme Precipitation

Figure 1 displays the composite precipitation percentile and corresponding time series of the annual number of days of extreme precipitation for the Indochina Peninsula cluster. The extreme precipitation is concentrated over the southern Indochina Peninsula (**Figure 1A**). Its annual occurrence number exhibits a significant upward trend at the 99% confidence level. Such an upward trend might be contributed by the amplified decadal variability in the 21st century, when there was an anomalously high number of days of extreme precipitation during 2003–2015. In contrast, the decadal variability generally fluctuates around the annual mean in the 20th century. The amplified decadal variability in the 21st century suggests a potential abrupt change in extreme precipitation over the Indochina Peninsula.

To begin with, we introduce the daily LMP in terms of stream function anomalies that are directly associated with extreme precipitation (Xie et al., 2017; Zhao et al., 2017). **Figure 2** displays the composite 850- and 200-hPa stream function and corresponding anomalies and 700-hPa specific humidity anomalies overlaid with horizontal wind anomalies during days of extreme precipitation. The reason that we chose 700 hPa for specific humidity is that its value is not too small and its anomaly is stronger compared to 850 hPa (**Supplementary Figure S3**). The LMP is characterized by an enhanced typical summer monsoon pattern (Zhang et al., 2002). Specifically, the 850-hPa LMP features a dipole pattern with a zonally elongated Mascarene high and a deepened monsoon trough from northern India to the South China Sea (**Figure 2A**). Due to this intensified dipole, the low-level

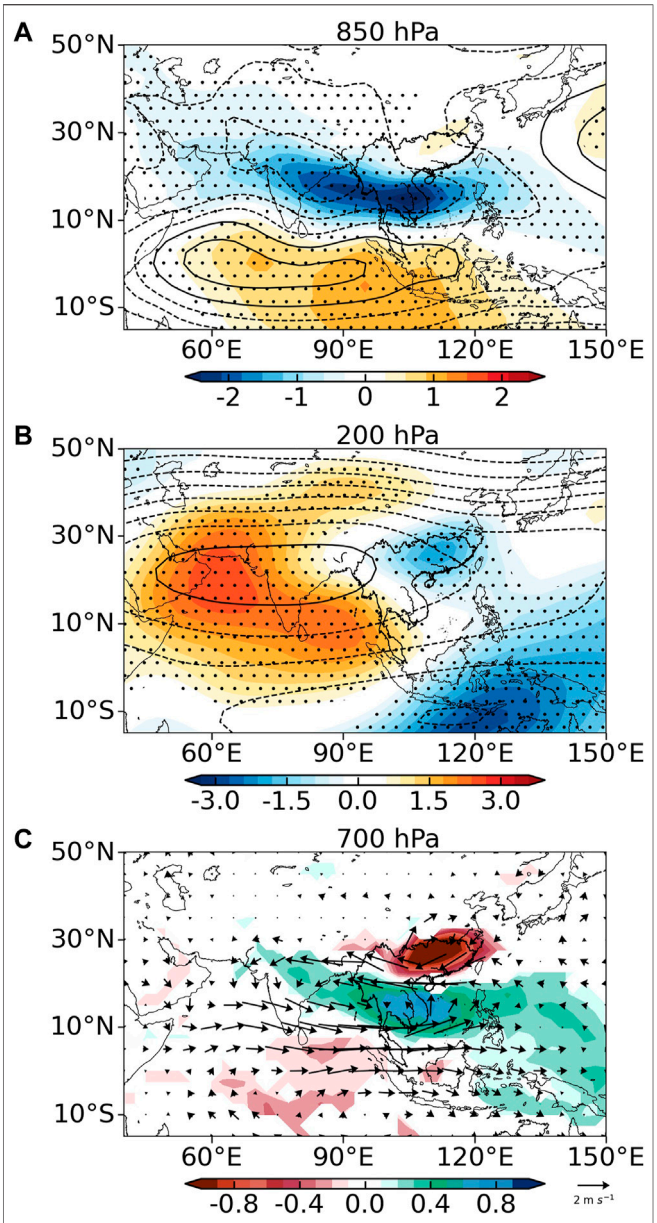

FIGURE 2 | Composite stream function (contours; units: 10^6 m^2 s^{-1}) and corresponding anomalies relative to the climatological mean (shading) associated with extreme precipitation at **(A)** 850 hPa and **(B)** 200 hPa. Contours are drawn at intervals of 3 and 10 for **(A**, **B)**, respectively. **(C)** is the composite 700-hPa specific humidity anomalies (shading, units: g kg^{-1}) and horizontal wind anomalies (arrows, units: m s^{-1}). Stippling in **(A**, **B)** and shading in **(C)** indicate composite values that are statistically significant at the 90% confidence level.

westerly jet is enhanced between the dipole from Somalia to the South China Sea (**Figure 2C**). As such, this cyclonic anomaly circulation accumulates water vapor from both the Indian Ocean and the South China Sea to the Indochina Peninsula, resulting in an increased water vapor over there. In the upper level (**Figure 2B**), the South Asian high is amplified from the Arab Peninsula southeastward to the Malay Peninsula. The amplified South Asian high enhances the divergent circulation in the upper level and thus the upward motions over the Indochina Peninsula, which facilitates convections for extreme precipitation. As such, the amplified South Asian high also favors the enhancement of the low-level monsoon dipole (e.g., the 850-hPa LMP). The LMP characterized by an intensification of the Asian monsoon configuration favors both water vapor transport to the Indochina Peninsula and convective activity, which tends to induce extreme precipitation.

Change in the Large-Scale Meteorological Pattern

As mentioned above, the enhanced decadal variability of the annual occurrence of extreme precipitation in the 21st century suggests a potential transition. To verify this speculation, we apply a running *t*-test method to the time series of the annual number of days of extreme precipitation to obtain its change point (Fu and Wang, 1992). As anticipated, there is a transition year in 2003, which is statistically significant at the 95% confidence level (**Figure 3**). Accordingly, the entire period can be divided into two subperiods of 1951–2002 and 2003–2015. In comparison with the period 1951–2002, there is a greater mean number of extreme precipitation days during 2003–2015. This change coincides with decadal shifts in well-known long-term climate modes such as the PDO and the Atlantic Multidecadal Oscillation (Liu et al., 2020). We discuss the potential influence of the PDO on extreme precipitation over the Indochina Peninsula in **Section 3.4**.

Figure 4 shows the differences in the LMPs and water vapor associated with extreme precipitation during 2003–2015 and 1951–2002. In comparison with the LMPs associated with extreme precipitation during 1951–2002, the monsoon pattern is intensified during 2003–2015. In the lower troposphere (**Figure 4A**), the monsoon trough is deepened over northern India, whereas it is weakened over the Malay Peninsula. To the south, the zonally elongated Mascarene high magnifies and extends northward. As a result, the gradient between this dipole intensifies, which enhances the low-level westerly jet

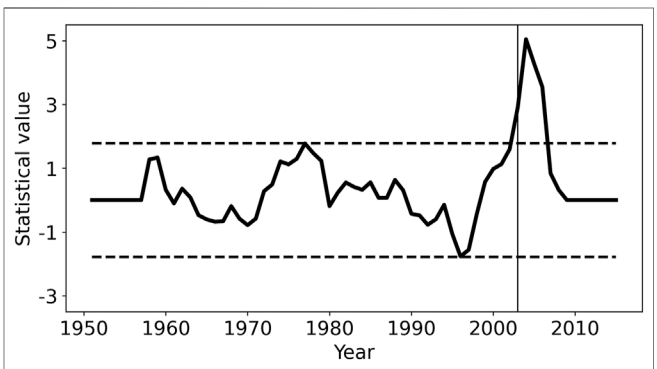

FIGURE 3 | Decadal shift in the total number of days of extreme precipitation according to a running *t*-test and Lepage test, respectively. The dashed lines represent the critical values at the 95% significance level, and the thin vertical line denotes the change year of 2003.

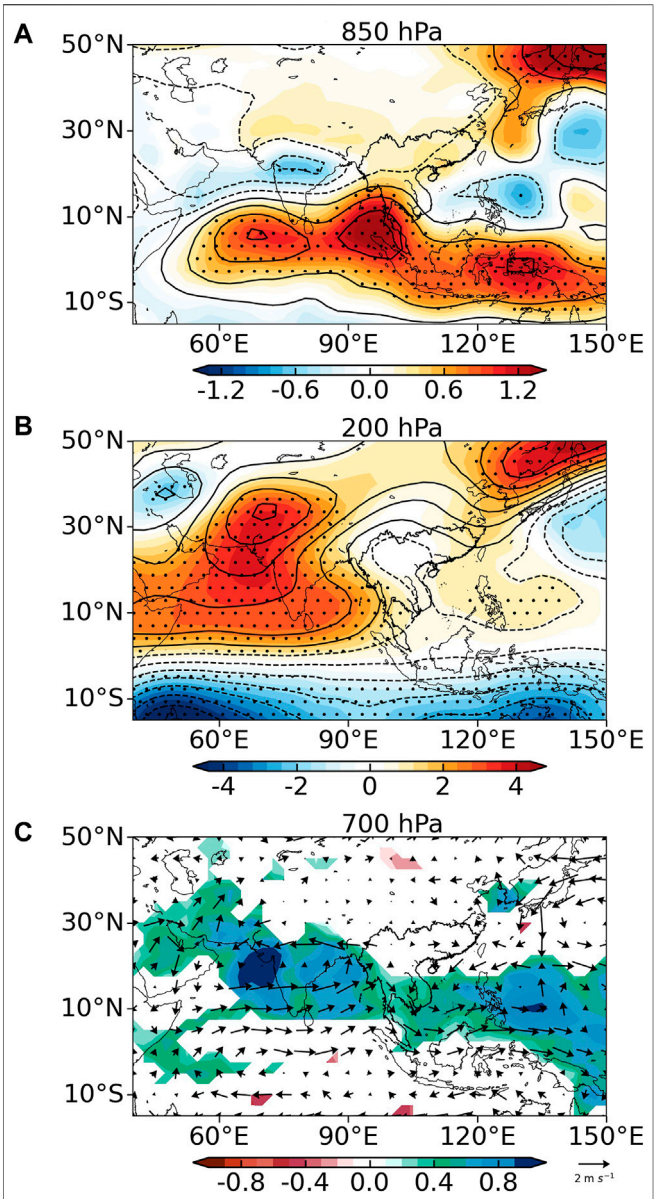

FIGURE 4 | Differences in composite stream functions (contours; units: 10^6 m^2 s^{-1}) associated with extreme precipitation during the subperiods of 1951–2002 and 2003–2015 at **(A)** 850 hPa and **(B)** 200 hPa. Contours are drawn at intervals of 0.5 and 1 in **(A**, **B)**, respectively. **(C)** is the differences of composite 700-hPa specific humidity (shading, units: g kg^{-1}) and horizontal wind (arrows, units: m s^{-1}) during the subperiods. Stippling in **(A**, **B)** and shading in **(C)** indicate composite values that are statistically significant at the 90% confidence level.

from Somalia to the Indochina Peninsula (**Figure 4C**), which favors the transport of water vapor from the Indian Ocean to the Indochina Peninsula. Meanwhile, a weak negative anomaly can be seen over the South China Sea, which also helps convey water vapor from the South China Sea to the Indochina Peninsula. An increased water vapor is observed over the Indochina Peninsula (**Figure 4C**). At 200 hPa (**Figure 4B**), a meridional dipole pattern resides over Asia, indicating a further amplification and westward displacement of the South Asian high, which further intensifies the upward motions for extreme precipitation over the Indochina Peninsula. Following the intensification of the LMPs, extreme precipitation becomes more frequent during the period 2003–2015 compared with 1951–2002.

Change in Water Vapor Transport

Given the significant change in the LMP associated with extreme precipitation, it is of interest to investigate the change in water vapor transport and the possible driving factors. To explore these two aspects, we use the Lagrangian analysis tool LAGRANTO to calculate the 5-day backward trajectories of air masses associated with extreme precipitation over the region of 98°–109°E and 10°–17°N (**Figure 1A**). The trajectory density is then calculated by counting the number of trajectory points within each $1^\circ \times 1^\circ$ grid box using the density tool of LAGRANTO.

Figures 5A–C show the trajectory density patterns for the extreme precipitation in the two subperiods. There are two major channels of water vapor: one along the low-level westerly jet over the Indian Ocean and the other along the gyre of the monsoon trough over the South China Sea (**Figures 5A,B**). In comparison with those during 1951–2002, both of water vapor channels displace southward during 2003–2015 (**Figure 5C**). Moreover, the water vapor channel over the Indian Ocean bends southward over Sri Lanka owing to the deepened monsoon trough over India. The different trajectory densities of the air masses suggest that the water vapor channel over the Indian Ocean is weakened over the Bay of Bengal and displaced southward in accordance with the enhanced low-level westerly jet. By contrast, although the westerly over the South China Sea weakens, the trajectory density of air masses is increased.

However, there is a deficiency in the trajectory density of air masses, in which not all trajectories include large values of water vapor for precipitation. To address this issue, we apply PSCF analysis to each air mass trajectory to reveal the potential water vapor sources (**Figures 5D,E**). As seen from **Figure 5D**, the water vapor for the extreme precipitation during the period 1951–2002 is largely contributed by the South China Sea channel, which is conveyed by the gyre of the monsoon trough. Meanwhile, the large values of water vapor in the channel over the Indian Ocean are distributed from the south to Sri Lanka northeastward to the Indochina Peninsula.

In contrast, the water vapor of extreme precipitation during the period 2003–2015 is primarily contributed by the Indian Ocean channel (**Figures 5E,F**). Despite the reduced trajectory density of air masses over the Bay of Bengal, the PSCF increases not only over the Bay of Bengal but also the Indian Ocean. The result suggests that there could be more water vapor in the atmosphere over the Indian Ocean during the period 2003–2015. Since the low-level westerly jet is enhanced owing to the intensification of the LMP (**Figures 5A–C**), the higher wind speed helps water to evaporate from the ocean. In contrast, the westerly is weakened over the South China Sea during the period 2003–2015 compared with during 1951–2002. Therefore, the decelerated wind suppresses the evaporation of water from the South China Sea. Meanwhile, the decelerated wind leads to air masses lingering over the South China Sea, which results in a

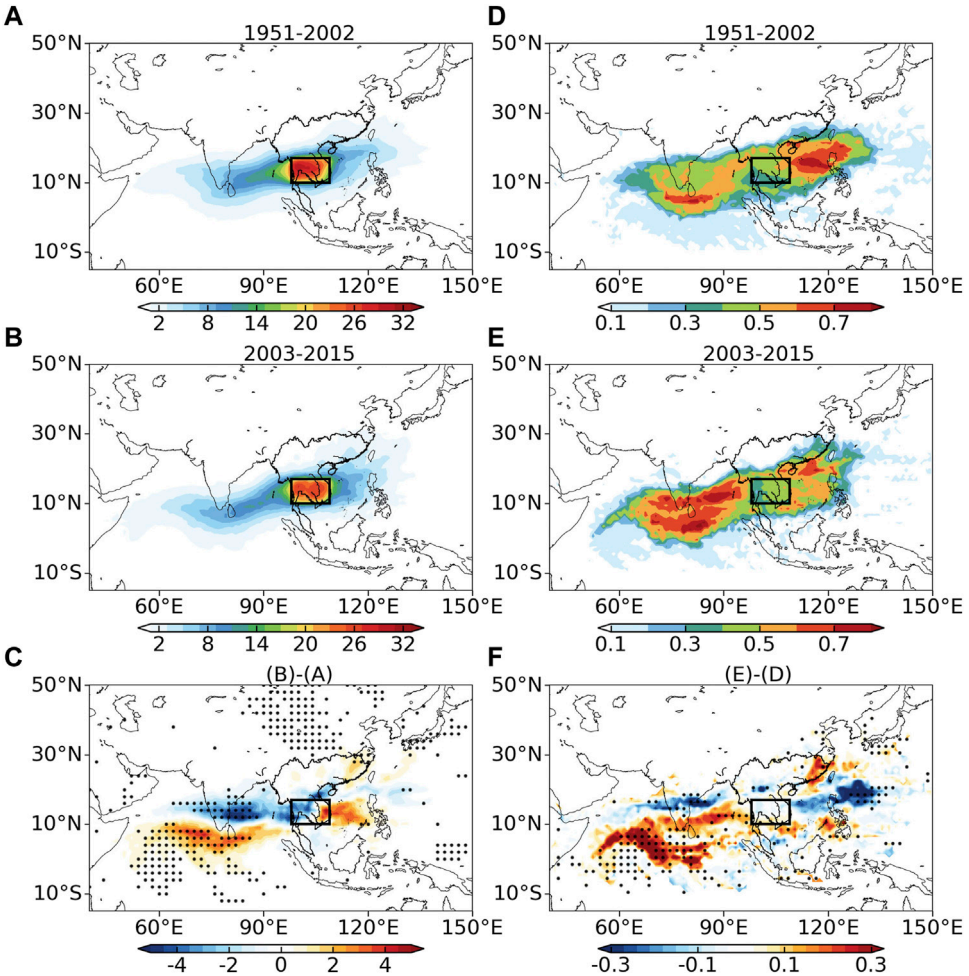

FIGURE 5 | Trajectory density patterns for the extreme precipitation during **(A)** 1951–2002, **(B)** 2003–2015, and **(C)** their differences. **(D–F)** as in **(A–C)** but for the PSCF. Only differences that are statistically significant at the 90% confidence level are stippled in **(C, F)**.

higher density of air masses. In spite of the increased trajectory density of air masses over the South China Sea, the PSCF decreases.

The water vapor channel over the Indian Ocean agrees with the findings of Stojanovic et al. (2021), who identified this as the dominant moisture source for precipitation over Vietnam. In comparison with their study, we found an additional moisture source over the South China Sea and a parallel water vapor channel over the Bay of Bengal for the larger occurrence number of extreme precipitation during 2003–2015. These results are in contrast to the general view that extreme precipitation requires more water vapor sources.

In comparison with the Lagrangian perspective and PSCF analysis, water vapor flux from the Eulerian perspective may provide anomalous westward water vapor fluxes over the South China Sea due to the easterly anomaly (**Figures 4C** and **6F**). The PSCF analysis of the backward trajectories of air masses can rule out this potential error.

To corroborate the elevated water vapor in the 21st century, **Figure 6** displays the climatological mean total column water vapor and vertically integrated water vapor flux and their anomaly fields associated with extreme precipitation for the two subperiods. The water vapor exhibits a circular distribution around the Indochina Peninsula, with the largest value over the Bay of Bengal (**Figures 6A,B**). These large values of water vapor are transported by the low-level westerly jet over the Indian Ocean and the cross-equatorial flow from the Australian high to the South China Sea. In comparison with that over the South China Sea, the water vapor flux is larger over the Indian Ocean and converges over the Bay of Bengal because of the topography.

Undoubtedly, water vapor increases over most of the region from the period 1951–2002 to 2003–2015 (**Figure 6C**), since climate warming leads to the atmosphere being able to hold more water vapor. Water vapor elevates more evidently over the Bay of Bengal than the South China Sea. A close inspection of **Figure 6C** shows enhanced northeastward water vapor flux associated with the deepened monsoon trough over India and the amplified Mascarene high. By contrast, the northward water vapor flux

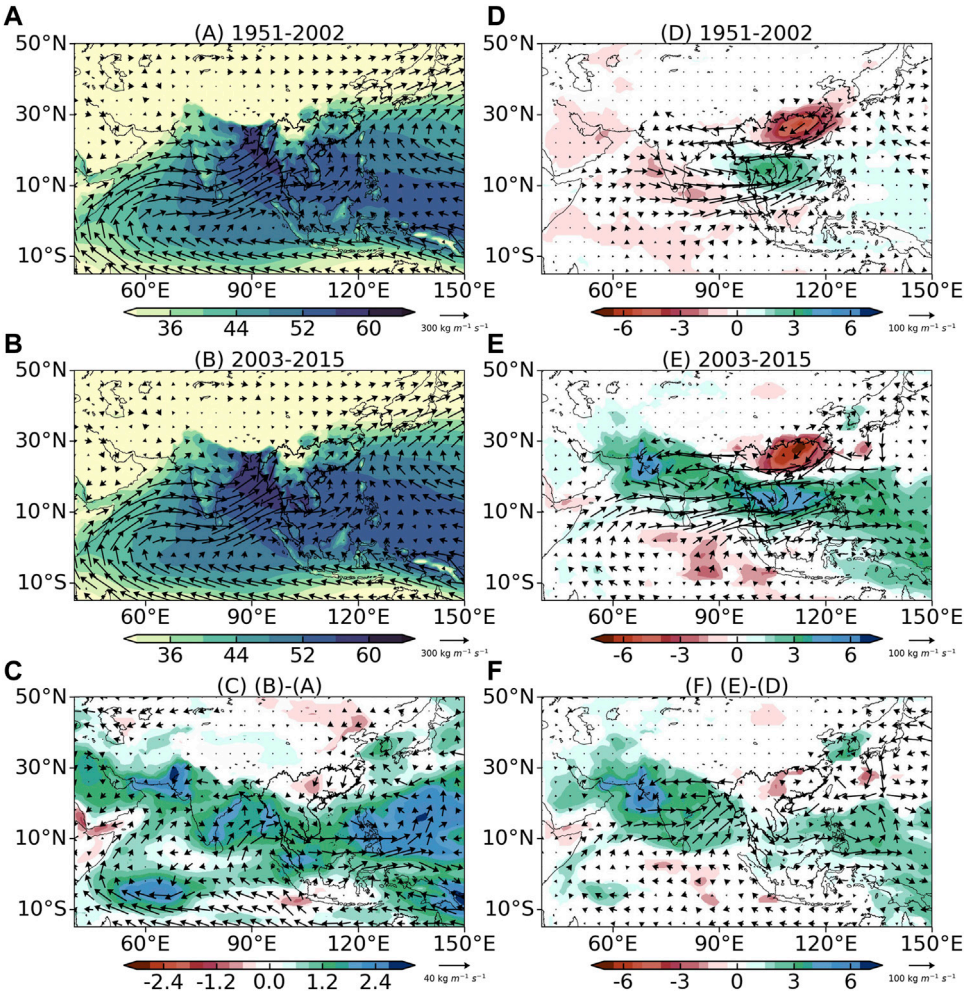

FIGURE 6 | Climatological mean total column water vapor (shading; units: kg m^{-2}) and vertically integrated water vapor flux (arrows; units: kg m^{-1} s^{-1}) during **(A)** 1951–2002, **(B)** 2003–2015, and **(C)** their differences. **(D–F)** as in **(A–C)**, but for the anomaly fields associated with extreme-precipitation days. Only differences that are statistically significant at the 90% confidence level are shaded in **(C–F)**.

is weakened over the South China Sea. Therefore, the change of the climatological mean flow over the Bay of Bengal, compared to the South China Sea, provides a more favorable water vapor condition for the extreme precipitation over the Indochina Peninsula in 2003–2015.

Considering the days of extreme precipitation, the mean fields of total column water vapor and vertically integrated water vapor flux generally resemble those of the climatological mean field but with enhanced water vapor over the Indochina Peninsula and eastward water vapor flux over the Indian Ocean (figure not shown). During 1951–2002, the positive water vapor anomaly is confined over the Indochina Peninsula to the South China Sea, which is contributed by eastward water vapor flux from the Indian Ocean and westward water vapor flux from the South China Sea associated with the enhanced monsoon dipole (**Figure 6D**). In contrast, during 2003–2015, the positive water vapor anomaly dominates the Arab Sea via Indochina to the subtropical Pacific Ocean, which is associated with the eastward water vapor flux from Somalia (**Figure 6E**). The differences of water vapor and flux between two subperiods feature amplified water vapor and enhanced eastward transport over India via Indochina to the subtropical Pacific Ocean (**Figure 6F**), which is consistent with the increased climatological mean water vapor and eastward water vapor flux and the intensification of the LMP.

Association With Pacific Decadal Oscillation

It is well recognized that El Niño–Southern Oscillation (ENSO), one of the strongest SST signals in interannual climate variability, exerts a significant impact on the interannual variability of monsoon precipitation over the Indochina Peninsula (Zhang et al., 2002; Ge et al., 2021; Wu and Zhu, 2021). To investigate the potential influence of SST anomalies on the extreme precipitation over the Indochina Peninsula, we construct an LMP index by projecting each daily 850-hPa stream function

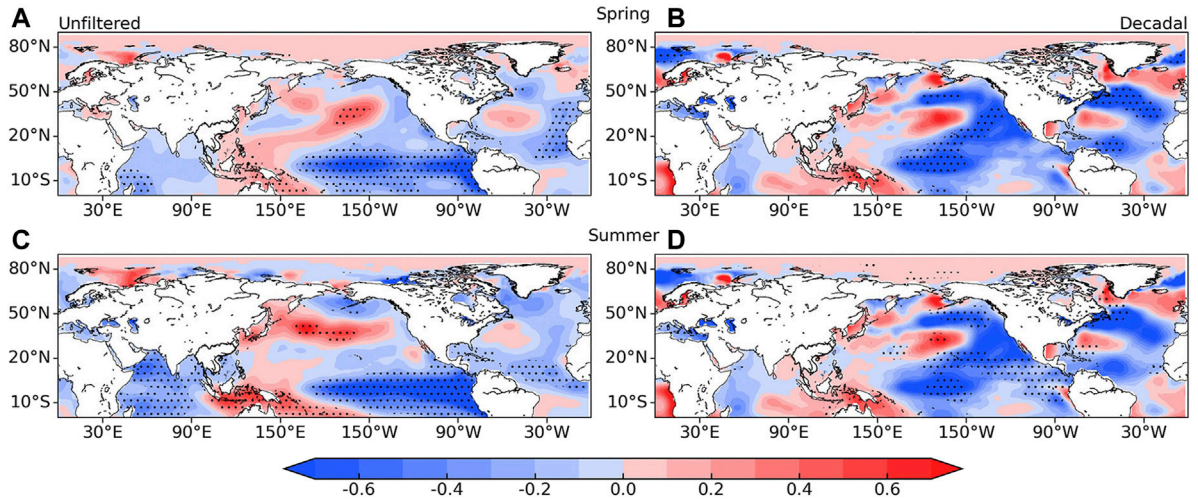

FIGURE 7 | Regression maps of SST anomalies (unit: °C) during **(A)** spring and (**B**) summer against unfiltered time series of LMP indices. **(C**, **D)** as in **(A**, **B)**, but for the decadal time series of LMP indices. Stippling indicates regression coefficients that are statistically significant at the 90% confidence level.

anomaly pattern (ψ') onto the LMP (ψ_{LMP}) using a pattern amplitude projection (Xie et al., 2017):

$$\text{LMP index} = \frac{A^{-1}\int_A a^2\psi'\psi_{\text{LMP}}\cos\phi d\lambda d\phi}{A^{-1}\int_A a^2(\psi_{\text{LMP}})^2\cos\phi d\lambda d\phi}$$

where A represents the area of the LMP (15S°–30°N, 60°–125°E), which encompasses the anomalous circulation directly associated with extreme rainfall; a is the mean radius of the Earth; and λ and ϕ are the longitude and latitude, respectively. This LMP index measures both the phase and amplitude of the LMP simultaneously (Xie at al., 2017).

Figure 7 displays regression maps of the SST during spring and summer against the unfiltered and decadal time series of the detrended LMP index. On the interannual time scale, the LMP is obviously associated with the La Niño pattern (**Figures 7A,C**), which agrees with prior studies regarding the influence of ENSO on monsoon precipitation over the Indochina Peninsula (Zhang et al., 2002; Ge et al., 2021; Wu and Zhu, 2021). Ge et al. (2021) showed that La Niño induces a cyclonic circulation over both the western North Pacific and the Bay of Bengal and thus brings in more water vapor from the Pacific and Indian Oceans for the monsoon precipitation over the Indochina Peninsula.

In addition, the midlatitude North Pacific central-western SST is significantly warm, and the tropical central-eastern Pacific and North Pacific North American west coast SSTs are anomalously cold, indicative of the negative phase of the PDO (Mantua et al., 1997). Given that the unfiltered time series of the LMP index is primarily contributed by the interannual variability, we remove this time scale by applying a 10-year Gaussian filter. The regression map of SST anomalies against the decadal time series of the LMP index confirms that the LMP is indeed correlated with the negative phase of the PDO. To verify the influence of the PDO on the LMP and extreme precipitation, **Figure 8** displays the probability density function (PDF) of the LMP index and occurrence of extreme precipitation stratified by the PDO phases (±1 standard deviation) for summer. The PDF of LMP indices is right-skewed during the negative phase of the PDO (**Figure 8A**). Meanwhile, the occurrence of extreme precipitation is also most frequent during the negative phase of the PDO (**Figure 8B**). The result suggests that the negative phase of the PDO in the 21st century contributes substantially to the increased occurrence number of days of extreme precipitation over the Indochina Peninsula *via* populating larger values of the LMP indices.

We acknowledge that not all larger value of the LMP indices can induce extreme precipitation over the Indochina Peninsula. Even though a larger value of the LMP index does not produce extreme precipitation, it is likely to induce intense rainfall. Cheng et al. (2021) noted that the LMP in terms of stream function anomalies is contaminated by the global warming signal, which increases the stream function value in the Northern Hemisphere. If the LMP is defined in terms of relative vorticity, the relationship between such an LMP and the PDO would strengthen.

DISCUSSION

Since the period of May–October includes the decay stage of the summer monsoon, a natural question arises: there must be some extreme precipitation that is not associated with the summer monsoon, particularly in October. To answer this question, we investigated the relationships between extreme precipitation and tropical cyclone and MJO. We calculated the relative frequency of tropical cyclone and OMI associated with extreme precipitation during periods of May–August and September–October normalized by the number of years and months.

Figure 9 displays the relative frequency of tropical cyclone center associated with extreme precipitation over 1951–2015 and its difference between two subperiods of 1951–2002 and

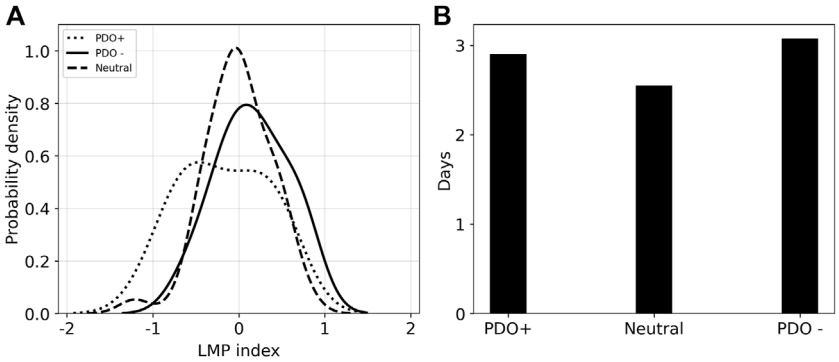

FIGURE 8 | (A) PDF of LMP indices and **(B)** the relative frequency of extreme precipitation during different phases of the PDO.

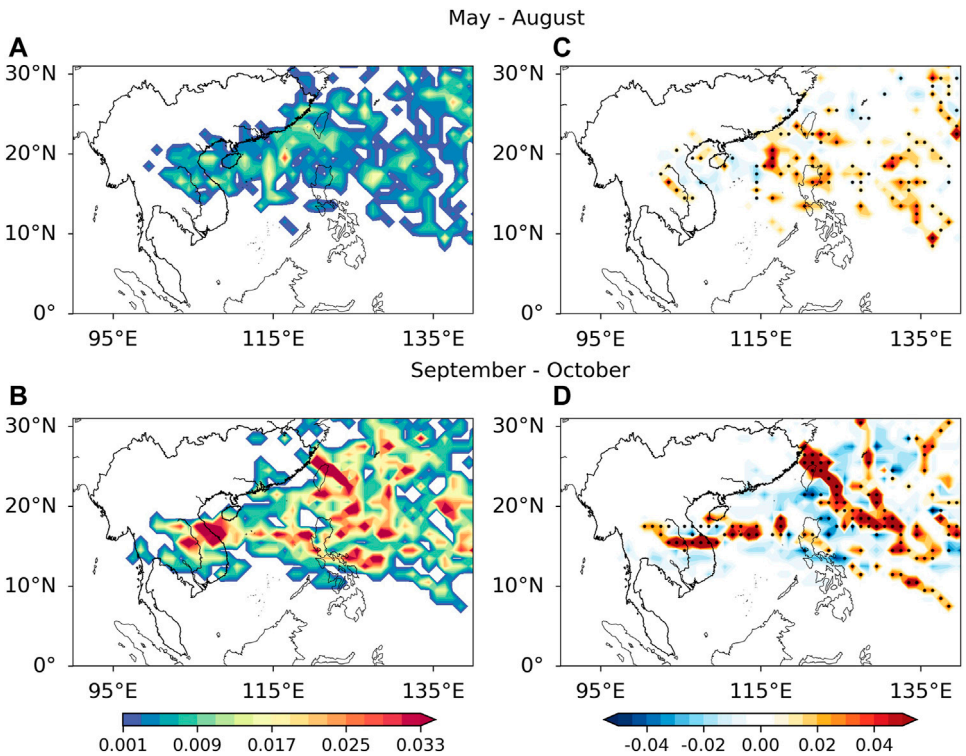

FIGURE 9 | The relative frequency of tropical cyclone center associated with extreme precipitation during **(A)** May–August and **(B)** September–October over 1951–2015. **(C, D)** as in **(A, B)**, but for the differences in frequency of tropical cyclone center associated with extreme precipitation during the subperiods of 1951–2002 and 2003–2015. Only differences that are statistically significant at the 90% confidence are stippled in **(C, D)**.

2003–2015. During May–August, tropical cyclones associated with extreme precipitation are confined to the northeastern Indochina Peninsula (**Figure 9A**). In contrast, tropical cyclones associated with extreme precipitation during September–October not only increase in number but also dominate the southern Indochina Peninsula (**Figure 9B**). The result suggests that tropical cyclones contribute more to extreme precipitation during the decay stage of summer monsoon than the peak of summer monsoon. Considering the difference between two subperiods (**Figures 9C,D**), an apparent increase is seen over central Indochina during September–October. Therefore, the increase of extreme-precipitation-associated tropical cyclone also provides some contributions to the more extreme-precipitation days during 2003–2015 compared to 1951–2002, particularly during the decaying stage of the summer monsoon.

A parallel analysis is performed for extreme precipitation associated with MJO (**Figure 10**). Extreme precipitation is mainly associated with phases 5–7 of MJO that correspond to pronounced convections from India via Indochina to the western Pacific and stream function anomalies resembling

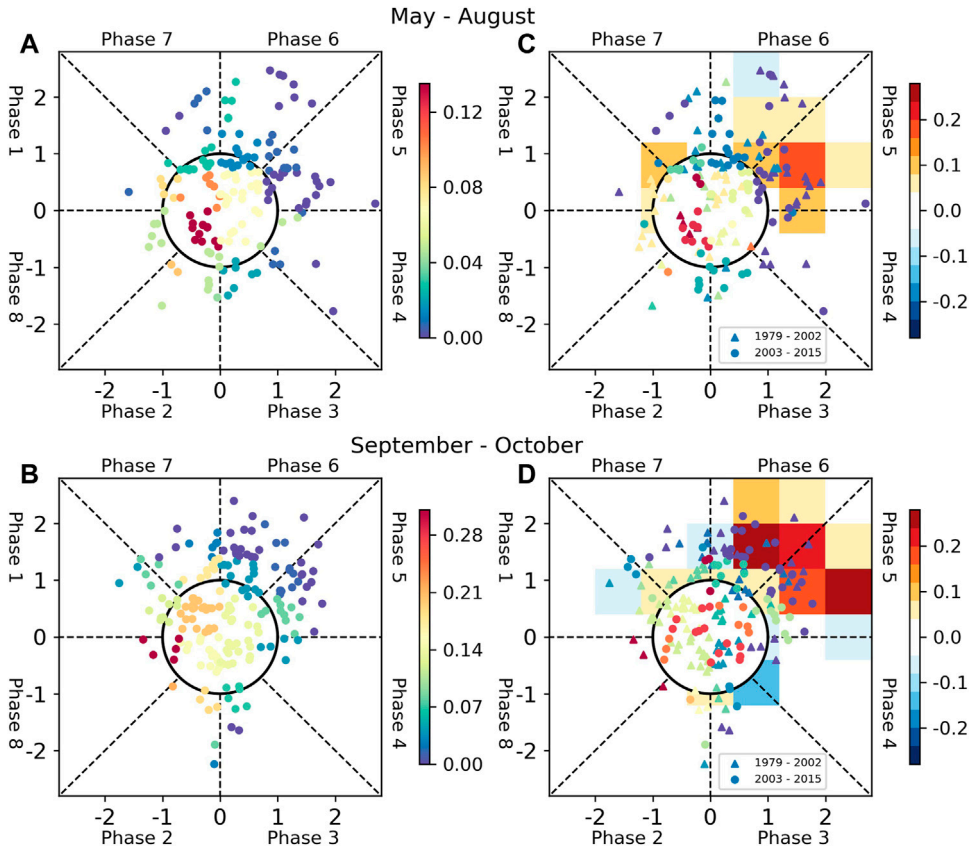

FIGURE 10 | Phase plots of OMI associated with extreme precipitation during **(A)** May–August and **(B)** September–October over 1951–2015. The color shading indicates the relative frequency of OMI in each 0.7 × 0.7 bin. **(C, D)** as in **(A, B)**, but for the differences (shading) in frequency of OMI during the subperiods of 1951–2002 and 2003–2015.

the LMP (see https://psl.noaa.gov/mjo/mjoindex/pdf/psi850.1x.20ns.omi.amp1.096.jja.7912.pdf). In comparison with May–August, there are more extreme-precipitation days associated with phases 5–7 of MJO during the decaying stage of the summer monsoon (**Figures 10A,B**). The result indicates that phases 5–7 of MJO contribute more to extreme precipitation during the decaying stage of the summer monsoon. Considering the change between two subperiods of 1951–2002 and 2003–2015 (**Figures 10C,D**), there are positive frequency anomalies of extreme precipitation associated with phases 5 and 6 of MJO, which have stronger convections over the Indochina Peninsula than phase 7 of MJO. Therefore, phases 5 and 6 act to increase occurrence frequency of extreme precipitation during 2003–2015 compared to 1951–2002, particularly during the decaying stage of the summer monsoon.

The tropical cyclone and MJO provide contributions to occurrence frequency of extreme precipitation during the decay stage of the summer monsoon and thus to the decadal variability of extreme precipitation over the Indochina Peninsula. However, they both carry a large amount of water vapor and may be implicitly included in the change of the foregoing water vapor analysis.

SUMMARY

The decadal change in extreme precipitation over the Indochina Peninsula during the rainy season (May–October) during 1951–2015 is investigated in this study. The annual occurrence number of days of extreme precipitation exhibits a significant upward trend, possibly contributed by the amplified decadal variability during the period 2003–2015. A running *t*-test shows an abrupt change in the year 2003 for the annual occurrence number of days of extreme precipitation. Therefore, this study focuses on the change in extreme precipitation between the two subperiods of 1951–2002 and 2003–2015 in terms of changes of circulation pattern and water vapor transport from the Lagrangian perspective.

The extreme precipitation is associated with an intensified monsoon dipole pattern in which the monsoon trough is deepened from northern India to the Indochina Peninsula and the Mascarene high is amplified. Therefore, the low-level westerly jet is enhanced from Somalia to the Indochina Peninsula and a monsoon trough gyre over the South China Sea. The analysis with the Lagrangian tool shows that these two flows constitute two major water vapor channels: one along the low-level westerly jet over the Indian Ocean and the other from the South China Sea.

The monsoon pattern is intensified from the subperiod of 1951–2002 to that of 2003–2015. The monsoon trough is deepened over northern India, and the Mascarene high is amplified, which results in an intensification and southward displacement of the low-level westerly jet over the Indian Ocean. Meanwhile, the acceleration of wind speed increases the evaporation of water from the Indian Ocean. Therefore, the PSCF analysis reveals that the contributions of water vapor from the Bay of Bengal and the Indian Ocean both increase. In contrast, the wind speed is decelerated over the South China Sea and thereby leads to lingering air masses over the South China Sea, which can suppress the evaporation of water from the sea. Despite more air mass trajectories over the South China Sea, the contribution of water vapor from the South China Sea decreases.

The present study primarily focuses on the changes in the atmospheric circulation pattern and water vapor for the change in extreme precipitation and preliminarily discusses a possible influence of SST anomalies—particularly ENSO and the PDO. The negative phase of the PDO populates larger values of the LMP and thus enhances the water vapor channel over the Indian Ocean, resulting in an abnormally high frequency of extreme precipitation in the 21st century. In future work, we will carry out atmospheric general circulation model experiments to explore this pathway between the PDO and extreme precipitation over the Indochina Peninsula.

DATA AVAILABILITY STATEMENT

The original contributions presented in the study are included in the article/**Supplementary Material**, further inquiries can be directed to the corresponding author.

AUTHOR CONTRIBUTIONS

ZC drafted the first version of the paper. ZX writing, editing, and responding of the review. All authors provided feedback on the paper.

FUNDING

This research is jointly supported by the National Key Research and Development Program of China (Grant 2016YFA0601500), the National Natural Science Foundation of China (Grants 41861144014 and 41875078), and the Huaneng Group Technology Project (Phase 1) "Offshore Wind Power and Intelligent Energy System" (No. HNKJ20-H88).

ACKNOWLEDGMENTS

The authors are grateful to two reviewers for their instructive suggestions and comments. We thank the Joint Laboratory of Offshore Wind Power and Intelligent Energy System for providing the funding. We thank the Atmospheric Dynamics Group, Institute for Atmospheric and Climate Science, ETH Zurich for providing LAGRANTO *via* https://iacweb.ethz.ch/staff/sprenger/lagranto/ and Michael Sprenger for providing help with running it.

SUPPLEMENTARY MATERIAL

The Supplementary Material for this article can be found online at: https://www.frontiersin.org/articles/10.3389/feart.2021.758664/full#supplementary-material

REFERENCES

Alexander, L. V., Zhang, X., Peterson, T. C., Caesar, J., Gleason, B., Klein Tank, A. M. G., et al. (2006). Global Observed Changes in Daily Climate Extremes of Temperature and Precipitation. *J. Geophys. Res.* 111, D05109. doi:10.1029/2005JD006290

Bengtsson, L. (2010). The Global Atmospheric Water Cycle. *Environ. Res. Lett.* 5, 025202. doi:10.1088/1748-9326/5/2/025202

Chang, C.-P., Wang, Z., McBride, J., and Liu, C.-H. (2005). Annual Cycle of Southeast Asia-Maritime Continent Rainfall and the Asymmetric Monsoon Transition. *J. Clim.* 18, 287–301. doi:10.1175/JCLI-3257.1

Cheng, Z. L., Xie, Z. W., Bueh, C., Gong, Y. F., Jian, J., and Lai, S. (2021). Spatiotemporal Characteristics of Extreme Precipitation in Indochina Peninsula and South China. *Chin. J. Atmos. Sci. Accepted*. in Chinese.

Chhin, R., Shwe, M. M., and Yoden, S. (2019). Time-lagged Correlations Associated with Interannual Variations of Pre-monsoon and post-monsoon Precipitation in Myanmar and the Indochina Peninsula. *Int. J. Climatol.* 40, 3792–3812. doi:10.1002/joc.6428

Christensen, J. H., and Christensen, O. B. (2003). Severe Summertime Flooding in Europe. *Nature* 421, 805–806. doi:10.1038/421805a

Faikrua, A., Pimonsree, S., Wang, L., Limsakul, A., Singhruck, P., and Dong, Z. (2020). Decadal Increase of the Summer Precipitation in Thailand after the Mid-1990s. *Clim. Dyn.* 55, 3253–3267. doi:10.1007/s00382-020-05443-8

Fu, C. B., and Wang, Q. (1992). The Definition and Detection of the Abrupt Climatic Change. *Chin. J. Atmos. Sci.* 16, 482–493. doi:10.3878/j.issn.1006–9895.1992.04.11

Ge, F., Zhi, X., Babar, Z. A., Tang, W., and Chen, P. (2017). Interannual Variability of Summer Monsoon Precipitation over the Indochina Peninsula in Association with ENSO. *Theor. Appl. Climatol.* 128, 523–531. doi:10.1007/s00704-015-1729-y

Ge, F., Zhu, S., Sielmann, F., Fraedrich, K., Zhu, X., Zhang, L., et al. (2021). Precipitation over Indochina during the Monsoon Transition: Modulation by Indian Ocean and ENSO Regimes. *Clim. Dyn.* 57, 2491–2504. doi:10.1007/s00382-021-05817-6

Gimeno, L., Nieto, R., Drumond, A., Castillo, R., and Trigo, R. (2013). Influence of the Intensification of the Major Oceanic Moisture Sources on continental Precipitation. *Geophys. Res. Lett.* 40, 1443–1450. doi:10.1002/grl.50338

Grotjahn, R., Black, R., Leung, R., Wehner, M. F., Barlow, M., Bosilovich, M., et al. (2015). North American Extreme Temperature Events and Related Large Scale Meteorological Patterns: a Review of Statistical Methods, Dynamics, Modeling, and Trends. *Clim. Dyn.* 46, 1151–1184. doi:10.1007/s00382-015-2638-6

Hersbach, H., Bell, B., Berrisford, P., Hirahara, S., Horányi, A., Muñoz-Sabater, J., et al. (2020). The ERA5 Global Reanalysis. *Q.J.R. Meteorol. Soc.* 146, 1999–2049. doi:10.1002/qj.3803

Huang, B., Thorne, P. W., Banzon, V. F., Boyer, T., Chepurin, G., Lawrimore, J. H., et al. (2017). Extended Reconstructed Sea Surface Temperature, Version 5 (ERSSTv5): Upgrades, Validations, and Intercomparisons. *J. Clim.* 30, 8179–8205. doi:10.1175/JCLI-D-16-0836.1

Huang, R. H., Chen, J. L., and Liu, Y. (2011). Interdecadal Variation of the Leading Modes of Summertime Precipitation Anomalies over Eastern China and its Association with Water Vapor Transport over East Asia. *Chin. J. Atmos. Sci.* 35, 589–606. doi:10.3878/j.issn.1006-9895.2011.04.01

Kohonen, T. (2001). *Self-Organizing Maps*. 3rd Edition. Berlin: Springer Press. doi:10.1007/978-3-642-56927-2

Lai, S., Xie, Z., Bueh, C., and Gong, Y. (2020). Fidelity of the APHRODITE Dataset in Representing Extreme Precipitation over Central Asia. *Adv. Atmos. Sci.* 37, 1405–1416. doi:10.1007/s00376-020-0098-3

Liu, Y., Chen, H., Zhang, G., Sun, J., Li, H., and Wang, H. (2020). Changes in Lake Area in the Inner Mongolian Plateau under Climate Change: The Role of the Atlantic Multidecadal Oscillation and Arctic Sea Ice. *J. Clim.* 33, 1335–1349. doi:10.1175/JCLI-D-19-0388.1

Lu, X., Yu, H., Ying, M., Zhao, B., Zhang, S., Lin, L., et al. (2021). Western North Pacific Tropical Cyclone Database Created by the China Meteorological Administration. *Adv. Atmos. Sci.* 38, 690–699. doi:10.1007/s00376-020-0211-7

Mantua, N. J., Hare, S. R., Zhang, Y., Wallace, J. M., and Francis, R. C. (1997). A Pacific Interdecadal Climate Oscillation with Impacts on salmon Production. *Bull. Amer. Meteorol. Soc.* 78, 1069–1079. doi:10.1175/1520-0477(1997)078<1069:APICOW>2.0.CO;2

Meng, H. F., Zhang, M. J., Wang, S. J., Qiu, X., Zhou, S. E., Zhang, Y. N., et al. (2020). Precipitation Isotope Characteristics and Water Vapor Source Analysis in the Upper Reaches of the Heihe River. *J. Glaciol. Geocryol.* 42, 937–951. doi:10.7522/j.issn.1000-0240.2020.0068

Promchote, P., Simon Wang, S.-Y., and Johnson, P. G. (2016). The 2011 Great Flood in Thailand: Climate Diagnostics and Implications from Climate Change. *J. Clim.* 29, 367–379. doi:10.1175/JCLI-D-15-0310.1

Salamalikis, V., Argiriou, A. A., and Dotsika, E. (2015). Stable Isotopic Composition of Atmospheric Water Vapor in Patras, Greece: A Concentration Weighted Trajectory Approach. *Atmos. Res.* 152, 93–104. doi:10.1016/j.atmosres.2014.02.021

Schemm, S., Nummelin, A., Kvamstø, N. G., and Breivik, Ø. (2017). The Ocean Version of the Lagrangian Analysis Tool LAGRANTO. *J. Atmos. Ocean. Technol.* 34, 1723–1741. doi:10.1175/JTECH-D-16-0198.1

Sprenger, M., and Wernli, H. (2015). The LAGRANTO Lagrangian Analysis Tool - Version 2.0. *Geosci. Model. Dev.* 8, 2569–2586. doi:10.5194/gmd-8-2569-2015

Stojanovic, M., Nieto, R., Liberato, M. L. R., Sorí, R., Vázquez, M., and Gimeno, L. (2021). Tracking the Origins of Moisture over Vietnam: The Role of Moisture Sources and Atmospheric Drivers on Seasonal Hydroclimatic Conditions. *Int. J. Climatol.* 41, 5843–5861. doi:10.1002/joc.7156

Takahashi, H. G., Fujinami, H., Yasunari, T., Matsumoto, J., and Baimoung, S. (2015). Role of Tropical Cyclones along the Monsoon Trough in the 2011 Thai Flood and Interannual Variability. *J. Clim.* 28, 1465–1476. doi:10.1175/JCLI-D-14-00147.1

Tang, B., Hu, W., and Duan, A. (2021). Assessment of Extreme Precipitation Indices over Indochina and South China in CMIP6 Models. *J. Clim.* 34, 7507–7524. doi:10.1175/JCLI-D-20-0948.1

Wang, A. P., Zhu, B., Yin, Y., Jin, L. J., and Zhang, L. (2014). Aerosol Number Concentration Properties and Potential Sources Areas Transporting to the Top of Mountain Huangshan in Summer. *China. Environ. Sci.* 34, 852–861. doi:10.3969/j.issn.1000-6923.2014.04.008

Wu, R., and Zhu, P. (2021). Interdecadal Change in the Relationship of Indochina Peninsula May Precipitation to ENSO. *Int. J. Climatol.* 41, 2441–2455. doi:10.1002/joc.6968

Xie, Z., Black, R. X., and Deng, Y. (2017). The Structure and Large-Scale Organization of Extreme Cold Waves over the Conterminous United States. *Clim. Dyn.* 49, 4075–4088. doi:10.1007/s00382-017-3564-6

Yang, Y., and Wu, R. (2019). Seasonal Variation of Precipitation over the Indochina Peninsula and its Impact on the South China Sea spring Warming. *Int. J. Climatol.* 39, 1618–1633. doi:10.1002/joc.5904

Yatagai, A., Kamiguchi, K., Arakawa, O., Hamada, A., Yasutomi, N., and Kitoh, A. (2012). APHRODITE: Constructing a Long-Term Daily Gridded Precipitation Dataset for Asia Based on a Dense Network of Rain Gauges. *Bull. Am. Meteorol. Soc.* 93, 1401–1415. doi:10.1175/BAMS-D-11-00122.1

Zeng, Y., and Hopke, P. K. (1989). A Study of the Sources of Acid Precipitation in Ontario, Canada. *Atmos. Environ. (1967)* 23, 1499–1509. doi:10.1016/0004-6981(89)90409-5

Zhang, R., Chu, Q., Zuo, Z., and Qi, Y. (2021). Summertime Moisture Sources and Transportation Pathways for China and Associated Atmospheric Circulation Patterns. *Front. Earth Sci.* 9, 756943. doi:10.3389/feart.2021.756943

Zhang, R., Sun, C., Zhu, J., Zhang, R., and Li, W. (2020). Increased European Heat Waves in Recent Decades in Response to Shrinking Arctic Sea Ice and Eurasian snow Cover. *NPJ Clim. Atmos. Sci.* 3, 7. doi:10.1038/s41612-020-0110-8

Zhang, Y., Li, T., Wang, B., and Wu, G. (2002). Onset of the Summer Monsoon over the Indochina Peninsula: Climatology and Interannual Variations*. *J. Clim.* 15, 3206–3221. doi:10.1175/1520-0442(2002)015<3206:OOTSMO>2.0.CO;2

Zhao, S., Deng, Y., and Black, R. X. (2017). A Dynamical and Statistical Characterization of U.S. Extreme Precipitation Events and Their Associated Large-Scale Meteorological Patterns. *J. Clim.* 30, 1307–1326. doi:10.1175/JCLI-D-15-0910.1

Zhou, T. J., Yu, R. C., Zhang, X. H., Yu, Y. Q., Li, W., Liu, H. L., et al. (2001). Features of Atmospheric Moisture Transport, Convergence and Air–Sea Freshwater Flux Simulated by the Coupled Climate Models. *Chin. J. Atmos. Sci.* 25, 596–608. doi:10.3878/j.issn.1006-9895.2001.05.03

Conflict of Interest: JY was employed by China Huaneng Group Co., Ltd.

The remaining authors declare that the research was conducted in the absence of any commercial or financial relationships that could be construed as a potential conflict of interest.

Publisher's Note: All claims expressed in this article are solely those of the authors and do not necessarily represent those of their affiliated organizations, or those of the publisher, the editors and the reviewers. Any product that may be evaluated in this article, or claim that may be made by its manufacturer, is not guaranteed or endorsed by the publisher.

frontiers in Environmental Science

ORIGINAL RESEARCH
published: 09 December 2021
doi: 10.3389/fenvs.2021.759547

Projecting Hydrological Responses to Climate Change Using CMIP6 Climate Scenarios for the Upper Huai River Basin, China

Guodong Bian[1,2,3,4], *Jianyun Zhang*[1,2,3,4], *Jie Chen*[1], *Mingming Song*[2,3,4], *Ruimin He*[2,3,4], *Cuishan Liu*[2,3,4], *Yanli Liu*[2,3,4], *Zhenxin Bao*[2,3,4], *Qianguo Lin*[5] *and Guoqing Wang*[2,3,4]*

[1]State Key Laboratory of Water Resources and Hydropower Engineering Science, Wuhan University, Wuhan, China, [2]Nanjing Hydraulic Research Institute, Nanjing, China, [3]Yangtze Institute for Conservation and Development, Nanjing, China, [4]Research Center for Climate Change, Ministry of Water Resources, Nanjing, China, [5]College of Environmental Science and Engineering, North China Electric Power University, Beijing, China

The influence of climate change on the regional hydrological cycle has been an international scientific issue that has attracted more attention in recent decades due to its huge effects on drought and flood. It is essential to investigate the change of regional hydrological characteristics in the context of global warming for developing flood mitigation and water utilization strategies in the future. The purpose of this study is to carry out a comprehensive analysis of changes in future runoff and flood for the upper Huai River basin by combining future climate scenarios, hydrological model, and flood frequency analysis. The daily bias correction (DBC) statistical downscaling method is used to downscale the global climate model (GCM) outputs from the sixth phase of the Coupled Model Intercomparison Project (CMIP6) and to generate future daily temperature and precipitation series. The Xinanjiang (XAJ) hydrological model is driven to project changes in future seasonal runoff under SSP245 and SSP585 scenarios for two future periods: 2050s (2031–2060) and 2080s (2071–2100) based on model calibration and validation. Finally, the peaks over threshold (POT) method and generalized Pareto (GP) distribution are combined to evaluate the changes of flood frequency for the upper Huai River basin. The results show that 1) GCMs project that there has been an insignificant increasing trend in future precipitation series, while an obvious increasing trend is detected in future temperature series; 2) average monthly runoffs in low-flow season have seen decreasing trends under SSP245 and SSP585 scenarios during the 2050s, while there has been an obvious increasing trend of average monthly runoff in high-flow season during the 2080s; 3) there is a decreasing trend in design floods below the 50-year return period under two future scenarios during the 2050s, while there has been an significant increasing trend in design flood during the 2080s in most cases and the amplitude of increase becomes larger for a larger return period. The study suggests that future flood will probably occur more frequently and an urgent need to develop appropriate adaptation measures to increase social resilience to warming climate over the upper Huai River basin.

Keywords: climate change, CMIP6, hydrological modeling, flood, Huai River basin

OPEN ACCESS

Edited by:
Yulei Xie,
Guangdong University of Technology, China

Reviewed by:
Xihui Gu,
China University of Geosciences Wuhan, China
Yuliang Zhou,
Hefei University of Technology, China

***Correspondence:**
Guoqing Wang
gqwang@nhri.cn

Specialty section:
This article was submitted to Interdisciplinary Climate Studies, a section of the journal Frontiers in Environmental Science

Received: *16 August 2021*
Accepted: *18 November 2021*
Published: *09 December 2021*

Citation:
Bian G, Zhang J, Chen J, Song M, He R, Liu C, Liu Y, Bao Z, Lin Q and Wang G (2021) Projecting Hydrological Responses to Climate Change Using CMIP6 Climate Scenarios for the Upper Huai River Basin, China. Front. Environ. Sci. 9:759547. doi: 10.3389/fenvs.2021.759547

1 INTRODUCTION

Climate change associated with global warming, mainly owing to the rise of greenhouse gas emissions in the atmosphere, has caused an increase of the evapotranspiration over the land surface, which in turn has accelerated the hydrological cycle and altered the hydrological element (Arnell and Gosling, 2013; Schewe et al., 2014; Wang et al., 2017). Recently, several studies have already suggested signs of adverse impacts on availability of water resources due to global warming in different regions around the world (Feyen et al., 2012; Yoon et al., 2016; Byun et al., 2018; Gu et al., 2020). Moreover, there is strengthened evidence that the global water cycle will continue to intensify as global temperatures rise, with precipitation and surface water flows projected to become more variable over most land regions (IPCC, 2021). A warmer climate will intensify very wet and very dry weather and climate events. These extreme events are expected to trigger further, leading to increasing weather-related hazards such as destructive flooding or drought, which possibly pose tremendous societal, economic, and environmental challenges around the world. Therefore, it is of great necessity to enhance the understanding of future changes in the hydrological responses and flood characteristics under the context of climate change to provide support for appropriate adaptation strategies and water resources management.

In recent years, the global climate models have been proven to be the most versatile and effective tool for producing potential climatic scenarios in the future by many studies, which have been extensively applied in investigating the effects of climate change on the hydrological cycle and water resource management (Masood et al., 2015; Amin et al., 2017; Zhuan, et al., 2018). However, the coarse grids of GCMs are generally unable to acquire climate variability at the basin scale; the downscaling techniques are developed to convert GCM outputs with coarse resolution to a finer scale for generating daily series of climate variables representing the future climatic scenarios. Compared to dynamic downscaling techniques, statistical downscaling methods are more widely used owing to their relatively good performance and inexpensive computational expense (Shen et al., 2018; Gu et al., 2020). Moreover, the bias correction approaches are usually used considering their convenience and good ability in identifying extreme climatic features among those statistical downscaling methods (Ahmadalipour et al., 2018). Based on the results of the aforementioned techniques, a hydrological model can be used to project and evaluate future changes in hydrological characteristics from global and regional perspectives (Jung and Chang., 2011; Alkama et al., 2013; Li et al., 2015; Winsemius et al., 2016; Glenn et al., 2017; Wang et al., 2020). For example, Koirala et al. (2014) used runoff outputs from 11 AOGCMs from phase 5 of the Coupled Model Intercomparison Project (CMIP5) to evaluate the changes in global streamflow. They found that high flow had a rising trend over northern high latitudes of Eurasia and North America, Asia, and eastern Africa under emission scenario RCP4.5 and RCP8.5, while mean and low flows were both projected with a decreasing trend in Europe, Middle East, southwestern United States, and Central America. Zheng et al. (2018) projected the changes of future climate and runoff for the south Asia region under the RCP8.5 scenario using 42 CMIP5 GCMs, three downscaling techniques, and an H08 model. Their results indicated that the change in precipitation was the main driving factor leading to the increase in future runoff throughout most of the study region.

Moreover, flood is the most serious disaster related to climate, and it is projected to become more frequent and intense as global warming (IPCC., 2013; Du et al., 2019; IPCC, 2021). Due to the characteristics of the basin and river networks, the Huai River basin is the worst hit area threatened by frequent flood disasters since ancient times, and the flood severity of this area ranks first among the major rivers over China. Recently, the basin-wide floods in 1991, 2003, and 2007 are acknowledged as the most destructive events on record in the Huai River basin, which have resulted in considerable losses with millions of emergency relocation and billions of economy loss (Zhang and You, 2014). These associated socioeconomic damages in the Huai River basin will be even more progressively intensified under the background of climate change. Therefore, investigating the changes in flood characteristics over the Huai River basin is of great importance to formulate regional flood risk mitigation measures for future climatic scenarios. The conventional approach to calculate future design floods is using historical data only by fitting probability distribution functions, while it may not truly reflect the probable future scenario of extreme events due to the climate change. To overcome these shortcomings, climate models and projections are widely employed. In the previous studies, they found that results of the CMIP5 models have shown strong agreement on an array of flood variations (Silva and Portela, 2018; Nam et al., 2019; Tabari, 2020). For instance, Nyaupane et al. (2018) employed the variable infiltration capacity (VIC) model to analyze the change in flood frequency under various future emission scenarios from CMIP5 data for the study basin. They found that there existed a rising trend of the future streamflow in the study area, and the future flood with a 100-year return period likely would be more than 2 times the present flood with a 100-year return period, highlighting the likelihood of the intensification of the risk of future flooding. Gao et al. (2020) used four GCMs drawn from CMIP5 in conjunction with GR4J model to evaluate the variations of future extreme floods in the context of climate change in the Qu river basin of east China under RCP4.5 and RCP8.5 scenarios. They applied the POT method and generalized Pareto distribution and found that a rising tendency of design floods was projected at most cases in the future climate scenarios for the study area.

Despite global climate models from CMIP5 projections effectively providing some useful information on how climate change will affect the future flood, it is necessary to re-evaluate the status of these effects once new datasets and research approaches become available (Cook et al., 2020). Hence, the release of the latest and most advanced climate models from phase 6 of the Coupled Model Intercomparison Project (CMIP6) provides a new opportunity to obtain more credible understanding of influences of climate change on hydrology and to review conclusions from previous community modeling efforts. Thus, the specific purposes of this study are to investigate variations in

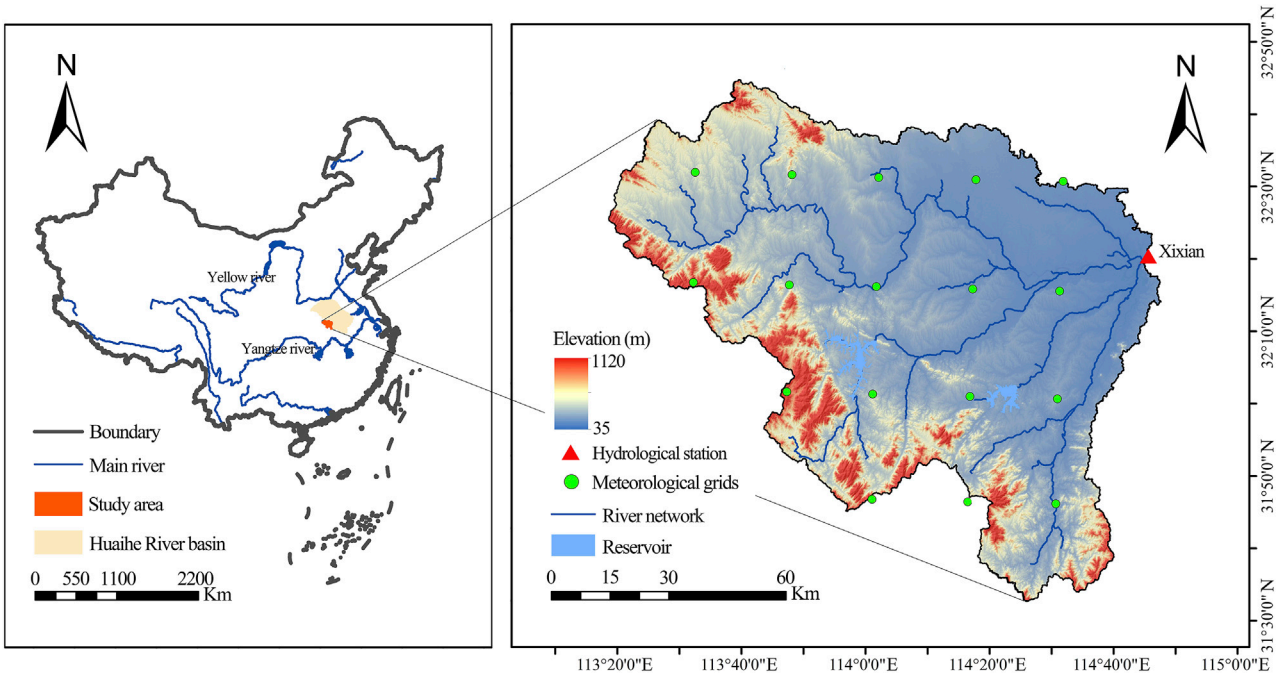

FIGURE 1 | Location, topography, and river network of the upper Huai River basin, and the distribution of meteorological grids and hydrological stations.

precipitation, runoff, and flood for the upper Huai River basin under a series of 21st-century development and radiative forcing scenarios informed by the CMIP6 models. The structure of this article contains the following five sections: First, **Section 2** introduces the detailed information of the study area and data. Then the employed approaches are described in **Section 3**, including the downscaling technique, hydrological model, and the POT approach. **Section 4** evaluates the potential influences of climate change on future runoff and flood. Finally, the discussion and conclusion are detailed in **Sections 5**, **6**, respectively.

2 STUDY AREA AND DATA

2.1 Study Area

The Huai River basin is located between 30°55′N–38°20′ 30°55′38°20′N and 111°55′E–120°45′E111°55′120°45′, between the Yellow River and the Yangtze River (**Figure 1**). It originates in Tongbai Mountain of Henan Province and flows into the Yangtze River, flowing through four provinces (i.e., Henan, Anhui, Shandong, and Jiangsu provinces). The total area of the Huai River basin is 191,200 km^2, and the length of the main channel is 1,000 km. The Xixian basin is located in the upper reaches of the Huai River, with a catchment area of 10,191 km^2, which is chosen for study in this study. The Xixian basin is located in the transition zone of warm temperature region and northern subtropical zone. The main crops are rice and wheat in this area. The multi-year average air temperature is 15.4°C. The long-term average annual rainfall is 1,028 mm (calculated by the data from 1980 to 2014). Rainfall for the flood season (from June to September) is mainly affected by monsoon, and more than half of the precipitation (~60%) falls in the flood season. Owing to the monsoon and windward mountain terrain conditions, flood has become the most serious natural hazard in the Huai River basin.

2.2 Data

In this study, the 1980–2014 daily precipitation and temperature data are obtained from observational gridded datasets, with a 0.25° horizontal resolution, which can be downloaded from the website of the National Meteorological Information Center of the China Meteorological Administration (http://cdc.cma.gov.cn/). These observational gridded datasets are interpolated from observations of nearly 2,400 quality-proven stations all over China (Xu et al., 2009). Moreover, the Thiessen polygon method is used to calculate the basin-averaged daily precipitation and temperature data by the gridded datasets for the study basin. The 1980–2014 daily runoff data of Xixian station are obtained from the Hydrology Bureau of the Huai River basin.

To analyze the future climatic scenarios, four GCM outputs (BCC-CSM2-MR, CanESM5, CESM2, and MRI-ESM2-0) from the latest CMIP6 are chosen under two SSP-RCP scenarios (i.e., SSP245 and SSP585). Meanwhile, we downloaded the essential model outputs (daily precipitation and daily temperature) for both the historical period (1980–2014) and future period (2015–2100). The detailed information of the chosen models is listed in **Table 1**. According to the latest studies (O'Neill et al., 2013; Simpkins, 2017; Su, et al., 2021), the state-of-the-art scenarios become more plausible as the

TABLE 1 | Detail information of four selected GCMs from CMIP6.

No.	Model name	Abbreviation	Horizontal resolution	Modeling center
1	BCC-CESM2-MR	BCC	~1.125° × 1.121°	Beijing Climate Center, China
2	CanESM5	CanESM	~2.8125° × 2.7906°	Canadian Center for Climate Modeling and Analysis, Canada
3	CESM2	CESM	~1.25° × 0.9424°	National Center For Atmospheric Research, United States
4	MRI-ESM2-0	MRI	~1.125° × 1.1215°	Meteorological Research Institute, Japan

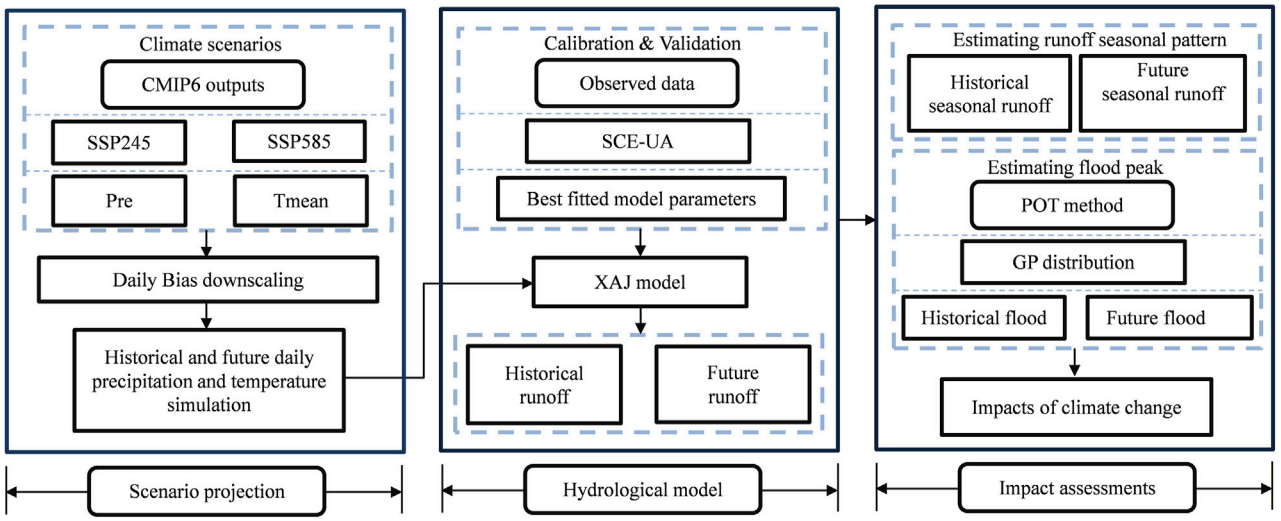

FIGURE 2 | Methodology framework of future climate change impacts on seasonal runoff pattern and flood characteristics in the Xixian basin.

shared socioeconomic pathways (SSPs) work in harmony with RCPs by shared policy assumptions. There are five SSP scenarios that represent the possible future socioeconomic conditions and describe various combinations of mitigation and adaptation challenges, including SSP1: sustainability; SSP2: middle of the road; SSP3: regional rivalry; SSP4: inequality; and SSP5: fossil fuel development (Huang et al., 2019; Su et al., 2021). Among these scenarios, SSP245 and SSP585 are selected for this study as the updated versions of the RCP 4.5 and RCP8.5 scenarios from CMIP5.

3 METHODOLOGIES

3.1 Methodology Framework

Figure 2 displays the methodology framework of this study, including three major modules of climate scenario projection, hydrological model, and impact assessment. The module of scenario projection produces climatic scenarios during historical and future periods. The hydrological model module involves the calibration and validation of the XAJ model and calculation of daily runoff simulation under historical and future climatic scenarios. The impact assessments module is applied to investigate the runoff seasonality variations and to quantify the potential impacts of climate change on future design flood.

3.2 Xinanjiang Hydrological Model

The XAJ model, a conceptual hydrological model, is developed by Zhao (1992). The physical basis of this model is the theory that runoff generation occurs until the saturated condition of soil water is reached. The XAJ model involves 16 free parameters (see **Table 2**) and has been extensively and successfully applied in runoff simulation and flood forecasting for the humid and semi-humid zones over China. The detail of the XAJ model can be found in Zhang et al. (2012). The basin-average daily precipitation and daily potential evapotranspiration (PET) data are calculated as the inputs of this model, and then the discharge at the basin outlet is the final output. The PET is calculated by the Oudin temperature–based method (Oudin et al., 2005) in this study. Although this method requires only average daily temperature data as input, it has been proved to be an alternative to other complex methods, such as the Penman method, for the hydrological simulations (Oudin et al., 2005). Specifically, the formulas for potential evapotranspiration are presented as follows:

$$PET = \frac{R_e}{\lambda\rho}\frac{T_a + 5}{100} \quad if \quad T_a + 5 > 0$$
$$PET = 0 \quad if \quad T_a + 5 \le 0, \tag{1}$$

where PET refers to the potential evapotranspiration (mm day^{-1}), R_e refers to extraterrestrial radiation (MJ m^{-2} day^{-1}), depending

TABLE 2 | Parameters of XAJ model.

Rank	Parameters	Description	Unit	Range
1	KC	Ratio of PET to the pan evaporation		[0.6, 1.2]
2	WUM	Tension water capacity of upper layer	mm	[5, 20]
3	WLM	Tension water capacity of lower layer	mm	[60, 90]
4	C	Deeper evapotranspiration coefficient		[0.08, 0.18]
5	WM	Areal mean tension water capacity	mm	[120, 220]
6	B	Exponential of the distribution of tension water capacity		[0.1, 0.4]
7	IMP	Ratio of impervious area to the total area of the basin		[0.01, 0.02]
8	SM	Free water storage capacity	mm	[10, 50]
9	EX	Exponential of distribution water capacity		[1, 1.5]
10	KG	Outflow coefficient of free water storage to the groundwater flow		[0.2, 0.6]
11	KI	Outflow coefficient of free water storage to the interflow		[0.2, 0.6]
12	CS	Recession constant of surface water storage		[0.4, 0.7]
13	CI	Recession constant of interflow storage		[0.5, 0.9]
14	CG	Recession constant of groundwater storage		[0.99, 1]
15	KE	Residence time of water	h	[0.5, 1.5]
16	XE	Muskingum coefficient		[0, 0.5]

only on latitude and Julian day, λ refers to the latent hear flux (MJ kg^{-1}), ρ refers to the density of water (kg m^{-3}), and Ta is mean daily air temperature (°C).

Furthermore, we select the shuffled complex evolution optimization algorithm (SCE-UA, Duan et al., 1992) to calibrate the XAJ hydrological model. The Kling–Gupta efficiency (KGE) is selected as the evaluation index in this study, and the objective function is to maximize the KGE value during calibration. The KGE value could be calculated as follows (Gupta et al., 2009):

$$KGE = 1 - \sqrt{(r-1)^2 + (\alpha-1)^2 + (\beta-1)^2}, \tag{2}$$

where r indicates Pearson's linear correlation coefficient between the observed and simulated streamflow, α is the ratio of standard deviations of observed and simulated streamflow, and β is the ratio of the mean value of observation and simulations. The value of KGE ranges from $-\infty$ to 1, with KGE = 1 indicating a perfect fit between the observed and simulated series.

3.3 Daily Bias Correction Approach

The DBC approach is an empirical statistical downscaling approach and has recently been used to correct the systematical errors of raw GCM scenarios (Chen et al., 2013b). The procedures of these methods are calculated as follows: First, the precipitation occurrence of each GCM output is revised by a determined threshold defined month by month from the historical period, which can ensure that the corrected historical precipitation has the same frequency as observations. Then those thresholds are employed to correct the frequency of rainy days for the future period. Furthermore, the daily precipitation distribution of each month is revised by multiplying (or adding) the quantile ratios (or differences) between the observations and GCM simulations during the historical period. Finally, those quantile ratios (or differences) are applied to correct distribution of daily precipitation during the future period. Definitely, these procedures can also be used for temperature correction. The formulas can be expressed as follows:

$$\begin{aligned} P_{adj,d} &= P_{GCM,d} \times \left(P_{obs,Q}/P_{GCM,ref,Q}\right) \\ T_{adj,d} &= T_{GCM,d} \times \left(T_{obs,Q}/T_{GCM,ref,Q}\right), \end{aligned} \tag{3}$$

where the subscript Q is a quantile for a month, the subscript d is a specific day in the historical or future period, and the subscript adj is the corrected variables.

3.4 Peak Over Threshold Method

In this study, the POT approach is employed to extract a number of flood samples each year that are required to exceed the threshold S determined by certain criteria. Compared to annual maximum series method (AMS), this method has the core advantage, allowing more reasonable events to be identified as "floods" for extreme value analysis. Thus, the POT method can not only overcome the shortcoming of short historical data but also provide a more comprehensive description of the "flood" process (Lang et al., 1999). Accordingly, this method has been commonly employed in the estimation of extreme precipitation and temperature and the frequency analysis of flood runoff, and so on (Solari et al., 2017; Lee et al., 2019; Bian et al., 2020; Yang et al., 2020). In this study, the POT method is conducted for flood frequency analysis. The first key step is to ensure that the sampled flood events satisfy the independence condition. Here, the criteria evaluated by Silva et al. (2012) are employed, which indicates that the successive two flood peaks can be accepted when they meet the following formula:

$$\begin{aligned} D &< 5\,days + \log(A) \\ Q_{\min} &< \frac{3}{4}\min(Q_1, Q_2), \end{aligned} \tag{4}$$

where D refers to the interval time between two flood peaks in days, A denotes the basin area in km^2, and Q_1 and Q_2 are the magnitudes of two flood peaks in m^3/s, respectively.

In addition, an appropriate threshold is required to determine to guarantee that the frequency distribution of floods meets a Poisson function, which is another key point here. The mean number of over-threshold events per year μ should be more than

TABLE 3 | List of evaluation metrics for precipitation and temperature.

No.	Evaluation metrics (mean)	No.	Evaluation metrics (quantile)
1	Daily	14	0.1
2	January	15	0.2
3	February	16	0.3
4	March	17	0.4
5	April	18	0.5
6	May	19	0.6
7	June	20	0.7
8	July	21	0.8
9	August	22	0.9
10	September	23	0.99
11	October		
12	November		
13	December		

two times per year as recommended by Mediero et al. (2014). Therefore, the mean annual number of flood events is set as $\mu = 3$ under the independence assumption in this study. Last, the extracted series of flood peaks are fitted with a generalized Pareto (GP) distribution.

4 RESULTS

4.1 Bias Correction Performance of Global Climate Models

The performances of GCMs are discrepant for different climate variables among various climate regions; thus, there is no common conclusion on how to select suitable GCMs in a particular basin. Therefore, it is necessary to assess the performances of the chosen models (i.e., BCC, CanESM, CESM, and MRI models) in order to investigate the influences of climate change on seasonal runoffs and floods in the Xixian basin. The systematical errors of raw GCM outputs are tackled by the DBC method. Afterward, 23 metrics (**Table 3**) are selected to describe mean and extreme values of precipitation and temperature series under climate change. The raw GCM simulations have the same historical period 1980–2014 with the observed data.

Figure 3 is a color-coded "portrait diagram" showing the deviations of precipitation and temperature before and after DBC method during the historical period. It is can be seen that raw outputs of precipitation and temperature from four GCMs exhibit obvious deviations. The raw precipitations of GCMs deviate from observed precipitations by more than ±50% for most metrics, whereas the deviations of temperature are generally above ±2°C. However, the systematic biases of GCMs are significantly reduced after the DBC. The biases of precipitation effectively reduce to below 5% in most cases for the selected GCMs, and as for temperature, the biases reduce to lower than 0.1°C. Overall, the performances of bias correction for both precipitation and temperature simulation of GCMs are satisfied for the research requirement. Those results indicate that the DBC method is reliable for reproducing future climate variables in the study basin.

4.2 Projected Variations of Precipitation and Air Temperature

The long-term changes of annual mean precipitation and temperature over the upper Huai River basin are detected

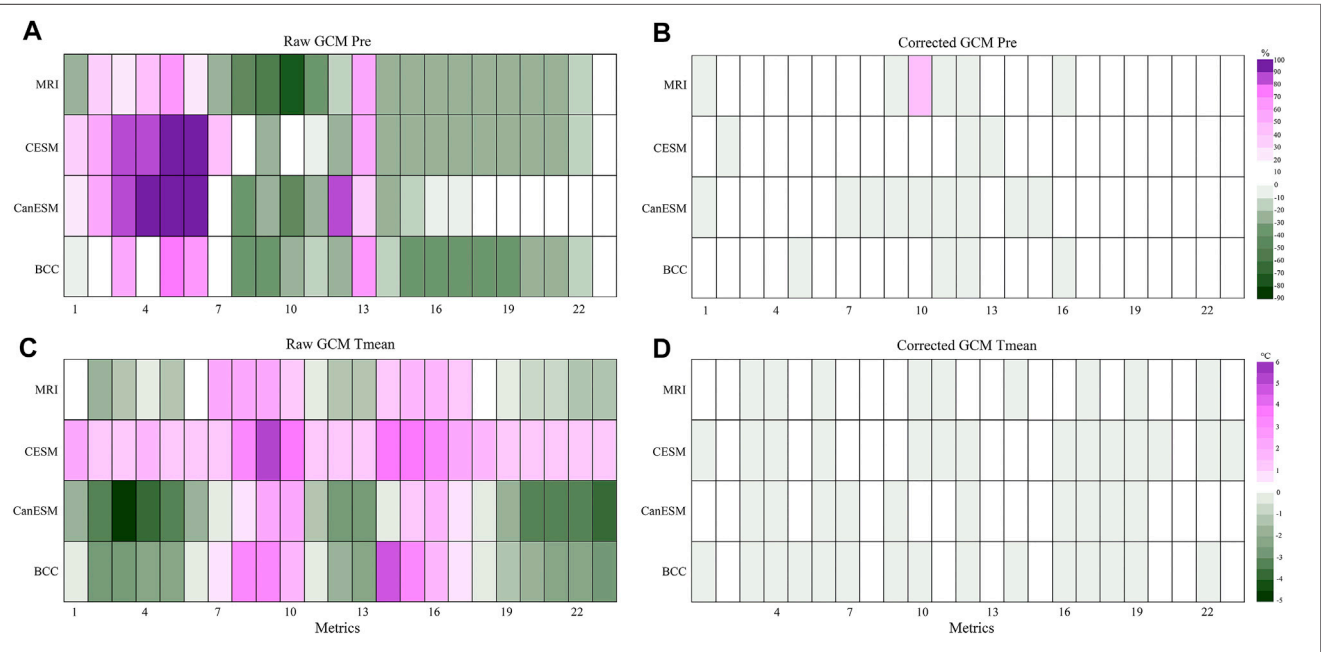

FIGURE 3 | Portrait diagram of daily precipitation relative deviation (%) and temperature absolute deviation (°C) for the selected GCMs before and after DBC method in Xixian basin. The *x*-axis represents the 23 metrics, whereas the *y*-axis represents the GCMs.

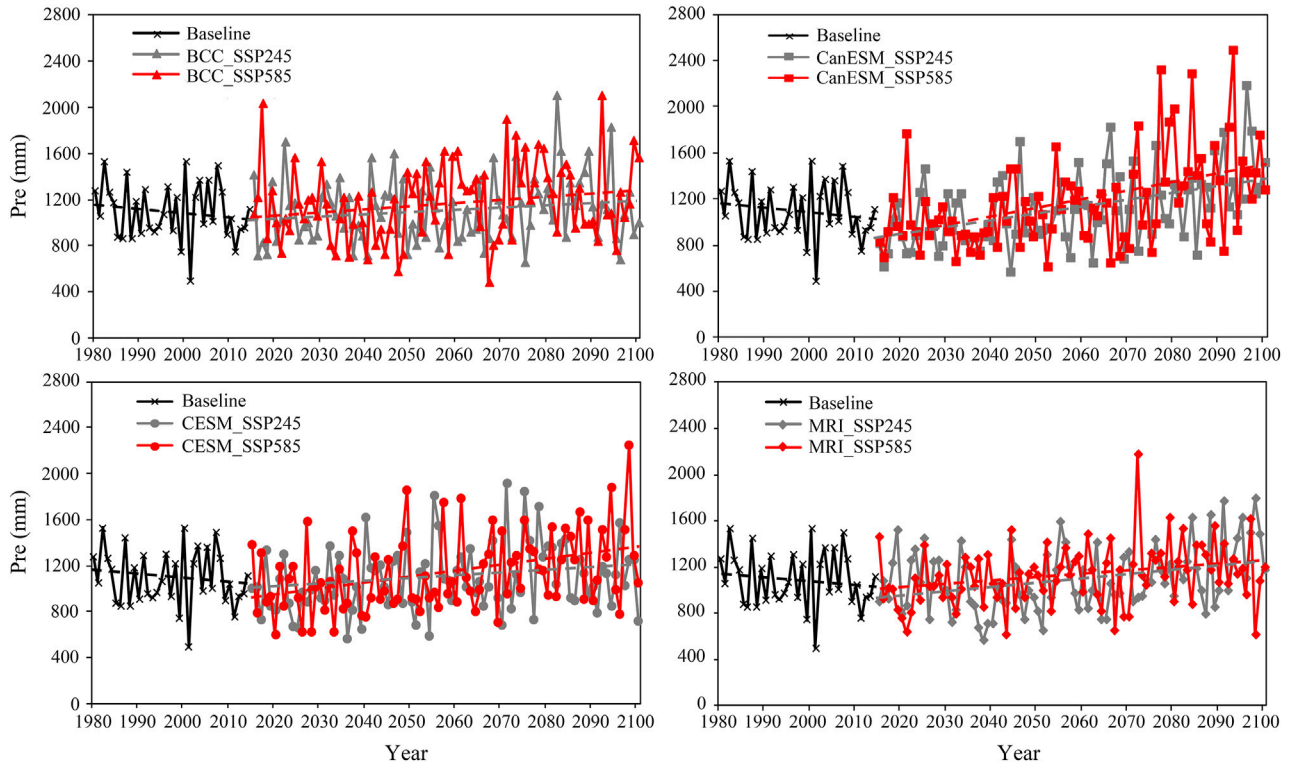

FIGURE 4 | Trend results of annual mean precipitation for each GCM in the Xixian basin from 1980 to 2100.

during the period of 1980–2100 for each GCM under two different SSP–RCP scenarios (SSP245 and SSP585). Relative to the change of precipitation over the baseline period, there is a general rising trend during the future period, although the rising rate varies with different GCM and SSP scenarios (**Figure 4**). More specifically, BCC model projects the highest increasing rate of annual mean precipitation with a rising rate up to 28 mm per decade under SSP585 scenarios, while the minimum rising rate of annual mean precipitation with 10.3 mm per decade is projected by the MRI model. For SSP245 scenario, the increasing tendency of precipitation is more insignificant than that under SSP585 scenario.

In the field of the long-term tendency of annual mean temperature, **Figure 5** shows that a significant increasing trend in temperature is observed during the period 1980–2100, and more significant increasing changing of temperature is observed under SSP585 scenario compared to the SSP245. In detail, the CanESM model releases the most pronounced warming signal, which projects that the annual average temperature has a significant rising rate of 0.37°C and 0.57°C per decade under SSP245 and SSP585 scenarios, respectively. The MRI model exhibits the most optimistic warming condition with an increase of 0.23°C and 0.33°C per decade under the two scenarios, respectively. The BCC and CESM models project that annual average temperature has a significant increase with a rate of 0.28 and 0.23°C per decade under SSP245, respectively, and with a maximum rate of 0.37°C per decade under SSP585 scenarios.

4.3 Calibration and Validation Results of Xinanjiang Model

In this study, XAJ model is adopted to simulate hydrological processes in the Xixian basin. Initially, we used the basin-averaged precipitation and temperature data during 1980–1999 to carry out the calibration of the XAJ model, and then the optimum model parameters are obtained with the largest KGE value. The 15-year period during 2000–2014 are used for model validation. To further investigate the performance of the XAJ model, the Nash–Sutcliffe efficiency coefficient (NSE) and relative bias (PBIAS) criteria are also employed.

Table 4 presents the results of calibration and validation periods for the Xixian basin. Furthermore, the comparisons between observed and simulated runoffs in two periods at the daily and monthly scale are presented in **Figure 6**, which suggest that the XAJ model performs well in the study basin though with overestimates or underestimates in the flood peaks in some cases. From **Table 4**, it can be seen that the KGE values are 0.86 and 0.91, respectively, at the monthly scale, and 0.79 and 0.82 at the daily scale for calibration and validation periods. In addition, the NSEs are 0.88 and 0.86, respectively, at the monthly scale, and 0.74 and 0.71 at the daily scale, and the PBIAS of the calibration

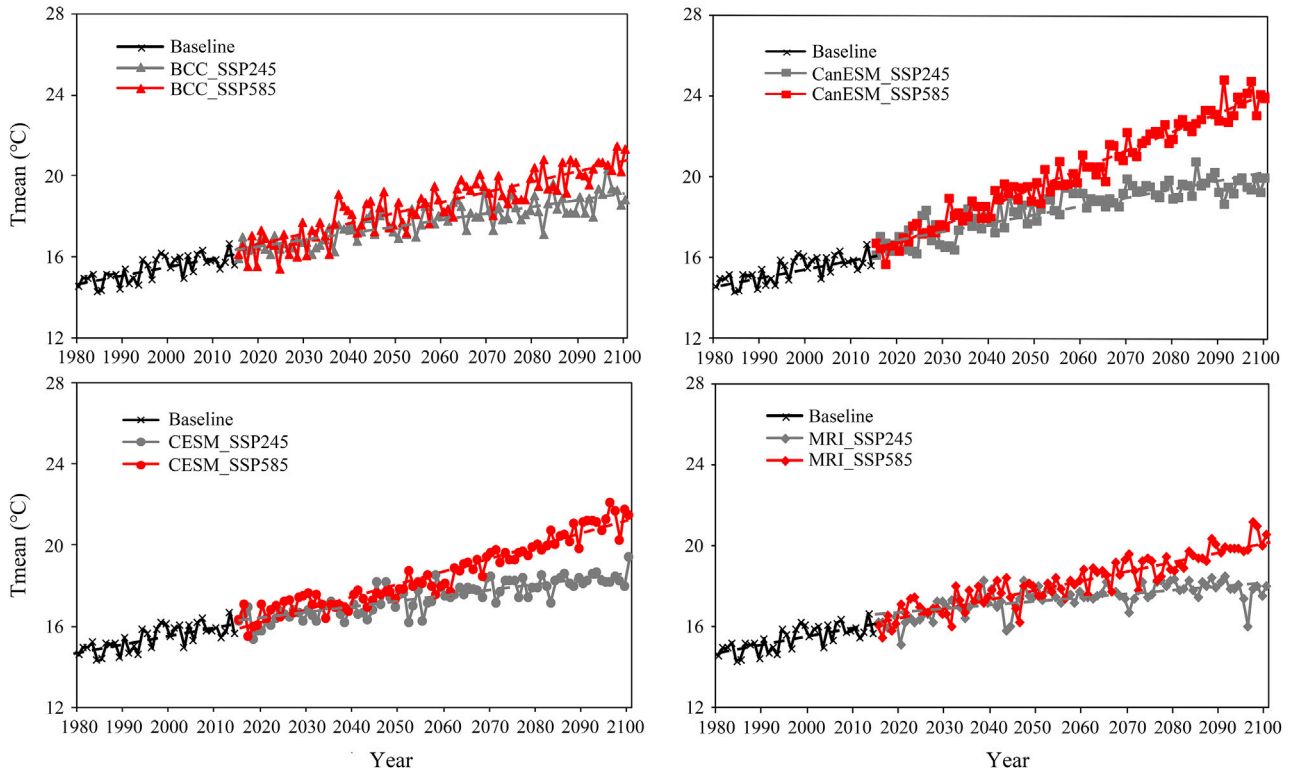

FIGURE 5 | Trend results of annual average air temperature for each GCM in the Xixian basin from 1980 to 2100.

TABLE 4 | Evaluation of the XAJ model performance at daily and monthly time step.

	Period	KGE	NSE	PBIAS(%)
Daily	Calibration (1980–1999)	0.79	0.74	1.4
	Validation (2000–2014)	0.82	0.71	9.7
Monthly	Calibration (1980–1999)	0.86	0.88	1.4
	Validation (2000–2014)	0.91	0.86	9.7

and validation are both lower than 10%. These results indicate that the XAJ model can perform satisfactorily so that it can be used to project hydrological scenarios in subsequent research.

4.4 Impacts of Climate Change on Runoff Seasonal Pattern

To investigate the influence of climate change on monthly runoff over the Xixian basin, the XAJ model is used to simulate runoffs during the historical period (1980–2014) and two future periods: 2050s (2031–2060) and 2080s (2071–2100). **Figure 7** demonstrates the monthly average runoff during the two future periods for each GCM under SSP245 and SSP585 scenarios. Broadly speaking, the selected GCMs perform similarly for change of monthly runoff under two scenarios, but there still exist some differences. Under SSP245 scenario, all GCMs project that runoffs of most months are generally smaller than those in the baseline period over the 2050s, while runoffs of high-flow season over the 2080s are larger than those in the baseline period, reflected in May to September. Moreover, the change patterns of seasonal runoffs under SSP585 scenario are similar to those under SSP245 scenario during the two future periods. These can be explained by the fact that precipitation simulations in the 2050s are equal to or less than those in the baseline period under SSP245 and SSP585 scenarios, while the higher temperature is projected. Thus, the projected monthly runoffs are smaller in the 2050s than those in the baseline period. In contrast, the precipitation simulations in the 2080s are obviously larger than those in the baseline period, which results in higher monthly runoffs. In addition, compared with SSP245, the monthly runoffs under SSP585 scenario are obviously higher, especially for high-flow months.

Then, we further analyzed the variations of monthly runoff between the baseline and the two future periods under SSP245 and SSP585 scenarios, as shown in **Figure 8**. There is a large discrepancy between the changing trends of average monthly runoffs in the two future periods. During the 2050s, the monthly average runoffs in most months have seen decreasing trends for each GCM under SSP245 and SSP585 scenarios, generally occurring in the low-flow season such as January to April and September to December. It can be seen that the monthly average runoffs are lower than that in baseline period and have decreased by about 10 and 8% under SSP245 and SSP585 scenario, respectively. These indicate that there will be more serious

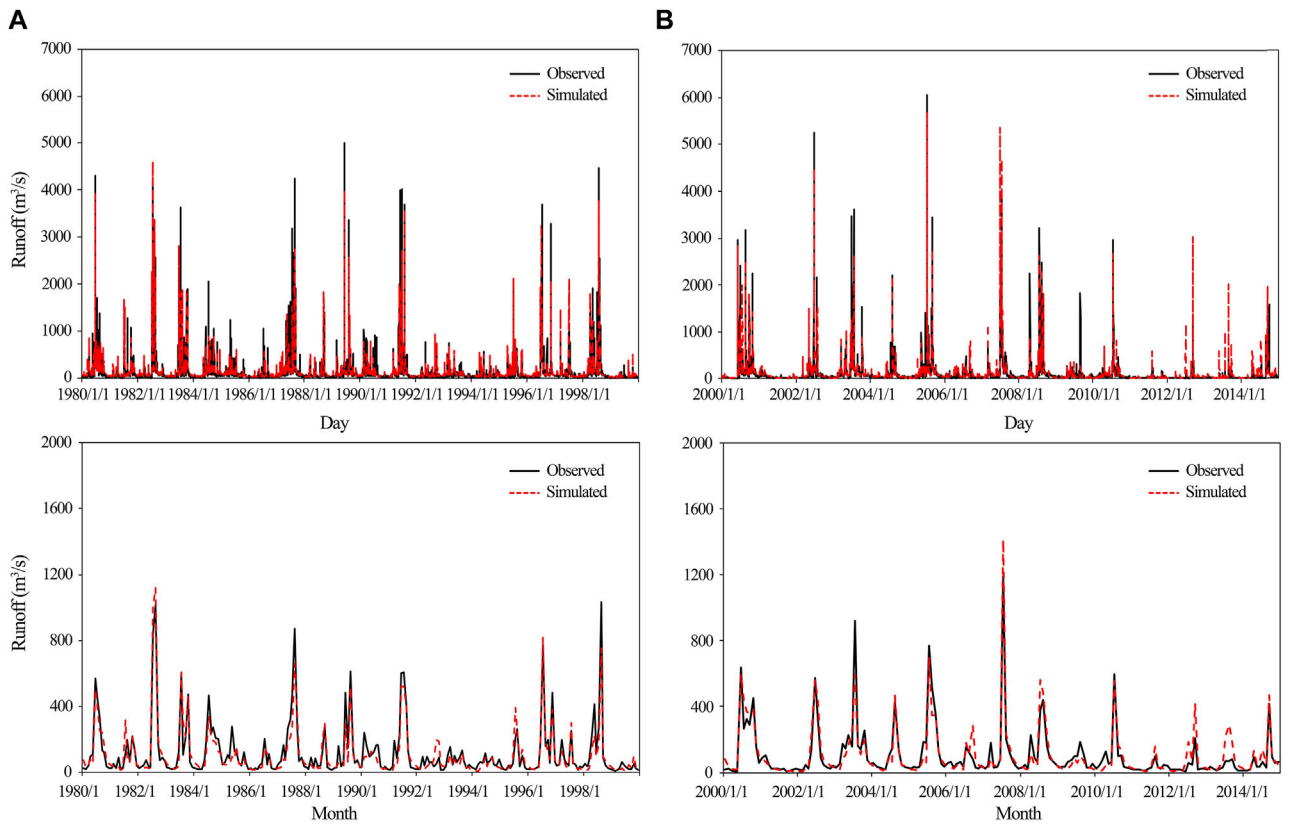

FIGURE 6 | Performance of XAJ model for the calibration **(A)** and validation **(B)** periods at daily and monthly scale in the Xixian basin.

water shortage and higher risk of drought during the 2050s in the upper Huai river basin. In addition, **Figure 8** shows that there has been an obvious increasing trend of monthly average runoff in the high-flow season during the 2080s. In detail, compared to the baseline period, the GCMs project that the monthly runoffs have generally increased by about 29% from May to September under the SSP245 scenario. Under the SSP585 scenario, the monthly runoffs are projected to increase by approximately 39% from May to September. These may be caused by increasing seasonal precipitation in high-flow season under two future scenarios. Thus, there will be higher flood risk in high-flow season during the 2080s in the upper Huai river basin, especially under the SSP585 scenario, which also are proved in subsequent analyses of impacts of climate change on design floods.

4.5 Impacts of Climate Change on Design Floods

In order to analyze the changes of flood frequency, the flood peaks are extracted by the POT method in this study, which has been certified to be more reasonable than the annual maximum sampling approach (Mediero et al., 2014; Bian et al., 2020). Moreover, the L-Moment approach (Hosking and Wallis, 1997) is used to estimate the parameters of GP distribution. The design floods under SSP245 and SSP585 scenarios for each GCM during the two future periods are demonstrated in **Figure 9**. It can be seen that the change patterns of design floods are quite different between the 2050s and 2080s for each GCM under SSP245 and SSP585 scenarios. In detail, during the 2031–2060, the design floods are generally lower than those in baseline period for small return period under the two scenarios for each GCM. However, BCC and CanESM models project that the design flood with a 100-year return period is obviously bigger than that in baseline period under SSP585 scenario. As for the 2080s, there have been the obviously larger design floods for all GCMs under SSP245 scenarios comparing to the near future period. When the return period exceeds 20 years, the design floods of 2080s are larger than those of baseline period. Moreover, the design flood runoffs are projected to increase more significantly when the return periods increase. Under SSP585 scenarios, the design floods of 2080s are larger than those of baseline period when the return period exceeds 10 years. In addition, the flood magnitude with the same return period is greater than that under SSP245 scenario. These indicate that flood extremes are projected to increase during the future periods in the upper Huai River basin, especially under SSP585 scenario.

To further investigate the results as mentioned above, the changes of future floods are calculated for the 10, 20, 50, and 100-year return period, shown in **Figure 10**. It can be observed that the design floods of the 100-year return period are increasing for all GCMs under the SSP245 and SSP585 scenarios during the 2050s, especially the CanESM model, which exhibits the largest

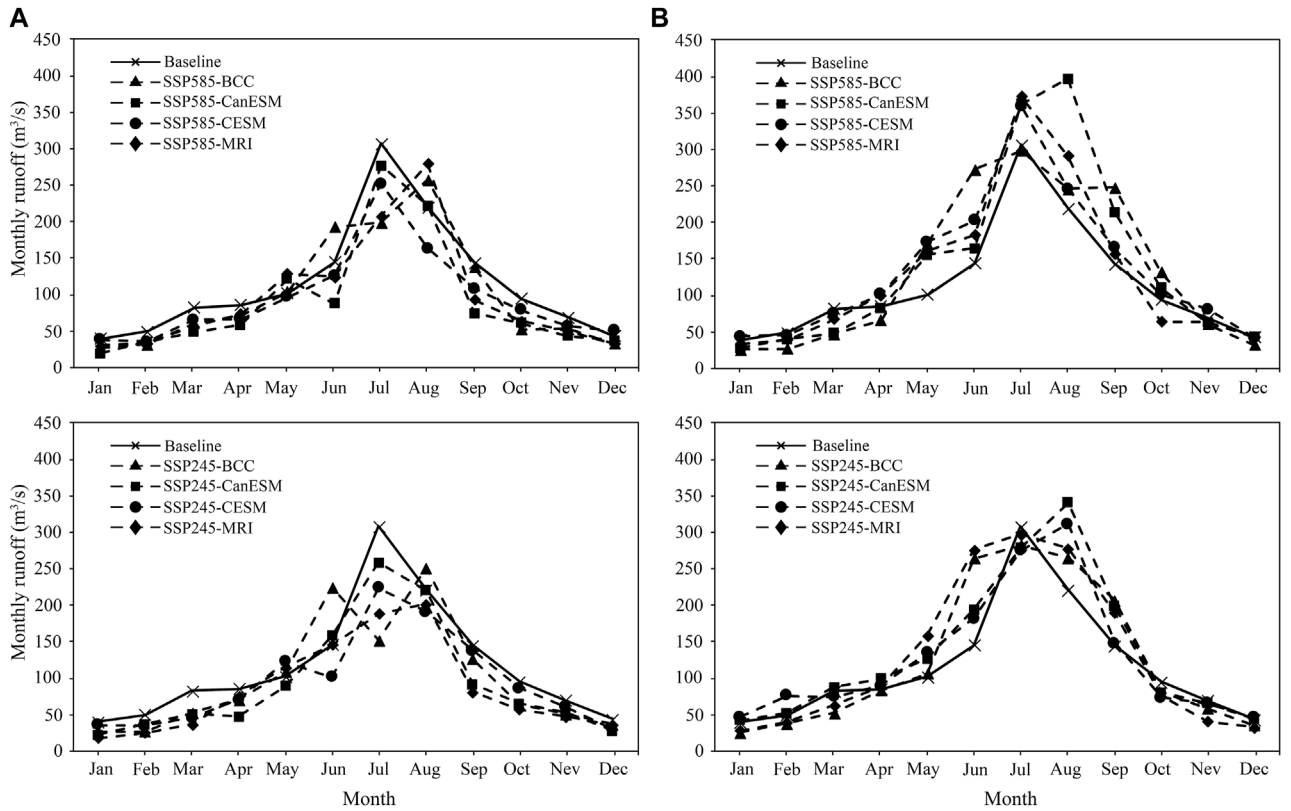

FIGURE 7 | Seasonal runoffs of different GCMs under SSP245 **(bottom)** and SSP585 **(top)** scenarios during two future periods 2050s **(A)** and 2080s **(B)**. "Baseline" denotes the results in the baseline period. "SSP245_BCC" denotes the results of BCC model under SSP245 scenario in the future period that as well applies to the other seven abbreviations.

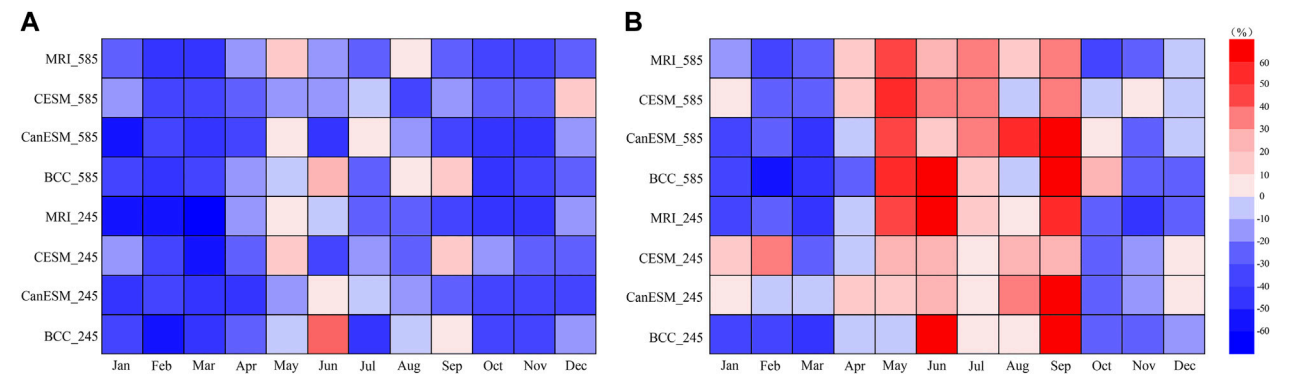

FIGURE 8 | Relative change results of seasonal runoffs during two future periods 2050s **(A)** and 2080s **(B)** to the historical period.

increasing rate with the 17.9 and 38.4% under SSP245 and SSP585 scenarios, respectively. However, there has been a general decreasing tendency of the design floods with 50, 20 and 10-year return periods during the 2050s under SSP245 scenario. As the return period decreases, the reducing range of design flood runoffs is exacerbated. In addition, **Figure 10** demonstrates that the change patterns of design floods for 2080s show great differences from those in 2050s. All GCMs project obvious increasing trends of the design floods for all return periods under the two scenarios, except the design floods with a 10-year return period of CESM and MRI. In detail, CanESM projects that under SSP585 scenario, the rising rate of design floods for the 100-year and 50-year return periods in the 2080s can go up to 106 and 72%, respectively. For the BCC model, the design floods for

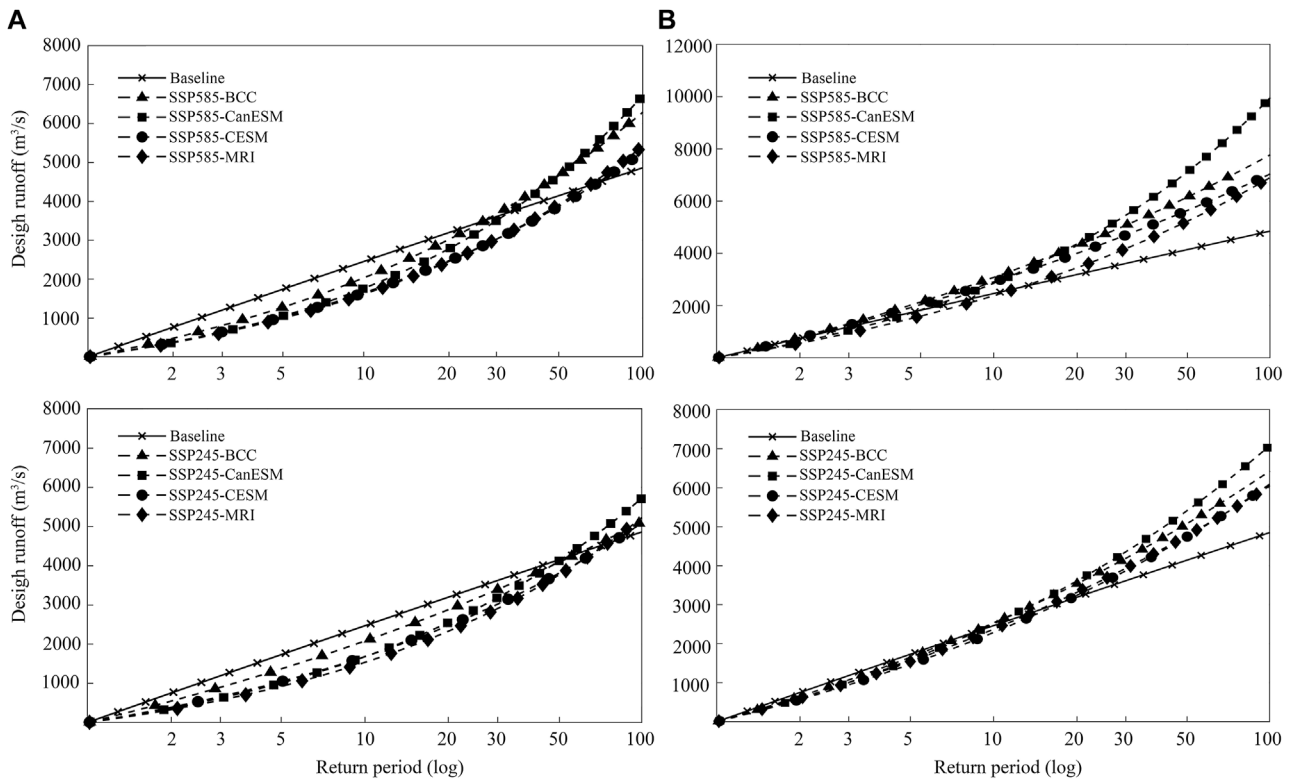

FIGURE 9 | Design floods of different return periods for various GCMs under SSP245 **(bottom)** and SSP585 **(top)** scenarios during two future periods 2050s **(A)** and 2080s **(B)**.

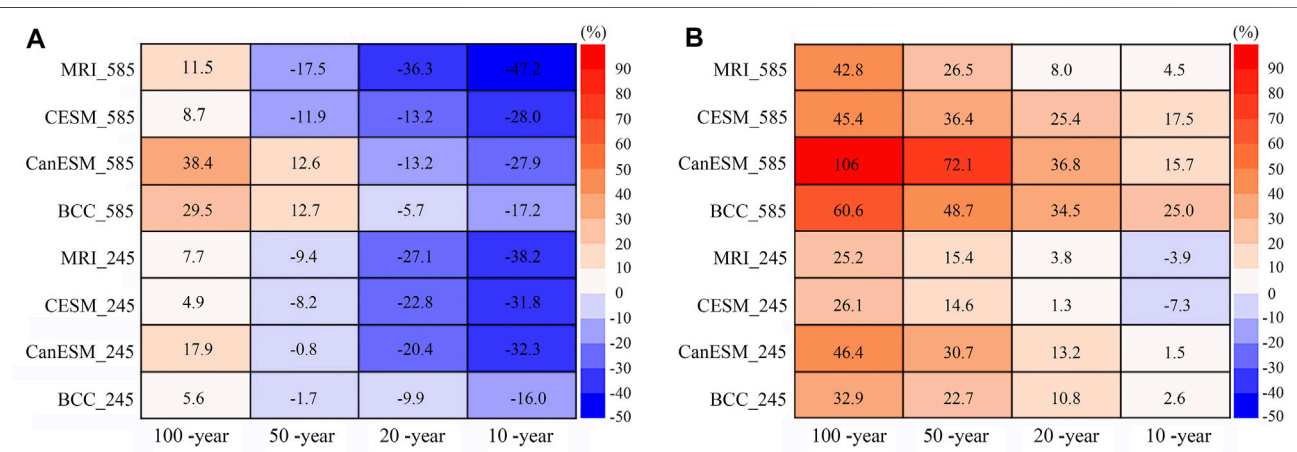

FIGURE 10 | Relative changes of design floods with 100-year, 50-year, 20-year, and 10-year return periods during two future periods 2050s **(A)** and 2080s **(B)** to the baseline period.

100-year and 50-year return periods increase by 60.6 and 48.7%, respectively, under SSP585 scenario. CESM model projects that the increasing rates of design floods for these two return periods are 45.4 and 36.4%, respectively, under SSP585 scenario, and those of MRI model increase by 42.8 and 26.5%, respectively. However, under SSP245 scenario, the increases of design floods with 100-year and 50-year return periods are far below that under the SSP585 scenario. These could be explained by the fact that the heavier emission of gas such as SSP585 scenario causes the larger extreme precipitation. These results indicate that the flood events are likely to occur more frequently during the far future period in the Xixian basin.

5 DISCUSSION

As we know, flood frequency is expected to increase as the hydrological cycle has been altered by climate change. This paper quantitatively evaluates the changes of future floods in response to climate change coupling of CMIP6 models and XAJ hydrological model in the Xixian basin. As expected, the main results demonstrated that extreme floods will increase under future climatic scenarios in the study area, which is consistent with the previous studies (Wang et al., 2018; Yang et al., 2020). Jin et al. (2017) used CMIP5 models to investigate the effects of climate change on flood in the upper Huai River basin during 2021–2050. They found that future floods were projected to increase under the RCP4.5 and RCP5.8 scenarios over the upper Huai River basin. The fact is that the heavier and more frequent precipitation extremes in future can be used to explain the intensification of extreme floods. Based on the Clausius–Clapeyron law, a 1 K increase in temperature is likely to cause the water vapor holding capacity to increase by about 7% (Trenberth et al., 2003). Therefore, a warmer atmosphere enables to supply more sufficient water vapor and enhances the occurrence of extreme precipitation. Although the physical mechanism of flood production is more complex, flood extremes are projected to increase when extreme precipitation events occur more frequently in the future. This has been confirmed by previous literature studies (Hirabayashi et al., 2013; Wu and Huang., 2015).

In this study, we use four CMIP6 GCMs, two SSP scenarios, one downscaling method, one hydrological model, and one frequent analysis approach to analyze the projections of possible changes range for future design floods during two time stages in the Xixian basin. The results show that GCM and SSP scenarios both cause large uncertainties in projections of floods under future climatic scenarios, which are in agreement with the previous literatures (Chen et al., 2013a; Basheer et al., 2016; Krysanova et al., 2017; Hattermann et al., 2018). Meanwhile, the discrepancy of the projected results from different GCM and SSP scenarios also emphasizes that the misleading conclusions may be drawn if only one GCM and SSP scenario is adopt for future climate change studies. In addition, there are some limitations in this study. First, we ignored the possible impacts of other important uncertainty sources in this study, involving downscaling methods, the structure and parameters of hydrological model, and the flood frequency distribution functions. Although many studies have suggested that GCMs generate much larger uncertainty comparing to those from downscaling techniques and hydrological models (Dobler et al., 2012; Karlsson et al., 2016; Das et al., 2018), this does not mean that the impacts of other uncertainty sourcing should be overlooked. Consequently, the next step of our study is to thoroughly analyze the uncertainties stemming from various uncertainty sources in the evaluation of effects of climate change on future floods. Second, human activities, including land-use change, water conservancy construction, and government policy, are another important driving factor affecting runoff and flood for the upper Huai River basin. Hence, future runoff responses to human activities and climate change are required to further accurately investigate in following works.

6 CONCLUSION

Based on four CMIP6 GCMs, this study investigates the potential influences of climate change on future seasonal runoffs and extreme floods in the upper Huai River basin. The statistical downscaling methods DBC is adopted to translate the GCM outputs with coarse resolution to regional and basin scale, and then the XAJ model is employed to simulate daily discharge for the baseline period (1980–2014) and two future periods: 2050s (2031–2060) and 2080s (2071–2100). The POT method and GP distribution are employed to estimate the changes in design floods for different return periods. The main conclusions are summarized as follows:

1) There is an insignificant increasing tendency of precipitation in the Xixian basin. The projection of annual mean precipitation has greater climate model uncertainty and roughly increases 11 mm (60 mm) under SSP245 (SSP585) scenario. In terms of the annual mean temperature, there is an obvious increasing trend with a rising rate of 0.59°C (0.36°C) per decade under SSP585 (SSP245) scenario.
2) The XAJ model performs well in simulating both monthly and daily runoffs demonstrated by validation results; thus, it enables to be employed to evaluate the potential influences of climate change on runoffs. Modeling outputs indicate that runoffs in most low-flow months have seen decreasing trends under SSP245 and SSP585 scenarios during the 2050s (2031–2060), while there has been an obvious increasing trend of most high-flow monthly average runoffs during the 2080s (2071–2100).
3) There is a pronounced increasing tendency in design floods with large return period under climate change. Especially the design flood for a 100-year return period is roughly projected to increase 42.8–106% for SSP585 scenario during the 2080s, and the amplitude of flood increase decreases with the decrease of the return period. For the 2050s period, design floods with small return periods have a decreasing trend under two scenarios, and as the return period decreases, the decreasing extent of design flood runoffs is exacerbated.

DATA AVAILABILITY STATEMENT

The original contributions presented in the study are included in the article/Supplementary Material, further inquiries can be directed to the corresponding author.

AUTHOR CONTRIBUTIONS

GB contributed to methodology, data curation, and writing—original draft preparation; JZ assisted with conceptualization and methodology; JC contributed to methodology, resources, and writing—review and editing; MS helped with data curation, visualization, and investigation; RH contributed to resources and writing—review and editing; CL supported in resources and writing—review and editing; YL contributed to resources and writing—review and editing; ZB

assisted with resources and writing—review and editing; QL helped with writing—review and editing; and GW supported in conceptualization, funding acquisition, supervision, and writing—review and editing.

FUNDING

The study has been financially supported by the National Natural Science Foundation of China (Grants: 41830863, 51879162, 5167090940, 91847301, 92047203, 51879164, and 52121006), and the National Key Research and Development Programs of China (Grants: 2017YFA0605002, 2017YFC0404602 and 2021YFC3200201) and the Belt and Road Fund on Water and Sustainability of the State Key Laboratory of Hydrology-Water Resources and Hydraulic Engineering, China (2019nkzd02, 2020nkzd01).

ACKNOWLEDGMENTS

We thank the reviewers and editors.

REFERENCES

Ahmadalipour, A., Moradkhani, H., and Rana, A. (2018). Accounting for Downscaling and Model Uncertainty in fine-resolution Seasonal Climate Projections over the Columbia River basin. *Clim. Dyn.* 50, 717–733. doi:10.1007/s00382-017-3639-4

Alkama, R., Marchand, L., Ribes, A., and Decharme, B. (2013). Detection of Global Runoff Changes: Results from Observations and CMIP5 Experiments. *Hydrol. Earth Syst. Sci.* 17 (7), 2967–2979. doi:10.5194/hess-17-2967-2013

Amin, M. Z. M., Shaaban, A. J., Ercan, A., Ishida, K., Kavvas, M. L., Chen, Z. Q., et al. (2017). Future Climate Change Impact Assessment of Watershed Scale Hydrologic Processes in Peninsular Malaysia by a Regional Climate Model Coupled with a Physically Based Hydrology Model. *Sci. Total Environ.* 575, 12–22. doi:10.1016/j.scitotenv.2016.10.009

Arnell, N. W., and Gosling, S. N. (2013). The Impacts of Climate Change on River Flow Regimes at the Global Scale. *J. Hydrol.* 486, 351–364. doi:10.1016/j.jhydrol.2013.02.010

Basheer, A. K., Lu, H., Omer, A., Ali, A. B., and Abdelgader, A. M. S. (2016). Impacts of Climate Change under CMIP5 RCP Scenarios on the Streamflow in the Dinder River and Ecosystem Habitats in Dinder National Park, Sudan. *Hydrol. Earth Syst. Sci.* 20, 1331–1353. doi:10.5194/hess-20-1331-2016

Bian, G. D., Du, J. K., Song, M., Zhang, X., Zhang, X., Li, R., et al. (2020). Detection and Attribution of Flood Responses to Precipitation Change and Urbanization: a Case Study in Qinhuai River basin, Southeast China. *Hydrol. Res.* 51 (2), 351–365. doi:10.2166/nh.2020.063

Byun, K., Chiu, C. M., and Hamlet, A. F. (2018). Effects of 21st century Climate Change on Seasonal Flow Regimes and Hydrologic Extremes over the Midwest and Great Lakes Region of the US. *Sci. Total Environ.* 650, 1261–1277. doi:10.1016/j.scitotenv.2018.09.063

Chen, J., Brissette, F. P., Chaumont, D., and Braun, M. (2013b). Finding Appropriate Bias Correction Methods in Downscaling Precipitation for Hydrologic Impact Studies over north America. *Water Resour. Res.* 49 (7), 4187–4205. doi:10.1002/wrcr.20331

Chen, J., Brissette, F. P., Chaumont, D., and Braun, M. (2013a). Performance and Uncertainty Evaluation of Empirical Downscaling Methods in Quantifying the Climate Change Impacts on Hydrology over Two North American River Basins. *J. Hydrol.* 479, 200–214. doi:10.1016/j.jhydrol.2012.11.062

Cook, B. I., Mankin, J. S., Marvel, K., Williams, A. P., Smerdon, J. E., Anchukaitis, K. J., et al. (2020). Twenty-First Century Drought Projections in the CMIP6 Forcing Scenarios. *Earth's Future* 8 (6), e2019EF001461. doi:10.1029/2019ef001461

Das, J., Treesa, A., and Umamahesh, N. V. (2018). Modelling Impacts of Climate Change on a River Basin: Analysis of Uncertainty Using REA & Possibilistic Approach. *Water Resour. Manage.* 32, 4833–4852. doi:10.1007/s11269-018-2046-x

Dobler, C., Hagemann, S., Wilby, R. L., and Stötter, J. (2012). Quantifying Different Sources of Uncertainty in Hydrological Projections in an Alpine Watershed. *Hydrol. Earth Syst. Sci.* 16, 4343–4360. doi:10.5194/hess-16-4343-2012

Du, H., Alexander, L. V., Donat, M. G., Lippmann, T., Srivastava, A., Salinger, J., et al. (2019). Precipitation from Persistent Extremes Is Increasing in Most Regions and Globally. *Geophys. Res. Lett.* 46 (11), 6041–6049. doi:10.1029/2019gl081898

Duan, Q., Sorooshian, S., and Gupta, V. (1992). Effective and Efficient Global Optimization for Conceptual Rainfall-Runoff Models. *Water Resour. Res.* 28 (4), 1015–1031. doi:10.1029/91wr02985

Feyen, L., Dankers, R., Bódis, K., Salamon, P., and Barredo, J. I. (2012). Fluvial Flood Risk in Europe in Present and Future Climates. *Climatic Change* 112, 47–62. doi:10.1007/s10584-011-0339-7

Gao, C., He, Z., Pan, S., Xuan, W., and Xu, Y.-P. (2020). Effects of Climate Change on Peak Runoff and Flood Levels in Qu River Basin, East China. *J. Hydro-environment Res.* 28, 34–47. doi:10.1016/j.jher.2018.02.005

Glenn, A., Paul, H., Donald, H. B., Hannaford, J., Renard, B., Stahl, K., et al. (2017). Climate-driven Variability in the Occurrence of Major Floods across North America and Europe. *J. Hydrol.* 552, 704–717. doi:10.1016/j.jhydrol.2017.07.027

Gu, L., Yin, J., Zhang, H., Wang, H. M., Yang, G., and Wu, X. (2020). On Future Flood Magnitudes and Estimation Uncertainty across 151 Catchments in mainland China. *Int. J. Climatol* 41, 779–800. doi:10.1002/joc.6725

Gupta, H. V., Kling, H., Yilmaz, K. K., and Martinez, G. F. (2009). Decomposition of the Mean Squared Error and NSE Performance Criteria: Implications for Improving Hydrological Modelling. *J. Hydrol.* 377, 80–91. doi:10.1016/j.jhydrol.2009.08.003

Hattermann, F. F., Vetter, T., Breuer, L., Su, B., Daggupati, P., Donnelly, C., et al. (2018). Sources of Uncertainty in Hydrological Climate Impact Assessment: a Cross-Scale Study. *Environ. Res. Lett.* 13, 015006. doi:10.1088/1748-9326/aa9938

Hirabayashi, Y., Mahendran, R., Koirala, S., Konoshima, L., Yamazaki, D., Watanabe, S., et al. (2013). Global Flood Risk under Climate Change. *Nat. Clim. Change* 3, 816–821. doi:10.1038/nclimate1911

Hosking, J. R. M., and Wallis, J. R. (1997). *Regional Frequency Analysis*. Cambridge, UK: Cambridge University Press, 224.

Huang, J., Qin, D., Jiang, T., Wang, Y., Feng, Z., Zhai, J., et al. (2019). Effect of Fertility Policy Changes on the Population Structure and Economy of china: from the Perspective of the Shared Socioeconomic Pathways. *Earth's Future* 7, 250–265. doi:10.1029/2018ef000964

IPCC (2013). "Summary for Policymakers," in *Climate Change 2013: The Physical Science Basis. Contribution of Working Group I to the Fifth Assessment Report of the Intergovernmental Panel on Climate Change*. TF Stocker, D Qin, G.-K. Plattner, M. Tignor, S. K. Allen, J. Boschung, et al. (Cambridge, UK: Cambridge University Press).

IPCC (2021). "Summary for Policymakers," in *Climate Change 2021: The Physical Science Basis. Contribution of Working Group I to the Sixth Assessment Report of the Intergovernmental Panel on Climate Change*. V Masson-Delmotte, PM Zhai, A. Pirani, et al. (Cambridge, UK: Cambridge University Press).

Jin, J., He, J., He, R., Liu, C., Zhang, J., Wang, G., et al. (2017). Impacts of Climate Change to Water Resources and Extreme Hydrological Event in the Huaihe River Basin. *Scientia Geographica Sinica* 37 (8), 1226–1233. doi:10.13249/j.cnki.sgs.2017.08.013

Jung, I.-W., and Chang, H. (2011). Assessment of Future Runoff Trends under Multiple Climate Change Scenarios in the Willamette River Basin, Oregon, USA. *Hydrol. Process.* 25 (2), 258–277. doi:10.1002/hyp.7842

Karlsson, I. B., Sonnenborg, T. O., Refsgaard, J. C., Trolle, D., Børgesen, C. D., Olesen, J. E., et al. (2016). Combined Effects of Climate Models, Hydrological Model Structures and Land Use Scenarios on Hydrological Impacts of Climate Change. *J. Hydrol.* 535, 301–317. doi:10.1016/j.jhydrol.2016.01.069

Koirala, S., Hirabayashi, Y., Mahendran, R., and Kanae, S. (2014). Global Assessment of Agreement Among Streamflow Projections Using CMIP5 Model Outputs. *Environ. Res. Lett.* 9 (6), 064017. doi:10.1088/1748-9326/9/6/064017

Krysanova, V., Vetter, T., Eisner, S., Huang, S., Pechlivanidis, I., Strauch, M., et al. (2017). Intercomparison of Regional-Scale Hydrological Models and Climate Change Impacts Projected for 12 Large River Basins Worldwide-A Synthesis. *Environ. Res. Lett.* 12, 105002. doi:10.1088/1748-9326/aa8359

Lang, S., Ouarda, T. B. M. J., and Bobee, B. (1999). Production of Microbial Glycolipids. *J. Hydrol.* 225 (3-4), 103–118. doi:10.1007/978-1-59259-261-6_9

Lee, O., Sim, I., and Kim, S. (2019). Application of the Non-stationary Peak-Over-Threshold Methods for Deriving Rainfall Extremes from Temperature Projections. *J. Hydrol.* 585, 124318. doi:10.1016/j.jhydrol.2019.124318

Li, L., Diallo, I., Xu, C.-Y., and Stordal, F. (2015). Hydrological Projections under Climate Change in the Near Future by RegCM4 in Southern Africa Using a Large-Scale Hydrological Model. *J. Hydrol.* 528, 1–16. doi:10.1016/j.jhydrol.2015.05.028

Masood, M., Yeh, P. J.-F., Hanasaki, N., and Takeuchi, K. (2015). Model Study of the Impacts of Future Climate Change on the Hydrology of Ganges-Brahmaputra-Meghna basin. *Hydrol. Earth Syst. Sci.* 19 (2), 747–770. doi:10.5194/hess-19-747-2015

Mediero, L., Santillán, D., Garrote, L., and Granados, A. (2014). Detection and Attribution of Trends in Magnitude, Frequency and Timing of Floods in Spain. *J. Hydrol.* 517, 1072–1088. doi:10.1016/j.jhydrol.2014.06.040

Nam, D., Hoa, T., Duong, P., Thuan, D., and Mai, D. (2019). Assessment of Flood Extremes Using Downscaled CMIP5 High-Resolution Ensemble Projections of Near-Term Climate for the Upper Thu Bon Catchment in Vietnam. *Water* 11 (4), 634. doi:10.3390/w11040634

Nyaupane, N., Thakur, B., Kalra, A., and Ahmad, S. (2018). Evaluating Future Flood Scenarios Using Cmip5 Climate Projections. *Water* 10 (12), 1866. doi:10.3390/w10121866

O'Neill, B. C., Kriegler, E., Riahi, K., Ebi, K. L., Hallegatte, S., Carter, T. R., et al. (2013). A New Scenario Framework for Climate Change Research: the Concept of Shared Socioeconomic Pathways. *Clim. Chang* 122, 387–400. doi:10.1007/s10584-013-0905-2

Oudin, L., Hervieu, F., Michel, C., Perrin, C., Andréassian, V., Anctil, F., et al. (2005). Which Potential Evapotranspiration Input for a Lumped Rainfall–Runoff Model?: Part 2—Towards a Simple and Efficient Potential Evapotranspiration Model for Rainfall–Runoff Modelling. *J. Hydrol.* 303, 290–306. doi:10.1016/j.jhydrol.2004.08.026

Schewe, J., Heinke, J., Gerten, D., Haddeland, I., Arnell, N. W., Clark, D. B., et al. (2014). Multimodel Assessment of Water Scarcity under Climate Change. *Proc. Natl. Acad. Sci. USA* 111, 3245–3250. doi:10.1073/pnas.1222460110

Shen, M., Chen, J., Zhuan, M., Chen, H., Xu, C.-Y., and Xiong, L. (2018). Estimating Uncertainty and its Temporal Variation Related to Global Climate Models in Quantifying Climate Change Impacts on Hydrology. *J. Hydrol.* 556, 10–24. doi:10.1016/j.jhydrol.2017.11.004

Silva, A. T., Portela, M. M., and Naghettini, M. (2012). Nonstationarities in the Occurrence Rates of Flood Events in Portuguese Watersheds. *Hydrol. Earth Syst. Sci.* 16 (1), 241–254. doi:10.5194/hess-16-241-2012

Silva, A. T., and Portela, M. M. (2018). Using Climate-Flood Links and CMIP5 Projections to Assess Flood Design Levels under Climate Change Scenarios: A Case Study in Southern Brazil. *Water Resour. Manage.* 32 (15), 4879–4893. doi:10.1007/s11269-018-2058-6

Simpkins, G. (2017). Progress in Climate Modelling. *Nat. Clim Change* 7, 684–685. doi:10.1038/nclimate3398

Solari, S., Egüen, M., Polo, M. J., and Losada, M. A. (2017). Peaks over Threshold (POT): A Methodology for Automatic Threshold Estimation Using Goodness of Fit P -value. *Water Resour. Res.* 53 (4), 2833–2849. doi:10.1002/2016wr019426

Su, B., Huang, J., Mondal, S. K., Zhai, J., Wang, Y., Wen, S., et al. (2021). Insight from CMIP6 SSP-RCP Scenarios for Future Drought Characteristics in China. *Atmos. Res.* 250, 105375. doi:10.1016/j.atmosres.2020.105375

Tabari, H. (2020). Extreme Value Analysis Dilemma for Climate Change Impact Assessment on Global Flood and Extreme Precipitation. *J. Hydrol.* 593, 125932. doi:10.1016/j.jhydrol.2020.125932

Trenberth, K. E., Dai, A., Rasmussen, R. M., and Parsons, D. B. (2003). The Changing Character of Precipitation. *B Am. Meteorol. Soc.* 84 (9), 1205–1218. doi:10.1175/bams-84-9-1205

Wang, G., Zhang, J., He, R., Liu, C., Ma, T., Bao, Z., et al. (2017). Runoff Sensitivity to Climate Change for Hydro-Climatically Different Catchments in China. *Stoch. Environ. Res. Risk Assess.* 31, 1011–1021. doi:10.1007/s00477-016-1218-6

Wang, S., Xu, H., Liu, L., Wang, Y., and Song, A. (2018). Projection of the Impacts of Global Warming of 1.5°C and 2.0°C on Runoff in the Upper-Middle Reaches of Huaihe River Basin. *J. Nat. Resour.* 33 (11), 1966–1978. doi:10.31497/zrzyxb.20171050

Wang, Y., Wang, Y., and Xu, H. (2020). Impacts of 1.5°C and 2.0°C Global Warming on Runoff of Three Inland Rivers in the Hexi Corridor, Northwest China. *J. Meteorol. Res.* 34 (5), 1082–1095. doi:10.1007/s13351-020-9152-4

Winsemius, H. C., Aerts, J. C. J. H., van Beek, L. P. H., Bierkens, M. F. P., Bouwman, A., Jongman, B., et al. (2016). Global Drivers of Future River Flood Risk. *Nat. Clim Change* 6, 381–385. doi:10.1038/nclimate2893

Wu, C., and Huang, G. (2015). Changes in Heavy Precipitation and Floods in the Upstream of the Beijiang River basin, South China. *Int. J. Climatol.* 35 (10), 2978–2992. doi:10.1002/joc.4187

Xu, Y., Gao, X., Shen, Y., Xu, C., Shi, Y., and Giorgi, F. (2009). A Daily Temperature Dataset over China and its Application in Validating a RCM Simulation. *Adv. Atmos. Sci.* 26 (4), 763–772. doi:10.1007/s00376-009-9029-z

Yang, Q., Gao, C., Zha, Q., and Zhang, P. (2020). Changes of Climate and Runoff under the Representative Concentration Pathways Scenarios in the Upper Reaches of the Huaihe River. *J. Anhui Agric. Sci.* 48 (3), 209–214.

Yoon, S.-K., Kim, J.-S., and Moon, Y.-I. (2016). Urban Stream Overflow Probability in a Changing Climate: Case Study of the Seoul Uicheon Basin, Korea. *J. Hydro-environment Res.* 13, 52–65. doi:10.1016/j.jher.2015.08.001

Zhang, D., Zhang, L., Guan, Y., Chen, X., and Chen, X. (2012). Sensitivity Analysis of Xinanjiang Rainfall-Runoff Model Parameters: a Case Study in Lianghui, Zhejiang Province, China. *Hydrol. Res.* 43, 123–134. doi:10.2166/nh.2011.131

Zhang, Y.-L., and You, W.-J. (2014). Social Vulnerability to Floods: a Case Study of Huaihe River Basin. *Nat. Hazards* 71 (3), 2113–2125. doi:10.1007/s11069-013-0996-0

Zhao, R. J. (1992). The Xinanjiang Model Applied in China. *J. Hydrol.* 135 (1–4), 371–381.

Zheng, H., Chiew, F. H. S., Charles, S., and Podger, G. (2018). Future Climate and Runoff Projections across South Asia from CMIP5 Global Climate Models and Hydrological Modelling. *J. Hydrol. Reg. Stud.* 18, 92–109. doi:10.1016/j.ejrh.2018.06.004

Zhuan, M.-J., Chen, J., Shen, M.-X., Xu, C.-Y., Chen, H., and Xiong, L.-H. (2018). Timing of Human-Induced Climate Change Emergence from Internal Climate Variability for Hydrological Impact Studies. *Hydrol. Res.* 49, 421–437. doi:10.2166/nh.2018.059

Conflict of Interest: The authors declare that the research was conducted in the absence of any commercial or financial relationships that could be construed as a potential conflict of interest.

frontiers in Ecology and Evolution

ORIGINAL RESEARCH
published: 14 December 2021
doi: 10.3389/fevo.2021.761251

A Stepwise-Clustered Simulation Approach for Projecting Future Heat Wave Over Guangdong Province

Jiayan Ren[1], Guohe Huang[1,2], Yongping Li[1], Xiong Zhou[1], Jinliang Xu[3], Zhifeng Yang[4], Chuyin Tian[2] and Feng Wang[1]*

[1] State Key Joint Laboratory of Environmental Simulation and Pollution Control, China-Canada Center for Energy, Environment and Ecology Research, UR-BNU, School of Environment, Beijing Normal University, Beijing, China, [2] Environmental Systems Engineering Program, University of Regina, Regina, SK, Canada, [3] Key Laboratory of Power Station Energy Transfer Conversion and System, North China Electric Power University, Ministry of Education, Beijing, China, [4] Guangdong Provincial Key Laboratory of Water Quality Improvement and Ecological Restoration for Watersheds, Institute of Environmental and Ecological Engineering, Guangdong University of Technology, Guangzhou, China

A heat wave is an important meteorological extreme event related to global warming, but little is known about the characteristics of future heat waves in Guangdong. Therefore, a stepwise-clustered simulation approach driven by multiple global climate models (i.e., GCMs) is developed for projecting future heat waves over Guangdong under two representative concentration pathways (RCPs). The temporal-spatial variations of four indicators (i.e., intensity, total intensity, frequency, and the longest duration) of projected heat waves, as well as the potential changes in daily maximum temperature (i.e., Tmax) for future (i.e., 2006–2095) and historical (i.e., 1976–2005) periods, were analyzed over Guangdong. The results indicated that Guangdong would endure a notable increasing annual trend in the projected Tmax (i.e., 0.016–0.03°C per year under RCP4.5 and 0.027–0.057°C per year under RCP8.5). Evaluations of the multiple GCMs and their ensemble suggested that the developed approach performed well, and the model ensemble was superior to any single GCM in capturing the features of heat waves. The spatial patterns and interannual trends displayed that Guangdong would undergo serious heat waves in the future. The variations of intensity, total intensity, frequency, and the longest duration of heat wave are likely to exceed 5.4°C per event, 24°C, 25 days, and 4 days in the 2080s under RCP8.5, respectively. Higher variation of those would concentrate in eastern and southwestern Guangdong. It also presented that severe heat waves with stronger intensity, higher frequency, and longer duration would have significant increasing tendencies over all Guangdong, which are expected to increase at a rate of 0.14, 0.83, and 0.21% per year under RCP8.5, respectively. Over 60% of Guangdong would suffer the moderate variation of heat waves to the end of this century under RCP8.5. The findings can provide decision makers with useful information to help mitigate the potential impacts of heat waves on pivotal regions as well as ecosystems that are sensitive to extreme temperature.

Keywords: heat wave, heat wave downscaling, future projection, climate variation, ecosystem

Abbreviations: CMIP5, coupled model intercomparison projected phase 5; GCMs, global climate models; RCPs, representative concentration pathways; RHW, relative heat wave; RHWI, average intensity of heat waves within a year; RHWTI, total intensity of heat waves within a year; RHWL, yearly sum of participating heat wave days; RHWF, the length of the longest heat wave event within a year.

OPEN ACCESS

Edited by:
Shan Zhao,
Shandong University, China

Reviewed by:
Dimitrios Melas,
Aristotle University of Thessaloniki, Greece
Peng Zhang,
Fudan University, China
Wei Sun,
Sun Yat-sen University, China

****Correspondence:***
Guohe Huang
huang@iseis.org

Specialty section:
This article was submitted to Interdisciplinary Climate Studies, a section of the journal Frontiers in Ecology and Evolution

Received: *19 August 2021*
Accepted: *17 November 2021*
Published: *14 December 2021*

Citation:
Ren J, Huang G, Li Y, Zhou X, Xu J, Yang Z, Tian C and Wang F (2021) A Stepwise-Clustered Simulation Approach for Projecting Future Heat Wave Over Guangdong Province. Front. Ecol. Evol. 9:761251. doi: 10.3389/fevo.2021.761251

INTRODUCTION

A heat wave, as one of the most frequent extreme events under climate warming, has caused a destructive social, economic, and ecological impacts around the world, giving rise to a number of weather-related human mortality, property losses, and ecosystem challenges (Perkins et al., 2012; Yang et al., 2013; Zhang L. et al., 2018; Zhu et al., 2018; Shiva et al., 2019; Vogel et al., 2019; Zheng et al., 2019; Ren et al., 2021a; Woolway et al., 2021). For example, northwest Atlantic was significantly affected by a heat wave occurred in 2012, which resulted in the massive loss of biological habitats, the depletion of biodiversity, the destruction of nutrient cycles, and the variation in the distribution of commercial fisheries species (Mills et al., 2013; Smale et al., 2019). A heat wave has also appreciably disrupted ecosystem services and goods (Suryan et al., 2021). In 2012, 30% of global ocean has experienced strong or severe heat waves, which increased to approximately 70% in 2016 (Hobday et al., 2018; Smale et al., 2019). Furthermore, an estimation conducted by Zhao et al. (2017) indicates that global yields of wheat, rice, maize, and soybean would be, respectively, reduced by 6.0, 3.2, 7.4, and 3.1% for each degree-Celsius increase in global mean temperature during 2029–2058 relative to 1981–2010. Several prominent heat wave events have struck many regions in recent years, conspicuous events occurred in China in 2006 and 2013 (Chen and Fan, 2007), in Europe in 2003 and 2006 (Rebetez et al., 2009), in Russia in 2010 (Hauser et al., 2016), in the United States in 2015 (Fewings and Brown, 2019), in India in 2015 (Ghatak et al., 2017), and in Australia in 2009 (Zhang et al., 2017). Heat wave activities are likely to intensify longer and severer in the coming decades, and are expected to have an increasing impact on the socioeconomic system (Perkins, 2015; Wang et al., 2018; Wu et al., 2020; Gha et al., 2021). Consequently, it is desired to project future heat waves and investigate their characteristics to provide valuable information for future mitigation and adaption strategies since they can induce an increasing threat in many parts of the world.

Warming in China has also increased at a rate of approximately 0.24°C per decade during 1951–2006, which has been almost double the global average increase of surface meant temperature at 0.13 per decade from 1956 to 2005 (Ding and Qian, 2011). Consequently, China is one of the countries that have suffered deadly heat waves in the past few decades (Chen and Fan, 2007; Sun et al., 2014; Gu et al., 2016). For instance, many cities in south China suffered high temperature that lasted 20–50 days from July to early September in 2003 (Ding and Qian, 2011). As one of the most economically developed and populated regions in China (Luo and Lau, 2017), Guangdong Province has also experienced deadly heat waves due to climate change (Wang W. W. et al., 2013; Luo and Lau, 2017; Wang et al., 2018). For example, in June–July 2004, a severe heat wave event with a maximum temperature exceeding 40°C that occurred has resulted in 39 deaths (Du et al., 2013) in the capital city of Guangdong (i.e., Guangzhou). Yang et al. (2013) explored the heat wave-related mortality in 2005 over Guangzhou and found that the average and a total number of deaths reached 12 and 145 during the heat waves, respectively. Moreover, the 2005 heat wave has led to an increase of 23% (34%) of non-accidental (cardiovascular) mortality. Thus, it is of great significance to explore the characteristics of heat waves in Guangdong in the 21st century.

Previously, there have been some studies investigating the projection of future heat waves in China (Zhou B. T. et al., 2014; Li et al., 2019; Guo et al., 2020). Based on the outputs of 24 GCMs from the coupled model intercomparison projected phase 5 (CMIP5) models under two RCPs, projected changes of temperature extremes in China have been analyzed by Zhou B. T. et al. (2014). They found that the duration of warm spell duration index would be 136 days under RCP8.5, and that, under RCP4.5, would be 87 days lower. Based on 12 GCMs, Guo et al. (2017) projected future heat waves in China and showed that the frequency and intensity of heat waves would have a more dramatic increase under more emission-intense scenarios. Li et al. (2019) projected the properties of the future heat waves over China on the basis of the multi-model ensemble of 10 CMIP5 models and illustrated that heat waves are likely to become more frequent (0.40 and 1.26 per decade) and more extreme (1.07 and 2.90 days per decade) under RCP4.5 and RCP8.5, respectively. In brief, the projected variations in heat waves are becoming more obvious.

However, in most of the previous pieces of research, the projections of future heat waves were conducted on the basis of direct outputs of GCMs. Guangdong is located in the south part of China and faces the South China Sea; strong air-sea interactions exist in coastal areas such as Guangdong, which involves small-scale climate processes that are not well-represented in GCMs due to their coarse resolution over 100 km. Furthermore, GCMs may have less than 10-grid points involved in Guangdong, which cannot reflect the climate variations sufficiently within the region. Moreover, existing studies of extreme climate events in the Guangdong were mostly focused on the characteristics of history heat waves and the associated possible influencing factors (Luo and Lau, 2017), as well as the evaluation of impacts (Du et al., 2013; Tao et al., 2013; Yang et al., 2013); the characteristics and patterns in future heat waves over Guangdong have not been assessed in detail.

Thus, as an extension of previous studies, this study aims to examine the temporal-spatial variations of future heat waves in Guangdong through a developed statistical downscaling model. It entails: (1) a stepwise-clustered simulation approach will be developed on the station scale to reproduce the high-resolution simulations in Guangdong; (2) the trend of projected daily maximum temperature (i.e., Tmax, 2006–2100) will be analyzed; (3) historical (1976–2005) and future (2006–2100) heat waves will be calculated based on the projection results; and (4) the temporal-spatial variations and trend of four heat wave indicators (i.e., intensity, total intensity, frequency, and the longest duration) will be analyzed. This study may be of great significance for the development of heat wave alert systems and the formulation of early adaptive actions to protect vulnerable regions and sensitive ecosystems in Guangdong that are exposed to the adverse effects of heat waves.

STEPWISE-CLUSTERED SIMULATION APPROACH FOR PROJECTING FUTURE HEAT WAVES

To reproduce the daily maximum temperature (i.e., Tmax) for the analysis of future heat waves, a stepwise-clustered simulation approach based on the stepwise clustering analysis (i.e., SCA) is developed. The framework of the developed approach is presented in **Figure 1**. SCA was introduced by Huang (1992) and has been widely used in pieces of environmental research, such as climate change, air pollution, process control, and hydrology prediction (Huang et al., 2006; Wang X. Q. et al., 2013; Li et al., 2015; Wang and Huang, 2015; Fan et al., 2016; Zhuang et al., 2016; Sun et al., 2019; Zhai et al., 2019; Duan et al., 2020; Ren et al., 2021b; Wang et al., 2021). These studies have indicated the SCA has satisfactory performance in projecting environmental processes with complex non-linear and dynamic relationships. Multivariate analysis of variance is the fundamental theory of SCA (Morrison, 1967; Fan et al., 2016; Wang X. et al., 2017). The projection is realized through the establishment of a cluster tree from inputs (i.e., predictors or independent variables) to outputs (i.e., predictands or dependent variables). An SCA cluster tree will be obtained after a series iteration process of cutting and merging of dependent variables according to the specific given criteria, and independent variables are used as references in the process (Huang et al., 2006). Previously, statistical downscaling methods mostly assume that the interested dependent variable is a function of independent variables (Wilby et al., 2002; Hessami et al., 2008; Gibson et al., 2017), while the improvements of the quality of downscaled simulation reproduced through such a function are likely to be limited relative to the raw GCMs' output owning to the complex climate system (Wilby et al., 2002; Wang X. Q. et al., 2013). However, the underlying complex relationships (including non-linear and discrete relationships) between dependent and independent variables can be revealed by the generated cluster tree without assuming the functional relationship compared to these downscaling methods (Wang X. Q. et al., 2013; Zhuang et al., 2016; Duan et al., 2020). Handling the complicated relationship among multiple dependent and independent variables at the same time is another significant advantage of SCA (Fan et al., 2015; Wang et al., 2021). In addition, heat wave, as one of the extreme climate events, the projection of which is also challenging due to the inherently complex relationship between predictors (i.e., large-scale coarse atmospheric variables) and predictands (i.e., local surface variables). Therefore, given the advantage of the SCA method and characteristics of heat waves, a stepwise-clustered simulation approach based on SCA is developed for heat wave projection in this study. Previous studies assumed that the developed relationship through the statistical downscaling method can hold for the future (Wu et al., 2017; Xu and Wang, 2019; Araya-Osses et al., 2020). Such a cluster tree then can be further employed for the projection of predictions once new predictors are available. A detailed process for SCA can be demonstrated as following five steps, which include the determination of the original inputs and outputs, establishment of the cutting and merging criterion, operation of cut and merge, output of the cluster tree and the operating rules, and projection for the study period. Following that, the developed stepwise-clustered simulation approach was used for statistically downscaling the GCMs outputs to generate high-resolution heat wave projections for Guagdong. Previous studies showed that extreme climate events (such as heat waves and temperature anomaly) were likely to become more frequent, longer duration and higher intensity during 1976–2005 and 2036–2095 over South China (including Guangdong) (Lewis and King, 2016; Almazroui et al., 2021; Ren et al., 2021b). Thus, to provide comparability results, outputs from the GCM projections are expected and divided into three 30-year periods, including the historical period (i.e., 1976–2005) and the future period (i.e., 2036–2065, 2050s; 2066–2095, 2080s) under RCP4.5 and RCP8.5. Variations of future climate in comparison with the historical period were then investigated to help better understand the possible future changes in heat waves.

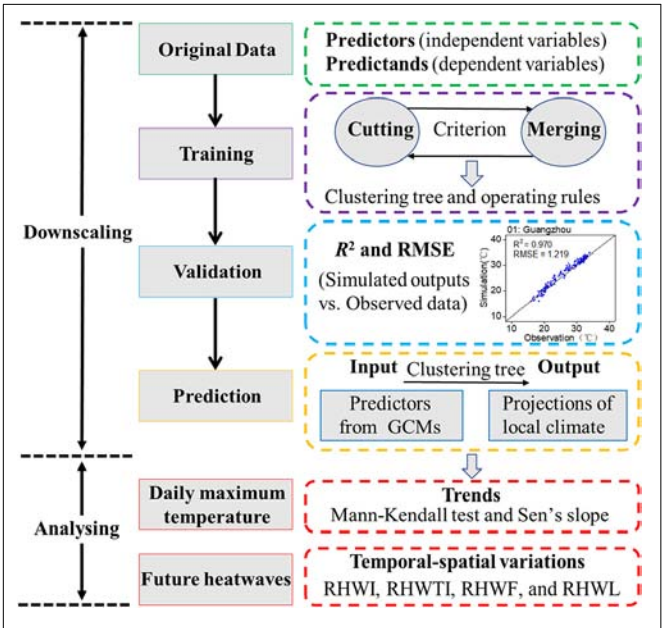

FIGURE 1 | The framework of the developed stepwise-clustered simulation approach.

The coefficient of determination (R^2) measures of the extent of a model explains variations in the data; the root mean squared error (RMSE) evaluates the variance of errors independent of sample size and characterizes the difference between simulations and observations. In this study, the performance of the developed approach for projecting future heat waves is evaluated based on the R^2 and RMSE values. The reliability of the approach increases as R^2 approaches one, and when it is equal to one, which indicates that all variations can be explained. In terms of RMSE, when the fit between simulations and observations is perfect, the RMSE would have a value of zero. Thus, the lower the value (close to zero), the better performance of the approach. R^2 and RMSE have been broadly used in the evaluation of climatic or hydrological models (Fan et al., 2015, 2016, 2017; Wang and Huang, 2015; Zhou et al., 2018; Sun et al., 2019;

Zhai et al., 2019; Duan et al., 2020; Li et al., 2020; Pramod et al., 2021). To assess the ability of the developed approach in reproducing the observations, the $R^2$and RMSE were used in this study and expressed as follows:

$$R^2 = \frac{\left[\sum_{i=1}^{n}\left(O_i-\bar{O}\right)\left(S_i-\bar{S}\right)\right]^2}{\sum_{i=1}^{n}\left(O_i-\bar{O}\right)^2\sum_{i=1}^{n}\left(S_i-\bar{S}\right)^2} \quad (1)$$

$$RMSE = \sqrt{\frac{\sum_{i=1}^{n}\left(S_i-Q_i\right)^2}{n-1}} \quad (2)$$

where n is the sample number in the training or validation dataset; O_i and S_i are the observed and simulated values in the i_{th} sample, respectively; and $\bar{O}$ itch $\bar{S}$ are the averages of O_i and S_i, respectively.

The Mann—Kendall test (i.e., MK test) is one of the most populated method for evaluating the variation trends in climatic studies (Gupta et al., 2018; Zhai et al., 2019; Mukherjee and Mishra, 2020; Farooq et al., 2021; Zhou et al., 2021). The MK test is a non-parametric procedure due to its advantages in considering the distribution of time series data as well as processing outlies (Mann, 1945; Kendall, 1948); the MK test is used to investigate the trends of variables (i.e., Tmax and heat wave indicators) in this study. A null hypothesis (H_0) assumes that time series of variables are specifically distributed contrary to the alternative hypothesis (H_1), which demonstrates an increasing or declining trend. The temporal trend of the MK test is identified based on the standardized test static (i.e., denoted as Z) as follows:

$$\begin{cases} Z_{ij} = \sum_{i=1}^{n-1}\cdot\sum_{j=i+1}^{N} sign\left(X_j - X_i\right) \\ sign\left(X_i - X_j\right) = \begin{cases} +1 & \text{if } \left(X_i - X_j\right) > 0 \\ 0 & \text{if } \left(X_i - X_j\right) = 0_i, \\ -1 & \text{if } \left(X_i - X_j\right) < 0_i \end{cases} \end{cases} \quad (3)$$

where X_i and X_j are the consecutive time series of the variables (i.e., Tmax and heat wave indicators), and n is the time series length of the variable. Z is the Kendall's test statistic; it can be an increasing trend (positive), a declining trend (negative), or a no trend (zero). The statistical significance of the trends is determined by the Z_{ij}, and the H_0 of no trend will be rejected when the absolute value of Z_{ij} is larger than 1.96. See Farooq et al. (2021) for more detailed information about the MK test.

Sen's slope is a non-parametric estimator that is applied to obtain variations in trends of the variable in a time series (Sen, 1968). In this study, the variables are Tmax and heat wave indicators. The rate of variation (Q_{med}) was calculated from the slopes (S) of all consecutive pairs of data (N).

$$Q_{med} = \begin{cases} \frac{S(N+1)}{2}, & \text{if } N \text{ is odd} \\ \frac{\frac{SN}{2}+S\left(\frac{N+2}{2}\right)}{2}, & \text{if } N \text{ is even} \end{cases} \quad (4)$$

The data trend is reflected by the Q_{med} sign, and a positive value of Q_{med} demonstrates an increase in variation, and *vice versa*.

AN OVERVIEW OF THE STUDY AREA

Guangdong Province (109°39′–117°19′E and 20°13′–25°31′N) is located in the south part of China and faces the South China Sea and adjacent to Macau and Hong Kong (**Figure 2**). Guangdong has a total area of about 1.798×10^5 km^2, with the total population of 0.115×10^3 million at the end of the year 2019 (Guangdong Statistical Yearbook, 2020). Guangdong has experienced rapid urbanization and developed as one of the largest economic provinces of China since 1989 (Luo and Lau, 2017; Liu et al., 2019; Yu et al., 2019). Continued urbanization throughout Guangdong contributes to the heat-island effect, and the occurrence, intensity, and duration of heat waves are expected to increase under climate warming (Zeng et al., 2006; Sun et al., 2012; Luo and Lau, 2017).

Guangdong is characterized by typical tropical and subtropical climates. Its climate has been changing dynamically due to the close relationship with large-scale atmospheric activities, such as East Asian monsoon and the North Pacific subtropical high (Luo and Lau, 2017). From 1976 to 2005, the average summer temperature is 32.3°C at 35 stations over Guangdong, while this in winter is 19°C. Guangdong has experienced a fluctuating rise in temperature since the 1980s. With the variation of average annual temperature as high as 0.03°C per year, the Pearl River Delta region is the main warming area of Guangdong (Yu et al., 2007). During 1986–2015, the annual temperature is 22°C (Wu et al., 2019). The annual precipitation is over 1,300 mm, nearly 60% of which is concentrated in the rainy season (i.e., June–August) (Wu et al., 2019). The surface air temperature increased at a rate of 0.13°C per decade in the capital of Guangdong (i.e., Guangzhou) during 1951–2004, while it is expected to increase rapidly in Guangdong in the coming decades (Liu et al., 2019). In the long-term adaption to climate change, Guangdong has experienced extreme climate events, such as heat waves, drought, and coastal flooding, which have resulted in losses and threats to the lives and safety (Zhu et al., 2014; Xu and Wang, 2019; Yu et al., 2019; He et al., 2020). For instance, Yang et al. (2013) investigated the impact of a diurnal temperature range on mortality in the capital of Guangdong and concluded that the increase in diurnal temperature of 1°C at 0–4 lag days would induce a 0.47% increase in non-accidental mortality. In addition, Zhang L. et al. (2018) quantified the mortality effects of future heat waves on human health; they found that the average annual loss of the elders ($\geq$65) would be 1,675 deaths per million in Guangzhou during 2051–2095 under RCP. Climate warming will induce extreme disastrous impacts to coastal cities, such as a sea level rise, the expansion of storm surge inundation areas, and ecosystem degradation of coastal wetlands, mangroves, and reefs (He et al., 2012; Rahmoun et al., 2016). He et al. (2012) assessed the sea level rising in China; the investigation illustrated that the sea level in Guangdong rose by 20 mm during 2001–2010 relative to 1991–2000. Moreover, it is estimated that, in 2030 and 2050, the average increase of the sea level in the Pearl River Delta will be approximately 20–33 and 50 mm, respectively. According to the prediction of Li et al. (1993), the low altitude of 1,500 km^2 below 0.4 m in the Pearl River Delta would be completely submerged when the sea level rises to 0.7 m in the middle of

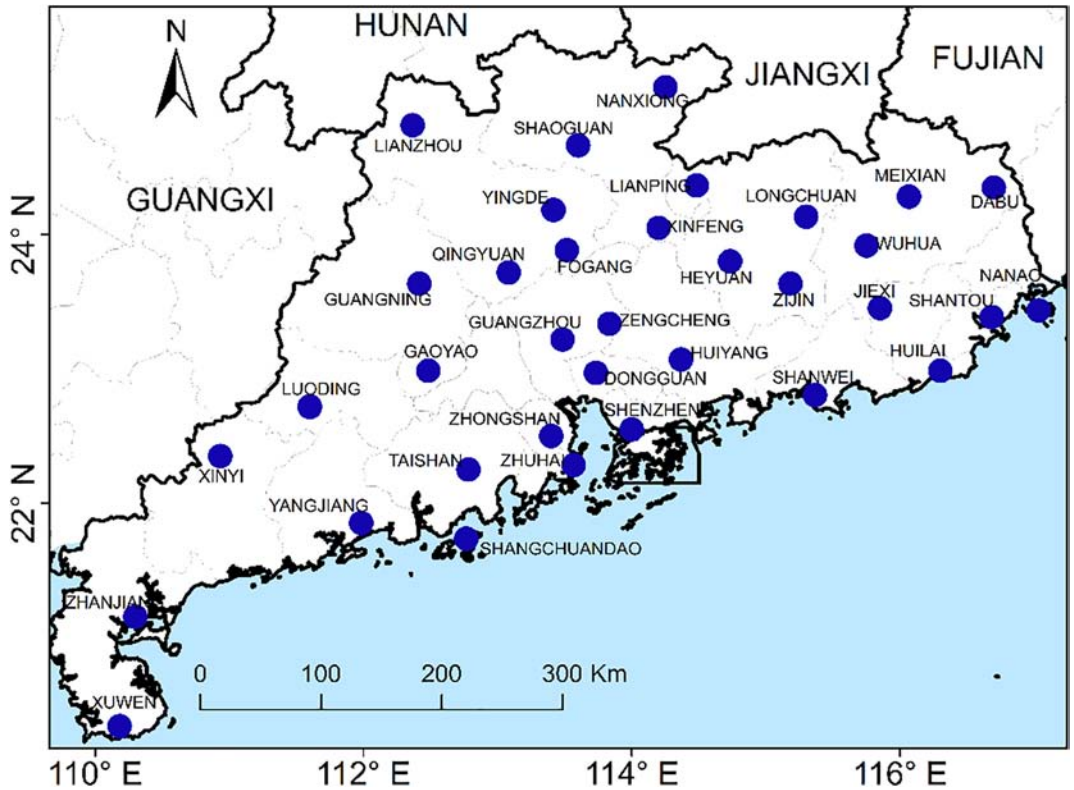

FIGURE 2 | Geographical positions of the 16 weather stations over Guangdong Province, China.

21st century. Thus, it is desired to improve our understanding of future heat waves in Guangdong and provide helpful guidance for improving our ability in projecting the variations of heat waves in that region.

In this study, 35 weather stations are selected. For each weather station, the observed Tmax from 1976 to 2005 was obtained from the National Meteorological Information Center.[1] The quality of the raw Tmax dataset was checked before analysis and used as a predictand of the heat wave downscaling model. The variables of reanalysis dataset were acquired through the National Centers for Environmental Prediction (NCEP/NCAR)[2] and were used as large-scale atmospheric predictors (**Table 1**). Through the correlation analysis, the seven most relevant large-scale atmospheric variables were chosen as predictors of Tmax (i.e., the bold font). The NCEP/NCAR dataset has been derived from the interpolation of daily observations since 1948 with a resolution of 2.5° × 2.5° (Kalnay et al., 1996). It has been used in many branches of climatological research (Simmons et al., 2004; Luo and Lau, 2017; Wang P. et al., 2017; Zhai et al., 2019), and its reliability is better for surface air temperature in the southern and eastern parts of China (Xu and Ding, 2001; Shi et al., 2007). The associated data (i.e., predictors and prediction) supporting the development of the heat wave downscaling model for the same period (i.e., the historical period, 1976–2005) were extracted. In addition, these data were further divided into two 15-year subsets, including 1976–1990 and 1991–2005. The former set was used for the training of the developed model, and the latter one was used to validate the performance of the developed model.

TABLE 1 | A list of NARR variables selected as predictors for Tmax.

NARR variables selected	Unit	Pressure level (hPa)
Geopotential height	m	500, 700, 850, and 1000
Near-surface air temperature	K	**2 m**
Air temperature	K	500, 700, **850**, and 1000
Near surface relative humidity	%	Surface
Relative humidity	%	500, 700, 850, and 1000
Near surface specific humidity	%	**Surface**
Specific humidity	%	500, 700, 850, and 1000
Eastward near surface wind	m s^{-1}	Surface
Eastward wind	m s^{-1}	10, 500, 700, 850, and 1000
Northward near surface wind	m s^{-1}	Surface
Northward wind	m s^{-1}	10, 500, 700, 850, and 1000
Pressure at surface	hPa	**Surface**
Sea level pressure	hPa	**Surface**
Precipitable water	Kg/m^2	**Surface**
Wind	m s^{-1}	Surface, 10, **500**, 700, 850, and 1000

The bold values denotes the selected predictors of predictand, i.e., the seven large-scale atmospheric variables that are most relevant to the Tmax.

[1] http://data.cma.cn

[2] https://www.esrl.noaa.gov/psd/

Daily gridded data from the four GCMs, i.e., Centre National de Recherches Météorologique CNRM-CM5 Model 5 (i.e., CNRM-CM5), Commonwealth Scientific and Industrial Research Organisation Mark 3.6.0 (i.e., CSIRO-Mk3.6.0), Institut Pierre Simon Laplace Model CM5A-MR (i.e., IPSL-CM5A-MR), and Model for Interdisciplinary Research on Climate Version Five (i.e., MIROC5) were downloaded from the CMIP5 dataset to analyze the future variations of heat waves in Guangdong (Li et al., 2019; Xu and Wang, 2019; Ren et al., 2021b). The four GCMs cover the historical and future simulations data under different emission scenarios. Their scenarios were developed based on their end-of-century radiative forcing, including RCP 2.6, RCP4.5, RCP 6.0, and RCP 8.5. Among which, RCP 4.5 is a stabilization scenario—its stabilization without an overshoot pathway to 4.5 Wm^{-2} at stabilization after 2100 (Clarke et al., 2007). RCP8.5 represents a high-emission global warming scenario; the rising radiative forcing would lead to 8.5 Wm^{-2} by the end of 21st century (Adeniyi, 2016). In this study, the four GCMs are re-gridded to the coarsest resolution (NCEP/NCAR data) through the bilinear interpolation method (Zhai et al., 2019). They were then extracted for the periods of 1976–2005 (i.e., historical) and 2006–2100 (i.e., under RCP4.5 and RCP8.5). The extracted data were used to develop the heat wave downscaling model and project the future heat wave. Especially, to provide comparability results, the GCM data from 1991 to 2005 (i.e., the validation period) were also prepared.

In general, a heat wave event is defined as a period during which the daily temperature (e.g., daily temperature of maximum, minimum, and mean) exceeds its threshold temperature and consecutive several days (Perkins et al., 2012; Wang P. et al., 2017; Shiva et al., 2019; Woolway et al., 2021). In this study, the daily maximum temperature (i.e., Tmax) exceeds the corresponding relative threshold for at least 4 consecutive days, which was used as the criterion to identify heat wave events in Guangdong and denoted as relative heat wave events (i.e., RHWs). The relative threshold (i.e., the 90th percentile of Tmax) was calculated based on centered 21-day moving window samples with observations during May to December in the historical period (i.e., 1976–2005). The total samples are 4,590 days (153 × 30). Following previous studies (Perkins et al., 2012; Pezza et al., 2012; Guo et al., 2017; Luo and Lau, 2017; Wang P. et al., 2017; Oliver et al., 2018; Fenner et al., 2019; Shiva et al., 2019), four indicators (i.e., intensity, total intensity, frequency, and the length of the longest event of RHW) are measured to quantify the properties of relative heat waves; their definitions are as follows:

- Average intensity of heat wave (RHWI): the average intensity of heat waves within a year, i.e., the average of cumulative value of the temperature biases when the daily maximum temperature exceeds its threshold temperature during the heat wave event within a year, calculating by averaging all participating event days; Eq. 5 summarizes the definition of RHWI (unit: °C/event).
- Total intensity of heat wave (RHWTI): the total intensity of heat waves within a year, i.e., the cumulative value of the temperature biases when the daily maximum temperature exceeds its threshold temperature during the heat wave event within a year; Eq. 6 summarizes the definition of RHWTI (unit: °C).
- Frequency of a heat wave (RHWF): the total number of days within a year that meet the relative heat wave criterion; Eq. 7 summarizes the definition of RHWF (unit: °C).
- The longest heat wave event (RHWL): the length of the longest heat wave event within a year; Eq. 8 summarizes the definition of RHWL (unit: days).

$$RHWI = \frac{\sum_i^N \sum_j^{D_i} \left(T_{ij} - TR_{ij}\right)}{N} \tag{5}$$

$$RHWTI = \sum_i^N \sum_j^{D_i} \left(T_{ij} - TR_{ij}\right) \tag{6}$$

$$RHWF = \sum_i^N \left(D_i\right) \tag{7}$$

$$RHWL = \max\left(D_i\right) \tag{8}$$

where N is the total number of occurred RHW during the study period. T_{ij} is the Tmax on Day j in the RHW, and TR_{ij} is the corresponding threshold temperature of T_{ij}. The intensity $\sum_j^{D_i}(T_{ij}-TR_{ij})$ of heat wave i is the sum of the temperature biases that exceed its threshold values during the duration D_i. And $max(D_i)$ is the length of the longest RHWs within a year.

RESULTS

Evaluation of the Statistical Downscaling Model

In this study, the stepwise-clustered simulation approach is developed and used for the heat wave downscaling. The 1976–2005 period is divided into two 15-year sets: 1976–1990 and 1991–2005, with one set used for training and the other for validation. To validate the performance of the developed model, the downscaling results for Tmax are shown with the corresponding simulations during 1991–2005 (**Figures 3**, **4**, **5**). In this study, 16 weather stations spatially distributed across Guangdong were selected as examples to present the associated results. **Figure 3** shows the validation results of the downscaling model. The determination coefficient (i.e., R^2) and RMSE between the NCEP reproduced dataset through the downscaling model and observations were calculated for the 16 weather stations. The R^2 values range from 0.950 to 0.987, and the RMSEs of all stations range from 0.863 to 1.730°C, evidencing that the NCEP-trained approach exhibits outstanding performance.

To validate the performance of the developed model, the R^2 values for the monthly average between the simulations of the four GCMs (i.e., CNRM-CM5, CSIRO-Mk3.6.0, IPSL-CM5A-MR, MIROC5, and their model ensemble) and the observed Tmax are also represented in **Figure 4**. Although the performance of the developed approach displays variations among stations over Guangdong, it can reproduce Tmax well. For instance, the

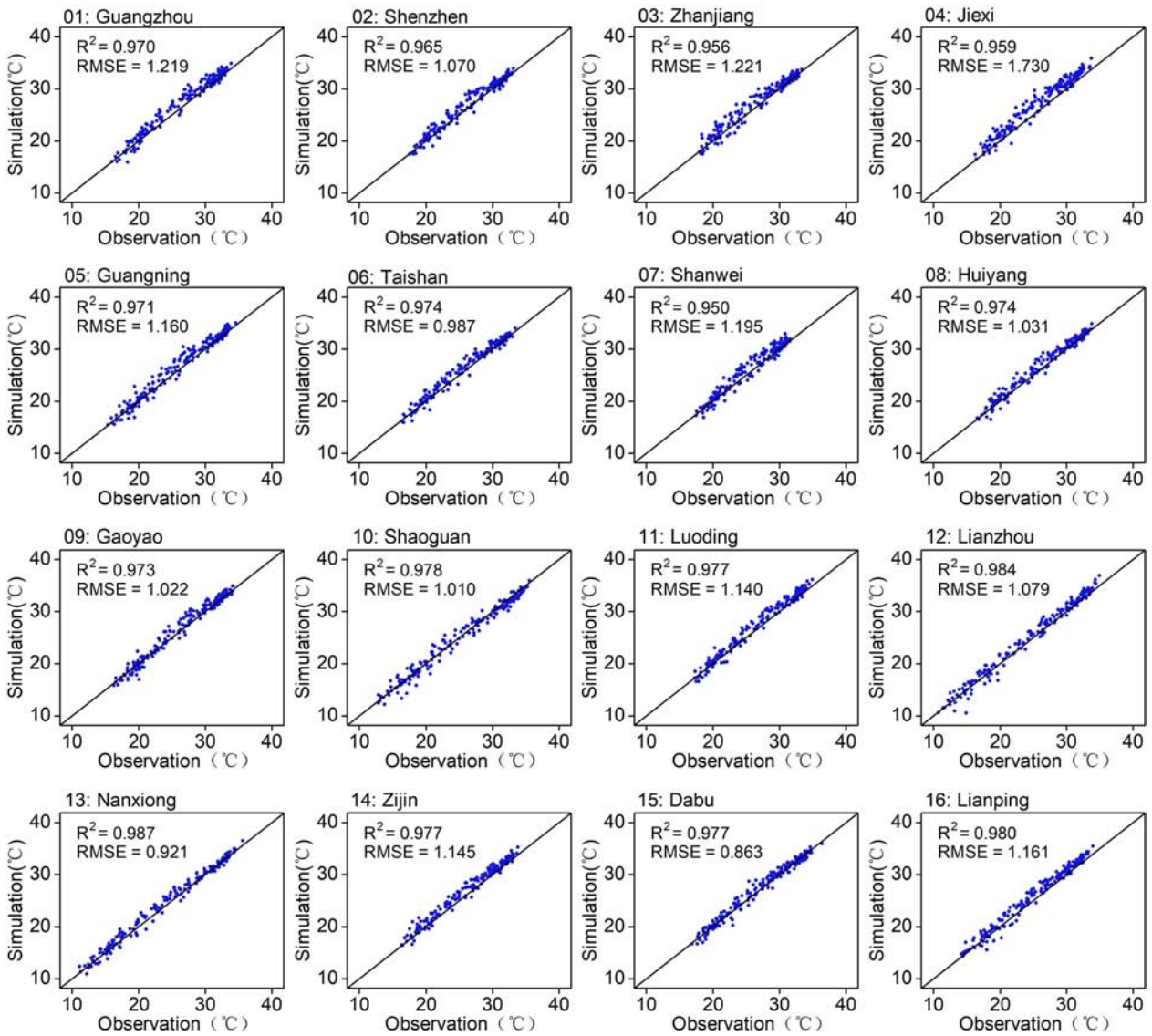

FIGURE 3 | Evaluation results for multiyear monthly average of Tmax between observed and NCEP/NARR reanalysis at the 16 selected weather stations, 1991–2005.

maximum R^2 value of 0.923 is related to the reproduced Tmax from the model ensemble. The results implied that the model ensemble can be an effective tool in the case of reproducing the observed Tmax at the 16 selected weather stations over Guangdong. Previous studies have also found the use of model ensemble reduced more the bias in the evaluation than using only a single GCM, thereby improving the reliability of climate projections (Webber et al., 2018; Qian et al., 2020; Ma et al., 2021). Similarly, it can be found that the developed approach also demonstrates significant performance in reproducing the observed Tmax from the four GCMs at the 16 selected weather stations (**Figure 5**). The comparison results of the monthly variations between the observed Tmax and reproduced values from GCMs during 1991–2005 possess similar trends, which means that the developed approach has significant ability in capturing present-day Tmax, especially for those reproduced by the model ensemble in the periods from May to October. In addition, Tmax is somewhat over- and underestimated by the single GCM. In detail, Tmax is somewhat overestimated by the CNRM-CM5 from March to April (e.g., Guangning and Shanwei), and underestimated by the MIROC5 during July to August (e.g., Nanxiong and Zijin). This is mainly due to the uncertainty of the model, which may be induced by differences in the model parameterization, emission concentration scenarios, and internal climate variability (Zhai et al., 2019; Ma et al., 2021). Therefore, it is essentially recommended to present the Tmax with the model ensemble from multiple GCMs' outputs to reduce potential biases.

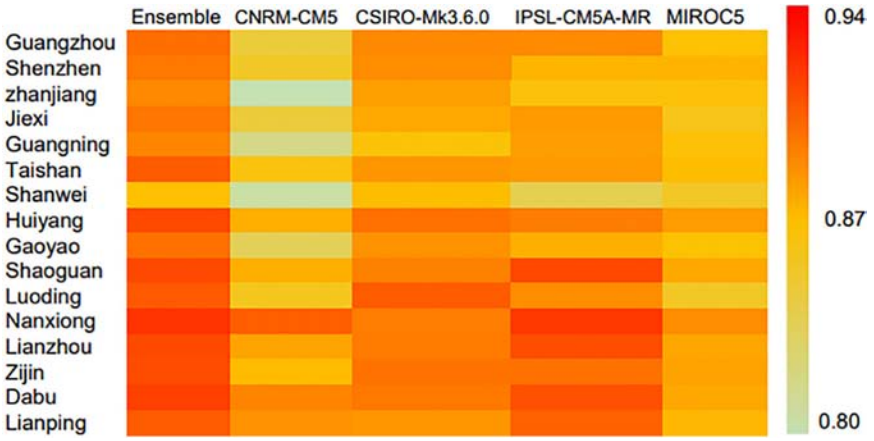

FIGURE 4 | Comparisons of the monthly average between observed Tmax and downscaled outputs from CNRM-CM5, CSIRO-Mk3.6.0, IPSL-CM5A-MR, MIROC5, and their ensemble, 1991–2005 [color bars represent the coefficient of determination (R^2) value between observed Tmax and downscaled outputs].

Characteristics of the Projected Daily Maximum Temperature

Projections of future temperature from the ensemble of four GCMs (i.e., CNRM-CM5, CSIRO-Mk3.6.0, IPSL-CM5A-MR, and MIROC5) are resulted from the developed approach. The characteristics of the projected Tmax in Guangdong are shown in **Figures 6**, **7**, **8**, **9** and **Table 2**. **Figures 6**, **7** provide the monthly trend of the projected average of Tmax at the 16 selected weather stations from 2006 to 2100 under RCP4.5 and RCP8.5. The trend of the projected Tmax is obtained by fitting the monthly time series data of each weather station using the *lowess* method (Zhai et al., 2019), which is displayed as a smooth bold red line. It provides a better understanding of the possible variations of future Tmax. The results indicate that there is a consistent increase at all 16 weather stations under RCP4.5 and RCP8.5. In detail, the highest increasing trend of the Tmax is likely to occur at Shaoguan (Nanxiong) under RCP4.5 (RCP8.5). Moreover, **Table 2** provides the trends of seasonal (spring, summer, autumn, and winter) and annual average of Tmax through the Mann–Kendall statistics and Sen's slope estimator test for 16 selected weather stations. These two test methods have been extensively used by previous studies to explore monotonic trends in climatic time series (Zhai et al., 2019; Farooq et al., 2021). It is pretty evident that all stations suggest significant increasing trends for their respective mean seasonal and annual of Tmax, with MK-p values less than.001. It indicated that Guangdong is likely to experience a warmer future. The increase is various among stations under RCP4.5 and RCP8.5. For instance, of all the seasons under two RCPs, the most remarkable increase is detected in spring, lesser in winter and summer, followed by autumn. Besides, Shaoguan presents the highest increasing trend of 0.075°C per year during summer under RCP8.5. On the annual time scale, the increase varies between 0.016°C per year (i.e., at Zhanjiang) and 0.030°C per year (i.e., at Shaoguan) under RCP4.5, while these range from 0.027°C (i.e., at Lianzhou) to 0.057°C (i.e., at Nanxiong) per year under RCP8.5. This is consistent with previous pieces of research that the climate in Guangdong will become warmer in the future (Sutton, 2009).

Figures 8, **9** show the most likely variations in monthly average Tmax at Guangdong during 2066–2095 in comparison with those in the historical period (1976–2005). The results present that the projected Tmax is increasing in all months to the end of this century under RCP4.5 and RCP8.5. In detail, the increase of projected Tmax during November, December, and February over Guangdong is more prominent relative to the increase in other months, especially August. Those increases can be similarly discovered over all 16 weather stations under two RCPs. In addition, it is noticeable that the increases of Tmax during 2066–2095 are more significant under RCP8.5. For example, the smallest projected variation of Tmax occurs in the weather station of Zhanjiang in August, which is likely to be 0.046°C, and the largest projected change would expand to 1.474°C in November (i.e., Shaoguan) under RCP4.5. While the projected variation ranges from 0.334°C (i.e., in August at the Zhanjiang station) to 2.985°C (i.e., in December at the Lianzhou station) under RCP8.5. Therefore, it can be inferred that a higher emission concentration will lead to a much higher variation in the Tmax. Consequently, the projected Tmax of the 16 selected weather stations in Guangdong will continue to increase by the end of this century under two RCPs.

Evaluation of Relative Heat Waves During the Historical Period

To evaluate the ability of the developed approach to simulating the historically observed heat waves, the spatial distributions between the observations and ensemble simulations of the four GCMs during 1976–2005 over Guangdong are presented in **Figures 10**, **11**. The spatial patterns of a 30-year average of RHW intensity and total intensity (i.e., RHWI and RHWTI) are shown in **Figure 10**. In terms of RHWI, it can be found that the stations in southwestern Guangdong experience higher observed heat wave intensity, exceeding 6.3°C/event per year (e.g., Xuwen, Zhanjiang, and Xinyi) (**Figure 10A**). In central

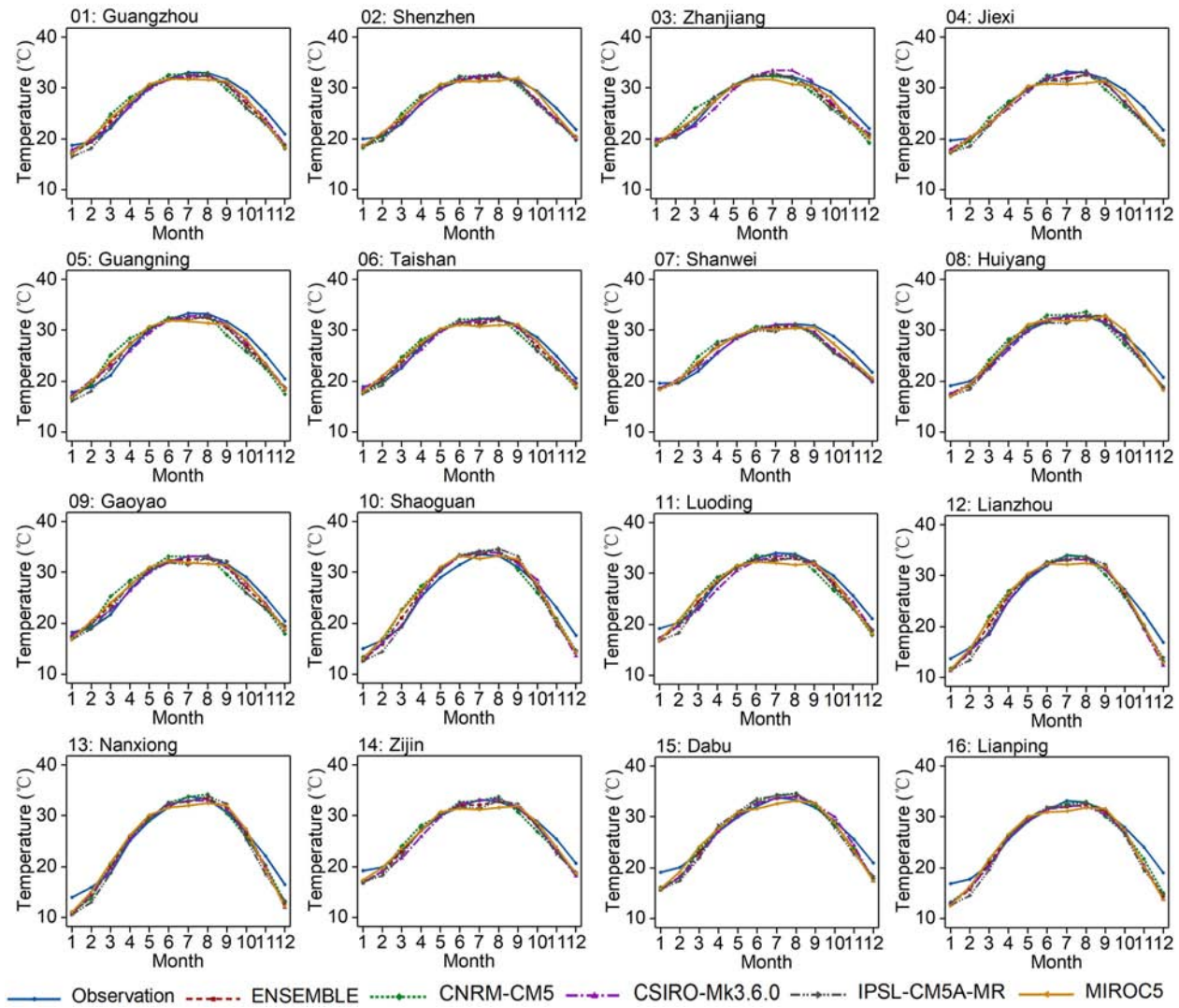

FIGURE 5 | Monthly variations of the observed Tmax and downscaled values for GCMs and their ensemble at the 16 selected weather stations, 1991–2005.

Guangdong and most of the coastal areas, the RHWI was low with values less than 2.7°C/event per year. This spatial pattern is consistent with the variations of HWM in this region in Luo and Lau (2018), which has slightly less constrained definitions. Those spatial characteristics might associate with the stronger solar radiation, the amplifying effect of El Niño, and the anomalous anticyclonic circulation (Luo and Lau, 2018; Wang et al., 2018). When it comes to the reproduced RHWI from the model ensemble, the overall spatial patterns of RHWI over Guangdong are well captured, although it is faintly overestimated (underestimated) in Lianzhou, Shaoguan, and Nanxiong (Meixian, Dabu, and Wuhua) over northern (eastern) Guangdong (**Figure 10B**). Similarly, the single GCM performs better in reproducing the spatial characteristics of RHWI, except for IPSL-CM5A-MR, which almost underestimated the whole Guangdong. CNRM-CM5, CSIRO-Mk3.6.0, and MIROC5 show overestimation in northern Guangdong and the surrounding stations of Guangzhou, while the rest stations are closer to the observed RHWI. Consequently, the spatial pattern of RHWI can be reasonably simulated by the model ensemble of the four GCMs.

The spatial distribution of the observed RHWTI is similar to that of the RHWI, which presents the higher values at most of the stations over southwestern Guangdong. However, the lower RHWTI values do not directly follow those of HWI (**Figure 10G**). In addition to the coastal areas of Guangdong, the stations with lower values no more than 2°C are also distributed in northeastern Guangdong, which has the highest altitude of the province. This supports previous investigation, suggesting that cooler sites at higher altitude will result in less severe heat waves (Wang et al., 2018; Woolway et al., 2021). CNRM-CM5 and MIROC5 exhibit similar distribution of observed RHWTI, overestimating it over central Guangdong (e.g., Guangzhou and Dongguan) (**Figures 10I,L**). Likewise, the CSIRO-Mk3.6.0

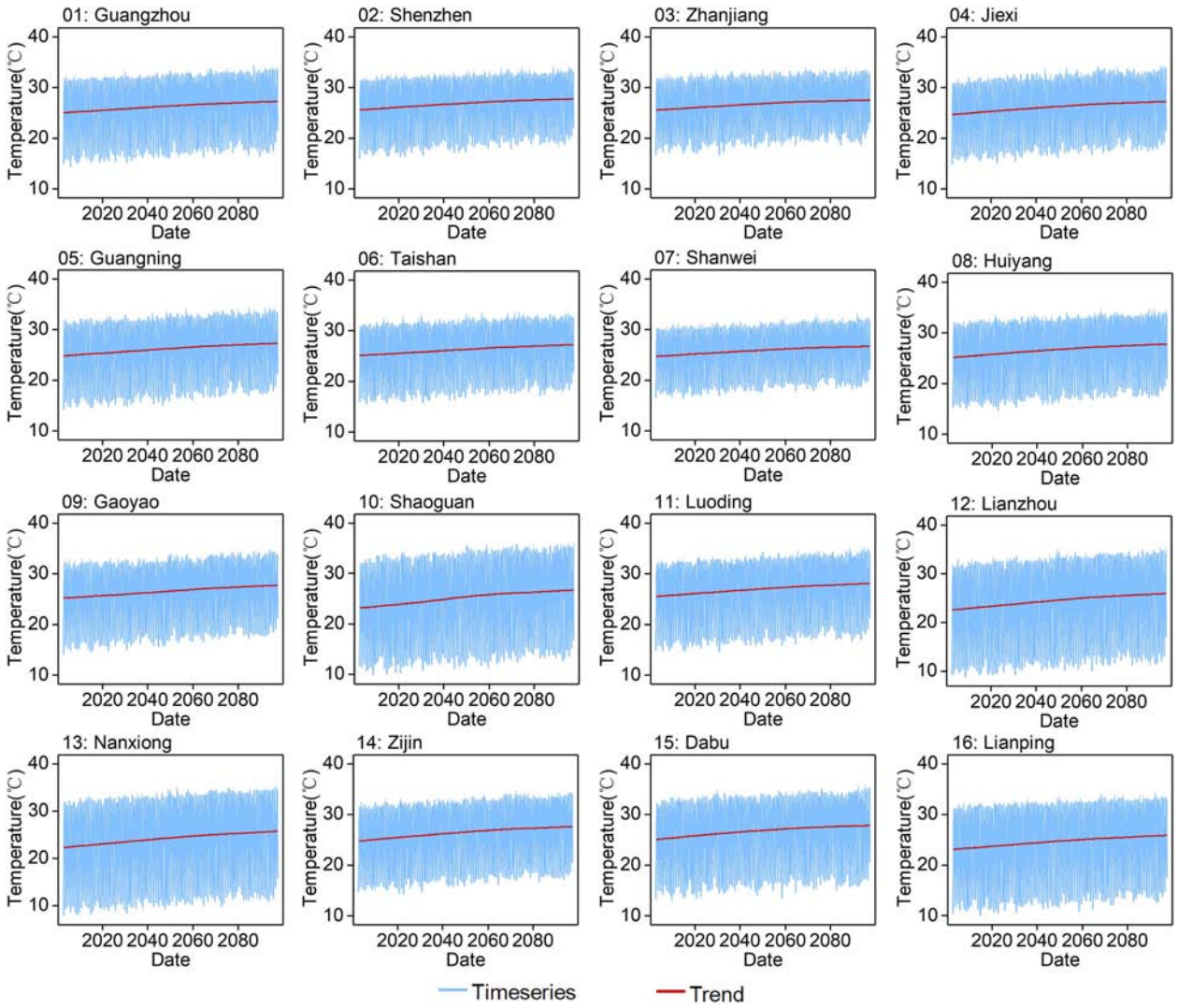

FIGURE 6 | Monthly projected Tmax of the ensemble of GCMs (i.e., CNRM-CM5, CSIRO-Mk3.6.0, IPSL-CM5A-MR, and MIROC5) from 2006 to 2100 under RCP4.5.

and IPSL-CM5A-MR underestimated RHWTI over eastern Guangdong (e.g., Meixian and Dabu) and overestimated RHWTI in the peripheral of Guangdong (e.g., Nanxiong and Huilai). As a result, the ensemble of the four GCMs is able to capture the spatial distributions of RHWTI well but shows under- and overestimation in eastern and central Guangdong, respectively.

Moreover, the spatial patterns of the frequency and the longest duration of relative heat waves (i.e., RHWF and RHWL) during the historical period (1976–2005) for all the weather stations over Guangdong are provided in **Figure 11**. The spatial pattern of observed and simulated RHWF is quite similar to that of RHWL. In terms of observations, the largest observed values of RHWF and RHWL distribute in the southwest region, such as Zhanjiang, with higher values exceeding 11.9 and 7 days per year, respectively (**Figures 11A,G**). However, the performance of GCMs in reproducing the spatial characteristics of RHWF and RHWL varies. For example, CNRM-CM5 and CSIRO-Mk3.6.0 can better reproduce the spatial distribution of RHWF and RHWL; although CNRM-CM5 overestimates the observed values in western (e.g., Guangning and Gaoyao) and eastern (e.g., Meixian and Dabu) Guangdong. The CSIRO-Mk3.6.0 slightly underestimated the RHWF and RHWL in the central-northern regions of Guangdong (e.g., Yingde and Cengcheng) and overestimated for the eastern region (e.g., Zijin). IPSL-CM5A-MR tends to underestimate the observed RHWF and RHWL in almost all Guangdong. MIROC5 reproduces the HWF and RHWL of more than 5 days per year in the central (e.g., Guangzhou and Dongguan) and coastal (e.g., Shenzhen and Huiyang) Guangdong, which slightly overestimated for these regions. The model ensemble simulates RHWF less than 3.4 days per year for the central Guangdong, which is consistent with the observations, while slightly underestimated (overestimated)

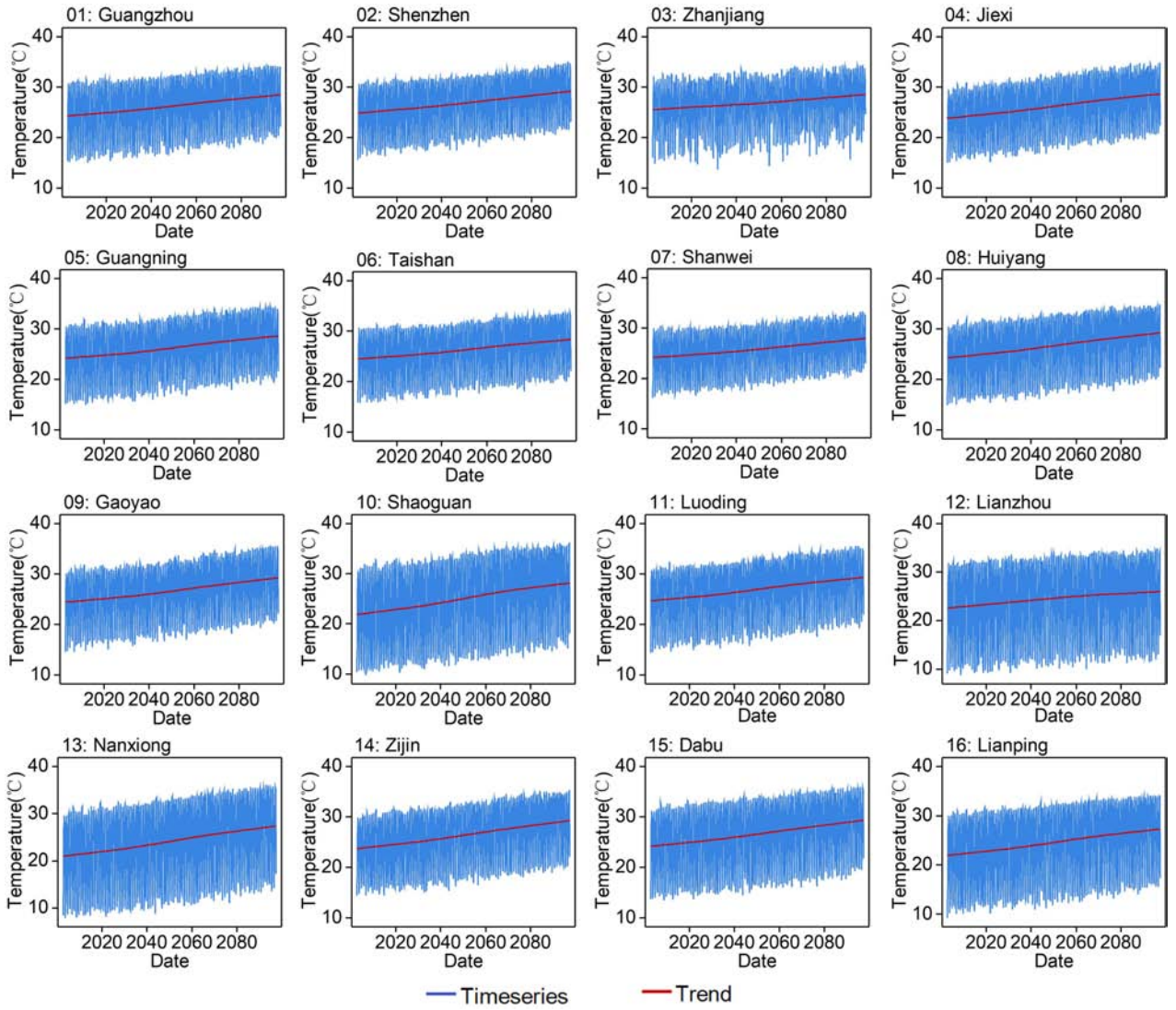

FIGURE 7 | Monthly projected Tmax of the ensemble of GCMs (i.e., CNRM-CM5, CSIRO-Mk3.6.0, IPSL-CM5A-MR, and MIROC5) from 2006 to 2100 under RCP8.5.

over marginal Guangdong, such as Shangchuandao (Huilai) (**Figure 11E**). The model ensemble of RHWL also performs well at capturing these, but the longest day of heat waves in the southwestern (i.e., Zhanjiang) and eastern (i.e., Longchuan and Wuhua) parts of Guangdong is a little underestimated (**Figure 11H**). Therefore, the model ensemble performs well in reproducing the RHWF and RHWL, even if there is a certain deviation between these GCMs. Thus, the ensemble of simulated outputs with multiple GCMs is suitable for the projection of heat waves.

Spatial Patterns of the Projected Heat Waves in Guangdong

Projections of future RHW over Guangdong are reproduced through the developed downscaling approach. To better understand the spatial variations of future RHW in the context of Guangdong, the projections in the 21st century are split into two 30-year periods, 2050s (i.e., 2036–2065) and 2080s (i.e., 2066–2095) under RCP4.5 and RCP8.5. For each indicator, the projected changes of future RHW relative to these during the historical period (i.e., 1976–2005) are calculated and shown in **Figure 12**. In detail, the indicators of intensity, total intensity, frequency, and the longest duration of relative heat waves (i.e., RHWI, RHWTI, RHWF, and RHWL) over Guangdong will be analyzed.

With the increase of emission concentration (i.e., from RCP4.5 to RCP8.5), the projected changes of RHW in Guangdong will gradually increase from the 2050s to 2080s, especially over the northern, southern, and eastern Guangdong. For example, the projected changes of RHWI in Guangzhou (i.e., central Guangdong) are most likely to be -0.36°C per event

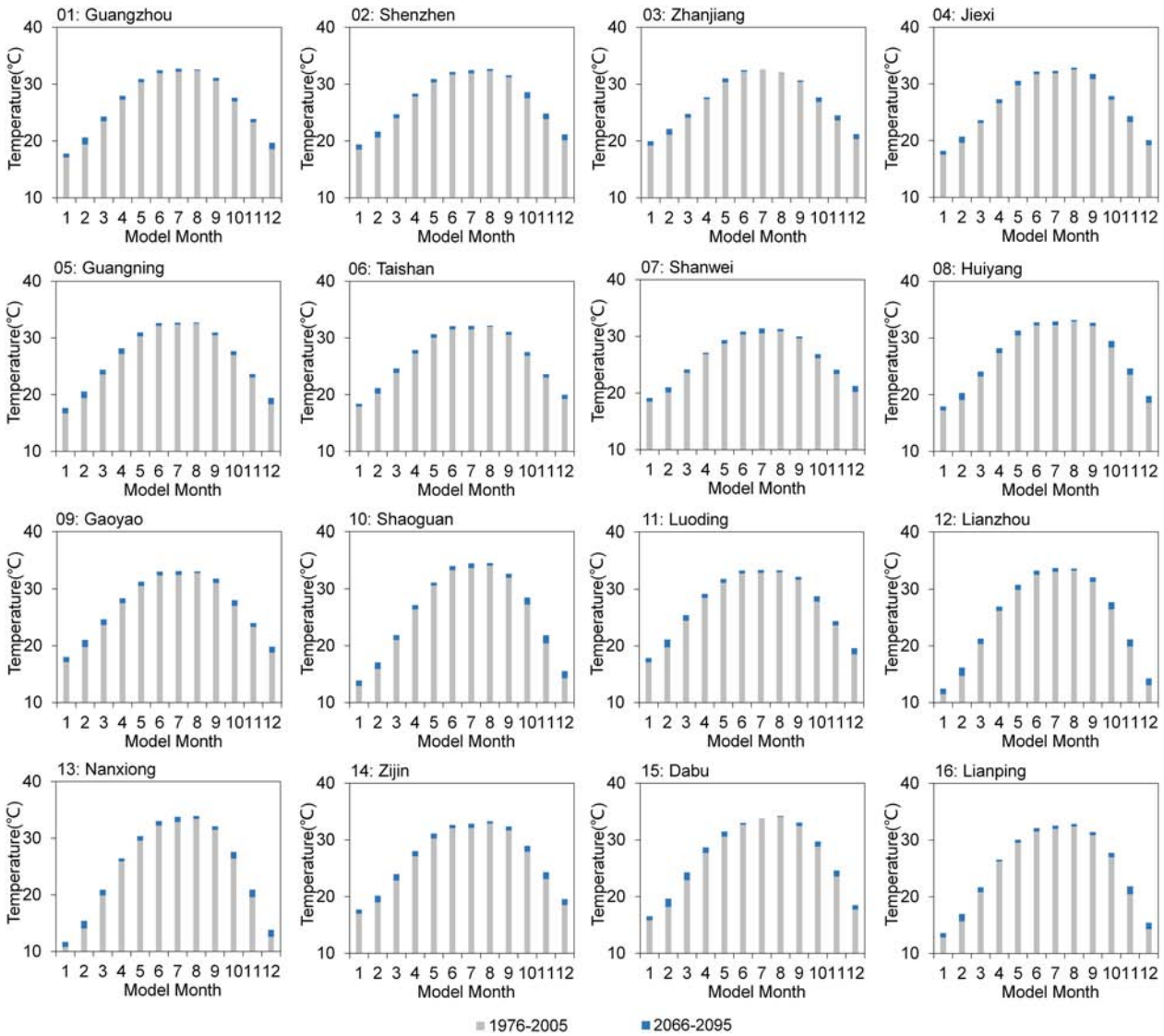

FIGURE 8 | Projected monthly variations of Tmax between 2066–2095 and 1976–2005 under RCP4.5.

(lower than 0°C per event) in the 2050s under RCP4.5, 1.81°C per event in the 2080s under RCP4.5, and 4°C per event to the end of this century (i.e., in the 2080s under RCP8.5) (**Figures 12A–C**). However, the annual average variation of RHWI in Shaoguan (i.e., northern Guangdong) is likely to be 1.6°C per event (surpassing 0°C per event) in the 2050s under RCP4.5, while the change value of projected RHWI in the 2080s under RCP4.5 is expected to be 3.14°C per event, and this would be as high as 6.1°C per event (surpassing 5.4°C per event) under RCP8.5 in the coming decades. In addition, there is a similarly increasing tendency in the ensemble simulations for RHWTI over Guangdong (**Figures 12D–F**). It is interesting to find that the annual average of projected variations of RHWTI across all Guangdong except the central region is more likely to exceed 24°C in the 2080s under RCP8.5.

In addition, the results of model ensemble reveal that there is an apparent increase in the spatial variations of RHWF and RHWL for all weather stations from 2050s to 2080s under two RCPs over Guangdong (**Figures 12G–L**). In detail, during the 2050s under RCP4.5, the projected variation values of RHWF are likely to range from -0.19 to 6.79 days, and the projected range of RHWL would be between -0.46 and 1.3 days. When it comes to the 2080s under RCP4.5, the projected changes of RHWF and RHWL are expected to expand to -0.08–20.65 and -0.12–5.28 days, respectively. It is clear that the higher change value centers of RHWF and RHWL are mainly distributed in the southwestern (e.g., Xinyi) and eastern (e.g., Wuhua) Guangdong. Consistent projected increases in RHWF and RHWL over Guangdong are found during the 2080s under RCP8.5. The distribution of RHWF shows that more frequent RHW is expected to occur in the eastern Guangdong under

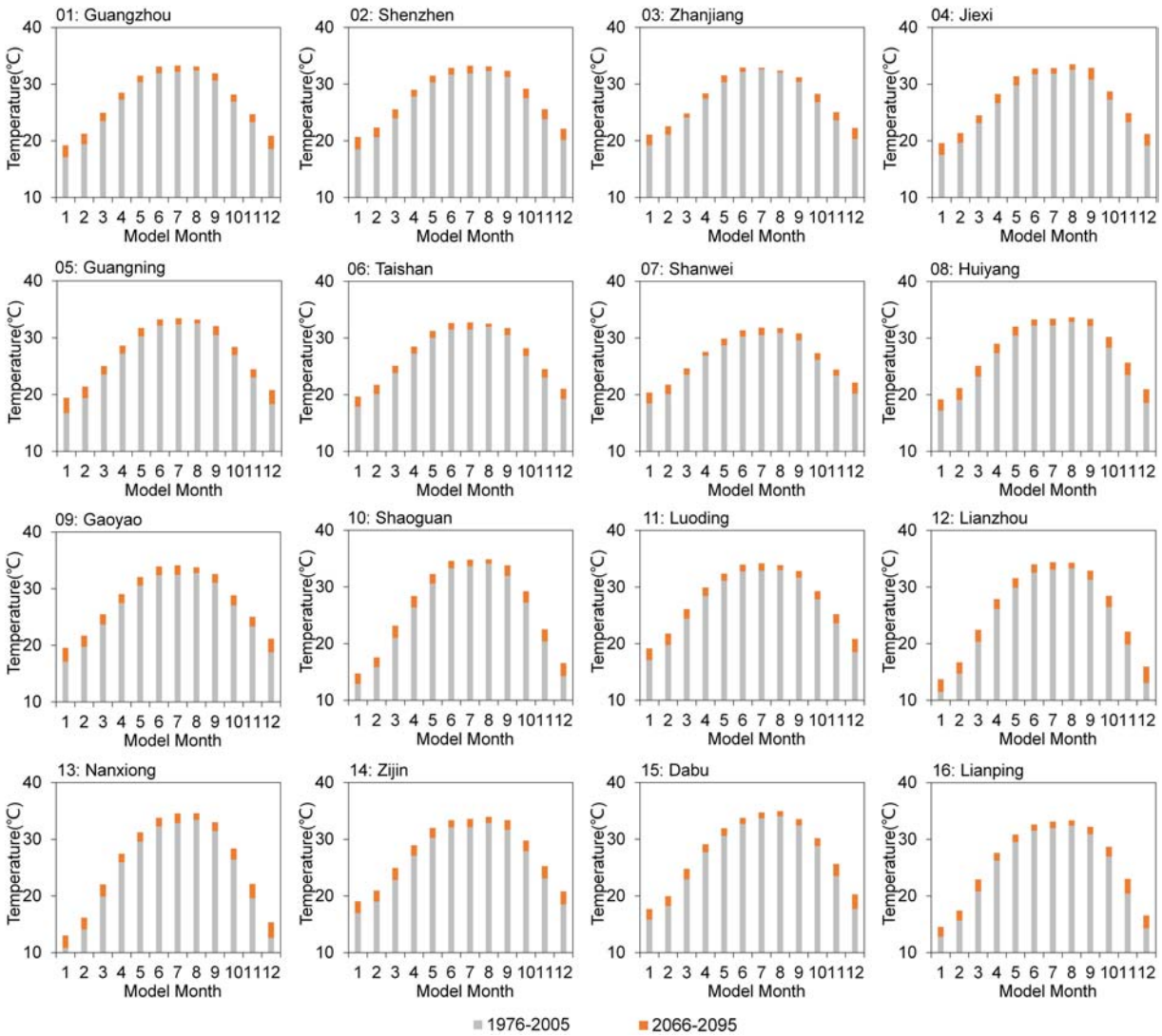

FIGURE 9 | Projected monthly variations of Tmax between 2066–2095 and 1976–2005 under RCP8.5.

RCP8.5, with the maximum increase of up to 31.92 days in the Longchuan station. More than 71% stations of Guangdong would also likely to experience longer-lasting heat waves with the RHWL variation exceeding 4 days under higher emission concentration. This is consistent with the observed values of severe heat waves over Guangdong in recent years (Luo and Lau, 2018; Wang et al., 2018), which are mainly due to influences of El Niño (Luo and Lau, 2018), while the lowest variation of RHWL is projected to be occurred along the western coast (i.e., Taishan) where the value is likely to be as low as 0.98 days in the 2080s under RCP8.5.

Interannual Variations of Future Heat Waves in Guangdong

To explore the interannual variations of RHW, the annual time series are constructed for each heat wave indicator (i.e., RHWI, RHWTI, RHWF, and RHWL) and subsequently averaged over Guangdong. The annual trends of RHW are estimated based on the Sen's slope estimator, and then, these, during the historical (i.e., 1976–2005) and future (i.e., 2066–2095) periods are compared to explore the possible contribution of global warming. In this study, at the 95% confidence level, the statistical significance of the change trends in annual heat waves is estimated through the MK test (Mann, 1945; Kendall, 1948). The obtained slope values for each indicator are illustrated in **Figure 13**.

All the indicators of RHW over Guangdong present clear interannual variations and show a significant (at the 95% confidence level) increasing trend during the historical and future periods. Among all the indicators, RHWI demonstrates the smallest increase (**Figure 13A**). Specifically, the average time series of RHWI reflect a remarkable increase in the historical period (0.11°C per event per year). However, in the 2080s, under

TABLE 2 | Sen's slope values (in °C/year) of annual and seasonal of Tmax (in °C) at the 16 weather stations in Guangdong for the period of 2006–2095.

	RCP4.5					RCP8.5				
Stations	**Spring**	**Summer**	**Autumn**	**Winter**	**Annual**	**Spring**	**Summer**	**Autumn**	**Winter**	**Annual**
01 Guangzhou	0.0272	0.0231	0.0205	0.0268	0.0189	0.0493	0.0484	0.0418	0.0441	0.0374
02 Shenzhen	0.0284	0.0217	0.0177	0.0265	0.0177	0.0522	0.0468	0.0421	0.0455	0.0377
03 Zhanjiang	0.0228	0.0214	0.0152	0.0262	0.0163	0.0408	0.0441	0.0298	0.0395	0.0303
04 Jiexi	0.0268	0.0287	0.0271	0.0269	0.0225	0.0496	0.0584	0.0553	0.0483	0.0445
05 Guangning	0.0302	0.0244	0.0250	0.0281	0.0216	0.0521	0.0500	0.0469	0.0493	0.0409
06 Taishan	0.0260	0.0222	0.0210	0.0246	0.0185	0.0452	0.0442	0.0406	0.0412	0.0353
07 Shanwei	0.0261	0.0200	0.0199	0.0222	0.0176	0.0485	0.0390	0.0416	0.0376	0.0338
08 Huiyang	0.0300	0.0277	0.0223	0.0316	0.0211	0.0566	0.0562	0.0466	0.0561	0.0427
09 Gaoyao	0.0284	0.0276	0.0273	0.0278	0.0226	0.0518	0.0569	0.0542	0.0503	0.0447
10 Shaoguan	0.0352	0.0377	0.0363	0.0425	0.0303	0.0650	0.0751	0.0616	0.0733	0.0543
11 Luoding	0.0305	0.0252	0.0241	0.0301	0.0217	0.0561	0.0513	0.0473	0.0528	0.0422
12 Lianzhou	0.0363	0.0348	0.0301	0.0423	0.0277	0.0363	0.0348	0.0301	0.0414	0.0277
13 Nanxiong	0.0371	0.0341	0.0306	0.0435	0.0286	0.0713	0.0692	0.0651	0.0745	0.0575
14 Zijin	0.0324	0.0295	0.0263	0.0324	0.0236	0.0624	0.0635	0.0579	0.0572	0.0493
15 Dabu	0.0323	0.0258	0.0241	0.0337	0.0220	0.0591	0.0503	0.0489	0.0642	0.0446
16 Lianping	0.0326	0.0261	0.0216	0.0368	0.0214	0.0628	0.0554	0.0459	0.0678	0.0441

All the trends at the 95% confidence level (MK p value < 0.001).

RCP4.5, RHWI shows a slight increase trend (0.1% per year) lower than that of the observation. When it comes to the 2080s under RCP8.5, RHWI increases at 0.14°C per event per year. As for RHWTI, the Sen's slope estimator of the observation has the largest increase compared with the other three indicators, for which the increment varied at a rate of 0.4°C per year during 1976–2005. In addition, RHWTI is also likely to experience most significant increase in the future under two RCPs. In detail, RHWTI would display the greatest increase of 1.41°C per year in the 2080s under RCP8.5, and 0.64°C per year under RCP4.5. The observed RHWF has a significantly increasing trend at a rate of 0.33% per year during the historical period. During 2066–2095, a rate of increment of RHWF under RCP8.5 (0.83% per year) almost doubles of that (0.42% per year) under RCP4.5. Similarly, for RHWL, the observed estimated slope shows an increase of 0.12% per year from 1976 to 2005, while a slightly higher rate of that (0.13% per year) is simulated in the 2080s under RCP4.5. The average time series of RHWL depict a noticeable increase (0.21% per year) to the end of this century under RCP8.5. Both intensity and frequency of heat waves are found to be increased substantially during the historical period. This is consistent with previous studies that Guangdong has suffered significantly high temperature and heat wave events over the past 64 years (especially after 2000) (Zeng et al., 2006; Luo and Lau, 2017; Zhang P. et al., 2018). These results reveal that warming has a significant and consistent impact on the increases of RHW across Guangdong. Moreover, all the four heat wave indicators present significant increasing trends in the future period (especially under RCP8.5), and those trends are also expected to increase greatly compared to the historical period. This further corroborates the results demonstrated in **Figure 12**, indicating that the climate change would also has a substantial impact on future heat waves.

To specifically evaluate the future variations of RHW with different intensities, in this study, the heat wave is classified into four categories based on the change ratio [(2080s under RCP8.5 minus historical)/historical] of RHWTI. The classification is denoted as mild (change ratio < 0.8), moderate ($0.8 \leq$ change ratio < 1.6), severe ($1.6 \leq$ change ratio < 2.4), and extreme (change ratio ≥ 2.4) variations. This classification is similar to many previous studies (Wang et al., 2018; Shiva et al., 2019; Woolway et al., 2021). The spatial distribution of the four RHW variational categories is shown in **Figure 13E**.

Among the four classifications, the projected change ratio presents that 60% weather stations over Guangdong would undergo the moderate variations of RHWs to the end of this century under RCP8.5 (**Figure 13E**), which are mainly distributed in the western half of Guangdong. Mild variation of RHWs is expected to occur in the most southwestern Guangdong (i.e., Zhanjiang and Xuwen) (**Figure 13E**), which may be due to the high total intensity of RHW in both the historical and future periods (**Figures 10**, **12**). The changes of RHW are comparatively severe and extreme in the eastern and coastal Guangdong, contrary to the results in **Figure 12**, which may be related to the low observed RHWTI during the historical period (**Figure 10**). The results depict a challenging situation that the projected change ratios from mild to extreme heat wave events are likely to increase significantly in the future, in the context of a dramatic increase in extremely high temperature in the coming decades (**Figures 6**, **7** and **Table 2**). Therefore, more attention should be paid to these regions on the adaption strategies as impacts from serious heat wave events are usually devastating, especially when they occur in populated regions and ecologically fragile areas (Cavanagh et al., 2016; Luo and Lau, 2017; Jos et al., 2018; Vogel et al., 2019).

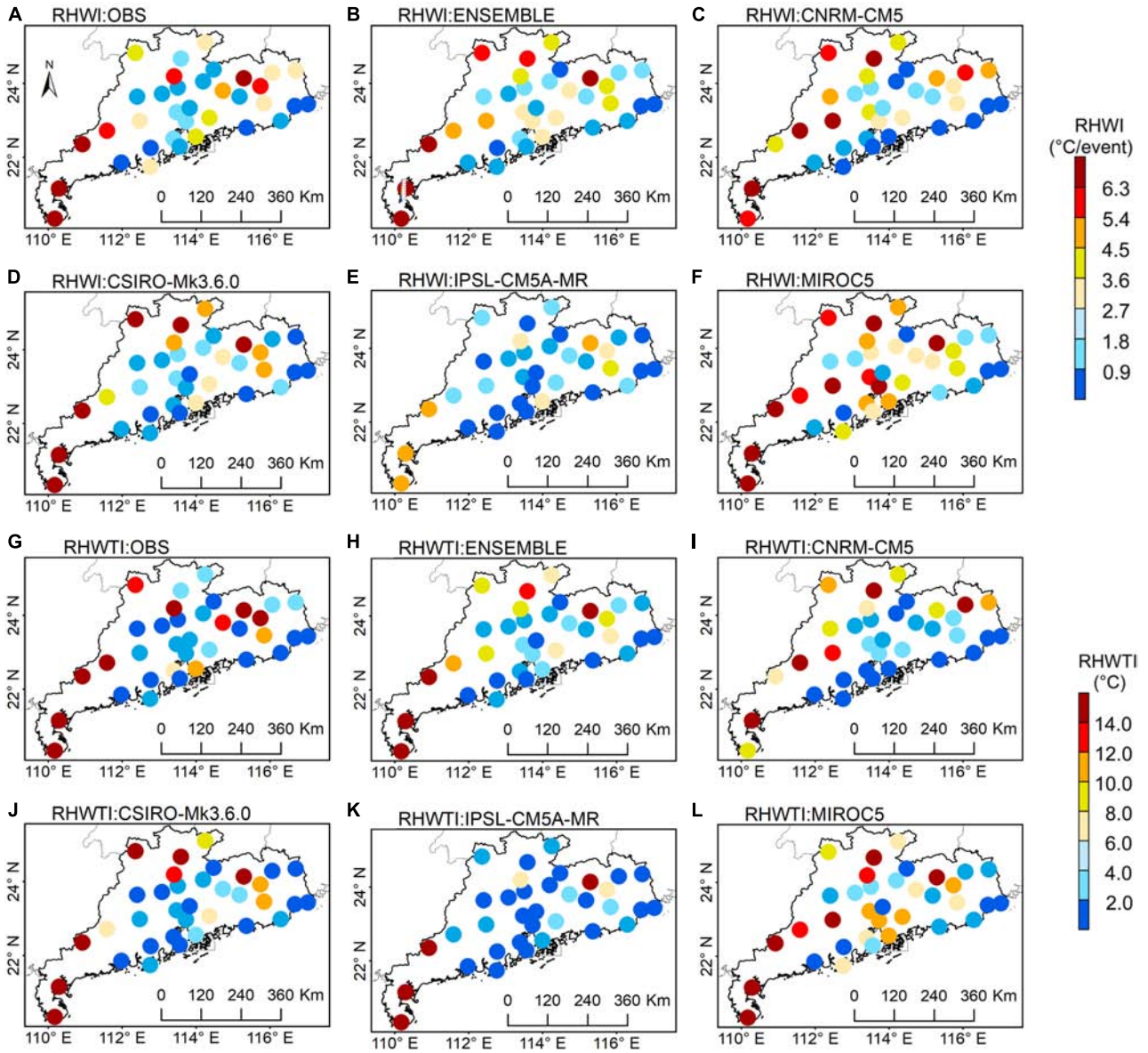

FIGURE 10 | The spatial distributions of observed **(A)** and simulated RHWI (unit: °C/event), driven by CNRM-CM5 **(C)**, CRIRO-Mk3.6.0 **(D)**, IPSL-CM5A-MR **(E)**, and MIROC5 **(F)** and the model ensemble **(B)**. Panels **(G–L)** are same as panels **(A–F)**, but for RHWTI (unit: °C).

CONCLUSION AND DISCUSSION

In this study, a stepwise-clustered simulation approach driven by multiple GCMs is developed for high-resolution projections of relative heat waves at station scale in the context of Guangdong. The evaluation results concluded that the developed approach performed very well in reproducing Tmax ($R^2 > 0.95$), and the model ensemble of four GCMs was superior to any single GCM in capturing the main features of current climatology. Subsequently, the model ensemble of 16 weather stations was selected to analyze the characteristics of projected Tmax, and then the assessment of temporal-spatial changes of projected RHW was extended to cover 35 weather stations in entire Guangdong, aiming to provide valuable information for mitigating the potential impact of severe heat waves.

The results suggest that Guangdong would experience a warmer climate in the coming decades under two RCPs. On the annual scale, the 16 selected weather stations would suffer a consistent increasing trend under RCP4.5 (i.e., 0.016–0.030°C per year) and RCP8.5 (i.e.,0.027–0.057°C per year). The most noteworthy seasonal increase was detected in spring. The highest monthly increase of Tmax was up to 1.474°C (2.985°C) in November (December) at Shaoguan (Lianzhou) under RCP4.5 (RCP8.5). The ability of the developed approach to reproduce the present heat wave was also evaluated, suggesting that the model ensemble can well capture the spatial distribution

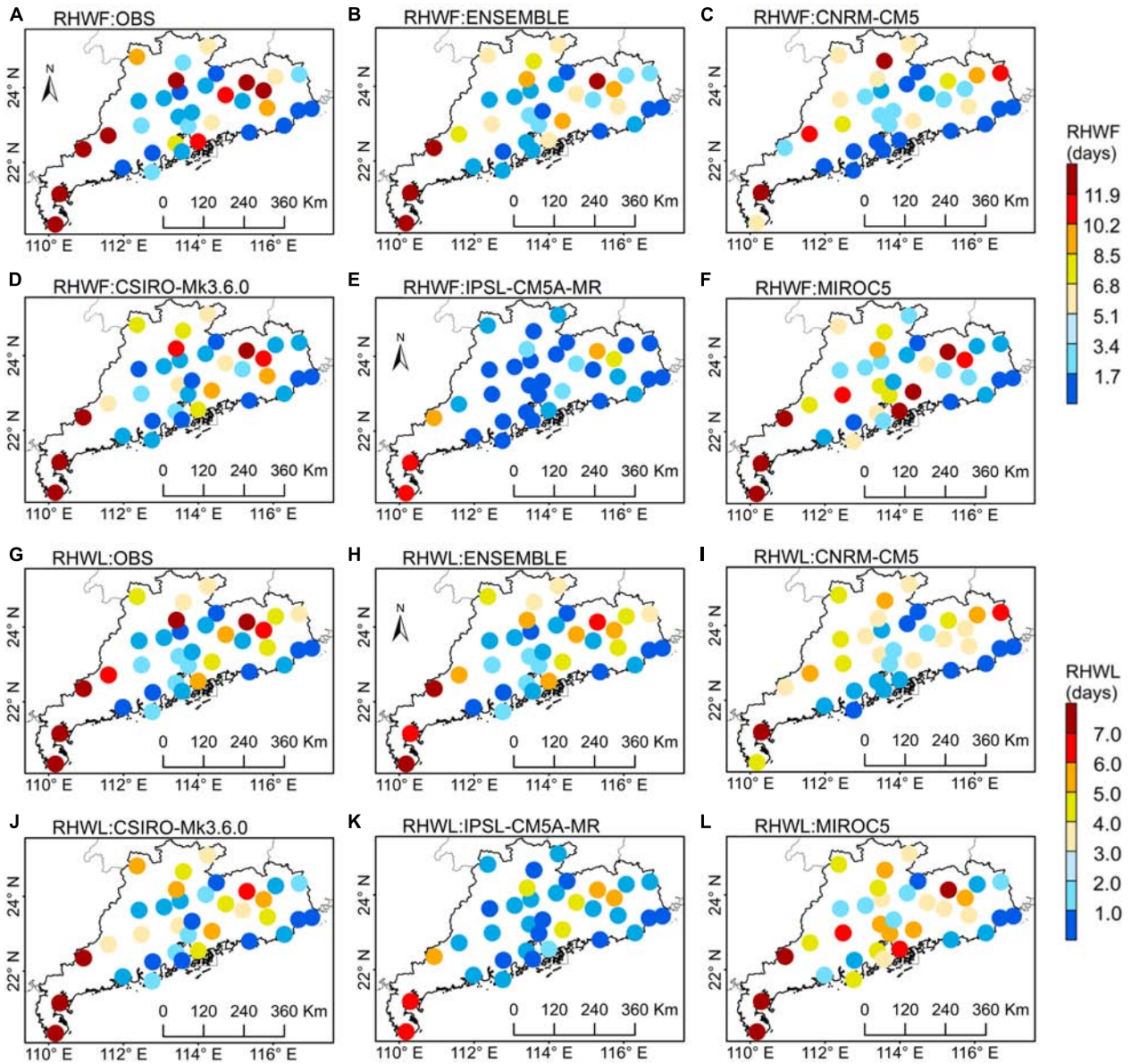

FIGURE 11 | Same as **Figure 9**, but for RHWF (**A–F**, unit: days) and RHWL (**G–L**, unit: days).

of RHW. Four indicators (i.e., RHWI, RHWTI, RHWF, and RHWL) were then used to evaluate the variations of RHW. The spatial patterns and interannual trends displayed that Guangdong would undergo severe RHW. The higher projected changes of RHW would be concentrated in eastern Guangdong under two RCPs, and Guangdong would experience the largest significant increase in RHWTI with 1.41 days per year under RCP8.5. Meanwhile, the variations of RHW were also quantitated into four categories (i.e., mild, moderate, severe, and extreme variations) based on the projected change ratio of RHWTI [(2080s under RCP8.5 minus historical)/historical]. Over 60% weather stations of Guangdong would suffer moderate variations in the 2080s under RCP8.5, followed by severe and extreme changes. Much more attention should be raised to those areas to adopt such variations.

Overall, the developed approach driven by multiple GCMs performed well in the high-resolution projections of RHW, while there is a certain bias in the simulation of extreme variables (e.g., temperature). Techniques to improve the projected quality of such a variable should be further investigated, such as considering the input of more GCMs or improving the downscaling approach. The results of this study can provide helpful information for policymakers and stakeholders to assess the impact of heat waves due to their devastating consequences for social, economic, and ecological sectors under global warming (Zhang L. et al., 2018; Vogel et al., 2019; Liu et al., 2020;

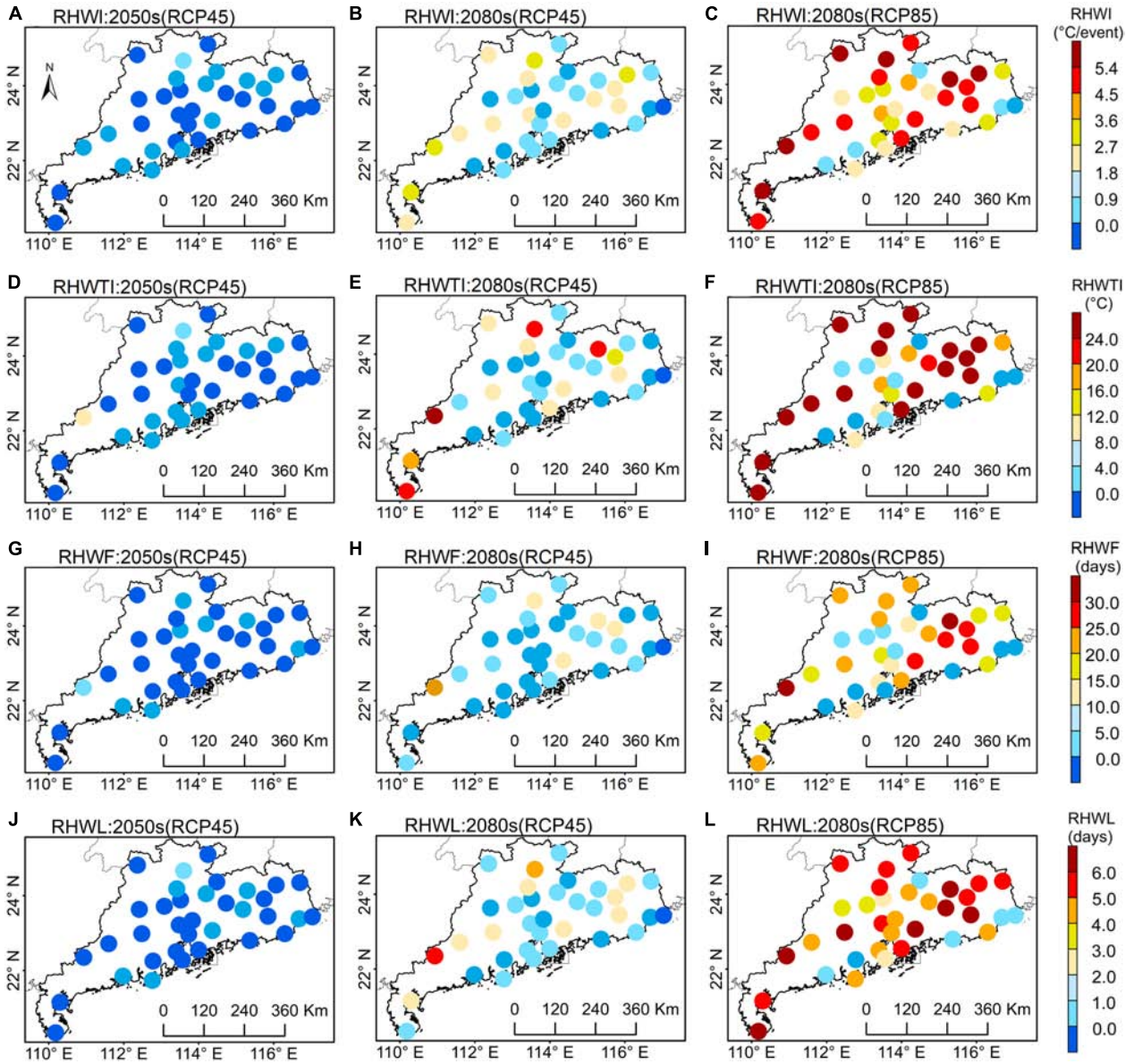

FIGURE 12 | The spatial patterns of the projected changes in relative heat wave indicators [RHWI (**A–C**, unit: °C/event), RHWTI (**D–F**, unit: °C), RHWF (**G–I**, unit: days), and RHWL (**J–L**, unit: days)] over Guangdong for the 2050s, 2080s driven by multi-GCMs under RCP4.5 and RCP8.5 scenarios (color dots represent average change value).

Sun et al., 2020; Woolway et al., 2021). The assessment of the impact of heat waves on social-economical-related sectors (e.g., human health, water resources, and energy demand) is supported by a lot of pieces of scientific evidence (Yang et al., 2013; Zhu et al., 2014; Xie et al., 2017; Zampieri et al., 2017; Mukherjee et al., 2020; Tian et al., 2021), which quantifies the negative or positive impact of heat waves on a regional or global scale. Moreover, heat waves (or temperature extremes) have also and will continue to have direct or indirect impacts on terrestrial and marine ecosystems (e.g., the carbon cycle, vegetation productivity, and global biodiversity), and disrupt the sustainable supply of ecological services and goods, thus affect the human well-beings (Zhou L. et al., 2014; Yuan et al., 2016; Jos et al., 2018; Smale et al., 2019; Wang et al., 2019; Zanatta et al., 2020; Liu et al., 2021). For example, exposure to heat waves would result in a decrease in vegetation productivity, crop yield, as well as weaken the terrestrial carbon sink (Zampieri et al., 2017; Wang et al., 2019; Font et al., 2021). Similarly, the widespread mortality of a diversity of taxa in the Mediterranean has also linked to the marine heat waves, which simplified the structure of critical habitats, destroyed the local biodiversity, and reduced the efficiency of natural carbon sequestration (Garrabou et al., 2009; Smale and Wernberg, 2013; Messori et al., 2020). Hundreds of millions of people benefit from these ecosystems; their services

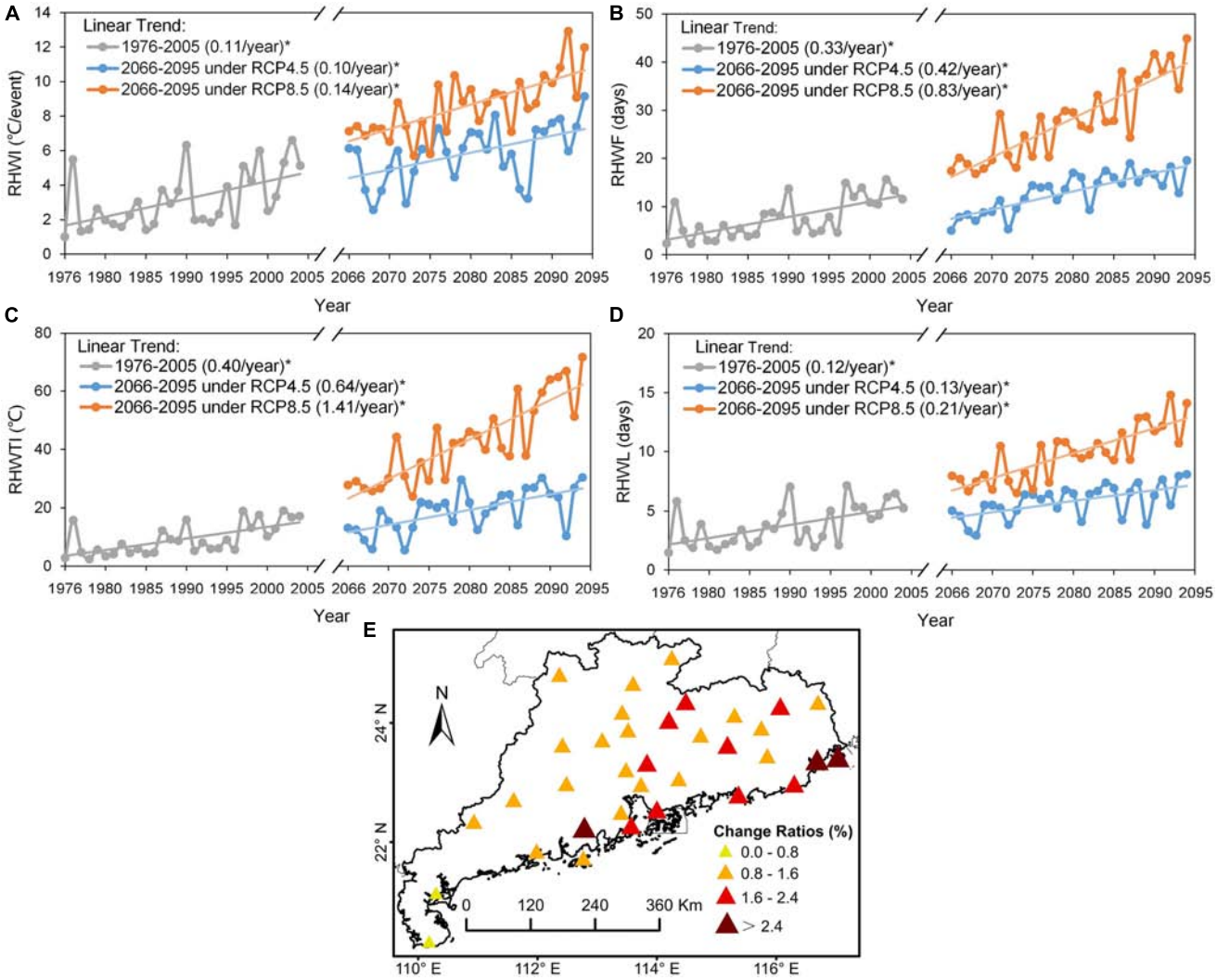

FIGURE 13 | Linear and scatter plots present the annual variations of averaged relative heat wave indicators across all of Guangdong during the historical period (1976–2005) and the future period (2066–2095) under RCP4.5 and RCP8.5 scenarios **(A–D)**. Panels **(A–D)** provided the relative heat wave indicators, consisting of intensity (i.e., RHWI), frequency (i.e., RHWF), accumulated intensity (i.e., RHWTI), and the longest duration (i.e., RHWL). Linear annual trends were estimated based on the Sen's slope estimator, and statistical significance in trends was determined based on the MK test. The numbers in the bracket represent the estimated slope, and the asterisks denote statistically significant trends (at the 95% confidence level). The spatial distribution of the projected change ratios [(2080s under RCP8.5 minus historical)/historical] for different categories of relative heat wave intensity from the model ensemble **(E)**. The categories are denoted as mild (change ratio < 0.8), moderate ($0.8 \leq$ change ratio < 1.6), severe ($1.6 \leq$ change ratio < 2.4), and extreme (change ratio ≥ 2.4) variations.

have considerable socioeconomic benefits (Cavanagh et al., 2016). Guangdong mangroves have the largest distribution in China; they play an irreplaceable role in protecting wetland ecosystems (Yu et al., 2007; Yang et al., 2018). The composition, structure, growth, and distribution of which are extremely sensitive to temperature (Yang et al., 2018). Discrete extreme events (such as heat waves) are beginning the key to shaping ecosystems through driving the sudden and drastic variations in the structure and function of the ecosystem (Smale et al., 2019). However, the quantitative exploration of the impact of heat waves on the ecosystem is still limited at present due to the heterogeneity of the temporal-spatial patterns and formation mechanism of heat waves (Mukherjee and Mishra, 2020; Ridder et al., 2020). The characteristics and variations of heat waves were investigated in this study, while the mechanism of which in Guangdong is needed to be explored. Besides, previous studies demonstrated that heat waves are often related to other heat wave-associated extreme events (e.g., drought) (Wu et al., 2020), the large-scale atmospheric variables (e.g., cloud cover and solar radiation) or teleconnections (e.g., El Nino Southern Oscillation, Pacific Decadal Oscillation, and North Atlantic Oscillation) (Luo and Lau, 2018; Mukherjee et al., 2020; Ridder et al., 2020). Therefore, it is necessary to explore the contribution of these influencing variables to the evolution of heat waves to promote our understanding of the mechanism of heat wave events and to further evaluate the potential impact of heat waves on population

and Guangdong's future related ecosystems such as mangroves to overcome the adverse effects of climate change. These will be the focus of our follow-up research.

DATA AVAILABILITY STATEMENT

The original contributions presented in the study are included in the article/supplementary material, further inquiries can be directed to the corresponding author.

AUTHOR CONTRIBUTIONS

GH, XZ, and JR conceived and designed the project. JR performed analyses and wrote the manuscript. GH and XZ revised the manuscript critically. YL, JX, ZY, CT, and FW reviewed the manuscript. All authors contributed to the article and approved the submitted version.

FUNDING

This research was supported by the Natural Sciences Foundation (U2040212 and 51779008), Strategic Priority Research Program of CAS (XDA20060302), MWR/CAS Institute of Hydroecology (1440020035), and the Natural Sciences and Engineering Research Council of Canada.

ACKNOWLEDGMENTS

We are grateful to the National Meteorological Information Center for providing the observed daily maximum temperature (http://data.cma.cn), the Working Group of World Climate Research Programme for Global Climate Models (GCMs), and National Centers for Environmental Prediction (NCEP/NCAR) (https://www.esrl.noaa.gov/psd/). We are also very grateful for the helpful inputs from the editor and anonymous reviewers.

REFERENCES

Adeniyi, M. O. (2016). The consequences of the IPCC AR5 RCPs 4.5 and 8.5 climate change scenarios on precipitation in West Africa. *Clim. Chang.* 139, 245–263. doi: 10.1007/s10584-016-1774-2

Almazroui, M., Saeed, F., Saeed, S., Ismail, M., Ehsan, M. A., Islam, M. N., et al. (2021). Projected changes in climate extremes using CMIP6 simulations over SREX regions. *Earth Syst. Environ.* 5, 481–497. doi: 10.1007/s41748-021-00250-5

Araya-Osses, D., Casanueva, A., Román-Figueroa, C., Uribe, J. M., and Paneque, M. (2020). Climate change projections of temperature and precipitation in Chile based on statistical downscaling. *Clim. Dyn.* 54, 4309–4330. doi: 10.1007/s00382-020-05231-4

Cavanagh, R. D., Broszeit, S., Pilling, G. M., Grant, S. M., Murphy, E. J., and Austen, M. C. (2016). Valuing biodiversity and ecosystem services: a useful way to manage and conserve marine resources? *Proc. R. Soc.* 283, 1–8. doi: 10.1098/rspb.2016.1635

Chen, H. B., and Fan, X. H. (2007). Some extreme events of weather, climate and related phenomena in 2006. *Clim. Environ. Res.* 12, 100–112. doi: 10.1002/jrs.1570

Clarke, L., Edmonds, J., Jacoby, H., Pitcher, H., Reilly, J., and Richels, R. (2007). *Scenarios of Greenhouse Gas Emissions and Atmospheric Concentrations. Sub-Report 2.1a of Synthesis and Assessment Product 2.1 by the U.S. Climate Change Science Program and the Subcommittee on Global Change Research*. Washington, DC: Department of Energy, Office of Biological and Environmental Research, 154.

Ding, T., and Qian, W. H. (2011). Geographical patterns and temporal variations of regional dry and wet heatwave events in China during 1960-2008. *Adv. Atmos. Sci.* 28, 322–337. doi: 10.1007/s00376-010-9236-7

Du, Y. D., Wang, X. W., Yang, X. F., Ma, W. J., Ai, H., and Wu, X. X. (2013). Impacts of climate change on human health and adaptation strategies in south China. *Adv. Clim. Chang. Res.* 4, 208–214. doi: 10.3724/sp.j.1248.2013.208

Duan, R. X., Huang, G. H., Li, Y. P., Zhou, X., Ren, J. Y., and Tian, C. Y. (2020). Stepwise clustering future meteorological drought projection and multi-level factorial analysis under climate change: a case study of the pearl river basin, China. *Environ. Res.* 196, 110368. doi: 10.1016/j.envres.2020.110368

Fan, Y., Huang, G., Li, Y., Wang, X., and Li, Z. (2016). Probabilistic prediction for monthly streamflow through coupling stepwise cluster analysis and quantile regression methods. *Water Resou. Manag.* 30, 5313–5331. doi: 10.1007/s11269-016-1489-1

Fan, Y. R., Huang, G. H., Li, Y. P., Wang, X. Q., Li, Z., and Jin, L. (2017). Development of PCA-based cluster quantile regression (PCA-CQR) framework for streamflow prediction: application to the Xiangxi River Watershed, China. *Appl. Soft Comput.* 51, 280–293. doi: 10.1016/j.asoc.2016.11.039

Fan, Y. R., Huang, W., Huang, G. H., Li, Z., Li, Y. P., Wang, X. Q., et al. (2015). A Stepwise-Cluster Forecasting Approach for Monthly Streamflows Based on Climate Teleconnections. *Stoch. Environ. Res. Risk Assess.* 29, 1557–1569. doi: 10.1007/s00477-015-1048-y

Farooq, I., Shah, A. R., Salik, K. M., and Ismail, M. (2021). Annual, seasonal and monthly trend analysis of temperature in kazakhstan during 1970-2017 using non-parametric statistical methods and GIS technologies. *Earth Syst. Environ.* 5, 1–21. doi: 10.1007/s41748-021-00244-3

Fenner, D., Holtmann, A., Krug, A., and Scherer, D. (2019). Heat waves in Berlin and Potsdam, Germany–Long-term trends and comparison of heat wave definitions from 1893 to 2017. *Int. J. Climatol.* 39, 2422–2437. doi: 10.1002/joc.5962

Fewings, M. R., and Brown, K. S. (2019). Regional structure in the marine heat wave of summer 2015 off the western united states. *Front. Mar. Sci.* 6:564. doi: 10.3389/fmars.2019.00564

Font, R. A., Khamis, K., Milner, A. M., Smith, G., and Ledger, M. E. (2021). Low flow and heatwaves alter ecosystem functioning in a stream mesocosm experiment. *Sci. Total. Environ.* 777:146067. doi: 10.1016/j.scitotenv.2021.146067

Garrabou, J., Coma, R., Bensoussan, N., Bally, M., Chevaldonn, P., Cigliano, M., et al. (2009). Mass mortality in Northwestern Mediterranean rocky benthic communities: effects of the 2003 heat wave. *Glob. Chang. Biol.* 15, 1090–1103. doi: 10.1111/j.1365-2486.2008.0-1823.x

Gha, B., Yx, C., Zh, D., Zr, E., Mz, F., Yang, C. G., et al. (2021). The assessment of current mortality burden and future mortality risk attributable to compound hot extremes in China. *Sci.Total Environ.* 777, 146219. doi: 10.1016/j.scitotenv.2021.146219

Ghatak, D., Zaitchik, B., Hain, C., and Anderson, M. (2017). The role of local heating in the 2015 Indian heat wave. *Sci. Rep.* 7:7707. doi: 10.1038/s41598-017-07956-5

Gibson, P. B., Perkins-Kirkpatrick, S. E., Alexander, L. V., and Fischer, E. M. (2017). Comparing Australian heat waves in the CMIP5 models through cluster analysis. *J. Geophys. Res. Atmos.* 122, 3266–3281. doi: 10.1002/2016JD025878

Gu, S. H., Huang, C. R., Bai, L., Chu, C., and Liu, Q. Y. (2016). Heat-related illness in China, summer of 2013. *Int. J. Biometeorol.* 60, 131–137. doi: 10.1007/s00484-015-1011-0

Guangdong Statistical Yearbook (2020). *Composition of Permanent Population*. Guangzhou: Guangdong Statistical Yearbook, 103–117.

Guo, J. H., Huang, G. H., Wang, X. Q., Wu, Y. H., Li, Y. P., Zheng, R. B., et al. (2020). Evaluating the added values of regional climate modeling over China

at different resolutions. *Sci. Total Environ.* 718:137350. doi: 10.1016/j.scitotenv.2020.137350

Guo, X., Huang, J., Luo, Y., Zhao, Z., and Xu, Y. (2017). Projection of heat waves over China for eight different global warming targets using 12 CMIP5 models. *Theor. Appl. Climatol.* 128, 507–522. doi: 10.1007/s00704-015-1718-1

Gupta, S., Goyal, M. K., and Sarma, A. K. (2018). Index-based study of future precipitation changes over Subansiri river catchment under changing climate. *J. Environ. Inform.* 34, 1–14. doi: 10.3808/jei.201700376

Hauser, M., Orth, R., and Seneviratne, S. I. (2016). Role of soil moisture versus recent climate change for the 2010 heat wave in western Russia. *Geophys. Res. Lett.* 43, 2819–2826. doi: 10.1002/2016GL068036

He, C. Y., Huang, G. H., Liu, L. R., Li, Y. P., Zhang, X. Y., and Xu, X. L. (2020). Multi -dimensional diagnosis model for the sustainable development of regions facing water scarcity problem: a case study for Guangdong, China. *Sci. Total. Environ.* 734, 139394. doi: 10.1016/j.scitotenv.2020.139394

He, X. J., Zhang, J. T., Ji, T. Y., Zhong, P., and Wang, W. T. (2012). Study on the sea level rising in the China coast and its adaptation strategy. *Mar. Forecasts* 29, 84–91.

Hessami, M., Gachon, P., Ouarda, T. B. M. J., and St-Hilaire, A. (2008). Automated regression-based statistical downscaling tool. *Environ. Modell. Softw.* 23, 813–834. doi: 10.1016/j.envsoft.2007.10.004

Hobday, A., Oliver, E., Sen, G. A., Benthuysen, J., Burrows, M., Donat, M., et al. (2018). Categorizing and naming marine heatwaves. *Oceanography* 31, 162–173. doi: 10.5670/oceanog.2018.205

Huang, G. H. (1992). A stepwise cluster analysis method for predicting air quality in an urban environment. *Atmos. Environ. Part B* 26, 349–357. doi: 10.1016/0957-1272(92)90010-P

Huang, G. H., Huang, Y. F., Wang, G. Q., and Xiao, H. N. (2006). Development of a forecasting system for supporting remediation design and process control based on NAPL-biodegradation simulation and stepwise-cluster analysis. *Water. Resour. Res.* 42, W06413. doi: 10.1029/2005WR004006

Jos, B., Filipe, F., Gardner, T. A., Hicks, C. C., Lennox, G. D., Erika, B., et al. (2018). The future of hyperdiverse tropical ecosystems. *Nature* 559, 517–526. doi: 10.1038/s41586-018-0301-1

Kalnay, E., Kanamitsu, M., Kistler, R., Collins, W., and Joseph, D. (1996). The ncep reanalysis project. *Biol. Am. Meteorol. Soc.* 77, 437–472.

Kendall, M. G. (1948). *Rank Correlation Methods*. Oxford: Griffin, doi: 10.1111/j.2044-8295.1934.tb00727.x

Lewis, S. C., and King, A. D. (2016). Evolution of mean, variance and extremes in 21st century temperatures. *Weather Clim. Extremes.* 15, 1–10. doi: 10.1016/j.wace.2016.11.002

Li, P., Fang, G., and Huang, G. (1993). Impacts on sea level rising on the economic development of zhujiang delta and countermeasures. *Acta Geogr. Sin.* 48, 527–534.

Li, Z., Guo, X., Yang, Y., Hong, Y., Wang, Z., and You, L. (2019). Heatwave trends and the population exposure over China in the 21st century as well as under 1.5°C and 2.0°C global warmer future scenarios. *Sustainability* 11, 1–21. doi: 10.3390/su11123318

Li, Z., Huang, G. H., Han, J. C., Wang, X. Q., Fan, Y. R., Cheng, G. H., et al. (2015). Development of a stepwise-clustered hydrological inference model. *J. Hydrol. Eng.* 20, 04015008. doi: 10.1061/(ASCE)HE.1943-5584.0001165

Li, Z., Li, J. J., and Shi, X. P. (2020). A two-stage multisite and multivariate weather generator. *J. Environ. Inform.* 35, 148–159. doi: 10.3808/jei.201900424

Liu, H. M., Ding, S. Y., and Ren, J. Y. (2021). Ecosystem services flow and its coupling evaluate of supply and demand–a case study of yihe river basin. *J. Environ. Inform. Lett.* 1–11. doi: 10.3808/jeil.202100072

Liu, T., Ren, Z., Zhang, Y., Feng, B., Lin, H., Xiao, J., et al. (2019). Modification effects of population expansion, ageing, and adaptation on heat-related mortality risks under different climate change scenarios in Guangzhou, China. *Int. J. Env. Res. Public Health* 16, 376. doi: 10.3390/ijerph16030376

Liu, X. C., Huang, G. H., and Chen, J. P. (2020). The development of inexact dual -objective programming for regional energy systems planning in Guang-Fo-Zhao region, China. *J. Clean. Prod.* 265:121351. doi: 10.1016/j.jclepro.2020.121351

Luo, M., and Lau, N. C. (2017). Heat waves in southern China: synoptic behavior, long-term Change, and urbanization effects. *J. Clim.* 30, 703–720. doi: 10.1175/JCLI-D-16-0269.1

Luo, M., and Lau, N. C. (2018). Amplifying effect of ENSO on heat waves in China. *Clim. Dynam.* 52, 3277–3289. doi: 10.1007/s00382-018-4322-0

Ma, D., Jing, Q., Xu, Y., Cannon, A., and Qian, B. (2021). Using ensemble-mean climate scenarios for future crop yield projections: a stochastic weather generator approach. *Clim. Res.* 83, 161–171. doi: 10.3354/cr01646

Mann, H. B. (1945). Nonparametric tests against trend. *Econometrica* 13, 245–259. doi: 10.2307/1907187

Messori, G., Bevacqua, E., Caballero, R., Coumou, D., and Zscheischler, J. (2020). Compound climate events and extremes in the midlatitudes: dynamics, simulation, and statistical characterization. *Biol. Am. Meteorol. Soc.* 102, 1–13. doi: 10.1175/BAMS-D-20-0289.1

Mills, K. E., Pershing, A. J., Brown, C. J., Chen, Y., Chiang, F. S., Holland, D. S., et al. (2013). Fisheries management in a changing climate lessons from the 2012 ocean heat wave in the northwest Atlantic. *Oceanography.* 26, 191–195. doi: 10.5670/oceanog.2013.27

Morrison, D. F. (1967). Multivariate statistical methods. *J. R. Stat. Soc. A Stat.* 130, 576. doi: 10.2307/2982527

Mukherjee, S., Ashfaq, M., and Mishra, A. K. (2020). Compound drought and heatwaves at a global scale: the role of natural climate variability-associated synoptic patterns and land-surface energy budget anomalies. *J. Geophys. Res. Atmos.* 125:E2019JD031943. doi: 10.1029/2019JD031943

Mukherjee, S., and Mishra, A. K. (2020). Increase in compound drought and heatwaves in a warming world. *Geophys. Res. Lett.* 48, 1–13. doi: 10.1029/2020GL090617

Oliver, E. C. J., Donat, M. G., Burrows, M. T., Moore, P. J., Smale, D. A., Alexander, L. V., et al. (2018). Longer and more frequent marine heatwaves over the past century. *Nat. Commun.* 9:1324. doi: 10.1038/s41467-018-03732-9

Perkins, S. E. (2015). A review on the scientific understanding of heatwaves-their measurement, driving mechanisms, and changes at the global scale. *Atmos. Res.* 164, 242–267. doi: 10.1016/j.atmosres.2015.05.014

Perkins, S. E., Alexander, L. V., and Nairn, J. R. (2012). Increasing frequency, intensity and duration of observed global heatwaves and warm spells. *Geophys. Res. Lett.* 39:L20714. doi: 10.1029/2012GL053361

Pezza, A. B., van Rensch, P., and Cai, W. J. (2012). Severe heat waves in Southern Australia: synoptic climatology and large scale connections. *Clim. Dyn.* 38, 209–224. doi: 10.1007/s00382-011-1016-2

Pramod, S., Sahib, L., Bibin, B. B., and Venkatachalapathy, R. T. (2021). Analysis of the effects of thermal stress on milk production in a humid tropical climate using linear and non-linear models. *Trop. Anim. Health. Prod.* 53, 1–7. doi: 10.1007/s11250-020-02525-x

Qian, B., Jing, Q., Smith, W., Grant, B., Cannon, A. J., and Zhang, X. (2020). Quantifying the uncertainty introduced by internal climate variability in projections of Canadian crop production. *Environ. Res. Lett.* 15:074032. doi: 10.1088/1748-9326/ab88fc

Rahmoun, T., Hassan, M., and Alhasan, W. (2016). Protection strategy for the coastal areas of climate change. *Res. J. Appl. Sci. Eng. Technol.* 12, 264–271. doi: 10.19026/rjaset.12.2333

Rebetez, M., Dupont, O., and Giroud, M. (2009). An analysis of the July 2006 heatwave extent in Europe compared to the record year of 2003. *Theor. Appl. Climatol.* 95, 1–7. doi: 10.1007/s00704-007-0370-9

Ren, J. Y., Liu, H. M., Ding, S. Y., and Cao, Z. H. (2021a). Spatio-temporal variation characteristics of water quality and its response to climate: a case study in Yihe River Basin. *J. Environ. Inform. Lett.* 6, 10–22. doi: 10.3808/jeil.202100070

Ren, J. Y., Huang, G. H., Li, Y. P., Zhou, X., Lu, C., and Duan, R. X. (2021b). Stepwise-clustered heatwave downscaling and projection for Guangdong Province. *Int. J. Climatol.* doi: 10.1002/joc.7393

Ridder, N. N., Pitman, A. J., Westra, S., Hong, X. D., and Zscheischler, J. (2020). Global hotspots for the occurrence of compound events. *Nat. Commun.* 11:5956. doi: 10.1038/s41467-020-19639-3

Sen, P. K. (1968). Estimates of the regression coefficient based on Kendall's tau. *J. Am. Stat. Assoc.* 63, 1379–1389. doi: 10.1080/01621459.1968.10480934

Shi, X., Xu, X., and Xie, L. (2007). Reliability analyses of anomalies of NCEP/NCAR reanalyzed wind speed and surface air temperature in climate change research in China. *Acta. Meteorol. Sin.* 21, 320–333. doi: 10.1021/am4044807

Shiva, J. S., Chandler, D. G., and Kunkel, K. E. (2019). Localized changes in heatwave properties across the United States. *Earths Future.* 7, 300–319. doi: 10.1029/2018EF001085

Simmons, A. J., Jones, P. D., Costa Bechtold, V., Beljaars, A. C. M., Källberg, P. W., Saarinen, S., et al. (2004). Comparison of trends and low-frequency variability in CRU, ERA-40, and NCEP/NCAR analyses of surface air temperature. *J. Geophys. Res. Atmos.* 109, 1–18. doi: 10.1029/2004JD005306

Smale, D. A., and Wernberg, T. (2013). Extreme climatic event drives range contraction of a habitat-forming species. *Proc. Biol. Sci.* 280:20122829. doi: 10.1098/rspb.2012.2829

Smale, D. A., Wernberg, T., Oliver, E. C. J., Thomsen, M., Harvey, B. P., Straub, S. C., et al. (2019). Marine heatwaves threaten global biodiversity and the provision of ecosystem services. *Nat. Clim. Chang.* 9, 306–312. doi: 10.1038/s41558-019-0412-1

Sun, Q., Wu, Z., and Tan, J. (2012). The relationship between land surface temperature and land use/land cover in Guangzhou, China. *Environ. Earth. Sci.* 65, 1687–1694. doi: 10.1007/s12665-011-1145-2

Sun, W., Shi, Q., Huang, Y., and Lv, Y. (2019). Ensemble learning enhanced stepwise cluster analysis for river ice breakup date forecasting. *J. Environ. Inform.* 1, 37–47. doi: 10.3808/jeil.201900005

Sun, X., Luo, X., Cao, G., Zhao, C., Xiao, J., Liu, X., et al. (2020). Associations of ambient temperature exposure during pregnancy with the risk of miscarriage and the modification effects of greenness in Guangdong, China. *Sci. Total Environ.* 702:134988. doi: 10.1016/j.scitotenv.2019.134988

Sun, Y., Zhang, X., Zwiers, F. W., Song, L. C., Wan, H., Hu, T., et al. (2014). Rapid increase in the risk of extreme summer heat in Eastern China. *Nat. Clim. Chang.* 4, 1082–1085. doi: 10.1038/nclimate2410

Suryan, R. M., Arimitsu, M. L., Coletti, H. A., Hopcroft, R. R., Lindeberg, M. R., Barbeaux, S. J., et al. (2021). Ecosystem response persists after a prolonged marine heatwave. *Sci. Rep.* 11:6235. doi: 10.1038/s41598-021-83818-5

Sutton, R. (2009). The potential to narrow uncertainty in regional climate predictions. *Biol. Am. Meteorol. Soc.* 90, 1095–1108.

Tao, L., Yan, J. X., Yong, H. Z., Yan, Q. H., and Ma, W. J. (2013). Associations between risk perception, spontaneous adaptation behavior to heat waves and heatstroke in Guangdong province, China. *BMC. Public Health* 13:913. doi: 10.1186/1471-2458-13-913

Tian, C., Huang, G., Lu, C., Zhou, X., and Duan, R. (2021). Development of enthalpy-based climate indicators for characterizing building cooling and heating energy demand under climate change. *Renew. Sust. Energ. Rev.* 143:110799. doi: 10.1016/j.rser.2021.110799

Vogel, M. M., Zscheischler, J., Wartenburger, R., Dee, D., and Seneviratne, S. I. (2019). Concurrent 2018 hot extremes across northern hemisphere due to human-induced climate change. *Earths Future* 7, 692–703.

Wang, F., Huang, G. H., Li, Y. P., Xu, J. L., Wang, G. Q., Zhang, J. Y., et al. (2021). A statistical hydrological model for Yangtze River watershed based on stepwise cluster analysis. *Front. Earth Sci.* 9:742331. doi: 10.3389/feart.2021.742331

Wang, P., Tang, J., Sun, X., Liu, J., and Fang, J. (2018). Spatiotemporal characteristics of heat waves over China in regional climate simulations within the CORDEX-EA project. *Clim. Dyn.* 52, 799–818. doi: 10.1007/s00382-018-4167-6

Wang, P., Tang, J., Sun, X., Wang, S., Wu, J., Dong, X., et al. (2017). Heat waves in China: definitions, leading patterns, and connections to large-scale atmospheric circulation and SSTs. *J. Geophys. Res. Atmos.* 122, 10679–10699. doi: 10.1002/2017JD027180

Wang, W. W., Zhou, W., Wang, X., Fong, S. K., and Leong, K. C. (2013). Summer high temperature extremes in southeast China associated with the East Asian jet stream and circumglobal teleconnection. *J. Geophys. Res. Atmos.* 118, 8306–8319. doi: 10.1002/jgrd.50633

Wang, X., Huang, G., Baetz, B., and Zhao, B. (2017). Probabilistic projections of regional climatic changes over the great lakes basin. *Clim. Dynam.* 49, 2237–2247. doi: 10.1007/s00382-016-3450-7

Wang, X. Q., and Huang, G. H. (2015). Impacts assessment of air emissions from point sources in Saskatchewan, Canada – a spatial analysis approach. *Environ. Prog. Sustain. Energy.* 34, 304–313. doi: 10.1002/ep.11948

Wang, X. Q., Huang, G. H., Lin, Q. Y., Nie, X. H., Cheng, G. H., and Fan, Y. R. (2013). A stepwise cluster analysis approach for downscaled climate projection – a Canadian case study. *Environ. Modell. Softw.* 49, 141–151. doi: 10.1016/j.envsoft.2013.08.006

Wang, X. R., Qiu, B., Li, W. K., and Zhang, Q. (2019). Impacts of drought and heatwave on the terrestrial ecosystem in China as revealed by satellite solar-induced chlorophyll fluorescence. *Sci. Total Environ.* 693:133627. doi: 10.1016/j.scitotenv.2019.133627

Webber, H., Ewert, F., Olesen, J. E., Müller, C., Fronzek, S., Ruane, A. C., et al. (2018). Diverging importance of drought stress for maize and winter wheat in Europe. *Nat.Commun.* 9:4249. doi: 10.1038/s41467-018-06525-2

Wilby, R. L., Dawson, C. W., and Barrow, E. M. (2002). sdsm — a decision support tool for the assessment of regional climate change impacts. *Environ. Modell. Softw.* 17, 145–157. doi: 10.1016/s1364-8152(01)00060-3

Woolway, R. I., Jennings, E., Shatwell, T., Golub, M., and Maberly, S. C. (2021). Lake heatwaves under climate change. *Nature* 589, 402–407. doi: 10.1038/s41586-020-03119-1

Wu, H., Chen, B., Snelgrove, K., and Lye, L. M. (2017). Quantification of uncertainty propagation effects during statistical downscaling of precipitation and temperature to hydrological modeling. *J. Environ. Inform.* 34, 139–148. doi: 10.3808/jei.201600347

Wu, X. Y., Hao, Z. C., Tang, Q. H., Singh, V. P., Zhang, X., and Hao, F. H. (2020). Projected increase in compound dry and hot events over global land areas. *Int. J. Climatol.* 41, 393–403. doi: 10.1002/joc.6626

Wu, Y., Tang, G., Gu, H., Liu, Y., Yang, M., and Sun, L. (2019). The variation of vegetation greenness and underlying mechanisms in Guangdong province of China during 2001–2013 based on MODIS data. *Sci. Total Environ.* 653, 536–546. doi: 10.1016/j.scitotenv.2018.10.380

Xie, Y., Crary, D., Bai, Y., Cui, X., and Zhang, A. (2017). Modeling grassland ecosystem responses to coupled climate and socioeconomic influences in multi-spatial-and-temporal scales. *J. Environ. Inform.* 33, 37–46. doi: 10.3808/jei.201600337

Xu, L., and Wang, A. (2019). Application of the bias correction and spatial downscaling algorithm on the temperature extremes from CMIP5 multimodel ensembles in China. *Earth Space Sci.* 6, 2508–2524. doi: 10.1029/2019EA000995

Xu, Y., and Ding, Y. (2001). Confidence analysis of NCEP/NCAR 50-year global reanalyzed data in climate change research in China. *J. Appl. Meter.* 2001, 337–347.

Yang, J., Liu, H. Z., Ou, C. Q., Lin, G. Z., Qin, Z., Shen, G. C., et al. (2013). Global climate change: impact of diurnal temperature range on mortality in Guangzhou, China. *Environ. Pollut.* 175, 131–136. doi: 10.1016/j.envpol.2012.12.021

Yang, J., Yuhua, H., Luo, Y., and Xue, C. (2018). Study on the distribution and dynamic change of mangrove in Guangdong. *Forestry Environ. Sci.* 34, 24–27.

Yu, X., Shen, M., Wang, D., and Imwa, B. T. (2019). Does the low-carbon pilot initiative reduce carbon emissions? Evidence from the application of the synthetic control method in Guangdong province. *Sustainability* 11:3979. doi: 10.3390/su11143979

Yu, Y., Liang, J. Y., Li, J. L., Xiao, Y. B., Qian, G. M., and Lv, Y. P. (2007). Assessment report on climate change of Guangdong(selection). *Guangdong Meteorol.* 29, 1–6.

Yuan, W., Cai, W., Chen, Y., Liu, S., Dong, W., Zhang, H., et al. (2016). Severe summer heatwave and drought strongly reduced carbon uptake in Southern China. *Sci. Rep.* 6:18813. doi: 10.1038/srep18813

Zampieri, M., Ceglar, A., Dentener, F., and Toreti, A. (2017). Wheat yield loss attributable to heat waves, drought and water excess at the global, national and subnational scales. *Environ. Res. Lett.* 12:064008. doi: 10.1088/1748-9326/aa723b

Zanatta, F., Engler, R., Collart, F., Broennimann, O., Mateo, R. G., Papp, B., et al. (2020). Bryophytes are predicted to lag behind future climate change despite their high dispersal capacities. *Nat. Commun.* 11:5601. doi: 10.1038/s41467-020-19410-8

Zeng, X., Qian, G. M., Chen, T. G., Zhang, J. Y., and Yu, K. F. (2006). Characteristics of urban heat-island effect in the coastal cities of Guangdong. *Meteorological* 11, 94–97. doi: 10.1111/j.1744-7917.2006.00098.x

Zhai, Y., Huang, G., Wang, X., Zhou, X., Lu, C., and Li, Z. (2019). Future projections of temperature changes in Ottawa, Canada through stepwise clustered downscaling of multiple GCMs under RCPs. *Clim. Dynam.* 52, 3455–3470. doi: 10.1007/s00382-018-4340-y

Zhang, L., Zhao, Z., Ye, T., Zhou, M., Wang, C., Yin, P., et al. (2018). Mortality effects of heat waves vary by age and area: a multi-area study in China. *Environ. Health* 17, 54. doi: 10.1186/s12940-018-0398-6

Zhang, P., Yan, J., Li, Y., Tang, B., and Wang, W. (2018). A study on the heatwave of Guangdong province and Guangxi in summer from 1960 to 2015. *J. Zhejiang Univ. (Science Edition)* 45, 73–81.

Zhang, Y., Nitschke, M., Krackowizer, A., De Ar, K., Pisaniello, D., Weinstein, P., et al. (2017). Risk factors for deaths during the 2009 heat wave in Adelaide,

Australia: a matched case-control study. *Int. J.Biometeorol.* 61, 35–47. doi: 10.1007/s00484-016-1189-9

Zhao, C., Liu, B., Piao, S. L., Wang, X. H., Lobell, D. B., Huang, Y., et al. (2017). Temperature increase reduces global yields of major crops in four independent estimates. *Proc. Natl. Acad. Sci. U.S.A.* 114:9326. doi: 10.1073/pnas.1701762114

Zheng, S. G., Huang, G. H., Zhou, X., and Zhu, X. H. (2019). Climate-change impacts on electricity demands at a metropolitan scale: a case study of Guangzhou, China. *Appl. Energ.* 261:114295. doi: 10.1016/j.apenergy.2019.114295

Zhou, B. T., Wen, Q. Z., Xu, Y., Song, L. C., and Zhang, X. B. (2014). Projected changes in temperature and precipitation extremes in China by the CMIP5 multimodel ensembles. *J. Clim.* 27, 6591–6611. doi: 10.1175/JCLI-D-13-00761.1

Zhou, L., Tian, Y., Myneni, R. B., Ciais, P., Saatchi, S., Liu, Y. Y., et al. (2014). Widespread decline of Congo rainforest greenness in the past decade. *Nature* 509, 86–90. doi: 10.1038/nature13265

Zhou, X., Huang, G. H., Wang, X. Q., and Cheng, G. H. (2018). Future changes in precipitation extremes over Canada: driving factors and inherent mechanism. *J. Geophys. Res. Atmos.* 123, 5783–5803. doi: 10.1029/2017JD027735

Zhou, X., Huang, G. H., Li, Y. P., Lin, Q. G., Yan, D. H., and He, X. J. (2021). Dynamical downscaling of temperature variations over the canadian prairie provinces under climate change. *Remote Sens.* 13:4350. doi: 10.3390/rs13214350

Zhu, J. X., Huang, G. H., Wang, X. Q., Cheng, G. H., and Wu, Y. H. (2018). High-resolution projections of mean and extreme precipitations over China through PRECIS under RCPs. *Clim. Dyn.* 50, 4037–4060. doi: 10.1007/s00382-017-3860-1

Zhu, Q., Liu, T., Lin, H., Xiao, J., Luo, Y., Zeng, W., et al. (2014). The spatial distribution of health vulnerability to heat waves in Guangdong province, China. *Glob. Health Action.* 7:25051. doi: 10.3402/gha.v7.25051

Zhuang, X. W., Li, Y. P., Huang, G. H., and Wang, X. Q. (2016). A hybrid factorial stepwise-cluster analysis method for streamflow simulation – a case study in Northwestern China. *Hydrol. Sci.* 61, 2775–2788. doi: 10.1080/02626667.2015.1125482

Conflict of Interest: The authors declare that the research was conducted in the absence of any commercial or financial relationships that could be construed as a potential conflict of interest.

Publisher's Note: All claims expressed in this article are solely those of the authors and do not necessarily represent those of their affiliated organizations, or those of the publisher, the editors and the reviewers. Any product that may be evaluated in this article, or claim that may be made by its manufacturer, is not guaranteed or endorsed by the publisher.

frontiers in Earth Science

ORIGINAL RESEARCH
published: 17 December 2021
doi: 10.3389/feart.2021.753757

Long-Term Spatial and Temporal Variation of Near Surface Air Temperature in Southwest China During 1969–2018

Jia Zhou[1,2] *and Tao Lu*[1]*

[1]Chengdu Institute of Biology, Chinese Academy of Sciences, Chengdu, China, [2]Division of Life Sciences and Medicine, University of Chinese Academy of Sciences, Beijing, China

Near surface air temperature (NSAT) is one of the most important climatic parameters and its variability plays a vital role in natural processes associated with climate. Based on an improved ANUSPLIN (short for Australian National University Spline) model which considers more terrain-related factors, this study analyzed the trends, anomalies, change points, and variations of NSAT in Southwest China from 1969 to 2018. The results revealed that the improved approach performed the best in terms of Mean Absolute Error (MAE), Root Mean Square Error (RMSE) and R-squared (R^2) comparing to the conventional ANUSPLIN and co-kriging methods. It has great potential for future meteorological and climatological research, especially in mountainous regions with diverse topography. In addition, Southwest China experienced an overall warming trend of 0.21°C/decade for annual mean NSAT in the period 1969–2018. The warming rate was much higher than mainland China and global averages, and statistically significant warming began in the late 1990s. Moreover, consistent warming and significant elevation-dependent warming (EDW) were observed in most parts of Southwest China, and the hiatus or slowdown phenomenon after the 1997/1998 EL Niño event was not observed as expected. Furthermore, the remarkable increase in winter and minimum NSATs contributed more to the whole warming than summer and maximum NSATs. These findings imply that Southwest China responds to global warming more sensitively than generally recognized, and climate change in mountainous regions like Southwest China should be of particular concern.

Keywords: temperature changes, improved ANUSPLIN method, change-point detection, spatial variation, temporal variation

OPEN ACCESS

Edited by:
Xander Wang,
University of Prince Edward Island, Canada

Reviewed by:
Ming Luo,
Sun Yat-Sen University, China
Ahmed Kenawy,
Mansoura University, Egypt

***Correspondence:**
Tao Lu
lutao@cib.ac.cn

Specialty section:
This article was submitted to Atmospheric Science, a section of the journal Frontiers in Earth Science

Received: *05 August 2021*
Accepted: *19 November 2021*
Published: *17 December 2021*

Citation:
Zhou J and Lu T (2021) Long-Term Spatial and Temporal Variation of Near Surface Air Temperature in Southwest China During 1969–2018. Front. Earth Sci. 9:753757. doi: 10.3389/feart.2021.753757

INTRODUCTION

Near surface air temperature (NSAT) is a key meteorological parameter involved in exchanges of energy and water in land-atmosphere interactions. It is also a key atmospheric variable with direct influence on physical and biological processes, including energy and water balances, nutrient cycling, growth and yield, carbon dynamics, and ecosystem adaption (Joly et al., 2011; Wang et al., 2017; Cui and Shi, 2021). NSAT is typically measured at a height of 2.0 m above the ground with high precision and high temporal resolution, through irregularly distributed meteorological stations (Wang et al., 2017). Understanding about the spatial-temporal variability of NSAT is required in hydrology,

meteorology, and ecology (Peng et al., 2019). Thus, it is important to assess how climate change has altered the NSAT in spatial and temporal terms, and to enhance our understanding of its variability. However, this is often limited by the spatial coverage of instrumental records, especially in regions where meteorological stations are insufficient and distributed unevenly in space (Ilori and Ajayi, 2020).

A typical way to fill in this gap is by adopting the interpolation method, which estimates plausible values based on the discrete known values (Nalder and Wein, 1998). As a result, interpolation is commonly applied to estimate the spatial distribution of NSAT for regional scales (Fick and Hijmans, 2017). However, it is known that no single interpolation method is optimal for all regions, and the performance of an interpolating method is strongly affected by many factors, e.g., sample distribution and density, surface type, data variance, data normality, grid resolution, as well as the interactions among these factors (Li and Heap, 2011). Consequently, there has been growing interest in the development of methods for interpolating *in-situ* gauged data from sparse networks (Khosravi and Balyani, 2019). So far, a number of interpolation methods have been developed to obtain spatially continuous NSAT from point station measurements, including inverse distance weighting, regression analysis, kriging, and spline methods (Wu and Li, 2013; Kayikci and Kazanci, 2016; Hadi and Tombul, 2018; Jiang et al., 2019; Collados-Lara et al., 2021).

Many studies have evaluated the spatial-temporal variations of NSAT around the globe. In general, they reported the consistent and significant increase in NSAT over the past 100 years (Ding et al., 2007; Ren et al., 2016; Luo and Lau, 2017; Amato et al., 2019; Zhou et al., 2020). For example, the global average NSAT was trending upward at 0.145°C/decade in 1951–2019 (Li et al., 2021). In China, the NSAT was increasing at 0.150°C/decade in 1959–2014 (Cui et al., 2017). Moreover, there was a hiatus or slowdown in the warming period following the 1997/1998 EL Niño event at both global and regional scales (Easterling and Wehner, 2009; Cahill et al., 2015; Fyfe et al., 2016; Sun et al., 2018; Lewandowsky et al., 2018; Risbey et al., 2018; Li et al., 2021). For China, some studies have also indicated about a slowdown in the warming trend since 1998 (Tang et al., 2012; Li et al., 2015), which is more pronounced than the global mean (Du et al., 2019).

The challenge of estimating NSAT is primarily in mountainous or high elevation areas, where instrumental records are not always available due to the paucity of weather stations (Wang et al., 2017; Collados-Lara et al., 2021). Earlier studies have demonstrated that co-kriging and ANUSPLIN (abbreviation for Australian National University Spline) are more suitable for sparse data in these regions (Hutchinson and Gessler, 1994; Price et al., 2000; Islam and Déry, 2017; Mohammadi et al., 2017; Zhao et al., 2019; Belkhiri et al., 2020; Cheng et al., 2020; Guo et al., 2020). An advantage of these two interpolation methods is that they can model the terrain effect by considering additional variables during interpolation process (Cuervo-Robayo et al., 2014). Nevertheless, in most cases, both co-kriging and ANUSPLIN would ignore some important terrain-related factors (such as slope and aspect), which could influence the amount of Sun radiation on land surface and then affect NSAT (Minder et al., 2010; Zhao et al., 2019; Persaud et al., 2020). Thus, it is reasonable to refine the interpolation results of NSAT by incorporating more terrain-related variables, especially in topographically heterogeneous regions (Price et al., 2000).

It was reported that mountainous areas are especially sensitive and vulnerable to climate change (Diaz and Bradley, 1997). Even relatively small climate changes could have major implications for animal, plant, and people living in these regions (Fan et al., 2011). Hence, man studies have been conducted to understand the associated impacts of climate change in mountainous regions (Lin et al., 2017; Li et al., 2020). Nevertheless, biases in results are generally inevitable due to limited *in-situ* instrumental records, which make quantifying the climate trend, and variability inherently difficult (Chen et al., 2018; Sun et al., 2018). Therefore, one of the current research challenges is to seek ways to fill these gaps and reduce uncertainties for the climate change investigation in data-scarce mountainous areas.

Southwest China, a region with varied and complex topography, has abundant mountainous regions, and is one of the most sensitive areas to climate change (Du et al., 2017; Qian et al., 2019). In addition, it is one of the key regions of grain production in China, with a grain yield of ~12% of national total. There were no consistent findings about the trends and variabilities of NSAT in Southwest China. For example, cooling trends in the southwestern parts of China were reported in 1951–2001 (Hu et al., 2003) and 1963–2012 (Dong et al., 2015). However, other studies have shown that in response to global warming, Southwest China has exhibited warming trends in 1961–2004 (Fan et al., 2011) and 1961–2012 (Wang, 2018). In addition, Ren et al. (2016) indicated about the warming in Southwest China during 1992–2011, against its cooling during 1973–1992. Except for the different study periods, another important reason for this inconsistency might be related to the failure of sparse weather stations in Southwest China to fully satisfy the requirements for NSAT estimation (Yang and Jiang, 2017).

Consequently, despite some previous reports on the general characteristics of NSAT in Southwest China, no consistent results were identified. Moreover, to date, few attentions have been paid to the accurate interpolation of climate variables, and the spatial and temporal features of NSAT over Southwest China are not well recognized. Thus, Southwest China presents a good opportunity to improve and test the interpolation method by comprehensively taking into account the terrain effects on NSAT. The key objectives of the current study are: 1) optimization of ANUSPLIN by incorporating more terrain-related factors to improve the accuracy of NSAT estimation; 2) evaluation of the performance of the improved interpolation method by comparing interpolated values to withheld station data, the WorldClim datasets and the HMTC datasets (short for gridded data sets cover China at 1 km × 1 km resolution); and 3) identification of the trends and spatio-temporal variability of NSAT during 1969–2018 over Southwest China.

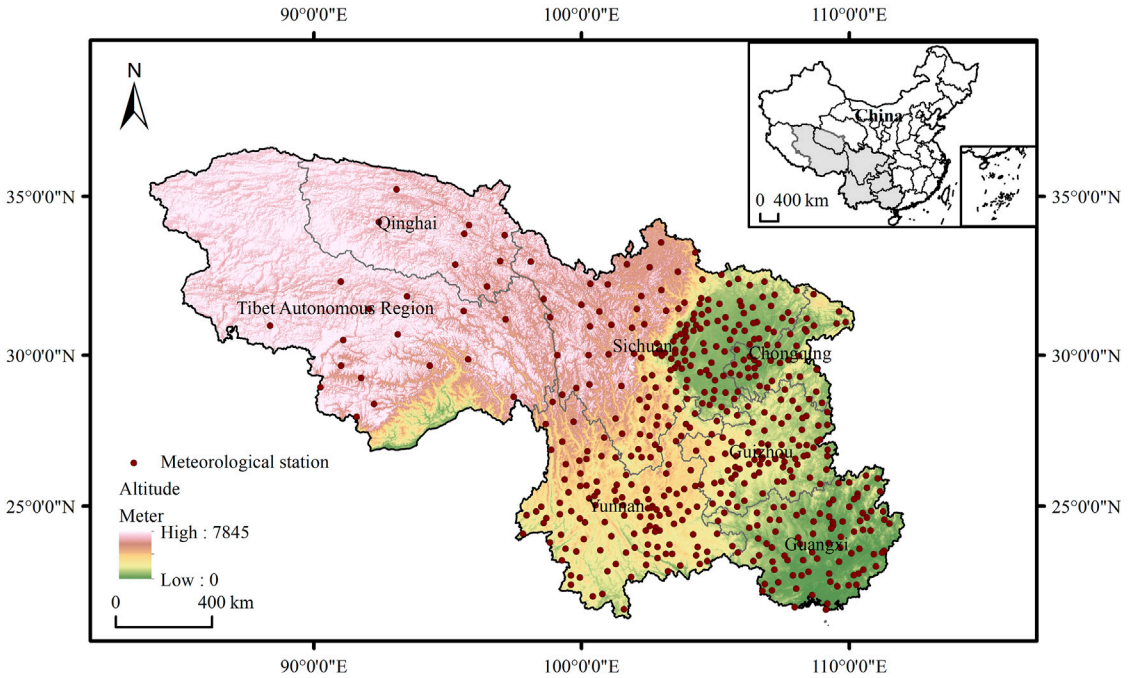

FIGURE 1 | Study area and 494 meteorological stations in Southwest China.

STUDY AREA AND MATERIALS

Study Area

The study area (83.87°E–112.07°E and 21.14°N–36.49°N) is located in Southwest China, including Guangxi, Guizhou, Chongqing, Yunnan, Sichuan, southern Qinghai and some parts of the Tibet Autonomous Region, with a total area of 2.33×10^6 km^2 (Xu et al., 2020) (**Figure 1**). The elevation in Southwest China presents a considerable variation with a difference of ~8,000 m, exhibiting complicated topographic structures (e.g., mountains, plateaus, hills, basins, and plains). Due to the wide range of latitudes and complex topography, Southwest China is characterized by a variety of climates and environments, ranging from monsoon region in the southeast zone to semi-arid region in the northwest zone (Jin and Wang, 2016). There are various ecosystems, including tropical rain forest, tropical seasonal rain forest, subtropical evergreen broad-leaved forest, and alpine vegetation (Gao et al., 2018).

Data Sources

Meteorological Data

NSAT datasets during 1969–2018 were downloaded from China Meteorological Data Service Center (http://data.cma.cn), covering 494 meteorological stations in Southwest China (**Table 1**). Its quality and uniformity were assessed by the National Meteorological Information Center. The data include daily and monthly averages, maximum and minimum temperatures. The annual and seasonal temperatures for each station were obtained by averaging the corresponding month temperatures. Specifically, the spring (T_{spring}), summer (T_{summer}), autumn (T_{autumn}), and winter (T_{winter}) denote the averages of March–May, June–August, September–November, and December–February, respectively.

Terrain Morphology Data

The Digital Elevation Model (DEM) at the spatial resolution of 90 m that was measured by the NASA Shuttle Radar Topographic Mission (SRTM). The DEM data were collected from the Computer Network Information Center, Chinese Academy of Sciences (http://www.gscloud.cn). In this study, the measures used were elevation, slope, and aspect. Prior to formal interpolation, we evaluated the performances of the DEM data with different spatial resolutions. We noticed that with the resolution of 500 m, the interpolation process can be completed with speed and the quality was satisfactory. Thus, all the terrain data were resampled to 500 m × 500 m, and the medians in each grid cell were used.

Other Air Temperature Datasets

The monthly mean near surface air temperature data for 1970–2000 on a 30 arc-second resolution grid were obtained from the WorldClim Data Portal (https://www.worldclim.org). The gridded data sets cover China at 1 km × 1 km resolution (HMTC) for the same period (Peng et al., 2019) were obtained from the National Earth System Science Data Center (http://www.geodata.cn). Specifically, WorldClim dataset is a set of global climate layers, while HMTC dataset was spatially downscaled from the 30 arc-minute resolution Climatic Research Unit (CRU) time series dataset. These reference

TABLE 1 | Datasets used to analyze NSAT in Southwest China.

Datasets	Year	Resolution		Sources
		Time	Space	
Meteorological data	1969–2018	Day	90 m	China Meteorological Data Service Center (http://data.cma.cn)
DEM				Computer Network Information Center, Chinese Academy of Sciences (http://www.gscloud.cn)
HMTC	1970–2000	Month	1 km	National Earth System Science Data Center (http://www.geodata.cn)
WorldClim	1970–2000	Month	30′	WorldClim Data Portal (https://www.worldclim.org)

datasets could provide detailed climatology data, and could be evaluated against the land-based observations. Moreover, they could reflect orographic effects, and are available for monthly mean, minimum and maximum NSATs.

METHODOLOGY

Improved ANUSPLIN Model

The ANUSPLIN is created using thin-plate smoothing splines, which make it suitable for interpolating climate data with large noises (Hutchinson and Gessler, 1994; Price et al., 2000; Guo et al., 2020). The noisy multivariable climatic data are treated as a function with one or more independent variables during the fitting process of a climatic surface, and thus can produce mean error lower than other interpolation methods (Islam and Déry, 2017; Zhao et al., 2019; Cheng et al., 2020). The theoretical statistical model is expressed as:

$$Z_i = f(x_i) + b^T y_i + e_i (i = 1, \ldots, N) \quad (1)$$

where Z_i represents the predicted value at location i; x_i is the spline independent variable as a multidimensional vector, and f represents a smoothing function of x_i which needs to be estimated; y_i is the independent covariable as a multidimensional vector, and b is the unknown coefficients for the y_i; n is the number of observational data. Each e_i is an independent, zero mean error term with variance $w_i\sigma^2$, where W_i is the known relative error variance and σ^2 is the error variance which is constant across all data points.

The traditional ANUSPLIN treats longitude and latitude as independent variables, with elevation as a covariate. To optimize the ANUSPLIN model, we improved it by incorporating more terrain-related factors, with slope, and aspect also as covariates (hereafter called M-ANUSPLIN).

Interpolation Methods

The NSAT parameters in Southwest China are estimated using co-kriging, ANUSPLIN and M-ANUSPLIN models, respectively. Due to the complex topography of the domain over Southwest China, we tested the performance of these models using different combinations of covariates (**Table 4**) to identify the best model in this region, and to find which variable contributes more to NSAT variability.

Model Assessment

To evaluate these models, a 10-fold cross validation test was conducted to assess the overall error of the interpolated NSAT grid. The advantage of 10-fold cross validation is that all observations are used for both training and validation, and each observation is used for validation exactly once. Thus, it is widely used to validate gridded observations (Appelhans et al., 2015; Yoo et al., 2018). In 10-fold cross validation for this study, the original observation data of 494 meteorological stations were randomly partitioned into ten subsamples. Of the ten subsamples, a single subsample was retained as the validation data for testing the model, and the remaining nine subsamples were used as training data. The cross validation process was then repeated ten times, with each of the ten subsamples used exactly once as the validation data. Hence, 10 different combinations of training and test sets were formed, and each of training and test pair was applied and evaluated. Final evaluation of 10-fold cross validation test was determined by the average mis-classification probability over the ten test sets to produce a single estimation.

Based on the results of 10-fold cross validation test, the statistical indices of Mean Absolute Error (MAE), Root Mean Square Error (RMSE) and R-squared (R^2) between predicted and observed values were selected as interpolation performance evaluation criteria. Briefly, MAE provides a measure of how far the estimate can be in error; RMSE provides a measure that is, sensitive to outliers; and R^2 provides the proportion of variation that is, explained by the predictor variables. The performance and bias were then compared by using the three indices, and the interpolation method with better performance was further selected. The calculation formulas of them are shown below:

$$MAE = \frac{1}{n}\sum_{i=1}^{n}|P_i - O_i| \quad (2)$$

$$RMSE = \sqrt{\frac{1}{n}\sum_{i=1}^{n}(P_i - O_i)^2} \quad (3)$$

$$R^2 = 1 - \frac{\sum_{i=1}^{n}(P_i - O_i)^2}{\sum_{i=1}^{n}(O_i - \bar{O})^2} \quad (4)$$

where P_i and O_i are the estimated NSAT and original observational NSAT at each station, respectively; $\bar{O}$ is the mean of observational NSAT; and n is the sample number.

Accuracy Comparison

To further examine the accuracy of obtained data set, two published and widely used air temperature products were compared. One is the 30 arc-second resolution grid product

obtained from WorldClim Data Portal (hereafter called WorldClim2), the other is the gridded data sets cover China at 1 km × 1 km resolution (hereafter called HMTC). Mean temperature values in time series of 1970–2000 derived from all datasets were compared. The M-ANUSPLIN and WorldClim2 values were resampled to 1 km × 1 km to render them consistent with the HMTC reference products.

Trend Analysis

A trend slope ratio analysis was examined to investigate the changing trends of NSAT for each pixel in 1969–2018 at both annual and seasonal scales. The formula is as follows (Vogelsang and Nawaz, 2017):

$$slope = \frac{n \times \sum_{i=1}^{n} i \times Tem_i - \sum_{i=1}^{n} i \sum_{i=1}^{n} Tem_i}{n \times \sum_{i=1}^{n} i^2 - \left(\sum_{i=1}^{n} i\right)^2} \quad (5)$$

where *slope* is the degree of change in *Tem*; *n* is the number of studied years; *i* is the order of year from 1 to 50 in the study period; and Tem_i is the average *Tem* in the *ith* year. Slope >0 means that the air temperature over *n* years increased (warming trend); while slope<0 signifies a decreasing trend (cooling trend). To test the significance of these trends, a significance test (F-test) was applied. According to the F-test, the trends were divided into categories of extremely significant ($p < 0.01$), significant ($0.01 < p < 0.05$), and non-significant level ($p > 0.05$).

A coefficient of variation (*CV*) index was also considered to evaluate the spatio-temporal variation of NSAT. The *CV* was calculated as follows (Yang and Jiang, 2017):

$$CV = \frac{1}{\overline{Tem}} \times \sqrt{\frac{1}{n-1} \sum_{i=1}^{n} \left(Tem_i - \overline{Tem}\right)^2} \times 100\% \quad (6)$$

where *CV* is the coefficient of variation for NSAT; $\overline{Tem}$ is the mean temperature; Tem_i is the temperature for year *i*; *n* is the number of studied years; *i* is the order of year from 1 to 50 in the study period. The significance test is carried out based on the *p* value. The CV is classified into three categories of weak variation ($0 < CV \leq 10\%$), medium variation ($10\% < CV \leq 100\%$) and strong variation ($CV > 100\%$).

Change Points Detection

For a long-term climatic dataset, it is expected to experience multiple changes rather than a single break (Khapalova et al., 2018). To detect and identify the time when significant changes for NSAT happened in the time series of 1969–2018, pruned exact linear time (PELT) was also conducted in this study. The superiority of PELT exists in the ability of accurate and fast detection and identification of multiple change-points (Killick et al., 2012).

RESULTS

Model Performance

Table 2 compares the MAE, RMSE and R^2 of the predicted NSAT parameters using different models over Southwest China in 1969–2018. Apparently, the prediction of M-ANUSPLIN model gave lower MAE and RMSE compared to the ANUSPLIN and co-kriging models for both annual and seasonal NSATs. The R^2 values of the M-ANUSPLIN model were 0.077–0.328°C above those of the other two models. Specifically, for annual parameters, relative to the ANUSPLIN and co-kriging models, the MAEs and RMSEs for the M-ANUSPLIN model were 0.02–0.04°C lower for mean temperature (T_{mean}); 0–0.02°C lower for maximum temperature (T_{max}); and 0.03–0.07°C lower for minimum temperature (T_{min}). For seasonal parameters, the MAEs and RMSEs for the M-ANUSPLIN model were also 0.01–0.04°C and 0–0.05°C lower than the ANUSPLIN and co-kriging models. These results indicate the improvement of the M-ANUSPLIN model by incorporating slope and aspect as interpolators. Moreover, **Table 2** also reflects the seasonal dependence of the model performance. In general, the MAEs and RMSEs decline in the order from winter to autumn to spring then to summer, while the R^2 basically has the opposite trend.

Figure 2 and **Table 3** show the performances of co-kriging, ANUSPLIN and M-ANUSPLIN models along altitudinal gradients. It can be seen that in general, the M-ANUSPLIN model has obvious advantages in regions with altitude <4,000 m, followed by the ANUSPLIN and co-kriging models. However, with the exception of elevation >4000 m, the MAE and RMSE of the M-ANUSPLIN model were slightly higher than those of the ANUSPLIN model. Moreover, in areas with altitude >4,000 m, all the three models generally gave overestimated values.

A summary of the performances of the ANUSPLIN and M-ANUSPLIN models were further compared using different combinations of covariates (**Table 4**). It can be seen that the incorporation of additional terrain-related factors resulted in more accurate results, and slope angle contribute more to NSAT than slope orientation.

Temporal Variation

Trends of Annual Temperature

The magnitude of change for annual mean NSAT ranged 15.20–16.81°C. **Figure 3** shows the annual variation of NSAT in the last 5 decades in Southwest China. It can be seen that over the whole region, with respect to the mean temperature during the period 1969–2018, the anomalies of mean temperature (T_{mean}) ranged −0.80 to 0.80°C; maximum temperature (T_{max}) ranged −0.93 to 1.07°C; while minimum temperature (T_{min}) ranged −0.77 to 0.96°C. In addition, T_{mean}, T_{max}, and T_{min} increased by 0.21°C/decade, 0.23°C/decade, and 0.28°C/decade over the past 50 years, respectively. Moreover, the warming rates for minimum temperature (0.28°C/decade) were greater than those for maximum temperature (0.23°C/decade), with T_{min} about 1.22 times of T_{max}.

Trends of Seasonal Temperature

The changes of seasonal NSAT for spring, summer, autumn and winter were 15.54–18.06°C, 22.15–24.13°C, 14.63–16.82°C, and 6.26–8.88°C, respectively. **Figure 4** indicates the similarity between the temporal patterns of the seasonal NSAT and the annual NSAT trends. Nevertheless, compared with annual NSAT,

TABLE 2 | 10-fold cross-validation results of the co-kriging, ANUSPLIN, and M-ANUSPLIN models.

Index	Models	Annual			Seasonal			
		T_{mean}	T_{max}	T_{min}	T_{spring}	T_{summer}	T_{autumn}	T_{winter}
MAE (°C)	M-ANUSPLIN	0.49	0.64	0.52	0.62	0.43	0.70	1.51
	ANUSPLIN	0.51	0.64	0.55	0.64	0.45	0.71	1.55
	Co-Kriging	1.16	1.27	1.86	1.26	1.15	1.39	1.83
RMSE(°C)	M-ANUSPLIN	0.77	1.02	0.79	0.95	0.68	1.15	2.37
	ANUSPLIN	0.81	1.04	0.86	0.98	0.73	1.18	2.37
	Co-Kriging	1.78	1.92	3.25	1.94	1.73	2.09	2.66
R^2	M-ANUSPLIN	0.974	0.939	0.979	0.967	0.978	0.935	0.715
	ANUSPLIN	0.970	0.937	0.975	0.964	0.975	0.932	0.713
	Co-Kriging	0.858	0.785	0.651	0.860	0.857	0.786	0.638

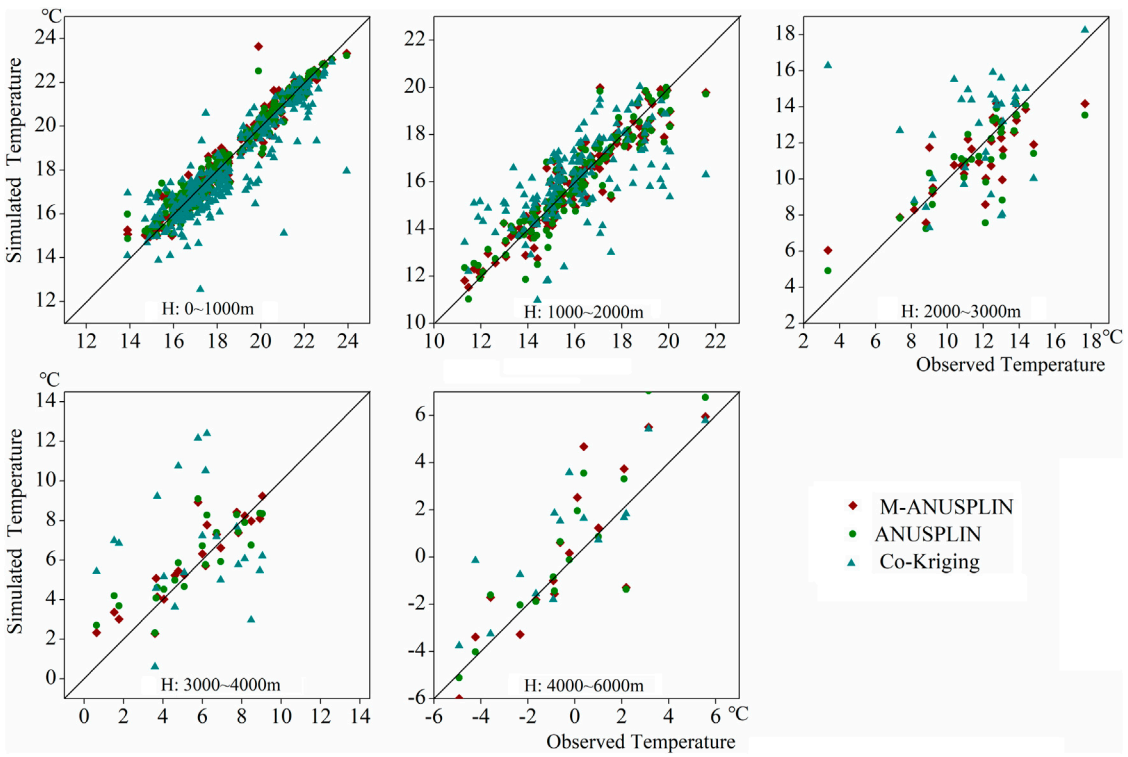

FIGURE 2 | The MAEs of co-kriging, ANUSPLIN, and M-ANUSPLIN models along altitudinal gradients.

TABLE 3 | Accuracy metrics of co-kriging, ANUSPLIN, and M-ANUSPLIN for the different altitudinal gradients.

Index	Models	$H_{0\sim1000\ m}$	$H_{1000\sim2000\ m}$	$H_{2000\sim3000\ m}$	$H_{3000\sim4000\ m}$	$H_{4000\sim6000\ m}$
MAE (°C)	M-ANUSPLIN	0.32	0.5	1.12	0.84	1.38
	ANUSPLIN	0.33	0.54	1.15	1.09	1.25
	Co-Kriging	0.74	1.26	2.42	3.16	1.83
RMSE (°C)	M-ANUSPLIN	0.47	0.71	1.53	1.11	1.83
	ANUSPLIN	0.46	0.75	1.68	1.37	1.78
	Co-Kriging	1.10	1.66	3.46	3.8	2.67
R^2	M-ANUSPLIN	0.953	0.880	0.643	0.778	0.535
	ANUSPLIN	0.954	0.863	0.572	0.666	0.561
	Co-Kriging	0.738	0.338	−0.822	−1.598	0.008

TABLE 4 | Comparisons of the ANUSPLIN model using different combinations of covariates.

Models	EDF freedom	√GCV	√MSR	√VAR
A_{ele}	436.9	0.69	0.61	0.65
A_{slope}	442.7	1.68	1.50	1.59
A_{aspect}	443.5	1.69	1.51	1.60
$A_{ele+slope}$	435.6	0.65	0.57	0.61
$A_{ele+aspect}$	435.8	0.69	0.61	0.65
$A_{aspect+slope}$	441.7	1.68	1.50	1.59
$A_{ele+aspect+slope}$	434.8	0.66	0.57	0.61
$A_{dem+aspect+slope}$	434.8	0.66	0.72	0.57

Note. EDF is the abbreviation for error degrees of freedom, GCV is for generalized cross validation, MSR is for mean square residual, and VAR is for data error variance estimate.

the temporal variations of seasonal NSAT could not be divided into cooling and warming phases clearly. Specifically, the temperature variations in summer were more stable than that in other seasons. Moreover, for spring, autumn and winter, the temperature variations showed stronger inter-annual fluctuations. This could lead to extreme weather events in Southwest China.

In **Figure 4**, the warming rate in summer (0.16°C/decade) was lower than those in spring (0.22°C/decade), winter (0.22°C/decade), and autumn (0.23°C/decade). This means that the most unnotable contribution to the warming in Southwest China as a whole comes from summer.

Change-Points of NSAT

Annual and seasonal variations of NSAT anomalies show that the overall warming over Southwest China started in the late 1990s and accelerated after it (**Figures 3**, **4**). Specifically, for mean temperature (T_{mean}), 18 out of 21 years were above the long-term average after 1998, while it was 3 out of 29 before 1998. This indicates that the NSAT of Southwest China was characterized by the transitions from cold to warm phases in the late 1990s.

To detect and identify the time when significant changes of NSAT occurred, the significant changes of each NSAT parameters were identified by using the PELT method at both annual and seasonal scales (as shown in **Figure 5**). It can be seen that the annual changes for maximum, average and minimum NSATs were quite similar to the seasonal changes. Moreover, there is strong evidence for the changes in all variables in the late 1990s and early 2000s. Specifically, for the annual mean temperature (T_{mean}) and maximum temperature (T_{max}), the significant changes began after 1997. While for the minimum temperature (T_{min}), there were two significant change points with both of them indicating a warming phase. The first change also started after 1997, and the second change began after 2011. Regarding the seasonal parameters, the change began after 1997, 2004, 1997, and 1985 for spring, summer, autumn and winter, respectively.

Overall, it is clear that most of the significant changes of NSAT occurred either in the late 1990s or in the early 2000s. Thus, in terms of NSAT variations, the late 1990s and early 2000s can be remarked as the abrupt change period in Southwest China.

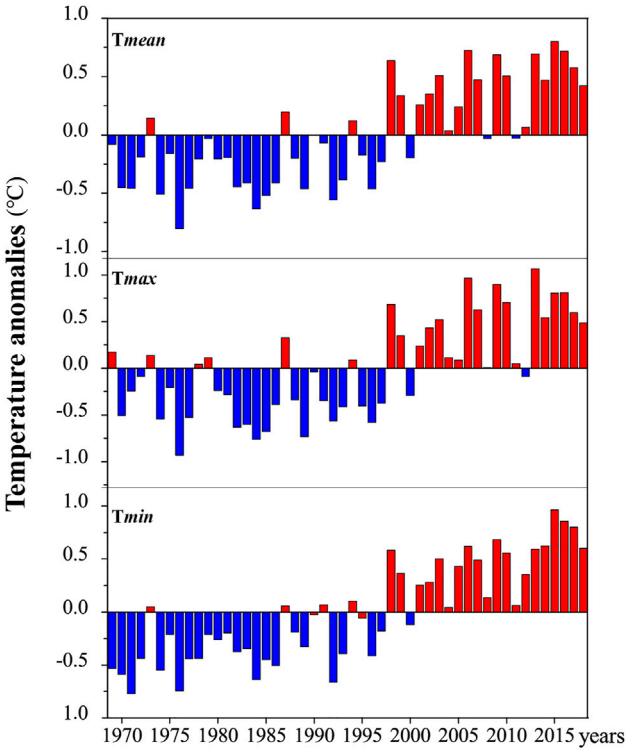

FIGURE 3 | Annual variations of NSAT anomalies in Southwest China for the period 1969–2018.

Spatial Variation of NSAT

To further probe into the spatial variation patterns of annual and seasonal NSATs over Southwest China, the variations with significance test were analyzed at the pixel scale. The area proportions occupied by extremely significant, significant and non-significant NSAT related indices are shown in **Figures 6**, **7**. It can be seen that the M-ANUSPLIN interpolation datasets can capture the detailed NSAT very well, and they can accurately represent the climate characteristics in Southwest China, such as the extremely significant cooling regions with high elevations (e.g., the northwest of Qinghai-Tibet Plateau), the non-significant warming regions with low elevations (e.g., the northeast of Sichuan Basin), and extremely significant warming regions in most part of the study area. Moreover, despite slight differences between the spatial variations of annual NSAT and those of the seasonal indices, they exhibited highly consistent characteristics. Specifically, for the mean annual NSAT, during the period 1969–2018, 85.66% of the study area showed extremely significant warming with the most notable increases in the southeast region. Areas occupied by non-significant warming accounted for 2.48%, followed by significant warming with 1.32%, leading to an overall warming tendency across Southwest China. Nevertheless, the northwest region experienced a contrary characteristic, with extremely significant, and significant cooling accounted for 8.35%. This could be attributed to the high altitude in this region, which belongs to the Qinghai-Tibetan Plateau. Regarding the mean seasonal NSAT, areas occupied by

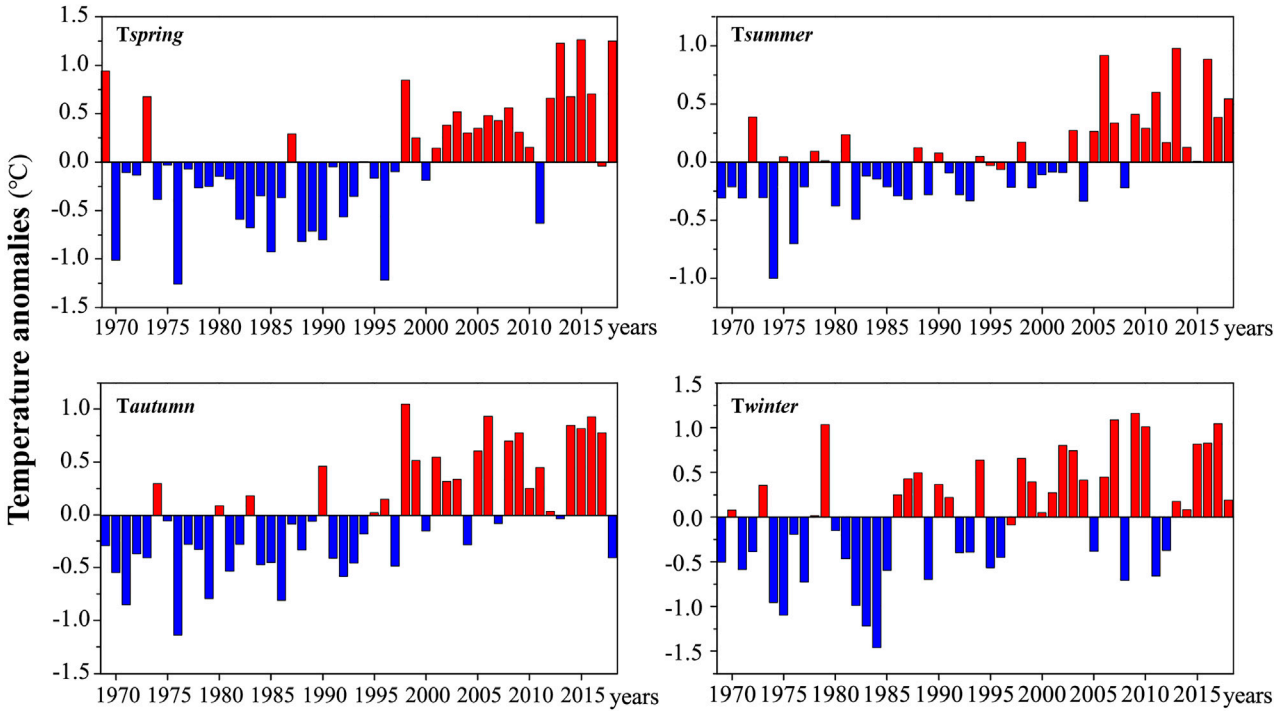

FIGURE 4 | Seasonal variations of NSAT anomalies in Southwest China for the period 1969–2018.

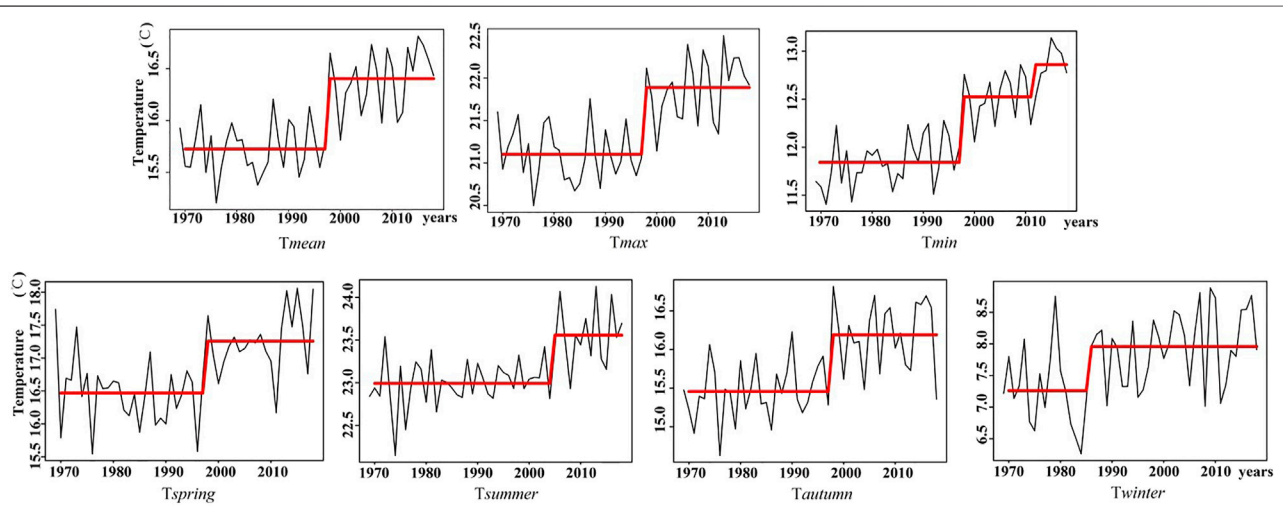

FIGURE 5 | Change-points for annual and seasonal NSATs in Southwest China for the period 1969–2018 (p-value < 0.05).

extremely significant warming in spring, summer, autumn and winter accounted for 63.48, 71.47, 72.36 and 54.77%, respectively. Otherwise, it can be seen that winter has the highest proportions for non-significant warming, comparing to other seasons (**Figure 7**).

Figure 8 shows the coefficient maps of variation (*CV*) index for NSAT over Southwest China. It indicates the high consistency of the CV index of annual NSAT with that of seasonal index over the past 50 years. Both annual and seasonal CV indices were generally stable and mainly dominated by weak or medium variations. Strong variations were mainly observed in high altitude regions, or in the combined section for encompassing plain and mountainous regions. For seasonal NSAT indices, it also mainly exhibited weak or medium variations, with different patterns in different seasons. Specifically, strong variations were identified in autumn and spring, followed by winter, while

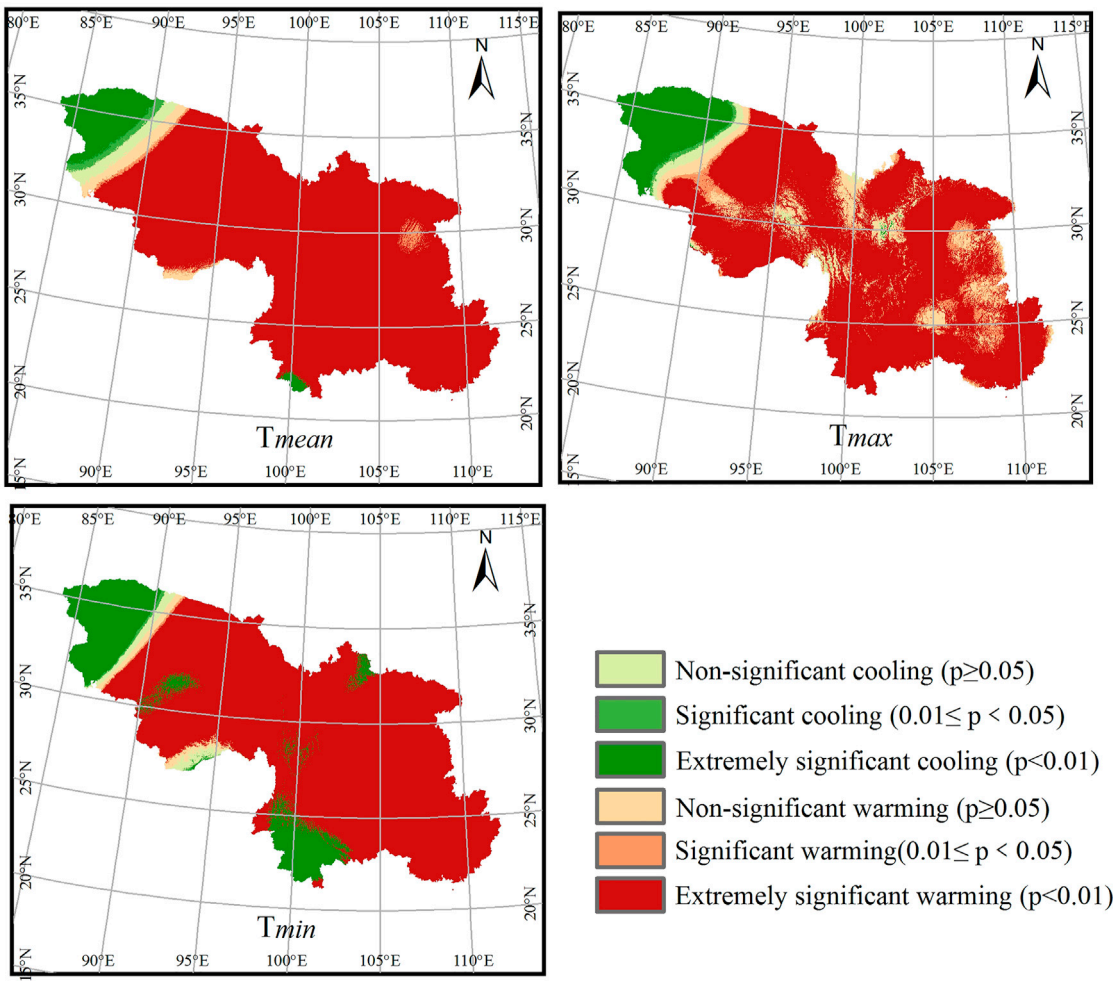

FIGURE 6 | Trends of annual NSAT over Southwest China for the period 1969–2018. Panels **(A–C)** correspond to the mean annual, mean annual maximum, and minimum temperatures, respectively.

summer was the most stable, denoting that autumn maybe more susceptible to the warming.

DISCUSSION

Priority of M-ANUSPLIN

Previous studies indicated that topographic information might be the key factor in climate indices prediction, especially in mountainous or high altitude areas with low density of meteorological stations (Gao et al., 2018; Peng et al., 2019). Therefore, it is possible that the precision of interpolation could be further improved by incorporating more detail terrain-related factors (Cheng et al., 2020). Nevertheless, traditional interpolation method is usually processed under the assumption that the NSAT is only dependent on the altitude. However, Šafanda (1999) demonstrated the strong dependence of NSAT on slope angle and orientation. Therefore, it is possible that the precision of interpolation for NSAT could be improved by considering slope angle and orientation in the interpolation process.

In this study, we included longitude and latitude as independent variables, and incorporated elevation, slope and aspect as covariates. We found that compared to the ANUSPLIN model, the MAE and RMSE values decreased by 0–5.77 and 1.96–8.86% for annual parameters, and 1.43–4.65 and 0–7.35% for seasonal parameters. As a result, the M-ANUSPLIN exhibited smaller deviation and performed better against other interpolation methods, especially in mountainous regions. However, our results also reflected the relatively poor performance of the M-ANUSPLIN model in regions with altitude >4,000 m, suggesting that it is not optimal for all regions.

Our study confirmed that slope is an important terrain-related factor in the interpolation process for NSAT (**Table 4**). As slope angle affects the temperature of surface objects by influencing the incidence angle and reflectivity of solar radiation, and then alters NSAT (Li et al., 2015; Peng et al., 2020). However, our study revealed the much smaller contribution of slope orientation to

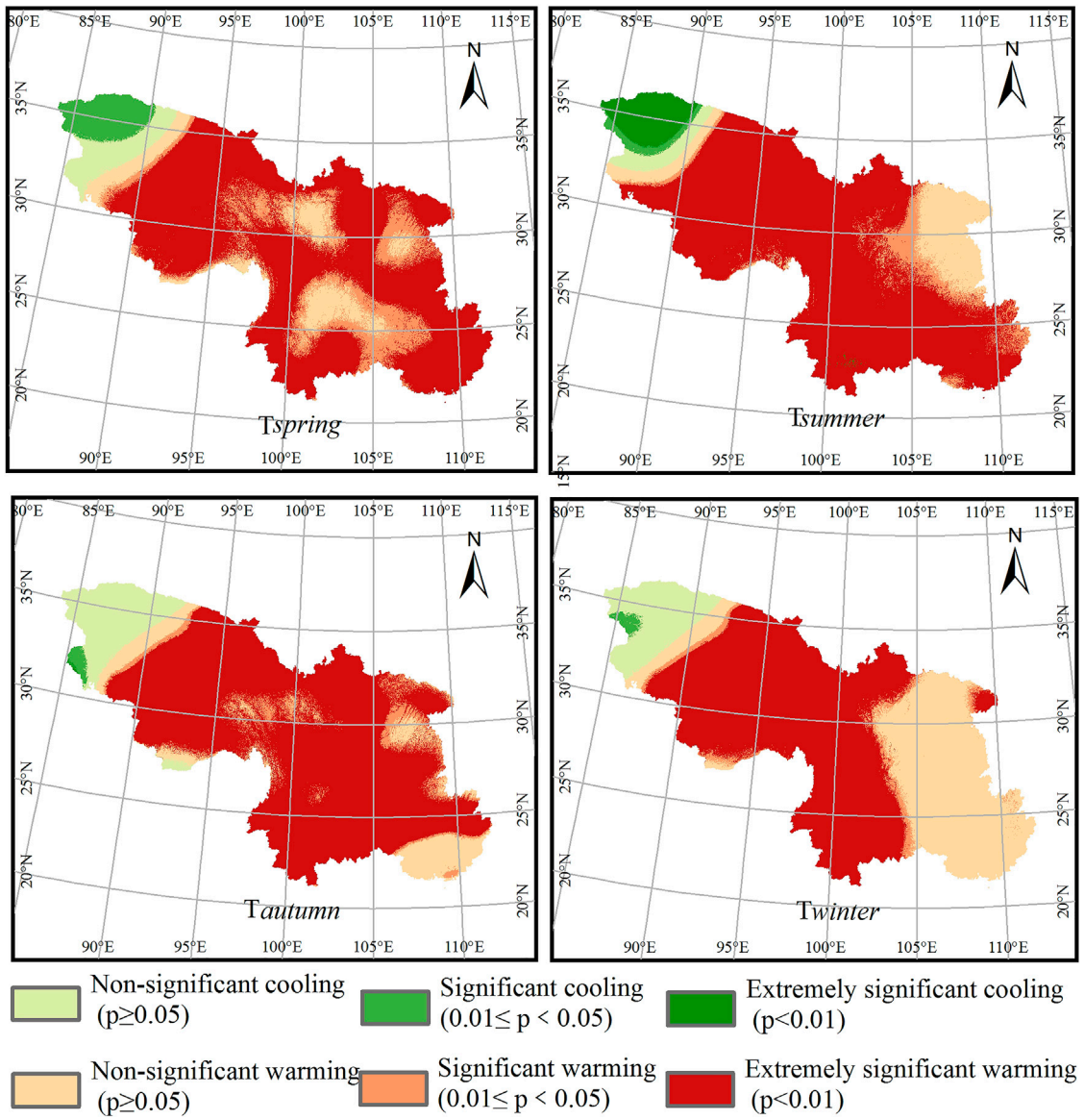

FIGURE 7 | Trends of NSAT over southwest China for the period 1969–2018. Panels **(A–D)** correspond to the mean spring, summer, autumn, and winter NSATs, respectively.

NSAT estimation than slope angle. This is not consistent with existing knowledge, which believes that slope orientation plays an important role in NSAT prediction. Earlier studies reported that in the middle latitudes of the Northern Hemisphere, the north slopes are generally colder at the same elevation than the south slopes because sunny aspects receive more direct solar radiation than northern aspects (Šafanda, 1999; Li et al., 2015). One reason for this inconsistent might be due to the different vegetation types in Southwest China. For example, Šafanda (1999) explained that the surface temperature in the meadow is higher than that in the forest because much of the Sun radiation is absorbed by the trees. Thus, the NSAT for meadows located at north slopes might be higher than the NSAT for forests located at south slopes. Another reason might be due to the existence and duration of the snow cover in high altitude regions, which can offset the effects of slope orientation on NSAT. Consequently, the effect of slope orientation on NSAT in Southwest China was smaller compared to those in other regions.

Comparisons With Other Datasets

To examine the accuracy of M-ANUSPLIN interpolated dataset, the predicted results were compared to both the WorldClim 2.0 dataset (Fick and Hijmans, 2017) and the HMTC dataset (Peng et al., 2019). The 10-fold cross validation test was used to evaluate the overall error of the interpolated NSAT grid obtained from each dataset and the original observation data of 494 meteorological stations (**Table 5**).

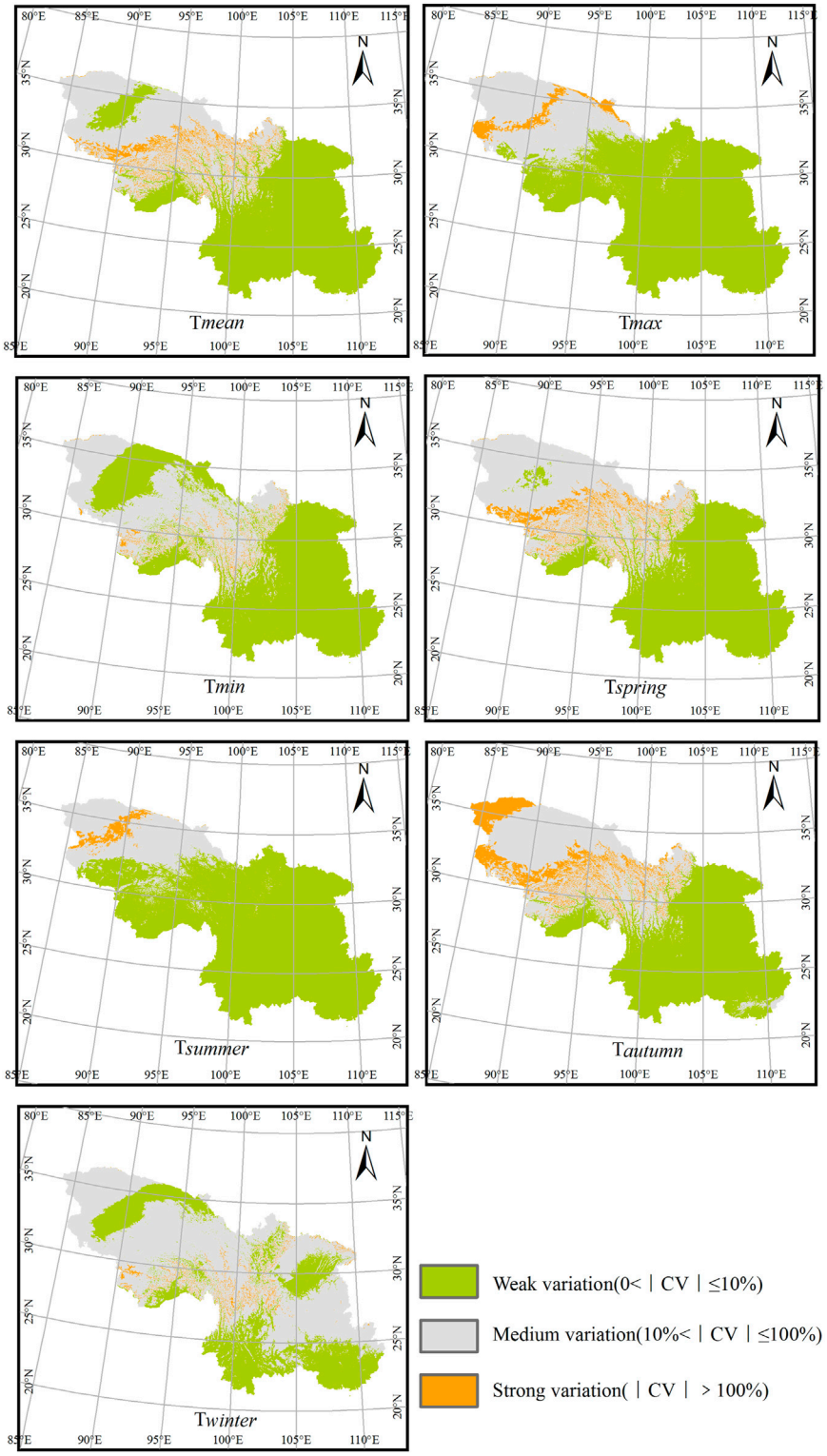

FIGURE 8 | Coefficient of variation (CV) index for NSAT over Southwest China for the period 1969–2018. Panels **(A–G)** correspond to the mean annual, mean annual maximum, mean annual minimum, mean spring, mean summer, mean autumn, and mean winter NSATs, respectively.

TABLE 5 | Comparisons of annual and seasonal climatology indices among different datasets.

Index	Datasets	Annual (°C)			Seasonal (°C)			
		T_{mean}	T_{max}	T_{min}	T_{spring}	$T_{summuer}$	T_{autumn}	T_{winter}
MAE(°C)	M-ANUSPLIN	0.50	0.69	0.53	0.64	0.54	0.73	0.60
	WorldClim2	0.66	0.87	0.71	0.91	0.66	1.40	0.75
	HMTC	0.72	1.51	1.13	0.99	0.68	1.39	0.87
RMSE(°C)	M-ANUSPLIN	0.83	1.14	0.82	1.00	1.09	1.18	0.98
	WorldClim2	1.03	1.36	1.11	1.35	1.13	2.87	1.14
	HMTC	1.19	1.97	1.54	1.57	1.23	2.83	1.30
R^2	M-ANUSPLIN	0.97	0.925	0.978	0.963	0.947	0.933	0.965
	WorldClim2	0.954	0.894	0.96	0.932	0.943	0.603	0.953
	HMTC	0.938	0.778	0.923	0.907	0.932	0.615	0.939

Table 5 lists the mean, maximum, minimum values for annual and seasonal NSAT variables obtained from different datasets. It can be seen that the climatology anomaly of M-ANUSPLIN dataset is the lowest comparing to the WorldClim 2.0 and the HMTC datasets. Specifically, the anomalies are relatively high for HMTC (0.72–1.51°C for MAE and 1.19–1.97°C for RMSE); intermediate for WorldClim2 (0.66–0.87°C for MAE and 1.03–1.36°C for RMSE); and the lowest for M-ANUSPLIN (0.50–0.69°C for MAE and 0.82–1.14°C for RMSE). The seasonal NSAT variables shows the similar trend, where HMTC gives the highest estimation error, followed by WorldClim2 and M-ANUSPLIN. The good performance of M-ANUSPLIN can be mainly attributed to two reasons. Firstly, in case of WorldClim2 and HMTC datasets, only ~300 sites and ~500 sites of *in-situ* observation stations were respectively used for interpolation, and therefore significant biases occurred due to the complex terrain (Peng et al., 2019). Secondly, the M-ANUSPLIN model incorporated more detailed topographic information than traditional models, and thus can capture NSAT features with better precision.

Overall, the results indicate that the improved M-ANUSPLIN model can produce more accurate NSAT values than traditional interpolation models, and has apparent advantages over other interpolation methods in complex terrain areas like Southwest China.

Study Limitations

Whilst this study demonstrated that the improved M-ANUSPLIN method can estimate more accurate NSAT than traditional models, especially in complex terrain areas like Southwest China, uncertainties still remain regarding the density of meteorological stations, input datasets and urbanization effect. Firstly, as gauge stations are relatively sparse in the western region of the study area, acquiring a correct distribution of NSAT through interpolation is difficult. The interpolated NSAT grid surface might contain some biases, which could introduce some uncertainty, especially in regions where the NSAT varies significantly in space and time. In addition, as the satellite SRTM product represents the average value in a 500 m × 500 m pixel, it does not provide the fine details and thus could not fully represent the real situation, which might also lead to additional biases.

Secondly, another source of uncertainty could be due to the input datasets. The NSAT is affected not only by topographical factors, but also closely related to other factors, e.g., vegetation and soil (Cho and Choi, 2014; Lensky et al., 2018). Moreover, as mentioned above, the effects of snow cover could be stronger than general expectation. It implies the need of careful interpretation of NSAT. Therefore, to further improve the accuracy of NSAT prediction, more information should be taken into account in the future.

Thirdly, the urbanization heat effect, which has a strong warming effect on NSAT (Kalnay and Cai, 2003; Ren et al., 2008; Luo and Lau, 2021), has not been considered in this study. This could cause an underestimation of NSAT, especially in the eastern region of Southwest China with a lot of big cities. Nonetheless, the results of this work should still, at least qualitatively, reveal the trends and spatial-temporal variations of NSAT in Southwest China over the past 50 years.

Lastly, elevation is an important factor affecting spatial variability of climate (Pepin et al., 2015). It is well known that for a stationary atmosphere, an increase in elevation leads to a subsequent decrease in air pressure and NSAT (You et al., 2008). According to EI Kenawy et al., 2009, different regions can experience different variations of NSAT, as each region has a unique terrain (Limsakul & Goes, 2008). Moreover, the variation of NSAT was not consistent between high and low land areas. Many studies suggested that NSAT increased more rapidly at higher than at lower elevations (Beniston, 2003; You et al., 2008; Pepin et al., 2015), which has been defined as elevation-dependent warming (EDW). However, this faster warming is not ubiquitous across the globe (Thakuri et al., 2019). In general, this study agrees with the previous studies of the EDW phenomenon with most high-altitude areas show significant warming. Nevertheless, we also observed a significant cooling trend in some high altitude regions like the northwestern part of Southwest China in the past 50 years. The reason for this phenomenon is still unclear, thus further investigation would be required.

CONCLUSION

This study enhanced the ANUSPLIN model by incorporating elevation, slope angle and orientation as covariates; and

constructed monthly NSAT datasets with a spatial resolution of 500 m in Southwest China from January 1969 to December 2018. The accuracy of the M-ANUSPLIN model was evaluated by analyzing error statistics based on comparisons between interpolated values against withheld stations data. Furthermore, we compared the M-ANUSPLIN predicted dataset against existing datasets. To our knowledge, this is one of the few studies which considered slope angle and orientation to account for the terrain effects on NSAT. The independent validation results confirmed the clear advantages of the optimized M-ANUSPLIN model against other interpolation methods in Southwest China. Our methodology therefore represents a significant and practical improvement in NSAT estimation. Therefore, it has great potential for meteorological and climatological research, especially in mountainous regions with diverse topography.

As mentioned above, during the period 1969–2018, consistent warming and significant EDW were found in most part of Southwest China, while some sporadic areas like northwestern region exhibited opposite trends. In general, Southwest China experienced an overall warming with a rate of 0.21°C/decade, obviously higher than mainland China and global averages. This implies that Southwest China is more sensitive to global warming than generally recognized. The warming mainly started in the late 1990s, and the hiatus or slowdown phenomenon was not observed as expected, and the NSAT experienced a persistent and even more significant warming after the 1997/1998 EL Niño event. This means that climate change in Southwest China should be of particular concern. Moreover, the increase of low temperature was significantly greater than that of high temperature, where the warming rate of T_{min} (0.28°C/decade) about 1.22 times of T_{max} (0.23°C/decade); and that of T_{winter} (0.22°C/decade) about 1.38 times of T_{summer} (0.16°C/decade). These indicate that the increases of T_{min} and T_{winter} contribute the most to the warming effect in Southwest China over the past 50 years.

DATA AVAILABILITY STATEMENT

The raw data supporting the conclusion of this article will be made available by the authors, without undue reservation.

AUTHOR CONTRIBUTIONS

JZ and TL conceived the study, performed the analysis, drafted the manuscript; TL supervised the project. All authors listed have made a substantial, direct, and intellectual contribution to the work and approved it for publication.

FUNDING

This research was supported by the Second Tibetan Plateau Scientific Expedition and Research program (2019QZKK04020301), the National Natural Science Foundation of China (42071238, 41371126), the Program for Biodiversity Protection of Ministry of Ecology and Environment of the People's Republic of China (9311341), the National Key Research and Development Program of China (2016YFC0502101).

REFERENCES

Amato, R., Steptoe, H., Buonomo, E., and Jones, R. (2019). High-Resolution History: Downscaling China's Climate from the 20CRv2c Reanalysis. *J. Appl. Meteorol. Clim.* 58 (10), 2141–2157. doi:10.1175/JAMC-D-19-0083.1

Appelhans, T., Mwangomo, E., Hardy, D. R., Hemp, A., and Nauss, T. (2015). Evaluating Machine Learning Approaches for the Interpolation of Monthly Air Temperature at Mt. Kilimanjaro, Tanzania. *Spat. Stat.* 14, 91–113. doi:10.1016/j.spasta.2015.05.008

Belkhiri, L., Tiri, A., and Mouni, L. (2020). Spatial Distribution of the Groundwater Quality Using Kriging and Co-kriging Interpolations. *Groundwater Sustain. Dev.* 11, 100473. doi:10.1016/j.gsd.2020.100473

Beniston, M. (2003). Climatic Change in Mountain Regions: A Review of Possible Impacts. *Climatic Change* 59, 5–31. doi:10.1007/978-94-015-1252-7_2

Cahill, N., Rahmstorf, S., and Parnell, A. C. (2015). Change Points of Global Temperature. *Environ. Res. Lett.* 10 (8), 084002. doi:10.1088/1748-9326/10/8/084002

Chen, X., Li, N., Zhang, Z., Feng, J., and Wang, Y. (2018). Change Features and Regional Distribution of Temperature Trend and Variability Joint Mode in mainland China. *Theor. Appl. Climatol* 132 (3-4), 1049–1055. doi:10.1007/s00704-017-2148-z

Cheng, J., Li, Q., Chao, L., Maity, S., Huang, B., and Jones, P. (2020). Development of High Resolution and Homogenized Gridded Land Surface Air Temperature Data: A Case Study over Pan-East Asia. *Front. Environ. Sci.* 8, 588570. doi:10.3389/fenvs.2020.588570

Cho, E., and Choi, M. (2014). Regional Scale Spatio-Temporal Variability of Soil Moisture and its Relationship with Meteorological Factors over the Korean peninsula. *J. Hydrol.* 516, 317–329. doi:10.1016/j.jhydrol.2013.12.053

Collados-Lara, A.-J., Fassnacht, S. R., Pardo-Igúzquiza, E., and Pulido-Velazquez, D. (2021). Assessment of High Resolution Air Temperature Fields at Rocky Mountain National Park by Combining Scarce Point Measurements with Elevation and Remote Sensing Data. *Remote Sensing* 13 (1), 113. doi:10.3390/rs13010113

Cuervo-Robayo, A. P., Téllez-Valdés, O., Gómez-Albores, M. A., Venegas-Barrera, C. S., Manjarrez, J., and Martínez-Meyer, E. (2014). An Update of High-Resolution Monthly Climate Surfaces for Mexico. *Int. J. Climatol.* 34 (7), 2427–2437. doi:10.1002/joc.3848

Cui, L. L., Shi, J., Du, H. Q., and Wen, K. M. (2017). Characteristics and Trends of Climatic Extremes in China during 1959-2014. *J. Trop. Meteorol.* 23 (4), 368–379. 1006-8775(2017) 04-0368-12.

Cui, L., and Shi, J. (2021). Evaluation and Comparison of Growing Season Metrics in Arid and Semi-arid Areas of Northern China under Climate Change. *Ecol. Indicators* 121, 107055. doi:10.1016/j.ecolind.2020.107055

Diaz, H. F., and Bradley, R. S. (1997). Temperature Variations during the Last century at High Elevations Sites. *Climatic Change* 36 (3-4), 253–279. doi:10.1023/A:1005335731187

Ding, Y., Ren, G., ZhaoXu, Z. Y., Xu, Y., Luo, Y., Li, Q., et al. (2007). Detection, Causes and Projection of Climate Change over China: An Overview of Recent Progress. *Adv. Atmos. Sci.* 24 (6), 954–971. doi:10.1007/s00376-007-0954-4

Dong, D., Huang, G., Qu, X., Tao, W., and Fan, G. (2015). Temperature Trend-Altitude Relationship in China during 1963-2012. *Theor. Appl. Climatol.* 122, 285–294. doi:10.1007/s00704-014-1286-9

Du, H., Hu, F., Zeng, F., Wang, K., Peng, W., Zhang, H., et al. (2017). Spatial Distribution of Tree Species in evergreen-deciduous Broadleaf Karst Forests in Southwest China. *Sci. Rep.* 7, 15664. doi:10.1038/s41598-017-15789-5

Du, Q., Zhang, M., Wang, S., Che, C., Ma, R., and Ma, Z. (2019). Changes in Air Temperature over China in Response to the Recent Global Warming Hiatus. *J. Geogr. Sci.* 29 (4), 496–516. doi:10.1007/s11442-019-1612-3

Easterling, D. R., and Wehner, M. F. (2009). Is the Climate Warming or Cooling. *Geophys. Res. Lett.* 36, L08706. doi:10.1029/2009GL037810

El Kenawy, A. M., López-Moreno, J. I., Vicente-Serrano, S. M., and Mekld, M. S. (2009). Temperature Trends in Libya over the Second Half of the 20th century. *Theor. Appl. Climatol* 98, 1–8. doi:10.1007/s00704-008-0089-2

Fan, Z.-X., Bräuning, A., Thomas, A., Li, J.-B., and Cao, K.-F. (2011). Spatial and Temporal Temperature Trends on the Yunnan Plateau (Southwest China) during 1961-2004. *Int. J. Climatol.* 31 (14), 2078–2090. doi:10.1002/joc.2214

Fick, S. E., and Hijmans, R. J. (2017). WorldClim 2: New 1-km Spatial Resolution Climate Surfaces for Global Land Areas. *Int. J. Climatol* 37 (12), 4302–4315. doi:10.1002/joc.5086

Fyfe, J. C., Meehl, G. A., England, M. H., Mann, M. E., Santer, B. D., Flato, G. M., et al. (2016). Making Sense of the Early-2000s Warming Slowdown. *Nat. Clim Change* 6 (3), 224–228. doi:10.1038/nclimate2938

Gao, J., Jiao, K., and Wu, S. (2018). Quantitative Assessment of Ecosystem Vulnerability to Climate Change: Methodology and Application in China. *Environ. Res. Lett.* 13 (9), 094016. doi:10.1088/1748-9326/aadd2e

Guo, B., Zhang, J., Meng, X., Xu, T., and Song, Y. (2020). Long-term Spatio-Temporal Precipitation Variations in China with Precipitation Surface Interpolated by ANUSPLIN. *Sci. Rep.* 10 (1), 81. doi:10.1038/s41598-019-57078-3

Hadi, S. J., and Tombul, M. (2018). Comparison of Spatial Interpolation Methods of Precipitation and Temperature Using Multiple Integration Periods. *J. Indian Soc. Remote Sens* 46 (7), 1187–1199. doi:10.1007/s12524-018-0783-1

Hu, Z.-Z., Yang, S., and Wu, R. G. (2003). Long-term Climate Variations in China and Global Warming Signals. *J. Geophys. Res.* 108 (19), 4614. doi:10.1029/2003JD003651

Hutchinson, M. F., and Gessler, P. E. (1994). Splines-more Than Just a Smooth Interpolator. *Geoderma* 62 (1-3), 45–67. doi:10.1016/0016-7061(94)90027-2

Ilori, O. W., and Ajayi, V. O. (2020). Change Detection and Trend Analysis of Future Temperature and Rainfall over West Africa. *Earth. Syst. Environ.* 4 (3), 493–512. doi:10.1007/s41748-020-00174-6

Islam, S. U., and Déry, S. J. (2017). Evaluating Uncertainties in Modelling the Snow Hydrology of the Fraser River Basin, British Columbia, Canada. *Hydrol. Earth Syst. Sci.* 21 (3), 1827–1847. doi:10.5194/hess-21-1827-2017

Jiang, S., Liang, C., Cui, N., Zhao, L., Du, T., Hu, X., et al. (2019). Impacts of Climatic Variables on Reference Evapotranspiration during Growing Season in Southwest China. *Agric. Water Manag.* 216, 365–378. doi:10.1016/j.agwat.2019.02.014

Jin, J., and Wang, Q. (2016). Assessing Ecological Vulnerability in Western China Based on Time-Integrated NDVI Data. *J. Arid Land* 8 (4), 533–545. doi:10.1007/s40333-016-0048-1

Joly, D., Brossard, T., Cardot, H., Cavailhes, J., Hilal, M., and Wavresky, P. (2011). Temperature Interpolation Based on Local Information: the Example of France. *Int. J. Climatol.* 31 (14), 2141–2153. doi:10.1002/joc.2220

Kalnay, E., and Cai, M. (2003). Impact of Urbanization and Land-Use Change on Climate. *Nature* 423 (6939), 528–531. doi:10.1038/nature01675

Khapalova, E. A., Jandhyala, V. K., Fotopoulos, S. B., and Overland, J. E. (2018). Assessing Change-Points in Surface Air Temperature over Alaska. *Front. Environ. Sci.* 6, 121. doi:10.3389/fenvs.2018.00121

Khosravi, Y., and Balyani, S. (2019). Spatial Modeling of Mean Annual Temperature in Iran: Comparing Cokriging and Geographically Weighted Regression. *Environ. Model. Assess.* 24 (3), 341–354. doi:10.1007/s10666-018-9623-5

Killick, R., Fearnhead, P., and Eckley, I. A. (2012). Optimal Detection of Changepoints with a Linear Computational Cost. *J. Am. Stat. Assoc.* 107, 1590–1598. doi:10.1080/01621459.2012.737745

Lensky, I. M., Dayan, U., and Helman, D. (2018). Synoptic Circulation Impact on the Near-Surface Temperature Difference Outweighs that of the Seasonal Signal in the Eastern Mediterranean. *J. Geophys. Res. Atmos.* 123, 11333–11347. doi:10.1029/2017JD027973

Lewandowsky, S., Cowtan, K., Risbey, J. S., Mann, M. E., Steinman, B. A., Oreskes, N., et al. (2018). Erratum: The 'pause' in Global Warming in Historical Context: II. Comparing Models to Observations (2018 Environ. Res. Lett . 13 123007). *Environ. Res. Lett.* 14 (4), 049601. doi:10.1088/1748-9326/aafbb7

Li, J., and Heap, A. D. (2011). A Review of Comparative Studies of Spatial Interpolation Methods in Environmental Sciences: Performance and Impact Factors. *Ecol. Inform.* 6, 228–241. doi:10.1016/j.ecoinf.2010.12.003

Li, Q., Sun, W., Yun, X., Huang, B., Dong, W., Wang, X. L., et al. (2021). An Updated Evaluation of the Global Mean Land Surface Air Temperature and Surface Temperature Trends Based on CLSAT and CMST. *Clim. Dyn.* 56 (1-2), 635–650. doi:10.1007/s00382-020-05502-0

Li, X., Li, L., Yuan, S., Yan, H., and Wang, G. (2015). Temporal and Spatial Variation of 10-day Mean Air Temperature in Northwestern China. *Theor. Appl. Climatol.* 119 (1-2), 285–298. doi:10.1007/s00704-014-1100-8

Li, Y., Zhang, D., Andreeva, M., Li, Y., Fan, L., and Tang, M. (2020). Temporal-spatial Variability of Modern Climate in the Altai Mountains during 1970-2015. *Plos. One* 15 (3), e0230196. doi:10.1371/journal.pone.0230196

Limsakul, A., and Goes, J. I. (2008). Empirical Evidence for Interannual and Longer Period Variability in Thailand Surface Air Temperatures. *Atmos. Res.* 87, 89–102. doi:10.1016/j.atmosres.2007.07.007

Lin, P., He, Z., Du, J., Chen, L., Zhu, X., and Li, J. (2017). Recent Changes in Daily Climate Extremes in an Arid Mountain Region, a Case Study in Northwestern China's Qilian Mountains. *Sci. Rep.* 7, 2245. doi:10.1038/s41598-017-02345-4

Luo, M., and Lau, N.-C. (2017). Heat Waves in Southern China: Synoptic Behavior, Long-Term Change, and Urbanization Effects. *J. Clim.* 30 (2), 703–720. doi:10.1175/JCLI-D-16-0269.1

Luo, M., and Lau, N. C. (2021). Increasing Human-Perceived Heat Stress Risks Exacerbated by Urbanization in China: A Comparative Study Based on Multiple Metrics. *Earth's Future* 9, e2020EF001848. doi:10.1029/2020EF001848

Minder, J. R., Mote, P. W., and Lundquist, J. D. (2010). Surface Temperature Lapse Rates over Complex Terrain: Lessons from the Cascade Mountains. *J. Geophys. Res.* 115, D14122. doi:10.1029/2009JD013493

Mohammadi, S. A., Azadi, M., and Rahmani, M. (2017). Comparison of Spatial Interpolation Methods for Gridded Bias Removal in Surface Temperature Forecasts. *J. Meteorol. Res.* 31, 791–799. doi:10.1007/s13351-017-6135-1

Nalder, I. A., and Wein, R. W. (1998). Spatial Interpolation of Climatic Normals: Test of a New Method in the Canadian Boreal forest. *Agric. For. Meteorology* 92 (4), 211–225. doi:10.1016/S0168-1923(98)00102-6

Peng, S., Ding, Y., Liu, W., and Li, Z. (2019). 1 Km Monthly Temperature and Precipitation Dataset for China from 1901 to 2017. *Earth Syst. Sci. Data* 11 (4), 1931–1946. doi:10.5194/essd-11-1931-2019

Peng, X., Wu, W., Zheng, Y., Sun, J., Hu, T., and Wang, P. (2020). Correlation Analysis of Land Surface Temperature and Topographic Elements in Hangzhou, China. *Sci. Rep.* 10 (1), 10451. doi:10.1038/s41598-020-67423-6

Pepin, N., Bradley, R. S., Diaz, H. F., Baraer, M., Caceres, E. B., Forsythe, N., et al. (2015). Elevation-dependent Warming in Mountain Regions of the World. *Nat. Clim. Change* 5, 424–430. doi:10.1038/nclimate2563

Persaud, B. D., Whitfield, P. H., Quinton, W. L., and Stone, L. E. (2020). Evaluating the Suitability of Three Gridded-datasets and Their Impacts on Hydrological Simulation at Scotty Creek in the Southern Northwest Territories, Canada. *Hydrological Process.* 34 (4), 898–913. doi:10.1002/hyp.13663

Price, D. T., McKenney, D. W., Nalder, I. A., Hutchinson, M. F., and Kesteven, J. L. (2000). A Comparison of Two Statistical Methods for Spatial Interpolation of Canadian Monthly Mean Climate Data. *Agr. For. Meteorol.* 101 (2-3), 81–94. doi:10.1016/S0168-1923(99)00169-0

Qian, H., Deng, T., Jin, Y., Mao, L., Zhao, D., and Ricklefs, R. E. (2019). Phylogenetic Dispersion and Diversity in Regional Assemblages of Seed Plants in China. *Proc. Natl. Acad. Sci. USA* 116 (46), 23192–23201. doi:10.1073/pnas.1822153116

Ren, G., Zhou, Y., ChuZhou, Z. J. X., Zhou, J., Zhang, A., Guo, J., et al. (2008). Urbanization Effects on Observed Surface Air Temperature Trends in north China. *J. Clim.* 21 (6), 1333–1348. doi:10.1175/2007JCLI1348.1

Ren, Y., Parker, D., Ren, G., and Dunn, R. (2016). Tempo-spatial Characteristics of Sub-daily Temperature Trends in mainland China. *Clim. Dyn.* 46 (9-10), 2737–2748. doi:10.1007/s00382-015-2726-7

Risbey, J. S., Lewandowsky, S., Cowtan, K., Oreskes, N., Rahmstorf, S., Jokimäki, A., et al. (2018). A Fluctuation in Surface Temperature in Historical Context: Reassessment and Retrospective on the Evidence. *Environ. Res. Lett.* 13 (12), 123008. doi:10.1088/1748-9326/aaf342

Šafanda, J. (1999). Ground Surface Temperature as a Function of Slope Angle and Slope Orientation and its Effect on the Subsurface Temperature Field. *Tectonophysics* 306, 367–375. doi:10.1016/S0040-1951(99)00066-9

Sun, X., Ren, G., Ren, Y., Fang, Y., Liu, Y., Xue, X., et al. (2018). A Remarkable Climate Warming Hiatus over Northeast China since 1998. *Theor. Appl. Climatol.* 133 (1-2), 579–594. doi:10.1007/s00704-017-2205-7

Tang, G. L., Luo, Y., Huang, J. B., Wen, X. Y., Zhu, Y. N., Zhao, Z. C., et al. (2012). Continuation of the Global Warming. *Clim. Chang. Res.* 8 (4), 235–242. (in Chinese). doi:10.3969/j.issn.1673-1719.2012.04.001

Tanır Kayıkçı, E., and Zengin Kazancı, S. (2016). Comparison of Regression-Based and Combined Versions of Inverse Distance Weighted Methods for Spatial Interpolation of Daily Mean Temperature Data. *Arab. J. Geosci.* 9 (17), 690. doi:10.1007/s12517-016-2723-0

Thakuri, S., Dahal, S., Shrestha, D., Guyennon, N., Romano, E., Colombo, N., et al. (2019). Elevation-dependent Warming of Maximum Air Temperature in Nepal during 1976-2015. *Atmos. Res.* 228, 261–269. doi:10.1016/j.atmosres.2019.06.006

Vogelsang, T. J., and Nawaz, N. (2017). Estimation and Inference of Linear Trend Slope Ratios with an Application to Global Temperature Data. *J. Time Ser. Anal.* 38 (5), 640–667. doi:10.1111/jtsa.12209

Wang, M., He, G., Zhang, Z., Wang, G., Zhang, Z., Cao, X., et al. (2017). Comparison of Spatial Interpolation and Regression Analysis Models for an Estimation of Monthly Near Surface Air Temperature in China. *Remote Sensing* 9 (12), 1278. doi:10.3390/rs9121278

Wang, S.-J. (2018). Spatiotemporal Variability of Temperature Trends on the Southeast Tibetan Plateau, China. *Int. J. Climatol* 38, 1953–1963. doi:10.1002/joc.5308

Wu, T., and Li, Y. (2013). Spatial Interpolation of Temperature in the United States Using Residual Kriging. *Appl. Geogr.* 44, 112–120. doi:10.1016/j.apgeog.2013.07.012

Xu, K., Wang, X., Jiang, C., and Sun, O. J. (2020). Assessing the Vulnerability of Ecosystems to Climate Change Based on Climate Exposure, Vegetation Stability and Productivity. *For. Ecosyst.* 7 (3), 23. doi:10.1186/s40663-020-00239-y

Yang, K., and Jiang, D. (2017). Interannual Climate Variability Change during the Medieval Climate Anomaly and Little Ice Age in PMIP3 Last Millennium Simulations. *Adv. Atmos. Sci.* 34 (4), 497–508. doi:10.1007/s00376-016-6075-1

Yoo, C., Im, J., Park, S., and Quackenbush, L. J. (2018). Estimation of Daily Maximum and Minimum Air Temperatures in Urban Landscapes Using MODIS Time Series Satellite Data. *ISPRS J. Photogrammetry Remote Sensing* 137, 149–162. doi:10.1016/j.isprsjprs.2018.01.018

You, Q., Kang, S., Pepin, N., and Yan, Y. (2008). Relationship between Trends in Temperature Extremes and Elevation in the Eastern and central Tibetan Plateau, 1961-2005. *Geophys. Res. Lett.* 35, L14704. doi:10.1029/2007GL032669

Zhao, H., Huang, W., Xie, T., Wu, X., Xie, Y., Feng, S., et al. (2019). Optimization and Evaluation of a Monthly Air Temperature and Precipitation Gridded Dataset with a 0.025° Spatial Resolution in China during 1951-2011. *Theor. Appl. Climatol.* 138 (1-2), 491–507. doi:10.1007/s00704-019-02830-y

Zhou, Z., Shi, H., FuLi, Q. T. X., Li, T., Gan, T. Y., Liu, S., et al. (2020). Is the Cold Region in Northeast China Still Getting Warmer under Climate Change Impact. *Atmos. Res.* 237, 104864. doi:10.1016/j.atmosres.2020.104864

Conflict of Interest: The authors declare that the research was conducted in the absence of any commercial or financial relationships that could be construed as a potential conflict of interest.

Publisher's Note: All claims expressed in this article are solely those of the authors and do not necessarily represent those of their affiliated organizations, or those of the publisher, the editors and the reviewers. Any product that may be evaluated in this article, or claim that may be made by its manufacturer, is not guaranteed or endorsed by the publisher.

frontiers in Environmental Science

ORIGINAL RESEARCH
published: 18 January 2022
doi: 10.3389/fenvs.2021.744462

A Bayesian-Model-Averaging Copula Method for Bivariate Hydrologic Correlation Analysis

Yizhuo Wen[1], *Aili Yang*[1]*, *Xiangming Kong*[2] *and Yueyu Su*[1]

[1]Key Laboratory for Environmental Biotechnology of Higher Education of Fujian Province, Xiamen University of Technology, Xiamen, China, [2]College of Fundamental Science, Beijing Polytechnic, Beijing, China

A Bayesian-model-averaging Copula (i.e., BMAC) approach was proposed for correlation analysis of monthly rainfall and runoff in Xiangxi River watershed, China. The BMAC approach was formulated by incorporating existing Bayesian model averaging (i.e., BMA) method and Archimedean Copula techniques (e.g., Gumbel-Hougaard, Clayton and Frank Copulas) within a general bivariate hydrologic correlation analysis framework. In this paper, the BMA method was applied to determine the marginal distribution functions of variables, and the Copula method was used to analyze the correlation. Results showed that: 1) the BMA method could improve the representation of the marginal distribution of hydrological variables with smaller corresponding errors; 2) the predictive joint distributions of monthly rainfall and runoff was much better calibrated by the Gumbel Copula according to criteria of the root mean square error (i.e., RMSE), Akaike Information Criterion (i.e., AIC) values, Anderson-Darling test (i.e., AD test), and Cramer-von Mises test (i.e., CM test); and 3) the bivariate joint probability and return periods of rainfall and runoff based on the optimal Copula function was characterized and the monthly rainfall and runoff presented a strong positive correlation based on Kendall and Spearman's rank correlation coefficients. Therefore, the BMAC approach performed reasonably well and can be further used to simulate runoff values according to the historical and predicted rainfall data. Highlights: 1) A Bayesian-model-averaging Copula method is proposed for correlation analysis; 2) the monthly rainfall and runoff in Xiangxi River watershed has a positive correlation. 3) Gumbel Copula is the best in modelling the joint distributions in the Xiangxi River watershed.

Keywords: archimedean copula, Bayesian model averaging, rainfall and runoff, Xiangxi river watershed, climate change

OPEN ACCESS

Edited by:
Yurui Fan,
Brunel University London,
United Kingdom

Reviewed by:
Md Shahid Latif,
University of Western Ontario, Canada
Wei Fang,
Xi'an University of Technology, China

***Correspondence:**
Aili Yang
yangaililoy@gmail.com

Specialty section:
This article was submitted to Interdisciplinary Climate Studies, a section of the journal Frontiers in Environmental Science

Received: *20 July 2021*
Accepted: *29 November 2021*
Published: *18 January 2022*

Citation:
Wen Y, Yang A, Kong X and Su Y (2022) A Bayesian-Model-Averaging Copula Method for Bivariate Hydrologic Correlation Analysis. Front. Environ. Sci. 9:744462. doi: 10.3389/fenvs.2021.744462

1 INTRODUCTION

Investigating the hydrological variables relations is of vital significance for flood control and water resource management (Fan et al., 2018). Univariate hydrological frequency analysis procedures are important tools for analyzing the change rules between rainfall and runoff (Andres-Domenech et al., 2015; Shin et al., 2015; Zhou et al., 2020). However, it cannot reflect the variation of variables effectively because it overlooks the joint effects of variables. In addition, variables of real-world hydrological systems are complicated with many factors, such as correlations and multidimensional characteristics in hydrological processes (Zhang et al., 2006; Zhang et al., 2007; Remesan et al., 2009; Reusser et al., 2010; Takbiri and Ebtehaj, 2017; Sun and Zhou, 2020). Consequently, statistical theories of joint probability analysis were undertaken for developing more effective methods in this field.

As a sufficient probabilistic analysis method for correlated multivariate events, Copula function has been widely applied to hydrological simulations (Aghakouchak et al., 2010; Chebana et al., 2012; Ma et al., 2013; Serinaldi, 2013; Madadgar and Moradkhani, 2014; Qiang et al., 2014; Li and Zheng, 2016; Nasr and Chebana, 2019.; Yang et al., 2019). One of the advantages is that the calculations of marginal distributions and correlation analysis in Copula function are relatively independent, which is the successful key to make the joint analysis of multivariate methods more popular (Favre et al., 2004; Shiau et al., 2007; Chebana and Ouarda, 2009; Sraj et al., 2015; Sugimoto et al., 2016; Lei et al., 2018). On the other hand, the inherent uncertainty has been proved by practices existing in any single frequency distribution model structure (See and Abrahart, 2001; Wu et al., 2022), which directly affects the reliability of hydrological prediction (Zhou et al., 2018). Therefore, a multi-model method is proposed to deal with the inherent uncertainty for improving the accuracy of hydrological modeling and forecasting. Currently, the multi-model combination methods include: the weighted average method, linear regression, and neural networks (DeChant and Moradkhani, 2014; Xu et al., 2017; Zhou et al., 2021). These methods are mainly based on different deterministic theories to form a more accurate synthesis simulation results, but rarely consider the uncertainty of the model structure. Therefore, a better method to reflect the uncertainty of the multi-model method is particularly important.

The Bayesian model averaging (BMA) method has been widely used to construct a simulation process with better description of variables' probabilities in areas of management, medicine, meteorology, etc. (Tsai, 2010; Fang et al., 2018; Zhang and Yang, 2018). It can efficiently handle the marginal probability distribution function (Zhang and Yang, 2012) and produce more accurate model synthesis results for the uncertain model structure. In this case, the obtained marginal distribution functions can be directly used as inputs of the Copula function. However, the adjunct process has not been used to study the correlation between rainfall and runoff, and thus its applicability remains to be further verified.

When considering the structure of the marginal distribution in the present hydrological field, a single model is usually used to calculate the hydrological frequency curve of each variable (Xu et al., 2021). General models of distribution of unique hydrological probabilities include primarily Gamma distribution, generalized extreme value distribution, lognormal distribution, etc. (Lu et al., 2021). According to the principle of the BMA method, it is found that we can construct a more suitable expression form for specific hydrological variables through this method and use this distribution form as a marginal distribution to calculate the Copula joint distribution function (Lin et al., 2021; Rahimi et al., 2021). Compare with the non-parametric method. Non-parametric methods are generally robust but ineffective. The precision of the parameter estimates is high. Ramsey proposed a method for modelling the core and imported histograms into the model. This method not only improves the accuracy of the estimate, but also increases the design speed (Ramsey, 2012). The nonparametric method gives more attention to sample distribution as it does not take the form of distribution. However, when the quantity of data is different, the parameter method is more stable because of the *a priori* assumption that it responds to a specific distribution. When the amount of data is small, using the parameter method and considering its underestimated risk can obtain better results (Zeng, 2014). Therefore, in this paper, we compare the marginal distribution among the parameter, nonparametric, and BMA methods to choose the best method of this study.

The objective of this article is to develop a BMA Copula (BMAC) approach for correlation analysis with rainfall-runoff in the Xiangxi River, the largest tributary of the Yangtze River in the Hubei part of the Three Gorges Reservoir area. In this system, the marginal distributions of monthly rainfall and runoff are simulated by the BMA method with better description in probability of each variable. Then correlation analysis between rainfall and runoff is constructed by the Gumbel Copula method. This paper aims to: 1) determine the variables' marginal distribution functions; 2) estimate the two-dimensional Copula function parameters and calculate the Kendall and Spearman's rank correlation coefficients to ascertain the optimal Copula function; and 3) characterize the bivariate joint probability and return periods of rainfall and runoff based on the optimal Copula function.

2 METHODOLOGY

2.1 Bayesian Model Averaging Theory

2.1.1 Bayesian Model Averaging

BMA is a statistical analysis method and can be used to infer a probabilistic prediction. It is a statistical analytical method that considers the uncertainty of the model itself. In this paper, the BMA method is applied to simulate the streamflow. Suppose that y is the forecasted variable, $\boldsymbol{F} = (f_1, f_2, \cdots f_k)$ is the all considered model predictions, and $\boldsymbol{M} = (y_1, y_2, \cdots y_t)$ is a given empirical probability distribution, where y_t is the experience distribution probability at t time. Considering the inherent uncertainty of a model, the posterior distribution of y under a given empirical probability distribution condition can be presented as:

$$p(y|F, M) = \sum_{k=1}^{k} p(f_k|M) p_k(y|f_k, M) \tag{1}$$

where $p(f_k|M)$ represents the posterior probability of a single distribution model f_k, $p_k(y|f_k, M)$ means the posterior distribution of y under a given model prediction f_k and data set M.

Let ω_k represent $p(f_k|M)$ with $\sum_{k=1}^{K} \omega_k = 1$. The posterior mean value and variance of the BMA prediction can be expressed as (Raftery et al., 2003; Duan et al., 2006):

$$E(y|M) = \sum_{k=1}^{K} p(f_k|M) E[p_k(y|f_k, M)] = \sum_{k=1}^{K} \omega_k f_k \tag{2}$$

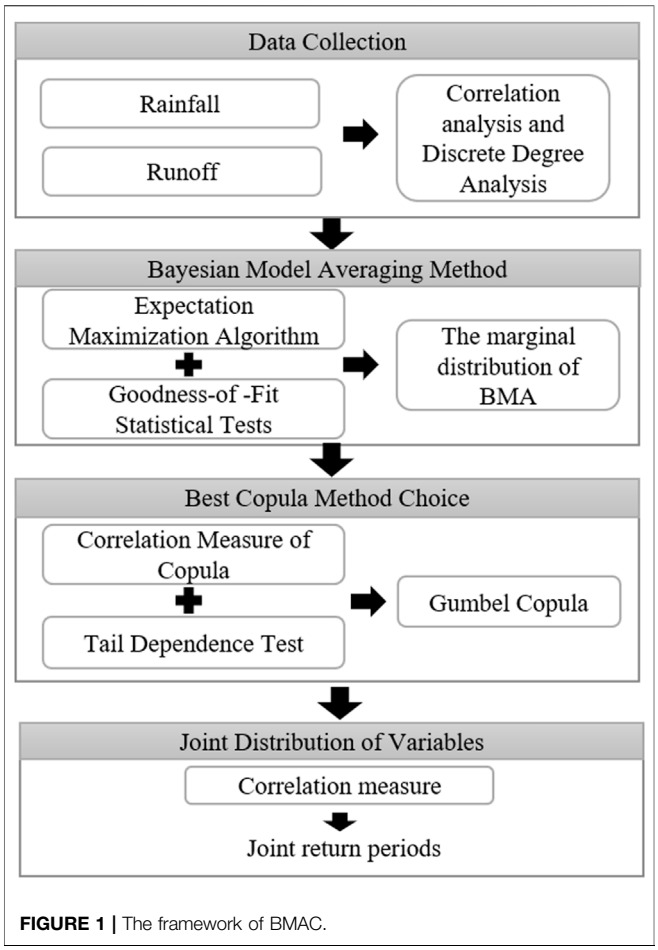

FIGURE 1 | The framework of BMAC.

$$Var(y|M) = \sum_{k=1}^{K}\omega_k\left(f_k - \sum_{i=1}^{K}\omega_i f_i\right)^2 + \sum_{k=1}^{K}\omega_k\sigma_k^2 \tag{3}$$

where σ_k^2 represents the variable variance when the empirical frequency and model prediction are M and f_k, respectively. The BMA mean value prediction can be calculated by the weighted average probability distributions for different optimal simulation. The two parts denoted by $\sum_{k=1}^{K}\omega_k(f_k - \sum_{k=1}^{K}\omega_i f_i)^2$ and $\sum_{k=1}^{K}\omega_k\sigma_k^2$ in **Eq. 3** mean the error between models and error of the model itself individually. Compared to deterministic multi-model combinations, BMA possesses more reliability in reflecting the uncertainty of distribution models.

2.1.2 Expectation Maximization Algorithm

To effectively calculate the weight and variance of BMA, the expectation-maximization (EM) method is introduced in this paper. EM is an iterative calculation method and has been widely used (Bilmes, 1998) to calculate the maximum likelihood estimation, and the obtained results show good effect especially in dealing with a great number of missing data. In detail, the EM algorithm can be illustrated as follows.

Considering the stability and convenience of calculation, the EM algorithm uses log-likelihood function (Duan et al., 2006). Assume the prediction error in time and space is independent, the log-likelihood function can be formulated as follows (Duan et al., 2006):

$$\ell(\omega_1, \cdots, \omega_k, \sigma^2) = \sum_{t=1}^{T}\log\left(\sum_{k=1}^{K}\omega_k g_k\left(y_t|f_{k,t}\right)\right) \tag{4}$$

Assume $Z_{k,t}$ is an unobserved variable, if at time t, f_k is the best prediction model, then $Z_{k,t} = 1$; otherwise, $Z_{k,t} = 0$. At any time t, only one of $\{Z_{1,t}, \cdots, Z_{k,t}\}$ is equal to 1 and the others are equal to zero. The key of applying the EM method is to switch steps between the expectation and maximization. It starts under an initial guess, such as assuming a value of $\theta^{(0)}$ for parameter θ. In the expectation (E) step, $Z_{k,t}$ is estimated by the given current guess value of θ. In the maximization (M) step, θ is estimated by the given current values of $Z_{k,t}$. These two steps are repeated until a predetermined accuracy meets the requirement. The detailed EM computation process is as follows.

Step 1. Initialization:

$$\text{Set}\quad j = 0, \omega_k^{(j)} = \frac{1}{k}, \sigma_k^{2}(j) = \frac{1}{k}\sum_{t=1}^{T}\frac{\left(\sum_{k=1}^{K}\left(y_t - f_{k,t}\right)^2\right)}{T} \tag{5}$$

where T is the number of data, and j is the number of iterations.

Step 2. Calculate the initial likelihood:

$$\begin{aligned}\ell\left(\theta^{(j)}\right) &= \log\left(\sum_{k=1}^{K}\omega_k \cdot p_k(y|f_k, M)\right)\\ &= \log\left(\sum_{k=1}^{K}\omega_k \cdot \sum_{t=1}^{T}g\left(y_t|f_{k,t}, \sigma_k^{(j)}\right)\right)\end{aligned} \tag{6}$$

Step 3. Implementation of the E-step operation:

$$\text{Set}\, j = j+1, Z_{k,t}^{(j)} = \frac{g\left(y_t|f_{k,t}, \sigma_k^{(j-1)}\right)}{\sum_{k=1}^{K}g\left(y_t|f_{k,t}, \sigma_k^{(j-1)}\right)}\quad k = 1, 2, \cdots, K,\quad t = 1, 2, \cdots, T \tag{7}$$

Step 4. Perform the M-step operation:

Calculate the weights of the single prediction model:

$$\omega_k^{(j)} = \frac{1}{T}\sum_{t=1}^{T}Z_{k,t}^{(j)} \tag{8}$$

Update the single forecast model variance:

$$\sigma^2(j) = \frac{\sum_{t=1}^{T}Z_{k,t}^{(j)} \cdot \left(y_t - f_{k,t}\right)^2}{\sum_{t=1}^{T}Z_{k,t}^{(j)}} \tag{9}$$

Update the value of the likelihood function $\ell(\theta^{(j)})$.

Step 5. Check convergence:

If $\ell(\theta^{(j)}) - \ell(\theta^{(j-1)})$ is less than or equal to 10^{-4}, then stop the operation; else return to the third step.

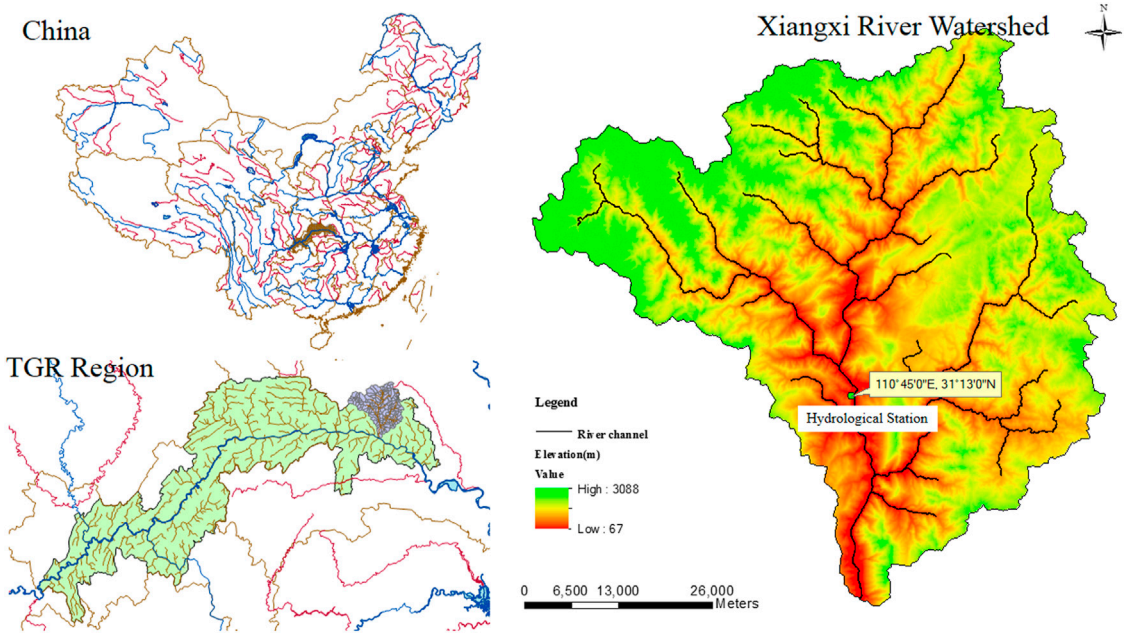

FIGURE 2 | The Studied are (Fan et al., 2016).

Readers can refer to McLachlan and Krishnan (McLachlan and Krishnan, 1997) for more detailed information of the EM algorithm.

2.1.3 Kernel Density Estimation

In statistics, the kernel density estimation (KDE) is a non-parametric way to estimate the probability density function of a random variable. KDE is a fundamental data smoothing problem where inferences about the population are made, based on a finite data sample (Li et al., 2022). Among the many non-parametric methods currently used, the KDE method proposed by Guo et al. (1996) is the most widely used, and the effect is the most ideal.

The estimation formula of the univariate kernel probability density function:

$$\hat{f}_x(x) = \frac{1}{nh}\sum_{i=1}^{n} k\left(\frac{x - x_i}{h}\right) \tag{10}$$

where n is the length of observed data x_i; $K(\cdot)$ is the kernel density function; and h is the window width, it determines the variance of the kernel function.

2.2 Copula Function Theory

Copula theory was proposed by Sklar (1959), which has many types of Copula functions, such as normality of Copula, t-Copula functions, and Archimedean Copula function family (Nelsen, 1999). Among them, Archimedean Copula function family, including Gumbel-Hougaard Copula function, Clayton Copula function, and Frank Copula functions, has characteristics of simplified structure, diversification, and practicability, which lead to relatively simple processes in constructing corrections among variables (Xie et al., 2020). Consequently, the Archimedean Copula function family could be an important method for hydrologic frequency analysis.

2.2.1. Archimedean Copula Function

Let u_i be the variable margin, θ be the parameter of the Copula function, the cumulative probability distribution of the three Archimedean Copula functions mentioned above can be expressed as follows:

(1) Gumbel-Hougaard Copula function

$$C(u_1, u_2 \cdots, u_t) = \exp\left\{-\left[(-\ln(u_1))^\theta + (-\ln(u_2))^\theta + \cdots + (-\ln(u_t))^\theta\right]^{\frac{1}{\theta}}\right\}; \theta \in [1, \infty) \tag{11}$$

$$\text{Expression of generator:} \quad \phi(t) = [-\ln(t)]^\theta \tag{12}$$

(2) Clayton Copula function

$$C(u_1, u_2, \cdots, u_t) = \left\{u_1^{-\theta} + u_2^{-\theta} + \cdots + u_t^{-\theta} - (t-1)\right\}^{\frac{1}{\theta}}; \theta \in (0, \infty)^\infty \tag{13}$$

$$\text{Expression of generator:} \quad \phi(t) = t^{-\theta} - 1 \tag{14}$$

(3) Frank Copula function

$$C(u_1, u_2, \cdots u_t) = -\frac{1}{\theta}\ln\left\{1 + \frac{[\exp(-\theta u_1) - 1][\exp(-\theta u_2) - 1]\cdots[\exp(-\theta u_t) - 1]}{[\exp(-\theta) - 1]^{t-1}}\right\}; \theta \in R \tag{15}$$

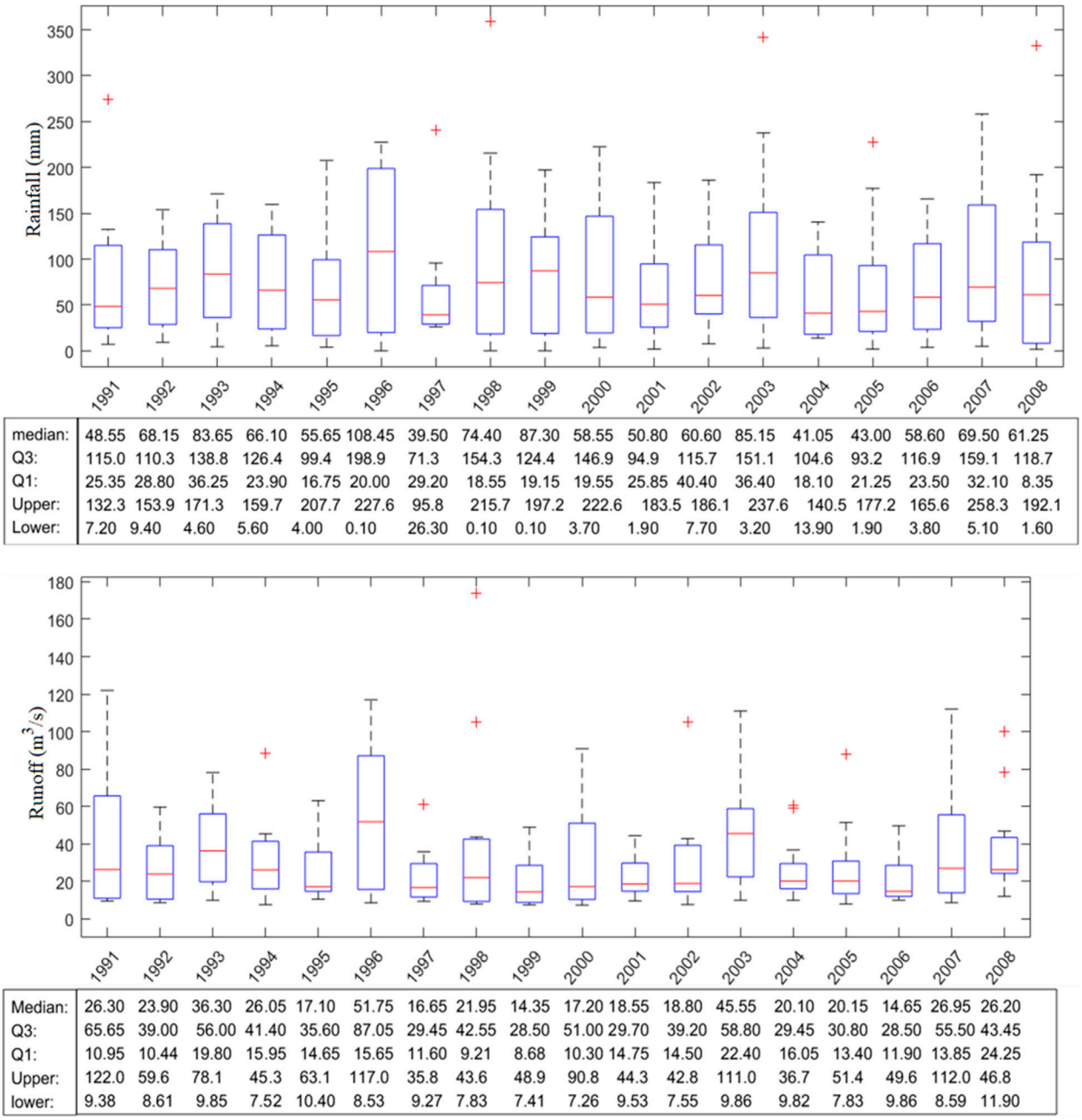

FIGURE 3 | The boxspots of monthly rainfall and runoff in the Xiangxi River watershed. Median id the midlevel line of the data, Upper and Lower are the maximum and minimum values, Q_1 and Q_3 are the lower and upper quantities.

$$\text{Expression of generator:} \quad \varphi = -\ln\frac{\exp(-\theta t)-1}{\exp(\theta)-1} \tag{16}$$

2.2.2 Correlation Measure of Copula

Correlation measure of random variables is used to describe the mutual dependence between random variables. There are many test metrics, in this study Kendall's rank correlation coefficient τ and Spearman's rank correlation coefficient ρ are used to evaluate the correlation of the streamflow variables. In detail, the corresponding Kendall's rank correlation coefficient τ and Spearman's rank correlation coefficient ρ_s for Copula function $C(u, v)$ can be expressed as follows:

$$\tau = 4\int_0^1\int_0^1 C(u,v)dC(u,v) - 1 \tag{17}$$

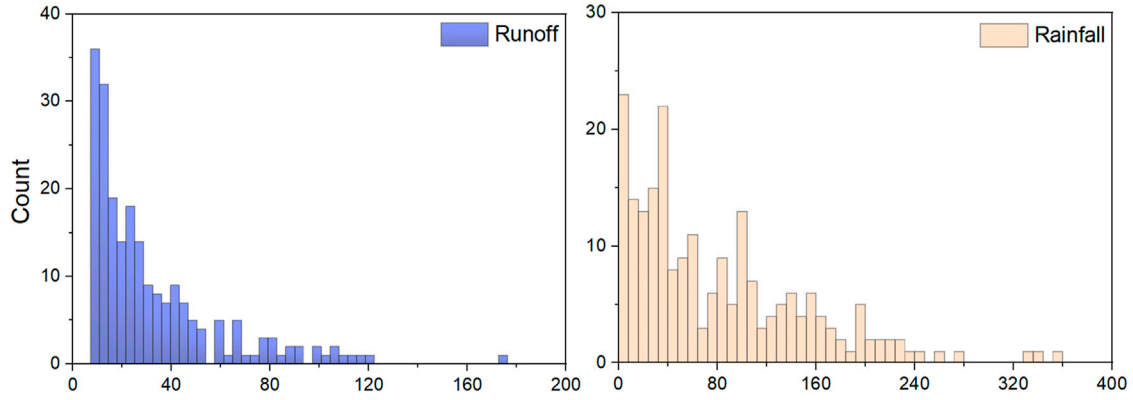

FIGURE 4 | The Histogram of mothly rainfall and runoff in the Xiangxi River watershed.

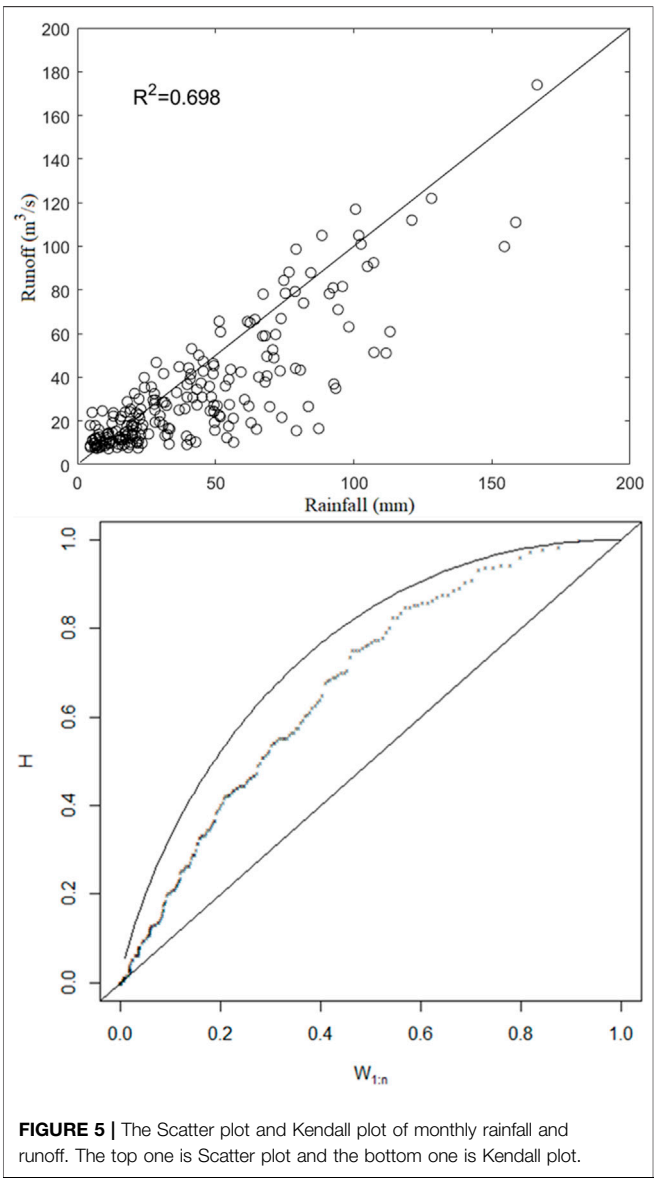

FIGURE 5 | The Scatter plot and Kendall plot of monthly rainfall and runoff. The top one is Scatter plot and the bottom one is Kendall plot.

TABLE 1 | The fitting parameters of probability distributions.

Probability distribution	Parameter	Rainfall	Runoff
Gam	a	32.76	2.91
	b	1557.46	31363.50
Gev	k	−0.34	0.18
	σ	8899.63	3.65
	μ	48177.10	63161.80
Log	μ	10.82	11.24
	σ	0.178	0.62
Weight			
BMA	Gam	0.9999996	0.00001
	Gev	3.90E-07	0.49844
	Log	6.79E-14	0.50155

$$\rho_s = 12\int_0^1\int_0^1 uvdC(u,v) - 3 = 12\int_0^1\int_0^1 C(u,v)dudv - 3 \quad (18)$$

2.2.3 Estimation of Copula Function Parameter

To estimate the parameter of Copula function, the exact maximum likelihood (EML) method is used (Dupuis, 2007). If the joint distribution function of t-dimensional continuous random variables $x_1, x_2, \cdots x_t$ can be expressed as $C(u_1, u_2, \cdots u_t)$, its maximum likelihood estimate can be calculated as follows (Dupuis, 2007):

Step 1. Establish the relevant likelihood function

The joint density function is expressed as:

$$c[(u_1, u_2, \cdots u_t); (\theta_1, \theta_2, \cdots, \theta_t), \alpha] = \frac{\partial^t C[(u_1, u_2, \cdots u_t); (\theta_1, \theta_2, \cdots, \theta_t), \alpha]}{\partial u_1 \partial u_2 \cdots \partial u_t} \quad (19)$$

Likelihood function is expressed as:

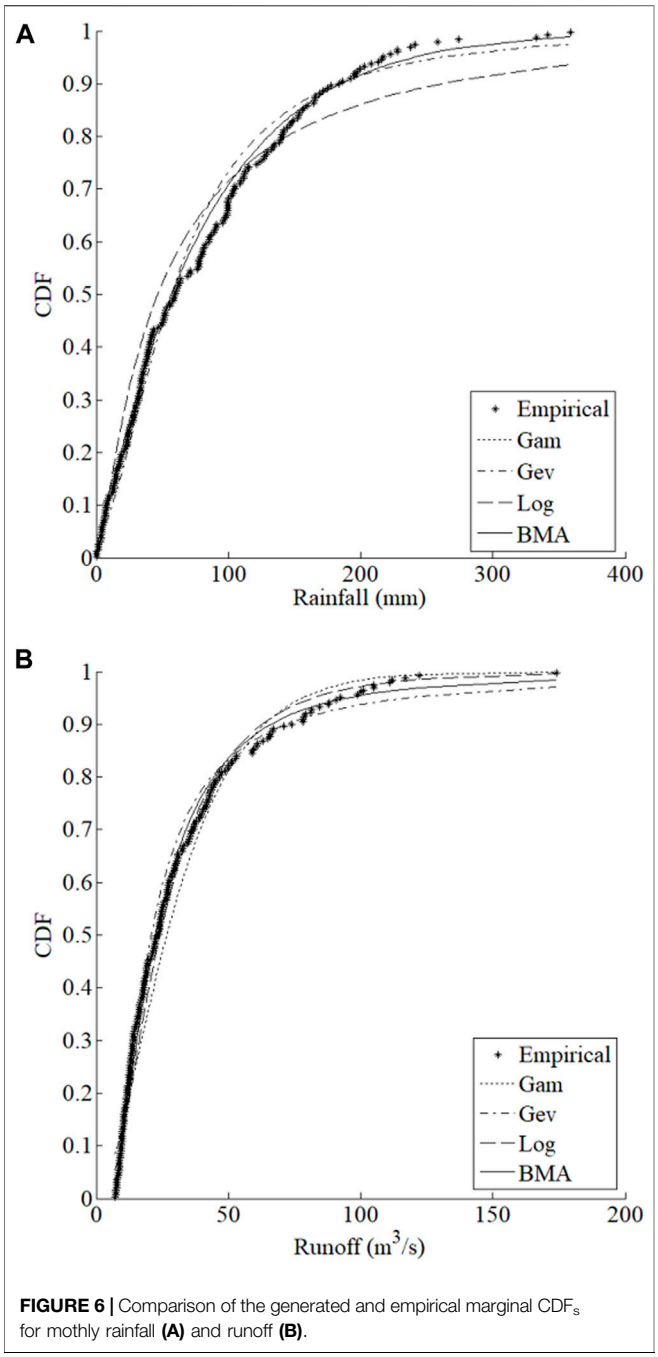

FIGURE 6 | Comparison of the generated and empirical marginal CDF_s for mothly rainfall **(A)** and runoff **(B)**.

TABLE 2 | The D, RMSE and AIC analysis for marginal distributions.

Probability distribution	D		RMSE		AIC	
	Rainfall	Runoff	Rainfall	Runoff	Rainfall	Runoff
Gam	0.061	0.097	0.024	0.056	−1624.15	−1242.93
Gev	0.083	0.065	0.038	0.0319	−1404.66	−1481.28
Log	0.097	0.079	0.059	0.0349	−1222.06	−1445.28
KDE	0.088	0.106	0.026	0.0313	−1570.65	−1490.51
BMA	0.060	0.061	0.023	0.0245	−1621.13	−1596.99

$$L[(\theta_1, \theta_2, \cdots, \theta_t), \alpha] = \prod_{i=1}^{n} c[(u_{i1}, u_{i2}, \cdots, u_{it}); (\theta_1, \theta_2, \cdots, \theta_t), \alpha] \tag{20}$$

Correspondingly, the log-likelihood function can be expressed as:

$$\ln L[(\theta_1, \theta_2, \cdots, \theta_t), \alpha] = \sum_{i=1}^{n} \ln c[(u_{i1}, u_{i2}, \cdots, u_{it}); (\theta_1, \theta_2, \cdots, \theta_t), \alpha] \tag{21}$$

Step 2. Solve the likelihood function

$$\left(\hat{\theta}_1, \hat{\theta}_2, \cdots, \hat{\theta}_t\right), \hat{\alpha} = \arg\max \ln L[(\theta_1, \theta_2, \cdots, \theta_t), \alpha] \tag{22}$$

where: $(\theta_1, \theta_2, \cdots \theta_t)$ are the unknown parameters of the distribution function for each margin; α is the associated unknown parameter in the Copula function.

2.3 Goodness-Of-Fit Statistical Tests

In order to perform the goodness-of-fit statistic tests for both univariate distribution and Copula functions the root mean square error (RMSE) and Akaike Information Criterion (AIC) are adopted to assess the validation of the BMAC method. RMSE can quantitatively analyze the results when the graph fitting effect is similar. To evaluate the performance and select the best fitted Copulas, the goodness-of-fit statistics test is conducted based on AIC (Akaike, 1974) and Cramér von Mises statistics (Genest et al., 2009).

$$MSE = \frac{1}{N-k} \sum_{i=1}^{N} \left(F_{em}(x_{i1}, x_{i2}, \cdots, x_{it}) - C(u_{i1}, u_{i2}, \cdots, u_{it})\right)^2 \tag{23}$$

$$RMSE = \sqrt{MSE} \tag{24}$$

where $F_{em}(x_{i1}, x_{i2}, \cdots, x_{it})$ is the value of empirical joint distribution; $C(u_{i1}, u_{i2}, \cdots u_{it})$ is the value of the predicted joint distribution; MSE is the mean square error; N is the length of the observed data; k is the number of unknown parameters in the model.

$$AIC = N \ln(MSE) + 2k \tag{25}$$

The Kolmogorov-Smirnov test (K-S test) is chosen because it is a useful nonparametric hypothesis test, which is primarily used to test if a set of samples comes from some probability distribution (Miller, 1956).

$$D = \max_{1 \le i \le n} \left| F^{est}\left(x \le x_{(i)}\right) - F^{obs}\left(x \le x_{(i)}\right) \right| \tag{26}$$

where $F^{est}(x \le x_{(i)})$ is the value of theoretical probability distribution; $F^{obs}(x \le x_{(i)})$ is the value of the empirical probability distribution; n is the length of the data.

The Anderson-Darling test (AD test) also has been chosen because of its excellent properties against a variety of alternatives, the test statistic is as follows (D'Agostino, 1986):

$$A_n^2 = -n - \frac{1}{n} \sum_{i=1}^{n} (2i-1) \cdot \left[\ln\left[F_s\left(H_{(i)}\right)\right] + \ln\left(1 - F_s\left(H_{(n-i+1)}\right)\right)\right] \tag{27}$$

TABLE 3 | Parameters estimation and correlation analysis of copula function.

Correlation	Ellipse copula		Archimedes copula		
	Gaussian copula	T Copula	Clayton copula	Gumbel copula	Frank copula
Upper	0.5283153	0.5293994	0.6655733	0.6695867	#
Lower	0.417623	0.4191937	0.6100611	0.7516461	#
Kendall	0.578918	0.5807679	0.4240182	0.5931158	0.5864246
Spearman	0.7738921	0.7694191	0.5938393	0.7799526	0.7887916

where: $H_{(1)} \le H_{(2)} \le \cdots \le H_{(n)}$ are values in ascending order; F_s is the distribution function of $\chi^2(2)$.

Specific calculation steps are as follows:

Step 1. Calculate the marginal distribution functions F_X and F_Y by the univariate empirical formula.

Step 2. Calculate $H(X,Y)$, obey $\chi^2(2)$ distribution.

$$H(X,Y) = \left[\Phi^{-1}(F_X)\right]^2 + \left[\Phi^{-1}(C(F_Y|F_X))\right]^2 \quad (28)$$

where: Φ^{-1} is the inverse function of the standard normal distribution.

Step 3. Calculate statistic value A_n^2.

Step 4. Estimate Copula parameter θ based on the marginal distribution function.

Step 5. Simulate and generate Copula random samples with Rosenblatt's transformation test method, find new Copula function parameter $\hat{\theta}$.

Step 6. Calculate a new $H^*(X^*, Y^*)$, and then calculate statistic value $\hat{A}_n^2$.

Step 7. Repeat steps 3 to 6 m times, obtain a sequence of $\hat{A}_n^2$, put the sequence in ascending order, and calculate the critical and statistical value of each sub-site.

Step 8. Compare the relationship between the statistic $\hat{A}_n^2$ and critical statistics. If the statistical value is lower than the critical one, the distribution of the results can be accepted; otherwise, reject the distribution results.

2.4 Bayesian-Model-Averaging Copula (BMAC) Method

In this study, the BMAC method would be proposed by combining the BMA and Copula methods into a general framework. In detail, the BMA method is used to determine the marginal distributions of monthly rainfall and runoff, and the Archimedean Copula method can be used to construct the joint distribution of monthly rainfall of runoff. Correspondingly, the BMAC method involves four steps: 1) determining the marginal distributions of monthly rainfall and runoff based on the principle of BMA and generating the values of weight through the EM method, 2) establishing the joint distributions by the Archimedean Copula (e.g., Gumbel-Hougaard Copula, Clayton Copula, and Frank Copula) method, 3) estimating the values of the Copula parameter θ through the maximum likelihood method, and 4) performing the goodness-of-fit statistic tests by RMSE, AIC, and AD test. The framework of the BMAC is shown in **Figure 1**.

3 CASE STUDY

3.1 Overview of the Studied Area

The Xiangxi River basin is located between 30.96 ~ 31.67° N and 110.47 ~ 111.13°E in the Hubei part of China, being the largest tributary of the Yangtze River in the Three Gorges Reservoir area (see **Figure 2**). It originates in the Shennongjia Nature Reserve, with the mainstream length of 94 km and a catchment area of 3,099 km^2 (Han et al., 2014). This region experiences a northern subtropics climate, and the main rainfall season is from May to September with the annual precipitation of 1,100 mm (Xu et al., 2009). In addition, the hydrological station mostly covering this river is called the Xiangshan Hydrological Station (110.45°E, 31.13°N).

In order to provide decision support for flood control and water resource management of the Xiangxi River basin, the hydrological frequency analysis of this region would be studied based on daily rainfall and runoff data (1991–2008) from Xingshan Hydrological Station in this study (see **Figure 3**). **Figure 3** demonstrates that rainfall and runoff in 1996 were relatively high, while rainfall and runoff in 1997 were relatively low. The annual distribution of runoff is primarily concentrated. The annual distribution of rainfall is rather dispersed. Annual rainfall and runoff during 1996 and 2007 were particularly sparse. Rainfall and runoff are strongly correlated. **Figure 4** demonstrates that the distribution of monthly rainfall and runoff are similar. The scatter plot demonstrates that the R-square value is 0.698 and the AUK value of the Kendall plot is 0.667. Both of them show a positive correlation (**Figure 5**).

3.2 Results Analysis

3.2.1 Comparison of Marginal Distributions

In the procedure of hydrological frequency analysis, the monthly rainfall and runoff probability distributions in the Xiangxi River basin are first estimated by the Gamma, the generalized extreme value, and the lognormal distributions, respectively. And then, the BMA-based marginal distributions are obtained according to the three estimated distributions. **Table 1** shows the fitting parameters of probability distributions.

Based on the weights and distribution parameters presented above, the BMA-based marginal distributions of monthly rainfall and runoff can be obtained. The Gamma distribution may account for a major proportion (99.99%) to produce the BMA-based marginal distribution of monthly rainfall; while the generalized extreme value distribution and lognormal distribution may account for almost the same proportion to produce the BMA-based marginal distribution of monthly runoff.

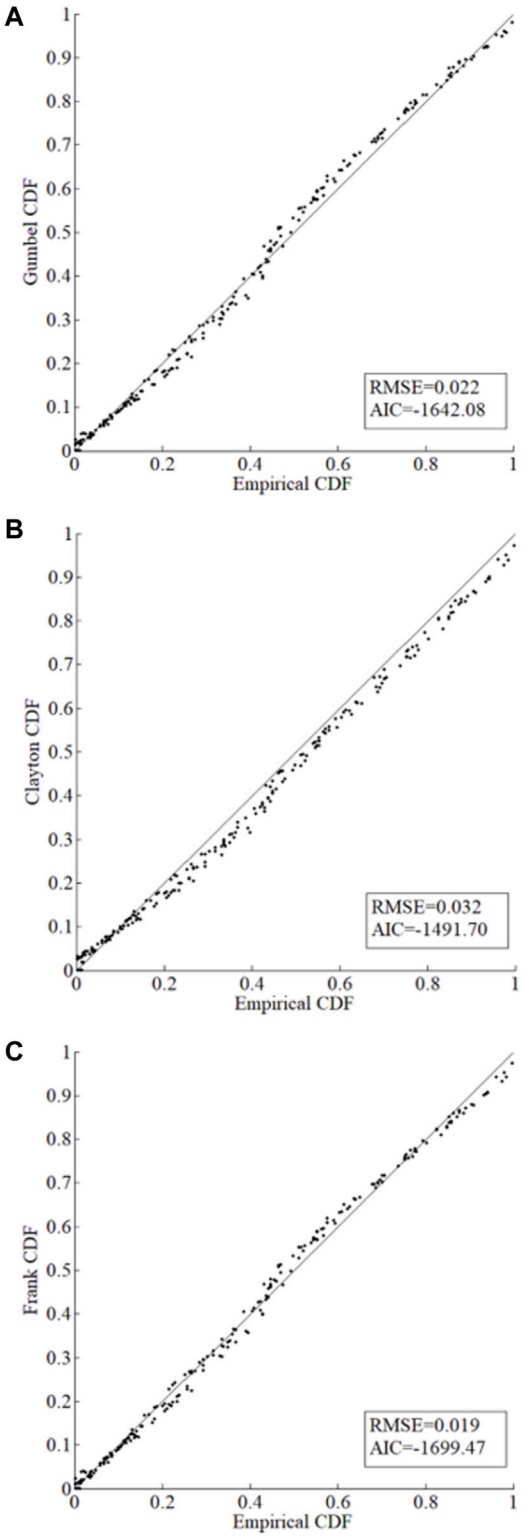

FIGURE 7 | Comparison of the theotrical and empircal joint CDFs for rainfall and runoff in Xiangxi River. **(A)** Gumbell-Hougard-Copula-based joint distribution. **(B)** Frank-Copula-based joint distribution, respectively.

The comparison of empirical and generated marginal cumulative distribution functions (CDFs) for monthly rainfall and runoff is shown in **Figure 6**. It indicates that the BMA-based marginal distribution may appropriately represent the univariate rainfall and runoff probability distributions. In order to clearly clarify, the D, RMSE, and AIC values for the marginal distributions obtained by the four methods are also calculated and presented in **Table 2**. In addition, to compare with the non-parametric methods, the KDE method is also calculated in the same way. Results D show that only the GEV and BMA methods pass the K-S test (the upper boundary of D is 0.092 while alpha is 0.05) in both rainfall and runoff. The obtained results indicate the corresponding errors of the BMA method are relatively smaller suggesting the accuracy of the marginal distributions generated by the BMA method is very excellent.

3.2.2 Comparison of Joint Distributions

After determining marginal distributions, the joint probability distributions of monthly rainfall and runoff in the Xiangxi River can be estimated by a Copula function. The estimation parameters for each Copula function are calculated based on the maximum likelihood estimation theory. In addition, according to the obtained parameters, the correlation coefficients can be calculated. Results are given in **Table 3**. It can be seen that the Kendall's rank correlation coefficient ranges from 0.42 to 0.59 and the Spearman's rank correlation coefficient ranges from 0.56 to 0.78. Therefore, it can be concluded that the monthly rainfall and runoff of the Xiangxi River have a relatively strong positive correlation.

According to **Table 3**, Gumbel-Hougaard-Copula-based joint distribution and Frank-Copula-based joint distribution are superior to the Clayton one based on the Kendall correlation and the Spearman correlation. Moreover, it shows that the estimation of the upper tail correlation coefficient should select the Gumbel Copula, the number is 0.6696. The estimation of the lower tail correlation coefficient should select

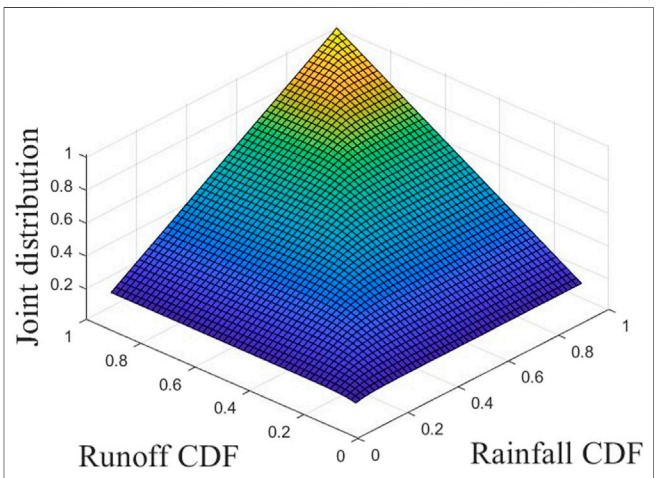

FIGURE 8 | The joint CDFs of rainfall and runoff.

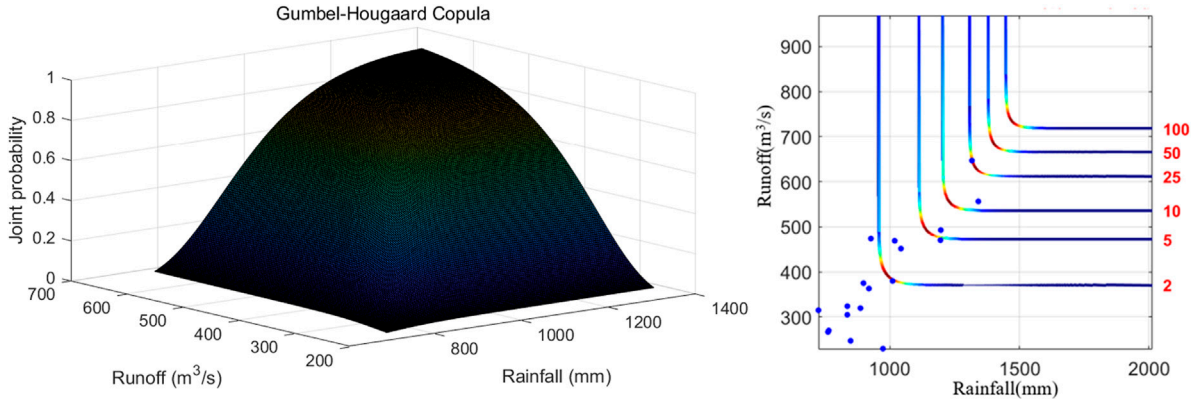

FIGURE 9 | Joint probability density and return periods of rainfall and runoff.

TABLE 4 | Goodness-of-fit of BMAC.

Fit test	Test statistics	α-the critical value of sub-sites				
		0.20	0.15	0.10	0.05	0.01
AD	0.97	1.47	1.69	1.97	2.30	3.55
CM	0.12	0.23	0.269	0.30	0.41	0.68

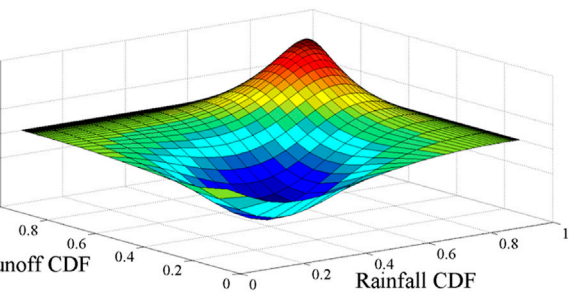

FIGURE 10 | Comparison of BMAC and MEGHC.

the Gumbel Copula, the number is 0.7516. Obviously, there are both upper tail correlation and lower tail correlation in the Xiangxi River. This conforms to research by Yang et al. (2016). Goodness-of-fit tests of empirical joint CDFs and theoretical joint CDFs are calculated for further analysis (as shown in **Figure 7**).

Comparing the results shown in **Figure 7**, it can be known that the joint distribution by Frank-Copula is close to the one by Gumbel-Hougaard-Copula in quantifying the relevant characteristics of monthly rainfall and runoff of the Xiangxi River. The RMSE of the Gumbel-Hougaard-Copula is less than the Clayton copula. The Frank-Copula function has no tail correlation and cannot capture the tail correlation between variables according to Xue (2018). Gumbel Copula performs better in the upper correlation while Clayton Copula performs better in the lower correlation (Jondeau, 2016). Therefore, the Gumbel Copula function would be chosen to construct the joint distribution of monthly rainfall-runoff pairs. The corresponding results are plotted and shown in **Figure 8**. **Figure 9** shows the combined probability density and return period of rainfall and runoff using the Gumbel Copula. It indicates that the extreme value of annual precipitation or annual runoff, the joint probability density is relatively small. When the annual runoff is constant, the greater the annual precipitation, the longer the time of return period is. In addition, the largest rainfall of observed data is 1,341.7 mm, the runoff of that year is 556.36 m^3/s. The return period is about 10 years, which is reasonable.

In this study, the AD test and the CM test also have been selected to investigate the suitability of the BMAC-based joint distributions in describing the dependencies for different rainfall-runoff pairs. The results are displayed in **Table 4**, and statistics A_n^2 are less than threshold values $A_{n,0.1}^{2(*)}$ ($\alpha = 0.1$) and $A_n^{2(*)}$ ($\alpha = 0.05$), where α is the significant level. Thus, the null hypothesis H_0 would be accepted. In total, it can be concluded that BMAC has a distinct superiority in modelling variable pairs.

3.2.3 Comparison of BMAC and MEGHC

In order to further clarify the efficiency of the BMAC method, a Maximum Entropy-Gumbel-Hougaard Copula (MEGHC) method proposed by Kong et al. (2015) has been applied for comparison. Accordingly, two joint distributions can be generated by the two methods, and the bias value between the two methods also can be obtained (shown in **Figure 10**). From **Figure 10**, the results are quite close to each other, and the great deviation value (i.e., absolute error) is 0.03, which illustrates that both of the two methods can be used to generate the joint distribution of the rainfall and runoff because of the best fitting effect. It also can be found that, under the condition of the CDF interval being 0–0.4, results obtained by the BMAC method are superior to the MEGHC method; while the CDF interval being 0.9–1, the MEGHC method may converge much faster. To some extent, the MEGHC method can better capture the characteristics of the upper tail dependence, which plays a great role in flood and drainage control and watershed design

work (Kong et al., 2015). However, in the situation of representing the uncertainty of the model structure, it is hard to find a suitable distribution to capture the characteristic of the hydrologic variable. Comparatively, the BMAC method can obtain a synthetic simulation result especially in exactly reflecting the variables' correlations.

4 CONCLUSION

In this study, a BMAC method has been proposed for assessing correlations of bivariate variables in hydrological processes. Through incorporating BMA and Copula functions within a general framework, BMAC can determine the marginal distribution functions of variables, and meanwhile analyze the correlation. To demonstrate the applicability, the developed BMAC method also has been adopted to investigate the hydrological frequency analysis of the Xiangxi River basin. The specific conclusions can be summarized as follows:

(1) Compared with the empirical and nonparametric marginal CDFs, the Bayesian model averaging method can improve the representation of the marginal distribution of hydrological variables and comprehensively capture the shape of empirical CDF with smaller corresponding errors.
(2) The goodness-of-fit statistical tests, consisting of RMSE, K-S, and AD test, indicate that the BMAC method is suitable for describing the statistical probabilities and the dependencies in the historical data of the Xiangxi River, China.
(3) There is a relatively strong positive correlation existing between the monthly rainfall and runoff. The Gumbel Copula would be best for modelling the joint distributions of monthly rainfall and runoff.
(4) Compared with the MEGHC method proposed by Kong et al. (2015), the BMAC method can obtain more accurate synthesis results when the model structure is evaluated as uncertain.
(5) The accuracy of the BMAC method in modelling the joint distribution of hydrological variables would be influenced by the performance of the marginal distribution of the variables and the algorithm used for estimating the unknown parameters in Copula functions. Consequently, further studies are required to analyze the uncertainty of the calculation process.

DATA AVAILABILITY STATEMENT

The raw data supporting the conclusion of this article will be made available by the authors, without undue reservation.

AUTHOR CONTRIBUTIONS

YW conceived and designed the method of BMAC, collected the data and analyzed the results, and wrote the manuscript. AY conceived and designed the method. XK collected the data and analyzed the results. YS analyzed the results. All authors read and approved the final manuscript.

FUNDING

This research was funded by the Natural Science Foundation of Fujian Province, China (2021J011180).

ACKNOWLEDGMENTS

The authors thank the support from the Hydrologic Bureau of Xingshan County.

REFERENCES

Aghakouchak, A., Bárdossy, A., and Habib, E. (2010). Conditional Simulation of Remotely Sensed Rainfall Data Using a Non-gaussian V-Transformed Copula. *Adv. Water Resour.* 33, 624–634. doi:10.1016/j.advwatres.2010.02.010

Akaike, H. (1974). A New Look at the Statistical Model Identification. *IEEE Trans. Automat. Contr.* 19, 716–723. doi:10.1109/tac.1974.1100705

Andrés-Doménech, I., García-Bartual, R., Montanari, A., and Marco, J. B. (2015). Climate and Hydrological Variability: the Catchment Filtering Role. *Hydrol. Earth Syst. Sci.* 19, 379–387. doi:10.5194/hess-19-379-2015

Bilmes, J. A. (1998). *A Gentle Tutorial of the EM Algorithm and its Application to Parameter Estimation for Gaussian Mixture and Hidden Markov Models*. Berkeley: Department of Electrical Engineering and Computer Science U. C, 1–13.

Chebana, F., Dabo-Niang, S., and Ouarda, T. B. M. J. (20122012). Exploratory Functional Flood Frequency Analysis and Outlier Detection. *Water Resour. Res.* 48. doi:10.1029/2011WR011040John Wiley & Sons

Chebana, F., and Ouarda, T. B. M. J. (2009). Index Flood-Based Multivariate Regional Frequency Analysis. *Water Resour. Res.* 45, W10435. doi:10.1029/2008WR007490

D'Agostino, R. (1986). *Goodness-of-Fit-Techniques*. Cleveland, OH, USA: CRC Press. ISBN 978-135-144-455-2.

Dai, Q., Han, D., Rico-Ramirez, M., and Srivastava, P. K. (2014). Multivariate Distributed Ensemble Generator: A New Scheme for Ensemble Radar Precipitation Estimation over Temperate Maritime Climate. *J. Hydrol.* 511, 17–27. doi:10.1016/j.jhydrol.2014.01.016

DeChant, C. M., and Moradkhani, H. (2014). Toward a Reliable Prediction of Seasonal Forecast Uncertainty: Addressing Model and Initial Condition Uncertainty with Ensemble Data Assimilation and Sequential Bayesian Combination. *J. Hydrol.* 519, 2967–2977. doi:10.1016/j.jhydrol.2014.05.045

Duan, Q., Ajami, N. K., Gao, X., and Sorooshian, S. (2007). Multi-model Ensemble Hydrologic Prediction Using Bayesian Model Averaging. *Adv. Water Resour.* 30, 1371–1386. doi:10.1016/j.advwatres.2006.11.014

Dupuis, D. J. (2007). Using Copulas in Hydrology: Benefits, Cautions, and Issues. *J. Hydrologic Eng.* 12, 383–393. doi:10.1061/(ASCE)1084-0699(2007)12:4(381)

Fan, Y., Huang, G., Zhang, Y., and Li, Y. (2018). Uncertainty Quantification for Multivariate Eco-Hydrological Risk in the Xiangxi River within the Three Gorges Reservoir Area in China. *Engineering* 4, 617–626. doi:10.1016/j.eng.2018.06.006

Fan, Y. R., Huang, W. W., Huang, G. H., Huang, K., Li, Y. P., and Kong, X. M. (2016). Bivariate Hydrologic Risk Analysis Based on a Coupled Entropy-Copula Method for the Xiangxi River in the Three Gorges Reservoir Area, China. *Theor. Appl. Climatol* 125, 381–397. doi:10.1007/s00704-015-1505-z

Fang, G., Guo, Y., Huang, X., Rutten, M., and Yuan, Y. (2018). Combining Grey Relational Analysis and a Bayesian Model Averaging Method to Derive

Monthly Optimal Operating Rules for a Hydropower Reservoir. *Water* 10, 1099. doi:10.3390/w10081099

Favre, A.-C., El Adlouni, S., Perreault, L., Thiémonge, N., and Bobée, B. (2004). Multivariate Hydrological Frequency Analysis Using Copulas. *Water Resour. Res.* 40. doi:10.1029/2003WR002456

Genest, C., Rémillard, B., and Beaudoin, D. (2009). Goodness-of-fit Tests for Copulas: A Review and a Power Study. *Insurance: Maths. Econ.* 44, 199–213. doi:10.1016/j.insmatheco.2007.10.005

Guo, S. L., Kachroo, R. K., and Mngodo, R. J. (1996). Nonparametric Kernel Estimation of Low Flow Quantiles. *J. Hydrol.* 185, 335–348. doi:10.1016/0022-1694(95)02956-7

Han, J.-C., Huang, G.-H., Zhang, H., Li, Z., and Li, Y.-P. (2014). Bayesian Uncertainty Analysis in Hydrological Modeling Associated with Watershed Subdivision Level: a Case Study of SLURP Model Applied to the Xiangxi River Watershed, China. *Stoch Environ. Res. Risk Assess.* 28, 973–989. doi:10.1007/s00477-013-0792-0

Jondeau, E. (2016). Asymmetry in Tail Dependence in Equity Portfolios. *Comput. Stat. Data Anal.* 100, 351–368. doi:10.1016/j.csda.2015.02.014

Kong, X. M., Huang, G. H., Fan, Y. R., and Li, Y. P. (2015). Maximum Entropy-Gumbel-Hougaard Copula Method for Simulation of Monthly Streamflow in Xiangxi River, China. *Stoch Environ. Res. Risk Assess.* 29, 833–846. doi:10.1007/s00477-014-0978-0

Lei, X.-H., Tan, Q.-F., Wang, X., Wang, H., Wen, X., Wang, C., et al. (2018). Stochastic Optimal Operation of Reservoirs Based on Copula Functions. *J. Hydrol.* 557, 265–275. doi:10.1016/j.jhydrol.2017.12.038

Li, F., and Zheng, Q. (2016). Probabilistic Modelling of Flood Events Using the Entropy Copula. *Adv. Water Resour.* 97, 233–240. doi:10.1016/j.advwatres.2016.09.016

Li, G., Wang, Y. X., Zeng, Y., and He, W. X. (2022). A New Maximum Entropy Method for Estimation of Multimodal Probability Density Function. *Appl. Math. Model.* 102, 137–152. doi:10.1016/j.apm.2021.09.029

Lin, K., Zhou, J., Liang, R., Hu, X., Lan, T., Liu, M., et al. (2021). Identifying Rainfall Threshold of Flash Flood Using Entropy Decision Approach and Hydrological Model Method. *Nat. Hazards* 108, 1427–1448. doi:10.1007/s11069-021-04739-0

Lu, L., Yuan, W., Su, C., Gao, Q., Yan, D., and Wu, Z. (2021). Study on the Early Warning and Forecasting of Flash Floods in Small Watersheds Based on the Rainfall Pattern of Risk Probability Combination. *Stoch Environ. Res. Risk Assess*. doi:10.1007/s00477-021-02059-0

Ma, M., Song, S., Ren, L., Jiang, S., and Song, J. (2013). Multivariate Drought Characteristics Using Trivariate Gaussian and Student T Copulas. *Hydrol. Process.* 27, 1175–1190. doi:10.1002/hyp.8432

Madadgar, S., and Moradkhani, H. (2014). Improved B Ayesian Multimodeling: Integration of Copulas and B Ayesian Model Averaging. *Water Resour. Res.* 50, 9586–9603. doi:10.1002/2014WR015965

McLachlan, G. J., and Krishnan, T. (1997). *The EM Algorithm and Extensions*. 2nd ed. Hoboken, NJ, USA: Wiley, 274. ISBN 978-047-120-170-0.

Miller, L. H. (1956). Table of Percentage Points of Kolmogorov Statistics. *J. Am. Stat. Assoc.* 51, 111–121. doi:10.1080/01621459.1956.10501314

Nasr, I. B., and Chebana, F. (2019). Multivariate L-Moment Based Tests for Copula Selection, with Hydrometeorological Applications. *J. Hydrol.* 579, 124151. doi:10.1016/j.jhydrol.2019.124151

Nelsen, R. B. (1999). *An Introduction to Copulas*. New York, NY, USA: Springer. ISBN 978-038-728-678-5.

Raftery, A. E., Balabdaoui, F., Gneiting, T., and Polakowski, M. (2003). "Using Bayesian Model Averaging to Calibrate Forecast Ensembles,". Technical Report, no. 440 (Seattle, Washington: Department of Statistics, University of Washington). doi:10.21236/ada459828

Rahimi, L., Deidda, C., and Demichele, C. (2021). Origin and Variability of Statistical Dependencies between Peak, Volume, and Duration of Rainfall-Driven Flood Events. *Sci. Rep.* 11, 1. doi:10.1038/s41598-021-84664-1

Ramsey, C. B. (2012). The Use of Kernel Density Estimates to Assist in the Identification of Volcanic Tephra. *Quatern. Int.* 2012, 279–280. doi:10.1016/j.quaint.2012.07.309

Remesan, R., Shamim, M. A., Han, D., and Mathew, J. (2009). Runoff Prediction Using an Integrated Hybrid Modelling Scheme. *J. Hydrol.* 372, 48–60. doi:10.1016/j.jhydrol.2009.03.034

Reusser, D. E., Buytaert, W., and Zehe, E. (2011). Temporal Dynamics of Model Parameter Sensitivity for Computationally Expensive Models with the Fourier Amplitude Sensitivity Test. *Water Resour. Res.* 47, W07551. doi:10.1029/2010WR009947

See, L., and Abrahart, R. J. (2001). Multi-model Data Fusion for Hydrological Forecasting. *Comput. Geosciences* 27, 987–994. doi:10.1016/S0098-3004(00)00136-9

Serinaldi, F. (2013). An Uncertain Journey Around the Tails of Multivariate Hydrological Distributions. *Water Resour. Res.* 49, 6527–6547. doi:10.1002/wrcr.20531

Shiau, J.-T., Feng, S., and Nadarajah, S. (2007). Assessment of Hydrological Droughts for the Yellow River, China, Using Copulas. *Hydrol. Process.* 21, 2157–2163. doi:10.1002/hyp.6400

Shin, M.-J., Guillaume, J. H. A., Croke, B. F. W., and Jakeman, A. J. (2015). A Review of Foundational Methods for Checking the Structural Identifiability of Models: Results for Rainfall-Runoff. *J. Hydrol.* 520, 1–16. doi:10.1016/j.jhydrol.2014.11.040

Sklar, A. (1959). *Fonctions de répartition à n dimensions et leurs marges, (N-dimensional distribution function and its margin in 1959)*, Vol. 8. Paris, French: Publications de l'Institut de Statistique de l'Uni- versité de Paris, 229–231.

Sraj, M., Bezak, N., and Brilly, M. (2015). Bivariate Flood Frequency Analysis Using the Copula Function: a Case Study of the Litija Station on the Sava River. *Hydrol. Process.* 29, 225–238. doi:10.1002/hyp.10145

Sugimoto, T., Bárdossy, A., Pegram, G. G. S., and Cullmann, J. (2016). Investigation of Hydrological Time Series Using Copulas for Detecting Catchment Characteristics and Anthropogenic Impacts. *Hydrol. Earth Syst. Sci.* 20, 2705–2720. doi:10.5194/hess-20-2705-2016

Sun, C., and Zhou, X. (2020). Characterizing Hydrological Drought and Water Scarcity Changes in the Future: A Case Study in the Jinghe River Basin of China. *Water* 12, 1605. doi:10.3390/w12061605

Takbiri, Z., Ebtehaj, A. M., and Foufoula-Georgiou, E. (2017). A Multi-Sensor Data-Driven Methodology for All-Sky Passive Microwave Inundation Retrieval. *Hydrol. Earth Syst. Sci.* 21, 2685–2700. doi:10.5194/hess-21-2685-2017

Tsai, F. T.-C. (2010). Bayesian Model Averaging Assessment on Groundwater Management under Model Structure Uncertainty. *Stoch Environ. Res. Risk Assess.* 24, 845–861. doi:10.1007/s00477-010-0382-3

Wu, R.-T., Jokar, M., Jahanshahi, M. R., and Semperlotti, F. (2022). A Physics-Constrained Deep Learning Based Approach for Acoustic Inverse Scattering Problems. *Mech. Syst. Signal Process.* 164, 108190. doi:10.1016/j.ymssp.2021.108190

Xie, W. P., Yang, J. S., Yao, R. J., and Wang, X. P. (2020). Impact Study of Impoundment of the Three Gorges Reservoir on Salt-Water Dy-Namics and Soil Salinity in the Yangtze River Estuary. *J. Environ. Inform.* 36, 11–23. doi:10.3808/jei.202000432

Xu, B., Huang, X., Mo, R., Zhong, P.-a., Lu, Q., Zhang, H., et al. (2021). Integrated Real-Time Flood Risk Identification, Analysis, and Diagnosis Model Framework for a Multireservoir System Considering Temporally and Spatially Dependent Forecast Uncertainties. *J. Hydrol.* 600, 126679. doi:10.1016/j.jhydrol.2021.126679

Xu, H., Taylor, R. G., Kingston, D. G., Jiang, T., Thompson, J. R., and Todd, M. C. (2010). Hydrological Modeling of River Xiangxi Using SWAT2005: A Comparison of Model Parameterizations Using Station and Gridded Meteorological Observations. *Quat. Int.* 226, 54–59. doi:10.1016/j.quaint.2009.11.037

Xu, Y., Huang, G., and Fan, Y. (2017). Multivariate Flood Risk Analysis for Wei River. *Stoch Environ. Res. Risk Assess.* 31, 225–242. doi:10.1007/s00477-015-1196-0

Xue, Y. (20182018). *Coupla-based Tail Correlation Theory and its Application*. Yichang, China: Sanxia University, 1–37.

Yang, A. L., Huang, G. H., Kong, X. M., and Hao, Z. D. (2016). Analysis of Rainfall-Runoff Correlation in Xiangxi River Basin Based on Maximum Entropy-Copula Method. *South-to-North Water Transfers Water Sci. Technol.* 14, 84–89. doi:10.13476/j.cnki.nsbdqk.2016.01.014

Yang, P., Xia, J., Zhang, Y., Zhan, C., and Sun, S. (2019). How Is the Risk of Hydrological Drought in the Tarim River Basin, Northwest China? *Sci. Total Environ.* 693, 133555. doi:10.1016/j.scitotenv.2019.07.361

Zeng, H. (2014). *Comparative Study on the Methods of Determining the Insurance Premium Rates of Crops in the Region*. Xinjiang, China: Xinjiang University of Finance and Economics.

Zhang, L., and Singh, V. P. (2006). Bivariate Flood Frequency Analysis Using the Copula Method. *J. Hydrol. Eng.* 11, 150–164. doi:10.1061/(ASCE)1084-0699(2006)11:2(150)

Zhang, L., and Singh, V. P. (2012). Bivariate Rainfall and Runoff Analysis Using Entropy and Copula Theories. *Entropy* 14, 1784–1812. doi:10.3390/e14091784

Zhang, L., and Singh, V. P. (2007). Bivariate Rainfall Frequency Distributions Using Archimedean Copulas. *J. Hydrol.* 332, 93–109. doi:10.1016/j.jhydrol.2006.06.033

Zhang, L., and Yang, X. (2018). Applying a Multi-Model Ensemble Method for Long-Term Runoff Prediction under Climate Change Scenarios for the Yellow River Basin, China. *Water* 10, 301. doi:10.3390/w10030301

Zhou, X., Huang, G., Li, Y., Lin, Q., Yan, D., and He, X. (2021). Dynamical Downscaling of Temperature Variations over the Canadian Prairie Provinces under Climate Change. *Remote Sensing* 13, 4350. doi:10.3390/rs13214350

Zhou, X., Huang, G., Wang, X., and Cheng, G. (2018). Future Changes in Precipitation Extremes over Canada: Driving Factors and Inherent Mechanism. *J. Geophys. Res. Atmos.* 123, 5783–5803. doi:10.1029/2017JD027735

Zhou, Y., Chang, F.-J., Chen, H., and Li, H. (2020). Exploring Copula-Based Bayesian Model Averaging with Multiple ANNs for PM2.5 Ensemble Forecasts. *J. Clean. Prod.* 263, 121528. doi:10.1016/j.jclepro.2020.121528

Conflict of Interest: The authors declare that the research was conducted in the absence of any commercial or financial relationships that could be construed as a potential conflict of interest.

frontiers in Earth Science

ORIGINAL RESEARCH
published: 26 January 2022
doi: 10.3389/feart.2021.755119

Water Resource Availability Assessment Through Hydrological Simulation Under Climate Change in the Huangshui Watershed of the Qinghai–Tibet Plateau

Zhenghui Fu[1], Yulei Xie[2], Yang Zhang[3], Xia Jiang[1], Huaicheng Guo[3] and Shuhang Wang[1]**

[1]National Engineering Laboratory for Lake Pollution Control and Ecological Restoration, State Environment Protection Key Laboratory for Lake Pollution Control, Chinese Research Academy of Environmental Science, Beijing, China, [2]Key Laboratory for City Cluster Environmental Safety and Green Development of the Ministry of Education, Institute of Environmental and Ecological Engineering, Guangdong University of Technology, Guangzhou, China, [3]College of Environment Sciences and Engineering, Peking University, Beijing, China

OPEN ACCESS

Edited by:
Andries Hof, PBL Netherlands Environmental Assessment Agency, Netherlands

Reviewed by:
Jeeban Panthi, University of Rhode Island, United States
Jing-Cheng Han, Shenzhen University, China
Yuliang Zhou, Hefei University of Technology, China

***Correspondence:**
Yulei Xie
xieyulei@gdut.edu.cn
Shuhang Wang
shuhang125126@163.com

Specialty section:
This article was submitted to Interdisciplinary Climate Studies, a section of the journal Frontiers in Earth Science

Received: *08 August 2021*
Accepted: *13 December 2021*
Published: *26 January 2022*

Citation:
Fu Z, Xie Y, Zhang Y, Jiang X, Guo H and Wang S (2022) Water Resource Availability Assessment Through Hydrological Simulation Under Climate Change in the Huangshui Watershed of the Qinghai–Tibet Plateau. Front. Earth Sci. 9:755119. doi: 10.3389/feart.2021.755119

The related dynamic change in meteorological and hydrological parameters is critical for available water resources, development management options, and making informed decisions. In this study, to enhance the resolution of the predicted meteorological and hydrological parameters under climate change, the statistical downscaling method (SDSM), the generalized regression neural network (GRNN) model, the Soil and Water Assessment Tool (SWAT) model, and the improved Tennant method were integrated into a framework. The available water resources were assessed in the Huangshui watershed of the Qinghai–Tibet Plateau, which has the highest average elevation in the world. The meteorological parameters were obtained by the SDSM model and the GRNN model. The SWAT model used the meteorological parameters to simulate the hydrological data under climate change scenarios. Considering the meteorological conditions and the high sediment content in the basin, the available water resources are evaluated by the improved Tennant method. The meteorological data of the Xining station from 1958 to 2011 were used to analyze the dynamic changes and mutation trends in the data. The results indicated that the precipitation would have a great increase during the wet season from May to September, and the flows and available water resources would decrease with increasing carbon emissions under different representative concentration pathways (RCPs).

Keywords: water resource assessment, downscaling models, climate change, GRNN model, SWAT

1 INTRODUCTION

The spatial and temporal dynamics of ecosystems are closely related to fluctuations in the climate. The meteorological parameters are severely affected by the climate change that cause the reallocation of water resources and lead to crisis of water utilization and threaten human lives (Song et al., 2019; Sharma and Goyal, 2020). In addition, as sensitive climate and ecosystem area, the meteorological data in the ecotone attracts major concern for fragile ecosystem management. The climate changes

are expected to produce large shifts in water distributions at unprecedented rates (Hanewinkel et al., 2013; Teng et al., 2020). Thus, predicting the meteorological parameters, the hydrological parameters, and the water resource availability in the ecotone areas under different climate change scenarios is important for planning and managing the ecological environment.

Previously, in order to meet the actual condition in regional scale, the downscaling methods were developed for improving the spatial resolution of the global climate models (GCMs) in climate change impact assessment (Thuiller et al., 2005; Delworth, 2006; Taylor et al., 2012; Hughes and Mazibuko, 2018). Among those methods, due to its relatively low computational requirements, the functional transformation downscaling method is the most commonly used downscaling method (Ghosh and Mujumdar, 2008; Guo et al., 2014). For example, Jeong et al. (2012) provided a multisite hybrid statistical downscaling procedure combining regression-based and stochastic weather generation approaches for multisite simulations of daily precipitation. Piras et al. (2015) advanced a statistical downscaling method to analyze the impacts of climate change on precipitation and discharges in a Mediterranean basin. Tang et al. (2016) developed statistical and dynamical downscaling methods to simulate the surface climate of China based on large-scale information from either reanalysis data or global climate models. Although the large-scale parameters, such as the atmospheric oscillation and the circulation patterns with slowly changing processes and low resolutions can be addressed by the downscaling process, the changing process of small-scale parameters (e.g., local temperature and precipitation) are needed to reflect for analyzing the response relationship between underlying surfaces and meteorological factors in hydrological simulations (Sillmann et al., 2013; Friedlingstein et al., 2014; Zhang et al., 2020).

Moreover, water resource availability refers to the largest one-time utilization quantity of local water resources within an expected time range under deduction of the ecological water demand, and the determination of ecological water demand is the key to evaluating water resource availability (Kattsov et al., 2007; Whitehead et al., 2009). The acceptable approaches to simulate ecological water demand can be divided into four categories, including the hydrological index method, hydraulic method, holistic method, and habitat method. Among these, as a typical representative of hydrological index measures, the Tennant method is widely used due to its convenient operation and high accuracy to determine the ratio of the ecological water demand to the average annual natural flow through the correlation between the flow in rivers and environmental quality of fish habitats (Yakup et al., 2018; Suwal et al., 2020; Joseph et al., 2021). However, the application of the Tennant method for permanent rivers in arid and semiarid areas still has some limitations. The Tennant method divides the year into two periods to calculate the recommended average percentage of runoff according to the amount of runoff monthly. At the same time, this method is mainly studied on the basis of considering the impact of runoff on fish and ecosystem, so it needs to be adjusted in the study area with high sediment content in rivers. So, it needs to be improved according to the actual situation and regional characteristics.

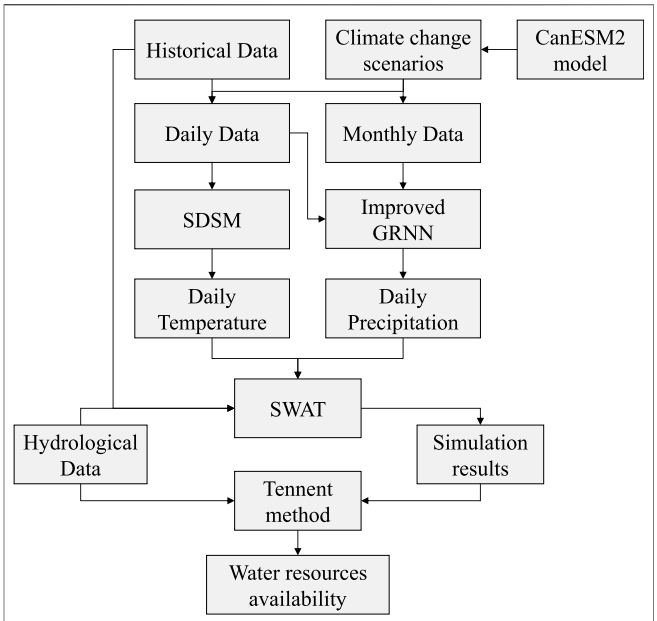

FIGURE 1 | The framework of evaluation method of available water resources.

Therefore, in consideration of the above limitation, the aim of this study is to develop a general framework through integration with the SDSM downscaling method, the GRNN model, the SWAT model, and the Tennent method for a comprehensive meteorological and hydrographic prediction, and available water resource assessment of the Huangshui watershed in the Qinghai–Tibet Plateau with the fragile ecological environment. For the framework, the SDSM downscaling method was applied for temperature prediction according to the large-scale observed meteorological data, and the GRNN model was advanced to improve the prediction accuracy of monthly precipitation. The predicted temperature and precipitation values were the main input parameters to the SWAT model to simulate more precise hydrologic data under different climate change scenarios, and the water availability within basin scale can be further obtained through the improvement of the Tennent method. The study results could analyze the available water resource for generating effective water resource management schemes and address the impacts of the climate change on ecotones in the basin.

2 METHODOLOGY

This study constructed a comprehensive assessment framework of water resource availability based on hydrological simulation under the impact of climate change. The methodology contains three parts. The first step is the development of future climate conditions including daily temperature with the SDSM method (**Section 2.1**) and precipitation with the GRNN model (**Section 2.2**). The second step involves using the downscaled daily

precipitation and temperature to simulate daily runoff using the SWAT model (**Section 2.3**). The third step involves using the hydrological data to calculate the water resource availability using the Tennant method (**Section 2.4**). To evaluate the SDSM model, the GRNN model, and the SWAT model, R2 and NSE are used (**Section 2.5**). **Figure 1** presents the general framework of the evaluation method of available water resources based on hydrological simulation under the impact of climate change. Historical data and climate change scenarios both include daily and monthly data. The daily data of historical data and climate change scenarios will be used to predict temperature through the SDSM model. The daily data and monthly data of historical data and climate change scenarios are used by the GRNN model, and the precipitation prediction results will be obtained.

2.1 Statistical Downscaling Model

Statistical downscaling model (SDSM) is an effective decision supporting tool with a robust statistical downscaling technique for assessing local climate change impacts (Wilby et al., 2002; Meenu et al., 2013). Under the present and future climate forcing, this model can facilitate the rapid development of the multiple, low-cost, and single-site scenarios of daily surface weather variables. The general equation for the SDSM is as follows:

$$R = F(L) \tag{1}$$

where R = predictand (a local climate variable), L = predictor (a set of large-scale climate variables), and F = deterministic/stochastic function conditioned by L and is estimated empirically from historical observations.

Statistical downscaling model (SDSM) is used to downscale temperature factor, which includes the daily maximum and minimum temperatures. The data required include the daily measured data of weather station and the daily large-scale meteorological data obtained by GCM. In order to achieve the purpose of this study, the software (SDSM v. 5.2) was used.

2.2 Generalized Regression Neural Network Model

Considering that the SDSM is not accurate enough for daily precipitation prediction, we built a new generalized regression neural network model (GRNN method) to predict precipitation, and the new method is suitable for the description of various nonlinear relations. This method is based on nonparametric regression. It takes the sample data as a posteriori condition, performs nonparametric estimation, and calculates the network output according to the maximum probability principle (Specht, 1991; Dalkilic et al., 2014). At present, it has been applied in many fields such as control decision system, structure analysis, and so on (Kumar and Malik, 2016). The network has the following obvious advantages: 1) No model parameters need to be trained, and the convergence speed is fast; 2) Based on radial basis function network, it has good nonlinear approximation performance, and has good adaptability to curve fitting problem. In this model, a network can be employed to

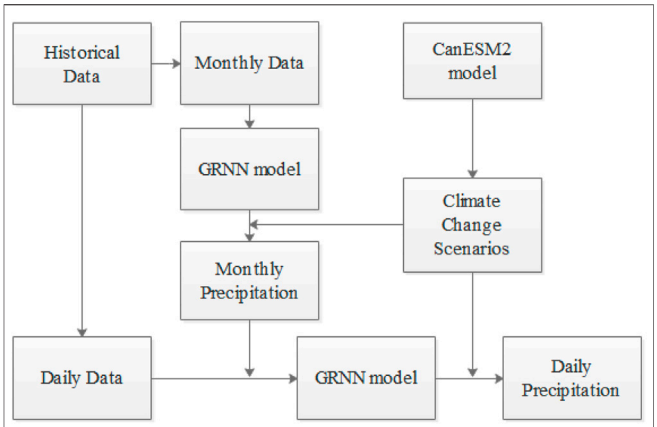

FIGURE 2 | The improved precipitation prediction model based on the generalized regression neural network (GRNN) model.

estimate a dependent variable from an independent variable through finite datasets (Cigizoglu and Alp, 2006). The theoretical foundation of the GRNN model is the kernel regression, which is a nonlinear regression analysis. The regression of the random variable y on the observed values X of random variable x can be found using:

$$E(y|X) = \frac{\int_{-\infty}^{0} y f(X,y)dy}{\int_{-\infty}^{0} f(X,y)dy} \tag{2}$$

where $f(X, y)$ is a known joint continuous probability density function. When $f(X, y)$ is unknown, it should be estimated from a set of observations of x and y. $f(X, y)$ can be estimated using the nonparametric consistent estimator suggested as follows:

$$\widehat{f}(X,Y) = \frac{1}{(2\pi)^{\frac{\rho+1}{2}}\sigma^{\rho+1}} \frac{1}{n}\sum_{i=1}^{n} \exp\left[-\frac{(X-X^i)^T(X-X^i)}{2\sigma^2}\right] \exp\left[-\frac{(Y-Y^i)^2}{2\sigma^2}\right] \tag{3}$$

where n = sample size, ρ = dimensionality of random variable x, and σ = smooth parameter.

By substituting **Eq. 3** into **Eq. 2**, and after solving the integration, the following equation will be obtained:

$$\widehat{Y}(X) = \frac{\sum_{i=1}^{n} y \exp\left[-\frac{(X-X^i)^T(X-X^i)}{2\sigma^2}\right]}{\sum_{i=1}^{n} \exp\left[-\frac{(X-X^i)^T(X-X^i)}{2\sigma^2}\right]} \tag{4}$$

Equation 4 is directly applicable to the issues involving numerical data. In order to improve the predictive accuracy caused by the nontemporality of daily precipitation, the GRNN model was improved to construct a two-layer GRNN model as shown in **Figure 2**. First, the first layer of the GRNN model is constructed, in which the monthly precipitation is predicted by multiple monthly scale factors. Second, the second-level GRNN model is constructed, which uses multiple

daily scale factors and monthly precipitation as input variables and daily precipitation as output variables to calibrate and verify the model. The model is composed of the two layers models. Through the gradual simulation and prediction, the nonlinear relationship between the large-scale meteorological data and the measured daily precipitation is obtained.

2.3 Hydrological Model

The Soil and Water Assessment Tool (SWAT) is a physically based semi-distributed hydrological model used to simulate the quantity and quality of surface water and can be also used to predict the impact of land use, land management practices, and climate change on hydrology (Arnold et al., 2012), and developed by the Agricultural Research Service (ARS) of the United States Department of Agriculture (USDA). The hydrological simulation in the SWAT model is mainly carried out through the hydrological module. The process is divided into two parts, land slope runoff and river channel runoff. The land slope runoff consists of precipitation process, rainwater trapped by plant canopy into soil, groundwater, and surface runoff (Nyika et al., 2020). The river channel runoff is mainly affected by the evaporation of water and infiltration of the river water. The balance equation of water quantity in this model is shown as follows:

$$SW_t = SW_0 + \sum_{i=1}^{t}\left(R_{day} - Q_{surf} - E_a - W_{seep} - Q_{gw}\right) \quad (5)$$

where SW_t = ultimate soil moisture content, SW_0 = antecedent soil moisture content, t = sample size, R_{day} = daily total precipitation, Q_{surf} = total surface runoff, E_a = the total evapotranspiration, W_{seep} = soil infiltration capacity and lateral flow volume, and Q_{gw} = total underground runoff.

2.4 Tennant Method of Water Resource Availability Assessment

The Tennant method is an operational method originated from the midwest of the United States, which can determine the ratio of ecological water demand in the average annual river flow and evaluate the degree of river ecology according to the analysis of the relationship between the flow of multiple rivers and the environmental quality of fish habitat (Abbaspour et al., 2007; Ateeq-Ur and Abdul, 2018). Specifically, 10% of the average flow is a minimum instantaneous flow recommended to sustain short-term survival habitat for most aquatic life forms, 30% of the average flow is recommended as a base flow to sustain standard survival conditions for most aquatic life forms, and 60% of the average flow provides the excellent habitat for most aquatic life forms. In addition, according to the monthly runoff changes and the growth conditions of fish and other aquatic organisms, the evaluation standard can also be divided into two periods from October to March and April to September. The Tennant method can be used in calculating the ecological water demand in permanent arid and semi-arid rivers. Practically, some appropriate improvements should be conducted based on the actual hydrological changes and the regional characteristics. In this study, as the largest tributary of the upper reaches of the Yellow River, the Huangshui River Basin suffered from serious soil erosion and high sediment content due to the influence of geological conditions and human factors. The sediment is mainly concentrated from June to September. Through the calculation of the average sediment transport in Xining station, the average sediment concentration is 2.45 kg/m^3. Therefore, in order to ensure that there are enough water resources in the Huangshui River to transport the sediment in the water to the downstream, it is necessary to increase the sediment transport water demand on the basis of the original Tennant method.

2.5. Model performance evaluation method

In this study, the determination coefficient (R^2) and Nash–Sutcliffe efficiency coefficient (NSE) were used to evaluate the accuracy of the simulation results. The formulas are shown as follows:

$$R^2 = \frac{\left[\sum_{i=1}^{n}\left(O_i - \bar{O}\right)\left(S_i - \bar{S}\right)\right]^2}{\sum_{i=1}^{n}\left(O_i - \bar{O}\right)^2\sum_{i=1}^{n}\left(S_i - \bar{S}\right)^2} \quad (6)$$

$$NSC = 1 - \frac{\sum_{i=1}^{n}\left(S_i - O_i\right)^2}{\sum_{i=1}^{n}\left(O_i - \bar{O}\right)^2} \quad (7)$$

where, i = the number of time series, $i = 1, 2..., n$; S_i = the ith modeled value; O_i = the ith observation; $\bar{S}$ = the average of modeled values; and $\bar{O}$ = the average of observations. R^2 ranges from 0 to 1. The NSE ranges from minus infinity to 1.

3 STUDY AREA AND DATA

3.1 Overview of the Huangshui Watershed

The Huangshui watershed, a semi-arid area with an average annual precipitation of less than 400 mm, is located in the upstream of the Yellow River. Moreover, this area is the core region of the Tibetan Plateau with the most dense population and the most developed economy. Therefore, as a transitional and ecologically fragile zone between the Tibetan Plateau and the Loess Plateau, this area has become a globally well-known ecologically vulnerable area with the characteristics of high ecological sensitivity, low environmental capacity, a weak capability to withstand interference, and poor stability (Song et al., 2009; Chen et al., 2015).

The Huangshui watershed has a total area of 10,337 km^2, and the overall terrain of the basin is high in the northwest and low in the southeast. The river originates from the mountains at an elevation of 4,300 m, and the total basin has elevations ranging from 2,100 to 5,000 m. The terrain of the river basin is complex and diverse, mainly including mountains, hills, valley basins, and other landforms. The upper reaches of the river are mainly canyons, while the middle and lower reaches are mainly wider canyons. The study area is located in the inland plateau continental climate, and belongs to a subhumid climate area. The area has a high elevation, a large amount of evaporation, and large temperature differences between day and night. The annual

precipitation is unevenly distributed in this region, and 60%–80% of the total precipitation is concentrated in the rainy season. Moreover, the dry season from November to February only accounts for approximately 3% of the annual precipitation. In addition, the river networks are arranged in dense, branching patterns, with more than 10 main tributaries.

3.2 Data Collection

The meteorological data were obtained from the standard weather station of the Yellow River upstream (1952–2011), which was provided by the "Comprehensive data platform of Ningxia-Inner Mongolia Reach of the Yellow River," National Key Basic Research Program of China. These data were measured on a daily time span, and the original format was ".txt." The data of the Menyuan meteorological station (W1) and Xining meteorological station (W2) are used in this study. The study data contained daily meteorological data for the upper reaches of the Yellow River and its surrounding areas from 1952 to 2011. The standard station data included air pressures, temperatures, humidity values, wind speeds, and 15 other factors.

The large-scale meteorological data obtained by GCM used to estimate the future trends in climate change came from the CanESM2 model (the second-generation Canadian Earth System Model), which was developed by CCCma (Canadian Centre for Climate Modeling and Analysis). The selected large-scale meteorological factors include the daily maximum near-surface air temperature (tasmax), daily minimum near-surface air temperature (tasmin), near-surface air temperature (tas), precipitation (pr), near-surface relative humidity (ths), surface air pressure (ps), total cloud fraction (clt), eastward near-surface wind (uas), and northward near-surface wind (vas). The data used in this study were based on CMIP5 (Coupled Model Intercomparison Project Phase 5), which included the historical scenario, RCP (representative concentration pathway) 2.6 scenario, RCP4.5 scenario, and RCP8.5 scenario (Park et al., 2018). These data had two kinds of time spans: daily and monthly. The original format was ".nc," and the data were spatial grid data with a spatial resolution of 2.5°.

The DEM (digital elevation model) was provided by the Geospatial Data Cloud site, Computer Network Information Center, Chinese Academy of Sciences (http://www.gscloud.cn/sources/accessdata/310?pid=302). The data were derived from the ASTER GDEM dataset based on the Advanced Spaceborne Thermal Emission and Reflectance Radiometer (ASTER) data developed by the National Aeronautics and Space Administration (NASA) and the Ministry of Economy, Trade, and Industry (METI) of Japan. The resolution of the DEM data used was 30 m, and the original format was ".tiff." Based on Landsat 8 remote-sensing images, the datasets were generated by manual visual interpretation. In the study area, the land use types included the cultivated land, forestland, grassland, water area, residential land, and unused land. These data were obtained from the data center of resources and environment science, Chinese Academy of Sciences and are 1-km resolution, remote-sensing monitoring data of the land use status of China in 2015 with the ".tiff" format. According to the analysis, grassland, forestland, and cultivated land were the main types in this region, accounting for 52.45, 20.82, and 18.02%, respectively. Construction land accounted for only 3.22% of the total area. The soil parameters were provided by the China Soil Map Based Harmonized World Soil Database (HWSD). The soil data were provided by the Nanjing Soil Institute for the second land survey in 1995, and the data resolution was 1 km with the ".tiff" format. Considering that the soil particle size grading standard in the HWSD is American standard, these data can be directly used to establish the SWAT model soil database. The division threshold was set at 2,000 ha, and the Xiaoxiaqiao section was selected as the outlet of the watershed. A total of 305 subbasins are generated, and the final division results are shown in **Figure 3D**. **Figures 3A–D** have been used in the SWAT model, and they are elevation, land use type, soil type, and subwatershed distribution.

In this study, the mainstream Huangshui River and its tributaries were simulated. The hydrological data are from eight hydrological stations in the basin, including Huangyuan station (H1), Xining station (H2), Dongjiazhuang station (H3), Xinachuan station (H4), Niuchang station (H5), Qiaotou station (H6), Chaoyang Station (H7), and Fujiazhai station (H8). The daily flow monitoring data from 2008 to 2015 were used as the hydrological data in this study. **Table 1** shows the results of the annual average flow of each hydrological station. Xining Station is located in the lower reaches of the Huangshui watershed, close to the exit of the basin, with an annual average flow of 39.99 m^3/s. As the second largest hydrological station, Chaoyang station is located in the upper reaches of the confluence point of the Beichuan River, the main tributary of the Huangshui River

TABLE 1 | Annual average flow of each hydrological station.

Year	Streamflow station (unit: m^3/s)							
	H1 (Huangyuan)	H2 (Xining)	H3 (Dongjiazhuang)	H4 (Xinachuan)	H5 (Niuchang)	H6 (Qiaotou)	H7 (Chaoyang)	H8 (Fujiazhai)
2008	7.32	29.55	2.13	3.41	4.95	10.62	14.95	4.14
2009	10.62	41.19	2.88	6.10	8.52	18.18	22.27	3.19
2010	9.30	37.57	3.21	4.65	7.12	18.19	20.26	3.21
2011	9.35	43.27	2.86	5.42	8.96	19.96	24.75	3.26
2012	12.01	45.60	3.55	6.70	8.74	18.67	22.34	3.75
2013	9.22	30.08	2.87	4.52	6.53	13.64	15.68	2.83
2014	10.55	51.20	3.00	5.21	10.31	21.53	24.55	4.21
2015	9.14	41.46	2.36	4.31	9.22	16.04	19.86	3.84
Average	9.69	39.99	2.86	5.04	8.04	17.10	20.58	3.55

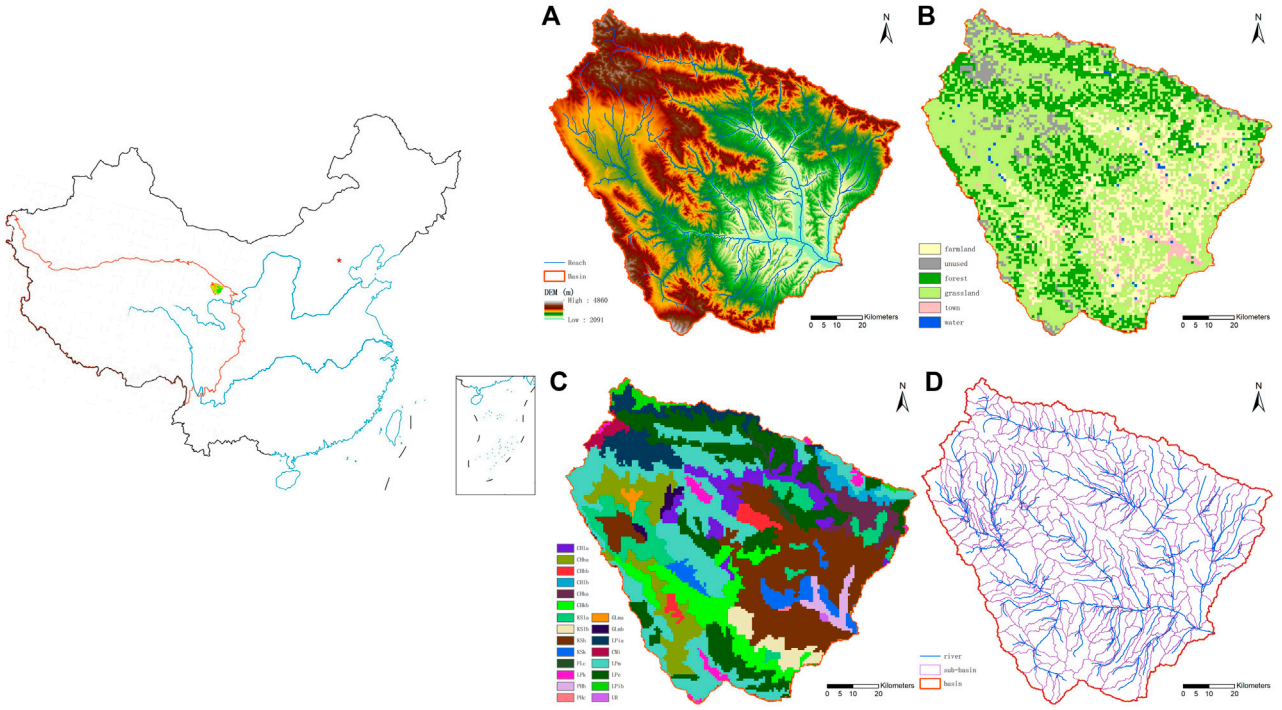

FIGURE 3 | The graphic digital elevation model (DEM) data **(A)**, land use data **(B)**, soil data **(C)**, and the divided threshold of the basin **(D)**.

basin, with an annual average flow of 20.58 m^3/s. According to the statistics on the multiyear hydrologic flow data, the hydrologic situations had markable changes in different years. For example, the annual average flow of the Xining station in 2008 was 29.55 m^3/s, which was only 57.7% of the annual average flow of 51.20 m^3/s in 2014.

The consistency of the time scales of the data utilized for the SDSM model, the GRNN model, and the SWAT model needs to be considered. The calibration periods, validation periods, and predictive periods were 1979–2000, 2001–2005, and 2021–2035, respectively, in the meteorological prediction section. In the hydrological simulation part, according to the daily hydrological data of the Huangshui watershed from 2008 to 2015, the relevant data from 2008 to 2013 were taken as the model training period, those of 2014–2015 were taken as the model validation period, and those of 2021–2035 were taken as the prediction period. In addition, the warm up period of the model was 3 years before the beginning time of the cycle.

4 RESULTS ANALYSIS AND DISCUSSION

4.1 The Prediction of the Meteorological Data

4.1.1 The temperature predictions by the Statistical Downscaling Method Model

The statistical parameter R^2 was used on the observation data and large-scale forecast of the daily maximum and minimum temperature from 1979 to 2000, and the R^2 values were approximately 0.9, which suggested that the temperature had a direct relation with the large-scale forecast factors and could be predicted directly. Moreover, the unconditional process analysis model of SDSM was applied to predict the monthly maximum and minimum average temperatures from 2021 to 2035.

The predicted (each year from 2021 to 2035) and observed (each year from 1958 to 2011) maximum temperatures and the average minimum temperatures in different months are presented in **Figure 4** and **Table 2**. Compared with the observed temperatures, the predicted maximum average temperatures of January, February, June, October, November, and December have an increasing tendency, and those of April, August, and September have an opposite tendency. However, the minimum average temperatures have an obvious increase in winter (November to February) and decrease slightly in summer (June to August). The prediction results suggested that considering the factors of climate change, the temperature fluctuation of the Huangshui watershed would become flatter, meaning that the temperature in winter would increase obviously, and the temperature difference within 1 year would decrease. The determination coefficients (R-squared) of the minimum temperature and maximum temperature were 0.77 and 0.62, respectively, and the Nash–Sutcliffe coefficients were 0.74 and 0.62. According to different season, the biggest change occurred in winter. The prediction maximum average temperatures will change from 2.87° to 7°, and the minimum average temperatures will change from −12.35° to −8°.

The annual average maximum temperatures and minimum temperatures of Xining station in the Huangshui watershed under different scenarios are shown in **Figure 5**. Under different scenarios, the average maximum temperatures and minimum temperatures at Xining station increased. The maximum temperature rose from

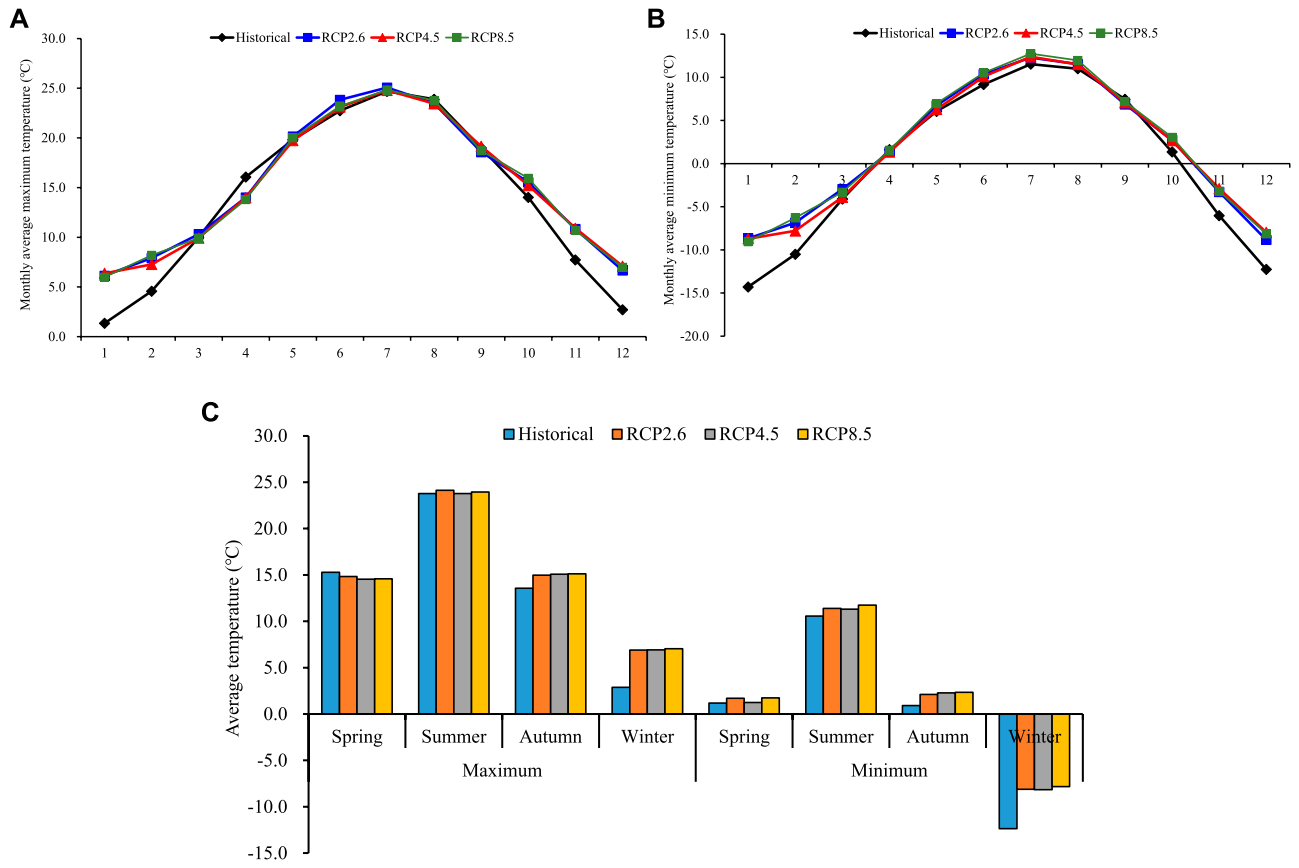

FIGURE 4 | The predicted results of the monthly average temperatures.

TABLE 2 | The results of daily maximum temperature and minimum temperature in different periods.

Period	Model		Max	Min
Calibration period (1979–2000)	Measured value		13.96	0.53
	Global climate model (GCM)		6.52	–5.93
Validation period (2001–2005)	Statistical downscaling method (SDSM)		14.73	1.08
	Measured value		14.50	–0.32
	GCM		7.61	–5.19
Prediction period (2021–2035)	Representative concentration pathway (RCP)2.6	SDSM	15.21	1.77
		GCM	8.40	–4.08
	RCP4.5	SDSM	15.08	1.67
		GCM	8.19	–4.25
	RCP8.5	SDSM	15.17	2.00
		GCM	8.34	–3.81

13.88° to 15.25°, 15.13°, and 15.21° in different scenarios. The minimum temperature rose from 0.08° to 1.82°, 1.72°, and 2.04°. Under the RCP8.5 scenario, the annual average maximum temperature showed an upward trend. However, in the RCP2.6 and RCP4.5 scenarios, the annual maximum temperatures showed certain downward trends. At the same time, the annual average minimum temperature showed an upward trend under the RCP85 scenario. Under the RCP2.6 and RCP4.5 scenarios, the annual average minimum temperatures presented certain downward trends. Overall, the maximum temperature and the minimum temperature showed the same trends under different scenarios. According to the analysis of different scenarios, the RCP2.6 scenario had a smaller temperature variation and stable climate between different years.

4.1.2 Precipitation Prediction by the Improved Generalized Regression Neural Network Model

Considering that daily rainfall is affected by atmospheric circulation, temperature, humidity, cloud cover, and other factors, seven factors (tas., pr., ths., ps., clt., uas., and vas.,)

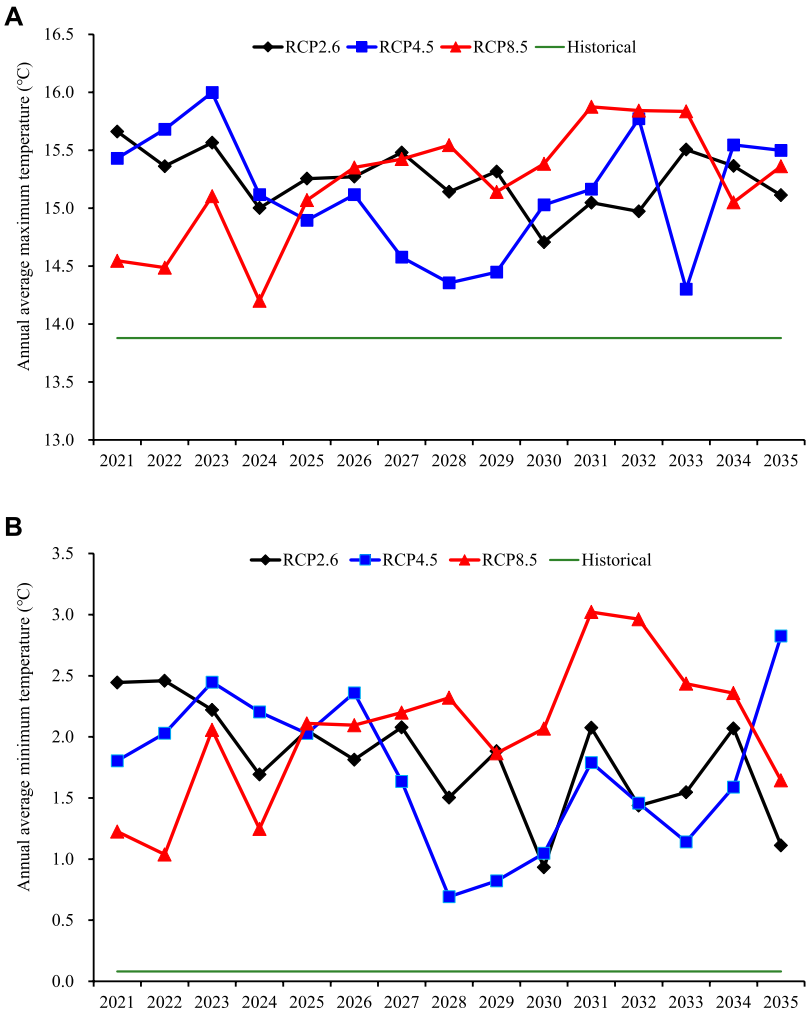

FIGURE 5 | The predicted results of the annual average temperatures.

were selected as large-scale meteorological factors to predict daily precipitation. The generalized regression neural network was constructed and trained by using the historical meteorological data from 1979 to 2000.

The daily precipitation in the verification period (2001–2005) is seen as the curve of the original net in **Figure 6**. The values of R^2 and NSE were 0.53 and 0.4, respectively, which were not sufficiently ideal. The forecast results of daily precipitation were also not ideal. This may be due to the strong randomness of daily precipitation on a daily time scale. To improve the predictive accuracy, the GRNN model was improved to construct a two-layer GRNN model in which the first layer took the monthly precipitation, monthly average near-surface air temperature, average near-surface wind, near-surface relative humidity, and surface air pressure as the inputs to predict the monthly precipitation. Then the monthly precipitation was induced into the second layer as the correction factor to predict the daily precipitation. The R^2 and NSE values obtained for the improved GRNN model were 0.72 and 0.70, respectively, suggesting that the accuracy of the results was improved and could reach a satisfactory level.

By combining the improved GRNN model with the large-scale meteorological data output by the CanESM2 model, the precipitation predictions of the Xining station under different RCPs were obtained. The annual average precipitation prediction results of the Xining station are shown in **Figure 7**. The annual average precipitation amounts of RCP2.6, RCP4.5, and RCP8.5 are 471.88, 486.98, and 485.67 mm, respectively, at Xining Station, which are very close. The annual average precipitation has an increasing tendency for RCP2.6 and RCP8.5, but a decreasing tendency for RCP4.5. Under the RCP2.6, RCP4.5, and RCP8.5 scenarios, the annual maximum precipitations are 568.06 mm at the year of 2028, 653.66 mm at the year of 2027, and 621.39 mm at the year 2034; the annual minimum precipitations are 372.00 mm at the year of 2024, 407.91 mm at the year 2035, and 383.45 mm at the year 2035.

The monthly precipitation predictions and the observed precipitation data of Xining station are shown in **Figure 8**. It can be seen from the figure that during the dry season (November to April), the precipitation amounts of different RCPs have no

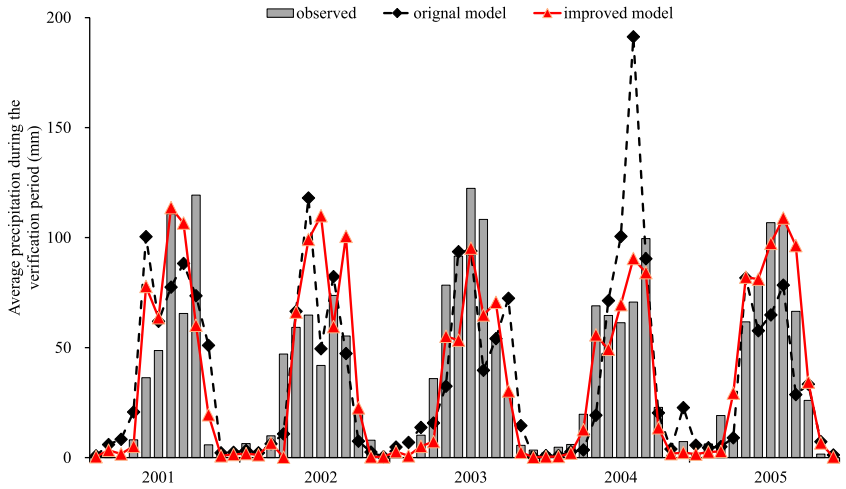

FIGURE 6 | The simulated and observed monthly precipitations in the verification period (2001–2005).

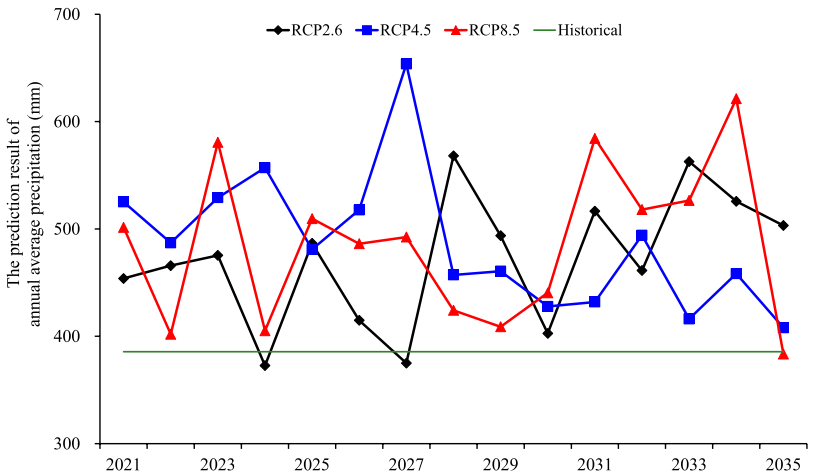

FIGURE 7 | The annual average precipitation prediction results of the Xining station.

obvious changes with the observed precipitation; however, for the precipitation of the wet season (May to September), the predicted precipitation has a large increase.

4.2 The Prediction of the Hydrologic Data

4.2.1 Calibration and Evaluation of the Parameters

The parameters used in this model were chosen as follows: First, the sensitivity ranking of the whole watershed parameters was conducted through the sensitivity analysis process, and the parameters ranked at the top were selected. At the same time, the parameters to be calibrated, their alternative methods, and initial rate determination range were determined in combination with the results of the SWAT manual and related research as well as the watershed related literature. Finally, 20 parameters and their initial value ranges were obtained. The original data in this paper were mainly used to calibrate the parameters and compare the simulation results with the final evaluation to determine the simulation effects of the model.

The daily flow rate data from 2008 to 2013 were set as the model calibration period, and those of 2014 and 2015 were set as the validation period of the model, and the 3 years before the calibration period were set as the model reheating period. The calibration was conducted for the eight hydrologic stations of the Huangshui watershed according to the principles of branches first and then main streams, up streams first and then down streams. The SWATCUP model was calibrated by the universal Sufi2 (Sequential Uncertainty Fitting Version 2) method, which takes the nondeterminacies of the input data, model structures, parameters, and metrical data into consideration and reflected the nondeterminacies to the ranges of the parameters. After the parameter calibration, the uncertainty interval at the 95% confidence level could contain most measured data.

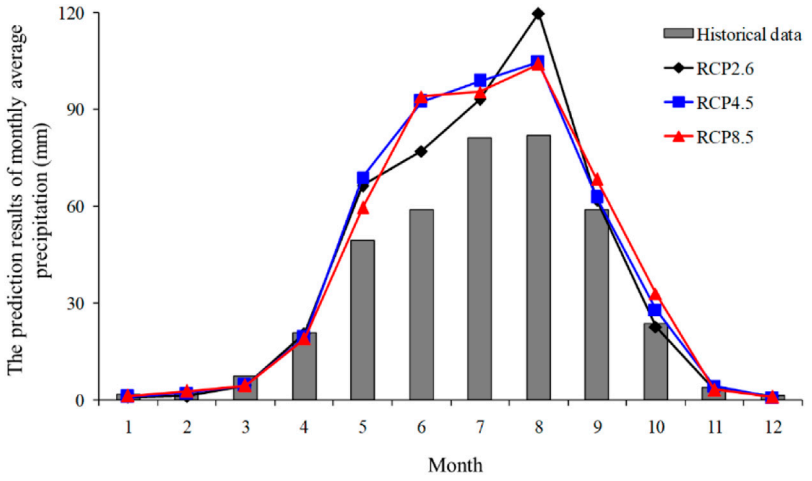

FIGURE 8 | The monthly precipitation predictions and the observed precipitation data.

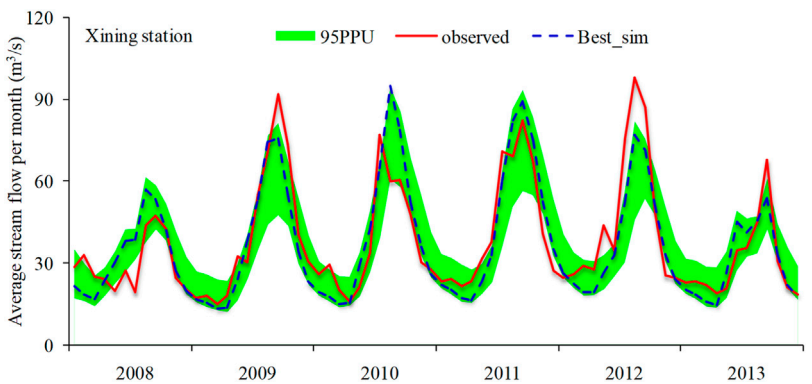

FIGURE 9 | The observed results of the calibration period, optimum simulation results, and 95% confidence interval.

The observed results of the calibration period, optimum simulation results, and 95% confidence interval are shown in **Figure 9**. It could be suggested that the SWAT model could simulate the monthly variation characteristics of the flow rates in the Huangshui watershed by the results of the calibration period. It was suggested that the single peak and multiple peaks in **Figure 9** were attributed to the flow-rate peaks. When there was one main heavy precipitation in a month or the times of precipitation were concentrated, a single peak appeared; when the heavy precipitation happened more than once in a month or the times of precipitation were dispersive, multiple peaks appeared.

According to the variation characteristics of the observed and simulated results, it was concluded that the simulated results had smaller fluctuation ranges and that the value variation was more stable. In the wet seasons of the second (2009) and fifth years (2012) of the calibration period, the observed results were all higher than the optimum simulated results. The R^2 and NSE values of most hydrologic stations are approximately 0.75 and 0.70, respectively, which can properly reflect the whole flow rates of the Huangshui watershed.

The observed and updated simulated flow rate results in the verification period of the Xining hydrologic station are shown in **Figure 10**. The observed and simulated values are well fitted, especially for Xining Station, which is upstream of the basin main exit and can effectively reflect the variation characteristics of the flow rate with time.

4.2.2 The Simulation and Prediction of the Hydrological Data

The parameters calibrated by the SWATCUP were input into the SWAT model to obtain runoff data at the exit of the Huangshui watershed from 2006 to 2015, which was set as the basic period. The average amount of runoff was 49.59 m^3/s, and 2007 and 2013 had the largest and smallest runoff amount, at 60.83 and 37.31 m^3/s, respectively. The runoff data were set as the basic data for the hydrological analysis under different climate change scenarios.

The predicted meteorological data at different RCPs were applied in the SWAT model with the calibrated parameters of the Huangshui Basin. The predicted runoff data at the exit of the

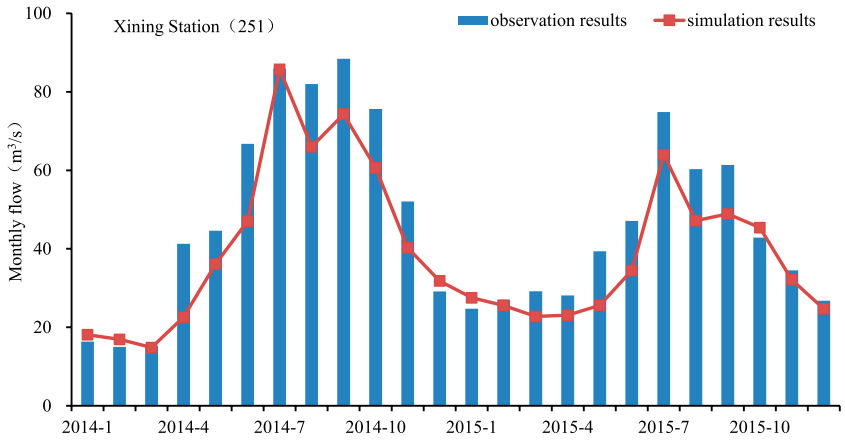

FIGURE 10 | The observed and updated simulated flowrate results in the verification period of Xining station.

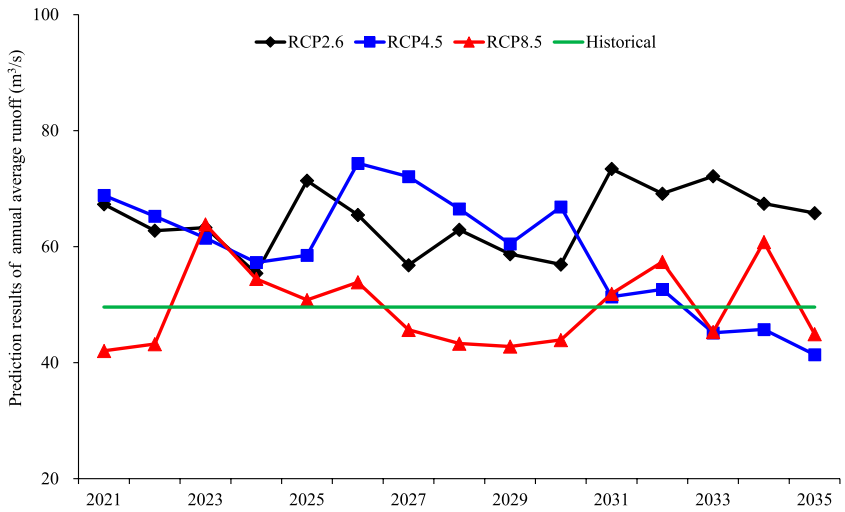

FIGURE 11 | The predicted runoff data at the exit of the basin under different representative concentration pathways (RCPs).

basin under different RCPs are shown in **Figure 11**. It was suggested that under different RCPs, there was a large distinction among the runoff data, and the runoff data were 64.59, 59.20, and 49.61 m^3/s for RCP2.6, RCP4.5, and RCP8.5, respectively. In addition, with the increase in CO_2 emission, the flow rate was larger than the flow rate between 2006 and 2015, which was 49.59 m^3/s.

4.3 Basin Water Availability Assessment

4.3.1 Analysis of Basin Ecological Water Demand

Based on monthly runoff, the original Tennant method divides the whole year into two periods and calculates the percentages of average annual flow. The first period is from October to March, and the second period is from April to September. Actually, the distinct regional characteristics and the monthly runoffs of the Huangshui watershed force the redivision of these two periods. According to the monthly average runoff data of the Xiaoxia Bridge section from 2006 to 2015, it is at the exit of the Huangshui River basin. It can be estimated that the annual average runoff of the Huangshui watershed is 49.59 m^3/s. The average runoff from December to April is almost under 30 m^3/s, which accounts for 22% of the annual overall runoff. Specifically, only runoff flow of 23.73 m^3/s can be found in March. In comparison, the average runoff in each month from May to November is above 40 m^3/s, which occupies 78% of the annual overall runoff. During the period from July to September, the average runoff can reach 80 m^3/s. Thus, this study divides the whole year into two periods, from December to April and from May to November. Moreover, in consideration of the convenience of calculation, different levels of runoff percentage are recommended based on the runoff ratios at different time periods.

In this study, the Huangshui River is the largest tributary of the Yellow River, which contains high sediment due to the influence of geological conditions and human factors. The detention period

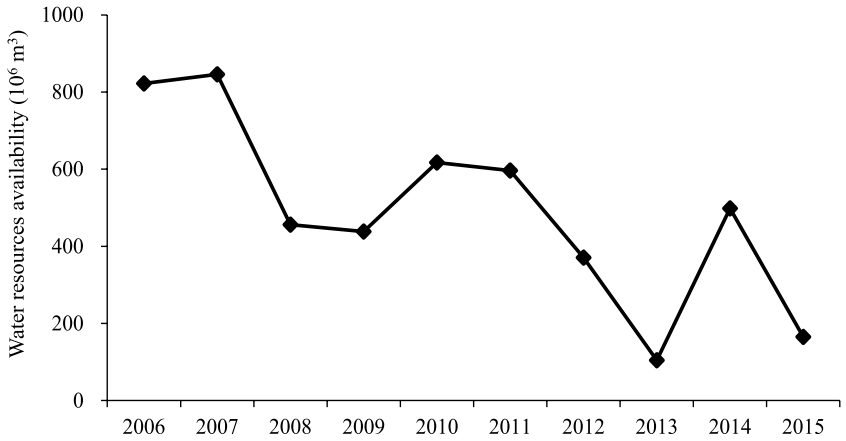

FIGURE 12 | The average water availability in the Huangshui River in the baseline period.

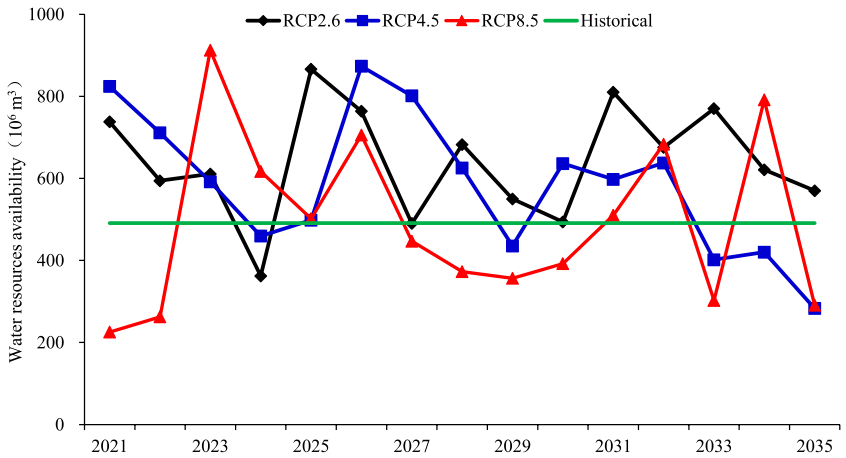

FIGURE 13 | The annual average water availability under different scenarios.

of the sediment is from June to September. From the annual calculation of the mean annual sediment transport at Xining station, the mean annual sediment content in the Huangshui River is 2.45 kg/m^3. Thus, it is necessary to attach the calculation of the sediment-carrying water volume on the original Tennant to ensure that the Huangshui River has enough water to transport the sediment in the water body downstream. Since sediment transport is mainly concentrated in the flood season, the sediment-carrying water volume of the Huangshui River during the flood season is 35 m^3/t.

The average annual sediment-carrying water volume in the Huangshui watershed is approximately 134 million m^3, accounting for 8.58% of the overall average annual runoff. The ecological water demand in the river channel accounts for 60.00% of the overall annual average runoff under the optimal conditions, and the proportion of the sediment-carrying water demand is 8.58%. Based on the results, the recommended final ecological base flow is 68.58% of the annual average runoff.

4.3.2 Basin Water Availability Assessment and Prediction

Since the total amount of basin water availability is equal to the difference between the basin average annual runoff and the ecological water demand, the basin hydrological simulation and the runoff under different climate scenarios can be predicted. **Figure 12** illustrates the water availability from 2006 to 2015. It is worth noting that the optimal mean annual ecological water demand in the Huangshui River is 1.072 billion m^3.

From 2006 to 2015, the mean annual average water availability in the Huangshui River was approximately 491 million m^3. The largest water availability was 846 million m^3 in 2007. The lowest value was 104 million m^3 in 2013, which accounted for 12.29% of

that in 2007. Taking the average annual runoff in different periods as input data, the ecological water demand in different planning periods under various scenarios can be calculated. The results of water availability in the Huangshui watershed are obtained during the forecast period under different concentration emission scenarios, as shown in **Figure 13**. In terms of the low-concentration emission scenario RCP2.6, the mean annual average water availability is 640 million m^3. The largest water availability is predicted to reach almost 833 million m^3 in 2025. In contrast, the lowest data point is predicted to be 362 million m^3 in 2024. Different results can be obtained in the medium concentration emission scenario RCP4.5. The mean annual average water availability will decline to 587 million m^3, accompanied by the largest data being 874 million m^3 in 2026 and the least data being 492 million m^3 in 2035. For the high concentration emission scenario RCP8.5, the water availability will witness a dramatic decrease, which falls to 492 million m^3. Evidently, the range of the water availability in scenario RCP8.5 will be the largest among the three different emission scenarios, accompanied by a maximum of 913 million m^3 in 2023 and a minimum of 225 million m^3 in 2021.

The results show that the Huangshui watershed is obviously affected by global climate change. With the increase in atmospheric CO_2 concentration and the further aggravation of greenhouse effects in the future, more obvious changes will be found in regional climate conditions. In the future, research and management in the Huangshui watershed need to fully consider the changes in temperature, precipitation, and other environmental factors. For example, when making a water resource allocation management plan, the decision-maker could make a flexible allocation plan in advance according to the change in trend of water resources available. Some emergency plans or engineering measures need to be developed in advance based on the predicted results. The results also indicate that climate change may have a positive effect on the ecological environment of the Qinghai–Tibet Plateau and other special regions. This means that rainfall in the region will increase as a result of climate change, and the temperature difference will decrease throughout the year. The region could shift from a semi-arid zone to a warm-humid zone, and ecosystems would benefit. The economic and social development of humanity in the region will also benefit from an increase in the availability of water resources.

In this study, the statistical downscaling method, the GRNN model, the SWAT model, and the improved Tennant method has been coupled. However, there are some shortcomings in this study, which need to be improved in several aspects. For example, in the further research, the researchers need to consider the response relationship between land use change and climate change. The hydrological change trend under the superposition of land use change and climate change should to be studied. The uncertainty in the research also needs to be considered, especially the problem of uncertainty amplification and superposition caused by the coupling of different methods. At the same time, the selection of large-scale meteorological data itself also needs repeated comparative analysis to select data sets with better applicability.

5 CONCLUSION

The Huangshui watershed is an ecologically fragile area on the Qinghai–Tibet Plateau of China. The meteorological and hydrological data of the Huangshui watershed were simulated under different climate change scenarios. In the simulation process, the temperature was predicted by the SDSM model; the precipitation data were simulated by the improved GRNN model; furthermore, the meteorological data were applied in the SWAT model to simulate the hydrologic processes at the basin scale under various climate change scenarios.

Through these simulations, it was determined that the basin temperatures were obviously changed by climate change, the improved GRNN model adopted in this study could effectively simulate the daily precipitation, and the R^2 and NSE values of the predicted results were significantly improved. Through the prediction results of the temperature and precipitation, the SWAT model could effectively simulate and predict the hydrological changes in the basin under the influence of climate change.

Moreover, the improved Tennant method is tailor-made for the variety of hydrological characteristics and the high sediment content in the river basin. The conclusion can be drawn that climate change has a great impact on water availability. The downscaling methods combined with the SWAT model and the calculation method of water availability have been proven effective in the study area. It was predicted that the temperature of the studied region would become flatter on the existing basis. Also, the precipitation would have a great increase in the wet season from May to September. In addition, the runoff of the Huangshui watershed and the water resource availability would decrease with increasing carbon emissions under different representative concentration pathway (RCP) scenarios. Moreover, the study could also provide an effective method to assess the regional hydrology and climate systems affected by climate change in ecotones similar to the Huangshui watershed.

DATA AVAILABILITY STATEMENT

The raw data supporting the conclusion of this article will be made available by the authors, without undue reservation.

AUTHOR CONTRIBUTIONS

ZF, YX, and HG designed the research. ZF wrote the original draft of this manuscript. YZ and XJ performed the analysis of the data and results. YX and SW revised the manuscript. All authors contributed to the article and approved the submitted version.

FUNDING

This research was funded by the Central Public-Interest Scientific Institution Basal Research Fund of Chinese Research Academy of Environmental Science (2020YSKY-014), the National Key

Research and Development Program of China (2016YFA0601502), the Program for Guangdong Introducing Innovative and Entrepreneurial Teams (2019ZT08L213), Beijing Natural Science Foundation (No. 9212001), and the National Natural Science Foundation of China (51609003).

SUPPLEMENTARY MATERIAL

The Supplementary Material for this article can be found online at: https://www.frontiersin.org/articles/10.3389/feart.2021.755119/full#supplementary-material

REFERENCES

Abbaspour, K. C., Yang, J., Maximov, I., Siber, R., Bogner, K., Mieleitner, J., et al. (2007). Modelling Hydrology and Water Quality in the pre-alpine/alpine Thur Watershed Using SWAT. *J. Hydrol.* 333, 413–430. doi:10.1016/j.jhydrol.2006.09.014

Arnold, J. G., Daniel, N. M., Philip, W. G., Karim, C. A., and Manoj, K. J. (2012). SWAT: Model Use, Calibration, and Validation [J]. *Trans. Asabe* 55, 1549–1559. doi:10.13031/2013.42256

Ateeq-Ur, R., and Abdul, G. (2018). Impact Assessment of Rainfall-Runoff Simulations on the Flow Duration Curve of the Upper Indus River-A Comparison of Data-Driven and Hydrologic Models [J]. *Water* 10 (7), 876. doi:10.3390/w10101411

Chen, D. L., Xu, B. Q., Yao, T. D., Guo, Z. T., Cui, P., Chen, F. H., et al. (2015). Assessment of Past, Present and Future Environmental Changes on the Tibetan Plateau [J]. *Chin. Sci. Bull.*, 3025–3035. doi:10.1360/n972014-01370

Cigizoglu, H. K., and Alp, M. (2006). Generalized Regression Neural Network in Modelling River Sediment Yield. *Adv. Eng. Softw.* 37 (2), 63–68. doi:10.1016/j.advengsoft.2005.05.002

Dalkilic, Y., Okkan, U., and Baykan, N. (2014). Comparison of Different Ann Approaches in Daily Pan Evaporation Prediction[J]. *J. Water Resource Prot.* 6 (4), 319–326. doi:10.4236/jwarp.2014.64034

Delworth, T. L. (2006). GFDL's CM2 Global Coupled Climate Models. Part I: Formulation and Simulation Characteristics [J]. *J. Clim.* 19 (19), 643–674. doi:10.1175/jcli9016.1

Friedlingstein, P., Meinshausen, M., Arora, V. K., Jones, C. D., Anav, A., Liddicoat, S. K., et al. (2014). Uncertainties in CMIP5 Climate Projections Due to Carbon Cycle Feedbacks. *J. Clim.* 27 (2), 511–526. doi:10.1175/jcli-d-12-00579.1

Ghosh, S., and Mujumdar, P. P. (2008). Statistical Downscaling of GCM Simulations to Streamflow Using Relevance Vector Machine. *Adv. Water Resour.* 31 (1), 132–146. doi:10.1016/j.advwatres.2007.07.005

Guo, Y., Li, J., and Li, Y. (2014). Seasonal Forecasting of North China Summer Rainfall Using a Statistical Downscaling Model. *J. Appl. Meteorology Climatology* 53 (7), 1739–1749. doi:10.1175/jamc-d-13-0207.1

Hanewinkel, M., Cullmann, D. A., Schelhaas, M.-J., Nabuurs, G.-J., and Zimmermann, N. E. (2013). Climate Change May Cause Severe Loss in the Economic Value of European forest Land. *Nat. Clim Change* 3 (3), 203–207. doi:10.1038/nclimate1687

Hughes, D. A., and Mazibuko, S. (2018). Simulating Saturation-Excess Surface Run-Off in a Semi-distributed Hydrological Model. *Hydrological Process.* 32 (17), 2685–2694. doi:10.1002/hyp.13182

Jeong, D. I., St-Hilaire, A., Ouarda, T. B. M. J., and Gachon, P. (2012). Multisite Statistical Downscaling Model for Daily Precipitation Combined by Multivariate Multiple Linear Regression and Stochastic Weather Generator [J]. *Climatic Change* 114 (3-4), 567–591. doi:10.1007/s10584-012-0451-3

Joseph, N., Preetha, P. P., and Narasimhan, B. (2021). Assessment of Environmental Flow Requirements Using a Coupled Surface Water-Groundwater Model and a Flow Health Tool: A Case Study of Son River in the Ganga basin. *Ecol. Indicators* 121, 107110. doi:10.1016/j.ecolind.2020.107110

Kattsov, V. M., Walsh, J. E., Chapman, W. L., Govorkova, V. A., Pavlova, T. V., and Zhang, X. (2007). Simulation and Projection of Arctic Freshwater Budget Components by the IPCC AR4 Global Climate Models. *2007* 8 (3), 571–589. doi:10.1175/jhm575.1

Kumar, G., and Malik, H. (2016). Generalized Regression Neural Network Based Wind Speed Prediction Model for Western Region of India [J]. *Proced. Comp. Sci.* 93, 26–32. doi:10.1016/j.procs.2016.07.177

Meenu, R., Rehana, S., and Mujumdar, P. P. (2013). Assessment of Hydrologic Impacts of Climate Change in Tunga-Bhadra River basin, India with HEC-HMS and SDSM. *Hydrol. Process.* 27 (11), 1572–1589. doi:10.1002/hyp.9220

Nyikadzino, B., Chitakira, M., Muchuru, S., and Muchuru, S. (2020). Rainfall and Runoff Trend Analysis in the Limpopo River basin Using the Mann Kendall Statistic. *Phys. Chem. Earth, Parts A/B/C* 117, 102870. doi:10.1016/j.pce.2020.102870

Park, C.-E., Jeong, S.-J., Joshi, M., Osborn, T. J., Ho, C.-H., Piao, S., et al. (2018). Keeping Global Warming within 1.5 °C Constrains Emergence of Aridification. *Nat. Clim Change* 8 (1), 70–74. doi:10.1038/s41558-017-0034-4

Piras, M., Mascaro, G., Deidda, R., and Vivoni, E. R. (2015). Impacts of Climate Change on Precipitation and Discharge Extremes through the Use of Statistical Downscaling Approaches in a Mediterranean basin. *Sci. Total Environ.* 543, 952–964. doi:10.1016/j.scitotenv.2015.06.088

Sharma, A., and Goyal, M. K. (2020). Assessment of the Changes in Precipitation and Temperature in Teesta River basin in Indian Himalayan Region under Climate Change. *Atmos. Res.* 231, 104670. doi:10.1016/j.atmosres.2019.104670

Sillmann, J., Kharin, V. V., Zwiers, F. W., Zhang, X., and Bronaugh, D. (2013). Climate Extremes Indices in the CMIP5 Multimodel Ensemble: Part 2. Future Climate Projections. *J. Geophys. Res. Atmos.* 118 (6), 2473–2493. doi:10.1002/jgrd.50188

Song, X., Yang, G., Yan, C., Duan, H., Liu, G., and Zhu, Y. (2009). Driving Forces behind Land Use and Cover Change in the Qinghai-Tibetan Plateau: a Case Study of the Source Region of the Yellow River, Qinghai Province, China. *Environ. Earth Sci.* 59 (4), 793–801. doi:10.1007/s12665-009-0075-8

Song, Y., Linderholm, H. W., Wang, C., Tian, J., Huo, Z., Gao, P., et al. (2019). The Influence of Excess Precipitation on winter Wheat under Climate Change in China from 1961 to 2017. *Sci. Total Environ.* 690, 189–196. doi:10.1016/j.scitotenv.2019.06.367

Specht, D. F. (1991). A General Regression Neural Network. *IEEE Trans. Neural Netw.* 2, 568–576. doi:10.1109/72.97934

Suwal, N., Kuriqi, A., Huang, X. F., Delgado, J., Młyński, Da., and Walega, A. (2020). Environmental Flows Assessment in Nepal: The Case of Kaligandaki River [J]. *Sustainability* 12 (21), 1–23. doi:10.3390/su12218766

Tang, J., Niu, X., Wang, S., Gao, H., Wang, X., and Wu, J. (2016). Statistical Downscaling and Dynamical Downscaling of Regional Climate in China: Present Climate Evaluations and Future Climate Projections. *J. Geophys. Res. Atmos.* 121 (5), 2110–2129. doi:10.1002/2015jd023977

Taylor, K. E., Stouffer, R. J., and Meehl, G. A. (2012). An Overview of CMIP5 and the Experiment Design. *Bull. Am. Meteorol. Soc.* 93 (4), 485–498. doi:10.1175/bams-d-11-00094.1

Teng, M., Zeng, L., Hu, W., Wang, P., Yan, Z., He, W., et al. (2020). The Impacts of Climate Changes and Human Activities on Net Primary Productivity Vary across an Ecotone Zone in Northwest China. *Sci. Total Environ.* 714, 136691. doi:10.1016/j.scitotenv.2020.136691

Thuiller, W., Lavorel, S., Araujo, M. B., Sykes, M. T., and Prentice, I. C. (2005). Climate Change Threats to Plant Diversity in Europe. *Proc. Natl. Acad. Sci.* 102 (23), 8245–8250. doi:10.1073/pnas.0409902102

Whitehead, P. G., Wilby, R. L., Battarbee, R. W., Kernan, M., and Wade, A. J. (2009). A Review of the Potential Impacts of Climate Change on Surface Water Quality. *Hydrological Sci. J.* 54 (1), 101–123. doi:10.1623/hysj.54.1.101

Wilby, R. L., Dawson, C. W., and Barrow, E. M. (2002). Sdsm - a Decision Support Tool for the Assessment of Regional Climate Change Impacts. *Environ. Model. Softw.* 17 (2), 145–157. doi:10.1016/s1364-8152(01)00060-3

Yakup, K., Aydın, H. D., and Zehra, Y. (2018). Comparison of Environmental Flow Assessment Methods with a Case Study on a Runoff River–type Hydropower Plant Using Hydrological Methods [J]. *Environ. Monit. Assess.* 190 (12), 1–15. doi:10.1007/s10661-018-7107-3

Zhang, L., Zhao, Y., Hein-Griggs, D., Janes, T., Tucker, S., and Ciborowski, J. J. H. (2020). Climate Change Projections of Temperature and Precipitation for the great lakes basin Using the PRECIS Regional Climate Model. *J. Great Lakes Res.* 46 (2), 255–266. doi:10.1016/j.jglr.2020.01.013

Conflict of Interest: The authors declare that the research was conducted in the absence of any commercial or financial relationships that could be construed as a potential conflict of interest.

Publisher's Note: All claims expressed in this article are solely those of the authors and do not necessarily represent those of their affiliated organizations, or those of the publisher, the editors and the reviewers. Any product that may be evaluated in this article, or claim that may be made by its manufacturer, is not guaranteed or endorsed by the publisher.

Advantages of publishing in Frontiers

OPEN ACCESS
Articles are free to read for greatest visibility and readership

FAST PUBLICATION
Around 90 days from submission to decision

HIGH QUALITY PEER-REVIEW
Rigorous, collaborative, and constructive peer-review

TRANSPARENT PEER-REVIEW
Editors and reviewers acknowledged by name on published articles

Frontiers
Avenue du Tribunal-Fédéral 34
1005 Lausanne | Switzerland

Visit us: www.frontiersin.org
Contact us: frontiersin.org/about/contact

REPRODUCIBILITY OF RESEARCH
Support open data and methods to enhance research reproducibility

DIGITAL PUBLISHING
Articles designed for optimal readership across devices

FOLLOW US
@frontiersin

IMPACT METRICS
Advanced article metrics track visibility across digital media

EXTENSIVE PROMOTION
Marketing and promotion of impactful research

LOOP RESEARCH NETWORK
Our network increases your article's readership